Title

Electronic Structure Modelling of Catalysis and Complex Systems: Theory, Analysis and Application

Author

Loipersberger, Matthias

Publication Date

2021

Peer reviewed|Thesis/dissertation

Electronic Structure Modelling of Catalysis and Complex Systems: Theory, Analysis and Application

by

Matthias Loipersberger

A dissertation submitted in partial satisfaction of the

requirements for the degree of

Doctor of Philosophy

in

Chemistry

in the

Graduate Division

of the

University of California, Berkeley

Committee in charge:

Professor Martin Head-Gordon, Chair
Professor Teresa Head-Gordon
Professor Ali Mesbah

Summer 2021

Electronic Structure Modelling of Catalysis and Complex Systems: Theory, Analysis and Application

Abstract

Electronic Structure Modelling of Catalysis and Complex Systems: Theory, Analysis and Application

by

Matthias Loipersberger

Doctor of Philosophy in Chemistry

University of California, Berkeley

Professor Martin Head-Gordon, Chair

This thesis contributes to three areas of electronic structure theory: First, chapters 2 to 5 cover the development of energy decomposition schemes based on absolutely localized orbitals (ALMO-EDA). In chapter 2, the second-order Møller-Plesset perturbation theory (MP2) based version of this decomposition scheme is generalized to restricted and unrestricted open-shell. This new method allows to decompose the interaction energy of radical species at the MP2 level. Furthermore in chapter 3, a variational forward-backward (VFB) approach is presented to decompose the overall charge transfer (CT) stabilization energy into contributions from forward and backward donation for the density functional theory (DFT) based ALMO-EDA scheme. The two "one-way" CT states are variationally relaxed such that the associated nuclear forces can be readily obtained. In chapter 4, the DFT based ALMO-EDA scheme is extended to intermolecular interactions in the solution phase by the development of ALMO-EDA(solv); a scheme that allows the application of continuum solvent models within the framework of energy decomposition analysis.

Second, the performance of second- and third-order Møller-Plesset perturbation (MP3) theory wavefunction methods is probed for non-covalent interactions in chapter 5. The κ-regularization improves the energetics in almost all data sets for both MP2 and OOMP2. Scaled MP3 using κ-OOMP2 reference orbitals provides the most accurate results among all tested methods for non-covalent interactions across all data sets.

Third in chapters 6–8, a robust computational model is presented to study mechanisms of molecular catalysts for the CO_2 reduction reaction (CO2RR) to CO using DFT calculations. This model is applied and refined by the mechanistic studies of four pyridine based catalysts. In chapter 5, the bipyridine based $[Fe(bpy^{NHEt}PY2)(H_2O)_2]^{2+}$ system is studied. In chapter 7, the mechanisms of $[Co^{II}(qpy)(H_2O)_2]^{2+}$ and $[Fe^{II}(qpy)(H_2O)_2]^{2+}$ (with qpy = quaterpyridine) are investigated using DFT calculations to shed light on the contrasting catalytic pathways. In chapter 8, a terpyridine(tpy)-based iron polypyridine complex,

$[Fe(tpyPY_2Me)]^{2+}$, is investigated in a combined experimental and computational approach to elucidate the different mechanisms at low and high overpotentials.

to my family Sophia, Florian, Thomas and Mama for their unconditional support.

Contents

Contents **ii**

List of Figures **v**

List of Tables **xii**

1 Introduction **1**
1.1 Quantum Mechanics in Chemistry 2
1.2 Quantum Chemistry 5
1.3 Computational Catalysis 22
1.4 Outline 36

2 MP2-EDA for Radicals **42**
2.1 Introduction 42
2.2 Theory 44
2.3 Computational Details 49
2.4 Results 51
2.5 Conclusion 62

3 Variational Charge Transfer Analysis **64**
3.1 Introduction 64
3.2 Theory 67
3.3 Computational Details 71
3.4 Results 72
3.5 Conclusions 89
3.6 SCF equations for generalized SCF-MI 91
3.7 Nuclear gradient for generalized SCF-MI 92

4 Continuum Solvation in ALMO-EDA **95**
4.1 Introduction 95
4.2 Theory 98
4.3 Computational Details 102
4.4 Results 103

4.5 Conclusions . . . 121

5 Limits of MPX for Non-Covalent Interactions 123
5.1 Introduction . . . 123
5.2 Overview of Benchmark Sets . . . 126
5.3 Overview of Methodology . . . 127
5.4 Computational Details . . . 129
5.5 Results and Discussion . . . 131
5.6 Conclusions . . . 149

6 Mechanistic Study of an Fe-Bpy based catalyst 153
6.1 Introduction . . . 153
6.2 Computational Model . . . 156
6.3 Results and Discussion . . . 158
6.4 Hydroxyl Substituent . . . 171
6.5 Alternative Catalysis Cycles . . . 171
6.6 Conclusion . . . 174

7 Mechanistic Insights into Co-qpy and Fe-qpy Cat. 175
7.1 Introduction . . . 175
7.2 Computational Model . . . 179
7.3 Results . . . 181
7.4 Comparison and Discussion . . . 201
7.5 Conclusion . . . 203

8 Influence of Overpotential on an Iron Terpyridine Complex for CO_2 Reduction 207
8.1 Introduction . . . 207
8.2 Computational Model . . . 210
8.3 Results and Discussion . . . 211
8.4 Conclusions . . . 228

Bibliography 231

A MP2-EDA for Radicals 278
A.1 Long-Range Behavior of each Energy Component . . . 278
A.2 TA13 Benchmark Set . . . 280
A.3 Complexes between Halogenated Benzene Radical Cation and Water . . . 283
A.4 Anionic CO_2 radical N-heterocycle complexes . . . 286

B Variational Charge Transfer Analysis 289
B.1 Additional results for BH_3 complexes . . . 289
B.2 Additional results for complexes between CO and BeY (Y = O or CO_3) . . . 291

B.3 Additional results for complexes between $[Ru(II)(NH_3)_5]^{2+}$ and π-acidic ligand series 296

C Continuum Solvation in ALMO-EDA **299**
C.1 Additional results for the validation of ALMO-EDA(solv) 299
C.2 Additional results for the $[FeTPP(CO_2^{\bullet -})]$ derivatives 302
C.3 Additional results for the substituted terphenyl$\cdots CO_2$ complexes 305

D Limits of MPX for Non-Covalent Interactions **312**
D.1 Optimal c_3 Coefficients 313
D.2 Box Plots 320

E Mechanistic Study of an Fe-Bpy based catalyst **328**
E.1 Comparison of Different DFT functional 328
E.2 Doubly Reduced Intermediates 332
E.3 Further Information about pK_a values 337
E.4 Additional Information about Intermediates in the Cycle 338

F Mechanistic Insights into Co-qpy and Fe-qpy Cat. **341**
F.1 Additional Information on Possible Intermediates 341
F.2 HER 345
F.3 Full Cycles Including a Third Reduction 347
F.4 Functional Dependency 351
F.5 CASSCF 363

G Influence of Overpotential on an Iron Terpyridine Complex for CO_2 Reduction **366**

List of Figures

1.1 Schematic representation the ALMO-EDA procedure 18
1.2 Illustration of charge transfer orbitals and a schematic aEDA PES 20
1.3 Illustration of the functional dependence of the spin gap in an iron(II) complex. 24
1.4 Thermodynamic cycle for calculating the change in free energy during a redox process. 29
1.5 Thermodynamic cycle for calculating the change in free energy for the dissociation of an acid. 31
1.6 Schematic concept of a homogeneous catalyst 36

2.1 A representation for each of the three types of double excitations for a two-fragment system 45
2.2 Illustration of the degenerate electronic configuration of the $Cl^{\bullet}$ radical, which then yields distinct frozen energies for the $Cl^{\bullet}\cdots H_2O$ complex depending on the initial orientation of the $Cl^{\bullet}$ spin density. 50
2.3 Two competing binding motifs for the interaction between a halogenated benzene radical cation ($C_6H_5X^{+\bullet}$) and a water molecule 54
2.4 Optimized geometries for two isomers of the halogenated benzene radical cation–water complex 54
2.5 Individual EDA terms for the two binding motifs of the water–bromobenzene radical cation complex 55
2.6 Changes in the total interaction energy and individual EDA terms for the heavier halogenated benzene radical cations relative to the fluorobenzene results with the two bonding motifs of the $H_2O\cdots C_6H_5X^{+\bullet}$ complexes. 56
2.7 Term-by-term energy differences between the IHB and IXB binding motifs of the $H_2O\cdots C_6H_5X^{+\bullet}$ complexes. 57
2.8 Different binding motifs for the association of a ${CO_2}^{-\bullet}$ with nitrogen heterocycles 58
2.9 Geometries of the four possible isomers using both binding motifs for the reaction of a ${CO_2}^{-\bullet}$ with nitrogen heterocycles 59
2.10 RMP2-EDA results for the carbamate and hydrogen bonding motifs of ${CO_2}^{-\bullet}$. 60
2.11 Relative EDA results for the carbamate and hydrogen bonding motifs of ${CO_2}^{-\bullet}$ 61

3.1 Schematic illustration of the three SCF-MI stages 70

3.2 Potential energy surface for $H_3N{-}BH_3$ and $OC{-}BH_3$ . . . 73
3.3 The key COVPs in $OC{-}BH_3$ . . . 74
3.4 Key COVPs contrasting the π backbonding for both OC−BeY complexes . . . 77
3.5 Potential energy surface for each ALMO-EDA intermediate state for OC−BeO . 78
3.6 Shift in ν_{CO} as a function of the intermolecular distance for XY−BeO . . . 81
3.7 Key COVPs for the $NN{-}[Ru(NH_3)_5]^{2+}$ complex . . . 84
3.8 Key COVPs for the Ru complexes . . . 85
3.9 Electron density difference between the CTf and Pol states for Ru complexes . 86
3.10 Potential energy surface for $XY{-}[Ru(NH_3)_5]^{2+}$ . . . 86

4.1 Summary of all FeTPP derivatives investigated in this study. . . . 98
4.2 Summary of all OPP derivatives investigated in this study. . . . 98
4.3 Illustration of the ALMO-EDA(solv) scheme . . . 100
4.4 Left y-axis: distance dependence of $\Delta E^{(0)}_{\mathrm{ELEC}}$, $\Delta E^{\mathrm{el}}_{\mathrm{SOL}}$, and $\Delta E^{(\mathrm{s})}_{\mathrm{ELEC}}$ for the $Na^+\cdots Cl^-$ model complex in C-PCM water . . . 104
4.5 Schematic illustration of the solvent effect on the $Na^+\cdots Cl^-$ electrostatic interaction . . . 105
4.6 ALMO-EDA(solv) results for the $H_2O\cdots Na^+$ complex in different solvents . . . 106
4.7 Simplified steps in the catalytic pathway of FeTPP leading to the activated CO_2 intermediate. . . . 109
4.8 Spin density of the doubly reduced CO_2 iron complex . . . 110
4.9 Optimized geometries of the doubly reduced CO_2 iron complex with varying substitutions . . . 110
4.10 Differential ALMO-EDA(solv) results relative to the unsubstituted $FeTPP(CO_2)^{2-}$ complex . . . 112
4.11 Information on EDA results of $FeTPP(CO_2)^{2-}$ . . . 113
4.12 Optimized geometries for Fe-o-imid-$(CO_2)^-$ . . . 115
4.13 Optimized structures of unsubstituted and substituted p-terphenyl$\cdots CO_2$ radical anion complexes . . . 118
4.14 Substituent effects on the differences in total interaction energies as well as the ELEC and POL components between the reactant and product states. . . . 119
4.15 ALMO-EDA(solv) results for reactant and product complexes between p-terphenyl and CO_2 with different substituent groups. . . . 120

5.1 Dependence of the the root-mean square deviation on the scaling of the third-order energy (c_3) in the S66 training set . . . 132
5.2 Boxplots of the S22 and S66 data-sets: . . . 137
5.3 Histogram of the absolute deviation of MP2, κ-MP2, κ-OOMP2 and MP2.5:κ-OOMP2 . . . 142
5.4 Boxplots of the NCED data category . . . 142
5.5 Dependence of the the root-mean square deviation on the scaling of the third-order energy (c_3) for the whole NCED data data category . . . 143

5.6 Boxplots of the Orel26rad data set . . . 147
5.7 PES scan of the π-stacked benzene dimer, CH_3NH_2 dimer and water dimer . . . 148

6.1 The catalytic system $[Fe(bpy^{NHEt}PY2\,Me)L_2]^{2+}$ (L = CH_3CN), a CO_2 reduction catalyst with high selectivity against hydrogen evolution reaction. . . . 156
6.2 Proposed mechanism for using $[Fe(bpy^{NHEt}PY2\,Me)L_2)]^{2+}$. . . . 159
6.3 Optimized geometry and spin densities of the reduced complexes . . . 160
6.4 MO diagrams of the reduced complexes . . . 161
6.5 Candidates for the doubly reduced intermediates . . . 161
6.6 Functional dependence of $([Fe(bpy^{NHEt}PY2\,Me)]^0)$ . . . 163
6.7 Schematic illustration of the four possible CO_2 binding modes (MLC = metal ligand cooperation). . . . 163
6.8 Geometry and MO of the CO_2 adduct . . . 165
6.9 Geometries of the key transition states . . . 166
6.10 Free energy landscape of both CO2RR and HER pathways . . . 169
6.11 Geometries of for the transition states for a possible formation of a hydride . . . 170
6.12 Possible HER mechanism involving . . . 171
6.13 Geometries of the and key parameters of the transition states for HER . . . 172
6.14 Alternative cycles involving cooperatively bound CO_2. . . . 173

7.1 Proposed catalytic pathways by Robert *et al.* . . . 178
7.2 Naming scheme for intermediates used throughout the manuscript. . . . 181
7.3 Proposed mechanism for the selective CO_2 to CO reduction using $[Co(qpy)L_2]^{2+}$ 182
7.4 Geometry and spin densities of the Co complex . . . 183
7.5 Proposed mechanism for CO_2 to CO reduction using $[Co(qpy)L_2]^{2+}$ and incorporating a third reduction . . . 187
7.6 Schematic MO diagram of the important intermediates in the cycle . . . 190
7.7 Geometrical parameters of Co intermediates . . . 190
7.8 Geometrical parameters of the protonation steps of Co intermediates . . . 191
7.9 Proposed mechanism for the selective CO_2 to CO reduction using $[Fe(qpy)L_2]^{2+}$ 192
7.10 Geometry and spin density of the iron complex . . . 194
7.11 Schematic MO diagram of the important intermediates in the cycle (Fe) . . . 195
7.12 Geometrical parameters of both possible CO_2 adduct intermediates of the Iron catalyst . . . 198
7.13 Geometrical parameters of both transition states (Fe) . . . 198
7.14 Geometrical parameters of the protonation intermediates (Fe) . . . 199
7.15 Free energy landscape of the most likely CO2RR pathways of both Coqpy and Feqpy . . . 201
7.16 Schematic MO diagram of both doubly reduced intermediates . . . 205
7.17 Schematic MO diagram of both doubly reduced CO_2 adducts . . . 206

8.1 Overview of select iron polypyridyl molecular catalyst platforms for CO_2 to CO reduction . . . 209
8.2 Electrochemical characterization of $^1[Fe]^{2+}$ . . . 212
8.3 Proposed mechanistic pathways for the low overpotential regime . . . 213
8.4 Spin densities and schematic MO diagrams . . . 215
8.5 Proposed mechanistic cycles for the high overpotential regime . . . 223
8.6 Free energy landscape of the CO_2RR . . . 224
8.7 Experimental kinetic analysis of $^1[Fe]^{2+}$ . . . 225
8.8 Free energy landscape of the CO_2RR and HER pathway . . . 226
8.9 Chemical structures of second-sphere functionalized polypyridyl catalysts for improved performance based on our mechanistic understanding . . . 228
8.10 ALMO-EDA(solv) results for CO_2 adduct $^1[Fe{-}CO_2]^0$ . . . 229

A.1 Log-Log plot for the decay of both the frozen and polarization terms for UMP2 and RMP2 . . . 279
A.2 The main COVP for the hydrogen-bonded and the halogen-bonded form of the $H_2O\cdots C_6H_5Br^{+\bullet}$ complex . . . 283
A.3 Spin densities for the CO_2 radical species . . . 286
A.4 Most significant COVP for charge transfer in the hydrogen-bonded $Im{-}CO_2{}^{-\bullet}$ complex . . . 286

B.1 Decay of the total forward and backward CT energies . . . 289
B.2 Electron density difference between the Pol and Frz states for BeO adducts . . . 291
B.3 Shifts in C−O bond length (Δr(CO)) as a function of the intermolecular distance for BeO adducts . . . 292
B.4 Key COVPs illustrating the σ and π donations in OC−BeO . . . 292
B.5 Decay of the forward CT stabilization energy ($E_{\mathrm{CTf}}{-}E_{\mathrm{Pol}}$) with the intermolecular (X−Be) . . . 293
B.6 PES for each ALMO-EDA intermediate state for $H_3N{-}[Ru(NH_3)_5]^{2+}$ . . . 296

C.1 Electrostatic and non-electrostatic components (in kJ/mol) of the solvent contribution (ΔE_{SOL}) to the $H_2O\cdots Na^+$ interaction in different solvents . . . 300
C.2 ALMO-EDA(sol) results (in kJ/mol) for the $H_2O\cdots Cl^-$ complex in different solvents . . . 301
C.3 Electrostatic and non-electrostatic components of the solvent contribution (ΔE_{SOL}) to the $H_2O\cdots Cl^-$ interaction in different solvents . . . 301
C.4 Spin density of $CO_2{}^{\bullet-}$ (isovalue: 0.08 a.u.) optimized with ωB97X-V/def2-TZVPP). 302

D.1 Dependence of the the root-mean square deviation on the scaling of the third-order energy (c_3) in the A24 data set aTZ with CBS reference (a); aTZ with aTZ reference (b) . . . 313

D.2 Dependence of the the root-mean square deviation on the scaling of the third-order energy (c_3) in the A24 data set aTZ with CBS reference (a); aQZ with CBS reference (b) . . . 314
D.3 Dependence of the the root-mean square deviation on the scaling of the third-order energy (c_3) in the S66 data set . . . 315
D.4 Dependence of the the root-mean square deviation on the scaling of the third-order energy (c_3) in the A24 (a), DS14 (b), HSG (c) and S22 (d) data sets; RMSD in kcal/mol; four scaled MP2.X methods (MP2.X, MP2.X:OOMP2, MP2.X:κ-OOMP2, κMP2.X:κ-OOMP2). . . . 316
D.5 Dependence of the the root-mean square deviation on the scaling of the third-order energy (c_3) in the X40 (a), HW30 (b), NC15 (c) and AlkBind12 (d) data sets; RMSD in kcal/mol; four scaled MP2.X methods (MP2.X, MP2.X:OOMP2, MP2.X:κ-OOMP2, κMP2.X:κ-OOMP2). . . . 317
D.6 Dependence of the the root-mean square deviation on the scaling of the third-order energy (c_3) in the CO2Nitrogen16 (a), HB49 (b) and Ionic43 (c) data sets; RMSD in kcal/mol; four scaled MP2.X methods (MP2.X, MP2.X:OOMP2, MP2.X:κ-OOMP2, κMP2.X:κ-OOMP2). . . . 318
D.7 Dependence of the the root-mean square deviation on the scaling of the third-order energy (c_3) in the TA13 (a), HB49 (b), Bauza30 (c), CT20 (d) data sets, XB51 (e) and Orel26rad (f); RMSD in kcal/mol; four scaled MP2.X methods (MP2.X, MP2.X:OOMP2, MP2.X:κ-OOMP2, κMP2.X:κ-OOMP2). . . . 319
D.8 Box-plots of the data-sets A24: (a) MP2 methods, (b) MP3 methods; DS14: (c) MP2 methods, (d) MP3 methods . . . 320
D.9 Box-plots of the data-sets HB15: (a) MP2 methods, (b) MP3 methods; HSG: (c) MP2 methods, (d) MP3 methods . . . 321
D.10 Box-plots of the data-sets X40: (a) MP2 methods, (b) MP3 methods; HW30: (c) MP2 methods, (d) MP3 methods . . . 322
D.11 Box-plots of the data-sets NC15: (a) MP2 methods, (b) MP3 methods; AlkBind12: (c) MP2 methods, (d) MP3 methods . . . 323
D.12 Box-plots of the data-sets CO2Nitrogen16: (a) MP2 methods, (b) MP3 methods; HB49: (c) MP2 methods, (d) MP3 methods; Ionic43 . . . 324
D.13 Box-plots of the data-sets TA13: (a) MP2 methods, (b) MP3 methods; XB18: (c) MP2 methods, (d) MP3 methods . . . 325
D.14 Box-plots of the data-sets Bauza30: (a) MP2 methods, (b) MP3 methods; XB18: (c) MP2 methods, (d) MP3 methods . . . 326
D.15 Box-plots of the data-sets XB51: (a) MP2 methods, (b) MP3 methods; Orel26rad: (c) MP2 methods, (d) MP3 methods . . . 327

E.1 Geometry and electron density and MOs of the η^2 coordinated CH_3CN adduct . 332
E.2 MOs of ${}^3_0 1^4$ before and after the CASSCF calculation . . . 334
E.3 MOs of ${}^3_0 1^5$ before and after the CASSCF calculation . . . 335
E.4 Spin density the doubly reduced η^2 CO_2 adduct ${}^3_0 1^5$. . . . 338

E.5 Spin density the transition state forming the doubly reduced η^2 CO_2 adduct ${}^{3}_{0}1^{5}$. 338
E.6 Geometry of the κ-O CO_2 adduct ${}^{3}_{0}3^{5}$ (distances in Å). 339
E.7 Geometry of ${}^{5}_{1}3^{5}$ (distances in Å). 339
E.8 Geometry of for a CO2 adduct involving metal ligand cooperation (${}^{5}_{0}2^{5CC}$)(distances in Å). 339
E.9 Geometry of the transition state of a protonation of the activated acetonitrile using H_2O as the proton source (distances in Å). The barrier is over 30 kcal/mol. 340
E.10 Bonding orbitals illustrating the dative σ bond of the CO_2 adduct 340

F.1 Side view of both the doubly reduced Feqpy and Coqpy 341
F.2 Geometrical parameters of all three CO_2 adducts discussed in the cycle with an explicit water added to stabilze the CO_2 342
F.3 Geometrical parameters for a phenoxide complex after the first protonation yielding ${}^{2}[\mathbf{3Co}(5)]^{+}$ 343
F.4 Geometrical parameters for the Transition state of the first protonation of ${}^{3}[\mathbf{2Fe}(5)]^{0}$ where the water molecule acts as a ligand. 343
F.5 Geometrical parameters for the Transition state of the second protonation of ${}^{5}[\mathbf{3Fe}(5)]^{+}$ where the water molecule acts as a ligand. 344
F.6 Geometrical parameters of the transition states for the protonation steps 344
F.7 Proposed mechanism for the a possible HER mechanism using $[Co(qpy)L_2]^{2+}$ . . 345
F.8 Proposed mechanism for the a possible HER mechanism using $[Fe(qpy)L_2]^{2+}$ . . 346
F.9 Proposed mechanism for the selective CO_2 to CO reduction including a possible third reduction using $[Co(qpy)L_2]^{2+}$ 347
F.10 Proposed mechanism for the selective CO_2 to CO reduction including a possible third reduction using $[Fe(qpy)L_2]^{2+}$ 348
F.11 Geometrical parameters of the transition states for the EEEC pathway (Co) . . 349
F.12 (a) Possible doubly reduced di-carbonyl (S = 0) intermediate resulting in a partial dissociation of the qpy ligand; (b) relaxed PES scan for the doubly reduced singlet and triplet carbonyl complexes 350
F.13 Spin densities for all viable spin states for both $[\mathbf{1Co}(5)]^{+}$ and $[\mathbf{1Co}(4)]^{0}$ using ωB97X-D (isovalue:0.05). 358
F.14 Spin densities for all viable spin states for both $[\mathbf{1Co}(5)]^{+}$ and $[\mathbf{1Co}(4)]^{0}$ using B3LYP (isovalue:0.05). 358
F.15 Spin densities for all viable spin states for both $[\mathbf{1Co}(5)]^{+}$ and $[\mathbf{1Co}(4)]^{0}$ using B97-D (isovalue:0.05). 359
F.16 Spin densities for all viable spin states for both $[\mathbf{1Fe}(5)]^{+}$ and $[\mathbf{1Fe}(4)]^{0}$ using ωB97X-D (isovalue:0.05). 359
F.17 Spin densities for all viable spin states for both $[\mathbf{1Fe}(5)]^{+}$ and $[\mathbf{1Fe}(4)]^{0}$ using B3LYP (isovalue:0.05). 360
F.18 Spin densities for all viable spin states for both $[\mathbf{1Fe}(5)]^{+}$ and $[\mathbf{1Fe}(4)]^{0}$ using B97-D (isovalue:0.05). 360

F.19 Functional dependence of the key molecular orbitals of: (a) $^{2}[\mathbf{1Co}(4)]^{0}$ and $^{2}[\mathbf{2Co}(5)]^{0}$; (b) $^{1}[\mathbf{1Fe}(4)]^{0}$ and $^{3}[\mathbf{2Fe}(5)]^{0}$. 361
F.20 Functional dependence of the structure of $^{2}[\mathbf{2Co}(5)]^{0}$. 361
F.21 Functional dependence of the structure of $^{3}[\mathbf{2Fe}(5)]^{0}$. 362
F.22 Natural Orbitals of $^{2}[\mathbf{1Co}(4)]^{0}$ 364
F.23 Natural Orbitals of $^{1}[\mathbf{1Fe}(4)]^{0}$ 364

G.1 Geometry of key intermediates of the low overpotential mechanism 367
G.2 Transition states for the second protonation 368
G.3 Transition states for the formation of a hydride 369
G.4 OH substituted pyridine 369
G.5 Complete mechanistic pathways investigated for the first catalytic regime and the second catalytic regime 370

List of Tables

1.1 Jacob's ladder of density functional approximations. 16
1.2 Reduction potentials of CO_2 and proton reduction 36

2.1 RMP2-EDA results for the TA13 benchmark set 53

3.1 Vertical ALMO-EDA results for $H_3N{-}BH_3$ and $OC{-}BH_3$ 73
3.2 Adiabatic ALMO-EDA results of the $OC{-}BH_3$ complex 74
3.3 Vertical ALMO-EDA results for the four BeY–carbonyl adducts. 77
3.4 Adiabatic ALMO-EDA results for the four X−BeY adducts 80
3.5 Vertical ALMO-EDA results for the transition metal complexes 83
3.6 Metal-ligand distance r(M−X) and bond length of the diatomic ligand r(X−Y) . 87
3.7 Adiabatic ALMO-EDA results for the shifts in the vibrational frequency 87
3.8 Shifts in the stretching frequency of N_2, CO, and BF of the Ru complexes (CTf geometry) 88
3.9 Shifts in the stretching frequency of N_2, CO, and BF of the Ru complexes (Tot geometry) 88

4.1 Strength of internal QM electrostatics ($\Delta E^{(0)}_{\mathrm{ELEC}}$) and the effect of solute-solvent electrostatic interaction for a $Na^+ \cdots Cl^-$ 104

5.1 Non-covalent interaction data-sets used to evaluate the performance of various methods in this work 127
5.2 Summary and short description of all perturbation theory methods used in this study 130
5.3 Results of the NCED data category 133
5.4 Results of the NCD data category 134
5.5 Optimal scaling parameter for the MP3 energy contribution (c_3) for S66 and its subcategories 136
5.6 Results of MP3:ωB97X-V and MP2.5:ωB97X-V for A24, S22, Ionic43, TA13 and Orel26rad 150
5.7 Comparison of MP2.5:κ-OOMP2 and MP2.5:ωB98X-V for for A24, S22, Ionic43, TA13 and Orel26rad 150

6.1 Reduction potentials of CO_2 and proton reduction at pH = 7 versus NHE. [155, 522] . . . 154
6.2 Relative Gibbs free reaction energies and barriers for the formation of CO_2 adducts after the second reduction . . . 166
6.3 The activation energies and pK_a values of both protonation steps . . . 168

7.1 Effect of introducing a substituent at at the qpy . . . 189
7.2 Possible pathways for the protonation processes in the catalytic cycle for Feqpy 196
7.3 Possible pathways for the third reduction in the catalytic cycle for Feqpy . . . 197

8.1 Key benchmark metrics of the three pyridine based catalyst platforms . . . 209

A.1 UMP2-EDA results for the TA13 benchmark set . . . 281
A.2 RMP2-EDA results for the TA13 benchmark set . . . 282
A.3 RMP2-EDA results for the halogenated benzene radical cations interacting with H_2O . . . 284
A.4 Comparison of RMP2-EDA against DFT-based ALMO-EDA for the halogenated benzene radical cation–water complexes . . . 285
A.5 RMP2-EDA results for the Py$-CO_2^{+\bullet}$ and Im$-CO_2^{+\bullet}$ complexes . . . 287
A.6 Comparison of RMP2-EDA against DFT-based ALMO-EDA for the Py$-CO_2^{+\bullet}$ and Im$-CO_2^{+\bullet}$ complexes . . . 288

B.1 Decomposition of the frozen interaction energy at the minimum-energy structures using the "quasiclassical" scheme . . . 290
B.2 Vertical ALMO-EDA results for OC$-BH_3$ with the B97-D and ωB97X-D . . . 290
B.3 Adiabatic ALMO-EDA molecular properties results for the OC$-BH_3$ complex . 290
B.4 Decomposition of the frozen interaction energy at the minimum-energy structures of the CO−BeY complexes using the "quasiclassical" scheme with the B3LYP functional . . . 291
B.5 Vertical ALMO-EDA results for the four CO−BeY complexes using B97-D and ωB97X-D . . . 293
B.6 Adiabatic ALMO-EDA molecular properties results for the four X−BeY adducts using B97-D . . . 294
B.7 Adiabatic ALMO-EDA molecular properties results for the four X−BeY adducts using ωB97X-D . . . 295
B.8 Decomposition of the frozen interaction energy at the minimum-energy structures of the transition metal complexes using the "quasiclassical" scheme with the B3LYP functional . . . 296
B.9 Vertical ALMO-EDA results for the transition metal complexes using the B3LYP, B97-D and ωB97X-D functionals . . . 297
B.10 Metal-ligand distance r(M−X) and bond length of the diatomic ligand r(X−Y) using B97-D . . . 297
B.11 Adiabatic ALMO-EDA results with B97-D . . . 298

B.12 Metal-ligand distance r(M−X) and bond length of the diatomic ligand r(X−Y) using ωB97X-D 298
B.13 Adiabatic ALMO-EDA results with ωB97X-D 298

C.1 Strength of internal QM electrostatics ($\Delta E^{(0)}_{\mathrm{ELEC}}$) and the effect of solute-solvent electrostatic interaction on binding ($\Delta E^{\mathrm{el}}_{\mathrm{SOL}}$) for $Na^+\cdots Cl^-$ 300
C.2 Geometry distortion (GD) term for the CO_2 fragment with different fragmentation schemes (in kJ/mol). 302
C.3 Fe−CO_2 bond length (in Å) for all CO_2 adducts investigated in this study . . . 303
C.4 ALMO-EDA(solv) results in CH_3CN solvent for all the different derivatives of the doubly reduced FeTPP−CO_2 adducts 303
C.5 Gas phase ALMO-EDA results for the selected derivatives of the doubly reduced FeTPP−CO_2 complexes 304
C.6 ALMO-EDA(solv) results with ωB97X-V for the reactant- and product-state complexes of the electron-transfer reaction from terphenyl$^{\bullet-}$ to CO_2 in CH_2Cl_2 . . . 306
C.7 ALMO-EDA(solv) results with ωB97X-V for the reactant- and product-state complexes of the electron-transfer reaction from terphenyl$^{\bullet-}$ to CO_2 in gas phase . . 307
C.8 ALMO-EDA(solv) results with B3LYP-D3 for the reactant- and product-state complexes of the electron-transfer reaction from terphenyl$^{\bullet-}$ to CO_2 in CH_2Cl_2 . 308
C.9 ALMO-EDA(solv) results with B3LYP-D3 for the reactant- and product-state complexes of the electron-transfer reaction from terphenyl$^{\bullet-}$ to CO_2 in gas phase 309
C.10 Mulliken charge population (e^-) on the CO_2 moiety in the fully relaxed reactant and product states of the terphenyl$\cdots CO_2$ complex with different substituent groups 310
C.11 Differential interaction energies (in kJ/mol) between the reactant and product complexes ($\Delta\Delta E_{\mathrm{INT}}$) and the differences between the monomer energies in the reactant and product complexes (ΔE_{PREP} 311

E.1 Comparison of the crystal structure of the initital complex ${}^5_0\mathbf{1}^6$ with the optimized geometries of the three functionals used in this study. 328
E.2 Adiabatic spin gap ($\Delta_{hs/ls}G = G(hs) - G(ls)$) ${}^3_0\mathbf{1}^5$ to ${}^3_0\mathbf{1}^4$ using different functionals. 329
E.3 Key reaction of the catalytic cycle using ωB97M-V with the constraint of remaining on the high spin (quintet) surface 329
E.4 Adibatic quintet-triplet gap using ωB97M-V for the both 4 ($_0\mathbf{1}^4$) and 5 ($_0\mathbf{1}^5$) coordinated isomers of doubly reduced complex, the doubly reduced CO_2 adduct ($_0\mathbf{2}^5$) and the carboxy intermediate ($_0\mathbf{3}^5$) (free energies in kcal/mol). 329
E.5 Key reaction of the catalytic cycle using ωB97X-D. 330
E.6 Key reaction of the catalytic cycle using B3LYP-D3. 330
E.7 Key reaction of the catalytic cycle using B97-D. 331
E.8 Isomerization energy from ${}^3_0\mathbf{1}^5$ to ${}^3_0\mathbf{1}^4$ using different functionals 333
E.9 Natural orbital occupation number (NOON) of the CASSCF calculations. 336

E.10 Comparison of free energies and computed pK_a values acetonitrile to experimental values taken from Ref. [551] using the experimental solvation energy for H^+ . . . 337
E.11 The activation energies and pK_a values of both protonation steps 337

F.1 Mulliken spin population of the Co center (χ(Co)) of the doubly reduced complex 342
F.2 Reduction potentials for $[Co^{II}(qpy)(H_2O)_2]^{2+}$ using different DFT functionals . . 353
F.3 Reduction potentials for $[Fe^{II}(qpy)(H_2O)_2]^{2+}$ using different DFT functionals . . 354
F.4 ωB97X-D: reaction of the catalytic cycle for $[Co^{II}(qpy)(H_2O)_2]^{2+}$. 355
F.5 ωB97X-D: reaction of the catalytic cycle for $[Fe^{II}(qpy)(H_2O)_2]^{2+}$ 355
F.6 B3LYP-D3: reaction of the catalytic cycle for $[Co^{II}(qpy)(H_2O)_2]^{2+}$ 356
F.7 B3LYP-D3: reaction of the catalytic cycle for $[Fe^{II}(qpy)(H_2O)_2]^{2+}$ 356
F.8 ωB97M-V: reaction of the catalytic cycle for $[Co^{II}(qpy)(H_2O)_2]^{2+}$. 357
F.9 ωB97M-V: reaction of the catalytic cycle for $[Fe^{II}(qpy)(H_2O)_2]^{2+}$. 357
F.10 Natural orbital occupation number (NOON) of the CASSCF calculations of the two doubly reduced intermediates. 365

Acknowledgments

This thesis would not have been possible without the assistance, efforts and encouragement of so many people. First and foremost, I would like to thank Martin Head-Gordon for supporting my efforts to return to Berkeley as a graduate student. I am extremely grateful for the countless meetings and thoroughly enjoyed the positive atmosphere in both the group and individual meetings. I profited tremendously not only from your expertise but also from watching your approaching new problems. Your enthusiasm for science was always motivating for me and your patient and polite nature made it easy for me to discuss all sorts of problems. Furthermore, I am grateful for all the guidance, excellent advice and freedom I received. You encourage me to try (not always successfully) to work on side projects and allowing me to explore many interesting avenues provided by the unique research environment here at Berkeley.

Secondly, I would like to thank all other professors with whom I worked with during the last five years. I thank Teresa Head-Gordon for being on my thesis committee and my qualifying exam chair. I enjoyed working on the joint projects and being part of the weekly force field meetings. Your enthusiasm, drive and commitment to your students was inspiring to see. In addition, I would like to thank Ali Mesbah for being both on my qualifying exam and my thesis committee, Chris Chang for very fruitful discussions on catalysis and excellent feedback on various manuscripts, Jeff Long for fruitful discussion on catalysis, Polly Arnold and Dean Toste for interesting discussions about EDA for transition metal complexes. I also want to acknowledge several professors at LMU Munich for their excellent efforts in teaching and drawing my interest to theoretical chemistry: Prof. Ochsenfeld, Prof. de Vivie-Riedle, Prof. Klüfers and Prof. Böttcher.

Thirdly, I want to thank the whole MHG research group for providing stimulating and fun research environment. In particular I want to thank my three mentors in the group Joonho, Yuezhi and Julien, who have been invaluable for my development as a researcher: I want to thank Joonho Lee for teaching me everything about method development, coding and debugging in Q-Chem. I could profit tremendously from working with you on a daily basis on science problems and your work ethic was certainly leading by example; I want to thank Yuezhi Mao, I enjoyed working with you on various EDA projects and I learned a lot from your detailed feedback and our discussions about science. I am also thankful for your patience in teaching me how to structure and write manuscripts. I am grateful that you took the time for our weekend meetings half-way between Stanford and Berkeley after you had left the group. I want to thank Julien Panetier, who taught me a lot about computational catalysis and how to use Q-Chem properly; your patience and friendly nature made it very easy for me to get started quickly. Furthermore, I want to thank "Saint" Luke Bertels for being the good soul of the MHG group, keeping me well fed by providing an endless supply of Skittles and chips, and as former captain of his school math team helping me double checking tedious derivations. I want to thank Srimukh Prasad[2] for working (struggling) together on learning about the EDA theory, programming in Q-Chem and all the fun times together in the office. I want to thank Dip Hait for many interesting late-night discussions,

for being a reliable reference for DFT questions and for organizing our theory events. I want to thank James Shee for many "science workouts" at the track during the pandemic. I want to thank Alex Zech for being a fun office mate and teaching me various concepts of computer science. I want to thank Christopher Stein for interesting science discussions and hosting many unforgettable BBQ events, Tim Stauch for keeping me motivated during my early struggles, Ainara Nova for all her efforts helping me with the computation of reduction potentials. I would like to thank Jessie Woodcock for swiftly resolving of all administrative issues. I want to thank Alec White and the Q-Chem team, especially Xintian Feng and Evgeny Epifanovsky, for being very helpful when encountering technical difficulties and for hosting us at several visits. I want to thank my interns Dan Chu, Delmar Cabral and Tim Schramm; it was a lot of fun mentoring every one of you and I hope you learned as much as from me as I did from you.

I am also grateful for having excellent experimental collaborators with Jeff Derrick and David Jaramillo; the discussions about chemistry and your enthusiasm and genuine interest about theory collaboration made working with both of you a lot of fun and resulted in very successful joint projects. I also want to thank all my other collaborators and coauthors for all their efforts on joint projects.

Lastly, I want to thank my whole family for their enormous support during my academic journey, I want to thank my two brothers for their constant support, their visits and for taking the load off me whenever necessary so I could solely focus on this dissertation for the last five years. I want to thank my mom for her unconditional support during my whole academic journey. Without your constant support and cheers, this would certainly not have been possible. In the end, I want to thank my partner Sophia for being the rock through all the ups and down of graduate school. Your constant support and cheers especially in the beginning and during the qualifying exam were invaluable. I am extremely grateful for all your support and your personal sacrifices over this last five years, and I look forward what the future holds for us.

Chapter 1

Introduction

In 1929, Paul Dirac made a bold claim about the influence of quantum mechanics on chemistry: *"The underlying physical laws necessary for the mathematical theory of [...] the whole of chemistry are thus completely known"*[1]. However, he also admits: *" The difficulty is only that the exact application of these laws leads to equations much too complicated to be soluble. It therefore becomes desirable that approximate practical methods of applying quantum mechanics should be developed"*[1]. His claim about the (dark) future of chemistry did initially not find much attention among chemists.[2] In hindsight, it is apparent that Dirac's claim about chemistry was too bold as it is still a thriving field of research; however, it is undeniable that the laws of quantum mechanics (QM) had a huge impact. QM provides a framework to understand and predict the behavior of the electrons in molecules, which at the core governs chemical reactivity. The field of quantum chemistry, more specifically electronic structure theory, is concerned with developing these *"approximate practical methods of applying quantum mechanics"* [1]. Exciting progress has been made over the last decades due to many ground breaking theoretical developments and the rapid development of computational power (Moore's law). To-date, electronic structure calculations are routinely performed to gain insights into the bonding situation in molecules, predicting reaction energetics and rates with an accuracy of a few kcal/mol.[3–5] In the field of catalysis, electronic structure calculations can yield invaluable mechanistic insights into the catalytic pathways, which usually involve many transient species (often) not possible to track experimentally. These mechanistic studies can provide explanations for the origin of activity and selectivity as well as the cause of any intrinsic limitations. In the future, electronic structure theory will have an even stronger influence as advances in both machine learning[6] and quantum computing[7] may leverage it to have a disrupting impact not only in quantum chemistry but chemistry as a whole.

This thesis is concerned with three aspects of electronic structure theory. First, the development of novel methods in the realm of energy decomposition analysis and its applications, this topic spans chapters 2 to 4; second, the performance of perturbation theory based wave function methods for non-covalent interactions in chapter 5; third the modelling of catalytic pathways for homogeneous CO_2 reduction catalysts and rational catalyst design based on

those models, this topic spans chapters 6 to 8. The first chapter of this thesis provides proper background and literature overview with the objective to facilitate the understanding of the core research chapters 2–8. Consequently, this first chapter is based on standard textbooks of quantum mechanics such as reference [8] and quantum chemistry such as references [9–12].

1.1 Quantum Mechanics in Chemistry

The postulates of quantum mechanics offer a theoretical framework to predict chemical observables *ab initio*. The (non-relativistic time dependent) Schrödinger equation[13] constitutes the central equation in quantum mechanics and describes the dynamics of quantum particles such as electrons:

$$i\hbar\frac{\partial}{\partial t}\left|\Psi\right\rangle = \hat{H}\left|\Psi\right\rangle \quad , \tag{1.1}$$

where $\hat{H}$ denotes the Hamiltonian operator and $|\Psi\rangle$ denotes the wave function of the system. Solving for the eigenvalues and eigenfunction of $\hat{H}$ in the time-independent Schrödinger equation yields the total energy of the quantum system:

$$\hat{H}\left|\Psi_n\right\rangle = E_n\left|\Psi_n\right\rangle \ , \tag{1.2}$$

where $n = 0$ denotes the ground state, E_0 the ground state energy of the system and $n = 1, 2, ..., K$ denotes the first, second and K^{th} excited state. This thesis is only concerned with the ground state energy and wave function; thus, the subscript is dropped. The wave function represents the quantum system and is the key for obtaining desired properties of the system.

The Hamiltonian operator for a molecule consisting of M nuclei with charge Z and N electrons has the following form (in atomic units):

$$\hat{H} = -\sum_{i=1}^{N}\frac{1}{2}\nabla_i^2 - \sum_{A=1}^{M}\frac{1}{2M_A}\nabla_A^2 - \sum_{i=1}^{N}\sum_{A=1}^{M}\frac{Z_A}{r_{iA}} + \sum_{i=1}^{N}\sum_{j>i}^{N}\frac{1}{r_{ij}} + \sum_{A=1}^{M}\sum_{B>A}^{M}\frac{Z_A Z_B}{R_{AB}} \ , \tag{1.3}$$

where r_{iA} denotes the distance between the i^{th} electron and A^{th} nuclei, r_{ij} the distance between the i^{th} and j^{th} electron and R_{AB} the distance between nuclei A and B.
In short hand notation:

$$\hat{H} = \hat{T}_e + \hat{T}_N + \hat{V}_{eN} + \hat{V}_{ee} + \hat{V}_{NN} \quad ,$$

where $\hat{T}_e$ denotes the kinetic energy operator of the electrons, $\hat{T}_N$ the kinetic energy operator for nuclei and $\hat{V}_{eN}$, $\hat{V}_{ee}$, $\hat{V}_{NN}$ the Coulomb potential operator for electron-nuclei, electron-electron and nuclei-nuclei, respectively. The wave function of such a quantum system depends on the coordinates of both electrons ($\mathbf{x}$, spin and spatial) and nuclei ($\mathbf{R}$): $\Psi = \Psi(\mathbf{x}, \mathbf{R})$.

The nuclei move several order of magnitude slower than electrons; therefore, a feasible approximation is the description of electrons in a static field of nuclei as proposed by Born and

Oppenheimer [14]. This allows a separation of variables and the wave function is factorized into two parts: (i) an electronic wave function $\Psi_{el} = \Psi_{el}(\mathbf{x}; \mathbf{R})$, depending on the coordinates of the electrons and parametrically on the nuclei position ($\mathbf{R}$); (ii) the nuclear wave function $\Upsilon(\mathbf{R})$, only dependent on the nuclei coordinates. This allows to neglect of the effect of $\hat{T}_N$ on the electronic wave function and $\hat{V}_{NN}$ can be treated as a constant term. Thus, solving for electronic wave function simplifies to (for a set of fixed nuclei coordinates $\mathbf{R}$):

$$\hat{H}_{el} \left|\Psi_{el}\right\rangle = E_{el} \left|\Psi_{el}\right\rangle \quad , \tag{1.4}$$

with $\hat{H}_{el} = \hat{T}_e + \hat{V}_{eN} + \hat{V}_{ee} + \hat{V}_{NN}$

Solving the electronic Schrödinger equation for various nuclear geometries yields a high $(3M-6)$ dimensional potential energy surface $V(\mathbf{R}) = E_{el}(\mathbf{R})$. Stationary points are important for describing chemical reactions. Minima correspond to stable reactants and products, which determine the direction of the chemical reaction, and saddle points correspond to transition states (TS), which determine the rate of the chemical reaction.

The electronic wave function is a many-body wave function of electrons (fermions), which is associated with a high dimensional Hilbert space. In classical physics, the state space S of n particles, each described by an m dimensional vector space S_i, yields an nm dimensional state space for the many-body system; the individual particle spaces combine via a direct sum: $S = \bigoplus_{i=1}^{n} S_i$. In contrast, quantum one-particle Hilbert spaces $\mathcal{H}_a$ combine into the many-body Hilbert space $\mathcal{H}$ via the tensor product: $\mathcal{H} = \bigotimes_{i=1}^{n} \mathcal{H}_i$, resulting in a Hilbert space of dimension m^n. In other words, exponential growth with number of particles.

Furthermore, a fermionic wave function must obey the anti-symmetry relation:

$$\left|\Psi(\mathbf{x}_1, \mathbf{x}_2, ..., \mathbf{x}_n)\right\rangle = - \left|\Psi(\mathbf{x}_2, \mathbf{x}_1, ..., \mathbf{x}_n)\right\rangle \quad , \tag{1.5}$$

which also implies that the wave function must vanish if two electrons are in the same quantum state (Pauli exclusion principle). Slater determinants fulfill this requirement and are defined as:

$$\left|\Phi\right\rangle = \frac{1}{\sqrt{N!}} \begin{vmatrix} \chi_1(1) & \chi_1(2) & \dots & \chi_1(N) \\ \chi_2(1) & \chi_2(2) & & \\ \vdots & & \ddots & \\ \chi_N(1) & & & \chi_N(N) \end{vmatrix} , \tag{1.6}$$

where χ_i denotes a one-electron function (spin-orbital). Given a complete basis of spin-orbitals $\{\chi_p\}$, the space can be partitioned into occupied and virtual orbitals (unoccupied):

$$\hat{I} = \hat{P} + \hat{Q} \quad , \tag{1.7}$$

where $\hat{I}$, $\hat{P}$ and $\hat{Q}$ are the projectors for the total, occupied and virtual space, respectively.

General orbitals are denoted with $p, q, r, ...$, occupied orbitals with $i, j, k, ...$ and $a, b, c, ...$ represent virtual orbitals. The n-particle Hilbert space can be decomposed into subspaces of Slater determinants. Based on the degree of substitution from a reference determinant $\left|\Phi_0\right\rangle$

(comprised of the occupied orbitals), subspaces of singly, doubly,... to n-fold substitution of occupied and virtual orbitals can be defined as[15]:

$$\mathcal{H} = 0 \oplus S \oplus D \oplus T \oplus ... \oplus n \quad , \tag{1.8}$$

where 0 denotes the subspace of the reference determinant, S the subspace of singly substituted determinants, D the subspace of all doubly substituted determinants, and so on. Thus, the electronic wave function can be expanded as:

$$|\Psi\rangle = c_0 |\Phi_0\rangle + \sum_{ia} c_i^a |\Phi_i^a\rangle + \sum_{ia} \sum_{j>i,b>a} c_{ij}^{ab} \left|\Phi_{ij}^{ab}\right\rangle + ... \quad , \tag{1.9}$$

where $|\Phi_i^a\rangle$ denotes a singly substituted determinant and $\left|\Phi_{ij}^{ab}\right\rangle$ a doubly substituted determinant and so on. This expansion is called full configuration interaction (FCI). The number of determinants grows combinatorially with increasing number of electrons; thus, this full expansion is only feasible for a very small number of electrons. Accurate approximation of the electronic ground state energy of molecules at the lowest possible computational cost is the heart of the matter in quantum chemistry. For instance, efficient truncation of the expansion in a compact orbital representations allows one to approximate $|\Psi\rangle$ in a subspace, e.g. the subspace $0 \oplus S \oplus D$.

1.2 Quantum Chemistry

This thesis is concerned with the solution to the electronic Schrödinger equation (equation 1.4) and thus the "el" subscripts are dropped in the following. This chapter is based on the textbooks [9, 11, 16]. Furthermore, reference [17] provides an excellent introduction to the Hartree-Fock method and references [18, 19] and [20] to density functional theory.

Hartree-Fock Method

The Hartree-Fock (HF) Method approximates $|\Psi\rangle$ as a single Slater determinant:

$$|\Psi\rangle \approx |\Phi_{HF}\rangle \tag{1.10}$$

The HF method approximates the pairwise Coulombic electron-electron interactions in a mean-field; i.e. the potential experienced by the i^{th} electron is the average potential of the remaining electrons. The HF method does not correlate electrons with opposite spin.[21]

The variational principle provides an ansatz to obtain an optimal set of occupied orbitals. It states that the energy E_{HF} can never be lower than the true ground state energy E_0. Thus, the best approximation for a single Slater determinant is obtained by minimizing the energy of the expectation value with respect to a set of occupied orbitals $\{\chi_i\}$ comprising the Slater determinant $\Phi(\{\chi_i\})$:

$$E_{el} \leq E_{HF} = \min_{\{\chi_i\}} \frac{\langle \Phi(\{\chi_i\})|\hat{H}|\Phi(\{\chi_i\})\rangle}{\langle \Phi(\{\chi_i\})|\Phi(\{\chi_i\})\rangle} \tag{1.11}$$

Assuming orthonormal orbitals, the HF energy can be expressed in terms of the orbitals using the Slater-Condon rules [22, 23]:

$$E_{HF} = \sum_{i=1}^{N} \langle i|\, \hat{h}\, |i\rangle + \frac{1}{2} \sum_{i,j=1}^{N} \langle ij||ij\rangle \ , \tag{1.12}$$

where N denotes the number of occupied orbitals and the $\hat{h}(\mathbf{x}_1)$ is defined as the one-particle operator:

$$\hat{h}(\mathbf{x}_i) = -\frac{1}{2}\nabla_i^2 - \sum_{A}^{N} \frac{Z_A}{\mathbf{r}_{iA}} \tag{1.13}$$

and the resulting integral defined as

$$\langle i|\, \hat{h}\, |j\rangle = \int d\mathbf{x}_1 \chi_i^*(\mathbf{x}_1) h(\mathbf{x}_1) \chi_j(\mathbf{x}_1) \ , \tag{1.14}$$

The two-electron integrals $\langle ij||kl\rangle$ are defined as

$$\langle ij||kl\rangle = \langle ij|kl\rangle - \langle ij|lk\rangle \tag{1.15}$$

and $\langle ij|kl\rangle$ as:

$$\langle ij|kl\rangle = \int d\mathbf{x}_1 d\mathbf{x}_2 \chi_i^*(\mathbf{x}_1)\chi_j^*(\mathbf{x}_2)\frac{1}{\mathbf{r}_{12}}\chi_k(\mathbf{x}_1)\chi_l(\mathbf{x}_2) \ . \tag{1.16}$$

The canonical Hartree-Fock equations emerge to obtain the set of orbitals that minimize equation 1.11 with the constraint of orthonormal orbitals:

$$\hat{f}\chi_i = \varepsilon_i\chi_i \quad i = 1, 2, 3, ... \ , \tag{1.17}$$

where ε_i denotes the i^{th} eigenvalue (orbital energy) and the Fock-operator $\hat{f}$ is defined as:

$$\begin{aligned} \hat{f}(\mathbf{x}_1) &= \hat{h}(\mathbf{x}_1) + \sum_j^N (\hat{J}_j - \hat{K}_j) \\ \hat{J}_j(\mathbf{x}_1)\chi_i(\mathbf{x}_1) &= \left[\int d\mathbf{x}_2 \chi_j^*(\mathbf{x}_2)\frac{1}{\mathbf{r}_{12}}\chi_j(\mathbf{x}_2)\right]\chi_i(\mathbf{x}_1) \\ \hat{K}_j(\mathbf{x}_1)\chi_i(\mathbf{x}_1) &= \left[\int d\mathbf{x}_2 \chi_j^*(\mathbf{x}_2)\frac{1}{\mathbf{r}_{12}}\chi_i(\mathbf{x}_2)\right]\chi_j(\mathbf{x}_1) \ , \end{aligned} \tag{1.18}$$

where $\hat{J}$ denotes the coulomb operator and $\hat{K}$ the exchange operator. The Fock operator is a one-particle operator, which approximates the two-body electron-electron interaction as an effective one-particle operator via the Hartree-Fock potential $\hat{v}^{HF}$:

$$\hat{v}^{HF} = \sum_j^N \hat{J}_j + \hat{K}_j \quad . \tag{1.19}$$

The Fock operator itself depends on the orbitals and exact solutions to the "pseudo-eigenvalue problem" only exist for very small systems. In practice, one usually introduces a basis and solves this equation in a self-consistent way (see below).

Most commonly, one solves either the restricted HF equations (RHF) for closed shell systems or the unrestricted HF equations for open-shell systems (UHF) where the spin part is integrated out. As a spin orbital can be represented as:

$$\chi(\mathbf{x}) = \phi_i(\mathbf{r})s(\omega)$$

where $\phi(\mathbf{r})$ is the spatial orbital and s is either α or β depending on the spin coordinate.

This yields the RHF equations:

$$\hat{f}\phi_i = \varepsilon_i\phi_i \ . \tag{1.20}$$

and the RHF Fock operator (using $n = N/2$):

$$\hat{f}(\mathbf{r_i}) = \hat{h}(\mathbf{r_i}) + \sum_j^n (2\hat{J}_j(\mathbf{r_i}) - \hat{K}_j(\mathbf{r_i})) \tag{1.21}$$

This spatial integro-differential equation is in practice solved by introducing a set of fixed basis functions and solved iteratively via the self-consistent field procedure (SCF). In doing so, the integro-differential equation is transformed into a matrix equation that is much easier to solve (see below).[24]

The molecular orbitals (MOs) $\{\phi_p\}$ are linearly expanded in a set of K known basis functions $\{\omega_\mu : \mu = 1, 2..., K\}$:

$$\phi_p = \sum_{\mu=1}^{K} C_{\mu p}\omega_\mu \qquad p = 1, 2, ..., K \ . \tag{1.22}$$

A basis function is usually based on the spherical harmonics for the angular part, a *gaussian type orbital* (GTO) for the radial part and are usually called atomic orbitals (AOs, abbreviated with Greek letters $\mu, \nu, ...$) and the expansion is called linear combination of atomic orbitals (LCAO).

Using equations 1.20 and 1.22 yields a matrix equation for the MO vectors $\underline{C_p}$, the Roothaan-Hall equation [24]:

$$\underline{\underline{\mathbf{F}}}\ \underline{\underline{\mathbf{C}}} \ = \ \underline{\underline{\mathbf{S}}}\ \underline{\underline{\mathbf{C}}}\ \underline{\underline{\varepsilon}} \ . \tag{1.23}$$

An element of the representation of the Fock operator in the AO basis ($F_{\mu\nu}$) has the following form:

$$F_{\mu\nu} = h_{\mu\nu} + \sum_{\kappa,\lambda=1}^{K} P_{\kappa\lambda}\left[2(\mu\nu|\kappa\lambda) - (\mu\lambda|\kappa\nu)\right] \ , \tag{1.24}$$

the matrix element $h_{\mu\nu}$ is defined as $h_{\mu\nu} = \langle\omega_\mu|\,\hat{h}\,|\omega_\nu\rangle$ and the 4-center-2-electrons integrals as: $(\mu\nu|\kappa\lambda) = \int d\mathbf{r}_1 d\mathbf{r}_2 \omega_\mu^*(\mathbf{r}_1)\omega_\nu(\mathbf{r}_1)\frac{1}{\mathbf{r}_{12}}\omega_\kappa^*(\mathbf{r}_2)\omega_\lambda(\mathbf{r}_2)$. The matrix elements of the one particle density matrix $\underline{\underline{\mathbf{P}}}$ are defined as:

$$P_{\mu\nu} = \sum_{i=1}^{n} C_{\mu i}^* C_{\nu i} \ . \tag{1.25}$$

The matrix $\underline{\underline{\mathbf{S}}}$ denotes the overlap matrix of the AOs since the basis functions need not be orthogonal: $S_{\mu\nu} = \langle\mu|\nu\rangle$.

The Fock matrix depends on the occupied orbital vectors of the coefficient matrix $\underline{\underline{\mathbf{F}}}(\underline{\underline{\mathbf{C}}})$; thus equation 1.23 is solved iteratively in the SCF procedure:

1. Specify molecular coordinates $\{\mathbf{R}\}$, charge and multiplicity
2. Compute integrals for $\underline{\underline{\mathrm{h}}}$ and $\underline{\underline{\mathrm{S}}}$
3. Obtain initial guess for $\underline{\underline{\mathrm{P}}}$
4. Build the Fock matrix (equation 1.24)
5. Diagonalize $\underline{\underline{\mathrm{F}}}$ and get new $\underline{\underline{\mathrm{C}}}$ and $\underline{\underline{\mathrm{P}}}$

6. Check SCF convergence based on E^{HF} and $\underline{\underline{P}}$ change

7. Stop or go back to step 4 if not converged

In case of UHF, the variational flexibility is increased by allowing the coefficients for the α and β spaces to be different:

$$\chi_p = \begin{cases} \sum_\mu^K C_{\mu p}^\alpha \omega_\mu^\alpha \\ \sum_\mu^K C_{\mu p}^\beta \omega_\mu^\beta \end{cases} \tag{1.26}$$

This ansatz yields an α density ($\underline{\underline{P}}^\alpha$), a β density ($\underline{\underline{P}}^\beta$) and a Fock operator for each spin state that depends on the total spin density ($\underline{\underline{P}} = \underline{\underline{P}}^\alpha + \underline{\underline{P}}^\beta$) resulting in two coupled matrix equations similarly to equation 1.23 called the Pople-Nesbet equations [25]. It is noteworthy that this ansatz can break spin symmetry as the expectation value for $\hat{S}^2$ is defined as:

$$\langle \Phi_{UHF} | \hat{S}^2 | \Phi_{UHF} \rangle = S_{exact}^2 + N^\beta - \sum_{i=1}^{N_\alpha} \sum_{j=1}^{N_\beta} \left| S_{ij}^{\alpha\beta} \right|^2 \quad , \tag{1.27}$$

where S_{exact}^2 denotes the good quantum number for the respective spin multiplicity, N^β the number of electrons in the β space and $S_{ij}^{\alpha\beta}$ the overlap of the spatial orbitals i in the α space and j in the β space. There are two main reasons why UHF breaks spin symmetry: First, the system cannot be properly described by a RHF single determinant, e.g. for bond dissociation or metallic systems with various configurations similar in energy, denoted as essential symmetry breaking. Second, the system can be represented as single RHF determinant; this is called artificial symmetry breaking and can be avoided by including explicit electron-electron correlation in the SCF procedure (*vide infra*) [26]. Another approach to enforce spin symmetry is to enforce constraints on the orbitals by forcing singly and doubly occupied orbitals to be orthogonal and doubly occupied orbitals to be identical in both α and β space; this ansatz is called restricted-open shell HF (RO-HF).

The HF method, even at the basis set limit, only yields an approximation to the electronic Schrödinger equation (1.4); this energy is called the Hartree-Fock limit energy. The HF method does not correlate electrons with opposite spins and the missing energy to reach the exact electronic energy is called correlation energy ($E_{corr} = E_{el} - E_{HF}$). The missing correlation can be incorporated with the use of post-HF methods such as Møller-Plesset Perturbation theory or density functional theory (*vide infra*).

An alternative approach to HF is provided by Pople and Head-Gordon via an orbital optimization [27] ansatz. The goal is to find a unitary transformation, which yields the eigenvectors of the Fock operator in the MO space:

$$\underline{\underline{C'}} = \underline{\underline{C}}\,\underline{\underline{U}} \tag{1.28}$$

the unitary matrix can be expressed in terms of the exponential of an anti-Hermitian X matrix:

$$\underline{\underline{U}} = e^{(\underline{\underline{X}})} \tag{1.29}$$

The matrix exponential can be Taylor expanded:

$$\underline{\underline{U}} = \underline{\underline{I}} + \underline{\underline{X}} + \frac{1}{2}\underline{\underline{X}}\ \underline{\underline{X}} + ... \quad . \tag{1.30}$$

As only the mixing of occupied and virtual orbitals changes the energy, the new rotated MOs ($|p'\rangle$) can be obtained by expanding the occupied-virtual sub-block of the matrix to first order:

$$|i'\rangle = |i\rangle + \sum_a \theta_{ai} |a\rangle \tag{1.31}$$

and

$$|a'\rangle = |a\rangle - \sum_i \theta_{ai} |i\rangle \quad , \tag{1.32}$$

where θ_{ai} denotes an element of the occupied-virtual sub-block of $\underline{\underline{X}}$.
The expansion is used in the HF energy functional (using the closed shell expression for HF):

$$E_{RHF} = 2\sum_i h_i + \sum_{ij} 2(ii|jj) - (ij|ji) \tag{1.33}$$

(or the MP2-energy functional, see equation 1.62). Taking a derivative with respect to the orbital rotation coefficients (θ_{ai}) yields the gradient for the energy:

$$\frac{\partial E_{RHF}}{\partial \theta_{ai}} = 4F_{ai} \tag{1.34}$$

The expression can then be minimized to yield the optimal set of occupied orbitals, for a very robust algorithm see reference [28].

SCF for Molecular Interactions

SCF for Molecular Interactions (SCF-MI) is a constraint SCF procedure, where the system is partitioned into fragments and each fragment's MOs are only expanded in the AOs of that fragment; in contrast, the canonical MOs are usually delocalized over all AOs. This constraint enforces a block diagonal coefficient matrix yielding absolutely localized molecular orbitals (ALMOs, see references [29–31] for a detailed discussion):

$$\left|\phi_{(Xp)}\right\rangle = \sum_{\mu \in X} \left|\omega_{(X\mu)}\right\rangle C_{(X\mu)(Xp)} \quad , \tag{1.35}$$

where (Xp) denotes the p^{th} MO on fragment X and $\left|\omega_{(X\mu)}\right\rangle$ the μ^{th} AO on fragment X. It follows from this constraint that the ALMOs cannot be orthogonal to each other. Therefore, a bi-orthogonal set, the contravariant orbitals $\{|\phi^p\rangle\}$, is introduced and the energy can be expressed in a mixed co and contravariant basis (see reference [15] for a an excellent overview of quantum chemistry in a non-orthogonal single-particle basis):

$$E_{SCFMI} = \left\langle \Phi_{ALMO} \middle| H \middle| \Phi^{ALMO} \right\rangle \tag{1.36}$$

$$E_{SCFMI} = 2\sum_{X}^{F}\sum_{i\in X}\left\langle\phi_{(Xi)}\middle|\hat{h}\middle|\phi^{(Xi)}\right\rangle + \sum_{X,Y}^{F}\sum_{i\in X j\in Y} 2(\phi_{(Xi)}\phi^{(Xi)}|\phi_{(Yj)}\phi^{(Yj)}) - (\phi_{(Xi)}\phi^{(Yj)}|\phi_{(Yj)}\phi^{(Xi)}) \ , \tag{1.37}$$

where F denotes the total number of fragments. Then, a fragment-wise orbital gradient can be obtained to ensure only mixing of occupied and virtual orbitals on fragment:

$$\left.\frac{\partial E_{SCFMI}}{\partial\theta^{(Wa)(Wi)}}\right|_{\theta=0} = 4\left[\sum_{X}\left\langle\phi_{(Wa)}(1-\hat{P})\middle|F\middle|\phi_{(Xj)}\right\rangle\sigma^{(Xj)(Wk)}\sigma_{(Wk)(Wi)}\right]_{(Wa)(Wi)} \quad , \tag{1.38}$$

where $\theta^{(Wa)(Wi)}$ denotes the orbital rotation parameter for fragment W. The problem can be cast into a generalized eigenvalue equation similarly to equation 1.23 by projection of the Fock operator[29, 30] in a fragment subspace yielding fragment-blocked eigenvalue equations:

$$\underline{\underline{F}}^{X}\underline{\underline{C}}^{X} = \underline{\underline{S}}^{X}\underline{\underline{C}}^{X}\underline{\underline{\varepsilon}}^{X} \quad , \tag{1.39}$$

where $\underline{\underline{F}}^{X}$ denotes an AO Fock matrix projected into fragment space X (see references [29–31] for the definition), $\underline{\underline{C}}^{X}$ the X^{th} block of the coefficient matrix, $\underline{\underline{S}}^{X}$ the X block of the AO overlap matrix and $\underline{\underline{\varepsilon}}^{X}$ the orbital energies for fragment X. The converged SCF-MI solution represents a state which naturally forbids charge transfer (CT) between the two fragments[32, 33] and is thus used as as a key intermediate in the ALMO based energy decomposition method described below.

Møller-Plesset Perturbation Theory

In wave function-based quantum chemistry the Hartree-Fock (HF) mean field reference determinant $|\Phi_{HF}\rangle$ is the foundation of post-HF methods. The missing energetic effect of other determinants is typically approximated by low-order Møller-Plesset (MP) perturbation theory[34, 35] or by infinite order coupled cluster theory,[36, 37] truncated at low levels of excitations from $|\Phi_0\rangle$ such as double or triple excitations. This approach yields a good compromise between computational cost and amount of correlation energy recovered.

In MP perturbation theory, the Fock operator is used as the unperturbed Hamiltonian:

$$\hat{H}^{(0)} = \sum_{i}\hat{f}(\mathbf{x_i}) \tag{1.40}$$

$$\hat{V} = \hat{H} - \hat{H}^{(0)} \quad . \tag{1.41}$$

Both the energy and the wave function are expanded around the unperturbed wave function and energy using the perturbation parameter λ:

$$E_{el} = E_{MP0} + \lambda E_{MP1} + \lambda^2 E_{MP2} + \lambda^3 E_{MP3} + ... \tag{1.42}$$

$$|\Psi_{MP}\rangle = |\Phi_{HF}\rangle + \lambda\left|\Psi^{(1)}\right\rangle + \lambda^3\left|\Psi^{(2)}\right\rangle + ... \ , \tag{1.43}$$

where E_{MPi} and $\left|\Psi^{(i)}\right\rangle$ denotes the i^{th} order correction to the energy and wave function, respectively. The corresponding perturbation equations are for zeroth order (assuming a (pseudo) canonical basis for the Fock operator):

$$\hat{f}\left|\Phi_{HF}\right\rangle = E_{MP0}\left|\Phi_{HF}\right\rangle \tag{1.44}$$

where E_{MP0} is the sum of orbital energies $\sum_i \epsilon_i$ which is not equal to E_{HF} because of double counting of the electron-electron interaction.

The first order correction is:

$$E_{MP1} = \left\langle \Phi_{HF}|V|\Phi_{HF}\right\rangle = -\frac{1}{2}\sum_{ij}\left\langle ii||jj\right\rangle \quad . \tag{1.45}$$

Note this correction resolves the double counting issue and recovers E_{HF}; hence, $E_{HF} = E_{MP0} + E_{MP1}$.

The second order energy correction depends on the first order wave function:

$$\left|\Psi^{(1)}\right\rangle = \sum_{ia} t_i^a \left|\Phi_i^a\right\rangle - \sum_{ia}\sum_{j>i,b>a} t_{ij}^{ab}\left|\Phi_i^a\right\rangle \quad , \tag{1.46}$$

where t denotes the amplitudes of the excited Slater determinant and the second order energy (single excitations do not contribute due to Brillouin's theorem):

$$E_{MP2} = \left\langle \Phi_{HF}\middle|V\middle|\Psi^{(1)}\right\rangle = \sum_{ia}\sum_{j>i,b>a} t_{ij}^{ab}\left\langle \Psi^{HF}\middle|V\middle|\Psi_{ij}^{ab}\right\rangle \tag{1.47}$$

where the t amplitudes are defined as

$$t_{ij}^{ab} = -\frac{\left\langle ij||ab\right\rangle}{\epsilon_a + \epsilon_b - \epsilon_i - \epsilon_j} \tag{1.48}$$

$$\tag{1.49}$$

and the resulting second order energy correction :

$$E_{MP2} = -\frac{1}{4}\sum_{ijab}\frac{\left|\left\langle ij||ab\right\rangle\right|^2}{\epsilon_a + \epsilon_b - \epsilon_i - \epsilon_j} \tag{1.50}$$

The third order energy correction is defined as:

$$E_{MP3} = \left\langle \Psi^{(1)}\middle|V\middle|\Psi^{(1)}\right\rangle \tag{1.51}$$

resulting in:

$$\begin{aligned} E_{\mathrm{MP3}} = & \frac{1}{8}\sum_{ijabcd}\left(t_{ij}^{ab}\right)^*\left\langle ab||cd\right\rangle t_{ij}^{cd} \\ & + \frac{1}{8}\sum_{ijklab}\left(t_{ij}^{ab}\right)^*\left\langle kl||ij\right\rangle t_{kl}^{ab} \\ & - \sum_{ijkabc}\left(t_{ij}^{ab}\right)^*\left\langle kb||ic\right\rangle t_{kj}^{ac} \quad . \end{aligned} \tag{1.52}$$

The Hylleraas functional, J_H, is a variational formulation that when minimized yields the first order wave function and MP2 energy; thus this approach can be used to obtain the MP2 energy in another orbital basis than the canonical[38] or for the evaluation of the MP2 energy with non-stationary t-amplitudes such as a trial wave function $\left|\tilde{\Psi}\right\rangle$:

$$J_H[\tilde{\Psi}] = \left\langle \Psi^{(0)} \middle| V - E_{MP1} \middle| \tilde{\Psi} \right\rangle + \left\langle \tilde{\Psi} \middle| H^{(0)} - E_{MP0} \middle| \tilde{\Psi} \right\rangle + \left\langle \tilde{\Psi} \middle| \hat{V} - E_{MP1} \middle| \Psi^{(0)} \right\rangle \tag{1.53}$$

or in a more compact matrix-vector notation:

$$J_H[\tilde{\mathbf{t}}] = \tilde{\mathbf{t}}^\dagger \mathbf{\Delta} \tilde{\mathbf{t}} + \tilde{\mathbf{t}}^\dagger \mathbb{I} + \mathbb{I}^\dagger \tilde{\mathbf{t}} \quad , \tag{1.54}$$

where $\tilde{\mathbf{t}}$ is a vector composed of the wave function amplitudes $\tilde{t}_{ij}^{ab}$, $\mathbb{I}$ is a vector composed of two-electron integrals, $\langle ij||ab\rangle$, and $\mathbf{\Delta}$ is a supermatrix whose elements are defined as:

$$\Delta_{\binom{ab}{ij},\binom{cd}{kl}} = \left\langle \Psi_{ij}^{ab} \middle| \hat{F} - E_{MP0} \middle| \Psi_{kl}^{cd} \right\rangle \quad . \tag{1.55}$$

It can be derived from the second order energy expression[16]:

$$E^{(2)} = \left\langle \Psi^{(0)} \middle| V \middle| \Psi^{(1)} \right\rangle \quad . \tag{1.56}$$

The first order equation is projected with the first order wave function:

$$\left\langle \Psi^{(1)} \middle| H^{(0)} - E_{MP0} \middle| \Psi^{(1)} \right\rangle = \left\langle \Psi^{(1)} \middle| E_{MP1} - V \middle| \Psi^{(0)} \right\rangle \quad . \tag{1.57}$$

Next, equation 1.57 is added to equation 1.56 to obtain the Hylleraas functional in equation 1.53; obviously for $\left|\tilde{\Psi}\right\rangle = \left|\Psi^{(1)}\right\rangle$, E_{MP2} is retained.

For real wave functions and if intermediate normalization ($\left\langle \tilde{\Psi} \middle| \Psi^{(0)} \right\rangle = 0$) is enforced, the expression simplifies to:

$$J_H[\tilde{\Psi}] = \left\langle \tilde{\Psi} \middle| H^{(0)} - E_{MP0} \middle| \tilde{\Psi} \right\rangle + 2 \left\langle \tilde{\Psi} \middle| V \middle| \Psi^{(0)} \right\rangle \tag{1.58}$$

and variation of the functional results in:

$$\delta J_H = 2 \left\langle \delta\tilde{\Psi} \middle| H^{(0)} - E_{MP0} \middle| \tilde{\Psi} \right\rangle + 2 \left\langle \delta\tilde{\Psi} \middle| V \middle| \Psi^{(0)} \right\rangle \quad . \tag{1.59}$$

Therefore, the stationary condition is the first order equation with $\left|\Psi^{(1)}\right\rangle$ as a solution:

$$(H^{(0)} - E_{MP0}) \left|\tilde{\Psi}\right\rangle = V \left|\Psi^{(0)}\right\rangle \quad . \tag{1.60}$$

Thus, the first order wave function and second order energy can be obtained by making the Hylleraas functional stationary with respect to the t-amplitudes:

$$J_H[\tilde{\Psi}] \geq E_{MP2} \quad . \tag{1.61}$$

The Hylleraas functional can be added to the HF energy expression to yield the MP2 Lagrangian, an orbital optimized (OO) MP2 energy functional; see references [39, 40] for a more detailed presentation. The OOMP2 energy is minimized with respect to the orbital rotation parameters (instead of the HF energy functional) and it depends on occupied orbitals, virtual orbitals ($\{\chi_p\}$) and the t-amplitudes t:

$$E^{OOMP2}[\{\chi_p\}, t] = E^{HF}[\{\chi_i\}] + J_H[\{\chi_p\}, t] \quad . \tag{1.62}$$

Analogously to equation 1.34 an orbital gradient can be obtained with an identical ansatz but more algebra, see reference [39] for the final expression and derivation. The new set of orbitals produced by the OOMP2 ansatz often recovers spin symmetry through incorporation of dynamic correlation in the orbital optimization procedure (in case of artificial spin symmetry breaking of the HF orbitals).

Density-Functional Theory

Density functional theory (DFT) is –by far– the most popular quantum chemical method because of its balance between computational cost and accuracy. Its theoretical foundation lies in the two Hohenberg-Kohn theorems[41] which state:

Theorem 1. *The external potential $v^{ext}(r)$, and hence the total energy, is a unique functional of the electron density $\rho(r)$.*

Theorem 2. *The ground state energy can be obtained variationally: The density that minimizes the total energy is the exact ground state density.*

Therefore, there exists a one-to-one mapping between the electronic energy of the system and the electron density. Instead of computing/approximating the m^N dimensional wave function of a system of N electrons (exponentially growing in complexity), it is sufficient to compute the three dimensional electron density $\rho(\mathbf{r})$ for the same system. The ground state energy can be expressed as a functional of the electron density:

$$E[\rho(\mathbf{r})] = \min_{\rho(\mathbf{r})} \left(F_U[\rho(\mathbf{r})] + \int d\mathbf{r} v_{ext}[\rho(\mathbf{r})] \right) \quad , \tag{1.63}$$

where F_U denotes an (unknown) universal functional and V_{ext} the system specific external potential. The Thomas-Fermi-Dirac functional (TFD)[42] was an early approximation attempt purely based on the electron density for a system with M nuclei:

$$E[\rho(\mathbf{r})] = T_e[\rho(\mathbf{r})] + E_{ee}[\rho(\mathbf{r})] - \sum_A^M \int d\mathbf{r} \frac{Z_A \rho(\mathbf{r})}{|\mathbf{R}_A - \mathbf{r}|} \quad , \tag{1.64}$$

where T_e denotes the kinetic energy functional, E_{ee} electron-electron repulsion energy (containing a Coulomb and exchange part) and $\mathbf{R}_A$ the position of the A^{th} nuclei. Unfortunately

even with several extensions, the accuracy of this orbital free ansatz is poor due to the large error in the kinetic energy functional [43].

Alternatively, orbitals are reintroduced via the Kohn-Sham (KS) framework, which laid the foundation of accurate density functional theory [44]. The kinetic energy is computed via a reference system of non-interacting electrons, which is identical to the true density of the N electron system:

$$T_S = -\frac{1}{2}\sum_i^N \langle\chi_i|\nabla_i^2|\chi_i\rangle \quad , \tag{1.65}$$

where the set of spin orbitals $\{\chi_i\}$ yields the true ground state electron density:

$$\rho_S(\mathbf{r}) = \sum_i^N \sum_{s\in\alpha,\beta} |\chi_i(\mathbf{r},s)|^2 = \rho(\mathbf{r}) \quad . \tag{1.66}$$

The universal functional F_U is separated into:

$$F_U[\rho(\mathbf{r})] = T_S[\rho(\mathbf{r})] + J[\rho(\mathbf{r})] + E_{XC}[\rho(\mathbf{r})] \quad , \tag{1.67}$$

where $J[\rho(\mathbf{r})]$ denotes the classical Coulomb energy functional and E_{XC} denotes the exchange-correlation energy functional, which encapsulates several missing pieces: first, the residual of the true kinetic energy ($T[\rho(\mathbf{r})] - T_s[\rho(\mathbf{r})]$); second, non-classical effects such as the self-interaction correction, exchange and correlation of the electron-electron interaction ($E_{ee}[\rho(\mathbf{r})] - J[\rho(\mathbf{r})]$). The exchange-correlation potential V_{XC} is then defined as the functional derivative of E_{XC}:

$$V_{XC} = \frac{\delta E_{XC}}{\delta\rho} \quad . \tag{1.68}$$

The set of orbitals ($\{\chi_i\}$) can be obtained, similarly to HF, via the Kohn-Sham equations:

$$\hat{f}^{KS}(\mathbf{r}) = \hat{h} + \int d\mathbf{r}\frac{\rho(\mathbf{r})}{|\mathbf{r}-\mathbf{r}'|} + V_{XC} \tag{1.69}$$

$$\hat{f}^{KS}\chi_i = \epsilon_i\chi_i \quad . \tag{1.70}$$

Those equations can be transformed into a set of matrix equations and solved iteratively similarly to the Roothaan-Hall equations (1.23):

$$\underline{\underline{\mathbf{F}}}^{KS}\ \underline{\underline{\mathbf{C}}} = \underline{\underline{\mathbf{S}}}\ \underline{\underline{\mathbf{C}}}\ \underline{\underline{\varepsilon}}\,, \tag{1.71}$$

where $\underline{\underline{\mathbf{F}}}^{KS}$ represents $\hat{f}^{KS}$ in the AO basis; see reference [45] for a detailed derivation. The KS-DFT approach can yield the exact electron density and energy given the exact V_{XC} is used. Unfortunately, the exact exchange-correlation potential is (also) unknown. Several approximations exist and they are organized in different rungs on the so-called Jacob's ladder based on the sophistication of the approximation (see table 1.1) [46]. However in

contrast to wave function methods, there is no guaranteed systematic improvement in the approximation.

The first rung is the local density approximation (LDA); it treats the density as an infinite uniform electron gas to calculate E_{XC}. The exchange-correlation functional only depends on the scalar value of the electron density. The contributions in E_{XC} are split into the exchange (E_X) and correlation (E_C) ($E_{XC} = E_X + E_C$). The exchange term can take the analytic form of the uniform electron gas [47], while the correlation term is approximated, for example, by fitting to quantum Monte-Carlo data in the PW92 functional [48]. This approximation already leads to good predicted molecular geometries, a reasonable description of the molecular electronic structure, and a qualitative description of thermochemistry. However, bond energies are overestimated by up to 20 kcal/mol referenced to high level coupled cluster methods [20].

The second rung contains generalized gradient approximations (GGA). In the GGA formalism, a functional dependence on the reduced spin-density gradient, s_σ, is introduced: $s_\sigma = |\bigtriangledown \rho_\sigma|/\rho_\sigma^{4/3}$, where σ denotes the spin $\sigma \in \{\alpha, \beta\}$, whereas α and β are treated separately. Two of the most popular exchange functionals are PBE [49] and B88 [50]. GGA exchange functionals lead to an improvement in accuracy in comparison to the LDA, yielding semi-quantitative accuracy for a wide range of problems in chemistry [20, 51]. The third rung, called meta-GGA, include the kinetic energy density ($|\nabla\rho(\mathbf{r})|^2$), two popular functionals in this rung are TPSS [52] and M06-L[53].

The fourth and most popular rung in chemistry contains hybrid density functionals. The purely local functional of the previous rungs suffer from (nonphysical) self-interaction error in the Coulomb energy functional, which is not properly canceled in all approximate exchange-correlation functionals.[54, 55] This can be partially alleviated by incorporating Hartree-Fock exchange. On the one hand, LDA and GGA functionals tend to overestimate binding energies. On the other hand, the HF method underestimates these energies. These two can be combined in hybrid functionals to yield improved accuracy. Hybrid GGA functionals combine Hartree-Fock exchange with LDA and GGA exchange and correlation functionals:

$$E_{XC}^{H} = c_x E_x^{HF} + E_{XC}^{DFA} \ , \tag{1.72}$$

where E_x^{HF} is the HF exchange, E_{XC}^{DFA} the density functional approximation to the exchange-correlation energy, and c_x is typically ranging from 0.1 to 0.5. The parameter c_x is usually referred to as the "amount of exact exchange" (given in %). This approach was first proposed by Becke [56] and –by far– the most popular (hybrid) density functional is B3LYP, a combination of the B88 exchange functional and the VWN1RPA and LYP correlation functionals with exact exchange [50, 56, 57]. It achieves overall good accuracy for a wide range of problems [20, 51, 58]. Density functional theory is excellent in modeling interactions in the local region, but fails for large separations. Hartree-Fock has naturally incorporated long range exchange interactions in the exchange integral, but lacks correlation effects that are significant in the local region. Long-range corrected hybrid functionals or range separated hybrids (RSH) combine the strengths of the two by a smooth transition from density functional theory in the short range to Hartree-Fock exact exchange in the long range (up to

100%) [59, 60]. The exchange-correlation functional E_{XC}^{RSH} is defined as follows:

$$E_{XC}^{RSH} = c_x^{LR} E_x^{LR-HF} + c_x^{SR} E_x^{SR-HF} + (1-c_x^{LR}) E_X^{LR-DFA} + (1-c_x^{SR}) E_X^{SR-DFA} + E_C^{DFA} \ , \quad (1.73)$$

where the superscripts LR and SR denote long range and short range, respectively. A popular example is the ωB97X functional. It performs better for standard thermochemistry calculation and greatly reduces errors for problems involving self-interaction [61].

The fifth and final rung contains the double-hybrid functionals and they incorporate not only exact exchange but also a correlated wave function theory such as MP2 (*vide supra*) to further incorporate missing dynamical correlation. Therefore, the energies do not only depend on the occupied KS-orbitals but also on the virtual orbitals. Popular double hybrid functionals are B2PLYP[62] or ωB97M(2)[63].

There exist many strategies for the design of DFAs, which has led to an enormous number of different functionals to date. The number of parameters in the DFA vary significantly from 0 empirical parameters, e.g. in TPSS, to over 40 parameter in MN15 [64]. The highly parameterized functionals can yield very high accuracy for specific energetics or properties but also leads to poor transferability. This makes extensive benchmarking of DFAs an important aspect of DFT. A detailed assessment of the performance of many density functionals for a wide range of systems and properties can be found in references [20, 51, 58].

Rung name	Variable	Example
5. Double hybrid	$\rho(\mathbf{r})$,$\nabla\rho(\mathbf{r})$, $\nabla^2\rho(\mathbf{r})$, { χ_i, χ_a }	ωB97M(2)
4. Hybrid	$\rho(\mathbf{r})$,$\nabla\rho(\mathbf{r})$, $\nabla^2\rho(\mathbf{r})$, { χ_i}	B3LYP
3. meta-GGA	$\rho(\mathbf{r})$,$\nabla\rho(\mathbf{r})$, $\nabla^2\rho(\mathbf{r})$	TPSS
2. GGA	$\rho(\mathbf{r})$,$\nabla\rho(\mathbf{r})$	PBE
1. LDA	$\rho(\mathbf{r})$	SPW92

Table 1.1: Jacob's ladder of density functional approximations.

Several problems occur when DFT is used to describe electronic structure: First, long range dispersion interactions between unbound chemical species are not well reproduced by many commonly used functionals [65]. However, this problem is largely solved in modern density functional theory by Grimme with the addition of an empirical dispersion correction term (E^{D3})[66, 67]:

$$E_{DFT-D3} = E_{KS-DFT} + E_{D3} \ . \quad (1.74)$$

The empirical correction can be added to "traditional" functionals like B3LYP yielding B3LYP-D3. In modern density functionals, the correction is often directly incorporated such as B97-D3[62] and ωB97X-D3[68]. Another less empirical solution to this problem is the development of non-local correlation functionals[69], which is used for example in ωB97M-V[70].

The second problem is poor cancellation between the electron self-interaction present in the Coulomb term and the exchange energy. This error favors delocalized electronic configurations and overestimates their stability. Therefore, reaction barriers are often underestimated if the TS has a more delocalized electronic structure [20]. Another example is the correct relative energy prediction of the different spin states in first row transition metal complexes in the absence of strong field ligands. The calculated spin-state splitting for a given complex varies almost linearly with the proportion of exact Hartree-Fock exchange included in an otherwise constant functional. Increased exact exchange contributions lead to lower relative energies for higher-spin states (or higher energies for low-spin states). As a consequence, pure GGA functionals which do not contain any HF exchange overestimate the stability of the low-spin configurations [58].

Thirdly, the KS-DFT framework uses a single Slater determinant; consequently, it is difficult to describe systems with significant amount of static correlation. A solution is broken symmetry DFT (BS-DFT) in the unrestricted KS framework (UKS).[71–74] In analogy to UHF, α and β spatial orbitals can differ, which results in spin symmetry breaking of the reference determinant as shown in equation 1.27 and is often referred to as a spin-contaminated state. This state yields an electron density which corresponds well to the electron density of the real antiferromagnetic state but qualitatively incorrect spin-densities.[75] The magnetic coupling can be estimated with the Heisenberg-Dirac-van Vleck Hamiltonian ($\hat{H}^{HDvV}$)[76]:

$$\hat{H}^{HDvV} = -J_{ab}\left(\hat{\mathbf{S}}_a \cdot \hat{\mathbf{S}}_b\right) \quad , \tag{1.75}$$

where J_{ab} denotes the magnetic coupling constant between two spin centers a and b and $\hat{\mathbf{S}}_i$ is the spin angular momentum of center i. J_{ab} can be calculated with BS-DFT[77]:

$$J_{ab} = \frac{E^{BS} - E^{HS}}{\langle S^2\rangle^{HS} - \langle S^2\rangle^{BS}} \tag{1.76}$$

where BS denotes the broken symmetry and HS the spin-pure high-spin state. This approach can yield high accuracy for systems with a few centers[78–80] but fails for pathological cases like the multi-metal cluster, e.g. the P-cluster[81].

Energy Decomposition Analysis

"Give us insight and numbers" stated Frank Neese in a recent perspective article on the requirements of modern quantum chemistry [5]. He argues that accurate energies alone are not enough to advance the understanding of pressing chemical problems like nitrogen fixation. Chemists often optimize interactions; thus they face questions such as "How dominant are classical electrostatic interactions?", or "how important are orbital donor-acceptor interactions?". Those insights are invaluable to engineer a given interaction, such as optimizing the second coordination sphere moiety for the binding of CO_2 to a catalyst (see chapter 4). Consequently, energy decomposition analysis methods (EDA) play a vital part in the modern

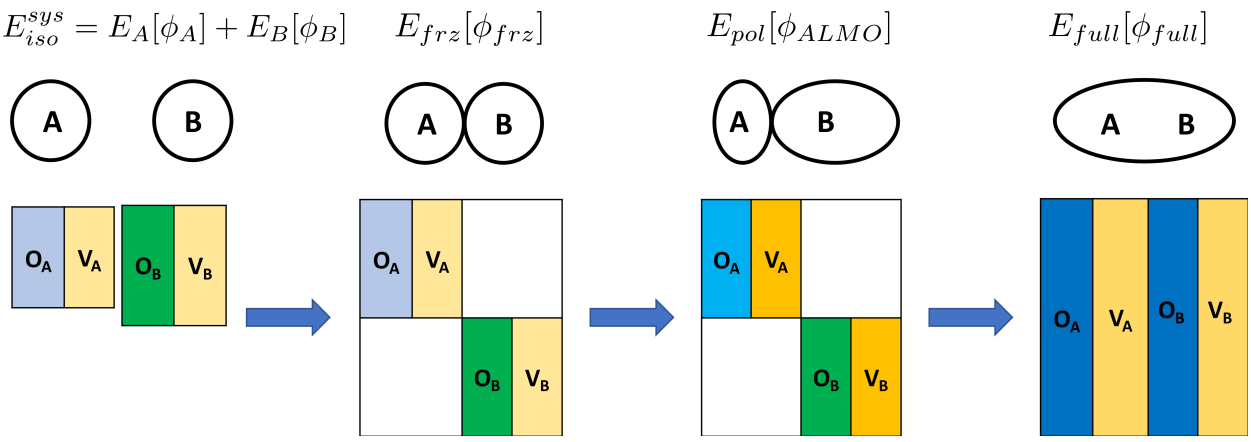

Figure 1.1: Schematic representation of the change of the electron density and the MO coefficient matrix during the ALMO-EDA procedure.

quantum chemist's toolkit to provide in-depth insights into important interactions. Those methods usually aim to decompose the intermolecular binding energy ΔE_{INT} defined for a molecular complex comprising F molecules:

$$\Delta E_{INT} = E_{TOT} - \sum_{i=1}^{F} E_i \quad , \tag{1.77}$$

E_{TOT} denotes the electronic energy of the supersystem and E_i the electronic energy of the i^{th} fragment (individual molecule).

Unfortunately, there is no unique approach to such a decomposition; hence, several schemes are available with different philosophies leading to controversial discussions [82]. This thesis focuses on the absolutely localized molecular orbital EDA (ALMO-EDA) scheme[83, 84] and is based on a recent review article [85]. The binding energy is decomposed in four terms:

$$\Delta E_{INT} = \Delta E_{GD} + \Delta E_{FRZ} + \Delta E_{POL} + \Delta E_{CT} \quad , \tag{1.78}$$

where ΔE_{GD} denotes the geometry distortion energy, ΔE_{FRZ} the frozen energy, ΔE_{POL} the polarization energy and E_{CT} the charge transfer energy. These four terms correspond to energy differences of five intermediate states with different constraints explained below and shown in figure 1.1. First, the energies are calculated fragmentwise with the optimized geometries of the m isolated molecules: $E_{iso} = \sum_i E_i$, which corresponds to the reference state of ΔE_{INT}. Second, the frozen intermediate energy is computed from the isolated fragments evaluated at the system geometry: $E_{iso}^{sys} = \sum_i E_i^{sys}$, where E_i^{sys} denotes the unconstrained electronic energy of the i^{th} molecule at the supersystem geometry. The energy distortion term is then defined as: $\Delta E_{GD} = E_{iso}^{sys} - E_{iso}$ and comprises the energy required to distort isolated molecules in the geometry they adopt in the supersystem complex.

Third, the frozen state energy E_{frz} is computed for the supersystem with "frozen" orbitals. The frozen orbitals are subject to the constraint that the orbitals of the isolated fragments are unmodified (taken from the E_i^{sys} states), denoted ϕ_i for the i^{th} fragment; the union of all frozen orbitals of each fragments form the supersystem frozen MOs: $\phi_{FRZ} = \phi_1 \oplus \phi_2 \oplus ... \oplus \phi_m$. This constraint excludes any energy lowering due to polarization and charge transfer. The frozen energy is then defined as: $\Delta E_{FRZ} = E_{frz} - E_{iso}^{sys}$. It contains the following physical components: (i) classical electrostatics, (ii) dispersion, (iii) Pauli repulsion (see below for a detailed definition of these components). The energy contribution of each component can be separated by further decomposition of the frozen energy [86]:

$$\Delta E_{FRZ} = \Delta E_{ELEC} + \Delta E_{DISP} + \Delta E_{PAULI} \quad . \tag{1.79}$$

Fourth, the polarized state energy E_{pol} is obtained using an SCF-MI procedure described in the HF section (SCF-MI can likewise be performed with KS-DFT). It allows for orbital rotation on each fragment while keeping the fragment block structure of the MO coefficient matrix. This constrained SCF procedure yields the ALMOs which, by construction, do not allow charge transfer between fragments but polarization of each fragment. The polarization energy is defined as $\Delta E_{POL} = E_{pol} - E_{frz}$.

Fifth, an unconstrained final state calculation yields delocalized canonical orbitals of the supersystem complex ϕ_{full}. The charge transfer energy can be decomposed in pairwise donor-acceptor orbital interactions [87, 88].

The following passage defines each physical component of the EDA briefly:

Classical electrostatics are the Coulomb interactions of the charges and charge distributions of the fragments, it can be expressed for two fragments A and B in the non-overlapping limit as

$$\Delta E_{elec}(AB) = \iint d\mathbf{r}_1 d\mathbf{r}_2 \rho_A(\mathbf{r}_1) \frac{1}{\mathbf{r}_{12}} \rho_B(\mathbf{r}_2) \quad ,$$

where ρ_i denotes the total (electron and nuclei) charge distribution of fragment i. It can either be repulsive or attractive and has polynomial distance dependence with $1/R$ for charged-charged fragments, $1/R^2$ for ion-dipole interactions and so on.

Dispersion or London force, is an quantum mechanical attractive interaction. Correlated electron fluctuations lead to favorable induced dipole–induced dipole interactions. The interaction is usually weak but becomes significant for large systems as it grows with the number of electrons. The leading long range decay is $1/R^6$.

Pauli Repulsion arises from the overlap of the electron densities of the fragments when compressed into the supersystem complex. The anti-symmetry requirement of the fermionic wave function forbids electrons with the same spin to occupy the same space. Therefore, the Pauli repulsion "force" distorts the fragment electron densities, which is accompanied by a loss of kinetic energy reflected in the (repulsive) Pauli repulsion energy. As it depends on the overlap of orbitals, it decays exponentially with distance ($e^{-\alpha R}$).

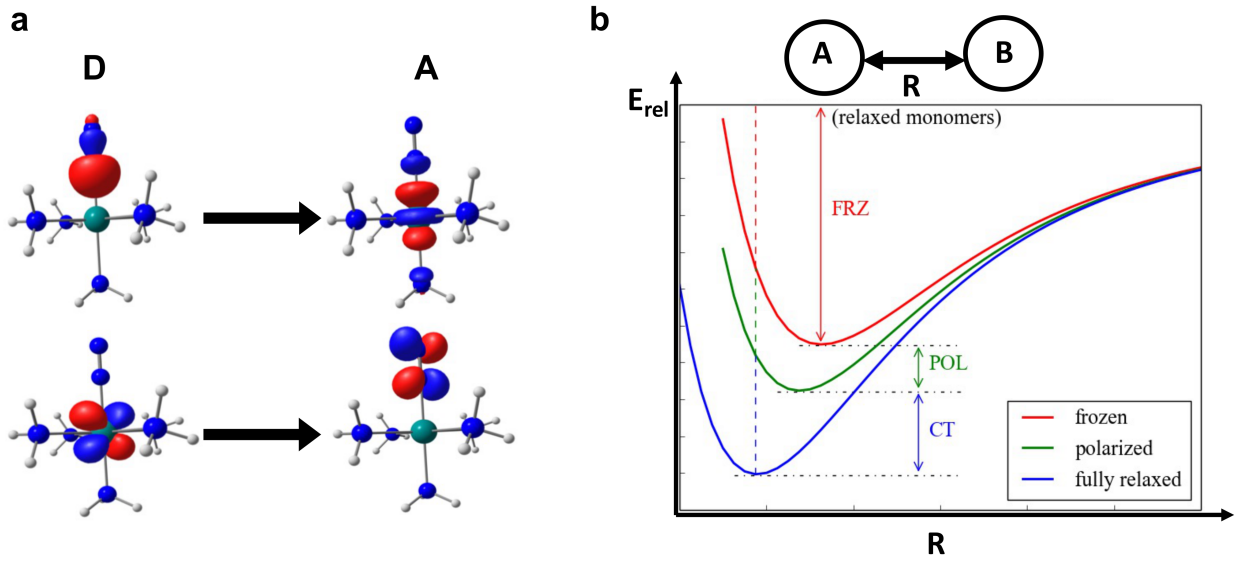

Figure 1.2: a) key donor-acceptor orbital pairs of the charge transfer for a $N_2{-}[Ru(II)(NH_3)_5]^+$ complex; b) schematic PES for the frozen, polarized and fully relaxed PES for in the adiabatic EDA picture (relative energies against the isolated monomer energy).

Polarization describes favorable intra-fragment relaxation of the electron densities due to the presence of the other fragments in the supersystem. Thus, polarization can be understood as the response of the fragment's electron density to the rest of the complex. In the long range it is dominated by the response to the electric field of the remaining complex. Thus, the leading long range decay is $1/R^4$ when a dipole responds to a monopole field.

Charge Transfer is the inter-molecular orbital mixing between donor and acceptor orbitals from different fragments such as a dative bond from a Lewis base to a Lewis acid. The charge transfer energy decays exponentially as it depends on the overlap of the orbitals ($e^{-\alpha' R}$). The important donor and acceptor orbitals can be extracted from the EDA calculation with a pair-wise charge transfer decomposition scheme[87, 88] and are illustrated for a pentaamine(dinitrogen)ruthenium(II) complex ($N_2{-}[Ru(II)(NH_3)_5]^+$) in figure 1.2 (a). The key CT orbitals recover the well established Dewar–Chatt–Duncanson model [89, 90] for π-acidic ligand (such as N_2) with σ forward donation and π back bonding.

The EDA scheme introduced above is evaluated at a single geometry (aside from the geometric distortion term), and therefore is commonly denoted as vertical EDA (vEDA). However, the definition of the new intermediate energy states (E_{frz} and E_{pol}) allows one to optimize the geometry or compute observables such as the vibrational modes at those constrained intermediates. This yields for example bond distances without the effect of charge transfer on the polarized surface or allows one to probe the effect of electrostatics,

polarization or charge transfer on the blue shift in certain hydrogen bonds' vibrational frequencies[91]. In addition, the adiabatic energy decomposition (aEDA) can be defined, where the complex geometry is optimized on each surface; as illustrated here for the polarization energy ΔE^{ad}_{POL}:

$$\Delta E^{ad}_{POL} = E_{pol}(\mathbf{R_{pol}}) - E_{frz}(\mathbf{R_{frz}}) \tag{1.80}$$

where $E_{pol}(\mathbf{R_{pol}})$ denotes E_{pol} at the optimal geometry on the polarized surface ($\mathbf{R_{pol}}$) and $E_{frz}(\mathbf{R_{frz}})$ denotes E_{frz} at the optimal geometry on the frozen surface ($\mathbf{R_{frz}}$). This concept is illustrated schematically in figure 1.2 (b).

1.3 Computational Catalysis

> *"In theory there is no difference between theory and practice, while in practice there is"* -Benjamin Brewest

Computational chemistry has become a core part of catalysis research as modeling of the reaction mechanism can provide vital insights into the catalytic pathway. It is possible to predict complete catalytic pathways based on thermodynamics and kinetics, identifying transient intermediates and transition states. This can be achieved by employing state-of-the-art electronic structure methods to compute –among many examples– Gibbs free energies, reaction rates, redox potentials and pK_a values. In addition, these calculations provide electronic structure information about key intermediates, such as the localization of additional electrons upon reduction. These insights illuminate intrinsic limitation in catalytic rates, degradation pathways, the origin of selectivity and form the basis of rational improvements and design of catalysts. The success of computational catalysis studies for a broad spectrum of topics in homogeneous catalysis is illustrated by these review articles [92–96] and in particular for homogeneous CO_2 reduction in reference [97].

Despite this indisputable success, computational mechanistic studies must employ simplifications in order to simulate complex reaction conditions in a feasible manner. Consequently, it is not (yet) possible to obtain a comprehensive mechanistic picture solely by computational studies. Noyori and Richmond express their scepticism about computational catalysis quite dramatically: *"The conclusions derived from an unrealistic assumption are far from truth, and confuse and mislead the community"* and further note: *"We should appreciate solid experimental evidence more than frivolous computations. This prevailing trend is harmful to the community"*[98]. This illustrates the importance of cross-validation of both experimental and computational findings to synthesize robust mechanistic insights. The quantum chemistry methods and models must be carefully calibrated and supplemented by experimental methods, prediction errors estimated and the robustness of the findings probed. There are various experimental methods which can be used to cross validate computational findings, for example, cyclic voltammetry, X-ray diffraction, Mössbauer spectroscopy, X-ray absorption spectroscopy and stopped-flow kinetics technique. The interested reader is referred to references [99] and [100].

This section presents the conceptional framework for the modelling of catalytic cycles and major challenges that must be addressed to avoid *"frivolous computations"*. The presentation focuses on the modelling of homogeneous CO_2 reduction catalysis as chapters 6–8 are concerned with mechanistic studies of various homogeneous electrocatalysts for the two-proton two-electron reduction of CO_2 to CO. There are several factors which govern the success of computational catalytic mechanism studies; they are briefly outlined below and closely follow reference [101]:

- Accurate electronic energies
- Treatment of enthalpic and entropic effects

- Solvation
- Kinetic Model
- Conformer Analysis

These topics are discussed in the following sections; lastly, a brief overview is given on artificial photosynthesis, namely the role of CO_2 reduction reaction (CO2RR) and the importance of efficient catalysts to motivate the mechanistic studies in sections 6–8.

Calculation of Thermodynamic Properties

In this section the methods used to calculate thermodynamic properties are introduced; namely the reaction free energy in different standard states, acid dissociation constants (pK_a values) and reduction potentials. In addition, the limits and accuracy are elucidated to allow for a comparison to experimental data.

Electronic Energies

The electronic energy E_{el} constitutes the main part of the free energy and consequently any inaccuracies translate to large inaccuracies in the free energy calculations. The most popular electronic structure method is -without a doubt- KS-DFT (see section 1.2). DFT offers the best compromise between accuracy and speed for typical systems in computational catalysis ($>$ 50 atoms, containing transition metals), with a formal scaling of $\mathcal{O}(N^4)$ [20, 51, 102].

Alternative correlation wave function methods such as perturbation theory or coupled cluster based methods perform poorly [39, 103] unless higher order terms are included making them computationally unfeasible for larger systems [104]. A promising alternative to DFT are local approximation of correlation methods such as local coupled cluster but their usage requires careful tuning of various parameters to obtain both accurate and fast results [105–107].

However regarding DFT calculations, a daunting question remains: Which functional should be used? The number of available DFT functionals is enormous and (quickly) growing; for example, over 200 DFT functionals are available in the Q-Chem software package[108]. Unfortunately, the optimal functional is highly system specific and therefore screening of various DFT functionals for the problem at hand is essential. In the case of homogeneous electrocatalysis for CO_2 reduction, first row transition metal complexes with bulky chelating ligands and a weak ligand field are used as catalysts. These systems have small spin gaps and several possible stable coordination geometries. Both coordination geometry and spin state greatly influence reaction pathways; thus, a high prediction accuracy is necessary. Different DFT functionals will produce biased results based on their parameters: First, the spin gap (energy difference between the high-spin and low-spin configuration) in transition metal complexes depends almost linearly on the amount of exact exchange used in the functional.

As a consequence, local GGA functionals, which do not contain any HF exchange, overestimate the stability of the low-spin configuration and functional with a large amount of exact exchange will favor the high-spin configuration [58]. The recommendations for the accurate prediction of spin gaps also varies dramatically in the literature from 0% exact exchange [109] to 15%[110] and 20% – 30% [111]. The spin state bias is illustrated in figure 1.3 for an iron(II) d^6 complex (investigated in more detail in chapter 8). The experimentally determined spin gap is $\sim$ 1kcal/mol (favoring the low-spin configuration) and DFT functionals predict a wide range of different energy gaps.

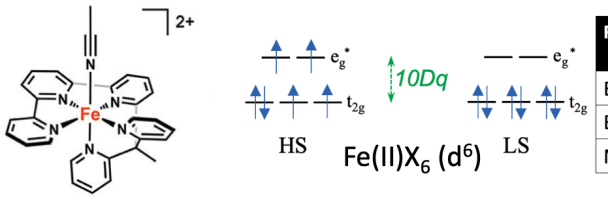

Functional	HF-exchange [%]	Spin Gap [kcal/mol]
B97-D	0	8.9
B3LYP	20	1.1
MN15	44	−2.3

Figure 1.3: Illustration of the functional dependence of the spin gap in an iron(II) complex.

Second, long range dispersion forces are not included in many density functionals. This can systematically bias results towards lower coordination numbers if the dative bonds to the metal are weak. However, this shortcoming of DFT can readily be addressed by empirical dispersion corrections [66, 112] or nonlocal correlation functionals[69]. Many modern density functionals include these by default such as B97-D[62] or ωB97M-V [70].

Third, reaction barriers are often underestimated if the transition state has a more delocalized electronic structure. This originates from poor cancellation between the electron self-interaction present in the Coulomb term and the exchange energy. This error favors delocalized electronic configurations and overestimates their stability. Consequently, local functionals with no exact exchange like B97-D underestimate barrier heights significantly; this is illustrated in the comprehensive review [20] (figure 26) where B97-D exhibits RMSDs for barrier height of $\sim$8 kcal/mol and RSHs like ωB97M-V with 100% long range and 15% short range exact exchange exhibits RMSDs of $\sim$2 kcal/mol.

Fourth, static or strong correlation cannot properly be described by DFT within the KS framework as it generates densities from a single Slater-determinant. Problems with static correlation can for example arise in reduced intermediates of a catalytic cycle. In many cases the additional electrons localize in non-innocent ligand moieties and are stabilized by exchange interactions with unpaired electrons at the metal center (see chapters 6–8). These weak metal-ligand bonds have small energy gaps between bonding and anti-bonding orbitals resulting in partial occupation of various orbitals. Thus, multi-determinant wave function methods such as complete active space SCF (CASSCF) are required to describe this bonding situation properly. However, in many cases broken-symmetry DFT can be used (see section 1.2). This approach can yield remarkably high accuracy [78–80] although it is known to fail for pathological cases [81]. Unfortunately, the accuracy of BS-DFT prediction

is functional- and system-dependent.[113] Specifically for polypyridyl complexes investigated in this study local functionals predict more accurate results [114, 115]. Therefore, it requires deep understanding of the electronic structure of the targeted system to recognize if BS-DFT can be used and if so to converge the SCF to the target BS-DFT state [103].

Fifth, converging results (close) to the basis set limit is desirable to avoid basis set artifacts. A small basis will bias results towards higher coordination numbers because of the basis set superposition error [116]. In case of DFT a triple zeta (preferably quadruple zeta) basis can typically yield results sufficiently close the basis set limit [20]. However, for wave function methods larger basis sets or extrapolation schemes are necessary [117]. The most economical compromise (also used in this thesis work) between accuracy and cost is to run the geometry optimization and frequency calculation with a smaller basis set, followed by a single point calculation with a larger basis set.

Calculation of Gibbs Free Energies

The electronic energy E_{elec} obtained from quantum chemistry refers to the energy of a single molecule in vacuum at 0 K. This is seldom a good approximation for chemistry. Most reactions happen at finite temperature and in macroscopic quantities. Therefore, these large ensembles of molecules are governed by macroscopic properties such as the Gibbs free energy or enthalpy. This section briefly summarizes the key approximations and equations which make it possible to augment electronic energies to obtain these desired thermodynamic quantities. This section is based on reference [10].

The core approximation for this procedure is the ideal gas approximation: The system is treated as a canonical ensemble of an ideal gas (fixed temperature T, volume V and particle number N) with an ensemble partition function $Q(N, V, T)$. The ideal gas approximation reduces the ensemble partition function Q to be only expressed in terms of the partition function of a single molecule q:

$$Q(N, V, T) = \frac{q(V, T)^N}{N!} \quad . \tag{1.81}$$

Furthermore, the molecular partition function q is assumed to be separable into electronic, translational, rotational and vibrational contributions:

$$q(V, T) = q_{elec}(T) q_{trans}(V, T) q_{rot}(T) q_{vib}(T) \quad . \tag{1.82}$$

The desired thermodynamic properties can be obtained by partial differentiation of Q. The internal energy U is defined as

$$U = k_B T^2 \left(\frac{\partial ln Q}{\partial T} \right)_{N,V} \quad , \tag{1.83}$$

where k_B denotes the Boltzmann's constant and the enthalpy H is defined as

$$H = U + PV \quad . \tag{1.84}$$

The entropy S is defined as

$$S = k_B lnQ + k_B T \left(\frac{\partial lnQ}{\partial T} \right)_{N,V} \tag{1.85}$$

and Gibbs free energy G is given by:

$$G = H - TS \quad . \tag{1.86}$$

The separability of the partition function results in additive contributions to U and S:

$$U = U_0 + U_{elec} + U_{trans} + U_{rot} + U_{vib} \tag{1.87}$$

$$S = S_{elec} + S_{trans} + S_{rot} + S_{vib} \tag{1.88}$$

The internal energy U at 0 K is defined as:

$$U_0 = E_{el} + \epsilon_{ZPE} \quad , \tag{1.89}$$

where ϵ^{ZPE} denotes the zero-point vibrational energy. The vibrations of the molecule are approximated by a harmonic potential around the stationary point (geometry) on the Born-Oppenheimer PES. The correction term arises then from the quantum mechanical treatment of the harmonic oscillator where the lowest vibrational energy level is not zero. ϵ^{ZPE} is defined as:

$$\epsilon^{ZPE} = \frac{1}{2} \sum_{i}^{M} \hbar \omega_i \quad , \tag{1.90}$$

where $\hbar$ denotes the reduced Planck's constant, ω the vibrational frequency and M the number of vibrational modes.

The individual contributions to the partition function from equation 1.82 are discussed below:

Electronic Contributions: The electronic partition function is usually set to be simply $q_{elec} = 1$, assuming no degeneracy at the ground state and large energy gaps between the electronic ground state and excited states. Thus, the contribution to both the internal energy beyond U_0 and the entropy are zero.

Translational Contributions: The molecule is treated as a particle in a large cubic box with volume V which yields the following partition function:

$$q_{trans}(V,T) = \left(\frac{2\pi M k_B T}{h^2} \right)^{3/2} V \quad , \tag{1.91}$$

where M denotes the molecular mass. This yields the following contributions:

$$U_{trans} = \frac{3}{2} RT \quad , \tag{1.92}$$

where R denotes the gas constant and the entropy is defined as

$$S_{trans} = R\left(ln\left(\left[\frac{2\pi M k_B T}{h^2}\right]^{3/2}\frac{V}{N_A}\right)+\frac{5}{2}\right) \quad . \tag{1.93}$$

In the standard state V corresponds to 24.5 L (1 atm and 298 K).

Rotational Contributions: The molecule is treated as a quantum mechanical rigid-rotor which yields the following partition function (for a general case):

$$q_{rot}(T) = \frac{\sqrt{\pi I_A I_B I_C}}{\sigma}\left(\frac{8\pi^2 k_B T}{h^2}^{3/2}\right) \quad , \tag{1.94}$$

where I_X denotes a principal component of inertia. This results in the following contributions:

$$U_{rot} = \frac{3}{2}RT \tag{1.95}$$

$$S_{rot} = R\left(ln\left(\left[\frac{8\pi^2 k_B T}{h^2}\right]^{3/2}\frac{\sqrt{\pi I_A, I_B, I_C}}{\sigma}\right)+\frac{2}{2}\right) \tag{1.96}$$

Vibrational Contributions: The vibrations of the molecules are assumed to be separable and are approximated as quantum harmonic oscillators. This results in the following partition function (assuming a non-linear molecule):

$$q_{vib}(T) = \prod_i^{3K-6}\frac{1}{1-e^{-h\omega_i/(k_B T)}} \quad , \tag{1.97}$$

where K denotes the number of atoms. This results in the following contributions:

$$U_{vib} = R\sum_i^{3K-6}\frac{h\omega_i}{k_B(e^{h\omega_i/k_B T}-1)} \tag{1.98}$$

$$S_{vib} = R\left[\sum_i^{3K-6}\frac{h\omega_i}{k_B T(e^{h\omega_i/k_B T}-1)} - ln\left(1-e^{-h\omega_i/k_B T}\right)\right] \quad . \tag{1.99}$$

Solvation

The accurate but efficient description of solvation effects is crucial for catalytic pathways. Ideally the effect of solvation is treated with full molecular simulations and statistical mechanics, for example the role of thermal flucuation was identified to be critical for binding of CO to the electrocatalyst in heterogeneous catalysis.[118] However, implicit solvation models offer the best compromise between accuracy and computational cost and are, therefore, used most commonly. The polarizable continuum model (PCM)[119, 120] treats the solvent

as a polarizable medium with a dielectric constant ϵ, which differs for each solvent, e.g. ϵ(MeCN) = 35.7. The cavity is constructed from a union of atom-centered spheres using different radii for each atom (UFF radii or Bondi radii[121]). The electric charge distribution of the molecule will polarize the medium, which in turn acts back on the solute, thereby producing an electrostatic stabilization inducing a change in the electronic structure of the solute. The interaction with the solvent model must therefore be calculated via an iterative procedure. In addition to the electrostatic contribution, dispersion interactions between solute and solvent lead to further stabilization and are included empirically in some models such as the SMX models[122] (though not PCM itself).

The solvation free energy is approximated as the energy difference between the gas phase electronic energy E_{gas} and the implicit solvation electronic energy E_{solv}:

$$\Delta G_{solv} \approx E_{solv} - E_{gas} \ . \tag{1.100}$$

The models are parameterized to estimate solvation free energies and build upon the models described above to estimate free energies in the gas phase. The accuracy is quite remarkable for uncharged species in polar solvents typically within 1 kcal/mol versus experiment. The error is larger for charged species with up to 5 kcal/mol (for small organic molecules and ions).[123] This difference in accuracy for charged and neutral species introduces biases for reaction steps where the charge changes during the reaction, for example, a reduction process or a protonation; see further discussion below. The performance for charged systems can sometimes be improved by adding a single explicit solvent molecule to incorporate an additional explicit local solute-solvent interaction. This improves solvation energies of systems where the charge is localized on a few exposed heteroatoms. By helping to account for strong hydrogen bonding interactions between the anion and the solvent [124]. However, one drawback of this method is how to decide when to incorporate explicit solvent molecules and for bigger systems one must determine the number of water molecules and their optimal position.[125]

Furthermore, the change in the standard $\Delta G^{\circ\rightarrow *}$ state from 1 atm in the gas phase to 1 M in solution must be taken into account (for a detailed derivation see Ref [125]):

$$\Delta G^{\circ\rightarrow *} = RT \cdot ln(24.4654) = 1.89 \text{ kcal/mol} \qquad (\text{for } T = 298 \ K) \ . \tag{1.101}$$

Therefore, the Gibbs free energy in solution ΔG°_{solv} is defined as:

$$G^{\circ}_{solv} = G^{\circ}_{gas} + \Delta G_{solv} + \Delta G^{\circ\rightarrow *} \ . \tag{1.102}$$

This allows to compute reaction energies of m products and n reactants:

$$\Delta_R G^{\circ}_{solv} = \sum_i^m a_i G^{\circ}_{solv}(i) - \sum_j^n a_j G^{\circ}_{solv}(j) \quad , \tag{1.103}$$

where a_x denotes the stochiometric reaction coefficient.

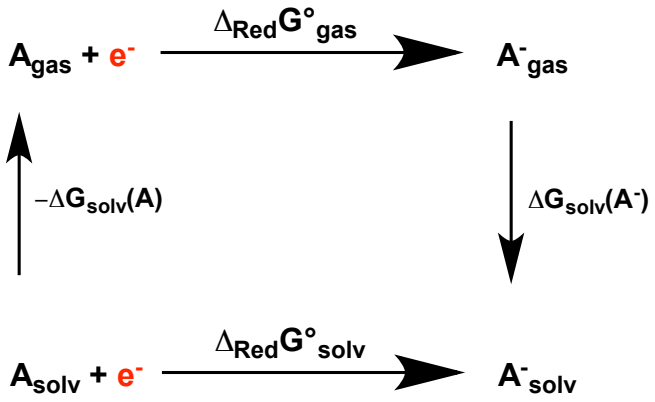

Figure 1.4: Thermodynamic cycle for calculating the change in free energy during a redox process.

Calculation of Reduction Potentials

The change in Gibbs free energies for a reduction event in solution $\Delta_{Red}G^{\circ}_{solv}$ is obtained by the thermodynamic cycle depicted in figure 1.4:

$$\Delta_{Red}G^{\circ}_{solv} = G^{\circ}_{gas}(A^{-}) + \Delta G_{solv}(A^{-}) - G^{\circ}_{gas}(A) - \Delta G_{solv}(A) \ . \tag{1.104}$$

The Gibbs free energy change is then used to calculate an absolute potential via:

$$E^{abs}_{calc} = -\frac{\Delta_{Red}G^{\circ}_{solv}}{nF} \ , \tag{1.105}$$

where F is the Faraday constant and n the number of electrons. However, experimental potentials are always reported versus a reference electrode like the standard hydrogen electrode. Therefore, the absolute potential of a reference electrode ($E^{abs}_{exp}(Reference)$) must be subtracted from E^{abs}_{calc} to obtain comparable values (the unit and reference are given in brackets):

$$E^{0}_{calc}[V \text{ vs Reference}] = E^{abs}_{calc}[V] - E^{abs}_{exp}(\text{Reference})[V] \ . \tag{1.106}$$

These absolute values are experimentally determined [126]. However, the values of the reference electrode can vary from experiment to experiment, depending on the solvent, electrolyte and the reference electrode itself. The experimental variations as well as the systematic errors introduced by the theoretical approach (i.e. choice of functional, basis set and solvent model) usually lead to deviations of approximately 200 mV relative to the experiment [127].

Alternatively and often more satisfactory, experimental redox potentials can be reported with respect to a reference couple (RC), e.g. the Ferrocene/Ferrocenium couple ($[Fc]^{0/+}$) as an internal standard.

$$E^{0}_{exp}[V \text{ vs RC}] = E^{0}_{exp}[V \text{ vs Reference}] - E^{0}_{exp}(\text{RC})[V \text{ vs Reference}] \ , \tag{1.107}$$

where E^0_{exp} is the experimental redox potential.

The same approach can be used for the reduction potentials calculated with DFT. Using a reference couple as internal reference, a reduction of the systematic error is achieved with accuracy of ~ 100 mV compared to experimental values [128]. This improved accuracy can be explained by both the decrease in the computational systematic error because of favorable error cancellation and preclusion of an experimentally measured absolute potential. The origin of the systematic errors in the calculations are extensively discussed in section 1.3. The potentials are calculated as follows:

$$E^0_{calc}[V \text{ vs RC}] = E^{abs}_{calc}[V] - E^{abs}_{calc}(\text{RC})[V] \ . \tag{1.108}$$

To minimize systematic errors the internal references should be measured under the exact same experimental conditions and computed with the exact same level of theory. In addition, the internal reference should contain a transition metal of the same row [128]. Therefore, in this thesis the $Fc^{0/+}$ couple was used as an internal reference.

Calculation of pK_a Values

The pK_a value is used by chemists to classify the acidity of a molecule. Its calculation using only first principals quantum mechanical methods is briefly introduced in the following. This section is based on the two reviews [125, 129] and they should be consulted for further details. For the acid dissociation reaction of an acid HA in a solvent S the following equilibrium can be formulated:

$$HA_s \rightleftharpoons A^-_s + H^+_s \tag{1.109}$$

and the associated equilibrium constant K_a can be calculated:

$$K_a = \frac{[\text{A}^-][\text{H}^+]}{[\text{HA}]} \ , \tag{1.110}$$

where [HA], [A^-] and [H^+] correspond formally to the activities of the acid HA, the corresponding base A^- and a proton. However, in practice simple concentrations are used for liquid systems with low acid concentrations. The pK_a is then defined as:

$$pK_a = -log(K_a) \ . \tag{1.111}$$

K_a can also be calculated from the Gibbs free reaction energy $\Delta_r G^\circ_{solv}$:

$$\Delta_r G^\circ_{solv} = -RTln(K_a) = -2.303 \cdot RTlog(K_a) \ . \tag{1.112}$$

Since the Gibbs free energy is a state function, a thermodynamic cycle can be used to obtain $\Delta_r G^\circ_{solv}$. It is calculated according to the cycle depicted in figure 1.5:

$$\Delta_r G^\circ_{solv} = G^\circ_{solv}(A^-) + G^\circ_{solv}(H^+) - G^\circ_{solv}(HA) \ . \tag{1.113}$$

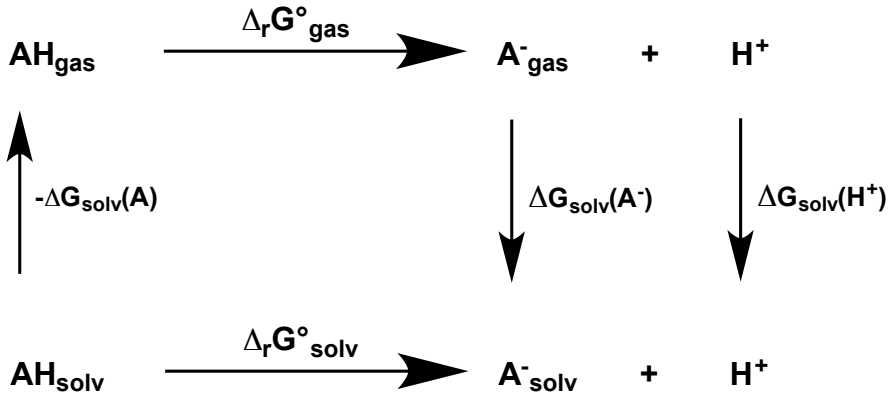

Figure 1.5: Thermodynamic cycle for calculating the change in free energy for the dissociation of an acid HA. The free energies of HA and A^- are obtained from converged gas phase calculations and the solvation energies from C-PCM calculations. For the free energy of the proton the experimental value −264.58 kcal/mol is used (see text for details).

The Gibbs free energies of HA and A^- are obtained in the same way as illustrated earlier in this section. However, the Gibbs free energy of a proton cannot be calculated using quantum chemical methods because it does not have any electrons. $G^\circ_{gas}(H^+)$ can be calculated using the Sackur-Tetrode equation yielding −6.28 kcal/mol for 1 M in the standard state at 298 K and 1 atm pressure [125]. Unfortunately, the value for the solvation energy $\Delta G_{solv}(H^+)$ is less certain and different values have been reported in recent years because it is difficult to measure an isolated ion [125]. The value which is currently used is −260.2 kcal/mol for 1 M in the standard state [130]. This value is also used in the computational CO_2 reduction literature [131–133]. Furthermore, the change in standard state from 1 atm gas phase to 1 M solution phase must be taken into account which is 1.89 kcal/mol at 298 K. Adding up these values leads to $G^\circ_{solv}(H^+) = -264.6$ kcal/mol. Employing this experimental value makes it challenging to compute accurate pK_a values because an error of only 1.36 kcal/mol leads to a deviation of 1 pK_a unit [134]. Besides the already discussed error due to introducing experimental solvation values, other factors need to be considered to minimize errors in the pK_a calculations.

The greatest source of error is the calculation of the solvation energies of A^- and HA. This leads to a different accuracy in solvation energies of the acid HA and the base A^-. Therefore, the difference $\Delta\Delta G_{solv}(HA)$, which is defined as:

$$\Delta\Delta G_{solv}(HA) = \Delta G_{solv}(A^-) - \Delta G_{solv}(HA) \ , \tag{1.114}$$

is dominated by the solvation energy of the anion; thus, the systematic errors tend to *not* cancel out. This is one of the main reasons for the deviations of experimental and calculated pK_as. The RMSD error for a set of small neutral (in)organic acids is 4–11 units [133, 135].

Another way to avoid the experimental value of $G^{\circ}_{solv}(H^+)$ and have error cancellation in both the gas phase reaction and solvation energies is the isodesmic reaction scheme [125, 129, 136]. Instead of a direct calculation of the dissociation reaction, the difference is calculated to a known reference system (BH):

$$HA_s + B_s^- \rightleftharpoons A_s^- + BH_s$$

and with the associated $\Delta_r G^{\circ}_{solv}$ and the known pK_a of the reference the pK_a is calculated:

$$pK_a(HA) = \frac{\Delta_r G^{\circ}_{solv}}{2.303RT} + pK_a(BH) \ . \tag{1.115}$$

In this reaction the usage of a proton is avoided; in addition, the net charge on both sides of the reaction is balanced, which allows cancellation of the systematic error in the solvation energies for charged species. This approach has the capability to produce Gibbs free reaction energies within a few tenth of a kcal/mol for organic acids in various solvents yielding considerably more accurate pK_a values [129]. In case of transition metal systems, the pK_a prediction for hydride complexes of the first, second and third transition metal row achieved an accuracy of 1.9 pK_a units using the same reference for all molecules [136]. However, this approach is only valid if the pK_a of a reference system is known and also similar to the unknown one. Furthermore, the degree of error cancellation also depends on the similarity of the investigated and reference system in electronic structure and geometry.

A similar approach is presented by Muckerman *et al* [135], they also realized the significance of the systematic solvation error $\Delta\Delta G_{solv}$ and suggested a linear correction by fitting a training set of acids to their experimental values in order to obtain a correction term for $\Delta_r G^{\circ}$. They were able to reduce the RMS significantly for a test set of neutral acids from 11.3 to 1.3 pK_a units with this approach and claim an accuracy of 2 units. They emphasize the importance of choosing a suitable training set for each problem, e.g. they classified different training sets for neutral and cationic acids. This ansatz has the same problems as the above discussed isodesmic reaction approach.

The systems investigated in this thesis do not have suitable reference molecules for the isodesmic ansatz. In addition, the calculation of explicit solvent molecules for every protonated species is not tractable. Therefore, all pK_a values are directly calculated using $G^{\circ}_{solv}(H^+) = -264.6$ kcal/mol but as extensively discussed in this section the values should only be compared to each other but not to experimental values due to uncertainties. However, work in this thesis computes free energies for the protonation reactions with carbonic acid H_2CO_3 instead of a proton. This has two advantages, it resembles the experimental conditions and leads to better error cancellation in the computation as the charge is conserved over the reaction step.

Kinetic Model

Accelerating the overall reaction rate k is the core ability of a catalyst. Thus, catalysis is an intrinsically kinetic effect which should be reflected in the modeling. The metric of a

catalyst activity is the turnover frequency (TOF) number of cycles per catalyst per second:

$$TOF = \frac{N}{[C]t} \quad , \tag{1.116}$$

where N denotes the total turnover number of cycles, $[C]$ the catalyst concentration and t time (assuming first order in the catalyst and in the steady state). The whole cycle can be decomposed in a series of elemental reaction steps with rates $k_1, k_2, ..., k_n$ and reaction free energies $\Delta_r G_1, \Delta_r G_2, ..., \Delta_r G_n$. However, experimentally only the overall rate k and free energy $\Delta_r G$ can be determined.

The Eyring Theory connects the k_x of a single elementary step with stationary points on the PES: reactants (minima) and transition states (saddle points). The activation energy $\Delta G^{\ddagger}_{solv}$ is defined as the Gibbs free energy difference between the TS and the reactants. The rate constant k of a reaction depends on $\Delta G^{\ddagger}_{solv}$:

$$k = \frac{k_B T}{h}\, e^{-\Delta G^{\ddagger}_{solv}/RT} \ . \tag{1.117}$$

In a first approach to compute the overall TOF, all the elementary steps of the cycle can be coupled with quasi-stationary concentrations, which leads to complicated systems of equations [137]. A second approach is to estimate the overall TOF from the slowest elementary step in the cycle: $TOF \approx k_x$ and the associated reactant and transition state are denoted rate limiting intermediate and rate limiting step. This approach, however, is a crude approximation especially if multiple steps are important or if the rate limiting intermediate is not in the same step as the transition state. A third approach is the energetic span model, which is currently one of the most popular models [138–140].

This model connects the free energy landscape of the DFT based catalytic cycles with the experimentally measured turnover frequencies using Eyring transition state theory. The model couples the elementary reaction steps in the energy representation (the natural representation of quantum chemistry) instead of the rate representation discussed above. The key assumption behind the energetic span model are: first, transition state theory is valid; second, the system is in a steady state; third, the intermediates undergo fast relaxation [138, 139]. The TOF can be expressed in the following way (see references [138] and [139] for the derivation):

$$TOF = \frac{k_B T}{h} \frac{e^{-\Delta_r G/RT} - 1}{\sum_{ij}^{N} e^{(T_i - I_j - \delta G_{ij})/RT}} = \frac{\Delta}{\sum_{ij}^{N} M_{ij}} \quad , \tag{1.118}$$

where $\Delta_r G$ denotes the free energy of the global reaction, T_i the free energy of i^{th} transition state and I_j the free energy of the j^{th} intermediate, and $\delta G_{ij} = \Delta_r G \quad \forall i \geq j$ (when the intermediate appears after the transition state in the cycle) or $\delta G_{ij} = 0$ otherwise.

The TOF is often dominated by a single transition state and intermediate denoted as TOF-determining transition states (TDTS) and the TOF-determining intermediates (TDI). Thus, equation 1.118 is dominated by single term of the sum in the denominator and the

TOF can be approximated as:

$$TOF \approx \frac{k_B T}{h} e^{\delta E/RT} \quad , \tag{1.119}$$

where $\delta E = TDTS - TDI + \delta G_{ij}$. This energy difference is called the TOF determining energetic span. It is important to realize that the TDI and TDTS are not necessarily the highest or lowest states and must not be necessarily adjoined in a single step. The identification of these intermediates is the basis for rational improvements of the catalyst.

However, the TOF is not necessarily controlled by a single intermediate or transition state. The influence of a single state can be expressed by the degree of rate control $X_{TOF,i}$, which is defined as the normalized influence of a certain rate constant E_i on the overall rate of the reaction [140, 141]:

$$X_{TOF,i} = \left| \frac{1}{TOF} \frac{\partial TOF}{\partial E_i} \right| \tag{1.120}$$

This yields the following equations for the influence of intermediates X_{TOF,I_k} and transition states X_{TOF,T_k}:

$$X_{TOF,I_k} = \frac{\sum_i M_{ik}}{\sum_{ij} M_{ij}} \tag{1.121}$$

$$X_{TOF,T_k} = \frac{\sum_j M_{kj}}{\sum_{ij} M_{ij}} \tag{1.122}$$

The range of X_{TOF} is between 0 and 1, where 0 denotes that the species has no influence on the TOF and 1 denotes that the species solely controls the TOF. The AUTOF program[1] automatically generates both TOF and X_{TOF} based on the computed cycles with a simple input file [138, 139, 142].

Conformation Analysis

To date, it is easily possible to use quantum mechanical DFT calculations to simulate systems with over 100 atoms. As the number of atoms grows, the conformer space grows exponentially and reaction pathways/ networks become complex. This makes it increasingly difficult to identify the global minimum for each intermediate or transition state, which can have detrimental effects on the reliability of the predicted reaction pathway. This can be illustrated for the reduction of the iron complex in figure 1.3: The isomer space includes different (broken symmetry) spin states, coordination numbers, and partial dissociation of the chelating ligand. It is not possible to explore the whole isomer space, therefore, chemical intuition and creativity are key for exploring the isomer space efficiently and accurately.

Alternatively, force fields or semi-empirical methods can be used to screen a larger space. Lowest energy isomers are then used in the quantum mechanical calculations.[143] Another

[1] It can be downloaded free of charge from `https://www.bgu.ac.il/~kozuch/software.html`

approach is the automated generation of structures, which are then used as guess structures in the quantum chemistry calculations.[144, 145] In addition, machine learning models like random forests or neural networks can be utilized in reaction mechanism discovery and catalyst design. This interesting emerging field is, however, beyond the scope of this thesis and the interested reader is referred to references [146–148].

Artificial Photosynthesis and CO_2 Reduction

Anthropogenic CO_2 emission has risen significantly since the beginning of the industrial revolution[149] resulting in unprecedented high atmospheric CO_2 concentrations of 420 ppm in 2020[150]. The green-house effect of CO_2 has detrimental environmental implications such as global warming and acidification of the ocean [151]. Simultaneously, natural fuel resources are diminishing which makes the conversion of CO_2 into high energy fuels a promising long term solution [152]. In order to achieve a net carbon emission free society, the transformation of CO_2 should be coupled to renewable energy sources such as solar power. Nature already provides a successful template for such a process: Photosynthesis uses sunlight to convert CO_2 and H_2O into glucose and oxygen. Consequently, artificial photosynthesis has emerged as a prominent research field in chemistry [153–156]. This process is multifaceted and requires innovation in various aspects: efficient light harvesting, e.g. via solar cells; efficient CO_2 capture and storage and efficient electrocatalysts for the CO_2 reduction reaction (CO2RR). This thesis focuses on the last point: electrocatalysts for CO2RR. There are various approaches such as biological [157], photochemical [158], electrochemical [159–161], photoelectrochemical reduction[155, 159] or reduction by hydrogenation [162].

The inertness of CO_2 is illustrated by the negative potential required for the one electron reduction, summarized in table 1.2. However, proton coupled electron transfers requires significantly less negative potentials. There is a plethora of possible products and a short summary for each possible oxidation state is shown in table 1.2; a comprehensive overview is presented in reference [163]. Among those products, CO is economically most viable due to its usage in the Fischer-Tropsch process [164]. Another key take-away from table 1.2 is that the hydrogen evolution reaction (HER) is a possible side reaction feasible at similar potentials which is why substrate selectivity is another important aspect to consider. In order to operate at a small overpotential, with fast reaction rates and product selectivity, the employment of electrocatalysts is critical.

Homogeneous electrochemical reduction is a promising candidate because of its high substrate and product selectivity ($> 90\%$) good turnover rates and tunability [165–167]. The concept of an electrocatalyst is illustrated in figure 1.6. In the uncatalyzed system, the electrochemical reaction takes place directly at the electrode without a catalyst and requires a high overpotential to achieve fast reaction rates. In contrast, a homogeneous electrocatalyst gets reduced at the electrode at a lower overpotential and diffuses in the double layer to then transfer the electrons to CO_2. In addition to facilitating the electron transfer, it can also catalyze other elementary reaction steps like protonation and thereby both reduce overpotential and increase rates [168]. Even further improvements in rates is

Table 1.2: Reduction potentials of CO_2 and proton reduction at pH = 7 versus the standard hydrogen electrode.[163]

Reaction			Potential
$CO_2 + e^-$	$\longrightarrow$	$CO_2^{\bullet -}$	$E^0 = -1.90$ V
$CO_2 + 2\,H^+ + 2\,e^-$	$\longrightarrow$	$CO + H_2O$	$E^0 = -0.53$ V
$CO_2 + 4\,H^+ + 4\,e^-$	$\longrightarrow$	$H_2CO + H_2O$	$E^0 = -0.48$ V
$CO_2 + 6\,H^+ + 6\,e^-$	$\longrightarrow$	$H_3COH + H_2O$	$E^0 = -0.38$ V
$CO_2 + 8\,H^+ + 8\,e^-$	$\longrightarrow$	$CH_4 + 2\,H_2O$	$E^0 = -0.24$ V
$2\,H^+ + 2e^-$	$\longrightarrow$	H_2	$E^0 = -0.42$ V

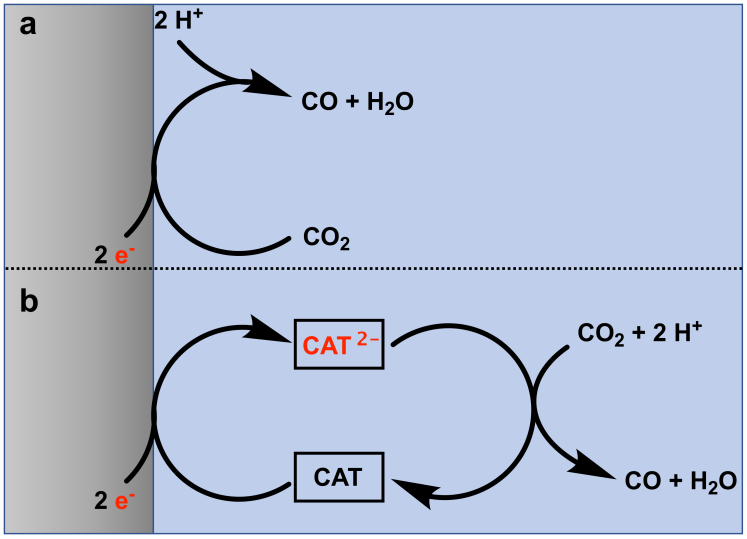

Figure 1.6: Schematic concept of (a) an uncatalyzed CO_2 reduction reaction and (b) a homogeneous electrocatalyst (the silver surface corresponds to the electrode and the blue surface to the double layer).

possible with a flow cell, achieving a current density comparable to a heterogeneous catalyst and a selectivity above 95% [169]. Alternatively, activity can be improved by incorporating the catalyst into metal/covalent organic frameworks [170, 171].

1.4 Outline

The chapters two, three and four are concerned with the development of energy decomposition methods. The fifth chapter surveys the accuracy of various perturbation theory methods

for non-covalent interactions, and the remaining three chapters provide mechanistic studies for various polypyridine based catalysts for the reduction of CO_2 to CO. In more detail:

Chapter 2: To study intermolecular interactions involving radicals at the correlated level, the Energy Decomposition Analysis scheme for Second-Order Møller-Plesset Perturbation Theory based on Absolutely Localized Molecular Orbitals (ALMO-MP2-EDA) is generalized to unrestricted and restricted open-shell MP2. The benefit of restricted open-shell MP2 is that it can provide accurate binding energies for radical complexes where density functional theory can be error prone due to delocalization errors. As a model application, the open-shell ALMO-MP2-EDA is applied to study the first solvation step of halogenated benzene radical cations, where both halogen and hydrogen bonded isomers are possible. We determine that the lighter halogens favor the hydrogen-bonded form, while the iodine-substituted species prefers halogen bonding due to larger polarizability and charge transfer at the halogen. As a second application, relevant to the activation of CO_2 in photoelectrocatalysis, complexes of $CO_2{}^{-\bullet}$ interacting with both pyridine and imidazole are analyzed with ALMO-MP2-EDA. The results reveal the importance of charge transfer into the π^* orbital of the heterocycle in controlling the stability of the carbamate binding mode, which is favored for pyridine, but not for imidazole. This work has been published in reference [172].

Chapter 3: To facilitate the understanding of charge transfer (CT) effects in dative complexes, we propose a variational forward-backward (VFB) approach to decompose the overall CT stabilization energy into contributions from forward and backward donation in the framework of energy decomposition analysis based on absolutely localized molecular orbitals (ALMO-EDA). Such a decomposition is achieved by introducing two additional constrained intermediate states in which only one direction of CT is permitted. These two "one-way" CT states are variationally relaxed such that the associated nuclear forces can be readily obtained. This allows for a facile integration into the previously developed adiabatic EDA scheme so that the molecular property changes arising from forward and back donation can be separately assigned. Using ALMO-EDA augmented by this VFB model, we investigate the energetic, geometric, and vibrational features of complexes composed of CO and main group Lewis acids (BH_3, $BeO/BeCO_3$), and complexes of the N_2, CO, and BF isoelectronic series with $[Ru(II)(NH_3)_5]^{2+}$. We identify that the shift in the stretching frequency of a diatomic π-acidic ligand (XY), such as CO, results from a superposition of the shifts induced by permanent electrostatics and backward CT: permanent electrostatics can cause an either red or blue shift depending on the alignment of the XY dipole in the dative complex, and this effect becomes more pronounced with a more polar XY ligand; the back-donation to the antibonding π orbital of XY always lowers the X−Y bond order and thus red-shifts its stretching frequency, and the strength of this interaction decays rapidly with the intermolecular distance. We also reveal that while σ forward donation contributes significantly to energetic stabilization, it affects the vibrational feature of XY mainly by shortening the intermolecular distance, which enhances both the electrostatic interaction and backward CT

but in different rates. The synergistic effect of the forward and backward donations appears to be more significant in the transition metal complexes, where the forward CT plays an essential role in overcoming the strong Pauli repulsion. These findings highlight that the shift in the XY stretching frequency is not a reliable metric for the strength of π back-donation. Overall, the VFB-augmented EDA scheme that we propose and apply in this work provides a useful tool to characterize the role played by each physical component that all together lead to the frequency shift observed. This work has been published in reference [173].

Chapter 4: To facilitate computational investigation of intermolecular interactions in the solution phase, we report the development of ALMO-EDA(solv), a scheme that allows the application of continuum solvent models within the framework of energy decomposition analysis (EDA) based on absolutely localized molecular orbitals (ALMOs). In this scheme, all the quantum mechanical states involved in the variational EDA procedure are computed with the presence of the solvent environment so that solvation effects are incorporated in the evaluation of *all* its energy components. After validation on several model complexes, we employ ALMO-EDA(solv) to investigate substituent effects on two classes of complexes that are related to molecular CO_2 reduction catalysis. For $[FeTPP(CO_2{-}\kappa C)]^{2-}$ (TPP = tetraphenylporphyrin), we reveal that two ortho substituents which yield most favorable CO_2 binding, $-N(CH_3)_3{}^+$ (TMA) and $-OH$, stabilize the complex via through-structure and through-space mechanisms, respectively. The Coulombic interaction between the positively charged TMA group and activated CO_2 is found to be largely attenuated by the polar solvent. Furthermore, we also provide computational support for the design strategy of utilizing bulky, flexible ligands to stabilize activated CO_2 via long-range Coulomb interactions, which creates biomimetic solvent-inaccessible "pockets" in that electrostatics is unscreened. For the reactant and product complexes associated with the electron transfer from the *p*-terphenyl radical anion to CO_2, we demonstrate that the double terminal substitution of *p*-terphenyl by electron-withdrawing groups considerably strengthens the binding in the product state while moderately weakens that in the reactant state, which are both dominated by the substituent tuning of the electrostatics component. These applications illustrate that this new extension of ALMO-EDA provides a valuable means to unravel the nature of intermolecular interactions and quantify their impacts on chemical reactivity in solution. This work has been published in reference [174].

Chapter 5: This chapter systematically assesses the influence of reference orbitals, regularization and scaling on the performance of second- and third-order Møller-Plesset perturbation theory wavefunction methods for non-covalent interactions (NCI). Testing on 19 data sets (A24, DS14, HB15, HSG, S22, X40, HW30, NC15, S66, AlkBind12, CO2Nitrogen16, HB49, Ionic43, TA13, XB18, Bauza30, CT20, XB51 and Orel26rad) covers a wide range of different NCI including hydrogen bonding, dispersion, and halogen bonding. Inclusion of potential energy surfaces from different hydrogen bonds and dispersion-bound complexes gauges accuracy for non-equilibrium geometries. 15 methods are tested. In notation

where nonstandard choices of orbitals are denoted as method:orbitals, these are MP2, κ-MP2, SCS-MP2, OOMP2, κ-OOMP2, MP3, MP2.5, MP3:OOMP2, MP2.5:OOMP2, MP3:κ-OOMP2, MP2.5:κ-OOMP2, and κ-MP3:κ-OOMP2, κ-MP2.5:κ-OOMP2, MP3:ωB97X-V, and MP2.5:ωB97X-V. Furthermore, we compare these methods to the ωB97M-V and B3LYP-D3 density functionals as well as CCSD. We find that the κ-regularization (κ = 1.45 a.u. was used through-out) improves the energetics in almost all data sets for both MP2 (in 17 out of 19 data sets) and OOMP2 (16 out of 19). The improvement is significant (e.g. the RMSD for the S66 data set is 0.29 kcal/mol for κ-OOMP2, versus 0.67 kcal/mol for MP2), and for interactions between stable closed shell molecules, not strongly dependent on the reference orbitals. Scaled MP3 (with a factor of 0.5) using κ-OOMP2 reference orbitals (MP2.5:κ-OOMP2) provides significantly more accurate results for NCIs across all data sets with non-iterative $\mathcal{O}(N^6)$ scaling (S66 data set RMSD: 0.10 kcal/mol). Across the entire data set of 356 points, the improvement over standard MP2.5 is approximately a factor of two: RMSD for MP3:κ-OOMP2 is 0.25 kcal/mol vs 0.50 kcal/mol for MP2.5. The use of high-quality density functional reference orbitals (ωB97X-V) also significantly improves the results of MP2.5 for NCI over a Hartree-Fock orbital reference. All our assessments and conclusions are based on the use of the medium-sized aug-cc-pVTZ basis to yield results that are directly compared against complete basis set limit reference values. This work has been published in reference [175].

Chapter 6: A solar-driven conversion of CO_2 into fuels by artificial photosynthesis would not only mitigate the greenhouse effect but also provide an alternative to obtain fuels in a renewable fashion. To this end, the new iron polypyridine catalyst $[Fe(bpy^{NHEt}PY2)L_2]^{2+}$ (L = H_2O, CH_3CN) was recently developed for the electrochemical reduction of CO_2 to CO. In this study, we performed density functional theory (DFT) electronic structure calculations to shed light on a possible pathway for CO_2 reduction and the origin of the selectivity between CO_2 versus hydrogen evolution reaction. The metal center remains Lewis acidic throughout the reduction process due to ligand loss and mainly ligand based reduction stabilized by antiferromagnetic coupling to a high-spin Fe(II) center. This results in a high barrier for hydride formation but a facile addition and activation of CO_2 via an η^2 coordination and stabilizing hydrogen bonding by the amine group. The second unoccupied equatorial coordination site opens up the possibility for an intramolecular protonation with a coordinated water ligand. This facilitates protonation because not only CO_2 but also the proton source H_2O is activated and properly aligned for a proton transfer due to the $Fe-OH_2$ bond; consequently, both protonation steps are facile. The moderate ligand field allows a rapid ligand exchange for a second intramolecular protonation step and facilitates an exergonic CO release. The lower selectivity of the related $[Fe(bpy^{OH}PY2)L_2]^{2+}$ compound can be related to the more acidic second coordination sphere because it opens up the possibility of an intramolecular proton transfer which has a comparable barrier to CO_2 addition. This work has been published in reference [176].

Chapter 7: Both $[Co^{II}(qpy)(H_2O)_2]^{2+}$ and $[Fe^{II}(qpy)(H_2O)_2]^{2+}$ (with qpy = 2,2′:6′,2″:6″,2‴-quaterpyridine) are efficient homogeneous electrocatalysts and photoelectrocatalysts for the reduction of CO_2 to CO. The Co catalyst is more efficient in the electrochemical reduction while the Fe catalyst is an excellent photoelectrocatalyst (*ACS Catal.* **2018**,*8*, 3411–3417). This work uses density functional theory to shed light on the contrasting catalytic pathways. While both catalysts experience primarily ligand-based reductions, the second reduction in the Co catalyst is delocalized onto the metal via a metal-ligand bonding interaction, causing a spin transition and distorted ligand framework. This orbital interaction explains the experimentally observed mild reduction potential and slow kinetics of the second reduction. The decreased hardness and doubly occupied d_{z^2}-orbital facilitate a σ-bond with the CO_2-π^* in an η^1-κC binding mode. CO_2 binding is only possible after two reductions resulting in an EEC mechanism (E=electron transfer, C=chemical reaction), and the second protonation is rate-limiting. In contrast, the Fe catalyst maintains a Lewis acidic metal center throughout the reduction process because the metal orbitals do not strongly mix with the qpy-π^* orbitals. This allows to bind the activated CO_2 in an η^2 binding mode. This interaction stabilizes the activated CO_2 via a π-type interaction of a Fe-t_{2g} orbital and the CO_2-π^* and a dative bond of the oxygen lone pair. This facilitates CO_2 binding to a singly reduced catalyst resulting in an ECE mechanism. The barrier for CO_2 addition and the second protonation are higher than those for the Co catalyst and rate-limiting. This work has been published in reference [177].

Chapter 8: $[Fe(tpyPY_2Me)]^{2+}$ ($[Fe]^{2+}$) is an exceptional homogeneous catalyst for converting CO_2 into CO at low overpotentials with high selectivities at turnover frequencies faster than 100,000 s^{-1}. In our initial study of $[Fe]^{2+}$, we reported the design, synthesis, characterization, and electrocatalytic activity. Synthesis of the two-electron reduced product, $[Fe(tpyPY_2Me)]^0$, and extensive spectroscopic characterization supported the assignment of an open-shell singlet electronic structure that we attributed to the low thermodynamic barrier required to selectively reduce CO_2 (*J. Am. Chem. Soc.* **2020**, 142, 48, 20489). The mechanistic pathways through which $[Fe]^{2+}$ functions, however, are entirely unexplored. Electrochemical data shows the formation of two distinct catalytic regimes as a function of applied potential. This work uses a combined experimental and computational approach to shed light on these low and high overpotential mechanistic pathways. We propose that at low overpotentials,the catalyst undergoes a two electron reduction, two proton transfer mechanism (EECC) where turnover occurs through the dicationic iron complex, $[Fe]^{2+}$. Computational analysis further validated the importance of the singlet ground state electronic structure for CO_2 binding and the rate limiting step is the second protonation in this low overpoential regime. When more negative applied potentials are applied, an additional electron transfer event occurs through either a step-wise or a proton coupled electron transfer (PCET) pathway, allowing for catalytic turnover from the monocationic iron complex ($[Fe]^+$) via an ECEC mechanism. Comparison of experimental kinetic data obtained from variable controlled potential electrolysis experiments with direct product detection with calculated

rates obtained from the energetic span model support the PCET pathway as the most likely mechanism. Building upon the understanding gained from the detailed mechanistic analysis, we propose the design of an improved ligand framework that is predicted to stabilize the key transition states identified from our study and explore their electronic structures using an energy decomposition analysis. Taken together, this study illustrates the importance of establishing a working mechanistic understanding of new electrocatlaysts to direct the rational design of improved catalyst platforms. This work is submitted for publication.

Chapter 2

Energy Decomposition Analysis for Interactions of Radicals: Theory and Implementation at the MP2 Level with Application to Hydration of Halogenated Benzene Cations and Complexes between $CO_2^{-\bullet}$ and Pyridine and Imidazole

2.1 Introduction

Intermolecular interactions describe attractive or repulsive forces between molecular species that govern important chemical processes, like the formation and structure of biological macromolecules and a wide range of catalyst systems. [178–187] Their energy scale ranges from a few kJ/mol for weak van der Waals complexes to more than 150 kJ/mol for strong hydrogen bonds or metal ligand interactions. The origin of these interactions can be understood readily for simple cases like rare gas dimers which bind because of dispersion. However, it can be difficult to understand the interaction for a more complicated system such as a complex formed by cationic halogenated benzene radical and water, where other intermolecular terms such as electrostatics, polarization, and charge transfer are all in play.

Modern quantum chemical methods are able to predict most intermolecular binding energies quite accurately, but there lacks a direct bridge between these energies and chemical concepts. [5] To this end, energy decomposition analysis (EDA) [188–190] aims to unravel the origin of the interaction by decomposing the binding energy into chemically motivated components. Admittedly, the resulting decomposition cannot be uniquely defined in the overlapping regime, and consequently there are multiple approaches in the literature for providing chemical interpretations of molecular complexes. Important seminal EDA schemes

include the Kitaura-Morokuma (KM)-EDA that decomposes the Hartree-Fock (HF) interaction energy into electrostatic, Pauli repulsion, polarization and charge transfer contributions, [191–193] and the extended transition state (ETS) method developed by Ziegler and Rauk, which partitions interactions calculated from density functional theory (DFT) into electrostatics, Pauli repulsion, and orbital interaction. [194, 195]

A significant improvement to the KM-EDA for HF and DFT was made possible by the variational treatment of polarization, accomplished via imposing a fragment-blocking constraint on the molecular orbital (MO) coefficient matrix. [30, 196] Solving the resulting constrained variational equations leads to absolutely localized MOs (ALMOs) [31] that are used in the Block-Localized Wavefunction EDA (BLW-EDA)[197–199] and the ALMO-EDA [83, 84, 200] approaches, both of which separate the interaction energy into a “frozen" term and allow for separability of general induction into the polarization and charge transfer contributions. The frozen energy corresponds to the interaction between monomers with their MOs optimized for each isolated fragment, the polarization energy is then defined by the relaxation of each fragment's MOs in the presence of other fragments, and finally charge transfer corresponds to the energy lowering resulting from inter-fragment orbital mixing. Furthermore, each intermediate energy exhibits correct asymptotic behavior and is a well-defined variational quantity. Recently a second generation ALMO-EDA [84] was developed, which includes two further improvements: first, the frozen term can be further decomposed into contributions from Pauli repulsion, permanent electrostatics, and dispersion [86]; and second, the use of a basis constructed from fragment electric response functions (FERFs) in the ALMO-constrained SCF calculation enables a well defined basis set limit for the separation between polarization and charge transfer. [32] The resulting second generation ALMO-EDA scheme [84] also permits any underlying representation with no restriction to atomic orbitals. Other recent advances in ALMO-EDA include decomposition of molecular properties [201] and an extension to singly excited-state methods.[202, 203]

In principle, EDAs can be extended to more accurate interaction energies obtained from correlated wavefunctions methods.[204] The simplest correlation method is second-order Møller-Plesset perturbation theory (MP2), which is accurate and widely used for molecular interactions such as hydrogen bonding, [205, 206] as well as being fast and efficient with the use of density fitting or resolution of the identity (RI). [207, 208] MP2 also performs well for radical-solvent interactions, [209] provided that a restricted open shell reference is used when the HF reference is spin-contaminated. The KM scheme has been extended to post-HF methods such as MP2, by assigning the entire contribution from correlation energy to dispersion. [210] However, the inclusion of correlation also has an effect on electrostatic interactions, polarization and charge transfer, [211, 212] and thus other EDAs were developed to understand the full correlation effects on intermolecular binding. The local second-order Møller-Plesset perturbation theory (LMP2) approach naturally allows for a decomposition of the correlation energy into an intramolecular correlation, a dispersion and an ionic contribution. [213] However, MP2 can overestimate binding in dispersion-dominated interactions like π-stacking, [214–217] while coupled cluster theory provides significantly higher accuracy if triples are included (e.g. via CCSD(T)), albeit at significant computational cost. A similar

concept to LMP2 has been applied at the CCSD(T) level to define the Local Energy Decomposition (LED) scheme, which distinguishes between intra- and intermolecular correlation contributions. [218–221] Perhaps the most widely used EDA approach is symmetry-Adapted Perturbation Theory (SAPT), which computes the interaction energy via a perturbative expansion starting with non-interacting fragments. High-level SAPT with intramolecular correlation taken into account can yield accuracy comparable to CCSD(T),[222] and it decomposes the interaction energy into an electrostatic, an exchange, an induction and a dispersion term. [223–226]

We have developed an alternative post-HF approach, the ALMO-MP2-EDA scheme, [212, 227] which builds on local correlation models[228, 229] and on an earlier pilot effort[230] which did not correct the mean-field frozen and polarization terms for the effect of correlation. The original ALMO-MP2-EDA scheme was designed to decompose the correlation energy into the same terms as the mean-field ALMO-EDA scheme through the addition of an explicit dispersion term. The core idea was to assign the excitations that contribute to the MP2 energy into different classes (see Fig. 2.1): intra-fragment for frozen and polarization, charge conserving for dispersion and charge transferring for charge transfer. However, the previous ALMO-MP2-EDA scheme and implementation were both limited to interactions between closed-shell molecules. In this work the ALMO-MP2-EDA scheme is generalized to unrestricted and restricted open-shell MP2 to permit the study of intermolecular interactions of radicals with a correlated wavefunction method, for which DFT methods are shown to be error prone.[209, 231] We verify that the correct asymptotic behaviour of frozen, polarization, dispersion and charge transfer is operative, and the method is applied to understand the hydration of halogenated benzene radical cations. [232], as well as the different interaction motifs of the $CO_2^{-\bullet}$ radical anion with N-heterocycles in the gas phase. [233, 234]

2.2 Theory

The notation used in this manuscript employs indices i, j, k, ... for occupied orbitals, a, b, c, ... for virtual and p, q, r, ... for either. As far as possible, the discussion is presented in the spin-orbital basis. However, at some points we specifically discuss unrestricted spatial orbitals where $\bar{p}$ represents the β spin space. Labels for fragments are denoted as A, B, C ... and P, Q, R refer to the auxiliary (RI) basis functions.

Summary of MP2 Theory

The Hylleraas functional, J_H, is a variational formulation that when minimized yields the first order wave function and MP2 energy. The Fock operator ($\hat{F}$) is the usual choice for the zeroth-order Hamiltonian [38–40]:

$$J_H[\tilde{\Psi}] = \left\langle \Psi^{(0)} \middle| V - E^{(1)} \middle| \tilde{\Psi} \right\rangle + \left\langle \tilde{\Psi} \middle| H^{(0)} - E^{(0)} \middle| \tilde{\Psi} \right\rangle + \left\langle \tilde{\Psi} \middle| V - E^{(1)} \middle| \Psi^{(0)} \right\rangle \tag{2.1}$$

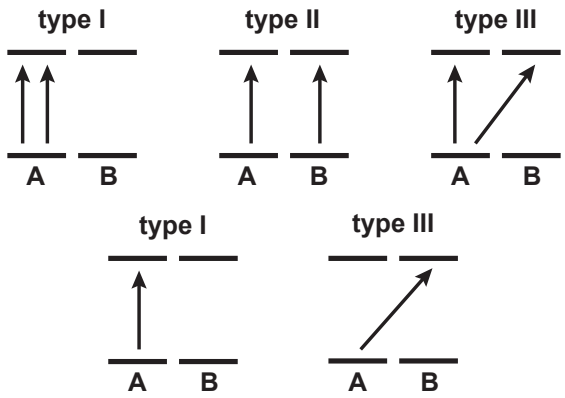

Figure 2.1: A representation for each of the three types of double excitations for a two-fragment system (A and B): on fragment (type I), charge conserving (type II) and charge transferring (III). In the case of RMP2 single excitations are also included, for which the on fragment and charge conserving constraints are identical. The lower level represents the occupied space and upper level the virtual space of each fragment.

or in a more compact matrix-vector notation:

$$J_H[\tilde{\mathbf{t}}] = \tilde{\mathbf{t}}^\dagger \boldsymbol{\Delta} \tilde{\mathbf{t}} + \tilde{\mathbf{t}}^\dagger \mathbb{I} + \mathbb{I}^\dagger \tilde{\mathbf{t}} \tag{2.2}$$

Here $\tilde{\mathbf{t}}$ is a vector composed of the wave function amplitudes, $\tilde{t}_{ij}^{ab}$, $\mathbb{I}$ is a vector composed of two-electron integrals, $\langle ij||ab\rangle$, and $\boldsymbol{\Delta}$ is a supermatrix whose elements are defined as:

$$\Delta_{\binom{ab}{ij},\binom{cd}{kl}} = \left\langle \Psi_{ij}^{ab} \middle| \hat{F} - E^{(0)} \middle| \Psi_{kl}^{cd} \right\rangle \tag{2.3}$$

Unlike restricted or unrestricted MP2, the choice of the zeroth-order Hamiltonian is not unique for ROHF, and, consequently, there are multiple approaches to MP2 with restricted open-shell HF references. Those approaches include ROMP2 by Amos *et al.*, [235] OPT1 and OPT2 by Murray and Davidson [236], HCPT by Hubač and Čársky [237], Z-averaged PT (ZAPT) by Lee and Jayatilaka [238], RMP2 by Knowles and co-workers [239] and ROHF-MBPT2 by Bartlett and co-workers [240]. This paper follows the RMP2 approach of Knowles *et al.* [239] where the occupied-occupied and virtual-virtual blocks of the pseudo-canonicalized $\hat{F}^\alpha$ and $\hat{F}^\beta$ are defined as the zeroth-order Hamiltonian. This results in similar equations to unrestricted MP2 (UMP2). However, Brillouin's theorem does not hold and therefore singles contributions are included in the first-order MP wave function, yielding the following open-shell RMP2 energy expression:

$$E^{(2)} = -\sum_{ia} t_i^a F_{ai} - \frac{1}{4} \sum_{ijab} t_{ij}^{ab} \langle ij||ab\rangle \tag{2.4}$$

Here as usual $\langle ij||ab\rangle = (ia|jb) - (ib|ja)$. After pseudo-canonicalization, the singles and doubles amplitudes are defined as

$$t_i^a = \frac{F_{ai}}{\epsilon_a - \epsilon_i} \tag{2.5}$$

$$t_{ij}^{ab} = \frac{\langle ij||ab\rangle}{\epsilon_a + \epsilon_b - \epsilon_i - \epsilon_j} \tag{2.6}$$

Of course in UMP2, $t_i^a = 0$. In RMP2, the energy is spin-pure (though the amplitudes are not).

We will also use the RI approximation for the two-electron integrals:

$$(ia|jb) \simeq \sum_Q^{N_{\text{aux}}} \left[\sum_P^{N_{\text{aux}}} (ia|P)(P|Q)^{-1/2}\right] \left[\sum_R^{N_{\text{aux}}} (Q|R)^{-1/2}(R|jb)\right] \tag{2.7}$$

$$= \sum_Q^{N_{\text{aux}}} B_{ia}^Q B_{jb}^Q$$

The MP2-EDA Scheme

The total binding energy is defined as the energy difference between the complex and the isolated non-interacting fragments. It can be divided into a geometry distortion term, which is the energy required to deform isolated fragments from their optimum geometry to their geometry in the complex, and the interaction energy at the supersystem geometry ($\Delta \mathrm{E}_{\mathrm{INT}}$). This interaction energy can be further partitioned into a mean-field contribution $\Delta \mathrm{E}_{\mathrm{INT}}^{\mathrm{HF}}$ and a correlation contribution $\Delta \mathrm{E}_{\mathrm{INT}}^{\mathrm{MP2}}$. In this work, the mean-field contribution is decomposed using the original ALMO-EDA scheme [83]:

$$\Delta \mathrm{E}_{\mathrm{INT}}^{\mathrm{HF}} = \Delta E_{\mathrm{FRZ}}^{\mathrm{HF}} + \Delta \mathrm{E}_{\mathrm{POL}}^{\mathrm{HF}} + \Delta E_{\mathrm{CT}}^{\mathrm{HF}} \tag{2.8}$$

The frozen and polarized intermediate energies are evaluated using constrained HF wave functions. At the frozen level, a single determinant is constructed by combining the isolated fragments into a supersystem using *unrelaxed* fragment MOs. This captures the HF-level electrostatic and Pauli repulsion contributions. For polarization, the MOs are variationally optimized subject to the fragment-blocking constraint, leading to polarized ALMOs from solving the locally projected SCF scheme (SCF-MI). [30, 31, 196, 241] This allows the electron densities on each fragment to adjust to the supersystem environment and naturally excludes charge transfer, which is finally obtained using the unconstrained HF energy.

The MP2 correlation energy is decomposed into the same terms by enforcing similar constraints; however, an additional term for dispersion naturally arises [212]:

$$\Delta \mathrm{E}_{\mathrm{INT}}^{\mathrm{MP2}} = \Delta \mathrm{E}_{\mathrm{FRZ}}^{\mathrm{MP2}} + \Delta \mathrm{E}_{\mathrm{POL}}^{\mathrm{MP2}} + \Delta \mathrm{E}_{\mathrm{DISP}}^{\mathrm{MP2}} + \Delta \mathrm{E}_{\mathrm{CT}}^{\mathrm{MP2}} \tag{2.9}$$

The intermediate energies are presented in this section, largely following the notations used previously [212] where energies are given parenthetical labels that indicate (system-size/basis-type) at each stage of the analysis. System-size will be either "frag" for a fragment, or "sys" for the supersystem.

At the mean-field level both frozen and polarized wave functions are constructed using fragment-blocked ALMO orbitals. The molecular orbitals in this basis are only orthogonal *within* each fragment. However, the MP2 energy expression is only well-defined for separated occupied and virtual spaces. Thus, both the frozen orbitals and converged ALMOs need to be properly prepared by projecting the occupied subspace out of the virtual orbitals. The occupied orbitals are then symmetrically orthonormalized [242] (globally) and the virtual orbitals are symmetrically orthonormalized on each fragment after being projected against the occupied space, yielding the pFRZ and pALMO basis, respectively. [212]. The MP2 contribution to frozen energy, which captures the pure electrostatic effects and Pauli repulsion, is obtained using

$$\Delta E_{\mathrm{FRZ}}^{\mathrm{MP2}} = \sum_{A}^{N_{\mathrm{frag}}} E_{\mathrm{frz}}(\mathrm{frag/pFRZ})_A - \sum_{A}^{N_{\mathrm{frag}}} E_{\mathrm{iso}}(\mathrm{frag})_A - \mathrm{ABSSE} \tag{2.10}$$

where $E_{\mathrm{iso}}(\mathrm{frag})_A$ is the standard MP2 energy of each fragment evaluated in the canonical basis and ABSSE refers to the auxiliary basis set superposition error (*vide infra*). The frozen MP2 energy of each fragment, $E_{\mathrm{frz}}(\mathrm{frag/pFRZ})_A$, is obtained by freezing both fragment orbitals and t-amplitudes. The Hylleraas functional is employed to evaluate the MP2 energy with non-stationary t-amplitudes, using the full system frozen Fock matrix in the pFRZ MO basis for each fragment.

However, the MP2 wave function is not stationary with respect to occupied-virtual (ov) orbital rotations (θ_{ai}). As a consequence, the relaxed second-order density matrix incorporating first-order orbital response effects is required for evaluting the frozen energy (see previous work by some of us for a more detailed derivation [212]). The final expression for the frozen energy has the following form:

$$E_{\mathrm{frz}A} = J_H[\mathbf{t}_{\mathbf{A}}^{\mathbf{iso}}, \mathbf{C}_A, \mathbf{F}_A] - 2\sum_{ia} P_{iaA}^{(2)} F_{iaA} \tag{2.11}$$

where $\mathbf{t}_{\mathbf{A}}^{\mathbf{iso}}$ refers to the isolated t-amplitudes in the canonical fragment basis, F_{iaA} is the frozen Fock matrix transformed into the pFRZ MO basis of each fragment, and the ov block of the second-order density matrix, $P_{ia}^{(2)} = -Z_{ia}$ (the so-called Z-Vector [243]). The Z-vector (Z_{ia}) is obtained by contracting the inverse of HF electronic hessian with the MP2 orbital gradient:

$$Z_{jb} = \sum_{ia} \left(\frac{\partial^2 E^{\mathrm{SCF}}}{\partial\theta_{ai}\partial\theta_{bj}} \right)^{-1} \frac{\partial E^{(2)}}{\partial\theta_{ai}} \tag{2.12}$$

The explicit expressions and derivations for these terms can be found elsewhere.[39, 40, 244]

For restricted open-shell MP2 methods like RMP2, the derivation of the Z-vector is more involved, and interested readers are referred to refs. [245, 246]. The important point is that the RMP2 CPSCF equation can be expressed in a form that is equivalent to UMP2 gradient theory. In summary, obtaining the frozen energy at the MP2 level requires calculating the t-amplitudes on each isolated fragment, evaluating the Hylleraas functional and solving a CPSCF equation for each fragment.

Next, the MP2 contribution to polarization energy is obtained using

$$\Delta \mathrm{E}_{\mathrm{POL}}^{\mathrm{MP2}} = \sum_{A}^{N_{\mathrm{frag}}} \mathrm{E}_{\mathrm{pol}}(\mathrm{frag/pALMO})_A - \sum_{A}^{N_{\mathrm{frag}}} \mathrm{E}_{\mathrm{frz}}(\mathrm{frag/frz})_A \tag{2.13}$$

After the SCF-MI is converged the ALMOs on each fragment are transformed into the pALMO basis. The ALMO basis allows the assignment of molecular orbitals to fragments. The polarization constraint, like the frozen system, permits only paired double substitutions on the same fragment. This allows for obtaining $\mathrm{E}_{\mathrm{pol}}$(frag/pALMO) with standard MP2 energy evaluation using the pALMO basis of each fragment.

The dispersion energy is obtained using

$$\Delta \mathrm{E}_{\mathrm{DISP}}^{\mathrm{MP2}} = \mathrm{E}_{\mathrm{ccc}}(\mathrm{sys/ALMO}) - \sum_{A}^{N_{\mathrm{frag}}} \mathrm{E}_{\mathrm{pol}}(\mathrm{frag/ALMO})_A \tag{2.14}$$

where the charge conserving correlation (CCC) constraint is imposed. This constraint only permits excitations that conserve the charge on each fragment as shown in Fig. 2.1 (types I and II). The CCCMP2 energy ($\mathrm{E}_{\mathrm{ccc}}$(sys/ALMO)) is evaluated for the whole system in the pALMO basis, which is neither orthonormal nor canonical. The derivative of the Hylleraas functional with respect to the amplitudes yields a set of linear equations to obtain the MP2 amplitudes:

$$\frac{\partial J_H^{\mathrm{CCC}}}{\partial \mathbf{t}^{\mathrm{CCC}}} = 0 \Rightarrow \boldsymbol{\Delta}^{\mathrm{CCC}} \mathbf{t}^{\mathrm{CCC}} = \mathbb{I}^{\mathrm{CCC}} \tag{2.15}$$

$$\sum_{i'j'a'b'} (\Delta^{\mathrm{CCC}})_{\binom{ab}{ij},\binom{a'b'}{i'j'}} (t^{\mathrm{CCC}})_{i'j'}^{a'b'} = \langle ij||ab\rangle^{\mathrm{CCC}} \tag{2.16}$$

where $\boldsymbol{\Delta}$ represents an 8 $^{\mathrm{th}}$-rank tensor that has the following form:

$$\left(\Delta^{\mathrm{CCC}}\right)_{\binom{ab}{ij},\binom{a'b'}{i'j'}} = -F_{ii'}g_{aa'}g_{jj'}g_{bb'} + g_{ii'}F_{aa'}g_{jj'}g_{bb'} - g_{ii'}g_{aa'}F_{jj'}g_{bb'} + g_{ii'}g_{aa'}g_{jj'}F_{bb'} \tag{2.17}$$

where $g_{rr'}$ refers to the MO-overlap matrix.

Utilizing the internal structure of $\boldsymbol{\Delta}$ tensor arising from the properties of the basis as well as the CCC constraint ($ia \in A$, i.e., pairs must be on the same fragment) simplifies the contraction on the left-hand side of Eq. 2.16. An efficient iterative algorithm to solve Eq. 2.16 was developed previously and is applied here as well. [227] The coupling terms

$\left((\Delta^{\mathrm{CCC}})_{\binom{ab}{ij},\binom{a'\bar{b}'}{i'\bar{j}'}}\right)$ for the same-spin (t_{ij}^{ab}) and opposite-spin ($t_{i\bar{j}}^{a\bar{b}}$) blocks of the t-amplitudes are zero. As a consequence, the three spin blocks of the t-amplitudes can be solved independently. In contrast to the same-spin case, the opposite-spin $\mathbf{\Delta}$ tensor has no symmetry between the first and third or between the second and fourth terms, rendering the contraction over the opposite-spin amplitudes in Eq. 2.16 twice as costly. Finally, the energy is obtained by contracting the amplitudes with the charge-conserving two-electron integrals in the pALMO basis. For RMP2, we also need to include the contribution from the singles. [239] The CCC constraint for singles is identical to the on-fragment constraint. Therefore, the singles contribution from the polarization calculation is added to obtain $\mathrm{E_{ccc}}$.

At last the MP2 contribution to charge transfer energy can be evaluated using

$$\Delta \mathrm{E}_{\mathrm{CT}}^{\mathrm{MP2}} = \mathrm{E(sys)} - \mathrm{E_{ccc}(sys/ALMO)} - \mathrm{BSSE} + \mathrm{ABSSE} \tag{2.18}$$

where E(sys) corresponds to the full MP2 energy of the supersystem, BSSE to the standard basis set superposition error in MP2 correlation energy calculated from applying a counterpoise correction, [116] and ABSSE to the auxiliary basis set superposition error, which corresponds to the difference between isolated fragment MP2 energies evaluated with and without auxiliary basis function on the ghost atoms. [212]

2.3 Computational Details

All geometries were fully optimized with ωB97X-D[68]/def2-TZVPPD[247, 248] and with an ECP for iodine [249] in the gas phase. The aug-cc-pVTZ basis set [250–252] in combination with the corresponding auxiliary basis [253, 254] was employed for the MP2-EDA calculations. Reference calculations for the interaction energies were performed with the double-hybrid ωB97M(2) functional [63] with either the def2-QZVPPD or def2-TZVPPD basis set,[248] with their corresponding auxiliary basis set and an ECP for iodine. [249, 255]

The electron density plots were visualized with an isovalue of 0.1 a.u., and a smaller isovalue (0.001 a.u.) was used for the density difference plots. A further analysis of CT using complementary occupied-virtual orbital pairs (COVPs) [87] is currently only available for mean-field methods, and thus we used EDA results with the ωB97M-V functional [70] to generated the COVPs (with an isovalue of 0.05 a.u.). ωB97M-V has been identified as one of the most accurate density functionals for intermolecular interactions by recent extensive benchmarks.[20, 256] Furthermore, the calculated ωB97M-V interaction energies were similar to the RMP2 results (see tables A.4 and A.6 in the appendix).

Implementation Details

We implemented the EDA scheme for RMP2 (UMP2) in a development version of the Q-Chem 5 package,[108] which comprises the following steps:

1. Perform fragment ROHF (UHF) and subsequently canonical MP2 calculations based on these references.
2. Evaluate the frozen HF energy and compute E_{frz} for each fragment (Eq. 2.11).
3. Perform an ROSCF-MI (USCF-MI) calculation enforcing fragment-blocking of the MO coefficients and subsequently evaluate E_{pol} for each fragment.
4. Iteratively solve for the CCC t-amplitudes and evaluate E_{ccc}.
5. Perform a fully relaxed ROSCF (USCF) calculation for the supersystem followed by a canonical MP2 calculation.
6. Perform ROSCF (USCF) and canonical MP2 calculations for each individual fragment with other fragments as ghost atoms for BSSE and ABSSE corrections.

In cases where the radical is a single atom (e.g. $Cl^{\bullet}$) or of a highly symmetric geometry (e.g. $^{\bullet}OH$), there can be multiple degenerate electronic configurations with the unpaired electron residing in different orbitals, yielding non-uniquely defined frozen states as illustrated by the $Cl^{\bullet}\cdots H_2O$ complex in Fig. 2.2. For such systems, it is desirable to obtain the orientation of fragment spin that yields the most favorable frozen energy. We achieve this by *recalculating* the isolated fragments after the SCF-MI step with the corresponding block of the ALMO coefficient matrix as the initial guess in combination with the Maximum Overlap Method (MOM). [257] Note that the proper alignment of the radical was suggested in the EDA scheme for chemical bonds previously developed by Levine *et al.* [258, 259]. To obtain the Z-vectors, we iteratively solve a CPSCF equation (either RO or U) for each fragment which avoids the direct inversion of the electronic hessian.

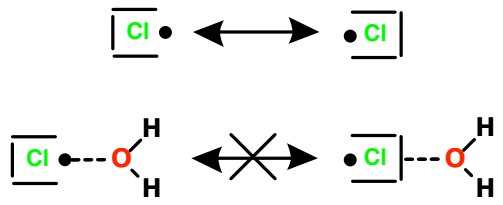

Figure 2.2: Illustration of the degenerate electronic configuration of the $Cl^{\bullet}$ radical, which then yields distinct frozen energies for the $Cl^{\bullet}\cdots H_2O$ complex depending on the initial orientation of the $Cl^{\bullet}$ spin density.

The linear equation to obtain the three sets of t-amplitudes (Eq. 2.16) follows an adaption of the efficient procedure of the closed-shell MP2-EDA scheme. [227] The initial guess is the t-amplitudes of the polarization calculations and a diagonal preconditioner is used to accelerate convergence. The construction of the charge conserving two-electron integrals for CCCMP2 follows a modified approach:

- Loop over all fragment pairs (AA, AB, AC, ...)
- For a given fragment pair AB, construct an intermediate $\mathbf{W}$ containing all two-electron integrals of the given fragment subspaces $W^{AB} = (i^A a^A | \bar{j}^B \bar{b}^B)$:

$$\mathbf{W}^{AB} = \mathbf{B}^{Q\dagger}_{ai\in A} \cdot \mathbf{B}^{Q}_{\bar{b}\bar{j}\in B}$$

- Map each $\mathbf{W}^{AB}$ into the $\mathbb{I}^{\mathrm{CCC}}$ tensor

All parts of the code are parallelized using a shared-memory programming model (OpenMP). The correct behavior of all terms were verified with simple test cases (see appendix A.1). The correct long-range decay of the polarization ($1/r^4$) was confirmed using an isolated lithium atom ($Li^{\bullet}$) interacting with an external charge. The correct long-range behavior of dispersion ($1/r^6$) and charge transfer (exponential) were confirmed with $He\cdots Li^{\bullet}$ complex (see Figs. A.1(a)–(d)).

2.4 Results

The method is first applied to the binary radical-solvent complexes from the TA13 benchmark set. [209] Next, we use this method to investigate the first solvation step of cationic halogenated benzene radicals. As the final example, we study the different interaction motifs of a $CO_2{}^{-\bullet}$ radical with N-heterocycles (pyridine and imidazole) in the gas phase. With UMP2, there is spin contamination in at least one example in all three sets of applications: $HF{-}CO^+$ in the TA13 benchmark set ($\langle S^2\rangle = 0.83$), the halogen-bonded chlorobenzene radical cation–water complex ($\langle S^2\rangle = 0.88$), and the $Py{-}CO_2{}^{-\bullet}$ complex ($\langle S^2\rangle = 0.94$). Furthermore, the RMSDs of UMP2 and RMP2 for the TA13 benchmark set (8.9 and 6.9 kJ/mol, respectively) suggest that RMP2 yields more accurate interaction energies. Hence, the following discussion focuses on the RMP2-EDA results only, which are also consistent with DFT-EDA (ωB97M-V) results (Tables A.4 and A.6 in the SI).

TA13 Benchmark Set

The TA13 benchmark set [209] includes thirteen binary radical-solvent complexes with non-bonded interactions, which are considered to be challenging non-covalent interactions for DFT due to a prominent self-interaction error. [20, 54, 55, 231] The popular B3LYP functional has an RMSD of 16.1 kJ/mol for the interaction energies, and ωB97M-V, the overall best-performing functional according to extensive benchmarking, has an RMSD of 11.5 kJ/mol.[20] Both UMP2 and RMP2 calculations were performed for the interaction energies on all 13 molecules with significantly smaller RMSD values of 8.9 and 6.9 kJ/mol (for full results see Tables A.1 (U) and A.2 (RO) in the appendix), respectively. The UMP2 vs. RMP2 difference stems mainly from the $CO^+{-}HF$ complex because UMP2 exhibits significant spin contamination ($\langle S^2\rangle = 0.83$ for the complex and 0.93 for the CO^+ monomer).

The correlation energy is significant in most cases: e.g., it accounts for $\sim 50\%$ of the binding energy for Al$-H_2O$. The frozen terms at the MP2 level are all positive as the perturbation theory tends to correct for the overestimation of the dipole moments of the HF reference (see Table A.2). The radical alignment scheme (see Sec. 2.3) is crucial for radicals with degenerate electronic configurations such as Cl$-OH_2$, for which there can be a difference up to 40 kJ/mol in the resulting frozen term otherwise, depending on how the fragment spins are aligned initially.

The RMP2-EDA results are presented in Table 2.1 and are categorized into three groups based on the interaction motifs: electron-rich metal-water complexes, electron-poor hemibonded complexes, and hydrogen-bonded complexes. Additional details are provided in Table A.2 in the appendix, such as the break-down into HF and correlation contributions. The electron-rich metal-water complexes (Li, Al, Be^+) display large polarization and relatively small charge transfer. This is already an interesting and surprising result, because it suggests that the strong interaction is primarily *non-bonded* rather than having a substantial covalent contribution, as had been inferred from natural bond orbital (NBO) analysis.[260] The optimized geometry of these complexes involves interaction of the O atom of water with the metal center, which is the main reason that CT from the electron-rich metal center to the solvent is somewhat suppressed. As a fraction of the binding energy, CT is most important for the Al$-H_2O$ complex, which also has a prominent contribution from dispersion.

The interaction of the family of electron-poor hemibonded complexes is mainly driven by charge transfer. Both Cl– and Br–water complexes show a significant charge transfer contribution to overcome Pauli repulsion at the frozen level. The cationic carbonyl complex with HF also shows a large CT contribution. However, in contrast to the halogen complexes, its short bond distance (r(O-F) = 1.8 Å) results in a strongly repulsive frozen term and the charged fragment induces significant polarization. The $NH_3{}^+-H_2O$ complex shows balanced contributions from all terms, which is more similar to the typical scenario of the hydrogen-bonded motifs.[83, 261] The strong electrostatic interaction renders the frozen term already attractive as the charge on the $NH_3{}^+$ radical and dipole moment of the water are favorably aligned. The charge also results in significant polarization. The last member of this group, F$-OH_2$, exhibits the largest error among the RMP2 interaction energies in this benchmark set. This complex has significant static correlation and is consequently not very accurately described by MP2 (or DFT) methods as discussed in ref. [209]. Hence, the EDA terms are just reported for completeness.

The hydrogen-bonded complexes have more balanced contributions from all energy components including significant charge transfer similar to results reported for closed-shell hydrogen bonding. [201, 261, 262] However, there are variations in the weight of these terms: the importance of charge transfer (measured relative to the total interaction energy) is higher for the more electropositive radicals such as CH_3 and BH_2, while complexes of the more electronegative radicals (NH_2, OH and $HNH_2{}^+$) exhibit stronger attractive electrostatic interaction (resulting in a less repulsive frozen term) and more significant polarization.

Table 2.1: RMP2-EDA results for the TA13 benchmark set evaluated with the aug-cc-pVTZ basis. Energies are in kJ/mol and r refers to the complex bond distance.

System	ΔE_{FRZ}	ΔE_{POL}	ΔE_{DISP}	ΔE_{CT}	ΔE_{TOT}	r(Å)
electron-rich metal-water complexes						
H_2O-Al	96.9	-86.1	-21.5	-16.7	-27.5	2.20
H_2O-Be^+	102.8	-306.9	-11.8	-42.7	-258.6	1.57
H_2O-Li	40.5	-66.2	-8.0	-11.5	-45.2	1.88
electron-poor hemibonded complexes						
H_2O-F	60.6	-9.5	-11.7	-36.3	3.1	2.11
H_2O-Cl	28.9	-7.1	-12.2	-19.7	-10.0	2.60
H_2O-Br	28.9	-8.5	-12.9	-17.6	-10.2	2.70
$HF-CO^+$	121.5	-101.8	-22.1	-117.4	-119.9	1.80
$H_2O-NH_3{}^+$	-14.3	-21.5	-12.3	-22.8	-70.8	2.32
hydrogen bonded complexes						
$HOH-CH_3$	6.8	-2.9	-5.5	-5.1	-6.7	2.33
$H_2O-HNH_2{}^+$	-3.2	-54.9	-13.5	-32.6	-104.2	1.54
$FH-BH_2$	11.1	-8.6	-5.6	-13.3	-16.4	2.22
$FH-NH_2$	12.9	-24.0	-9.9	-20.6	-41.7	1.75
FH−OH	5.7	-12.0	-6.6	-10.8	-23.7	1.81

Halogenated Benzene Radical Cation: Halogen or Hydrogen Bonding?

Ionic hydrogen bonds (IHBs) constitute a subclass of hydrogen bonding between radical ions and polar molecules with a binding energy ranging from -20 to -140 kJ/mol. [232, 263] Halogen bonds are defined according to IUPAC as a linear binding motif R−X···Y where X denotes a covalently bonded halogen atom acting as a Lewis acid (electron-poor) and Y is an electron-rich Lewis base (e.g. halide anion, water, etc.). [264] Halogen bonding is a type of intermolecular interaction that in part arises from the favorable electrostatic interaction between the halogen atom and the acceptor (Lewis base), which is often described in terms of the so-called σ-hole [265, 266]. However, many recent studies suggest that the $n \rightarrow \sigma^*$ charge transfer plays an important and even dominant role in halogen bonding.[267–272] While a consensus has almost been reached that permanent electrostatics alone is inadequate to describe halogen bonds, there is still an ongoing debate especially about the role of charge transfer. [266, 267, 269–274]

A recent study by El-Shall and co-workers discovered two competing mechanisms for the first hydration step of halogen-substituted benzene radical cations using mass-selected ion mobility spectroscopy. Depending on the halogen atom there is a preference for either IHBs, as depicted in Fig. 2.3(a), or ionic halogen bonds (IXBs), as depicted in Fig. 2.3(b). [232]

The authors found that $C_6H_5F^{+\bullet}$ solely forms IHB while $C_6H_5I^{+\bullet}$ solely forms IXB, and the chloro- and bromobenzene radical cations show an equilibrium between IXB and IHB isomers. [232] The substituent dependence of the IHB vs. IXB competition makes this class of systems interesting candidates for an EDA analysis. These insights on the control of halogen bonding strengths can be useful for the design of new catalysts.[275]

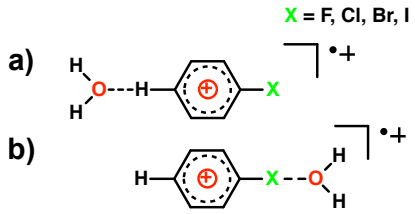

Figure 2.3: Two competing binding motifs for the interaction between a halogenated benzene radical cation ($C_6H_5X^{+\bullet}$) and a water molecule: (a) Ionic hydrogen bonding (IHB) and (b) ionic halogen bonding (IXB).

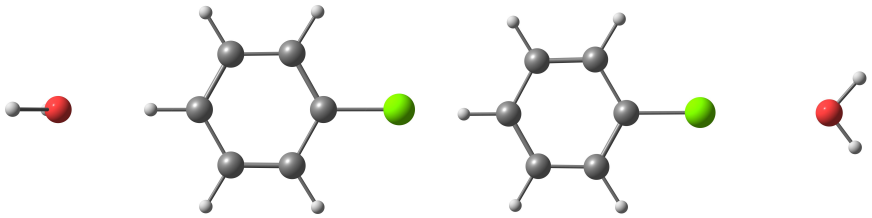

Figure 2.4: Optimized geometries for two isomers of the halogenated benzene radical cation–water complex: (a) the IHB structure ($r_{H\cdots O}$ in Å: F: 2.02, Cl: 2.04, Br: 2.05, I: 2.08); (b) the IXB structure ($r_{X\cdots O}$ in Å: F: 2.97, Cl: 2.78, Br: 2.78, I: 2.83).

The RMP2-EDA was employed to understand the competition between IHB and IXB in complexes of H_2O with $C_6H_5X^{+\bullet}$: a total of eight different isomers were analyzed. As an example, the optimized geometries of the IHB and IXB complexes formed by bromobenzene are shown in Fig. 2.4. All RMP2 interaction energies are in good agreement with the results of an accurate double-hybrid functional (ωB97M(2)) with the def2-TZVPPD basis (see Table A.3). Furthermore, it is verified that the trends in both the total interaction energies and the individual energy components are consistent with the results of DFT-based ALMO-EDA with ωB97M-V (see table A.4).

The full results for the bromobenzene–water complex are shown in Fig. 2.5, whose IHB and IXB isomers are of the closest total interaction energies (with the IXB isomer being slightly more favorable by 2.8 kJ/mol) among all halogenated benzene radicals investigated

here. The relative EDA energies with respect to fluorobenzene for both binding motifs are shown in Fig. 2.6, which help uncover the trends *within* each binding mode. Finally, the energy differences between IHB and IXB in the total interaction energies and each individual energy component is depicted in Fig. 2.7 to help understand the different binding preferences for each halogenated benzene radical cation.

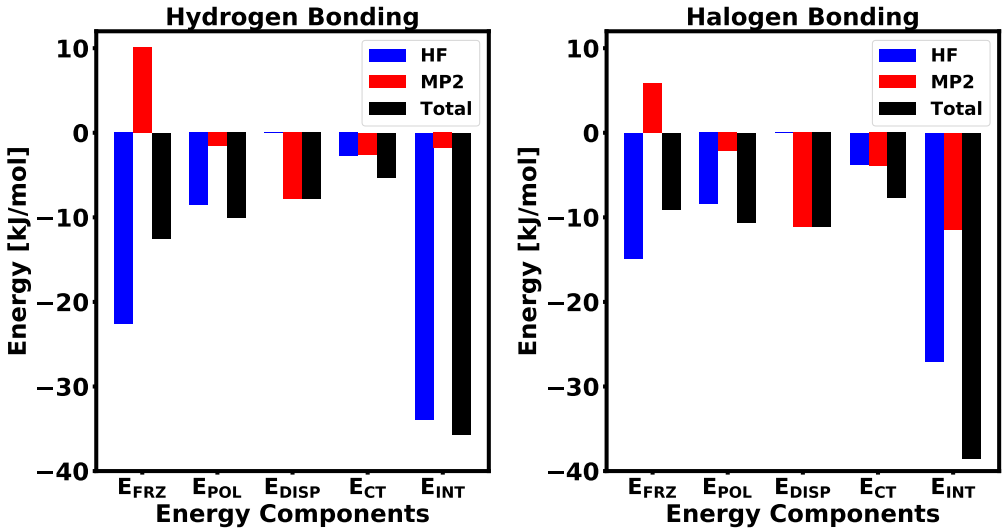

Figure 2.5: Individual EDA terms (in kJ/mol) for the two binding motifs of the water–bromobenzene radical cation complex, separated into HF and MP2 contributions.

The EDA results for the IHB bromobenzene radical cation (see the left panel of Fig. 2.5) show an interaction that is dominated by attractive frozen (due to permanent electrostatics) and polarization terms, and the contributions from dispersion and charge transfer are also not negligible. Although the MP2 contribution to the total IHB interaction energy is small, its contributions to the individual terms are not, especially its effect on the frozen term where MP2 corrects the overly attractive electrostatic interaction evaluated at the HF level.[211] The EDA results uncover a favorable error cancellation for the IHB motif at the HF level as the overestimated permanent electrostatic interaction compensates for the missing dispersion contribution that only arises at the MP2 level. The IXB motif has a more significant net MP2 contribution, and it is noteworthy that IXB is more favorable than IHB for this complex only when the effects of electron correlation are incorporated.

For the IHB isomers $H_2O\cdots C_6H_5X^{+\bullet}$, as shown in the left panel of Fig. 2.6, the magnitude of the total interaction energy monotonically decreases from lighter to heavier halogens. This trend stems mainly from the changes in the frozen and polarization terms (i.e. permanent and induced electrostatics), and can be readily rationalized with the increasing strength of the mesomeric effect (donating lone pairs to the benzene ring) of the halogens that makes the *para*-carbon more electron-rich and the C–H bond less polar. The CT term appears to be nearly independent of the halogen, which can be rationalized by analyzing the most

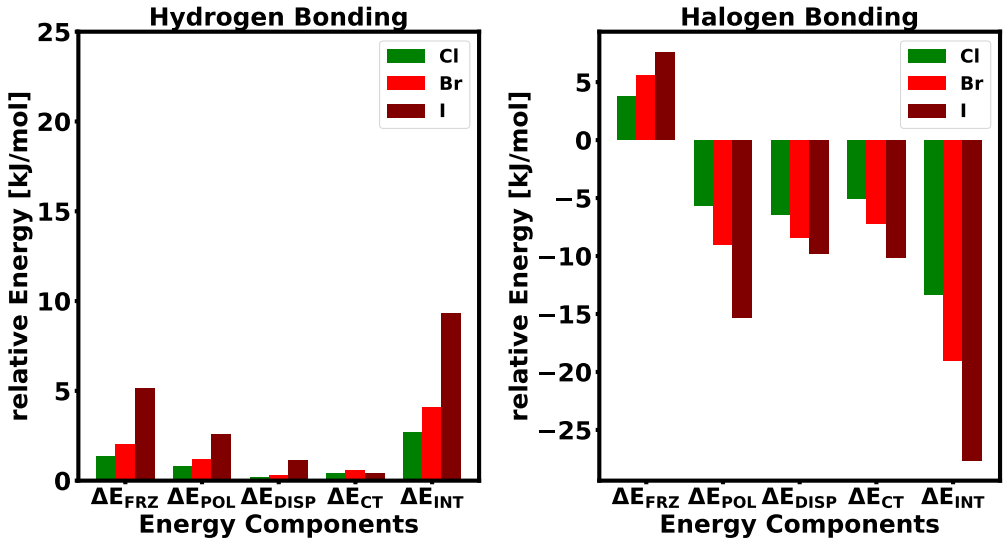

Figure 2.6: Changes in the total interaction energy and individual EDA terms for the heavier halogenated benzene radical cations relative to the fluorobenzene results with the two bonding motifs of the $H_2O\cdots C_6H_5X^{+\bullet}$ complexes.

important COVP. As shown in Fig. A.2(a) in the SI, the CT in the IHB isomer is primarily from the oxygen lone pair on H_2O to the C−H σ^* orbital. This acceptor orbital is not strongly affected by the *para*-substitution.

The EDA results for the IXB bromobenzene (the right panel of Fig. 2.5) show significant contributions from all terms with polarization and dispersion being the most important contributions. The MP2 term has the same sign for E_{POL} and E_{CT} but has an opposite sign for the frozen term, for the reason discussed above. The importance of all interaction energy components (permanent electrostatics, polarization, dispersion, and charge transfer) to overcome the Pauli repulsion for the IXB binding motif is in line with the conclusion reached by a previous study on halogen bonding by some of us.[270]

As shown in Fig. 2.6, the IXB interaction energy increases strongly for the heavier halogens. The interaction with fluorobenzene is the weakest, and in fact, the IXB isomer for fluorobenzene could only be obtained with a symmetry constraint (C_{2v}) in the geometry optimization (i.e. it is not the global minimum on the PES). The increase in halogen bond strength is mainly attributed to an increase in polarization, dispersion and charge transfer. The increase in dispersion and polarization can be rationalized by the increasing softness and ionic radius down the halogen series. Interestingly, the frozen term exhibits an opposite trend and is most favorable for the fluorobenzene, which is mainly attributed to the increase in Pauli repulsion as the halogen becomes more diffuse from F to I while the equilibrium X$\cdots$O distances do not change significantly (see the distances given in the caption of Fig. 2.4). The increase in charge transfer can be rationalized by analyzing the COVP (see Fig. A.2(b)): the charge transfer is dominated by the donation from the oxygen lone pair

to the C−X σ^* orbital whose energy is lowered (which facilitates CT) monotonically for the heavier halogens.

The comparison between the IHB and IXB isomers for each halogenated benzene radical cation is shown in Fig. 2.7, in which the differences (IHB − IXB) in both the total interaction energy and each individual component are plotted. The IHB is more favorable than the IXB motif by over 20 kJ/mol for fluorobenzene, while the interaction energies of IHB and IXB are very similar for both Cl- and Br-substituted benzene radical cations. Iodobenzene, on the other hand, prefers the IXB motif by more than 27 kJ/mol. This trend can be explained by the increase of polarization, dispersion, and charge transfer of the IXB motif due to the increasing softness, atomic radius, and lower-lying C−X σ^* from F to I contrasting with the almost constant behavior of the hydrogen bonding side.

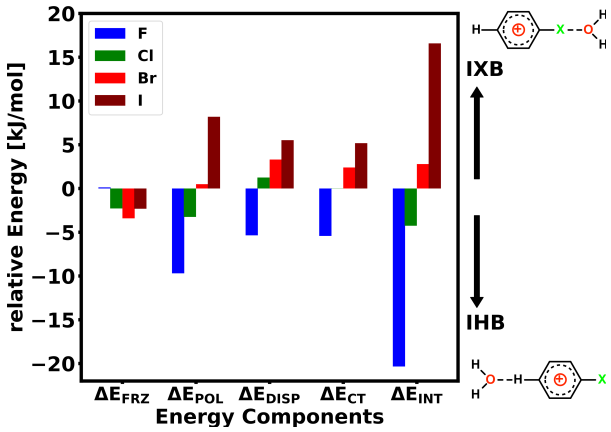

Figure 2.7: Term-by-term energy differences between the IHB and IXB binding motifs of the $H_2O\cdots C_6H_5X^{+\bullet}$ complexes.

Anionic CO_2 radical N-heterocycle complexes

Fossil fuel emission is yielding unprecedentedly high concentrations of CO_2 in the atmosphere, which acts as one of the main driving forces of global climate change. This has attracted considerable attention on artificial photosynthesis. [276, 277] Both pyridine (Py), C_6H_5N, and imidazole (Im), C_3N_2H, are known to be active catalysts in the photoelectrochemical conversion of CO_2. [278, 279] Interestingly, two distinct mechanisms are proposed for the initial CO_2 activation: pyridine forms a C−N bond via a carbamate intermediate; in contrast, imidazole forms a C−C bond with the C2 carbon. [279] In the quest for the elucidation of catalytic mechanisms, structural information about possible intermediates is both crucial and scarce.

Johnson and co-workers characterized possible intermediates via the reaction of both N-heterocycles with small anionic CO_2 clusters ($(CO_2)_m^{-\bullet}$, m=2−7) [280–282] in the gas

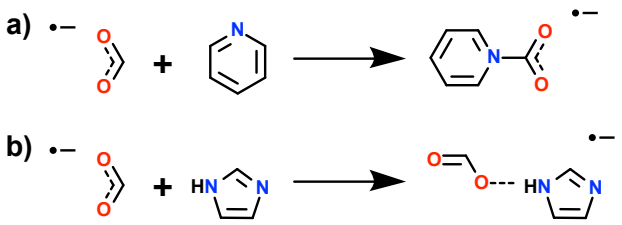

Figure 2.8: Different binding motifs for the association of a $CO_2^{-\bullet}$ with nitrogen heterocycles: (a) pyridine (Py) resulting in a carbamate radical anion and (b) imidazole (Im) resulting in hydrogen bonding.

phase. They obtained vibrational spectra of both anionic complexes: $Py{-}CO_2^{-\bullet}$ and $Im{-}CO_2^{-\bullet}$. [233, 234] The stable carbamate $Py{-}CO_2^{-\bullet}$ radical anion (Fig. 2.8(a)) was discovered by the reaction of $(CO_2)_m^{-\bullet}$ clusters with pyridine in the gas phase. [233, 283] The carbamate motif was identified via a C-N stretch feature in the vibrational predissociation spectra of $Py{-}CO_2^{\cdot -} \cdot (CO_2)_3$. [233] A similar study using imidazole instead of pyridine found a different interaction motif (Fig. 2.8(b)): hydrogen bonding of $CO_2^{-\bullet}$ to the H−N group yields a strong red-shift in the N-H stretching frequency. [234]

Since the different nature of these interactions could be relevant to their different catalytic mechanisms, we employ RMP2-EDA to gain insights into these two distinct binding motifs. In particular, by comparing the EDA results for the four complexes shown in Fig. 2.9 ($Py{-}CO_2^{-\bullet}$ and $Im{-}CO_2^{-\bullet}$ with two binding modes for each), we elucidate why different binding motifs are preferred by pyridine and imidazole. All RMP2 interaction energies are in good agreement with reference interaction energies calculated at the ωB97M(2)/def2-QZVPPD level of theory (see table A.5). Furthermore, the same trends in both the total interaction energies and the individual EDA terms are obtained using DFT-EDA with the ωB97M-V functional (see table A.6).

The calculated total binding energies are similar for $Py{-}CO_2^{-\bullet}$ and $Im{-}CO_2^{-\bullet}$, which are −140 and −104 kJ/mol, respectively. However, as shown in Fig. 2.10, the energy components reveal dramatically different nature of these interactions. The carbamate motif is strongly repulsive at the frozen level. This can be understood by the fact that the unpaired electron is localized in a CO_2 π^* orbital, which localizes most of the spin density on the carbon atom (see Fig. A.3(a)). In addition, the C−N bond distance is very short at only 1.49 Å, rendering the frozen term dominated by the Pauli repulsion between the lone pair of the N atom and the π^* of the $CO_2^{-\bullet}$-fragment. The polarization term is strongly attractive, which is most likely due to the redistribution of charges on the $CO_2^{-\bullet}$ fragment induced by the lone pair on nitrogen. This effect can be rationalized by the electron density difference of $CO_2^{-\bullet}$ with and without a partial negative charge ($0.5e^-$) located 1.5 Å away from the carbon atom on the bisector, which demonstrates how an electronegative species redistributes the spin density from C to both O atoms (see Fig. A.3(b)). CT also plays an important role in this interaction, and it is bidirectional with both forward and backward donations

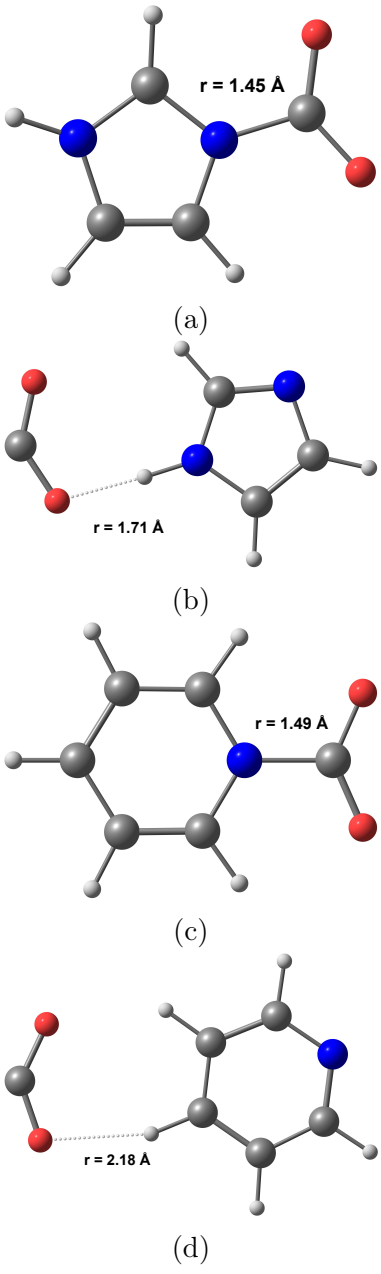

Figure 2.9: Geometries of the four possible isomers using both binding motifs for the reaction of a $CO_2^{-\bullet}$ with nitrogen heterocycles: (a) carbamate Im$-CO_2^{-\bullet}$; (b) hydrogen-bonded Im$-CO_2^{-\bullet}$; (c) carbamate Py$-CO_2^{-\bullet}$; (d) hydrogen-bonded Py$-CO_2^{-\bullet}$.

being significant. The spin density of the fully relaxed Py$-CO_2^{-\bullet}$ complex reveals a forward donation of the unpaired electron into the pyridine's π^* orbital (see Fig. A.3(c)). However, the bent O$-$C$-$O angle indicates a reduced CO_2 fragment, implying significant backward

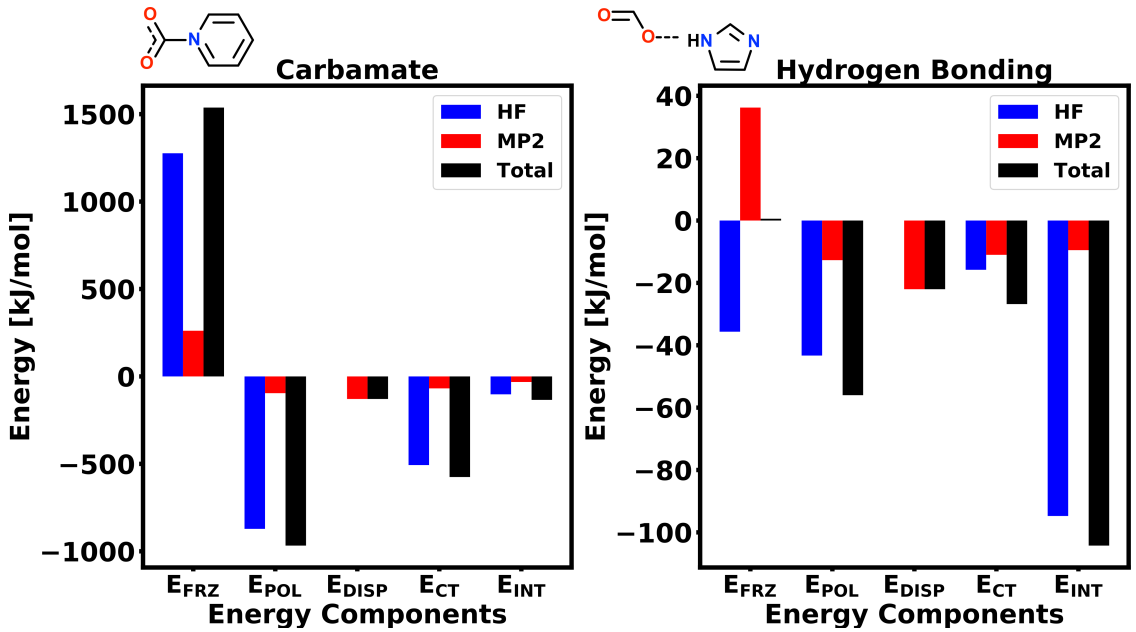

Figure 2.10: RMP2-EDA results (using the aug-cc-pVTZ basis) for the carbamate and hydrogen bonding motifs of $CO_2^{-\bullet}$, separated into HF and MP2 contributions.

CT from the lone pair into the CO_2 fragment. Note that polarization of the CO_2 fragment, as discussed above, makes the carbon more positive and thus more prone to nucleophilic attacks).

In contrast, the EDA fingerprints of the hydrogen-bonded Im$-CO_2^{-\bullet}$ complex (the right panel of Fig. 2.10) shows more balanced contributions from various components, which is similar to the IHB motifs discussed in Sec. 2.4. The O$-$H bond distance (1.71 Å) is slightly longer than the carbamate motif for Py$-CO_2^{-\bullet}$. The largest contribution comes from polarization, followed by also significant contributions from dispersion and charge transfer. The dominant role of polarization can be readily rationalized by the anionic CO_2 fragment that has large polarizability and the polar N$-$H bond. Interesting, the HF and MP2 contributions to the frozen term almost perfectly cancel each other for this complex, rendering the overall frozen term close to zero.

The experimentally observed Py$-CO_2^{-\bullet}$ carbamate has an interaction energy of -146.4 kJ/mol as calculated with RMP2. By contrast, the imidazole carbamate (Fig. 2.9(a)) is far less stable with an interaction energy of only -20.7 kJ/mol. The EDA components of the imidazole carbamate relative to the pyridine results are shown in the left panel of Fig. 2.11. The frozen interaction is significantly more repulsive for imidazole carbamate, which, however, is almost fully compensated by its more favorable polarization energy. There is also a significant decrease in CT from pyridine to imidazole, even though the latter is a stronger base and thus should exhibit a stronger forward donation from the nitrogen lone

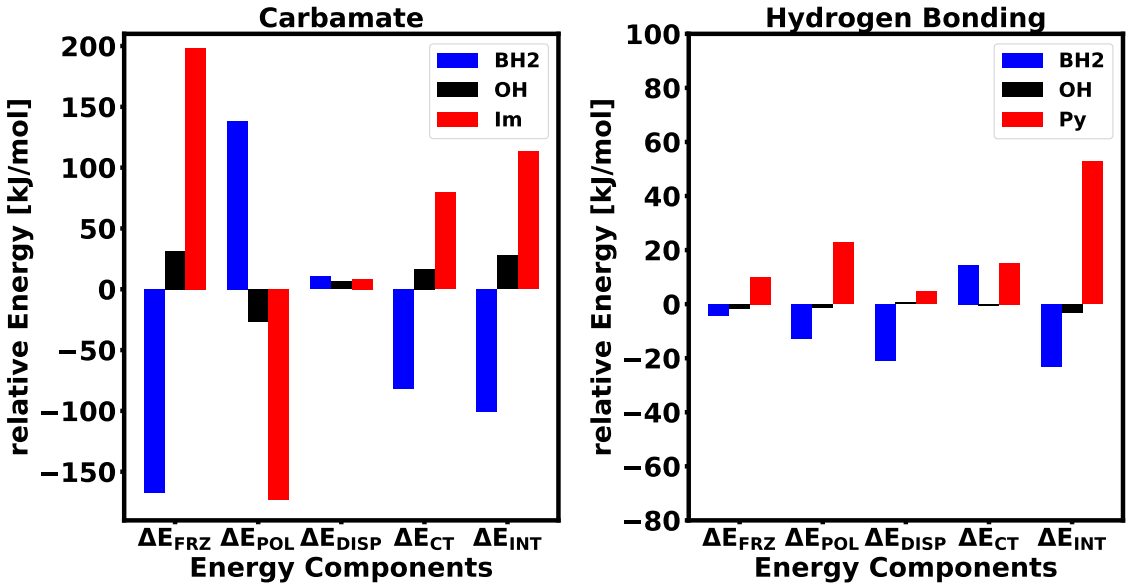

Figure 2.11: Left panel: comparison of the EDA components for the Py$-CO_2^{-\bullet}$ carbamate against those for its *para*-substituted (by $-$OH and $-BH_2$) derivatives and the imidazole carbamate; right panel: comparison of the Im$-CO_2^{-\bullet}$ hydrogen-bonded complex against the hydrogen binding of pyridine and its *para*-substituted derivatives with $CO_2^{-\bullet}$.

pair to $CO_2^{-\bullet}$. The results imply that this is insufficient to compensate for the less favorable back donation of the $CO_2^{-\bullet}$ fragment into the π^* orbital of imidazole.

To probe the effect of substituent groups on the Py$-CO_2^{-\bullet}$ carbamate complex, we separately place an electron-donating hydroxyl ($-$OH) group and an electron-withdrawing $-BH_2$ group at the *para* carbon. The energy components relative to the unsubstituted pyridine results are plotted on the left panel of Fig. 2.11. The $-BH_2$ group yields a more electron-deficient aromatic system, strengthening the interaction energy by $\sim$100 kJ/mol. The comparison against the unsubstituted case manifests its less repulsive frozen term as well as a less favorable polarization contribution, for which the differences largely cancel each other. The $-BH_2$ group also facilitates the donation from $CO_2^{-\bullet}$ to the lowered π^* orbital, as reflected by the markedly stronger charge transfer stabilization. An opposite effect is observed with the $-$OH group, which has a positive mesomeric effect by donating electron to the π-system, and it reduces the interaction energy with $CO_2^{-\bullet}$ by 28 kJ/mol. This net decrease mainly stems from the more repulsive frozen interaction and the weaker donation from $CO_2^{-\bullet}$ to the π^* orbital.

The RMP2 results for experimentally observed hydrogen-bonded Im$-CO_2^{-\bullet}$ yields an interaction energy of -104.2 kJ/mol, while the hydrogen-bonded Py$-CO_2^{-\bullet}$ complex (Fig. 2.9(d)) is only half as strongly bound (-51.5 kJ/mol). The EDA components of the hydrogen-bonded pyridine relative to the hydrogen-bonded imidazole complex are shown on the right panel

of Fig. 2.11. All energy components are destabilized upon the replacement of imidazole by pyridine. The N−H bond is more polar than C−H, which explains the more favorable electrostatic interaction as well as the stronger polarization of $CO_2^{-\bullet}$ in the complex with imidazole. The COVPs reveal a donation from $CO_2^{-\bullet}$ into the N−H σ^* orbital, which is more favorable than the donation into the C−H σ^*, elucidating the difference in CT (see Fig. A.4). This is similar to the trend observed in Sec. 2.4. In contrast to the carbamate motif, there is no clear substituent effect for the hydrogen bonding motif because the π system does not play a key role in this type of interaction as the same COVP implies.

2.5 Conclusion

In this work, we generalized the previously reported closed-shell MP2-EDA scheme [212, 227] to unrestricted and restricted open-shell MP2. This permits decomposition of the correlation energy of intermolecular interactions of radical systems into frozen, polarization, dispersion and charge transfer components. The scheme is efficiently implemented using OpenMP parallelism. In the case of a single atom or small radical fragments where the unpaired electron is located in a non-spherically symmetric orbital (e.g. $Cl^\bullet$), a proper alignment of the radical at the isolated fragment stage is necessary for obtaining unambiguously defined frozen and polarization energies.

Restricted open-shell MP2 is able to provide reasonably accurate binding energies for the radical-neutral complexes contained in the TA13 benchmark set, for which DFT can be error prone due to the self-interaction problem. The EDA analysis revealed that the different bonding motifs are driven by different energy components: the electron-rich metal-water complexes by polarization, the electron-poor hemibonded complexes by charge transfer, and the hydrogen bonded complexes show more balanced contributions from all terms.

The MP2-EDA was applied to study the first solvation step of halogenated benzene radical cations with water where two binding modes are possible: ionic hydrogen bonding and ionic halogen bonding. The EDA results show that IXB becomes more favorable as the halogen becomes heavier due to an increase in polarization, dispersion and charge transfer, whereas the IHB binding site is not strongly affected by the type of halogen. This makes the halogen bonding site more attractive for the iodobenzene-water complex.

Analysis of $CO_2^{-\bullet}$ interacting with pyridine as a carbamate and with imidazole via hydrogen bonding revealed very different fingerprints for these interactions. The carbamate shows very repulsive frozen interaction, strong polarization and bidirectional charge transfer. The hydrogen bonding motif exhibits balanced contributions from polarization, dispersion and charge transfer with a frozen term of very small magnitude. The carbamate motif is preferred by pyridine as it allows for a stronger charge transfer interaction, whereas the hydrogen bonding motif is preferred by imidazole because the more polar N−H bond results in stronger polarization of the $CO_2^{-\bullet}$ fragment. Furthermore, the importance of charge transfer into the π^* orbital of the heterocycle was discovered as a parameter to control the stability of the carbamate binding mode with a substituent effect.

While the MP2-EDA is already useful for chemical applications, as demonstrated by the examples presented here, further methodological development is still desirable in the future. Unlike the second generation ALMO-EDA for DFT that has a useful basis set limit for all terms [84], our current MP2-EDA scheme does not have this desirable feature. We hope to lift this limitation in future work. Additionally, it would be highly desirable to extend this approach from MP2 to recently developed methods based on regularized orbital-optimized MP2 (OOMP2) [26, 40, 284] and double-hybrid density functionals.[63, 285] Furthermore, extending it to higher-order MP approach using OOMP2 orbitals[286] as well as revisiting coupled-cluster methods [230] are needed when a more accurate description for electron-electron correlation effects is necessary.

Chapter 3

Variational Forward-Backward Charge Transfer Analysis Based on Absolutely Localized Molecular Orbitals: Energetics and Molecular Properties

3.1 Introduction

The stability of dative bonds in classical Lewis acid-base compounds is controlled by the effect of charge transfer (CT). [287] The widely used concept of donor-acceptor interaction stems from the assumption that charge flows from one fragment to another. In simple adducts like ammonia–borane or transition metal complexes with ligands that are σ-donors only (e.g. NH_3, H_2O), the assignment of the donor and acceptor moieties is straightforward, while in many other cases, the donor and acceptor moieties interchange their roles when different orbital interactions are considered, wherein the CT is bi-directional. The relative strength of the forward and backward CT and their cooperativity impose a substantial influence on the physical and chemical properties of these donor-acceptor systems.

Complexes formed by π-acidic ligands (e.g. CO, N_2, NO, etc.) with main group or transition metal Lewis acids serve as a prominent class of examples for bi-directional CT. The synergistic effect of the σ forward donation (ligand$\rightarrow$metal) and the π back-donation (ligand$\leftarrow$metal) is a well-established concept (Dewar-Chatt-Duncanson) [89, 90] and was extensively studied with various computational and analysis schemes. [87, 199, 288–292] The most prominent representative of this class of ligands is carbon monoxide (CO), which gives rise to the rich chemistry of a large variety of organometallic compounds ranging from mono-metal complexes (e.g. $[Ni(CO)_4]$ [293]) to small multi-metal clusters (e.g. $[Fe_2(CO)_9]$ [287, 294, 295]). Classical carbonyl compounds exhibit a red shift of 0–300 cm^{-1} in the CO stretching frequency (ν_{CO}) relative to that of the free CO molecule (2143 cm^{-1}), and the shift can be as large as 681 cm^{-1} for $Na_4[CrCO_4]$. [296] On the other hand, some

other metal-carbonyl complexes (especially cationic complexes) exhibit a blue shift in ν_{CO}, which were classified as "nonclassical" metal carbonyls. [297] Besides bonding with transition metals, CO also forms adducts with main group Lewis acids where the similar bi-directional CT is observed, including various boron compounds [83, 87, 298] and intramolecular B/N frustrated Lewis pairs [299]. Most recently, it was shown that CO is able to form octacarbonyl complexes with alkaline earth metals (Ca, Sr, and Ba) in their zero oxidation state [300] and a strongly red-shifted cationic monocarbonyl complex with Ba^+,[301] where the ns^2 electrons are promoted to the empty (n-1)d orbitals to facilitate the backbonding to CO, which further indicates the strong π-acidity of CO.

Dinitrogen (N_2), which is isoelectronic to CO, is considered to be a weaker σ-donor due to its more compact electron lone pair and also a weaker π-acceptor because of its larger HOMO-LUMO gap than CO, and consequently the coordination chemistry of N_2 is less rich. Nonetheless, since the discovery of the first complex with Ru(II),[302] many transition metal dinitrogen complexes have been synthesized (the interested reader is referred to the published reviews[303, 304]). The complexation of N_2 with transition metals is of crucial importance for artificial nitrogen fixation at ambient conditions, [305–312] which often involves the "activation" of the triple bond, i.e., the back-donation from the metal to the π^* antibonding orbital of N_2. In practice, one often measures how activated the N_2 is by measuring the red shift in its stretching frequency. The shift is about 200 cm^{-1} for the first reported $[Ru(II)(NH_3)_5N_2]^{2+}$ complex and increases to 400 cm^{-1} for a recently reported tris(phosphino)silyl osmium complex. [310] Gaining insights into how the chemical environment (such as the metal center and the ligand field) modulates the strength of the backward donation to N_2 will thus play an essential role in understanding the molecular mechanism of nitrogen fixation that facilitates the design of novel and highly efficient catalysts.

The strength of forwards and backwards direction of CT in the above-mentioned complexes depends on both the π-acidic ligand and the σ-acceptor moiety. To shed light on the nature of donor-acceptor interactions as well as the factors that govern their strength, one can resort to energy decomposition analysis (EDA) schemes [188–190] to unravel the effect of charge transfer (along with other binding forces) upon the formation of dative complexes. Originating from the pioneering Kitaura-Morokuma EDA,[192, 193] the early variational EDA approaches define CT as the mixing of one fragment's occupied orbitals into virtuals of other fragments. Therefore, starting with molecular orbitals (MOs) optimized on each fragment, one can quantify the energy contribution associated with the CT from one fragment (A) to another (B) by evaluating the change in SCF energy upon the inclusion of the A(occupied)$\rightarrow B$(virtual) relaxations into the variational degrees of freedom. This approach was widely used in early EDA methods, such as the reduced variational space (RVS) [313] and the similar constrained space orbital variation (CSOV) [314] schemes, to identify the forward and backward CT contributions between a pair of fragments. The natural bond orbital (NBO) analysis [315, 316] also employs a similar way to define CT between pairs of fragments although very different reference orbitals ("Lewis" orbitals prepared by the NBO procedure that remain strongly orthogonal even between fragments) are employed.

The more recently developed charge transfer analysis (CTA) based on absolutely local-

ized molecular orbitals (ALMOs) [87] is also able to separate the forward and backward CT contributions for each pair of molecules in a system. Starting from fragment orbitals that are variationally optimized within the supersystem (polarized ALMOs),[31] this approach approximates the CT stabilization energy using the energy lowering associated with a single Roothaan step, i.e., one diagonalization of the supersystem Fock matrix, which is further reformulated with unitary orbital rotations generated from a single-excitation operator ($\mathbf{X}_{\text{vo}}$).[317] The total stabilization energy can then be partitioned into contributions from forward and backward CT between different fragment pairs, which is achieved by evaluating the energetic stabilization associated with each off-diagonal block of $\mathbf{X}_{\text{vo}}$ in the polarized ALMO basis. Moreover, one can perform a singular value decomposition (SVD) on each off-diagonal block of $\mathbf{X}_{\text{vo}}$, yielding the complementary occupied-virtual pairs of orbitals (COVPs) that make the most significant contribution to the CT between a specific pair of fragments.[87]

While the schemes introduced above can separate the total CT energy into forward and backward contributions and even further into contributions from different pairs of donor and acceptor orbitals, most are unable to characterize the observable effects of CT. The recently developed adiabatic EDA scheme [201] (see Sec. 3.2) represents a systematic step forward to address this gap, which allows one to characterize the effects of CT (and other physical components) on molecular structures and vibrational frequencies. This approach has been employed to investigate observable shifts induced by intermolecular binding, such as the red or blue shifts in vibrational frequencies upon the formation of hydrogen or halogen bonds.[33, 91, 261, 270, 272] However, it has not been made generally possible yet to separate the observable effects of forward/backward CT in a manner that is similar to how the ALMO-CTA identifies the $A{\rightarrow}B$ and $B{\rightarrow}A$ contributions for a pair of fragments A and B,[87] even though such a partition is highly desirable in particular for interpretation purposes. One early exception was the already mentioned CSOV approach, which employed full SCF for one fragment in the field of e.g. frozen orbitals of the other. CSOV was applied for studies of CO bound to metal atoms and clusters.[314, 318, 319] We note that a decomposition scheme with a similar objective was recently formulated by deriving ALMO-based linear response equations, which, nonetheless, is limited to molecular properties that are only concerned with electronic degrees of freedom, such as static polarizabilities.[320, 321]

In this work, we extend the original formulation of the adiabatic ALMO-EDA by introducing two additional intermediate potential energy surfaces (PESs). Inspired by the RVS and CSOV approaches, on each of these surfaces one single direction of CT (either $A{\rightarrow}B$ or $B{\rightarrow}A$) is permitted while the other direction remains forbidden. The response of the acceptor fragment to such a one-directional CT, on the other hand, is captured by the intermediate state defined thereof. We obtain these "one-way" CT intermediate states via a special type of self-consistent field (SCF) calculation, whose details are given in Sec. 3.2. The variational feature of these two states renders the associated nuclear gradients readily attainable, and thus one can conveniently use them in the context of adiabatic EDA. This opens the door to an in-depth analysis for the effect of forward and backward donations on the energetic, structural, and vibrational features of dative complexes. In Sec. 3.4, we first validate the results produced by these two "one-way" CT states using two prototypical

borane complexes ($H_3N{-}BH_3$ and $OC{-}BH_3$). We then utilize this approach to investigate the carbonyl complexes of beryllium oxide and carbonate (Sec. 3.4), as well as the complexes composed of a series of π-acidic ligands and the pentaammineruthenium ($[Ru(II)(NH_3)_5]^{2+}$) moiety.

3.2 Theory

Vertical vs. Adiabatic ALMO-EDA

The ALMO-EDA scheme [83, 84] separates the overall intermolecular interaction energy, ΔE_{INT}, into contributions from frozen interaction (ΔE_{FRZ}), polarization (ΔE_{POL}), and charge transfer (ΔE_{CT}):

$$\Delta E_{\mathrm{INT}} = \Delta E_{\mathrm{FRZ}} + \Delta E_{\mathrm{POL}} + \Delta E_{\mathrm{CT}} \tag{3.1}$$

where the frozen term can be further decomposed into contributions from permanent electrostatics (ΔE_{ELEC}), Pauli repulsion ($\Delta E_{\mathrm{PAULI}}$), and dispersion interaction (ΔE_{DISP}).[84, 86, 322] Such a decomposition is usually performed at a single given geometry and thus we refer to this approach as the *vertical* ALMO-EDA thereafter. For details regarding the physical meaning and mathematical definition of each of these terms, we refer the reader to our previous publications.[84, 86]

Contrasting with the vertical EDA, recently we also proposed an *adiabatic* formulation of the ALMO-EDA in order to analyze the shifts in molecular properties induced by intermolecular interactions.[201] Instead of decomposing a single-point interaction at a fixed geometry, the geometry of the complex is relaxed at the initial (isolated fragments), intermediate (frozen and polarized), and final (full complex) stages of an ALMO-EDA procedure. As in the vertical version of ALMO-EDA, the frozen state is defined as an antisymmetric product of isolated fragment wavefunctions, and the polarized state is obtained by variationally optimizing the supersystem wavefunction with respect to the orbital rotations on each fragment.[83] These electronic states correspond to distinct PESs, and the geometry relaxation on each of them is facilitated by use of the associated analytical nuclear gradients. Optimization of the isolated fragment and fully relaxed complex geometries can be achieved by employing standard SCF nuclear gradients, and the gradients for the frozen and polarized states have been previously derived by some of us.[201]

The geometry relaxation on each intermediate surface allows one to obtain information on how each intermolecular interaction component modulates the structure of a complex. Moreover, one can perform harmonic frequency calculations at the stationary points evaluated on each surface, thereby obtaining the vibrational frequency shifts induced by each physical component of the interaction.[201]

Generalized SCF-MI

In the original formulation of ALMO-EDA,[83] the polarized yet CT-forbidden state is obtained by using the "SCF for molecular interaction" (SCF-MI) procedure, where one variationally optimizes a fragment-block-diagonal AO-to-MO coefficient matrix with respect to the orbital rotations on each fragment. The variational space of each fragment is thus determined by the span of AO basis functions associated with the atoms that belong to the same fragment. The one-particle density matrix (1PDM) can be constructed from ALMOs using

$$\mathbf{P} = \mathbf{C}_{\mathrm{o}}(\boldsymbol{\sigma}_{\mathrm{oo}})^{-1}(\mathbf{C}_{\mathrm{o}})^{T} \tag{3.2}$$

where $\mathbf{C}_{\mathrm{o}}$ refers to the MO coefficients for the occupied ALMOs, and $\boldsymbol{\sigma}_{\mathrm{oo}}$ denotes their overlap metric, which is obtained by transforming the AO overlap matrix ($\mathbf{S}$) into the basis formed by these occupied ALMOs:

$$\boldsymbol{\sigma}_{\mathrm{oo}} = (\mathbf{C}_{\mathrm{o}})^{T}\mathbf{S}\mathbf{C}_{\mathrm{o}} \tag{3.3}$$

The energy functional, $E = E[\mathbf{P}]$, can be minimized by solving locally projected SCF equations[30, 31, 196] or using gradient-based optimization algorithms (with respect to on-fragment orbital rotations).[32]

By introducing the concept of *fragment variational subspaces*, we propose a generalized formulation of SCF-MI. For a given fragment A, instead of using its full AO span ($\mathbb{I}_A$), we define its variational degrees of freedom as $\mathbb{G}_A$, where $\mathbb{G}_A$ is the space spanned by a set of vectors whose expansion coefficients in the AO basis are given by a matrix $\mathbf{G}_A$, i.e., $\mathbb{G}_A = \mathrm{span}\{\mathbf{G}_A\}$. The concatenation of subspace vectors for each fragment, $\mathbf{G} = [\mathbf{G}_A, \mathbf{G}_B, ...]$, defines the effective working basis for SCF-MI. The MOs can thus be represented as linear combinations of vectors in $\mathbf{G}$, whose coefficients are denoted as $\mathbf{C}^G = [\mathbf{C}^G_{\mathrm{o}}, \mathbf{C}^G_{\mathrm{v}}]$. By left-multiplying $\mathbf{C}^G$ with $\mathbf{G}$, one can retrieve the AO-to-MO coefficient matrix:

$$\mathbf{C} = [\mathbf{C}_{\mathrm{o}}, \mathbf{C}_{\mathrm{v}}] = \mathbf{G}[\mathbf{C}^G_{\mathrm{o}}, \mathbf{C}^G_{\mathrm{v}}] \tag{3.4}$$

and the 1PDM can thus still be calculated via Eq. (3.2).

Within generalized SCF-MI, one only requires $\mathbf{C}^G$ to be fragment-block-diagonal, while the vectors that span the variational subspace of a given fragment ($\mathbf{G}_A$, $\mathbf{G}_B$, ...) are allowed to be expanded by AO basis functions centered on other fragments. The vectors in $\mathbf{G}$ that belong to the same fragment are orthonormalized against each other for convenience, while interfragment orthogonality is usually not enforced. It is evident that the generalized SCF-MI scheme imposes a weaker constraint on the MO coefficient matrix than the original ALMO definition since the AO-to-MO coefficient matrix $\mathbf{C}$ need no longer be "absolutely localized", and in fact, if one chooses $\mathbb{G}_A = \mathbb{I}_A$ for each fragment, the original AO-based ALMO results will be recovered by generalized SCF-MI. Nevertheless, as $\mathbf{C}^G$ has a fragment-block-diagonal structure just like the $\mathbf{C}$ matrix in the original scheme, similar equations still hold for generalized SCF-MI once the quantities are properly transformed into the basis defined by $\mathbf{G}$. In last two section of this chapter, we show the the locally projected SCF

equation and the energy gradient with respect to on-fragment orbital rotations for generalized SCF-MI.

The generalized SCF-MI scheme was originally proposed to allow for a truncated virtual space for each fragment being used in the polarization step of ALMO-EDA,[32] thus providing a well-defined separation between polarization and charge transfer. In addition to that, by modifying the content of $\mathbf{G}$, one can solve a broad spectrum of variational optimization problems with varying degrees of freedom using the SCF-MI procedure. As an extreme example, if one uses the full AO span of the whole system ($\mathbb{I}$) as the variational subspace for each fragment, the full SCF result will be recovered by performing a generalized SCF-MI calculation.

Variational Forward-Backward Analysis of the CT contribution

Making use of the flexibility in variational space offered by generalized SCF-MI, we introduce two additional intermediate states into the ALMO-EDA. For a system comprising two fragments, we first denote the converged orbitals (expanded in AOs) at the polarization step as $[\mathbf{C}_{\mathrm{o},A}, \mathbf{C}_{\mathrm{v},A}] \cup [\mathbf{C}_{\mathrm{o},B}, \mathbf{C}_{\mathrm{v},B}]$, which are absolutely localized on fragments A and B, respectively. Note that within generalized SCF-MI, these orbitals can be used to define the variational space for the polarized wavefunction (shown as stage (a) in Fig. 3.1), and the corresponding MO coefficient matrix $\mathbf{C}^G$, according to Eq. (3.4), will be an identity matrix ($\mathbf{I}$). We then construct the virtual space for the full system that is strongly orthogonal to the occupied space, which is spanned by the orthonormalized projected virtual orbitals. The projected virtuals are defined as

$$\mathbf{C}_{\mathrm{v,proj}} = (\mathbf{I} - \mathbf{PS})\mathbf{C}_{\mathrm{v}} \tag{3.5}$$

and the orthonormalized vectors, $\mathbf{C}_{\mathrm{v,full}}$, are obtained through a canonical orthogonalization[323] of $\mathbf{C}_{\mathrm{v,proj}}$.

Now we construct two "one-way" CT surfaces: on the first surface, we allow $\mathbf{C}_{\mathrm{o},A}$ to be mixed with $\mathbf{C}_{\mathrm{v,full}}$ and $\mathbf{C}_{\mathrm{o},B}$ with $\mathbf{C}_{\mathrm{v},B}$, thus the corresponding $\mathbf{G}$ matrix has the form $[\mathbf{C}_{\mathrm{o},A}, \mathbf{C}_{\mathrm{v,full}}] \cup [\mathbf{C}_{\mathrm{o},B}, \mathbf{C}_{\mathrm{v},B}]$ (stage (b) in Fig. 3.1); on the second surface, we allow $\mathbf{C}_{\mathrm{o},B}$ to be mixed with $\mathbf{C}_{\mathrm{v,full}}$ while $\mathbf{C}_{\mathrm{o},A}$ only with $\mathbf{C}_{\mathrm{v},A}$, and the corresponding $\mathbf{G}$ matrix is $[\mathbf{C}_{\mathrm{o},A}, \mathbf{C}_{\mathrm{v},A}] \cup [\mathbf{C}_{\mathrm{o},B}, \mathbf{C}_{\mathrm{v,full}}]$ (stage (c) in Fig. 3.1). From the choice of variational spaces one can infer that $A \rightarrow B$ donation (but not $B \rightarrow A$) is allowed on the first of of these two surfaces, and that the response of the acceptor fragment B, called "repolarization", is also captured. The second surface is the reverse: $B \rightarrow A$ donation (but not $A \rightarrow B$) is allowed, with A being repolarized. Finally, as we mentioned above, if one chooses $\mathbf{G}$ to be $[\mathbf{C}_{\mathrm{o},A}, \mathbf{C}_{\mathrm{v,full}}] \cup [\mathbf{C}_{\mathrm{o},B}, \mathbf{C}_{\mathrm{v,full}}]$ (stage (d) in Fig. 3.1), the fully relaxed SCF surface will be recovered.

We note that the construction of these two "one-way" CT states is inspired by the previously developed RVS[313] and CSOV[314] schemes. One notable difference is that in these previous methods the variational space is constructed from orbitals calculated at the isolated fragment level, while here we start from variationally optimized ALMOs obtained in the polarization step. In addition, in RVS and CSOV only the occupied orbitals on the

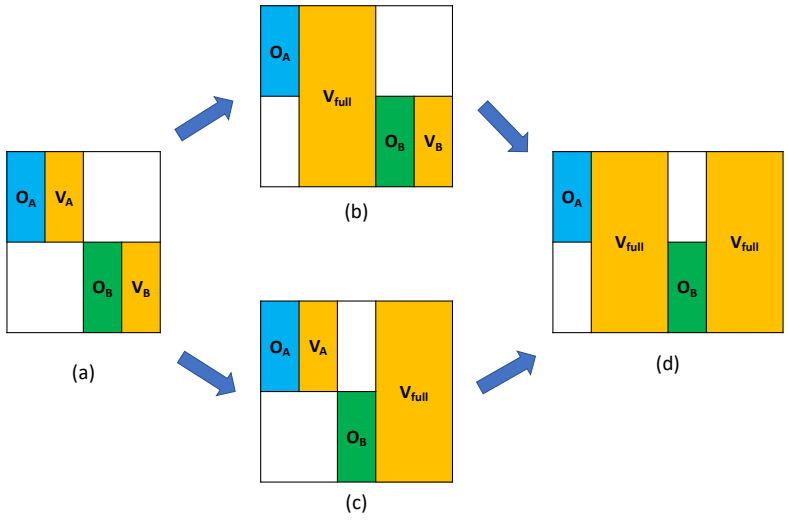

Figure 3.1: The form of **G** matrix in generalized SCF-MI at four different stages in adiabatic ALMO-EDA: (a) the polarized state without CT; (b) the $A \rightarrow B$ one-way CT state; (c) the $B \rightarrow A$ one-way CT state; (d) the fully relaxed SCF state.

donor fragment are relaxed while the acceptor fragment orbitals are frozen in their initial shape when considering a given direction of CT; in contrast, in our scheme both fragments are variationally relaxed on these "one-way" CT surfaces. For brevity, in the following we refer to our approach as illustrated in Fig. 3.1 as the *variational forward-backward* (VFB) analysis.

The overall CT stabilization energy in ALMO-EDA is defined as

$$\Delta E_{\mathrm{CT}} = E_{\mathrm{Tot}} - E_{\mathrm{Pol}} \tag{3.6}$$

where E_{Tot} is the unconstrained, fully relaxed SCF energy of the supersystem and E_{Pol} the energy of the polarized yet CT-forbidden state that is represented by Fig. 3.1(a). The stabilization effect of each direction of CT, denoted as ΔE_{CTf} ($A \rightarrow B$) and ΔE_{CTb} ($B \rightarrow A$), can be analogously defined:

$$\Delta E_{\mathrm{CTf}} = E_{\mathrm{CTf}} - E_{\mathrm{Pol}} \tag{3.7}$$

$$\Delta E_{\mathrm{CTb}} = E_{\mathrm{CTb}} - E_{\mathrm{Pol}} \tag{3.8}$$

where E_{CTf} and E_{CTb} are the energies of the variational forward and backward states represented by Figs.3.1(b) and 3.1(c), respectively. We adopt this convention because in our later examples we consistently choose fragment A to be a typical σ-donating Lewis base, such as NH_3, CO, etc., and fragment B a Lewis acidic moiety (e.g. BH_3 or $[Ru(NH_3)_5]^{2+}$). The total charge transfer energy can thus be partitioned into three terms:

$$\Delta E_{\mathrm{CT}} = \Delta E_{\mathrm{CTf}} + \Delta E_{\mathrm{CTb}} + \Delta E_{\mathrm{HO}} \tag{3.9}$$

where the higher-order (HO) term captures the non-additive contribution to energetic stabilization arising from the relaxation of electronic structure when both directions of CT are permitted simultaneously. This term is negative and relatively small in all examples investigated in this work (1–3% of the overall strength of ΔE_{CT} for the main group complexes and around 10% for the transition metal complexes). One should note that in the original ALMO-CTA scheme [87] the decomposition of the CT energy also yields the three terms on the right-hand side of Eq. (3.9) but uses a single *non-iterative* Roothaan-step correction upon the converged ALMO polarized state. Therefore, our scheme based on generalized SCF-MI serves as an alternative approach to decompose the energetic stabilization of CT with the advantage that the energies of the forward and backward CT states are strict upper bound to the full SCF energy. The results of these two approaches will be compared in Sec. 3.4.

One desirable feature of the present VFB scheme is that the forces associated with these two "one-way" CT states can be evaluated in the same way as the nuclear gradients for the polarized (AO-based SCF-MI) and fully relaxed (standard SCF) states (see the last section of this chapter for the mathematical details). Therefore, one can readily augment the adiabatic ALMO-EDA scheme with the PESs of these additional VFB states.

3.3 Computational Details

The generalized SCF-MI scheme has been implemented in the released version of Q-Chem 5.2.2. [108] On top of that, we enabled the energy and force calculations for the VFB "one-way" CT states, fully integrated into the adiabatic ALMO-EDA framework. The original AO-based SCF-MI scheme[31] is utilized in both vertical and adiabatic EDA calculations to separate the polarization and charge transfer contributions. To validate the CT energy decomposition results given by our VFB scheme, we compared them against the results of the original perturbative ALMO-CTA.[87] The latter approach was also used to generate the COVPs that help identify the key donor and acceptor orbitals. The COVP orbitals are plotted with an isovalue of 0.1 a.u. and density difference plots with an isovalue of 0.01 a.u.

All the energy and molecular property calculations were performed using the B3LYP functional [50, 56, 57] in combination with the def2-TZVPP[248] basis set unless otherwise specified. For the 4*d* transition metals (Ru and Tc), an effective core potential [249] was employed. The B3LYP functional was chosen because it provides adequate accuracy for CT-dominated complexes [20] and also decent agreement with experimental vibrational frequency shifts in all three application examples discussed in this work. In addition, we repeated all the calculations with two other functionals (B97-D [62] and ωB97X-D [68]). The functionals tested range from pure GGA (B97-D) to global and range-separated hybrid GGAs (B3LYP and ωB97X-D, respectively) and thus exhibit different extents of charge delocalization errors, [324] which consequently lead to the discrepancies in the predicted strength of CT and in the magnitude of frequency shift obtained. In general, B97-D produces the most red-shifted frequencies and ωB97X-D the least, since delocalization errors are largest for the pure GGA, and smallest for the range-separated hybrid. Nonetheless, our results

demonstrate that the qualitative trends given by the VFB analysis can all be reproduced with either of the three functionals (see Tables B.2, B.5–B.7, and B.9–B.13 in the appendix).

The optimized structures on different PESs were verified as true minima by examining the lowest harmonic frequency, and all the vibrational frequencies were computed with a finite-difference approach using the analytical nuclear gradients associated with each PES, for which the step size of atomic position displacement was set to be 10^{-3} Å. In Sec. 3.4, we report the frequency shift in the stretching mode of diatomic ligands N_2, CO, and BF (denoted by XY) relative to that calculated in the *isolated* (uncoordinated) state:

$$\Delta\nu_{\mathrm{XY}} = \nu_{\mathrm{XY}}(\mathrm{complex}) - \nu_{\mathrm{XY}}(\mathrm{free}) \tag{3.10}$$

A negative value of $\Delta\nu_{\mathrm{XY}}$ corresponds to frequency red shift and a positive value blue shift. The adiabatic EDA framework allows one to locate the energy minimum and obtain the associated harmonic frequencies on each individual PES: frozen (Frz), polarized (Pol), forward CT (CTf), backward CT (CTb) and fully relaxed (Tot).

As the geometry of a complex relaxes when moving from one PES to another, the shift in vibrational frequency calculated in such an adiabatic fashion arises not only from the distinction in constraints applied to different electronic states (i.e. the four states illustrated in Fig. 3.1) but also from the change in molecular structure. For instance, the inclusion of CT usually shortens the intermolecular distance, which, however, also enhances other effects such as those from electrostatic interactions. In order to estimate the strength of both the electronic and geometric effects of CT, one can perform a constrained geometry optimization in the Pol state with the intermolecular distance fixed at the CTf/CTb minimum-energy distance followed by a frequency calculation. The frequencies obtained thereof are denoted as ν_{XY}(Pol@CTf) and ν_{XY}(Pol@CTb), whose respective differences from the adiabatic CTf and CTb frequencies correspond to the pure electronic effect of forward and backward donation on the vibrational frequency shift:

$$\Delta\nu^{\mathrm{eff}}(\mathrm{CTx}) = \nu_{\mathrm{XY}}(\mathrm{CTx}) - \nu_{\mathrm{XY}}(\mathrm{Pol@CTx}) \tag{3.11}$$

where CTx stands for either CTf or CTb.

3.4 Results

Borane Complexes

The VFB decomposition of CT (see Sec. 3.2) yields two new PESs on which only one direction of CT is permitted. As the first step to validate this method, we analyze the $H_3N{-}BH_3$ complex in which the $H_3N{\rightarrow}BH_3$ forward donation dominates (see the large forward vs. backward ratio for this complex in Table 3.1). As shown in the left panel of Fig. 3.2, the surface that allows forward donation only (denoted as CTf) stays fairly close to the fully relaxed PES (Tot), whereas the one with $H_3N{\leftarrow}BH_3$ backward donation only (denoted as CTb) close

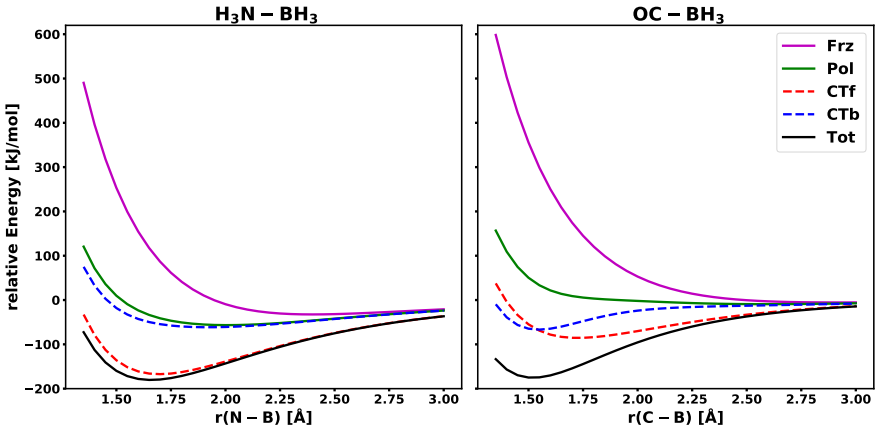

Figure 3.2: Potential energy surface (rigid scan) for each ALMO-EDA intermediate state (Frz, Pol, CTf, CTb, and Tot) for the two borane complexes. Left panel: $H_3N{-}BH_3$; right panel: $OC{-}BH_3$.

to the Pol surface, confirming that these two newly introduced intermediate states describe this simple mono-directional CT correctly.

We then move to the $OC{-}BH_3$ adduct that is known to have more involved bi-directional CT as many other carbonyl compounds do: a σ-type forward donation ($OC{\rightarrow}BH_3$) from the lone pair on CO into the empty p orbital on boron, and a π-type backbonding ($OC{\leftarrow}BH_3$) from the $B{-}H$ σ bonding orbitals to CO's empty π^* level, which are illustrated by the COVPs shown in Fig. 3.3. The vertical EDA results for this complex, as given in Table 3.1, reveal its strongly repulsive frozen interaction as well as the substantially favorable polarization and CT contributions. A further decomposition of the CT energy using the scheme introduced in this work suggests that the two directions of CT contribute almost equally in this complex.

Table 3.1: Vertical ALMO-EDA results for $H_3N{-}BH_3$ and $OC{-}BH_3$. The energies are in kJ/mol and the distance in Å. The ratio refers to $\Delta E_{CTf}/\Delta E_{CTb}$.

molecule	ΔE_{Frz}	ΔE_{Pol}	ΔE_{CTf}	ΔE_{CTb}	ΔE_{CT}	ΔE_{Tot}	ratio	r(X−B)
$H_3N{-}BH_3$	112.3	−147.2	−131.4	−15.6	−145.4	−180.3	8.0	1.658
$OC{-}BH_3$	331.8	−289.0	−104.0	−108.9	−218.1	−175.3	1.0	1.520

The five intermediate surfaces (Frz, Pol, CTf, CTb, and Tot) for $OC{-}BH_3$ are shown in the right panel of Fig. 3.2. While the vertical EDA results (Table 3.1) suggest that the forward and backward CT are almost equally strong for this system, one should note that this actually only holds around the equilibrium $N{-}B$ distance. Another remarkable feature is that the π-type backbonding decays faster than the forward donation right beyond the equi-

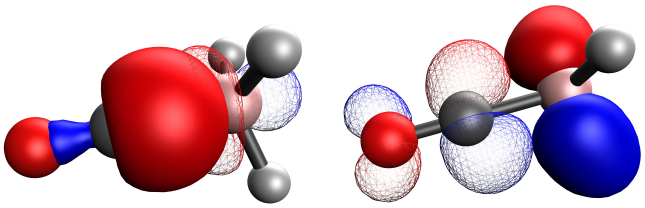

(a) (b)

Figure 3.3: The key COVPs in OC−BH_3 that illustrate its bi-directional CT: (a) σ-type and (b) π-type. The donor orbtial is shown as a solid isosurface while the acceptor orbital is shown as a mesh isosurface).

librium, rendering the latter as the dominant contribution to CT at long range. As shown in Fig. B.1 (appendix), this behavior can also be reproduced with the forward and backward CT contributions obtained from the perturbative ALMO-CTA.[87] This finding also holds for the metal complexes (see Figs. 3.5 and 3.10) and might be useful for kinetic control of carbonyl insertion/elimination reactions as the M−CO distance is usually elongated in transition states, where the forward CT plays a dominant role in the donor-acceptor interaction. In addition, Fig. B.1 also demonstrates that the forward and backward CT are dominated by the σ-type and the π-type COVPs, respectively, as the two perturbative stabilization energies are almost fully recovered by their dominant COVPs.

Table 3.2: Adiabatic ALMO-EDA results for the structural and vibrational parameters of OC−BH_3 complex. Δr(CO) and $\Delta\nu_{CO}$ refer to changes relative to the values of a free CO molecule (r(CO) = 1.125 Å and ν_{CO} = 2216 cm^{-1}). The experimental values are taken from Refs. [325] and [326].

Surface	r(CB) [Å]	Δr(CO) [Å]	$\Delta\nu_{CO}$ [cm^{-1}]
Frz	3.29	−0.001	8
Pol	3.18	−0.001	9
CTf	1.77	−0.010	108
CTb	1.54	0.001	24
Tot	1.52	0.004	−2
Exp	1.54	0.003	22

The importance of CT for this interaction is further highlighted by the adiabatic ALMO-EDA results (Table 3.2). On the fully relaxed surface, the obtained C−B and C−O bond distances and the shifts in ν_{CO} are in reasonable agreement with the previous theoretical studies and experimental values. [298, 325–327] The non-CT binding forces (frozen inter-

action and polarization) yield only a weakly bound adduct with the C−B distance, r(CB), being over 3 Å, and r(CB) is only shortened by ∼0.2 Å upon moving from the Frz to Pol surface. Allowing only forward donation drastically reduces the C−B distance to 1.77 Å, and with backward CT only the C−B distance is shortened even more, yielding a C−B distance of 1.54 Å that is already very close to the full equilibrium distance. The extraordinarily shortened intermolecular distance obtained on the CTb surface can be rationalized by the relatively weak Pauli repulsion in this complex, which is almost fully compensated by the favorable permanent electrostatics and polarization contributions even at a short intermolecular distance, and also by the rapid decay of CTb beyond equilibrium. This is in contrast to the transition metal complex cases (*vide infra*) where the synergy of CTf and CTb is required to overcome the stronger Pauli repulsion.

The calculated ν_{CO} on the fully relaxed surface is marginally red-shifted, while that on the Pol surface exhibits a small blue shift. The latter is in line with our previous work [33, 328] as well as other studies showing blue shifts in CO stretching frequency in the presence of an electric field along the C→O direction, such as in complexes where CO is bound to a metal cation, [329, 330] which is known as molecular Stark effect. This is because the dipole moment of CO increases when the C−O bond is contracted, which is favored by the electrostatic interaction between CO and the positively charged moiety. The blue shift is most prominent on the PES with forward CT only (CTf), which can be attributed to two effects: (i) the forward donation itself (electronic) and (ii) the shortened intermolecular distance r(CB) (geometric) that enhances the electrostatic interaction. The significance of these two effects can be estimated by optimizing the geometry of this complex in the Pol state with the C−B distance *constrained* at the minimum-energy r(CB) on the CTf surface (1.77 Å) and then evaluating the frequency shift. A blue shift of 105 cm^{-1} is obtained in this "Pol@CTf" state, which is almost identical to the blue shift on the CTf surface (108 cm^{-1}), indicating that the large blue shift caused by forward CT is almost solely a geometric effect, i.e., enhanced electrostatic interaction due to the shortened C−B distance.

With backward CT only, ν_{CO} is also moderately blue-shifted (24 cm^{-1}), for which the geometric and electronic effects can be separated in the same way as described above. With r(CB) fixed at 1.54 Å, the "Pol@CTb" frequency is significantly more blue-shifted (+184 cm^{-1} relative to free CO) than the "CTb@CTb" frequency, indicating that the back-donation, as expected, results in an effective red shift of 160 cm^{-1} by modifying the electronic structure of the CO moiety. This result, as well as the very small $\Delta\nu_{CO}$ in the fully relaxed complex, suggests that the shift in ν_{CO} is not always a reliable indicator for the strength of back-donation, as it can be largely compensated by the competing electrostatic force that blue-shifts ν_{CO}, which is nicely illustrated by this example. These results are in line with previous discussions in literature,[87, 327, 329] while our VFB approach is able to directly identify the origin of shifts in r(CB), Δr(CO), and $\Delta\nu_{CO}$.

In summary, our analysis of the two borane adducts above demonstrates that the VFB decomposition of charge-transfer effects yields qualitatively correct results as one would expect for these systems, validating its use in the applications presented below. It not only serves as an alternative scheme to separate the entire CT stabilization energy into forward

and backward contributions, but also directly probes their effects on shifts in observables.

Binding of CO with BeO and $BeCO_3$

A combined spectroscopic and theoretical study by Frenking *et al.* [331] investigated the binding of CO with beryllium oxide and carbonate (BeY with Y = O or CO_3) as well as the shifts in CO's stretching frequency (ν_{CO}). These beryllium compounds are strong Lewis acids that are even able to form adducts with noble gases. [332] In their study, carbonyl adducts of two binding modes with either the carbon or oxygen atom of CO interacting with the BeY moiety were isolated and characterized by IR spectroscopy,[331] which are denoted as the κC and κO modes in the following discussion, respectively. It was shown that ν_{CO} is red-shifted for κO carbonyls (-80 cm^{-1} for CO$-$BeO and -53 cm^{-1} for CO$-BeCO_3$) while blue-shifted for the κC isomers (43 cm^{-1} for OC$-$BeO and 122 cm^{-1} for OC$-BeCO_3$). The theoretical investigation demonstrated that the magnitude of interaction energies follows the order OC$-$BeO > OC$-BeCO_3$ > CO$-$BeO > CO$-BeCO_3$. Interestingly, the more strongly bound OC$-$BeO exhibits a significantly smaller blue shift than OC$-BeCO_3$. The EDA-NOCV (natural orbital for chemical valence) [190, 333] analysis for the two κC complexes revealed that their σ-type forward donations (OC$\rightarrow$BeY) are of similar strengths, while the π-type back-donation (OC$\leftarrow$BeY) is more pronounced in OC$-$BeO, which explained both its stronger interaction energy and less blue-shifted ν_{CO}. For the κO complexes, the contribution from CT is slightly weaker and the σ and π donations are of similar strength. Therefore, instead of backward CT, the authors attributed the red-shifted ν_{CO} in the κO complexes to the "reversed polarization" of CO relative to the κC complexes, which makes the C$-$O bond longer and less polar.

We compare the previous findings with the results of our more detailed VFB-EDA analysis including a decomposition of the shifts in ν_{CO}. The ALMO-EDA results at the equilibrium geometries of these four complexes (Table 3.3) are analyzed first. The comparison between the κC and κO binding modes for BeO reveals that the former is more stable by over 70 kJ/mol, and the difference is evenly distributed over all three EDA terms. The difference in ΔE_{Frz} results from the substantially more favorable electrostatic interaction under the κC mode, which overcomes its stronger Pauli repulsion. Upon polarization, one can observe a reduction of electron density on the distant atom for both binding modes, which is shown in Fig. B.3. The difference between their CT energies is mainly caused by the stronger back-donation in the κC complex (see Table 3.3), which can be rationalized via the COVPs obtained from the perturbative CT analysis (Fig. B.4(a) and Figs. B.4(c)–(e)): under the κC mode, the π^* acceptor orbital of CO (Fig. B.4(d)) has a better overlap with the π-donor orbital of BeO (Fig. B.4(c)) than that under the κO mode (Fig. B.4(e)), since the π^* orbital of CO is polarized towards the C atom.

The comparison between the BeO and $BeCO_3$ complexes (see Table 3.3) indicates that the carbonate analogues bind CO less strongly than the oxides mainly because of their less favorable CT contributions. The CTf/CTb ratios for the $BeCO_3$ complexes reveal the weaker back-donation in these complexes, which is consistent with the previous EDA-NOCV

Table 3.3: Vertical ALMO-EDA results (energies in kJ/mol) for the four BeY–carbonyl adducts. The ratio corresponds to the value of $E_{\mathrm{CTf}}/E_{\mathrm{CTb}}$ for each complex.

Adduct	ΔE_{Frz}	ΔE_{Pol}	ΔE_{CTf}	ΔE_{CTb}	ΔE_{CT}	ΔE_{Tot}	ratio
OC−BeO	11.4	−108.8	−26.5	−49.2	−77.9	−175.2	0.5
CO−BeO	31.4	−78.4	−29.8	−24.2	−54.9	−101.9	1.2
OC−$BeCO_3$	12.7	−93.9	−29.5	−14.9	−44.9	−126.1	2.0
CO−$BeCO_3$	27.0	−69.0	−28.3	−7.2	−35.6	−77.7	4.0

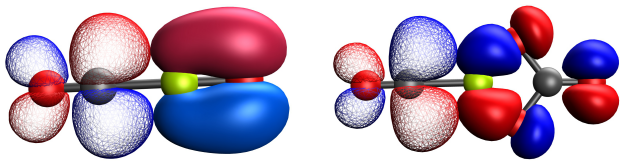

(a) (b)

Figure 3.4: Key COVPs contrasting the π backbonding for both OC−BeY complexes: (a) OC−BeO: (b) OC−$BeCO_3$. The donor orbitals are in solid colors and the acceptor orbitals are meshed.

results.[331] This can be elucidated by the smaller overlap between the π-donor orbital on $BeCO_3$ with the π^* orbital on CO as illustrated in Fig. 3.4. The comparison between the κC and κO isomers of the carbonate complex, on the other hand, shows the same trend as for the above-discussed BeO complexes. Finally, we note that the higher-order contribution is very small for this set of systems (3% of the overall CT energy for the complexes with BeO and ∼1% for those with $BeCO_3$), indicating that the decomposition of CT stabilization energy using the VFB approach yields nearly additive results for these Be complexes.

The PES scans for OC−BeO and CO−BeO are shown in Fig. 3.5. Both isomers (κC and κO) are only weakly bound in the frozen state with shallow minima located at 2.15 and 2.17 Å, respectively. Polarization strengthens the interactions and shortens the equilibrium Be−X distances of both isomers significantly. The κC complex is of a larger polarization energy, which can be rationalized by the chemically softer lone pair located on the C atom. Interestingly, given the characteristic difference between the lone pairs located on C and O, the energetic contributions from forward donation (from CO/OC to BeO) are of similar magnitude for these two complexes in the range of 1.5–1.8 Å. Nevertheless, the energetic contribution of forward CT (energy lowering relative to the Pol surface) does show a slower decay to zero in the long range under the κC mode, as one would expect based on the more diffuse electron lone pair on the C atom (see Fig. B.5 in the appendix). The backward donation, on the other hand, is of a greater strength in the κC complex, which is in line with

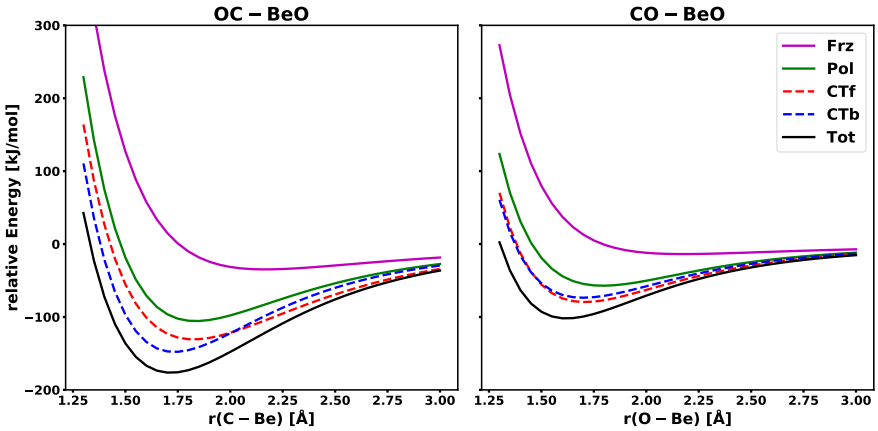

Figure 3.5: Potential energy surface (rigid scan) for each ALMO-EDA intermediate state (Frz, Pol, CTf, CTb, and Tot) for OC−BeO (left) and CO−BeO (right).

the vertical EDA results that were discussed above (Table 3.3). The strong back-donation in the κC complex also leads to a reduction of the Be−C distance by 0.1 Å, and the resulting intermolecular distance is only 0.016 Å longer than the full equilibrium distance.

The most pronounced difference between these two binding modes is observed when comparing their CTf against CTb surfaces for each of them: for CO−BeO, the forward and backward donations yield very similar energetic stabilization relative to the Pol state at all ranges; by contrast, OC−BeO exhibits markedly stronger backward CT than forward around the minimum-energy distance while the back-donation decays more rapidly, resulting in a crossover around 2 Å. Note that the faster decay of backward CT was also observed in the OC−BH_3 example discussed above (Sec. 3.4). Altogether, the CO molecule binds with BeO more strongly under the κC mode mainly because of the more favorable polarization and backward CT contributions. It is noteworthy that the equilibrium Be−X distance on the fully relaxed surface appears to be longer for the κC complex despite its stronger interaction. This, once again, can be rationalized by the more diffuse lone pair (σ-donor orbital) as well as the larger amplitude of the π-acceptor orbital on the C atom, with the former rendering the κC complex more prone to Pauli repulsion and thus energetically less favorable at a short distance, and the latter facilitating a considerable interaction strength at a comparatively large intermolecular separation.

The adiabatic ALMO-EDA results for OC−BeO and CO−BeO are shown in Table 3.4. The carbonyl stretching frequency (ν_{CO}) is blue-shifted by 102 cm^{-1} for the κC complex at the Frz level, accompanied by a contraction of the C−O bond by 0.01 Å. In contrast, the κO complex exhibits a moderate red shift of −28 cm^{-1} relative to the free ν_{CO} and correspondingly a lengthened C−O bond (by 0.004 Å). While Ref. [331] assigned the origin of the opposite frequency shifts in OC−BeO and CO−BeO to the "reversed polarization" of the C−O bond in these two complexes, our adiabatic ALMO-EDA results reveal that the

respective blue and red shifts in these two complexes already appear on the frozen surface where *no* orbital interaction (polarization or charge transfer) is involved. According to this result, one can elucidate the opposite shifts in ν_{CO} for these two complexes through the molecular Stark effect: since the Be atom carries partial positive charge and the dipole moment of CO (with oxygen as the positive end) increases upon the contraction of the C−O bond, a shortened C−O bond enhances the attractive electrostatic interaction and therefore is energetically favored, rendering ν_{CO} blue-shifted; on the contrary, a lengthened C−O bond is more favored by the electrostatic interaction in CO−BeO due to the opposite orientation of CO's permanent dipole, resulting in a red shift in ν_{CO}. These results are in agreement with the previous studies on classical (neutral) and non-classical (cationic) metal carbonyls. [33, 328–330, 334, 335]

The inclusion of polarization further enhances both the blue shift in OC−BeO and the red shift in CO−BeO. However, as the frequency shifts on the Pol surface are calculated at shortened intermolecular distances relative to those on Frz, these more pronounced frequency shifts again arise from both the geometric and electronic effects. While the forward donation to BeY imposes insignificant effects on the bond length and stretching frequency of CO, the back-donation substantially lowers ν_{CO} under both the κC and κO modes. With bi-directional CT, their ν_{CO}'s are further red-shifted relative to those on the CTb surface, which can be attributed to the non-additive relaxation of their electronic structure.

The two $BeCO_3$ complexes exhibit shifts in ν_{CO} that are comparable to those of the corresponding BeO complexes on the Frz, Pol, and CTf surfaces. The most pronounced difference originates from the much weaker backbonding from $BeCO_3$ than that from BeO, which is reflected in the much smaller changes in ν_{CO} from Pol to CTb for the $BeCO_3$ complexes (see Table 3.4). This is also consistent with the vertical EDA results shown in Table 3.3. Therefore, the significant blue shift in the fully relaxed OC−$BeCO_3$ complex is a consequence of the strong Stark effect, which significantly shortens the C−O bond and increases its stretching frequency, complemented with the weak back-donation from $BeCO_3$ that is inadequate to compensate for the blue-shifting effect.

The discussion in Sec. 3.4 regarding the shift in ν_{CO} nicely revealed that the enhanced electrostatic interaction upon the shortening of r(C−B) is the main contributor to the frequency shift on the CTf surface by calculating ν_{CO} in the "Pol@CTf" state. Here we employ a similar analysis to investigate the distance dependence of the effects of Frz, Pol, CTf, and CTb on ν_{CO}. Specific attention is paid to the shifts induced by each energy component at the full equilibrium X−Be distances (e.g. Frz@Tot) since all these effects are at their maximum strength there. For both OC−BeO and CO−BeO, we performed constrained geometry optimizations on each intermediate surface with r(X−Be) fixed at varying values and evaluated ν_{CO} at each given distance. The resulting frequency shifts relative to the free CO stretching frequency, which are denoted as $\Delta\nu_{CO}$, are plotted in Fig. 3.6 as a function of r(X−Be). It is clearly revealed that the overall frequency shifts are mainly determined by how the strength of permanent electrostatics, which is encompassed in the frozen term, compares to that of backward CT, and that both polarization and forward CT only result in moderate red shifts relative to ν_{CO} on the Frz surface. At the minimum-energy distance on the Tot surface, the

Table 3.4: Adiabatic ALMO-EDA results for the four X−BeY adducts (for a free CO molecule r(CO) = 1.125 Å and ν_{CO} = 2216 cm^{-1}). The distances are in Å and frequencies in cm^{-1}.

Property	Surface	OC−BeO	CO−BeO	OC−$BeCO_3$	CO−$BeCO_3$
r(CO)	Frz	1.115	1.129	1.117	1.129
r(CO)	Pol	1.112	1.132	1.113	1.132
r(CO)	CTf	1.112	1.133	1.112	1.134
r(CO)	CTb	1.121	1.137	1.114	1.132
r(CO)	Tot	1.122	1.141	1.115	1.135
r(X-Be)	Frz	2.148	2.167	2.345	2.324
r(X-Be)	Pol	1.833	1.793	1.888	1.845
r(X-Be)	CTf	1.823	1.707	1.868	1.727
r(X-Be)	CTb	1.733	1.700	1.831	1.812
r(X-Be)	Tot	1.717	1.620	1.810	1.695
$\Delta\nu_{CO}$	Frz	102	−28	80	−28
$\Delta\nu_{CO}$	Pol	141	−42	130	−46
$\Delta\nu_{CO}$	CTf	140	−51	133	−59
$\Delta\nu_{CO}$	CTb	44	−115	101	−54
$\Delta\nu_{CO}$	Tot	31	−160	95	−76
$\Delta\nu_{CO}$	Exp	43	−80	122	−53

CO−BeO isomer exhibits a minimal blue shift on the frozen surface (+13 cm^{-1} relative to free CO), small but still sizable red shifts induced by Pol (−44 cm^{-1} relative to Frz) and CTf (−13 cm^{-1} relative to Pol), and a significant red shift caused by CTb (−85 cm^{-1} relative to Pol). In contrast, the OC−BeO isomer exhibits a much more considerable blue shift on the frozen surface (+199 cm^{-1} relative to free CO). Despite the substantial red shift associated with the backward CT (−127 cm^{-1} relative to Pol), it is still inadequate to compensate for the strong blue shift induced by frozen interaction, leading to an overall blue-shifted ν_{CO}.

In summary, our VFB-EDA analysis reveals that the distinct frequency shifts in the κC and κO complexes of beryllium oxide and carbonate result from the competition between the electrostatic interaction and the backward CT from BeO or $BeCO_3$ to CO. The electrostatic interaction affects the CO stretching frequency through the Stark effect, rendering ν_{CO} strongly blue-shifted for the κC motif while moderately red-shifted for κO. Polarization and forward CT further increase the blue or red shift, mainly by shortening the intermolecular distance, which leads to enhanced Stark effect. The backward CT, which is more pronounced in the complexes with BeO, weakens the C−O bond under both binding modes. It offsets the blue shifts in the κC complexes while further red-shifts ν_{CO} in the κO ones. The results for the κO complexes demonstrate that significant red shift in ν_{CO} is possible even with a weak

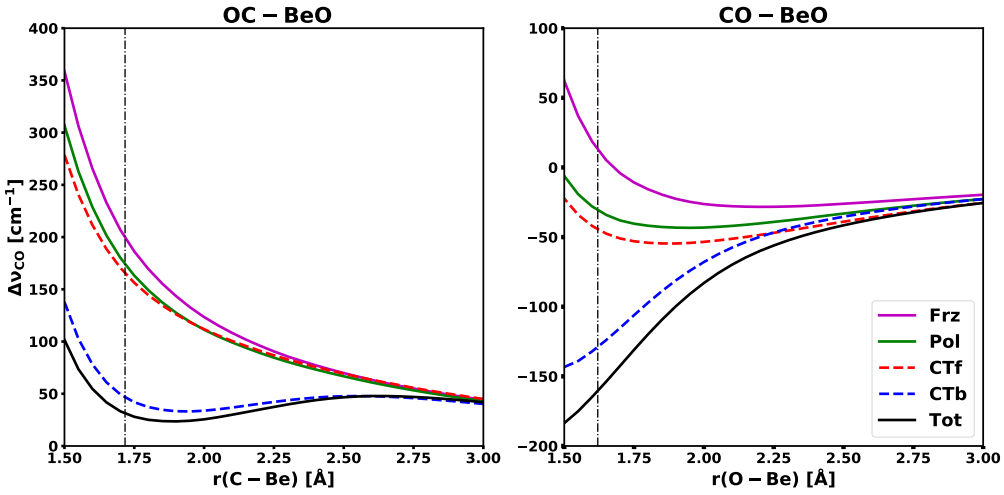

Figure 3.6: Shift in ν_{CO} (in cm^{-1}) as a function of the intermolecular distance in each intermediate state (relative to free CO) for OC−BeO (left) and CO−BeO (right). The frequencies are evaluated at complex geometries relaxed at each given Be−X distance. The black dashed lines indicate the full equilibrium distance for each complex.

back-donation if it is aligned with the electrostatic effect. Our results agree with Ref. [331] in explaining the stronger blue shift in OC−$BeCO_3$ than in OC−BeO while providing a distinct explanation for the opposite frequency shifts in the κC and κO complexes.

Pentaammineruthenium(II) Complexes of the Isoelectronic N_2, CO and BF

The red shift in CO or N_2's stretching frequency is often used as an indicator for the strength of the π-type metal-to-ligand back-donation, whereas the effect of the forward donation on this vibrational mode is small due to the non-bonding character of the σ-donating orbital (lone pair on the ligand). [329, 330, 336] Bistoni *et al.* recently investigated the effects of both σ forward and π backward donations on the C−O bond length and its stretching frequency using charge displacement analysis [337, 338] with a large set of classical and non-classical carbonyl complexes. [335] They found that ν_{CO} and r(CO) are in very good correlation with the strength of the π back-donation but not with the strength of the σ forward donation. The blue shift in non-classical carbonyl complexes, on the other hand, stems mainly from electrostatic interaction and polarization due to the positively charged metal moiety. Using the block-localized wavefunction (BLW) approach, Mo and co-workers obtained optimized structures and vibrational frequencies of a series of transition metal monocarbonyls with both directions of CT "quenched".[199, 334] They revealed that ν_{CO} is uniformly blue-shifted in both neutral and cationic transition metal monocarbonyls when CT is absent, and that CT always results in a red shift in ν_{CO}, which is more pronounced in neutral, classical complexes.

The blue shift induced by the transition metal moiety is in line with the Stark effect of CO in an electric field,[329, 330] and first arises even without polarization, i.e., on the frozen surface.[33, 328] The experimentally observed shift in ν_{CO} is thus a superposition of these effects and the net effect can be small since they induce shifts in opposite directions.

Boron monofluoride is also isoelectronic to CO and N_2, and was predicted to be both a stronger σ-donor and π-acceptor compared against CO. [339–341] It possesses a lower bond order and like CO, the dipole moment of BF is in the opposite direction of intuition, with the B atom as the negative pole. [342, 343] However, BF is only stable under extreme conditions, rendering its coordination compounds difficult to prepare. [344, 345] Nonetheless, recent work by Drance *et al.* reported the synthesis and characterization of a transition metal complex with a terminal coordinating BF ligand and demonstrated BF's σ-donor and π-acceptor properties. [346] Experimental evidence including NMR-, IR-, and Mössbauer-spectroscopy and X-ray crystallography suggests that BF is not only a stronger σ-donor than its isoelectronic counterparts (CO, N_2) but also a strong π-acceptor. Differing from the analogous complexes with CO and N_2 that exhibit red-shifted ligand stretching frequencies, the B−F stretching frequency, ν_{BF}, is markedly blue-shifted, which is seemingly contradictory to the assignment of BF as a strong π-acceptor.

Using the extended adiabatic ALMO-EDA with the VFB states, one is able to characterize and separate the effects of permanent and induced electrostatics, σ forward donation, and π back-donation on the structural and vibrational properties of a given complex. Here we provide a systematic study of octahedral transition metal complexes with the above-mentioned three isoelectronic ligands: N_2, CO, and BF. In order to compare these three ligands directly, we choose a $[Ru(II)(NH_3)_5]^{2+}$ framework because of its simplicity (homogeneous auxiliary ligands (NH_3) and low-spin singlet state) and its strong association with π-acidic ligands. Furthermore, the $[Ru(II)(NH_3)_5N_2]^{2+}$ cation is experimentally accessible and has been well characterized.[302]

The vertical ALMO-EDA results at the minimum-energy structure of each complex are summarized in Table 3.5. Starting with the ammine (NH_3) ligand that is a σ-donor only, we find that it exhibits a favorable frozen interaction due to the large dipole moment of NH_3. It also shows a relatively long Ru−N distance (2.2 Å), which gives rise to more favorable electrostatic interaction and weaker Pauli repulsion, respectively. Combined with ΔE_{Pol} (−46 kJ/mol), the total non-CT contribution is significant and constitutes ∼30% of the total interaction energy. The CT term, nonetheless, still makes the largest contribution to binding, and is strongly dominated by forward donation ($H_3N \rightarrow Ru$) as indicated by the large CTf/CTb ratio (10.8).

The three π-acidic ligands (N_2, CO, and BF) exhibit drastically different vertical EDA fingerprints than NH_3. Although both permanent electrostatics and polarization become more favorable in these complexes, they are overlaid by the stronger Pauli repulsion that increases from N_2 to BF (see Table B.8). Thus, CT becomes the key contributor to these interactions. As indicated by the large magnitude of both ΔE_{CTf} and ΔE_{CTb} values, CT in these complexes is of a typical bi-directional character, and the most significant COVPs (Figs. 3.7 and 3.8) clearly demonstrate σ forward donation and π back-donation. The total

Table 3.5: Vertical ALMO-EDA results for the transition metal complexes. The energies are in kJ/mol and the distance in Å. The ratio refers to $\Delta E_{CTf}/\Delta E_{CTb}$.

Complex	ΔE_{Frz}	ΔE_{Pol}	ΔE_{CTf}	ΔE_{CTb}	ΔE_{CT}	ΔE_{Tot}	ratio	r(M−X)
$H_3N{-}[Ru(NH_3)_5]^{2+}$	−11.6	−46.0	−102.4	−9.5	−113.4	−171.0	10.8	2.194
$NN{-}[Ru(NH_3)_5]^{2+}$	160.4	−70.1	−95.0	−99.5	−212.6	−122.4	1.0	1.951
$OC{-}[Ru(NH_3)_5]^{2+}$	283.2	−119.6	−190.0	−155.8	−392.8	−229.2	1.2	1.860
$FB{-}[Ru(NH_3)_5]^{2+}$	317.1	−171.0	−284.8	−130.0	−477.2	−331.1	2.2	1.871
$NN{-}[Fe(NH_3)_5]^{2+}$	82.4	−57.1	−42.1	−53.2	−100.9	−75.6	0.8	1.929
$NN{-}[Tc(NH_3)_5]^{+}$	263.8	−75.0	−94.6	−277.4	−414.7	−226.0	0.3	1.873

interaction strength of these complexes is in the order of N_2 < CO < BF, which is also in line with their relative strength of CT. The further decomposition of CT using the VFB approach reveals that N_2 is a much weaker σ-donor as well as a weaker π-acceptor than the more polar CO and BF. The increase in bond polarity (N_2 < CO < BF) in this isoelectronic series reduces the HOMO-LUMO gap, facilitating both forward and backward donation. The increase in the strength of CT with more polar ligands can also be rationalized with the COVPs shown in Figs. 3.7 (for N_2) and 3.8 (for CO and BF), which illustrate that more polar ligands are more favored as either σ-donor or π-acceptor. Interestingly, the relative strength of forward donation increases more rapidly than backward donation with the ligand polarity, as indicated by the increasing CTf/CTb ratio from N_2 to BF. It is also noteworthy that although BF is more polar than CO, which is supposed to yield an even better overlap of π^* with Ru(II)'s 4d orbitals, the back-donation towards BF is 25 kJ/mol less favorable than that towards CO and the interaction between BF and the Ru(II) moiety is dominated by the σ forward donation. These findings hold for different types of density functionals as shown in Table B.9 in the appendix.

The adiabatic EDA results (Table 3.6) show that the Ru(II) moiety binds the three π-acidic ligands (denoted as XY) only loosely on the Pol surface with the minimum-energy Ru−X distances ranging between 2.6–2.7 Å. This is in contrast to the main group beryllium carbonyls discussed in Sec. 3.4 above where short intermolecular distances were already observed on the Pol surface (see Table 3.4). In the case of N_2, introducing either the forward or backward CT shortens the Ru−X distance by ∼0.3 Å, indicating the similar σ-donating and π-accepting abilities of this ligand. For CO, the forward CT shortens the Ru−X distance more than backward CT, and this difference is further enlarged in the case of BF, where forward donation shortens the Ru−X distance by over 0.2 Å. This differs from the two main group examples ($OC{-}BH_3$ and OC−BeO) discussed in the above sections, where the adduct bond lengths on the CTb and fully relaxed surfaces are very similar because of the fast decay of CTb energy. For the Ru(II) complexes one can still observe similar fast decay of CTb as shown in Fig. 3.10. However, the strong Pauli repulsion between the lone pair on the XY

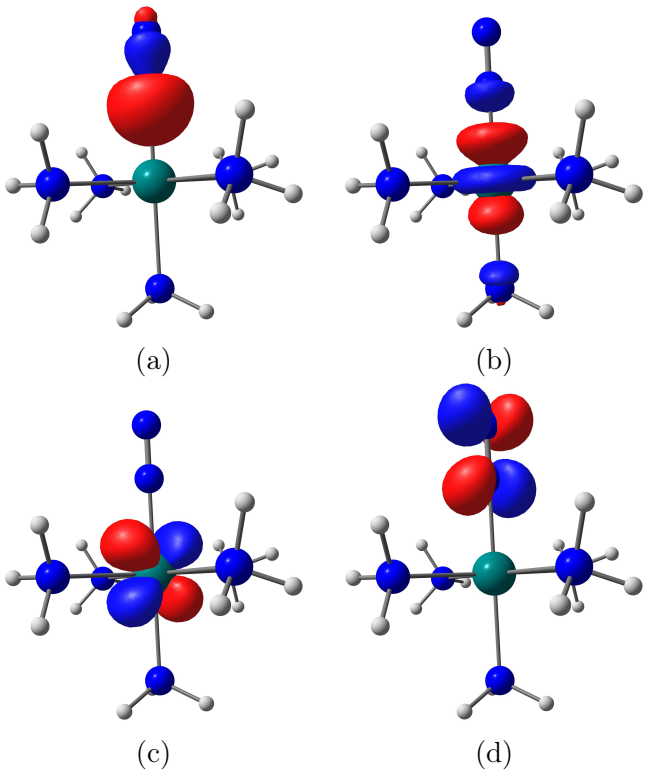

Figure 3.7: Key COVPs illustrating the σ- and π-type donations in NN$-[Ru(NH_3)_5]^{2+}$: (a) σ-donor, (b) σ-acceptor, (c) π-donor, and (d) π-acceptor.

ligand and the 4d electrons of Ru(II) do not allow for a shorter Ru$-$X distance without the presence of forward donation, even though it would greatly increase the strength of back-donation. The forward donation moves electron density from the lone pair of the ligand to Ru(II)'s empty d_{z^2} orbital and thereby reduces the Pauli repulsion, which is illustrated by the COVP acceptor orbital for σ-donation (Fig 3.7(b)) and the plots of electron density difference between the CTf and Pol states for N_2, CO, and BF (Figs. 3.9(a)–(c)). Therefore, the forward donation not only stabilizes the complex by itself but also enables stronger back-donation by reducing Pauli repulsion, which allows for a shorter M$-$X distance. This is not the case in the main group complexes where Pauli repulsion is not as prominent and can already be overcome by the non-CT contributions.

The comparison of the PES scans for these complexes with respect to the Ru$-$X distance (Fig. 3.10) further confirms the variation in the relative strength between the forward and backward CT. For the N_2 complex (left panel), CTf and CTb are of similar magnitude over the full range of the r(N$-$Ru), with CTb being marginally more favorable in the short range and a crossover taking place around 1.9 Å; for the CO complex (middle panel), the CTf surface is consistently of a lower energy than that of CTb although the gap between them is small. The BF ligand (right panel), on the other hand, is an even stronger σ-donor but a

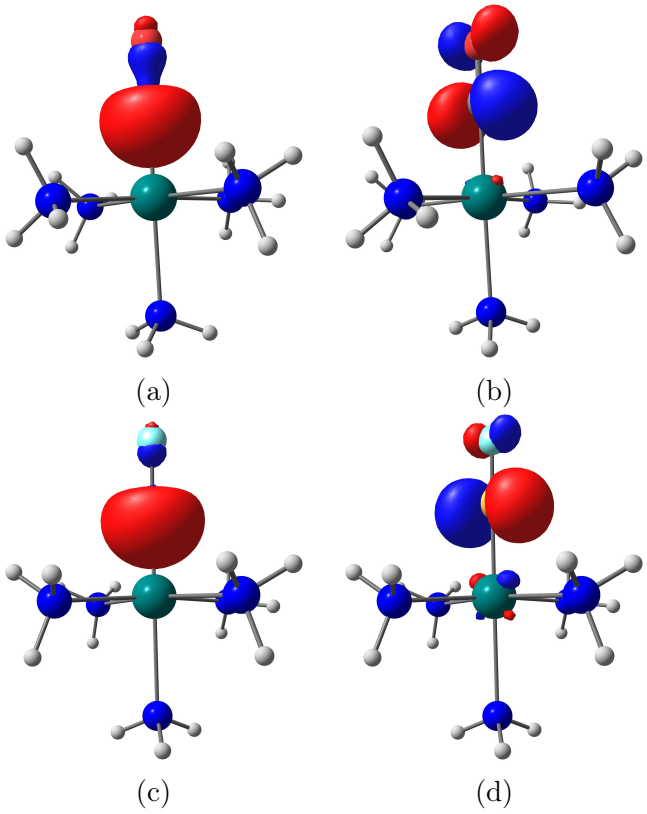

Figure 3.8: Key COVPs illustrating the σ- and π-type donations in OC$-$[Ru(NH$_3$)$_5$]$^{2+}$: (a) σ-donor, (b) π-acceptor, and in FB$-$[Ru(NH$_3$)$_5$]$^{2+}$: (c) σ-donor, (d) π-acceptor.

weaker π-acceptor, with a substantial gap between the CTf and CTb surfaces. Furthermore, from N_2 to BF the frozen surface becomes less favorable, while the stabilization effect due to of polarization (the difference between Frz and Pol) increases.

The IR shifts in the stretching frequency of these π-acidic ligands (see Table 3.7) show an opposite trend to the ordering of the strength of their CT energies (ΔE_{CT} in Table 3.5): a red shift of 150 cm^{-1} for N_2, a smaller red shift of 102 cm^{-1} for CO, and a blue shift of 123 cm^{-1} for BF. The origin of this seemingly counterintuitive trend can be unraveled by the frequency shifts ($\Delta\nu_{XY}$) evaluated on the Pol surface, where the blue shifts increase drastically from N_2 to BF. The blue shift in ν_{XY} for each complex is further increased at the equilibrium structures on the CTf surface, which, as in the OC$-$BH$_3$ and OC$-$BeO cases, is mainly a geometric effect as indicated by the close agreement between Pol@CTf and CTf@CTf frequencies in Table 3.8. The backward CT, on the other hand, lowers the frequencies relative to their values on the Pol surface for all three ligands, which, as indicated by the three right columns in Table 3.8, is truly an electronic effect. For the complex with N_2, the back-donation overpowers the weak electrostatic effect, yielding an overall red-shifted ν_{N_2}

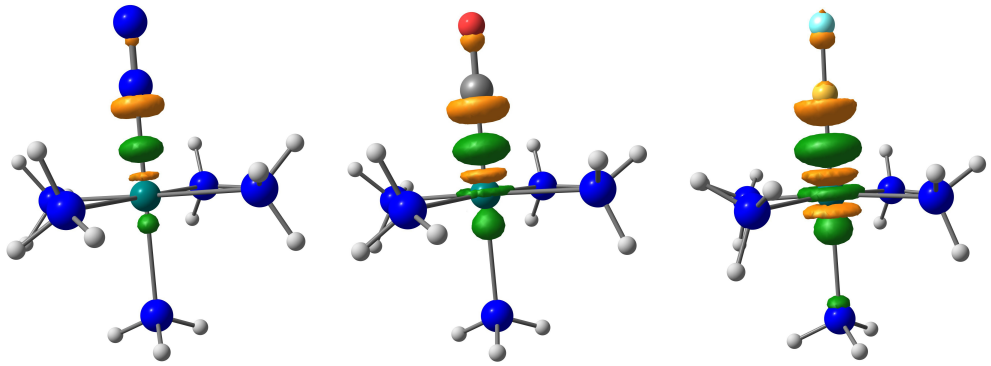

(a) (b) (c)

Figure 3.9: Electron density difference between the CTf and Pol states (plotted with isovalue 0.01 a.u.) for (a) $N_2{-}[Ru(NH_3)_5]^{2+}$, (b) $OC{-}[Ru(NH_3)_5]^{2+}$, and (c) $FB{-}[Ru(NH_3)_5]^{2+}$ (green: increase in electron density; yellow: decrease in electron density).

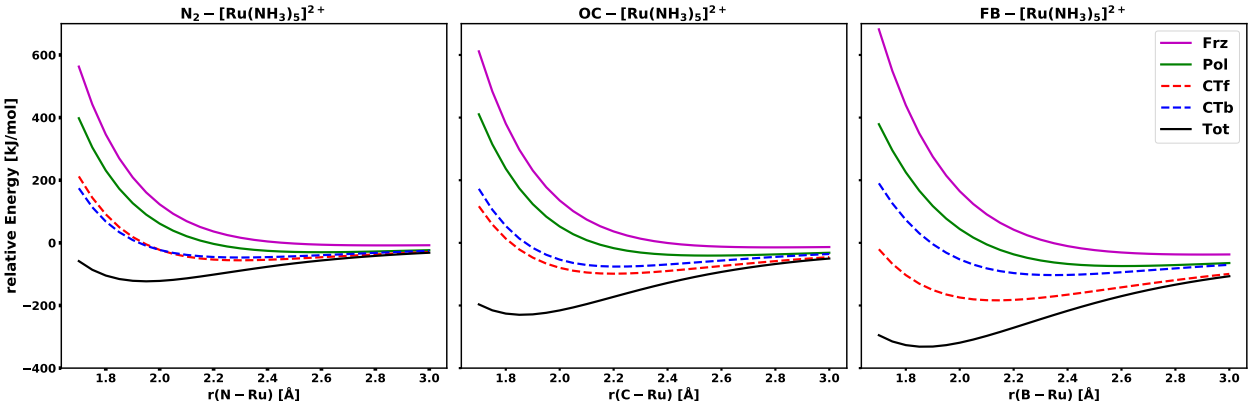

Figure 3.10: Potential energy surface (rigid scan) for each ALMO-EDA intermediate state (Frz, Pol, CTf, CTb, and Tot) for $N_2{-}[Ru(NH_3)_5]^{2+}$ (left), $OC{-}[Ru(NH_3)_5]^{2+}$ (middle), and $FB{-}[Ru(NH_3)_5]^{2+}$ (right).

on the CTb surface (-39 cm^{-1} relative to the free N_2 stretch). The red shift becomes much more pronounced (-150 cm^{-1}relative to free N_2) when both directions of CT are permitted, which can be explained by the combined effect of forward and backward CT in shortening the Ru$-$N distance. According to the adiabatic EDA results in Table 3.6, CTf and CTb shorten the Ru$-$N distance by 0.32 Å and 0.31 Å, respectively, and when combined they shorten the distance by 0.67 Å, indicating that their effects are almost additive in this case. The shortened Ru$-$N distance then strengthens both the electrostatic effect (blue-shifting) and the back-donation (red-shifting), whereas the latter plays a dominant role in this case.

The same mechanism applies to both the CO and BF complexes, where the bond short-

Table 3.6: Metal-ligand distance [r(M−X)] and bond length of the diatomic ligand [r(X−Y)] (both in Å) evaluated on the Pol, CTf, CTb, and Tot surfaces. In the isolated state, r(N−N) = 1.091 Å, r(C−O) = 1.125 Å, r(B−F) = 1.265 Å.

	r(M-X)				r(X-Y)			
Complex	Pol	CTf	CTb	Tot	Pol	CTf	CTb	Tot
NN−$[Ru(NH_3)_5]^{2+}$	2.625	2.308	2.318	1.951				
OC−$[Ru(NH_3)_5]^{2+}$	2.605	2.219	2.329	1.860	1.117	1.114	1.124	1.139
FB−$[Ru(NH_3)_5]^{2+}$	2.690	2.165	2.379	1.871	1.243	1.237	1.249	1.266
NN−$[Fe(NH_3)_5]^{2+}$	2.538	2.267	2.190	1.929	1.090	1.090	1.092	1.097
NN−$[Tc(NH_3)_5]^{+}$	2.638	2.388	2.091	1.873	1.090	1.089	1.115	1.133

Table 3.7: Adiabatic ALMO-EDA results for the shifts in the vibrational frequency of N_2, CO and BF ($\Delta\nu_{XY}$ in cm^{-1}) when associated with the transition metal moiety.

	$\Delta\nu_{XY}$			
Complex	Pol	CTf	CTb	Tot
NN−$[Ru(NH_3)_5]^{2+}$	11	25	−39	−150
OC−$[Ru(NH_3)_5]^{2+}$	74	109	−5	−102
FB−$[Ru(NH_3)_5]^{2+}$	143	208	108	123
NN−$[Fe(NH_3)_5]^{2+}$	7	16	−21	−80
NN−$[Tc(NH_3)_5]^{+}$	16	27	−236	−373

ening effects of CTf and CTb are also nearly additive. However, the relative strength of the blue-shifting electrostatic effect and the red-shifting backward CT, as well as their variation with the Ru−X distance, differs in each complex. The blue shifts on the Pol and CTf surfaces are more significant with more polar ligands, which is in line with the increasingly contracted r(X−Y) from N_2 to BF (see Table 3.6). The back-bonding to CO appears to exert a strong effect such that the frequency calculated on the CTb surface is red-shifted already (5 cm^{-1} relative to the free ν_{CO}). The synergy of forward and backward CT further results in a substantial red shift of 102 cm^{-1} in the fully relaxed complex, suggesting that the strength of backward CT increases more rapidly than the blue-shifting electrostatics with the shortening of the Ru−C distance. The back-bonding to BF, on the other hand, introduces a less pronounced red shift (35 cm^{-1} relative to ν_{BF} on the Pol surface) such that the frequency evaluated on the CTb surface is still strongly blue-shifted (108 cm^{-1} relative to the free ν_{BF}). More interestingly, with both directions of CT permitted, ν_{BF} becomes more blue-shifted relative to that on the CTb surface, which is opposite to the substantial red shifts induced by the synergistic effect of forward and backward CT found

in the N_2 and CO complexes, suggesting that the enhancement of the blue-shifting effect overshadows the increase in the strength of back-donation. This is confirmed by the strongly blue-shifted Pol@Tot frequency as shown in Table 3.9 (314 cm^{-1} relative to the free ν_{BF}), which is 142 cm^{-1} higher than the Pol@CTb frequency. The red shift induced by backward CT, on the other hand, is only increased by 55 cm^{-1} upon moving from the minimum-energy Ru−B distance on the CTb surface to that on the fully relaxed surface, and therefore it is overpowered by the enhanced blue-shifting electrostatic effect.

Table 3.8: Shifts in the stretching frequency of N_2, CO, and BF (in cm^{-1}) when associated with $[Ru(NH_3)_5]^{2+}$ with the Ru−X distance fixed at the optimum values on the CTf ("@CTf") and CTb ("@CTb") surfaces, respectively.

	$\Delta\nu_{XY}$@CTf			$\Delta\nu_{XY}$@CTb		
Complex	Pol	CTf	$\Delta\nu_{CTf}$	Pol	CTb	$\Delta\nu_{CTb}$
NN−$[Ru(NH_3)_5]^{2+}$	33	25	−8	32	−39	−71
OC−$[Ru(NH_3)_5]^{2+}$	107	109	2	92	−5	−97
FB−$[Ru(NH_3)_5]^{2+}$	207	208	1	172	108	−64

Table 3.9: Shifts in the stretching frequency of N_2, CO, and BF (in cm^{-1}) when associated with $[Ru(NH_3)_5]^{2+}$ evaluated at the fully relaxed minimum-energy Ru−X distance ("@Tot").

	$\Delta\nu_{XY}$@Tot			
Complex	Pol	CTf	CTb	Tot
NN−$[Ru(NH_3)_5]^{2+}$	105	83	−73	−150
OC−$[Ru(NH_3)_5]^{2+}$	217	188	7	−103
FB−$[Ru(NH_3)_5]^{2+}$	314	305	195	123

We then perform the same set of analyses on NN−$[Fe(NH_3)_5]^{2+}$, which is the 3d analogue of the Ru(II)−N_2 complex. The 3d electrons are more compact than 4d, resulting in an almost halved magnitude of the ΔE_{Frz} and ΔE_{CT} terms at the equilibrium structure compared to the values of the corresponding Ru(II) complex (see Table 3.5). Turning to the adiabatic EDA results (Table 3.6), the Fe−N distance optimized in the Pol state is ∼0.1 Å shorter than the corresponding Ru−N distance, which is consistent with the weaker Pauli repulsion exerted by the 3d orbitals. Nonetheless, once fully relaxed, r(Fe−N) is only ∼0.02 Å shorter than r(Ru−N) optimized in the same state, indicating the stronger effects of CT in the Ru(II) complex. One should also note that the forward CT has a weaker effect than backward CT on the Fe(II) complex, which is revealed by its CTf/CTb ratio (0.8) as well as the significantly larger Fe−N distance on the CTf surface than on CTb. The decomposition

of the shift in ν_{N2} follows the synergistic mechanism discussed above, whereas the overall red shift (relative to the free ν_{N2}) for the Fe(II) complex is slightly more than one half of that for the Ru(II) complex, which is consistent with the relative strength of their ΔE_{CTb} values in Table 3.5.

At last we investigate the Tc(I) complex with N_2, where the metal center is also of $4d^6$ configuration but has a different oxidation state. Compared to the Ru(II) complex, the frozen interaction at the equilibrium geometry is over 100 kJ/mol more repulsive (Table 3.5) due to the more diffuse d-orbitals of Tc(I), while their ΔE_{Pol} and ΔE_{CTf} terms only minimally differ. The backward CT, however, almost *triples* upon the replacement of Ru(II) with Tc(I), resulting in an overall CT stabilization energy that is over 200 kJ/mol more favorable in the latter. The results of adiabatic EDA further highlight the prominent contribution from back-donation in the Tc(I) complex, such as the significant elongation of the N−N bond (Table 3.6) and the substantial red shift in ν_{NN} (236 cm^{-1} relative the free N_2) that already appears on the CTb surface (Table 3.7). Despite the overwhelming dominance of CTb, the Tc−N distance on the CTb surface is still over 0.2 Å longer than the fully relaxed equilibrium distance. This demonstrates that even for strong π-donating metals, CTf still plays an important role in overcoming the Pauli repulsion to achieve the final metal-ligand distance. Surprisingly, the Ru(II) and Tc(I) complexes show similar N−N bond lengths and frequency blue shifts on the Pol and CTf surfaces. A closer look at the structures of these complexes reveals that the M−NH_3 distances are almost 0.1 Å shorter in the Ru(II) complex, indicating the stronger donation from the ammine ligands to Ru^{2+} that partially neutralizes its excessive positive charges. Finally, we note that the synergistic effect of forward and backward CT remains significant for the Tc(I) complex despite the dominance of backward CT, which is indicated by the further elongated r(N−N) and more red-shifted ν_{N_2} when both directions of CT are permitted.

3.5 Conclusions

Making use of the flexibility of the generalized SCF-MI scheme, we introduced two new intermediate states in which only one direction of CT is permitted under the ALMO-EDA framework. This allows us to separate a total CT stabilization energy into forward (CTf) and backward (CTb) contributions with a residual higher-order term. This new variational forward-backward (VFB) decomposition scheme yields similar results compared to the previously developed ALMO-CTA that employs a perturbative approach. An important difference is that, these two new intermediate states are each variationally optimized such that their energies are strict variational upper bounds to the full SCF energy and the nuclear forces associated with them can thus be readily computed, rendering it possible for one to identify the forward and backward CT contributions to the changes in structural and vibrational properties upon the formation of dative complexes.

As a proof-of-concept example, we first applied VFB analysis to the OC−BH_3 complex. The decomposition of ΔE_{CT} reveals that while CTf and CTb are of similar strength at

the minimum-energy distance, the backward donation from BH_3 to CO decays substantially faster in the long range. This steep distance dependence of the strength of back-donation, together with the relatively weak Pauli repulsion due to the electron-deficient nature of BH_3, elucidates the close agreement between the minimum-energy C−B distances on the CTb and Tot surfaces. The CO stretching frequency (ν_{CO}) in this system is only minimally shifted relative to that of the free CO, and the adiabatic ALMO-EDA results show that ν_{CO} is strongly blue-shifted on the CTf surface and moderately blue-shifted on the CTb surface, which are seemingly counterintuitive. We identified the significant blue-shifting effect of the electrostatic interaction as it shrinks the CO bond distance to increase the dipole moment of CO, which is further enhanced upon the shortening of the C−B distance driven by CT. This blue-shifting electrostatic effect largely cancels out the red-shifting effect of the back-donation.

We then applied VFB analysis to the carbonyl complexes of BeY (Y = O or CO_3), where CO is bound to the BeY moiety under either the κC or κO mode. At their equilibrium structures, the κC complexes are more strongly bound than their respective κO isomers, and the energy differences are rather evenly distributed betwee the Frz, Pol, and CTb terms. The CO stretching frequencies in the κC and κO complexes are blue- and red-shifted, respectively, which agree with the results in Ref. [331]. Using the adiabatic ALMO-EDA, we demonstrated that the opposite shifts in ν_{CO} originate from the frozen interaction, which can be attributed to the molecular Stark effect: depending on the orientation of the CO dipole to the Lewis acid, the electrostatic interaction induces a blue shift (κC) or a red shift (κO). Both Pol and CTb further increases the blue/red shift in the κC/κO complexes simply by shortening the intermolecular distances. The backward CT red-shifts ν_{CO} in both the κC and κO complexes and has a stronger effect in the former because of the larger amplitude of the π^* orbital on the C atom. Nevertheless, the backward CT is not of enough strength to overcome the blue-shifting electrostatics in the κC isomers, especially in the case of OC−$BeCO_3$ where the back-donation is particularly weak. The sizable red shifts in the κO complexes, on the other hand, result from the cooperation of the electrostatic effect and backward CT in elongating and weakening the O−C bond.

Finally we investigated the complexes of N_2, CO, and BF with the $[Ru(II)(NH_3)_5]^{2+}$ moiety. The vertical EDA results at the minimum-energy structures reveal that the total binding strength increases in the order of $N_2 < CO < BF$, which is attributed to the enhanced Pol and CT terms that overshadow increased Pauli repulsion. The adiabatic VFB-EDA results show that the contributions from CTf and CTb to the shortening of the Ru−X distance are almost additive, which differs from the scenarios of the complexes with main group Lewis acids (BH_3, BeO/$BeCO_3$) where intermolecular distance obtained on the CTb surface is already close to the full equilibrium distance. This result can be rationalized by stronger Pauli repulsion exerted by the d-electrons of the transition metal center, whose alleviation requires the assistance of forward CT. A counterintuitive trend is observed for the shifts in the stretching frequency of these ligands, with both ν_{N_2} and ν_{CO} red-shifted (-150 and -102 cm^{-1}, respectively) and ν_{BF} strongly blue-shifted ($+123$ cm^{-1}), which is not consistent with their relative strength of ΔE_{CTb}. Our further decomposition of the

frequency shifts demonstrated that the molecular Stark effect induces a stronger blue shift for a more polar π-acidic ligand, and its enhancement with the decrease of the Ru−X distance exceeds the red shift due to π back-donation, giving rise to the unusual blue shift in ν_{BF}.

In summary, our new VFB extension of the ALMO-EDA provides a useful tool to characterize the roles played by forward and backward CT in the formation of dative complexes, which complements the currently available ALMO-CTA scheme by allowing the decomposition of shifts in molecular properties. The application of VFB analysis to main group and transition metal complexes with π-acidic ligands further revealed that permanent electrostatics and π back-donation are the two crucial parameters in determining the shifts in vibrational frequencies ($\Delta\nu_{\mathrm{XY}}$). Our results highlighted that $\Delta\nu_{\mathrm{XY}}$ may become an unreliable metric for the strength of π back-donation because of the often pronounced electrostatic effect in the bonding regime.

3.6 SCF equations for generalized SCF-MI

Using 1PDM in the AO basis, the energy (objective function) of a generalized SCF-MI problem can be expressed as

$$E_{\mathrm{SCFMI}} = V_{\mathrm{nn}} + \mathbf{P}\cdot\mathbf{h} + \frac{1}{2}\mathbf{P}\cdot\mathbf{II}\cdot\mathbf{P} + E_{\mathrm{xc}}[\mathbf{P}] \tag{3.12}$$

which has the same form as the standard SCF-MI energy. The four terms on the right-hand side of Eq. (3.12) are nuclear repulsion energy, one-electron energy (kinetic energy and nuclei-electron attraction), two-electron energy (Coulomb and exact exchange), and exchange-correlation energy, respectively. Note that when non-hybrid (pure) functionals are used **II** reduces to the Coulomb repulsion between electrons.

The Stoll equation [196] for a given fragment X has the following form in generalized SCF-MI:

$$\begin{aligned}&\left[\mathbf{G}^T(\mathbf{I}-\mathbf{SP}+\mathbf{SP}_X^T)\mathbf{F}(\mathbf{I}-\mathbf{PS}+\mathbf{P}_X\mathbf{S})\mathbf{G}\right]_{XX}\mathbf{C}_X^G\\ &=[\mathbf{G}^T\mathbf{S}\mathbf{G}]_{XX}\mathbf{C}_X^G\boldsymbol{\epsilon}_X\end{aligned} \tag{3.13}$$

where one "X" in the subscript denotes columns corresponding to fragment X in a matrix and "XX" denotes both rows and columns corresponding to fragment X. $\mathbf{P}$ and $\mathbf{S}$ are the global 1PDM and the AO overlap matrix, respectively, $\mathbf{F}$ is the Fock matrix built from $\mathbf{P}$, and the fragment projector matrix $\mathbf{P}_X$ in the Stoll equation is defined as

$$\mathbf{P}_X = \left[\mathbf{G}\mathbf{C}_{\mathrm{o}}^G(\boldsymbol{\sigma}_{\mathrm{oo}}^{-1})\right]_X(\mathbf{C}_{\mathrm{o},X}^G)^T\mathbf{G}_X^T \tag{3.14}$$

Finally, $\boldsymbol{\epsilon}_X$ and $\mathbf{C}_X^G$ are the eigenvalues and eigenvectors (fragment MOs in the basis defined by $\mathbf{G}$) to be self-consistently obtained, respectively.

Besides solving locally projected SCF equations, one can also use gradient-based optimization algorithms to obtain variationally optimized $\mathbf{C}^G$. The gradient of energy with

respect to orbital rotations in the basis defined by $\mathbf{G}$ on a given fragment X ($\boldsymbol{\theta}^G_{\mathrm{ov},X}$) is

$$\frac{\partial E}{\partial \boldsymbol{\theta}^G_{\mathrm{ov},X}} = \left[(\boldsymbol{\sigma}^{-1}_{\mathrm{oo}})(\mathbf{C}^G_{\mathrm{o}})^T\mathbf{F}^G(\mathbf{I}^G - \mathbf{P}^G\mathbf{S}^G)\right]_{XX}\mathbf{C}^G_{\mathrm{v},X} + \text{c.c.} \tag{3.15}$$

where

$$\mathbf{F}^G = \mathbf{G}^T\mathbf{F}\mathbf{G} \tag{3.16}$$

$$\mathbf{S}^G = \mathbf{G}^T\mathbf{S}\mathbf{G} \tag{3.17}$$

$$\mathbf{P}^G = \mathbf{C}^G_{\mathrm{o}}(\boldsymbol{\sigma}^{-1}_{\mathrm{oo}})(\mathbf{C}^G_{\mathrm{o}})^T \tag{3.18}$$

and $\mathbf{I}^G$ is an identity matrix of $\mathbf{G}$'s column dimension. "c.c." refers to the complex of the previous term (transpose in the real case).

3.7 Nuclear gradient for generalized SCF-MI

Differentiating the generalized SCF-MI energy given by Eq. (3.12) with respect to the positions of nuclei yields

$$\begin{aligned} E^x_{\mathrm{SCFMI}} = V^x_{\mathrm{nn}} + \mathbf{P}\cdot\mathbf{h}^x + \frac{1}{2}\mathbf{P}\cdot\mathbf{II}^x\cdot\mathbf{P} + E^x_{\mathrm{xc}}[\mathbf{P}] + \sum_X E^{\boldsymbol{\theta}_X}_{\mathrm{SCFMI}}\cdot\boldsymbol{\theta}^x_X \\ + E^{\mathbf{S}}_{\mathrm{SCFMI}}\cdot\mathbf{S}^x + \sum_X E^{\mathbf{G}_X}_{\mathrm{SCFMI}}\cdot\mathbf{G}^{\boldsymbol{\phi}_X}_X\cdot\boldsymbol{\phi}^x_X \end{aligned} \tag{3.19}$$

The first four terms are of the same forms as these components in the nuclear gradient of a standard KS-DFT energy except for the specialized 1PDM. The variable $\boldsymbol{\theta}_X$ in the fifth term refers to the on-fragment rotations of MOs in the given basis defined by $\mathbf{G}$, which vanishes at the convergence of the generalized SCF-MI problem since by definition one would have $E^{\boldsymbol{\theta}_X}_{\mathrm{SCFMI}} = 0$.

The second last term in Eq. (3.19) arises from the fact that on each fragment both $\mathbf{G}_X$ and $\mathbf{C}^G_{\mathrm{o},X}$ are orthogonalized. Given $\mathbf{P} = \mathbf{G}\mathbf{C}^G_{\mathrm{o}}(\boldsymbol{\sigma}^{-1}_{\mathrm{oo}})(\mathbf{C}^G_{\mathrm{o}})^T\mathbf{G}^T$, using the chain rule we have

$$\begin{aligned} E^{\mathbf{S}}_{\mathrm{SCFMI}}\cdot\mathbf{S}^x &= \frac{\partial E}{\partial\mathbf{P}}\cdot\frac{\partial\mathbf{P}}{\partial\mathbf{S}}\cdot\mathbf{S}^x \\ &= \frac{\partial E}{\partial\mathbf{P}}\cdot\left(\sum_X\frac{\partial\mathbf{P}}{\partial\mathbf{C}^G_{\mathrm{o},X}}\cdot\frac{\partial\mathbf{C}^G_{\mathrm{o},X}}{\partial\mathbf{S}} + \frac{\partial\mathbf{P}}{\partial\boldsymbol{\sigma}_{\mathrm{oo}}}\cdot\frac{\partial\boldsymbol{\sigma}_{\mathrm{oo}}}{\partial\mathbf{S}} + \sum_X\frac{\partial\mathbf{P}}{\partial\mathbf{G}_X}\cdot\frac{\partial\mathbf{G}_X}{\partial\mathbf{S}}\right)\cdot\mathbf{S}^x \end{aligned} \tag{3.20}$$

The first term on the right-hand side of Eq. (3.20) vanishes because of the stationary condition $\partial E/\partial\mathbf{C}^G_{\mathrm{o},X} = \mathbf{0}$ for a generalized SCF-MI problem. The second term

$$\begin{aligned} \frac{\partial E}{\partial\mathbf{P}}\cdot\frac{\partial\mathbf{P}}{\partial\boldsymbol{\sigma}_{\mathrm{oo}}}\cdot\frac{\partial\boldsymbol{\sigma}_{\mathrm{oo}}}{\partial\mathbf{S}} &= \mathbf{F}\cdot\mathbf{C}_{\mathrm{o}}\frac{\partial(\boldsymbol{\sigma}^{-1}_{\mathrm{oo}})}{\partial\mathbf{S}}\mathbf{C}^T_{\mathrm{o}}\cdot\mathbf{S}^x \\ &= -\mathbf{F}\cdot\mathbf{C}_{\mathrm{o}}(\boldsymbol{\sigma}^{-1}_{\mathrm{oo}})\frac{\partial\boldsymbol{\sigma}_{\mathrm{oo}}}{\partial\mathbf{S}}(\boldsymbol{\sigma}^{-1}_{\mathrm{oo}})\mathbf{C}^T_{\mathrm{o}}\cdot\mathbf{S}^x \\ &= -(\mathbf{PFP})\cdot\mathbf{S}^x \end{aligned} \tag{3.21}$$

which possesses the same form as the overlap matrix contribution to the standard SCF gradient (the matrix **PFP** is often called the energy-weighted 1PDM).

Now we focus on the last term in Eq. (3.20). Without considering the fragment structure of $\mathbf{G}$, we have

$$\begin{aligned}
\frac{\partial E}{\partial \mathbf{G}} &= \mathbf{F} \cdot \frac{\partial \mathbf{P}}{\partial \mathbf{G}} \\
&= \mathbf{F} \cdot \left[\mathbf{C}_{\mathrm{o}}^{G} (\boldsymbol{\sigma}_{\mathrm{oo}}^{-1}) (\mathbf{C}_{\mathrm{o}}^{G})^{T} \mathbf{G}^{T} + \mathbf{G} \mathbf{C}_{\mathrm{o}}^{G} (\boldsymbol{\sigma}_{\mathrm{oo}}^{-1}) (\mathbf{C}_{\mathrm{o}})^{T} - \mathbf{C}_{\mathrm{o}} (\boldsymbol{\sigma}_{\mathrm{oo}}^{-1}) \frac{\partial \boldsymbol{\sigma}_{\mathrm{oo}}}{\partial \mathbf{G}} (\boldsymbol{\sigma}_{\mathrm{oo}}^{-1}) \mathbf{C}_{\mathrm{o}}^{T} \right] \\
&= \mathbf{C}_{\mathrm{o}}^{G} (\boldsymbol{\sigma}_{\mathrm{oo}}^{-1}) (\mathbf{C}_{\mathrm{o}}^{G})^{T} \mathbf{G}^{T} \mathbf{F} + \mathbf{F} \mathbf{G} \mathbf{C}_{\mathrm{o}}^{G} (\boldsymbol{\sigma}_{\mathrm{oo}}^{-1}) (\mathbf{C}_{\mathrm{o}})^{T} \\
&\quad - \mathbf{S}\mathbf{P}\mathbf{F}\mathbf{G} \mathbf{C}_{\mathrm{o}}^{G} (\boldsymbol{\sigma}_{\mathrm{oo}}^{-1}) (\mathbf{C}_{\mathrm{o}}^{G})^{T} - \mathbf{C}_{\mathrm{o}}^{G} (\boldsymbol{\sigma}_{\mathrm{oo}}^{-1}) (\mathbf{C}_{\mathrm{o}}^{G})^{T} \mathbf{G}\mathbf{F}\mathbf{P}\mathbf{S} \\
&= (\mathbf{I} - \mathbf{S}\mathbf{P}) \mathbf{F} \mathbf{G} \mathbf{C}_{\mathrm{o}}^{G} (\boldsymbol{\sigma}_{\mathrm{oo}}^{-1}) (\mathbf{C}_{\mathrm{o}}^{G})^{T} + \mathrm{c.c.}
\end{aligned} \tag{3.22}$$

While in the most general cases the right-hand side of Eq. (3.22) would be non-zero, it does vanish for the solutions to the generalized SCF-MI problems that correspond to the two "one-way" CT surfaces. We first reintroduce the fragmentation: without losing generality, we assume that fragment A is the donor fragment such that the left index of $\mathbf{G}_A$ covers all AO basis functions in the system:

$$\frac{\partial E}{\partial (G_A)^{\mu}_{\ As}} = [(\mathbf{I} - \mathbf{S}\mathbf{P}) \mathbf{F} \mathbf{G} \mathbf{C}_{\mathrm{o}}^{G} (\boldsymbol{\sigma}_{\mathrm{oo}}^{-1})]_{\mu}^{\ Ai} (C_{\mathrm{o}}^{G,T})_{\ Ai}^{As} \tag{3.23}$$

The variational subspace functions for fragment B, on the other hand, are only expanded by AOs on its own fragment

$$\frac{\partial E}{\partial (G_B)^{B\mu}_{\ \ Bs}} = [(\mathbf{I} - \mathbf{S}\mathbf{P}) \mathbf{F} \mathbf{G} \mathbf{C}_{\mathrm{o}}^{G} (\boldsymbol{\sigma}_{\mathrm{oo}}^{-1})]_{B\mu}^{\ \ Bi} (C_{\mathrm{o}}^{G,T})_{\ Bi}^{Bs} \tag{3.24}$$

We now show that the two derivatives above are both zero. The stationary condition for the generalized SCF-MI problem:

$$\begin{aligned}
&\frac{\partial E}{\partial (C_{\mathrm{o}}^{G})^{As}_{\ \ Ai}} = \mathbf{F} \cdot \frac{\partial \mathbf{P}}{\partial (C_{\mathrm{o}}^{G})^{As}_{\ \ Ai}} = 0 \\
\Longrightarrow\ & [(\mathbf{I}^{G} - \mathbf{S}^{G}\mathbf{P}^{G}) \mathbf{G}^{T} \mathbf{F} \mathbf{G} \mathbf{C}_{\mathrm{o}}^{G} (\boldsymbol{\sigma}_{\mathrm{oo}}^{-1})]_{\ As}^{Ai} = 0 \\
\Longrightarrow\ & (G^{T})_{\ As}^{\mu} [(\mathbf{I} - \mathbf{S}\mathbf{P}) \mathbf{F} \mathbf{G} \mathbf{C}_{\mathrm{o}}^{G} (\boldsymbol{\sigma}_{\mathrm{oo}}^{-1})]_{\mu}^{\ Ai} = 0
\end{aligned} \tag{3.25}$$

For our specific problem, the variational degrees of freedom for fragment A are essentially given by the full AO space without any further constraint. Therefore, we have

$$\frac{\partial E}{\partial (C_{\mathrm{o}}^{G})^{As}_{\ \ Ai}} = 0 \Leftrightarrow \frac{\partial E}{\partial (C_{\mathrm{o}})^{\mu}_{\ Ai}} = 0 \implies [(\mathbf{I} - \mathbf{S}\mathbf{P}) \mathbf{F} \mathbf{G} \mathbf{C}_{\mathrm{o}}^{G} (\boldsymbol{\sigma}_{\mathrm{oo}}^{-1})]_{\mu}^{\ Ai} = 0 \tag{3.26}$$

Similarly, for fragment B whose variational space is given by all AOs on that fragment, we have

$$\frac{\partial E}{\partial (C_{\mathrm{o}}^{G})^{Bs}_{\ \ Bi}} = 0 \Leftrightarrow \frac{\partial E}{\partial (C_{\mathrm{o}})^{B\mu}_{\ \ Bi}} = 0 \implies [(\mathbf{I} - \mathbf{S}\mathbf{P}) \mathbf{F} \mathbf{G} \mathbf{C}_{\mathrm{o}}^{G} (\boldsymbol{\sigma}_{\mathrm{oo}}^{-1})]_{B\mu}^{\ \ Bi} = 0 \tag{3.27}$$

Substituting Eqs. (3.26) and (3.27) into Eqs. (3.23) and (3.24), respectively, we get $\partial E/\partial \mathbf{G}_A = \mathbf{0}$ and $\partial E/\partial \mathbf{G}_B = \mathbf{0}$. Therefore, the last term in Eq. 3.20 also vanishes, suggesting that the overlap matrix contribution to the nuclear gradient can be computed in the same way as a standard SCF problem:

$$E^{\mathbf{S}}_{\mathrm{SCFMI}} \cdot \mathbf{S}^x = -(\mathbf{PFP}) \cdot \mathbf{S}^x \tag{3.28}$$

One should note that Eq. (3.28) only holds for special generalized SCF-MI problems where the variational subspace of each fragment has the same span as the AOs. In cases where this condition is not satisfied, e.g., the definition of each fragment's polarization subspace using fragment electrical response functions (FERFs), [32] one no longer has $\partial E/\partial \mathbf{G}_X = 0$.

The variable in the last term on the right-hand side of Eq. (3.19), $\boldsymbol{\phi}_X$, refers to the orbital rotations on a given fragment (X) at the polarization stage (the standard AO-based ALMO scheme), which also contributes to the variation of $\mathbf{G}$ with the displacement of nuclear positions. However, since we have shown above that $E^{\mathbf{G}_X}_{\mathrm{SCFMI}} = \mathbf{0}$ for this special problem, the last term in Eq. (3.20) can also be discarded. Taken all together, the nuclear gradients for the two "one-way" CT states are given by

$$E^x_{\mathrm{SCFMI}} = V^x_{\mathrm{nn}} + \mathbf{P} \cdot \mathbf{h}^x + \frac{1}{2}\mathbf{P} \cdot \mathbf{II}^x \cdot \mathbf{P} + E^x_{\mathrm{xc}}[\mathbf{P}] - (\mathbf{PFP}) \cdot \mathbf{S}^x \tag{3.29}$$

which is exactly of the same form as the standard SCF nuclear gradients.

Chapter 4

Consistent Inclusion of Continuum Solvation in Energy Decomposition Analysis: Theory and Application to Molecular CO_2 Reduction Catalysts

4.1 Introduction

Intermolecular interactions play an essential role in modern chemical research. Most chemical processes take place in solution, making it desirable to develop computational chemistry tools to model and analyze intermolecular interactions with solvent effects taken into account. The inclusion of solvent brings new challenges to the existing methods as solvation is able to modulate intermolecular interactions in a variety of ways. For interactions involving ionic species, the solvent helps stabilize the charged moieties while screening the long-range electrostatic interactions as a dielectric medium. Even for a neutral solute species, its electronic structure and related properties, such as multipole moments, may be altered by polar solvents, which in turn affects its interaction with other solute molecules. Such effects can impose profound influences on relative stability of intermolecular complexes as well as thermodynamics and kinetics of chemical reactions in solution. [347, 348]

Implicit solvent models, which typically treat the solvent environment as a dielectric continuum and ignore its molecular-level resolution, remain widely used in modern quantum chemistry calculations to incorporate solvation effects. [349–351] These methods are also known as self-consistent reaction field (SCRF) models, since the implicit solvent perturbs the quantum mechanical (QM) Hamiltonian via an external field, and the field itself depends on the QM electron density. Many variants of SCRF models that differ significantly in their formulation and complexity have been developed, including methods based on apparent surface charges (ASC),[119, 120, 122, 352–359] generalized Born models,[123, 360, 361] and models based on direct solution of inhomogeneous Poisson-Boltzmann equations. [362–366]

The popular conductor-like (C-PCM) [119, 120, 354] and integral-equation-formalism (IEF-PCM) [355, 356] polarizable continuum models are outstanding examples among the ASC models.

Energy decomposition analysis (EDA) [85, 188–190, 221] is a powerful tool that facilitates one's understanding of intermolecular interactions by quantifying the relative importance of various physically motivated components, such as permanent electrostatics, polarization, dispersion, etc. While there are many perturbative or variational EDA schemes available, these developments have been focusing on intermolecular interactions in vacuum. To extend the utility of EDA approaches to intermolecular interactions under solvent environment, it is natural to integrate existing EDA schemes with implicit solvent models, considering the wide usage of the latter for describing solute-solvent interactions with minimal computational cost. The simplest approach to achieve that is to include the solvent contribution to interaction energy as an *a posteriori* correction to the gas-phase EDA result. This approach was adopted, for instance, in the EDA scheme implemented in the ONETEP [367] linear-scaling density functional theory (DFT) program. [368, 369] While such an approach is applicable to most EDA schemes, it is not entirely satisfactory as it is unable to describe the solvation effect on each individual energy component.

In a pioneering effort to consistently incorporate solvent effect in an EDA procedure, Cammi et al.[370] modified the Kituara-Morokuma (KM)-EDA [192, 193] by adding the SCRF potential of the full dimer complex to the Fock matrix that was used to generate the energy components in this EDA scheme. Similar approaches were later proposed by Contador et al.[371] to study hydrogen-bonded complexes in solution, where the KM-EDA was applied to decompose interaction energies evaluated within "dimeric" cavities, and also by Gora et al.[372] where the intermolecular interaction (free) energy was separated into electrostatics, exchange-repulsion, delocalization, and reaction field (solvation) contributions. Fedorov and Kitaura extended their pair-interaction (PI)-EDA scheme [373] to treat intermolecular interactions in solution by combining the fragment molecular orbital (FMO) method[374] with PCM models,[375] in which they characterized two types of solvent effects: (i) screening of electrostatics and (ii) desolvation upon the formation of complex.

The EDA-PCM scheme developed by Su et al.,[376] which was based upon the localized molecular orbital (LMO)-EDA scheme,[210] is more closely related to the present work. It accounts for the solvation environment in two stages: (i) the isolated fragment orbitals (LMOs) are optimized with continuum solvent, and are then used to construct the intermediate states that are required for the evaluation of the electrostatics, exchange, repulsion, and polarization terms; (ii) a "desolvation" term, which describes the change in solute-solvent interaction energies associated with the destruction of monomer SCRFs and the formation of the full complex SCRF, is introduced in addition to the original LMO-EDA scheme. In the more recent generalized Kohn-Sham (GKS)-EDA, [377, 378] this same approach is used to incorporate the solvent contribution to the interaction free energy. While this is a rather sophisticated approach that integrates implicit solvation with a modern DFT-based EDA, the solvent reaction field is constructed only for the initial (isolated fragment) and final (full complex) states. Since it is not re-optimized for the intermediates, the solvent effect on each

individual term is still not explicitly characterized.

In this paper, we integrate SCRF implicit solvent models with energy decomposition analysis of DFT calculations based on absolutely localized molecular orbitals (ALMO-EDA), whose gas-phase version was previously developed by some of us. [83–85, 379] For brevity, we denote this new extension of the ALMO-EDA for studying non-covalent interactions in solution as "ALMO-EDA(solv)" throughout this paper. The second-generation ALMO-EDA method [84, 379] partitions the total interaction energy (ΔE_{INT}) into contributions from permanent electrostatics (ELEC), Pauli repulsion (PAULI), dispersion (DISP), polarization (POL), and charge transfer (CT):

$$\Delta E_{\mathrm{INT}} = \Delta E_{\mathrm{ELEC}} + \Delta E_{\mathrm{PAULI}} + \Delta E_{\mathrm{DISP}} + \Delta E_{\mathrm{POL}} + \Delta E_{\mathrm{CT}} \tag{4.1}$$

where the first three terms constitute the frozen interaction energy (ΔE_{FRZ}).[86] This decomposition relies on the definition of two intermediate states: (i) the frozen (FRZ) state, which is constructed as an antisymmetrized product of isolated fragment wavefunctions, and (ii) the polarized (POL) state, which is obtained from variationally relaxing the frozen wavefunction with respect to orbital rotations that are "absolutely localized" on each fragment.[31, 32] Differing from the scheme previously developed by Phipps et al.,[369] our new approach incorporates continuum solvent effects at all stages of the EDA procedure, namely, the isolated fragment states and FRZ, POL, and fully relaxed supersystem states. We validate and rationalize the results given by ALMO-EDA(solv) on the $Na^+\cdots Cl^-$ model complex as well as the potential energy curves of two ion-water ($H_2O\cdots Na^+$ and $H_2O\cdots Cl^-$) complexes, in which the solvation environments are treated with C-PCM (with no empirical non-electrostatic terms) [119, 120, 354] and the popular SMD model,[122] respectively.

We then utilize the ALMO-EDA(solv) scheme to investigate the role of intermolecular interactions in two distinct examples of catalyzed CO_2 reduction reactions: one is assisted by the $[Fe(II)TPP]^0$ catalyst (TPP = tetraphenylporphyrin) or its derivatives,[380] which facilitates the $2e^-/2H^+$ reduction of CO_2 to CO with fast turnover rates and high product selectivity at a low overpotential [100] by acting as an "electron mediator" between the electrode and CO_2 in solution and stabilizing intermediates such as adducts of activated CO_2; the other involves a single-electron transfer from a photoactivated and then reduced oligo(*p*-phenylenes) photocatalyst (OPP) to CO_2.[381] The catalysts investigated in this work for these two CO_2 reduction processes are summarized in Figs. 4.1 and 4.2, respectively. Electronic structure calculations and EDA can help provide vital insights into catalytic pathways by identifying key intermediates and characterizing substrate-catalyst interactions, allowing one to understand the origin of activity or selectivity as well as the cause of any intrinsic limitation of a catalyst. [131–133, 176] Many CO_2 reduction catalysts operate in aprotic polar solvents [100, 380–382], aqueous solutions[383], or water/organic solvent mixtures [384, 385]. In such cases, it is essential to incorporate solvation effects in electronic structure calculations for one to obtain meaningful and reliable energetic results, especially for adducts of activated CO_2 ($CO_2^{\bullet-}$) whose interactions with other species would be vastly different in the gas and solution phases.

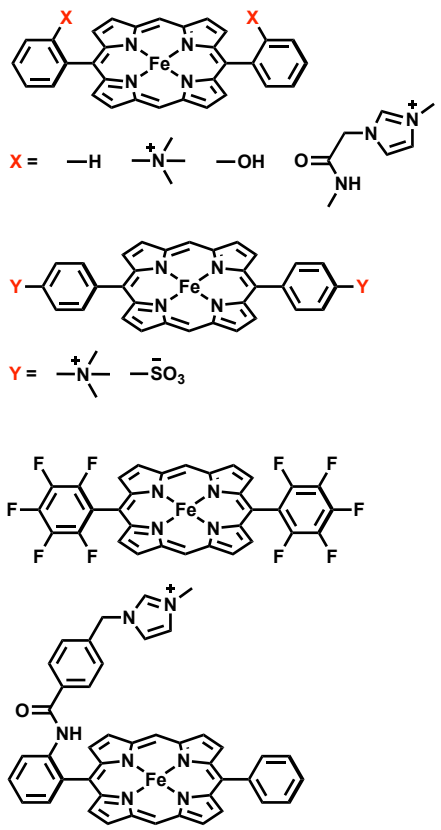

Figure 4.1: Summary of all FeTPP derivatives investigated in this study.

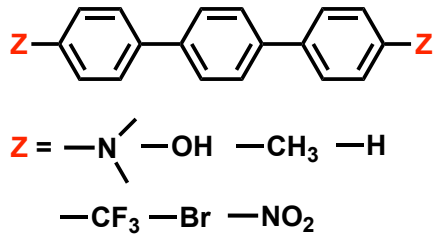

Figure 4.2: Summary of all OPP derivatives investigated in this study.

4.2 Theory

The overall procedure of ALMO-EDA(solv) is illustrated in Fig. 4.3, which, like the gas-phase second-generation ALMO-EDA (Eq. (4.1)), separates the total interaction into five terms:

$$\Delta E_{\mathrm{INT}}^{(\mathrm{s})} = \Delta E_{\mathrm{ELEC}}^{(\mathrm{s})} + \Delta E_{\mathrm{PAULI}}^{(\mathrm{s})} + \Delta E_{\mathrm{DISP}}^{(\mathrm{s})} + \Delta E_{\mathrm{POL}}^{(\mathrm{s})} + \Delta E_{\mathrm{CT}}^{(\mathrm{s})} \tag{4.2}$$

Here the superscript "(s)" indicates that the energetic terms are calculated with solvent taken into account. Unlike many other EDA schemes where the solvent contribution is treated as a correction to the EDA results in vacuum, our approach incorporates the solvation effect in all states (initial, intermediate and final) involved in the EDA. The interaction energy to be decomposed is given by the difference between the energy of the solvated, fully relaxed complex (stage (iv) in Fig. 4.3) and the sum of energies of isolated fragments that are individually solvated (stage (i) in Fig. 4.3), which, as in the gas-phase ALMO-EDA, can be first partitioned into contributions from frozen interaction (FRZ), polarization (POL), and charge transfer (CT):

$$\Delta E_{\mathrm{INT}}^{(\mathrm{s})} = E_{\mathrm{Full}}^{(\mathrm{s})} - \sum_A E_A^{(\mathrm{s})} \tag{4.3}$$

$$= \Delta E_{\mathrm{FRZ}}^{(\mathrm{s})} + \Delta E_{\mathrm{POL}}^{(\mathrm{s})} + \Delta E_{\mathrm{CT}}^{(\mathrm{s})} \tag{4.4}$$

The frozen interaction energy ($\Delta E_{\mathrm{FRZ}}^{(\mathrm{s})}$) describes the energy change upon the formation of a solvated complex from several individually solvated, non-interacting fragments *without* relaxing their orbitals. It corresponds to the energy change from (i) to (ii) in Fig. 4.1:

$$\Delta E_{\mathrm{FRZ}}^{(\mathrm{s})} = E_{\mathrm{FRZ}}^{(\mathrm{s})} - \sum_A E_A^{(\mathrm{s})} \tag{4.5}$$

To quantify the effect of the solvent on the interaction, we introduce a new term, ΔE_{SOL}, to describe the gain or loss of solute-solvent interaction energy upon the formation of the frozen complex:

$$\Delta E_{\mathrm{SOL}} = (E_{\mathrm{FRZ}}^{(\mathrm{s})} - E_{\mathrm{FRZ}}^{(0)}) - \sum_A (E_A^{(\mathrm{s})} - E_A^{(0)}) \tag{4.6}$$

where the superscript "(0)" denotes internal electronic energies of the solute (i.e. excluding solute-solvent interaction, but orbitals optimized with solvent). Subtracting ΔE_{SOL} from $\Delta E_{\mathrm{FRZ}}^{(\mathrm{s})}$ thus recovers $\Delta E_{\mathrm{FRZ}}^{(0)}$, which can be further decomposed into permanent electrostatics (ELEC), Pauli repulsion (PAULI), and dispersion (DISP) contributions as in vacuum:[86]

$$\begin{aligned} \Delta E_{\mathrm{FRZ}}^{(0)} &= \Delta E_{\mathrm{FRZ}}^{(\mathrm{s})} - \Delta E_{\mathrm{SOL}} \\ &= E_{\mathrm{FRZ}}^{(0)} - \sum_A E_A^{(0)} \\ &= \Delta E_{\mathrm{ELEC}}^{(0)} + \Delta E_{\mathrm{PAULI}}^{(0)} + \Delta E_{\mathrm{DISP}}^{(0)} \end{aligned} \tag{4.7}$$

The overall decomposition of the frozen interaction energy, including solvation, is thus given by

$$\Delta E_{\mathrm{FRZ}}^{(\mathrm{s})} = \Delta E_{\mathrm{SOL}} + \Delta E_{\mathrm{ELEC}}^{(0)} + \Delta E_{\mathrm{PAULI}}^{(0)} + \Delta E_{\mathrm{DISP}}^{(0)} \tag{4.8}$$

In this, the decomposition of the internal frozen interaction energy ($\Delta E_{\mathrm{FRZ}}^{(0)}$) is based on the "quasiclassical" scheme exclusively,[86, 322] where the electrostatic component, $\Delta E_{\mathrm{ELEC}}^{(0)}$, is defined as the Coulomb interaction between total charge distributions of isolated fragments.

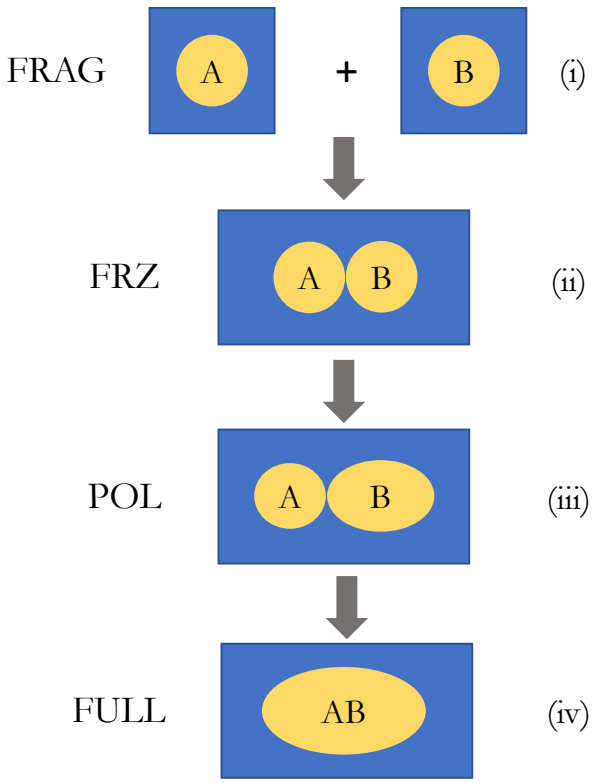

Figure 4.3: Illustration of the ALMO-EDA(solv) scheme: (i) isolated fragments that are individually solvated (the initial state); (ii) and (iii) the frozen (FRZ) and polarized (POL) intermediate states; (iv) the fully relaxed complex (the final state). Note that the shape of the molecular cavity for the complex remains the same across states (ii)–(iv), but the dielectric continuum (solvent) is polarized differently by the solute complex.

For most generic implicit solvent models, the solute-solvent interaction comprises both electrostatic and non-electrostatic components. While the description of the electrostatic component plays a pivotal role in the formulation of a solvent model, the non-electrostatic solute-solvent interaction is typically described by empirical, highly parameterized functions (e.g. the cavity-dispersion-solvent structure (CDS) term in the SMD model [122]) and sometimes even ignored. Upon the formation of a complex, the solute-solvent electrostatic interaction may be drastically changed due to the Coulomb interaction between induced charges that belong to different fragment cavities as well as modifications to the shape of molecular cavities. The overall effect of the change in solute-solvent electrostatic interaction, as we observe in practice, is often screening the electrostatic interaction between each fragment's "internal" charge distribution ($\Delta E^{(0)}_{\mathrm{ELEC}}$). The change in the non-electrostatic component of the solute-solvent interaction energy is usually of lesser importance compared

to the electrostatic component, and in most cases it supplies a destabilizing effect due to the reduction of total surface area of molecular cavities upon the formation of a complex. Bearing these considerations in mind, we separate ΔE_{SOL} into electrostatic ($\Delta E_{\mathrm{SOL}}^{\mathrm{el}}$) and non-electrostatic ($\Delta E_{\mathrm{SOL}}^{\text{non-el}}$) components: the former is combined with $\Delta E_{\mathrm{ELEC}}^{(0)}$, giving rise to a solvent-corrected electrostatic term that is denoted as $\Delta E_{\mathrm{ELEC}}^{(\mathrm{s})}$, and the latter is combined with $\Delta E_{\mathrm{PAULI}}^{(0)}$ because of their common short-ranged nature. The decomposition of the frozen term in ALMO-EDA(solv) (Eq. (4.8)) can thus be rewritten as

$$\begin{aligned}\Delta E_{\mathrm{FRZ}}^{(\mathrm{s})} &= (\Delta E_{\mathrm{SOL}}^{\mathrm{el}} + \Delta E_{\mathrm{ELEC}}^{(0)}) + (\Delta E_{\mathrm{PAULI}}^{(0)} + \Delta E_{\mathrm{SOL}}^{\text{non-el}}) + \Delta E_{\mathrm{DISP}}^{(0)} \\ &= \Delta E_{\mathrm{ELEC}}^{(\mathrm{s})} + \Delta E_{\mathrm{PAULI}}^{(\mathrm{s})} + \Delta E_{\mathrm{DISP}}^{(\mathrm{s})} \end{aligned} \tag{4.9}$$

One should note that in Eq. (4.9) we have assumed that $\Delta E_{\mathrm{DISP}}^{(\mathrm{s})} \approx \Delta E_{\mathrm{DISP}}^{(0)}$, that is, the dispersion interaction between fragments is unaffected by the presence of solvent except that the fragment wavefunctions are optimized with solvent. This assumption is plausible when the two interacting moieties are in close contact, especially when they reside in the same molecular cavity, but may become less justified when the two moieties are well-separated and reside in two non-overlapping cavities, since dispersion interaction, which can be viewed as interactions between fluctuating dipoles, may also be screened by the dielectric medium. [386] This many-body dispersion effect [387] seems non-trivial to include in a continuum solvent model, so we stick with this assumption for now and decompose the frozen interaction energy based on Eq. (4.9) in the rest of this paper.

The polarization energy ($\Delta E_{\mathrm{POL}}^{(\mathrm{s})}$) in ALMO-EDA(solv) is defined as the energy difference between the polarized intermediate state and the solvated frozen complex, which corresponds to the energy change from stage (ii) to (iii) in Fig. 4.3:

$$\Delta E_{\mathrm{POL}}^{(\mathrm{s})} = E_{\mathrm{POL}}^{(\mathrm{s})} - E_{\mathrm{FRZ}}^{(\mathrm{s})} \tag{4.10}$$

It describes the energetic stabilization associated with the intramolecular relaxation of each fragment in the presence of other fragments as well as the solvent environment. In DFT-based ALMO-EDA, the POL state is obtained by variationally minimizing the supersystem energy subject to the constraint that the polarized molecular orbitals (MOs) of each fragment are expanded in fragment-specific basis functions (either atomic orbitals (AO) or frozen occupied MOs plus fragment electrical response functions (FERFs)[32]), which is known as the "self-consistent field for molecular interaction" (SCF-MI) approach. [30, 31, 196] In each iteration of the SCF-MI calculation, the solvent reaction field will be re-equilibrated in accord with the updated electron density of the complex, ensuring that the response of the solvent to the change of solute electronic structure is incorporated in a self-consistent manner.

Finally, we perform a standard, unconstrained SCF calculation within the solvent environment, and the energy lowering relative to the POL state (from (iii) to (iv) in Fig. 4.3) is defined as the charge-transfer (CT) energy:

$$\Delta E_{\mathrm{CT}}^{(\mathrm{s})} = E_{\mathrm{Full}}^{(\mathrm{s})} - E_{\mathrm{POL}}^{(\mathrm{s})} \tag{4.11}$$

Note that the charge transfer process might be associated with charge redistribution in the complex, which in turn induces responses in the reaction field. Such an effect is captured by the self-consistent minimization of $E_{\text{Full}}^{(\text{s})}$ in the presence of solvent.

In summary, the energy decomposition given by the ALMO-EDA(solv) scheme is formally identical to its gas-phase counterpart. The explicit change in solute-solvent interaction energy upon the formation of complex is reflected in ΔE_{SOL}, which can be further partitioned into electrostatic and non-electrostatic components that serve as corrections to the internal ELEC and PAULI terms, respectively. The POL and CT contributions to the interaction are calculated with all involved intermediate states properly solvated, and hence the solvent effect on these terms will also be taken into account.

4.3 Computational Details

We implemented the ALMO-EDA(solv) scheme in a locally modified Q-Chem 5.2 software package,[108] which serves as an extension of the original routines for the second-generation ALMO-EDA for DFT calculations. [84, 379] While this scheme, in principle, should be compatible with most of the available SCRF models, in this work we demonstrate it with two widely used approaches: the conductor-like PCM (C-PCM) [119, 120, 354] and the SMD model.[122] The non-electrostatic effects of the solvent were ignored in our calculations using C-PCM, whereas the solvation free energy (ΔG_{S}) produced by SMD comprises both electrostatic and non-electrostatic contributions, which correspond to the "electronic-nuclear-polarization" (ENP) and the "cavity-dispersion-solvent structure" (CDS) terms, respectively:[122]

$$\Delta G_{\text{S}} = \Delta G_{\text{ENP}} + \Delta G_{\text{CDS}}$$

In the Q-Chem implementation of the SMD model, IEF-PCM [355, 356] is employed to describe the solute-solvent electrostatic interaction.

Both C-PCM and IEF-PCM require solving for discretized point charges on the surface of a molecular cavity. In our calculations using C-PCM, the molecular cavities were constructed using the union of a series of atom-centered spheres whose radii are determined using each atom's van der Waals radius from the Universal Force Field [388] scaled by a factor of 1.2. The boundary between solute and solvent constructed thereof is known as the solvent accessible surface (SAS). The calculations using SMD construct the molecular cavities in a similar manner but use its own set of atomic radii.[389] To ensure the smoothness of potential energy surfaces (PESs) associated with molecular complexes, the switching/Gaussian method developed by Lange and Herbert [358, 359] was employed in both C-PCM and SMD calculations, in which the atomic spheres are discretized using Lebedev grids rather than more traditional tessellation schemes (e.g. the GEPOL algorithm [390]). In this work, 302 Lebedev points were used for all atoms in our calculations using C-PCM or SMD.

Unless otherwise specified, the second-generation ALMO-EDA calculations are performed with the ωB97X-V functional, [391] which was shown to be one of the best-performing functionals for non-covalent interactions via extensive benchmarks [20, 392, 393] and gave excel-

lent results in our previous studies involving systems such as ion-water complexes. [33, 322, 394] The DFT calculations employ a (99, 590) grid (99 radial shells with 590 Lebedev points on each) for the integration of the exchange-correlation (XC) functional and the SG-1 grid [395] for the VV10 non-local correlation functional [69] in ωB97X-V. The decomposition of the frozen interaction energy in ALMO-EDA calculations follows the "quasiclassical" scheme [86, 322] exclusively in this work, as we have noted in Sec. 4.2. For the separation between POL and CT, the more sophisticated fragment electrical response function (FERF) method [32] featuring a well-defined basis set limit was used for the small model systems (Secs. 4.4 and 4.4), while the original ALMO scheme based on partition of the AOs [31, 83] was used for the applications in Secs. 4.4 and 4.4 with more moderate basis sets (def2-TZVPP and def2-TZVPD,[247, 248] respectively) given the substantial sizes of these systems.

4.4 Results

The sodium-chloride model complex

To validate the treatment of solvent effects in ALMO-EDA(solv), we first investigate a $Na^+\cdots Cl^-$ model complex where the two ions are separated by 20 Å and immersed in solvent with varying dielectric constant described by C-PCM. At the asymptotic limit, the strength of the electrostatic interaction between Na^+ and Cl^- in a dielectric medium is $1/\epsilon$ of that in vacuum according to Coulomb's law, where ϵ is the (relative) dielectric constant of the medium. This relation is reproduced by ALMO-EDA(solv) as demonstrated in Table 4.1. The $\Delta E^{(0)}_{\mathrm{ELEC}}$ term reflects the strength of the Coulomb interaction in vacuum, while $\Delta E^{\mathrm{el}}_{\mathrm{SOL}}$ is the correction from solute-solvent electrostatic interaction, which is an unfavorable term as its net effect is to damp the attractive Coulomb interaction between Na^+ and Cl^-. The sum of these two terms obtained in EDA calculations gives the effective (screened) electrostatic interaction in solution, $\Delta E^{(\mathrm{s})}_{\mathrm{ELEC}}$, whose relative strength against $\Delta E^{(0)}_{\mathrm{ELEC}}$ shows excellent agreement with the dielectric constants (ϵ) specified as an initial parameter in these calculations. This agreement can also be reproduced with the widely used IEF-PCM approach (see Table S1 in the ESI†), confirming that the treatment of solvent-screened permanent electrostatics in our EDA shows correct asymptotic behavior.

The distance dependence of the three electrostatics-related terms in Table 4.1 is shown in Fig. 4.4, where H_2O ($\epsilon = 78.2$) described by C-PCM is employed as the implicit solvent. At long range, the attraction between Na^+ and Cl^- is subjected to strong solvent screening, which renders the effective electrostatic interaction in solution minimal (e.g. at 5 Å $\Delta E^{(\mathrm{s})}_{\mathrm{ELEC}}$ is only -4.3 kJ/mol). Furthermore, the $\Delta E^{(0)}_{\mathrm{ELEC}}/\Delta E^{(\mathrm{s})}_{\mathrm{ELEC}}$ ratio stays close to the asymptotic limit (78.2) in this range, albeit with more pronounced deviation when moving closer. In contrast, at shorter distances (< 5 Å) this ratio decreases rapidly indicating less effective screening of the attractive electrostatics. At the minimum-energy distance (2.5 Å), $\Delta E^{(\mathrm{s})}_{\mathrm{ELEC}}$ gains appreciable magnitude (-140 kJ/mol) and the value of $\Delta E^{(0)}_{\mathrm{ELEC}}/\Delta E^{(\mathrm{s})}_{\mathrm{ELEC}}$ lowers to

Table 4.1: Strength (in kJ/mol) of internal QM electrostatics ($\Delta E^{(0)}_{\mathrm{ELEC}}$) and the effect of solute-solvent electrostatic interaction ($\Delta E^{\mathrm{el}}_{\mathrm{SOL}}$) for a $Na^+\cdots Cl^-$ complex separated by 20 Å calculated with ωB97X-V/def2-TZVPPD and C-PCM with varying dielectric constants. $\Delta E^{(\mathrm{s})}_{\mathrm{ELEC}} = \Delta E^{(0)}_{\mathrm{ELEC}} + \Delta E^{\mathrm{el}}_{\mathrm{SOL}}$ is the effective (screened) electrostatic interaction in solution.

ϵ	$\Delta E^{(0)}_{\mathrm{ELEC}}$	$\Delta E^{\mathrm{el}}_{\mathrm{SOL}}$	$\Delta E^{(\mathrm{s})}_{\mathrm{ELEC}}$	$\Delta E^{(0)}_{\mathrm{ELEC}}/\Delta E^{(\mathrm{s})}_{\mathrm{ELEC}}$
1	-69.47	0.00	-69.47	1.0
10	-69.47	62.52	-6.95	10.0
20	-69.47	65.99	-3.48	20.0
40	-69.47	67.73	-1.74	40.0
80	-69.47	68.60	-0.87	79.9

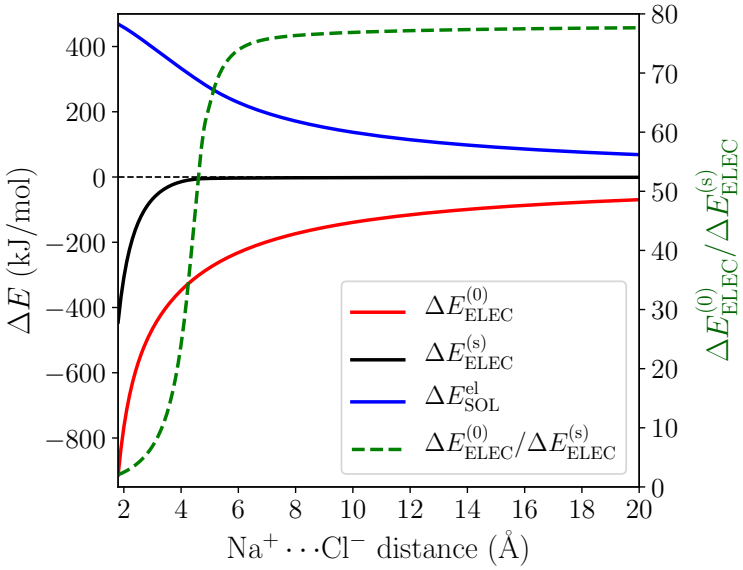

Figure 4.4: Left y-axis: distance dependence of $\Delta E^{(0)}_{\mathrm{ELEC}}$, $\Delta E^{\mathrm{el}}_{\mathrm{SOL}}$, and $\Delta E^{(\mathrm{s})}_{\mathrm{ELEC}}$ for the $Na^+\cdots Cl^-$ model complex in C-PCM water in the range of 1.8–20.0 Å; right y-axis: variation of the $\Delta E^{(0)}_{\mathrm{ELEC}}/\Delta E^{(\mathrm{s})}_{\mathrm{ELEC}}$ ratio with the $Na^+\cdots Cl^-$ distance (plotted with the green dashed curve).

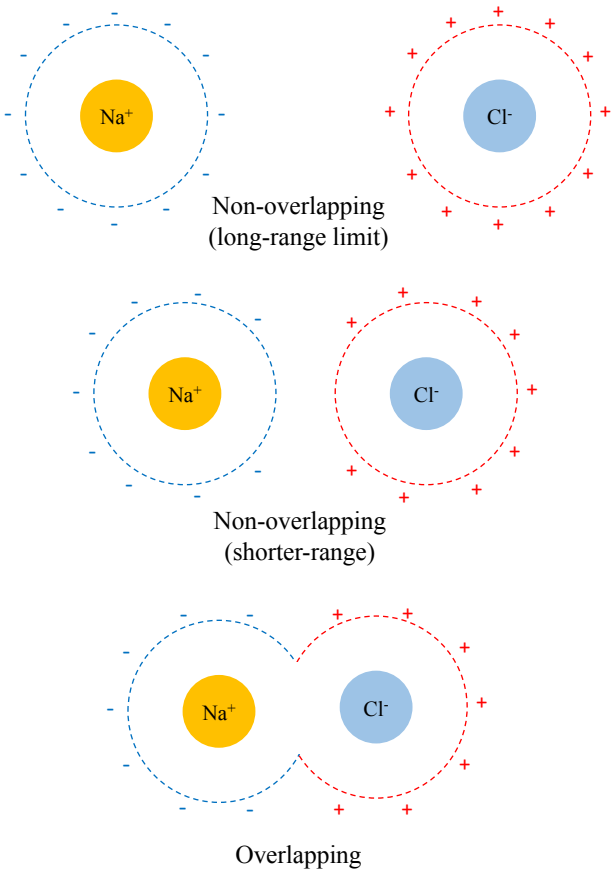

Figure 4.5: Schematic illustration of solvent effect on the $Na^+ \cdots Cl^-$ electrostatic interaction in the non-overlapping (upper and middle panels) and overlapping (lower panel) regimes. The dashed lines depict the cavities for each solute and "+" and "−" represent positive and negative surface charges, respectively.

4.1. Further examining the distance dependence of $\Delta E_{\mathrm{SOL}}^{\mathrm{el}}$ reveals an inflection point at 3.35 Å, i.e., the curve starts to *flatten* when moving to shorter distances.

The sharp contrast between the short- and long-range behavior of these terms can be rationalized schematically with Fig. 4.5. In the long-range limit (upper panel), the cavities for Na^+ and Cl^- are well-separated and the surface charges are mainly induced by their respective nuclei and electrons, yielding strong solvent screening of the long-range electrostatics. With the decrease in inter-fragment distance, even before the cavities start to overlap, the surface charges on each cavity will be influenced by both solutes (Na^+ and Cl^-) simultaneously, which then largely cancel each other in the inter-fragment region (see mid-panel of Fig. 4.5). This would result in weakened screening and potentially explains the modest increase in the deviation from the long-range limit for $\Delta E_{\mathrm{ELEC}}^{(0)}/\Delta E_{\mathrm{ELEC}}^{(\mathrm{s})}$. Finally, when the

two cavities start to overlap and merge with each other (for this system it occurs at 4.8 Å with our computational setup for PCM), as shown in the lower panel of Fig. 4.5, the dielectric solvent between the two fragments is "squeezed out" and the screening becomes even more incomplete. In addition, the inter-penetration of QM electron densities in the overlapping regime enhances the internal electrostatic attraction between Na^+ and Cl^-, which further contributes to the decrease in the value of $\Delta E^{(0)}_{\mathrm{ELEC}}/\Delta E^{(s)}_{\mathrm{ELEC}}$ since this short-ranged effect is subjected to almost no solvent screening. These effects, all together, result in only partial screening of the attractive internal electrostatics as well as the inflection point in the magnitude of $\Delta E^{\mathrm{el}}_{\mathrm{SOL}}$ at short $Na^+\cdots Cl^-$ distances.

Potential energy curves for ion-water interactions

As a further validation of ALMO-EDA(solv), we employ it to investigate the distance dependence of ion-water interactions ($H_2O\cdots Na^+$ and $H_2O\cdots Cl^-$) in three different solvents: toluene ($\epsilon = 2.37$), acetonitrile ($\epsilon = 37.5$), and water ($\epsilon = 78.3$). The gas-phase ALMO-EDA results for these systems are available in Ref. [322]. The long-range electrostatics in these systems can be depicted as charge-dipole interactions (R^{-2}), and in the short range polarization also contributes significantly to binding (especially in the $H_2O\cdots Na^+$ case). These strong interactions, however, will be diminished in solution due to solvent screening.

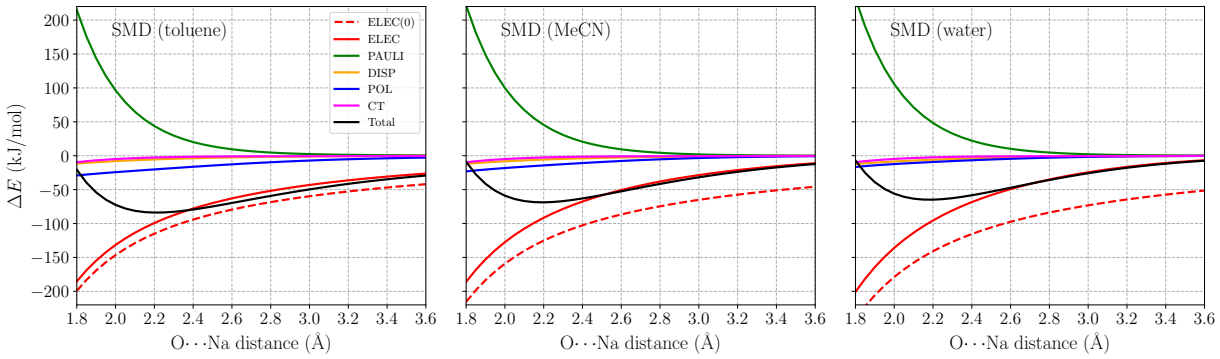

Figure 4.6: ALMO-EDA(solv) results (in kJ/mol) for the $H_2O\cdots Na^+$ complex in toluene, acetonitrile (MeCN), and water solutions with the $O\cdots Na^+$ distance ranging from 1.8 to 3.6 Å. All calculations are performed using ωB97X-V/def2-TZVPPD with the SMD solvent model. Terms in ALMO-EDA(solv) are represented with solid lines while the internal electrostatic interaction, denoted as "ELEC(0)", is shown as a dashed line.

Figure 4.6 shows the ωB97X-V/def2-TZVPPD total interaction energy and its components for the $H_2O\cdots Na^+$ complex vs $r_{\text{O-Na}}$ in the range of 1.8–3.6 Å. Permanent electrostatics makes the largest contribution to binding at this full range despite solvent screening. Comparing the results for different solvents, one remarkable feature is that the internal

electrostatic interaction, ELEC(0), becomes more favorable with the increase in solvent dielectric constant (from left to right in Fig. 4.6). This is because the dipole moment of an isolated H_2O molecule increases when placed in a more polar solvent environment. Nonetheless, since more polar solvent also screens more strongly, the total electrostatic interaction (ELEC) shows similar strength in both solvents around equilibrium (∼2.2 Å). The strength of long-range electrostatics and the total interaction energy, on the other hand, is governed by solvent screening, as evidenced by the smaller magnitude of ELEC at 3.6 Å in water vs toluene in Fig. 4.6.

Another energy component that is strongly impacted by solvent effects is polarization (POL). According to Ref. [322], the gas-phase polarization energy for $H_2O\cdots Na^+$ at 2.2 Å is around -25 kJ/mol, while this value reduces to around -9 kJ/mol in SMD water. Similar to long-range electrostatics, POL becomes less diminished when the solvent is less polar. The other three energy components, PAULI, DISP, and CT show much smaller variance with the change of solvent. They are apparently less affected by the solvent properties, at least within the present ALMO-EDA(solv) model.

Within the SMD model, the solvent contribution to binding can be further partitioned into electrostatic and non-electrostatic contributions. The distance dependence of these two terms as well as that of the overall ΔE_{SOL} is shown in Fig. S1 in the ESI†. The non-electrostatic (CDS) term has minimal significance compared to the electrostatic contribution and vanishes in the long range when the cavities of two fragments are fully separated. It is noteworthy that the non-electronic contribution to binding does *not* have a definite sign: among the three solvents here, $\Delta E_{\mathrm{SOL}}^{\text{non-el}}$ is exclusively positive for toluene while negative for acetonitrile and water. This is presumably a consequence of the CDS term in SMD aiming to account *in aggregate* for non-electrostatic solvation effects to better reproduce experimental solvation free energies.

The solvent electrostatic contribution ($\Delta E_{\mathrm{SOL}}^{\mathrm{el}}$), on the other hand, is repulsive over the full range (1.8–8.0 Å) for all three solvents. As in the $Na^+\cdots Cl^-$ case (Fig. 4.4(a)), this contribution first increases rapidly with the shortening of intermolecular distance, which damps the increasingly attractive internal electrostatic interaction. $\Delta E_{\mathrm{SOL}}^{\mathrm{el}}$ is more repulsive in solvents with larger dielectric constants, indicating their stronger screening capability. Moving into the overlapping regime, the solvent electrostatic term flattens first and then reaches a maximum when the $O\cdots Na^+$ distance is slightly below 3 Å, i.e., the magnitude of $\Delta E_{\mathrm{SOL}}^{\mathrm{el}}$ starts to decrease when the intermolecular distance is further shortened. This maximum in the solvent electrostatic contribution was also revealed by Su et al. with their LMO-EDA-PCM scheme for the water dimer. [376] We attribute this behavior to the merging of fragment cavities upon the formation of complex, which leads to diminished screening of the internal electrostatic interaction (*vide supra*).

In the ESI† we also show the analogues of Figs. 4.6 and S1 for the $H_2O\cdots Cl^-$ complex (Figs. S2 and S3). The ELEC and POL terms obtained from ALMO-EDA(solv) with different solvents (Fig. S2) show similar trends as in the $H_2O\cdots Na^+$ case except that the relative strength of solvent screening (indicated by their dielectric constants) has a more substantial impact on the electrostatic interaction and total interaction energy around the equilibrium

distance, rendering the intermolecular binding notably stronger in the least polar solvent (toluene). In addition, the location of the maximum in the solvent electrostatic contribution ($\Delta E^{\mathrm{el}}_{\mathrm{SOL}}$) varies from solvent to solvent: it appears at a notably longer $\mathrm{O}\cdots\mathrm{Cl}$ distance in H_2O than in the other two solvents. This distinction between solvents is more pronounced than in the $H_2O\cdots Na^+$ case where the maxima in $\Delta E^{\mathrm{el}}_{\mathrm{SOL}}$ with different solvents appear at similar distances.

Substituent effects on the stability of [FeTPP($CO_2^{\bullet -}$)] complexes: through-space vs. through-structure mechanisms

There is tremendous research interest in homogeneous electrochemical reduction of CO_2,[100, 155, 161] because CO_2 conversion to carbon-based fuels could underpin a future carbon-neutral economy. The initial step is activating CO_2, whose one-electron reduction potential is quite unfavorable (-1.90 V vs. NHE) by comparison with the reduction potential to convert CO_2 to more reduced products such as the $2e^-$ reduction to CO (-0.53 V vs. NHE). The first function of a catalyst is thus to stabilize the activated CO_2 as it drives the first reduction, and thereby reduce the thermodynamic overpotential. Molecular catalysts are of great interest for this purpose, in addition to enhancing turnover rates, and suppressing competitive side reactions such as the hydrogen evolution reaction (HER). Among available transition metal based catalysts, iron complexes have received particular attention because of the earth abundance of Fe and their low toxicity. To date, several iron catalysts with different ligand frameworks have been developed for the reduction of CO_2. [176, 384, 396–398] The most prominent family is $[\mathrm{Fe(II)TPP}]^0$ (TPP = tetraphenylporphyrin) [399, 400] and its derivatives. [380, 401–404] Mechanistic studies indicate that stabilizing the activated CO_2 adduct intermediate can substantially improve the performance of the catalyst. [168, 380, 382] An "electronic scaling electronic scaling relationship" (so-called because it reflects electronic substituent effects) between overpotential and turnover frequency (TOF) was previously established by stepwise fluorination of the phenyl groups in the TPP ligand framework. [402] The four derivatives FeTPP, FeF5TPP, FeF10TPP and FeF20TPP (full fluorination of zero, one, two and four phenyl rings, respectively) show a linear correlation between a favorable decrease in overpotential and an unfavorable decrease in TOF. This effect stems from stronger inductive effects that accompany the addition of $-$F substituents, which was referred to as a "through-structure" electronic effect. [402]

A subsequent experimental study[380] further demonstrated that charged substituents can break electronic scaling relationships. Introducing a positively charged trimethylammonio (TMA, $-NMe_3^+$) group to either the ortho or para position of each phenyl group, yielded tetra-trimethylanilinium-porphyrin complexes (Fe-*p*-TMA) and Fe-*o*-TMA). Unlike the fluorinated complexes, Fe-*o*-TMA exhibits high TOFs at a low overpotentials. In contrast, introducing the negatively charged sulfonate ($-SO_3^-$) group at the para positions to yield Fe-*p*-SUL results in lower TOF at higher overpotential relative to Fe(TPP) and Fe-o/p-TMA. Based on these results, the authors hypothesized that in these cases the strength of

CO_2 binding is not only controlled by the through-structure inductive effect of the electron-withdrawing groups but is more importantly modulated by the long-range (through-space) electrostatic interactions between these charged substituents and the negatively charged $CO_2^{\bullet-}$ moiety. This suggested mechanism could explain why Fe-*o*-TMA catalyzes CO_2 reduction at such high TOFs.[380] Further evidence for the importance of stabilizing the activated CO_2 adduct is provided by the ortho hydroxyl substituted TPP complex, tetrakis-(2′,6′,-dihydroxyphenyl)-porphyrin (CAT).[401] This derivative is also a more active catalyst than unsubstituted FeTPP, where the stabilization of activated CO_2 may also be due to favorable (through-space) interactions between the hydroxyl groups and negatively charged $CO_2^{\bullet-}$.

Here we employed the ALMO-EDA(solv) approach to gain insights into the stabilization mechanisms of activated CO_2 in the $[FeTPP(CO_2{-}\kappa C)]^{2-}$ adducts arising from the reaction of CO_2 with the doubly reduced $[FeTPP]^{2-}$ (formally Fe(0)) complex (see Scheme 4.7 for a simplified reaction scheme). The solvent MeCN was described by the C-PCM with the dielectric constant set to 35.88. [405] The electronic ground state of the complex is a (broken-symmetry) triplet in an η^1-κC binding mode, whose spin density contours (Fig. 4.8) reveal a significant amount of excess spin in the ligand framework as well as on the CO_2 moiety indicating reduction of both the CO_2 and the non-innocent TPP ligand. These reduced moieties are both antiferromagnetically coupled to the metal center as previously discussed in Ref. [382]. Therefore, this complex can be best represented as $[Fe(II)(TPP^{\bullet 3-})(CO_2^{\bullet-}{-}\kappa C)]^{2-}$. For brevity, in the following discussion we omit the "κC" notation that specifies the binding mode of CO_2 to the metal center.

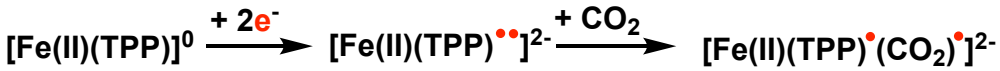

Figure 4.7: Simplified steps in the catalytic pathway of FeTPP leading to the activated CO_2 intermediate.

We illustrate the effects of different substituents by comparing the EDA results of complexes with varying substitutions ($-$H, $-NMe_3^+$, $-SO_3^-$, $-$OH) on the phenyl rings. To reduce the computational expense, we truncated these systems by removing two of the four phenyl groups based on the fact that the CO_2 moiety is positioned in such a way that only two substituent groups can strongly interact with it (see Fig. 4.9). In total, we compare six different CO_2 adducts with varying net charges due to the distinction in substituents: (a) the unsubstituted $[FeTPP(CO_2)]^{2-}$, (b) para $-NMe_3^+$ substituted [Fe-*p*-TMA-$(CO_2)]^0$, (c) ortho $-NMe_3^+$ substituted [Fe-*o*-TMA-(CO_2)], (d) para $-SO_3^-$ substituted [Fe-*p*-SUL-$(CO_2)]^{4-}$, (e) ortho $-$OH substituted [Fe-*o*-OH-$(CO_2)]^{2-}$, and (f) the perfluorinated FeTPP ($[FeF10TPP(CO_2)]^{2-}$) . The geometries of these complexes are shown in Fig. 4.9.

The results of the EDA calculations depend on the choice of reference states of both fragments, i.e., the electronic states they are in when they are infinitely separated. In

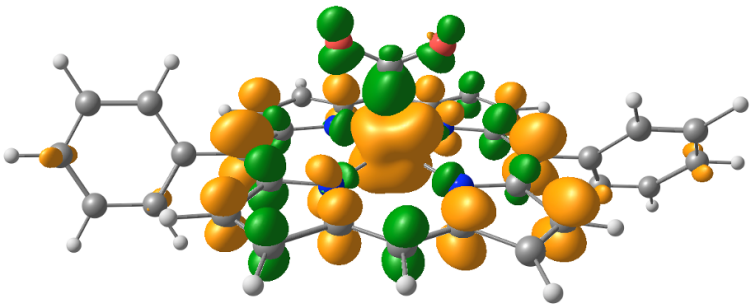

Figure 4.8: Spin density of the doubly reduced CO_2 adduct $[FeTPP(CO_2{-}\kappa C)]^{2-}$ (green: excess α spin; gold: excess β spin)

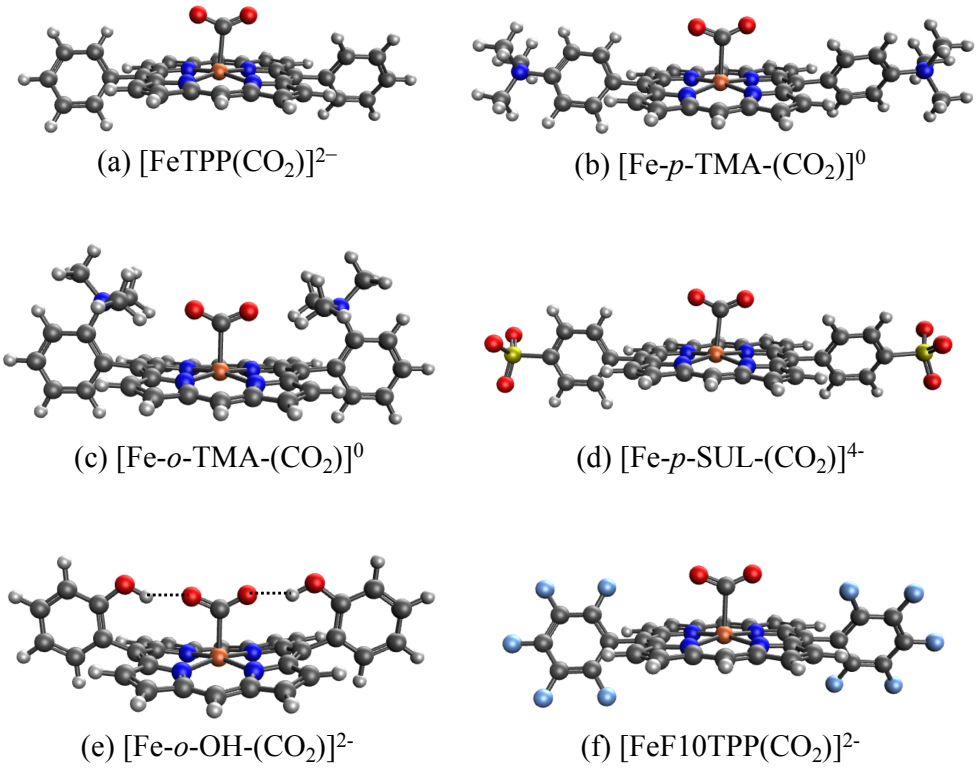

Figure 4.9: Optimized geometries for the $[FeTPP(CO_2{-}\kappa C)]^{2-}$ adduct with varying substitutions: (a) unsubstituted ($-H$); (b) para-trimethylammonio ($-NMe_3^+$); (c) ortho-trimethylammonio ($-NMe_3^+$); (d) para-sulfonate ($-SO_3^-$); (e) ortho-hydroxyl ($-OH$); (f) all-fluorinated ($-F$).

this example two fragmentation schemes are plausible: (i) the "natural" fragmentation that corresponds to reactants in the catalytic cycle, where a neutral CO_2 ($S = 0$) molecule is bound to a doubly reduced iron complex ($S = 1$); (ii) fragmentation based on the charge population of the final product complex, giving a singly reduced metal complex ($S = 3/2$) and a singly reduced (or activated) CO_2 radical anion ($CO_2^{\bullet-}$, $S = 1/2$). Our results show that the former fragmentation scheme is unsuitable here due to the drastic geometry distortion energy (> 200 kJ/mol) that is associated with the bending of a neutral CO_2 molecule, which would lead to EDA results that are dominated by this geometry distortion term and are thus less insightful (see Table S2 in the ESI†). In contrast, the geometry distortion term associated with the $CO_2^{\bullet-}$ moiety in the latter fragmentation scheme is minimal (less than 1 kJ/mol). Therefore, we selected the second fragmentation scheme in the following discussion, which corresponds to the binding of $CO_2^{\bullet-}$ with singly reduced FeTTP and its substituted derivatives.

Our choice yields (up to) two charged fragments where the net charge on the FeTPP moiety depends on the substituents. A comparison across all these compounds without considering the solvent effect would lead to unreasonably large variations in total interaction energy due to the large variation in gas-phase electrostatic interaction (see Table S5). Hence, we employ the new ALMO-EDA(solv) approach to better capture these interactions in solution. The EDA results for unsubstituted $[FeTPP(CO_2)]^{2-}$ are shown in Table S4 in the ESI†. This complex is subjected to strong Pauli repulsion (634 kJ/mol), which arises from the repulsion between the iron d-electrons and $CO_2^{\bullet-}$ whose excess spin density is mainly located on the carbon atom (see Fig. S4). The strongly favorable electrostatic interaction (−363 kJ/mol) makes the largest contribution to binding, and is comprised of (i) a moderate gas-phase ELEC term ($\Delta E^{(0)}_{\mathrm{ELEC}} = -94$ kJ/mol) and (ii) a substantially favorable contribution from solute-solvent interaction ($\Delta E_{\mathrm{SOL}} = -269$ kJ/mol). The former can be rationalized by the attractive short-range Coulomb interaction between the $CO_2^{\bullet-}$ moiety and the partially positive-charged iron center, and the latter reflects the solvent screening of the repulsive Coulombic interaction between $CO_2^{\bullet-}$ and the reduced π system of the TPP ligand. Despite the appreciable electrostatic contribution, the net frozen interaction is still strongly repulsive (+205 kJ/mol), and thus both POL (−135 kJ/mol) and CT (−123 kJ/mol) are essential to the stabilization of $CO_2^{\bullet-}$. The electron density difference between the frozen and polarized states reveals that the occupation of iron's d-orbitals changes due to interaction with $CO_2^{\bullet-}$. This is mainly to alleviate Pauli repulsion, via depopulating the $3d_{z^2}$ orbital (see Fig. 4.11(a)). The analysis of complementary occupied-virtual pairs (COVPs) [87] further demonstrates that the charge transfer in $[FeTPP(CO_2)]^{2-}$ is dominated by the donation from the odd-electron orbital of $CO_2^{\bullet-}$ into the vacant $3d_{z^2}$ orbital of Fe, where $CO_2^{\bullet-}$ acts as a σ-donor as illustrated in Fig. 4.11(b)).

To gauge the effect of the charged substituents (ortho- and para-TMA and para-sulfonate), we compare the total interaction energies and EDA components of these adducts against the results for the unsubstituted $[FeTPP(CO_2{-}\kappa C)]^{2-}$. The results are shown in Fig. 4.10(a). While para substitution with sulfonate groups alters the total charge of the CO_2 adduct from

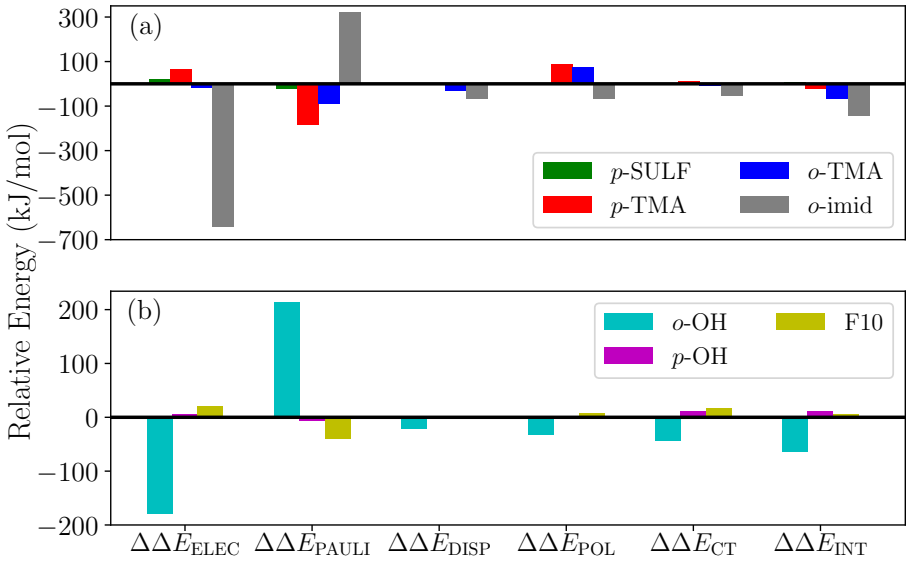

Figure 4.10: Differential ALMO-EDA(solv) results (in kJ/mol) relative to the unsubstituted $[FeTPP(CO_2)]^{2-}$ complex: (a) results for the charged substituent groups ($-NMe_3^+$,$-SO_3^-$, and the methylimidazolium-carrying group); (b) results for the substituent groups that retain the net charge of the unsubstituted complex (−OH, −F).

−2 to −4, its effect on the total interaction strength is small. The largest changes in the EDA components occur in the ELEC and PAULI terms: the former becomes slightly less favorable due to the more negatively charged TPP ligand, while the latter is diminished (becoming less unfavorable) by a similar amount, which is possibly related to the weak electron-withdrawing inductive effect of the sulfonate group and the slightly lengthened Fe−C distance in [Fe-*p*-SUL-$(CO_2)]^{4-}$ (see Table S3). Besides the changes in ELEC and PAULI that largely cancel each other, the effects of *p*-sulfonate on other energy components (DISP, POL, and CT) are negligible.

The *p*-TMA group changes the total charge of the CO_2 adduct from −2 to 0 and strengthens the total interaction by 21 kJ/mol relative to the unsubstituted FeTPP. Interestingly, the electrostatic interaction is made more repulsive by the *p*-TMA substitution relative to the unsubstituted adduct (by 67 kJ/mol), despite the presence of positively charged TMA groups that can favorably interact with $CO_2^{\bullet-}$. Indeed, if one performs EDA in the gas phase, the ELEC term in [Fe-*p*-TMA-$(CO_2)]^0$ is *stabilized* by ∼250 kJ/mol relative to unsubstituted $[FeTPP(CO_2)]^{2-}$. However, the electrostatic attraction between the *p*-TMA groups and $CO_2^{\bullet-}$ is screened to a large extent in the solvation environment due to the long distance between them ($r(N\cdots O) > 8$ Å for N in TMA and O in CO_2). Complemented by other secondary effects of the strongly electron-withdrawing TMA groups, the ELEC component

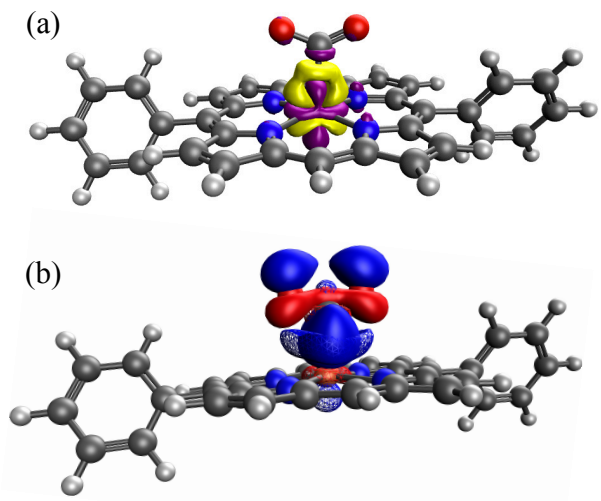

Figure 4.11: (a) Electron density difference between the FRZ and POL states (yellow: electron density increase, purple: electron density decrease); (b) the key COVPs illustrating the σ donation from the SOMO of $CO_2^{\bullet-}$ to Fe's d_{z^2} orbital (the donor and acceptor orbitals are plotted with solid and meshed isosurfaces, respectively).

in fact *destabilizes* [Fe-*p*-TMA-(CO_2)]^0 relative to the unsubstituted adduct.

Surprisingly, the largest change among EDA components appears to be the reduction in Pauli repulsion (-183 kJ/mol). This reduction *cannot* be solely explained by the change in the Fe$-$C distance since its value is almost identical in [Fe-*p*-SUL-(CO_2)]$^{4-}$ and [Fe-*p*-TMA-(CO_2)]^0 (see Table S4). We attribute it to the decrease in electron density at the iron center, which originates from the weaker coordination of the TPP ligand due to the strong electron-withdrawing inductive effect of the TMA groups and the rigidity of the porphyrin framework that inhibits the further shortening of the Fe$-$N distances. The polarization term is less favorable in [Fe-*p*-TMA-(CO_2)]^0 than that in the unsubstituted adduct, which, however, is a less substantial effect compared to the reduction in Pauli repulsion, and the relative changes in dispersion and charge transfer are of even less significance. Therefore, according to the results of ALMO-EDA(solv), the enhanced CO_2 stabilization resulting from the *p*-TMA substitution almost entirely arises from the reduction of Pauli repulsion stemming from the strong inductive effect of the TMA group, which is via a through-structure rather than through-space mechanism.

Moving the charged TMA groups closer to the $CO_2^{\bullet-}$ moiety in [Fe-*o*-TMA-(CO_2)]^0 yields more significant relative stabilization than *p*-TMA substitution (65 kJ/mol relative to the unsubstituted adduct). Surprisingly, the contribution to this relative stabilization from electrostatic interaction is only 16 kJ/mol, which serves as only the third largest contributor. As the distance between $CO_2^{\bullet-}$ and TMA is still long in [Fe-*o*-TMA-(CO_2)]^0 ($r(\mathrm{N}\cdots\mathrm{O}) = 3.8$ Å for N in TMA and O in CO_2), the favorable electrostatic interaction

remains strongly screened by the (implicit) solvent. As in the *p*-TMA case, the strong inductive effect of the TMA groups reduces Pauli repulsion by 89 kJ/mol, making the largest contribution to the enhanced stabilization. Note that the reduction in the Pauli term here is not as pronounced as that in the *p*-TMA case, which might result from the steric effect of the bulky methyl groups that are in close contact with $CO_2^{\bullet-}$. In addition, the Fe−C distance is slightly shorter in the *o*-TMA complex (r(Fe−C) = 2.06 Å (*o*-TMA) vs. 2.10 Å (*p*-TMA)), which implies a stronger baseline Pauli repulsion. The close contact between methyl groups and $CO_2^{\bullet-}$ also results in the strengthened dispersion interaction in the *o*-TMA adduct, which is 30 kJ/mol more favorable than that in the unsubstituted case and serves as the second largest contributor to the relative stabilization. Combining these factors together, in [Fe-*o*-TMA-(CO_2)]^0 we see stabilization of activated CO_2 via both through-space (enhanced dispersion and attractive electrostatics) and through-structure (reduction in Pauli repulsion due to the strong inductive effect of TMA) mechanisms, and our EDA results reveal the more significant role of the latter. The co-existence of these two mechanisms leads to larger stabilization of the *o*-TMA substituted adduct.

We next apply our EDA analysis to investigate the stabilization of activated CO_2 within two adducts whose total charge remains unchanged (−2) upon substitution: the ortho hydroxyl substituted adduct [Fe-*o*-OH-(CO_2)]$^{2-}$ and the F10 derivative. The results are shown in Fig. 4.10(b). The *o*-OH substitution stabilizes the CO_2 adduct by 64 kJ/mol, and the EDA results reveal a significantly strengthened electrostatic interaction and moderately increased DISP, POL, and CT components relative to the unsubstituted TPP adduct. Collectively these attractive terms outweigh the increase in Pauli repulsion. A pattern of this type is typical of EDA results for hydrogen bonds, [83, 84, 91], which in this case are formed between −OH groups at the ortho positions of phenyl and the oxygen atoms in $CO_2^{\bullet-}$ (see Fig. 4.9(c)) thanks to the short distance between them (r(H$\cdots$O) = 1.79 Å for H in *o*-OH and O in CO_2). When one moves the hydroxyl group to the para position (*p*-OH), no such hydrogen bonds can be formed and consequently there is no notable difference in any of the energy components relative to the unsubstituted adduct. This stark contrast between the results for the *o*-OH and *p*-OH substituted derivatives suggests that the −OH group at the ortho position stabilizes $CO_2^{\bullet-}$ almost exclusively via a through-space mechanism (hydrogen bonding). We note that the stabilization of activated CO_2 through hydrogen bonds can be further enhanced by precisely tuning the position of H-donor, which was achieved by Nichols et al. by introducing amide pendants at the ortho position of the meso phenyl groups.[406] In contrast to [Fe-*o*-OH-(CO_2)]$^{2-}$, the F10 derivative with only through-structure electron-withdrawing inductive effect does not lead to enhanced stabilization of CO_2 since the reduction in Pauli repulsion is far less pronounced than that in [Fe-*p*-TMA-(CO_2)]^0 or [Fe-*o*-TMA-(CO_2)]^0, which is then almost fully compensated by the diminished ELEC and CT contributions.

The EDA results for the TMA-substituted derivatives suggest that the strategy to stabilize activated CO_2 through long-range electrostatic attraction may not be fully effective in solution due to solvent screening. However, making use of the steric effects of the substituents, one may be able to create a solvent-free "cage" in which electrostatic interaction is almost unscreened. It was reported by Khadhraoui et al. that the introduction of four

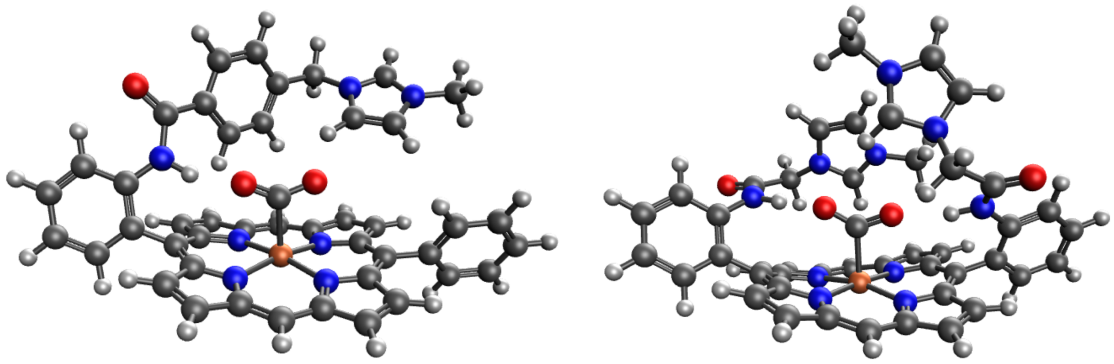

(a) [Fe-*o*-imid-(CO_2)]$^{2-}$ (b) [Fe-*o*-imid2-(CO_2)]$^{2-}$

Figure 4.12: Optimized geometries for (a) [Fe-*o*-imid-(CO_2)]$^{-}$, which carries one methylimidazolium-containing group that was reported in Ref. [407], and (b) [Fe-*o*-imid2-(CO_2)]$^{2-}$, which carries two modified methylimidazolium-containing groups.

bulky, methylimidazolium-containing groups at the ortho positions of the phenyl groups in FeTPP elevates its electrocatalytic activity. [407] Due to the substantial size of the substituent, we optimized the structure of the CO_2 adduct of this FeTPP derivative with only one methylimidazolium-containing "arm" included (reducing the negative charge from -2 to -1), which is denoted as [Fe-*o*-imid-(CO_2)]$^{-}$. The optimized structure of this adduct is depicted in Fig. 4.12(a). Differing from [Fe-*o*-TMA-(CO_2)]^{0}, the charged moiety (imidazolium ring) is far away from the central metal, excluding the possibility of any electron-withdrawing inductive effect from this positively charged substituent. A remarkable feature of the optimized structure is that this "long-arm" substituent folds over the activated CO_2 and thereby creating a small pocket that is inaccessible by solvent. The geometry also demonstrates that the activated CO_2 is stabilized by both the hydrogen bonding from the amide group and the electrostatic attraction from the positively charged methylimidazolium moiety: the H$\cdots$O distance in this hydrogen bond is 1.98 Å, and the distance between the mid-point of two N atoms in the imidazolium ring and the closest O atom in CO_2 is 4.55 Å.

Our results show that [Fe-*o*-imid-(CO_2)]$^{-}$ stabilizes CO_2 more strongly by -49.2 kJ/mol relative to the unsubstituted FeTPP (see Table S4 in the ESI†), similar to the *o*-OH and *o*-TMA cases. However, it should be noted that here we only included one substituent group ("arm") whereas the other derivatives are doubly substituted in our calculations. Therefore, once the two methylimidazolium-containing "arms" are both included, one can expect that this complex can stabilize activated CO_2 more than the *o*-OH and *o*-TMA derivatives. The ALMO-EDA(solv) results (Table S4) show that the dominant contributor to stabilization is electrostatic interaction (-85.9 kJ/mol), which stems from both the N$-$H$\cdots$O hydrogen bond and the positively charged methylimidazolium. The key difference from the *p*-TMA substituent is that this bulky ligand effectively "squeezes out" solvent from the

space in between the activated CO_2 and the positively charged moiety, rendering the attractive electrostatics nearly unscreened. Furthermore, as in the *o*-OH case, the strength of dispersion, polarization, and charge transfer is also enhanced by the introduction of this methylimidazolium-containing substituent, which, together with the gain in attractive electrostatics, contribute to this more stabilized CO_2 adduct.

In order to further optimize this interaction motif, we removed the phenyl group in the methylimidazolium-containing "arm", which moves the methylimidazolium moiety closer to the CO_2 moiety. The optimized structure for this adduct (denoted as [Fe-*o*-imid2-(CO_2)]^0 since the second substituent is added for a better comparison with the results of other derivatives) is shown in Fig. 4.12(b), in which the distance between the mid-point of two N atoms in the imidazolium ring and the closest O atom in CO_2 reduces to 3.74 Å. The stabilization energy relative to the unsubstituted adduct is −143.5 kJ/mol, which is significantly larger than that of the second most stabilized *o*-TMA and *o*-OH derivatives (see Fig. 4.10(a)). The relative stabilization arising from the electrostatic attraction is *by far* the strongest among the adducts that we investigated (−642.0 kJ/mol), and we estimate that −140 kJ/mol out of that stems from the two hydrogen bonds (see the "NH-ref" results in Table S4) and the rest (about −500 kJ/mol) from the imidazolium rings. These results indicate the importance of taking solvent effects into account if one wants to harness through-space Coulomb interaction in solution and pursue the promise of bulky, flexible substituents that can form a solvent-free "active" pocket mimicking that in enzymes to facilitate much stronger electrostatic interaction with CO_2.

It is important to point out that we focused here on the concept of strengthening the binding of activated CO_2 in adducts as that was presumed to accelerate catalysis. However, the substituents may also affect other intermediates in a catalytic cycle. This is illustrated by the ortho hydroxyl substituted TPP complex, CAT, where the hydroxyl group stabilizes the activated CO_2 and also leads to a fast intramolecular protonation pathway.[382] Ultimately, detailed mechanistic studies are necessary to understand the influence of each substituent on the TOF.

Electron transfer from terphenyl$^{\bullet-}$ to CO_2: substituent effects on the intermolecular binding of reactant and product complexes

An alternative to transition metal based catalysts for CO_2 reduction is organic (photo)redox catalysts, which can be more environment-friendly, economical, and are likewise highly tunable with substituents. [408] These catalysts access their electronic excited states through UV-Vis absorption and are subsequently quenched, yielding a reactive radical species that serves as the electron donor to CO_2. [408, 409] A prominent class of examples are oligo(*p*-phenylenes) (OPPs), which, for instance, are able to catalyze hydrocarboxylation from CO_2. [381] The introduction of different substituents alters the absorption wavelength but also impacts the rate of electron transfer. Some of us recently[410] investigated the substituent effects on the calculated rate of electron transfer (ET) reaction from an OPP radical

anion to molecular CO_2 using double terminal-substituted *p*-terphenyl as examples. We have shown that electron-donating groups (EDGs) facilitate this reaction in general by increasing the free energy driving force (ΔG in Marcus theory [411]) since they elevate the LUMO level of OPP. Besides the reductive potential of OPP/OPP$^{\bullet-}$, the difference in the association energies of the reactant (OPP$^{\bullet-}\cdots$CO$_2$) and product (OPP$\cdots$CO$_2^{\bullet-}$) complexes in solution, $\Delta\Delta E_{\mathrm{INT}} = \Delta E_{\mathrm{INT}}(\mathbf{R}_{\mathrm{r}}) - \Delta E_{\mathrm{INT}}(\mathbf{R}_{\mathrm{p}})$, also contributes to the free energy driving force ($\mathbf{R}_{\mathrm{r}}$ and $\mathbf{R}_{\mathrm{p}}$ denote optimized structures for the reactant and product states, respectively). Here we employ ALMO-EDA(solv) to investigate the substituent effects on the association energies of the reactant and product complexes in CH_2Cl_2 ($\epsilon = 8.93$) described by the SMD model, which will afford us deeper insight into how these chemical modifications affect the reactivity of OPPs as photoredox catalysts.

The geometries of the reactant and product complexes are directly taken from our previous work,[410] which were optimized on their respective diabatic PESs constructed from constrained DFT (CDFT) [412, 413] calculations at the B3LYP-D3(BJ)/6-311G(d,p) [56, 414, 415] level of theory with C-PCM. As illustrative examples, in Fig. 4.13 we show the optimized structures of the reactant and product complexes between CO_2 (or $CO_2^{\bullet-}$) and *p*-terphenyl$^{\bullet-}$ (or neutral *p*-terphenyl) substituted with dimethylamino ($-NMe_2$) and nitro ($-NO_2$) groups. Compared to the reactant complexes where CO_2 is linear and mainly interacting with one of the terminal phenyl groups, in the product state the CO_2 moiety is bent and moves closer to the middle ring of *p*-terphenyl. By contrast with the adducts with FeTPP where $CO_2^{\bullet-}$ is ligated to Fe through the κC mode (see Sec 4.4), here in the product state the two oxygen atoms of $CO_2^{\bullet-}$ are in closer contact with the *p*-terphenyl moiety, an orientation that is favored by these dispersion-dominated anion-π interactions (vide infra).

The substituent effect on the difference between interaction energies in the reactant and product states ($\Delta\Delta E_{\mathrm{INT}}$) in CH_2Cl_2 solution is exhibited in the upper panel of Fig. 4.14 with three electron-donating ($-NMe_2$, $-OH$, $-CH_3$) and three electron-withdrawing ($-Br$, $-CF_3$, $-NO_2$) groups. The strength of the electronic effects of these substituent groups can be characterized using their Hammett parameters[416] (σ_p): more negative (positive) σ_p indicates stronger electron-donating (withdrawing) ability. It is shown that the difference in interaction energies decreases monotonically with increases in σ_p, i.e., strong electron-withdrawing groups (EWGs) such as $-NO_2$ facilitate the stabilization of the product complex relative to the reactant. Relative to the unsubstituted species, the differential product stabilization by the strongest EWG, $-NO_2$, is over 10 kJ/mol. ALMO-EDA(solv) reveals that this prominent substituent effect is dominated by electrostatics despite the presence of solvent (see Table S6 in ESI† for the full EDA results). As shown in the left panel of Fig. 4.14, $\Delta\Delta E_{\mathrm{ELEC}}$ reproduces the trend in $\Delta\Delta E_{\mathrm{INT}}$ with only one marginal exception ($-CH_3$).

To demonstrate the effect of solvent on the trend in $\Delta\Delta E_{\mathrm{INT}}$ versus σ_p, we also performed ALMO-EDA calculations for the same set of complexes in vacuum (see Table S7 in ESI† for the complete results). The results for the total interaction energy and the ELEC component are shown in the lower panel of Fig. 4.14. While the same trend in $\Delta\Delta E_{\mathrm{INT}}$ (monotonically decrease with increasing σ_p) is reproduced without solvent, the magnitude of $\Delta\Delta E_{\mathrm{INT}}$ with different substituent groups exhibits a much wider range, which, once again, mainly results

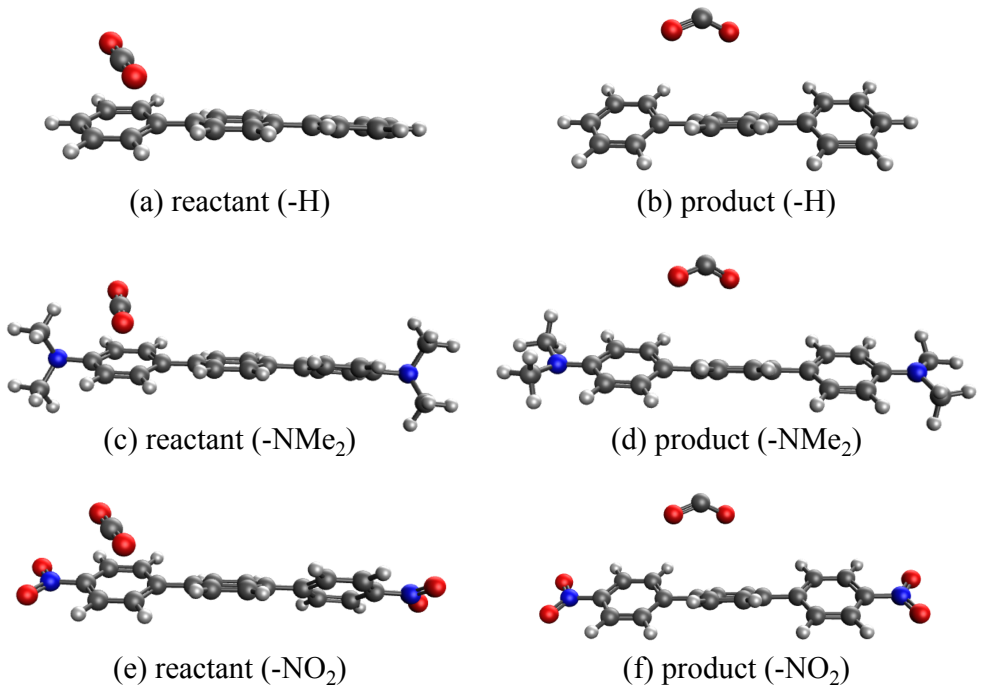

Figure 4.13: Optimized structures of unsubstituted and substituted *p*-terphenyl$\cdots CO_2$ radical anion complexes: (a) (b) unsubstituted reactant and product complexes; (c) (d) NMe_2-substituted; (e) (f) NO_2-substituted.

from the larger variation in $\Delta\Delta E_{\text{ELEC}}$ in vacuum. In contrast to the solution phase where the polarization component exhibits only minimal effects on $\Delta\Delta E_{\text{INT}}$, in the gas phase, POL stabilizes the product complex by ∼20 kJ/mol relative to the reactant for these complexes. The contrast between the upper and lower panels of Fig. 4.14 demonstrate the *attenuation* of substituent effects on the differential interaction energies due to solvent screening.

In our previous study[410] where the ALMO-EDA calculations were performed in vacuum at the B3LYP-D3(BJ)/6-311G(d,p) level of theory, we identified CT as another main contributor to the stabilization of the product complexes relative to the reactant ones and also to the trend in substituent effects. This contradicts the gas-phase ALMO-EDA results obtained here with ωB97X-V/def2-TZVPD, according to which CT only makes a minimal contribution to each complex's $\Delta\Delta E_{\text{INT}}$ (see the comparison between Tables S7 and S8 in the ESI†). We ascribe this discrepancy to the more substantial delocalization error [324, 417] associated with the B3LYP functional than that of ωB97X-V, which, as shown in Table S10 in the ESI†, is more pronounced in the gas phase. We refer the reader to Sec. S3 in the ESI† for a detailed discussion.

We then turn to the full ALMO-EDA(solv) results for the reactant and product complexes to gain further insights into the substituent effects on $\Delta\Delta E_{\text{INT}}$ revealed in Fig. 4.14.

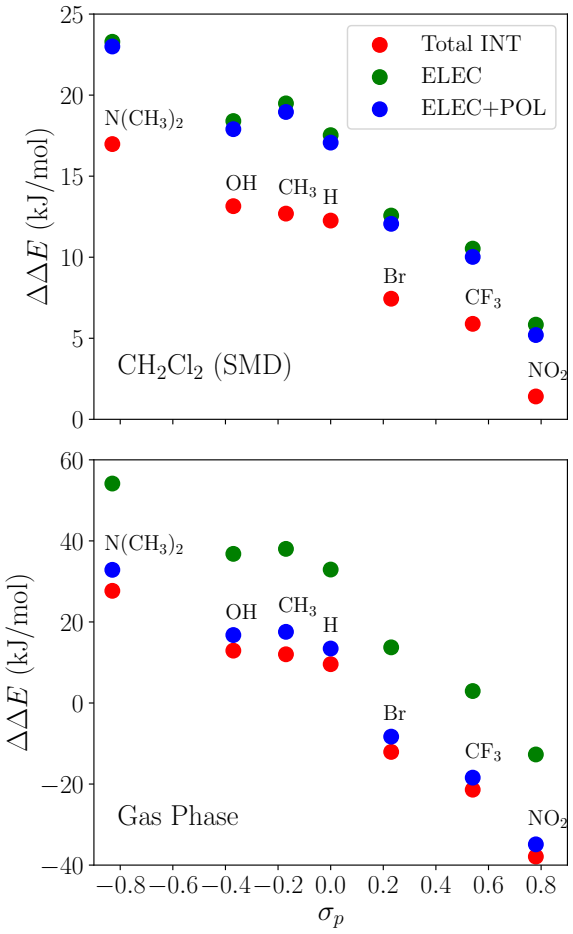

Figure 4.14: Substituent effects on the differences in total interaction energies as well as the ELEC and POL components (in kJ/mol) between the reactant and product states. The calculations are performed at the ωB97X-V/def2-TZVPD level of theory. The upper panel shows results in dichloromethane (CH_2Cl_2) solvent described by SMD and the lower panel shows gas-phase results. The x-axis shows the Hammett parameter of each substituent group.

The reactant complexes (Fig. 4.15(a)) are mainly bound by electrostatic and dispersion interactions, which, taken together, overcome the Pauli repulsion between p-terphenyl$^{\bullet-}$ (or its substituted derivatives) and the neutral CO_2 moiety. Moderate substituent effects are exhibited among the reactant complexes, where the EDGs yield more attractive total interactions in general (e.g. the NMe_2-substituted complex is more favorable than NO_2-substituted by $\sim$3 kJ/mol). This trend, as revealed by the EDA results, mainly stems from the enhancement in electrostatic interaction with stronger electron-donating substituents. The same trend is also

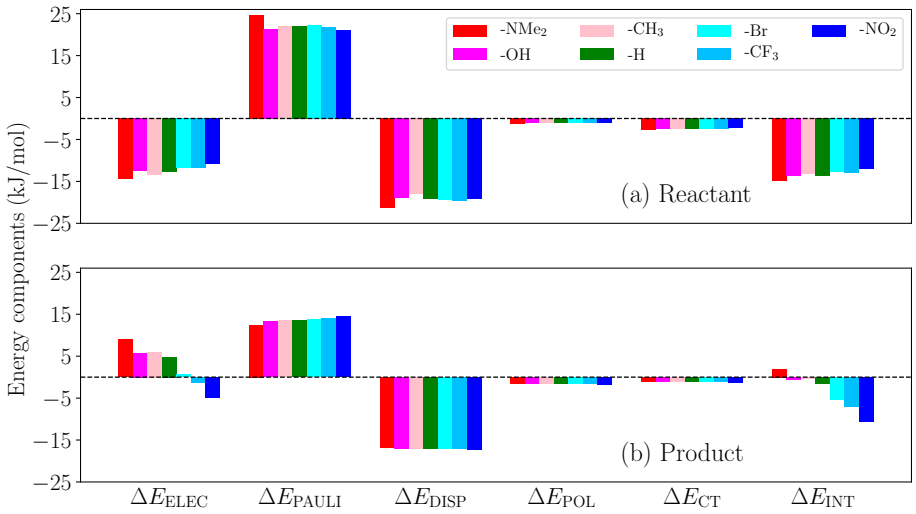

Figure 4.15: ALMO-EDA(solv) results (in kJ/mol) for (a) reactant and (b) product complexes between *p*-terphenyl and CO_2 with different substituent groups.

exhibited in the strength of POL and CT across different substituents, despite the relatively small magnitude of these two components. The product complexes, on the other hand, are not as strongly bound as in their respective reactant state, and they are mainly stabilized by dispersion interaction according to our EDA results (Fig. 4.15(b)). The magnitude of the total interaction is strongly impacted by the substituent group on the *p*-terphenyl moiety: with EDGs ($-NMe_2$, $-OH$, and $-CH_3$), the intermolecular binding between terphenyl and $CO_2^{\bullet-}$ is of only minimal strength (less favorable than -1 kJ/mol), while with EWGs ($-Br$, $-CF_3$, and $-NO_2$) the interaction becomes increasingly more favorable with the increase in substituent's electron-withdrawing ability (σ_p). Note that the resulting interaction energy for the NMe_2-substituted product complex is net repulsive ($+1.96$ kJ/mol), which most likely arises from the distinct levels of theory that were used in CDFT geometry optimizations [410] and ALMO-EDA(solv) calculations in the present paper. Similar to the reactant complexes, the substituent effects on the total interaction strength in the product state is also dominated by the ELEC component, where the EWGs are shown to strengthen the binding by reducing the electrostatic repulsion between $CO_2^{\bullet-}$ and the π electrons on the *p*-terphenyl moiety.

To summarize, the substituent effects on the intermolecular binding strength of the reactant and product *p*-terphenyl$\cdots CO_2$ radical anion complexes exhibit opposite trends, where EWGs diminish and enhance the interaction in the reactant and product states, respectively. While dispersion contributes significantly to binding in both states, the substituent effects are mainly controlled by the electrostatic component in both states despite the presence of solvent environment. These two opposite trends, combined together, lead to the trend shown in Fig. 4.14 where EWGs yield more strongly bound product complexes relative to

the reactant ones. Interestingly, the trend in $\Delta\Delta E_{\mathrm{INT}}$ with respect to varying σ_p is opposite to that in the total free energy change (ΔG) upon the electron transfer (ET), where EDGs yield more favorable driving forces.[410] This implies that although EWGs assist in stabilizing the product complexes, they are unable to reverse the trend in the free energy driving force dominated by the gap between the monomer energies before and after ET. In Table S11 in the ESI†, we show the comparison between $\Delta\Delta E_{\mathrm{INT}}$ and the energy associated with the reactant-to-product electronic transitions at the monomer level (denoted as ΔE_{PREP}) for this series of complexes.

4.5 Conclusions

In this work, we have developed the ALMO-EDA(solv) scheme to incorporate solvation effects described by dielectric continuum models into the second-generation ALMO-EDA based on DFT calculations.[84] This method possesses the following main features:

1. The implicit solvent environment is included in the construction of all states across the EDA procedure. Hence all energy differences (ΔE_{FRZ}, ΔE_{POL}, and ΔE_{CT}) are always computed between two consecutive states that are both properly solvated.

2. A new term, ΔE_{SOL}, is introduced to describe the direct change in solute-solvent interaction energy upon the formation of the frozen complex. In most generic cases, it comprises both electrostatic and non-electrostatic components, which can further be combined into the ELEC and PAULI components of the (internal) frozen interaction energy.

ALMO-EDA(solv) consistently incorporates continuum solvent effects, which permits study of solvation effects on each energy component in a systematic, physically motivated manner. To validate our EDA scheme, we first investigated the electrostatics-related terms using a solvated $Na^+\cdots Cl^-$ model complex. Our EDA reproduces the correct bulk limit for long-range electrostatics in solvent. We also rationalized diminished screening in the short range. We next analyzed the distance dependence of the energy components produced by ALMO-EDA(solv) for the $H_2O\cdots Na^+$ and $H_2O\cdots Cl^-$ complexes and demonstrated how solvents with varying dielectric constants affect the net strength of permanent electrostatics and polarization in these systems. The results further confirmed that ALMO-EDA(solv) yields physically sensible results for the energy components of these simple interactions in the solution phase and correctly reflects the trend in the relative strength of solvent effect.

We then employed ALMO-EDA(solv) to investigate more complex chemical systems related to catalysis of CO_2 reduction reactions. We first considered CO_2 complexes with $[Fe(II)TTP(CO_2^{\bullet-})]^{2-}$ (TPP = tetraphenylporphyrin) and its substituted derivatives.[380, 402] We found that the most strongly bound *o*-TMA-substituted complex is not mainly stabilized via through-space electrostatic attraction as was presumed (since the solvation environment screens this interaction significantly). Instead, it mainly benefits from reduced

Pauli repulsion compared to the unsubstituted $[\mathrm{FeTTP}(\mathrm{CO_2}^{\bullet-})]^{2-}$. This originates from the substantial electron-withdrawing inductive effect of the positively charged trimethylammonio groups that reduces electron density around the Fe center and give rise to a more Lewis acidic metal center. This stabilization is thus via a through-structure mechanism. Another strongly bound complex with *o*-OH substitution, in contrast, is mainly stabilized via hydrogen bonding between the *o*-OH groups and the negatively charged $\mathrm{CO_2}$ moiety, which is exclusively a through-space effect. Our study thus provides new insights into how substituent effects influence the ability of FeTPP to stabilize activated $\mathrm{CO_2}$. Inspired by the EDA results and the ligand reported in Ref. [407], we designed a bulky, floppy substituent group that contains a positively charged methylimidazolium moiety. When introduced to the ortho positions of the phenyl groups in FeTPP, they can create a solvent-inaccessible "pocket" in that stabilization of activated $\mathrm{CO_2}$ via long-range Coulomb interaction can be achieved due to the removal of solvent screening effects.

Second, we investigated complexes associated with the electron transfer reaction from *p*-terphenyl$^{\bullet-}$ (and its double terminal-substituted derivatives) to $\mathrm{CO_2}$. We demonstrated that differences between the interaction energies in the reactant and product states ($\Delta\Delta E_{\mathrm{INT}}$) are considerably modulated by the substituents, where electron-withdrawing groups were shown to stabilize the product complexes while moderately destabilizing the ones in the reactant state. Our EDA results further revealed that although dispersion plays an important role in the formation of both reactant and product complexes, the substituent tuning of $\Delta\Delta E_{\mathrm{INT}}$ is almost entirely achieved through modulating the electrostatic component (ΔE_{ELEC}) especially that in the product state. This example shows how ALMO-EDA(solv) assists in elucidating the nature of intermolecular interactions and mechanisms of chemical processes in the solution phase.

Finally, we shall note some of the limitations of the present ALMO-EDA(solv) scheme. First, as we have noted in Sec. 4.2, currently available DFT-based EDA schemes including our approach are most likely unable to fully describe the many-body solvent effect on dispersion interactions. Second, the current ALMO-EDA(solv) scheme is limited to the decomposition of single-point (*vertical*) interaction energies, and it is certainly desirable to further extend its capability to the analysis of molecular property shifts in solution based upon our previously developed *adiabatic* ALMO-EDA scheme.[201] This would require the development of nuclear gradients for the FRZ and POL intermediate states in the presence of implicit solvent. Besides these limitations from the perspective of EDA, one should also bear in mind that there are many other molecular approaches to describe solvent effects in modern theoretical chemistry that are more sophisticated than the relatively simple dielectric continuum model. It is an interesting challenge to make an EDA scheme compatible with those more advanced solvation models. These limitations, on the other hand, provide a wide range of future opportunities to further extend the treatment of solvation effects in ALMO-EDA calculations.

Chapter 5

Exploring the Limits of Second- and Third-Order Møller-Plesset Perturbation Theory for Non-Covalent Interactions: Importance of Regularization and Reference Orbitals

5.1 Introduction

Non-covalent intermolecular interactions (NCI) are important in many areas of chemistry ranging from catalysis to the structure of biological macromolecules. [174, 176, 177, 180–182, 186, 187, 398] For example, the network of hydrogen bonds and hydrophobic effects play a crucial role in the transmission rate of the highly contagious SARS-CoV-2 virus.[418] Electron correlation is essential for an accurate description of NCI.[419, 420] Dispersion is a type of NCI which is purely driven by electron-electron correlation as it is a long-range dynamic correlation effect with a well-known asymptotic behavior of $1/R^6$ where R is the distance between two fragments. Consequently, mean field methods like Hartree-Fock or approximate exchange correlation functionals within the Kohn-Sham density functional theory (KS-DFT) framework do not incorporate this effect unless an (empirical) correction term is applied.[65–67, 421] or a Van der Waals functional such as VV10[69] is included. Due to its highly accurate correlation treatment, coupled cluster theory with single, double, and perturbative triple excitations [CCSD(T)] is considered the "gold standard" for describing NCI.[214, 420] Unfortunately, this method exhibits a steep computational scaling ($\mathcal{O}(N^7)$, where N is the system size) and thus its canonical implementation is limited to small systems. Reduced scaling CCSD(T) methods are very promising but require care to ensure adequate numerical precision.[105–107]

Therefore, alternative methods are desirable to treat larger systems with a lower scaling

and ideally similar accuracy. Perturbation theory (PT) based methods such as second-order Møller-Plesset perturbation theory (MP2) can be employed with a $\mathcal{O}(N^5)$ scaling. However, conventional MP2 is known to overbind dispersion-dominated interactions[214–217] and modifications to MP2 have been explored[217, 422–425].

The first approach is to improve the reference orbitals used in MP2; instead of using Hartree-Fock (HF) orbitals, the MP2 energy can be determined via a self-consistent-field (SCF) procedure which includes the MP2 correlation energy yielding orbital-optimized MP2 (OOMP2) methods.[39, 426, 427]. For systems where the unrestricted HF (UHF) reference exhibits spin-contamination (artificial spin-symmetry breaking), its use as a reference determinant can lead to poor performance of MP2.[428–431] Orbital optimization at the MP2 level often reduces the degree of spin-contamination and improves energetics.[39, 426, 432] Despite the benefits of OOMP2 described above, it is not without its own pitfalls. Orbital optimization of the MP2 correlation functional can produce divergent energy contributions as the orbital energy difference denominator approaches zero. Overstabilization of bond-stretched configurations by OOMP2 leads to significant underestimation of harmonic vibrational frequencies.[433] OOMP2 also has difficulty transitioning smoothly from a spin-restricted (ROOMP2) to a spin-unrestricted (UOOMP2) solution via a Coulson-Fischer point, further limiting its applicability for bond-breaking.[434, 435]

Recently our group has explored regularization of the MP2 correlation energy to prevent its divergence at zero gap via a κ-regularizer[40]. The resulting methods, κ-MP2 and κ-OOMP2, use the following modified form of the MP2 correlation energy:

$$E_{\kappa-\mathrm{MP2}}(\kappa) = -\frac{1}{4}\sum_{ijab}\frac{|\langle ij||ab\rangle|^2}{\Delta_{ij}^{ab}}\left(1-e^{-\kappa\left(\Delta_{ij}^{ab}\right)}\right)^2 \quad . \tag{5.1}$$

where i and j are occupied orbital indices, a and b are unoccupied orbital indices, $\langle ij||ab\rangle$ is an element of the two-electron repulsion integral, and Δ_{ij}^{ab} is the orbital energy gap associated with orbitals i, j, a, b. The unregularized energy expression is recovered for large energy denominators while terms in the sum with small energy denominators are attenuated. The empirical κ parameter was trained for κ-OOMP2 on the TAE140 subset of the W4-11 set.[436] An optimized value of $\kappa = 1.45E_h^{-1}$ was shown to provide excellent results upon further testing on overall W4-11, RSE43[437], and TA13[209] sets. With this, κ-OOMP2 is fit to replace OOMP2 for general application. Complex restricted (cR) and complex general (cG) orbital extensions of κ-OOMP2 have also been developed.[26, 284]

The second approach is scaling or attenuated parts of the correlation energy: spin-component-scaled MP2 (SCS-MP2)[112, 422, 438–441] and orbital optimized SCS-MP2 (SCS-OOMP2)[39, 426] methods, which weight correlation contributions coming from same-spin and opposite-spin pairs of electrons differently. These techniques have also been applied to the second-order correlation contribution in several double-hybrid density functionals.[63, 442–445] However, different scaling parameters are necessary depending on the type of interaction (e.g. NCI) vs thermochemistry (TC).[440] Ochsenfeld and coworkers recently showed that MP2-F12 can yield good results for NCI when omitting expensive terms and re-scaling

the remaining components allowing an efficient calculation of large systems.[446] Another set of approaches are the attenuated MP2 methods that partially cancel basis set superposition errors with errors in MP2 itself to yield improved intermolecular interaction energies in finite basis sets.[423–425, 447]

Lastly, for further improvements, one may include the third-order terms in the MP perturbative expansion (MP3) which have the following correlation energy expression:

$$E_{\mathrm{MP3}} = \frac{1}{8}\sum_{ijabcd}\left(t_{ij}^{ab}\right)^{*}\langle ab||cd\rangle t_{ij}^{cd} + \frac{1}{8}\sum_{ijklab}\left(t_{ij}^{ab}\right)^{*}\langle kl||ij\rangle t_{kl}^{ab} - \sum_{ijkabc}\left(t_{ij}^{ab}\right)^{*}\langle kb||ic\rangle t_{kj}^{ac} \quad . \tag{5.2}$$

Despite its higher computational cost ($\mathcal{O}(N^6)$) compared to MP2, MP3 offers only a modest if any improvement over MP2 results. Specifically for weak NCI, MP3 does not improve the MP2 results.[112, 440, 448–452] However, Hobza and coworkers[450–452] suggested scaling the third-order correlation energy to interpolate between MP2 and MP3, e.g. MP2.5. These methods substantially improve binding energies for NCI and can even be used for radical systems[453]. Bozkaya and coworkers[432, 454–457] developed OOMP3 and OOMP2.5 and evaluated the performance of these methods on thermochemistry, kinetics, and NCI. OOMP2.5 was shown to outperform coupled cluster theory with single and double excitations (CCSD)[458, 459] on reaction energies and barrier heights [432] and perform comparably to CCSD(T)[460] for NCI[456]. These results motivated recent work in our group, where we developed an MP3 method using reference orbitals generated by κ-OOMP2, denoted as MP3:κ-OOMP2. Furthermore, scaling the third-order contribution was explored and 0.8 (MP2.8:κ-OOMP2) was determined to be an optimal scaling parameter to further improve the energetics.[286]

This previous work[286] showed promising results for both NCI and TC; however, the NCI analysis was limited to two small benchmark sets: A24[461], comprising 24 small dimer complexes and TA13, comprised of 13 radical-solvent complexes. This present work aims to provides a comprehensive analysis of NCI for novel MP2 and MP3 approaches by assessing 19 popular NCI benchmark sets (see Table 5.1). These data sets formed the basis for assessing the performance of DFT functionals for NCI in a previous study from our group.[20] We include various second- and third-order MP methods as well as the top performing DFT functional for NCI[20],ωB97M-V[70].

We do not want to overlook promising results with non-perturbative approaches. First, lower-order coupled cluster methods showed promising performance in atomization and reaction energies without any additional empirical parameters.[462] However, more benchmark data is necessary to test whether this high accuracy is transferable to NCI. Hobza and coworkers developed a same- and opposite-spin scaled CCSD method, specifically parameterized for NCI (SCS(MI)-CCSD)[463], parameterized on the S22 benchmark set[215]). The method performs remarkably well for the S66 (RMSD: 0.08 kcal/mol) and X40 (RMSD: 0.06 kcal/mol) NCI benchmark sets.[464, 465] In both cases the scaling is $\mathcal{O}(N^6)$ but iterative and thus more expensive than the perturbative approaches detailed above.

Modern density functionals (e.g ωB97M-V) perform excellent for all types of NCI when empirical dispersion corrections[66, 112] or nonlocal correlation functionals[69] are used.

We refer the interested reader to ref. [20] which includes an extensive comparison of many DFT functionals and various NCI data sets. However, approximate exchange correlation functionals incorporate many empirical parameters, which are often trained and/or tested on these benchmark sets[20, 63, 391]. Alternatively, there are promising NCI results obtained by employing the random phase approximation (RPA) as a correction to DFT,[466–468] as well as active development and testing of further corrections to RPA.[469–471] However, we note that radical systems or charged systems can still pose a problem for density functionals due to the self-interaction error.[20, 54, 55]

This paper is organized as follows: First, we give a short overview of the data sets used in this study which are separated in two categories NCED (non-covalent 'easy' dimers; easy refers to low sensitivity to the self-interaction error in these data sets) and NCD (non-covalent 'difficult' dimers). Second, we describe the electronic structure methods used in this study and the computational details. Third, we discuss the optimal scaling parameter for the third order methods for S66 and the whole NCED data category. Fourth, we discuss in detail the performance of each method in each data set and draw conclusion after both NCED and NCD data categories. Lastly, we conclude and summarize important findings in our work.

5.2 Overview of Benchmark Sets

The benchmark sets used in this study are inspired by the data categories for non-covalent interactions from ref. [20], which includes two data categories: "non-covalent easy dimers" (NCED) and "non-covalent difficult dimers" (NCD) (the classification "easy dimers" means that these systems are not sensitive to the self interaction error (SIE) of approximate exchange correlation functionals[20, 54, 55]).

The NCED data category includes thirteen equilibrium geometry data sets: A24[461], DS14[472], HB15[473], HSG[474], S22[215], X40[465], HW30[475], NC15[476], S66[464], Alk-Bind12[477], CO2Nitrogen16[478], HB49[479] and Ionic43[480]. These data sets cover a wide range of different NCI interaction motifs like classical hydrogen bonds, dispersion bound systems, ionic interactions and halogen bonding with various sub-classes such as π-stacking, aliphatic dispersion, halogen-π interactions, cyclic hydrogen bonds, charged-neutral and charged-charged ionic interactions; see Table 5.1 for a short description of each data set. We omitted the five non-equilibrium geometries data sets (NBC10[481], BzDC215[482], A21x12[483], S66x8[484], 3B-69-DIM[485]) in the overall statistical analysis. However, some data points in these data sets were included in the section about potential energy curve calculations.

The NCD is a collection of four non-covalent interactions:
TA13[209], XB18[486], Bauza30[487], CT20[488], XB51[486] and we extended the category by adding the Orel26rad[231] set. These are classified as difficult for DFT functionals because these systems are prone to the SIE.[20] We excluded all complexes with iodide in both halogen bonding sets following ref. [20]. In XB18 10 data points and XB51 30 data points were excluded analogous to ref. [20]. This data category covers neutral and charged radical

complexes, hydrogen bonding, halogen, chalcogen and pnicogen bonding; see Table 5.1 for a short description of each data set.

Name	Data-type	#	Description	Max(E)	Min(E)	Ref
A24	NCED	24	small non-covalent complexes	1.10	−6.53	[461]
DS14	NCED	14	sulfur based small non-covalent complexes	−0.85	−6.33	[472]
HB15	NCED	15	ionic hydrogen complexes	−11.46	−28.56	[473]
HSG	NCED	21	protein-ligand docking relevant non-covalent complexes	0.38	−19.08	[474]
S22	NCED	22	hydrogen-bonded and dispersion-bound complexes	−0.53	−20.64	[215]
X40	NCED	31	halogenated hydrocarbons non-covalent complexes	−0.49	−14.32	[465]
HW30	NCED	30	hydrocarbon water dimers	−0.66	−3.81	[475]
NC15	NCED	15	small non-covalent interactions	−0.02	−3.31	[476]
S66	NCED	66	hydrogen-bonded and dispersion-bound complexes	−1.39	−19.68	[464]
AlkBind12	NCED	12	unsaturated hydrocarbon dimers	−1.99	−4.65	[477]
CO2Nitrogen	NCED	16	polyheterocyclic CO_2 dimers	−1.18	−5.54	[478]
HB49	NCED	49	hydrogen bonding complexes	−1.75	−33.85	[479]
Ionic43	NCED	43	charged non-covalent complexes	−7.96	−120.80	[480]
TA13	NCD	13	binary radical-solvent complexes	−1.69	−64.20	[209]
XB18	NCD	8	halogen bonded dimers	−1.41	−8.60	[486]
Bauza30	NCD	30	halogen, chalcogen and pnicogen bonded complexes	−1.42	−46.42	[487]
CT20	NCD	20	ground state charge-transfer complexes	−0.32	−1.83	[488]
XB51	NCD	20	halogen bonded dimers	−0.74	−23.11	[486]
Orel26rad	NCD	26	aromatic radical dimer complexes	−1.89	−20.30	[231]

Table 5.1: Non-covalent interaction data-sets used to evaluate the performance of various methods in this work. These data sets were all taken from ref. [20]. # indicates the number of data points in each set. Max(E) and Min(E) denote the weakest and strongest interaction energy of the data set in kcal/mol, respectively.

5.3 Overview of Methodology

The majority of interaction energies reported in this work are computed without a geometric distortion term, meaning that the geometry of monomers are identical for the complex and in isolation. In this case, all energies are computed using the standard BSSE approach[116]:

$$\Delta E_{int} = E^{AB}_{AB}(AB) - E^{A}_{A}(AB) - E^{B}_{B}(AB) - E_{BSSE} \quad . \tag{5.3}$$

where $E^N_M(X)$ denotes the energy of $N \in \{A, B, AB\}$ in the basis of $M \in \{A, B, AB\}$ and in the geometry of X; AB denotes the supersystem of A and B. The basis set superposition

error correction[116] is defined as:

$$E_{BSSE} = E_{AB}^{A}(AB) + E_{AB}^{B}(AB) - E_{A}^{A}(AB) - E_{B}^{B}(AB) \quad . \tag{5.4}$$

The benchmark sets HB49, XB18, XB51 and TA13 include geometric distortion, meaning the reference states are optimized structures for both isolated and supersystem geometries. We use the following equation to compute interaction energies in accordance with reference [479]:

$$\Delta E_{int} = E_{AB}^{AB}(AB) - E_{A}^{A}(AB) - E_{B}^{B}(AB) - E_{BSSE} + E_{GD} \quad , \tag{5.5}$$

with the geometry distortion term[489] defined as:

$$E_{GD} = E_{A}^{A}(AB) + E_{B}^{B}(AB) - E_{A}^{A}(A) - E_{B}^{B}(B) \quad , \tag{5.6}$$

where (AB) correspond to the monomer geometry in the complex, (A) to the optimized isolated geometry of monomer A, and respectively for (B). This approach yields almost identical RMSDs to non-BSSE corrected values for ωB97M-V in ref. [20].

All perturbation methods used in this study are summarized in Table 5.2. All PT methods utilize an all-electron approach (no frozen core approximation) and the RI approximation. The non-iterative second-order methods include: standard MP2:

$$E_{MP2} = E_{HF} + E_{D}^{(2)} \quad , \tag{5.7}$$

κ-MP2 using the recently developed κ-regularizer[40] (using the recommended $\kappa = 1.45E_h^{-1}$ for the parameter) for the MP2 correlation energy:

$$E_{\kappa-MP2} = E_{HF} + E_{D}^{(2)}(\kappa) \quad , \tag{5.8}$$

this method is used to systematically assess the effect of regularization and orbital optimization in κ-OOMP2. We note, that the κ parameter is optimized for the orbital optimized variant, not the κ-MP2. In addition, spin-scaled (SCS) MP2 using 0.333 for same spin (ss) and 1.200 for opposite spin (os) scaling factors for the same spin and opposite spin correlation energy contribution of MP2 ($E_{ss}^{(2)}$ and $E_{os}^{(2)}$), as implemented in Q-Chem.[112]:

$$E_{SCS-MP2} = E_{HF} + c_{ss}E_{ss}^{(2)} + c_{os}E_{os}^{(2)} \quad , \tag{5.9}$$

The iterative second-order methods include orbital-optimized MP2 (OOMP2) and κ-regularized OOMP2 (κ-OOMP2) which minimize the E_{MP2} and $E_{\kappa-MP2}$ energy expressions stated above.

The third-order methods include: standard MP3 and MP2.5[450–452] which scales the third-order contribution (c_3) to the correlation energy by 0.5:

$$E_{MP2.5} = E_{HF} + E_{D}^{(2)} + c_3E_{D}^{(3)} \quad . \tag{5.10}$$

Additionally, we tested MP3 using OOMP2 reference orbitals (MP3:OOMP2); MP2.5 using OOMP2 reference orbitals (MP2.5:OOMP2); MP3 using κ-OOMP2 reference orbitals

where the regularizer is only applied for the generation of the the reference orbitals (MP3:κ-OOMP2); and MP2.5 using κ-OOMP2 reference orbitals (MP2.5:κ-OOMP2). For these non-HF reference orbitals, the MP2 energy includes the singles contributions, $E_S^{(2)}$:

$$E_S^{(2)} = -\sum_{ia} \frac{|F_{ia}|^2}{\epsilon_a - \epsilon_i} \quad , \tag{5.11}$$

where F_{ia} denotes an element of the occupied-virtual block of the Fock matrix. We also combined (scaled) MP3 and regularized MP2 where the regularizer is applied for the MP2 energy with κ-OOMP2 reference orbitals (κ-MP3:κ-OOMP2):

$$E_{\kappa-MP2.5} = E_{HF} + E^{(2)}(\kappa)_D + c_3 E_D^{(3)} \tag{5.12}$$

and the scaled version κ-MP2.5:κ-OOMP2. For these cases, $E_S^{(2)}$ is omitted.

Lastly, inspired by recent work in our group[490], we also investigate the effect of KS-DFT reference orbitals using ωB97X-V[391] for both MP2.5 and MP3, where we use the converged KS-DFT orbitals to evaluate the HF, MP2 and MP3 energy (in contrast to double hybrid functionals). This functional is among the most accurate for dipole moments[491], polarizabilities[492], electron density variances[493] and yielded among the most accurate reference orbitals for MP3 calculations[490]. Table 5.2 summarizes the range of perturbative methods assessed in this work.

5.4 Computational Details

All electronic structure calculations were performed with a local development version of Q-Chem (version 5.2.2)[108]. The MP2 and MP3 correlation energy calculations were performed with the RI approximation and correlate all electrons. We refer to RI-MP2 and RI-MP3 as simply MP2 and MP3, respectively. The MP3 calculations are performed with an amplitude direct approach which only requires the cubic storage overall.[494, 495] The aug-cc-pVTZ basis and the corresponding RI auxiliary basis were employed for all calculations[253, 254], except for parts of Orel26rad, TA13 and XB51. For Orel26rad, we used the more compact def2-tzvpd[247, 248] and corresponding auxiliary basis[255, 496, 497] for the larger systems due to computational efficiency; for TA13, we used the cc-pVQZ auxiliary basis for Li because there is no auxiliary basis for aug-cc-pVTZ; for XB51, we used the aug-cc-pVTZ-PP basis and the corresponding ECP and auxiliary basis for Br[249] and the frozen core approximation was employed to harmonize with the reference values which were also generated with aug-cc-pVTZ-PP and ECP for Br.[486]

All geometries and reference interaction energies were taken from ref. [20] (see references therein) with the exception of the Orel26rad data set, which was taken from ref. [231]. Note carefully that we compare our TZ-level calculations against reference values at the complete basis set limit. We do this to make the MP2 and MP3 calculations far more feasible than

Method	Orbitals	$E_S^{(2)}$	$E_D^{(2)}$	$E_S^{(3)}$	$E_D^{(3)}$
MP2	HF	0	✓	X	X
κ-MP2	HF	0	κ	X	X
SCS-MP2	HF	0	S	X	X
OOMP2	OOMP2	0	✓	X	X
κ-OOMP2	κ-OOMP2	0	κ	X	X
MP3	HF	0	✓	0	✓
MP2.5	HF	0	✓	0	S
MP3:OOMP2	OOMP2	✓	✓	X	✓
MP2.5:OOMP2	OOMP2	✓	✓	X	S
MP3:κ-OOMP2	κ-OOMP2	✓	✓	X	✓
MP2.5:κ-OOMP2	κ-OOMP2	✓	✓	X	S
MP3:ωB97X-V	ωB97X-V	✓	✓	X	✓
MP2.5:ωB97X-V	ωB97X-V	✓	✓	X	S
κ-MP3:κ-OOMP2	κ-OOMP2	X	κ	X	✓
κ-MP2.5:κ-OOMP2	κ-OOMP2	X	κ	X	S

Table 5.2: Summary and short description of all perturbation theory methods used in this study; X indicates that the contribution is not included, ✓means included, 0 indicates the contribution is identically to 0, and κ indicates regularized second order contribution ($\kappa = 1.45E_h^{-1}$), S indicates scaled second or third order contribution

if larger basis sets were used. We note that this affects the optimal scaling parameter (see figure D.2).

In addition, we performed density functional calculation using ωB97M-V with a fine integration grid (99 radial grid points and 590 Lebedev angular grid points) for quadrature, the resulting RMSD are almost identical to those reported in ref. [20]. Some small discrepancies (maximum deviation: 0.02 kcal/mol in DS14) can be explained with the different computational set-up (aug-cc-pVTZ with BSSE correction used here versus def2-QZVPPD[248, 498] without BSSE correction used in ref. [20]). The data for B3LYP-D3 is directly taken from ref. [20] and CCSD numbers are taken from the references for each data set. We performed the whole NCED data category with restricted HF (RHF) and ROOMP2. The same is true for the NCED data category with the exception of TA13 and Orel26rad. In TA13, we used UHF (and restricted open-shell HF (ROHF) just for MP2) and UOOMP2. In Orel26rad, we used ROHF for all HF methods and UOOMP2 for all OOMP2 methods including the composite MP3 methods.

5.5 Results and Discussion

The systems included in this study cover a wide range of NCI such as σ dispersion, π-stacking, hydrogen, halogen and ionic bonding; the complete list of 19 data sets was already shown in Table 5.1. The root-mean-square deviations (RMSD) are given in kcal/mol. We discuss equilibrium geometry data sets of the two data categories NCED (non-covalent: easy dimers) and NCD (non-covalent: difficult; with Orel26rad added) taken from an extensive benchmark work for DFT functionals.[20] In addition, we include potential energy surface (PES) scans for benzene, pyridine, water and methylamine dimers. We assess the performance of 15 methods (see Table 5.2) to systematically gauge the effect of scaling, reference orbitals and regularization. We compare these results to the top performing functional for NCI, ωB97M-V (based on ref. [20]). We also compare our results against those from a widely used exchange correlation functional B3LYP-D3, CCSD and SCS(MI)-CCSD wherever available. The results are summarized in tables 5.3 and 5.4. The SCS-MP2 results are consistently worse than regular MP2 as illustrated in tables 5.3 and 5.4.Consequently, we omit SCS-MP2 from most of the discussion below. In addition, we explore the option of using KS-DFT reference orbitals for MP3 and MP2.5 due to recent promising results employing this approach.[490]

Optimal Scaling of the Third-Order Energy

Both standard MP2 ($c_3 = 0.0$) and MP3 ($c_3 = 1.0$) (see equation 5.10) perform poorly for NCI as MP2 usually overbinds (too negative interaction energies) and MP3 underbinds (too positive interaction energies). Therefore, Hobza and coworkers[450–452] suggested scaling the third-order correlation energy to interpolate between MP2 and MP3. Thus, we expect an optimum scaling parameter between 0 and 1. In two previous studies,[286, 490] 0.8 was determined as the optimal scaling parameter (c_3) for the third-order energy contribution (see equation 5.10) using the W4-11 thermochemistry data set as a training set and CCSD(T) with aug-cc-pVTZ as a reference. However, other studies specifically for non-covalent interaction found a scaling factor of 0.5 yields good results for both MP3 and orbital optimized MP3.[432, 452] Therefore, we probed the scaling factor dependence for all four MP2.X methods (MP2.X, MP2.X:OOMP2, MP2.X:κ-OOMP2 and κ-MP2.X:κ-OOMP2) employed in this study. The results are depicted in figure 5.1 using the S66 benchmark set as a training set. A scale factor of around 0.5 is optimal for MP2.X, MP2.X:OOMP2 and MP2.X:κ-OOMP2 (optimal c_3 values were 0.45, 0.55, and 0.60 for MP2.X, MP2.X:κ-OOMP2, and MP2.X:OOMP2, respectively).

We stress again, however, that the c_3 coefficient is optimized in the medium sized aug-cc-pVTZ basis by training against CCSD(T)/CBS reference values. The c_3 parameter tends to shift to larger values for larger basis sets or when a CCSD(T)/aug-cc-pvtz reference is used (as in ref. [286] and [490]). MP2 tends to overestimate correlation energy with larger basis sets and consequently a higher amount of third order contribution becomes optimal. We illustrate this for the A24 benchmark set in figures D.1 and D.2.

Returning to figure 5.1, it is very interesting that both MP2.X:OOMP2 and MP2.X:κ-OOMP2 exhibit a sharper and deeper minimum than MP2.X. A more detailed look into the individual plots for each data set reveals that in many hydrogen bonding data sets (S66 hydrogen bonding subsection, HSG and HB49), Ionic43 and CT20 the minimum for MP2.X is at $c_3 = 0$ or very small. The optimal c_3 parameter for MP2.X:OOMP2 is always larger than MP2.X:κ-OOMP2 and notable deviations from $c_3 = 0.5$ are observed for A24 ($c_3 \sim 0.3$) and CT20 ($c_3 \sim 0.8$). The appendix D contains a plot for each of these data sets.

Furthermore, we combined both κ-regularization of the MP2 energy and scaling of the MP3 energy. We found, however, that the c_3 scaling factor was small and often did not yield a sizable improvement versus κ-OOMP2 (see figure 5.1). This is in accordance with the findings of our previous study.[286] Therefore this method is omitted from further discussion.

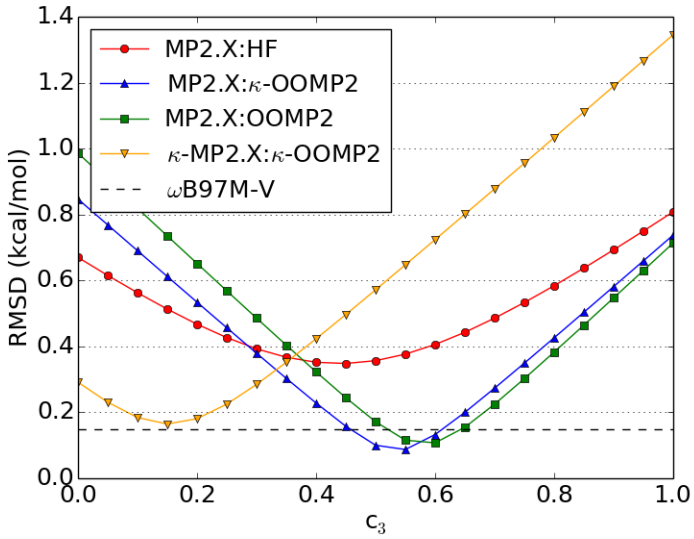

Figure 5.1: Dependence of the the root-mean square deviation on the scaling of the third-order energy (c_3) in the S66 training set; in kcal/mol; for four scaled MP2.X methods (MP2.X, MP2.X:OOMP2, MP2.X:κ-OOMP2, κMP2.X:κ-OOMP2); for reference, the RMSD of ωB97M-V is depicted as a flat line.

NCED

We discuss the S22 and S66 data sets in detail since they are the most popular benchmark sets for NCI and many findings are transferable to the other sets. The results for all data sets of that category are summarized in table 5.3.

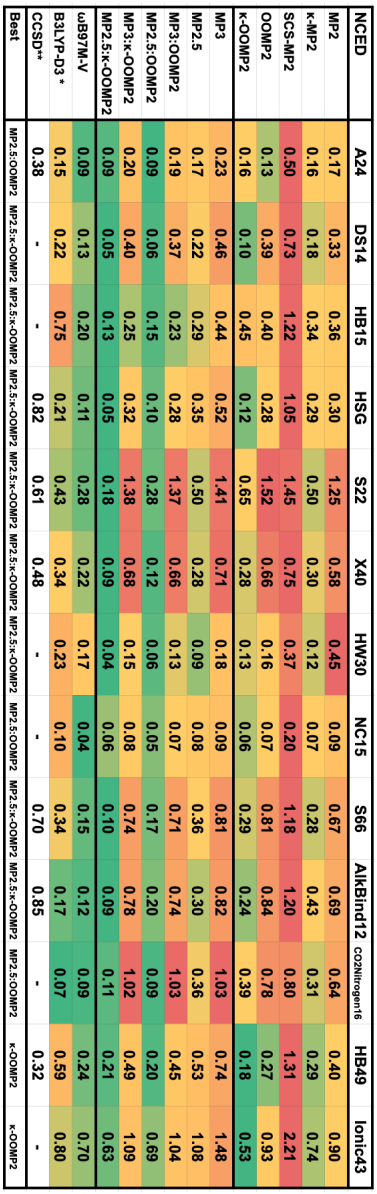

NCED	A24	DS14	HB15	HSG	S22	X40	HW30	NC15	S66	AlkBind12	CO2Nitrogen16	HB49	Ionic43
MP2	0.17	0.33	0.36	0.30	1.25	0.58	0.45	0.09	0.67	0.69	0.64	0.40	0.90
κ-MP2	0.16	0.18	0.34	0.29	0.50	0.30	0.12	0.07	0.28	0.43	0.31	0.29	0.74
SCS-MP2	0.50	0.73	1.22	1.05	1.45	0.75	0.37	0.20	1.18	1.20	0.80	1.31	2.21
OOMP2	0.13	0.39	0.40	0.28	1.52	0.66	0.16	0.07	0.81	0.84	0.78	0.27	0.93
κ-OOMP2	0.16	0.10	0.45	0.12	0.65	0.28	0.13	0.06	0.29	0.24	0.39	0.18	0.53
MP3	0.23	0.46	0.44	0.52	1.41	0.71	0.18	0.09	0.81	0.82	1.03	0.74	1.48
MP2.5	0.17	0.22	0.29	0.35	0.50	0.28	0.09	0.08	0.36	0.30	0.36	0.53	1.08
MP3:OOMP2	0.19	0.37	0.23	0.28	1.37	0.66	0.13	0.07	0.71	0.74	1.03	0.45	1.04
MP2.5:OOMP2	0.09	0.06	0.15	0.10	0.28	0.12	0.06	0.05	0.17	0.20	0.09	0.20	0.69
MP3:κ-OOMP2	0.20	0.40	0.25	0.32	1.38	0.68	0.15	0.08	0.74	0.78	1.02	0.49	1.09
MP2.5:κ-OOMP2	0.09	0.05	0.13	0.05	0.18	0.09	0.04	0.06	0.10	0.09	0.11	0.21	0.63
ωB97M-V	0.09	0.13	0.20	0.11	0.28	0.22	0.17	0.04	0.15	0.12	0.09	0.24	0.70
B3LYP-D3 *	0.15	0.22	0.75	0.21	0.43	0.34	0.23	0.10	0.34	0.17	0.07	0.59	0.80
CCSD**	0.38	-	-	0.82	0.61	0.48	-	-	0.70	0.85	-	0.32	-
Best	MP2.5:OOMP2	MP2.5:κ-OOMP2	MP2.5:κ-OOMP2	MP2.5:κ-OOMP2	MP2.5:κ-OOMP2	MP2.5:κ-OOMP2	MP2.5:κ-OOMP2	MP2.5:OOMP2	MP2.5:κ-OOMP2	MP2.5:κ-OOMP2	MP2.5:OOMP2	κ-OOMP2	κ-OOMP2

Table 5.3: Results of the NCED data category; RMSD in kcal/mol. For each data set all method cells are colored in a heatmap from green to yellow to red. Low RMSD are represented in green and high RMSD in red.

* B3LYP-D3(BJ) interaction energies were taken from ref. [20];** CCSD interaction energies for A24 and HSG were taken from ref. [392] (CCSD/aTZ), for S22 from ref. [463] (CCSD/CBS), for XB40 and S66 from ref. [465] (CCSD/CBS), for AlkBind12 from ref. [477] (CCSD/CBS), and for HB49 from ref. [499] (CCSD/aTZ).

NCD	TA13	XB18	Bauza30	CT20	XB51	Orel26rad
MP2	2.14	0.31	0.72	0.12	0.36	3.03
κ-MP2	2.46	0.26	0.98	0.10	0.36	1.53
SCS-MP2	2.65	0.75	2.33	0.34	0.82	2.12
OOMP2	0.96	1.01	1.76	0.22	1.27	7.70
κ-OOMP2	0.88	0.50	1.31	0.13	0.36	0.59
MP3	1.85	1.09	2.40	0.23	1.32	6.50
MP2.5	1.95	0.45	1.21	0.14	0.54	2.23
MP3:OOMP2	0.63	0.62	1.62	0.09	0.76	7.01
MP2.5:OOMP2	1.16	0.59	1.11	0.16	0.70	1.10
MP3:κ-OOMP2	0.62	0.71	1.81	0.10	0.88	5.92
MP2.5:κ-OOMP2	0.93	0.35	0.88	0.12	0.34	0.78
ωB97M-V	2.85	0.32	0.59	0.08	0.26	1.59
B3LYP-D3 *	3.85	0.37	1.87	0.28	1.04	5.67
CCSD**	0.89	0.66	-	-	0.67	-
Best	MP3:κ-OOMP2	κ-MP2	MP2	MP3:OOMP2	MP2.5:κ-OOMP2	κ-OOMP2

Table 5.4: Results of the NCD data category; RMSD in kcal/mol; RO-HF is used as a reference for the three MP2 methods in Orel26rad. For each data set all method cells are colored in a heatmap from green to yellow to red. Low RMSD are represented in green and high RMSD in red.
* B3LYP-D3(BJ) interaction energies were taken from ref. [20];** CCSD interaction energies for TA13 are taken from ref. [209] (CCSD/CBS); XB18 (CCSD/aQZ) and XB51 (CCSD/aTZ) were taken from ref. [486] and adjusted to the subset.

S22

The S22[215] benchmark set comprises 22 non-covalent interactions of model systems relevant to biological molecules. Typical systems are π-stacked aromatic systems like the benzene dimer or hydrogen bonded systems like the formic acid dimer. The two largest systems are adenine-thymine complexes (30 atoms). The set is divided into three subgroups: (i) hydrogen bonded complexes; (ii) dispersion-bound complexes; and (iii) mixed electrostatic and dispersion complexes.

Among the second order methods, MP2 is well-known to overbind dispersion-driven complexes[214–217], yielding a large RMSD of 1.25 kcal/mol and a mean signed deviation (MSD) of -0.45 kcal/mol. The largest deviations for MP2 are the π-stacked indole-benzene complex (-3.27 kcal/mol) and the adenine-thymine complex (-2.61 kcal/mol). Regularization damps the small gap correlation energy contributions which significantly decreases the RMSD to 0.50 kcal/mol for κ-MP2 (almost by a factor of 3). This is a remarkable improvement especially given that the κ value used in κ-MP2 was never trained on non-covalent interactions. The lower RMSD stems mainly from the improved binding energies of the π-stacked outliers described above: deviation of 1.18 kcal/mol for the indole-benzene complex and -1.18 kcal/mol for adenine-thymine complex. This is also seen in the boxplot of in figure 5.2 (a) where the spread of the error significantly decreases from MP2 to κ-MP2 and κ-OOMP2 to MP2.5:κ-OOMP2. By contrast, a currently more widely used MP2 variant, SCS-MP2

performs even worse than canonical MP2 for this data set. SCS-MP2 improves the performance of the π-stacked species e.g. deviation in the indole-benzene complex is -0.08 kcal/mol; however, this improvement in the dispersion category is accompanied by significant underbinding of hydrogen bonding, e.g. adenine thymine complex with 2.8 kcal/mol. This is further illustrated by both the mean signed deviation (MSD): 1.05 kcal/mol and the boxplots in figure 5.2. In total, the RMSD of SCS-MP2 is 1.45 kcal/mol performing worse than standard MP2.

For the MP3 methods, scaling MP3 correlation energy contribution improves the RMSD for all three sets of reference orbitals by $\sim$1 kcal/mol e.g., MP3:κ-OOMP2: 1.38 kcal/mol versus MP2.5:κ-OOMP2: 0.18 kcal/mol. Comparing the three scaled methods, the HF reference orbitals yield significantly worse binding energies (RMSD: 0.50 kcal/mol) than OOMP2 (RMSD: 0.28 kcal/mol), while κ-OOMP2 (RMSD: 0.18 kcal/mol) provides the best reference orbitals for scaled MP3. The box plots in figure 5.2 (a) and (b) show how all three MP2.5 methods significantly decrease the spread of the error in comparison to standard MP2.

Interestingly, for this dataset, the performance of the regularizer does not strongly depend on the reference orbitals, since both κ-MP2 (RMSD: 0.50 kcal/mol) and κ-OOMP2 (RMSD: 0.65 kcal/mol) yield similar accuracy. In addition, the comparison of κ-OOMP2 and OOMP2 show that improvements in the energetics mainly stem from the κ-regularizer (RMSD: OOMP2: 1.45 kcal/mol versus κ-OOMP2: 0.65 kcal/mol).

The two DFT functionals ωB97M-V (RMSD: 0.28 kcal/mol) and B3LYP (RMSD: 0.43 kcal/mol) perform less well than MP2.5:κ-OOMP2. In addition CCSD (CCSD/CBS) performs poorly with an RMSD of 0.61 kcal/mol[463] in comparison to MP2.5:κ-OOMP2; however, a scaled CCSD version, SCS(MI)-CCSD (RMSD: 0.06 kcal/mol)[463] outperforms MP2.5:κ-OOMP2 slightly; but the spin scaling parameters were trained on this data set[463].

In summary, the best performing method is MP2.5:κ-OOMP2 with an RMSD of 0.18 kcal/mol. The largest deviation is seen in the π-stacked adenine-thymine complex with -0.46 kcal/mol.

S66

The S66[464] benchmark set consists of 66 NCI. Similarly to S22, the data set covers a large variety of NCI relevant to biology with a more balanced representation of dispersion and electrostatic contributions. The interactions are also classified in three categories: (i) hydrogen bonds, (ii) dispersion and (iii) others/mixed. The largest data point is a pentane dimer (34 atoms).

Among the second-order methods both κ-OOMP2 and κ-MP2 are significant improvements on standard MP2. Similarly to S22, the improvements stem mainly from regularization and not orbital optimization which is illustrated by the RMSD of 0.28 kcal/mol for κ-MP2 and 0.29 kcal/mol for κ-OOMP2 versus standard MP2 0.67 kcal/mol. The boxplot in figure 5.2 illustrates this behaviour as MP2 shows a downwards bias and κ-MP2 (and κ-OOMP2) a significantly decreased spread in the data.

For the third-order methods, both scaling and κ-OOMP2 reference orbitals improve the energies; thus, the top performer is MP2.5:κ-OOMP2 with an RMSD of 0.10 kcal/mol. The largest MP2.5:κ-OOMP2 deviation is -0.41 kcal/mol for a π-stacked uracil complex. Both MP2.5 (RMSD: 0.36 kcal/mol) and MP3:κ-OOMP2 (RMSD: 0.74 kcal/mol) perform significantly less well than MP2.5:κ-OOMP2. As already mentioned, S66 was used as a training set to determine an optimal scaling parameter for the third-order correlation energy in the three MP3 methods surveyed and yielded optimal parameters of around 0.5 for each case, see table 5.5. This is consistent with results reported previously using HF reference orbitals.[450–452] Interestingly, this holds for each of the three subclasses in this set (see table 5.5 and figure D.3).

Method	c_3 tot	c_3 h-bonds	c_3 disp	c_3 mixed
MP2.X	0.45	0.45	0.45	0.40
MP2.X:κ-OOMP2	0.55	0.50	0.55	0.50
MP2.X:OOMP2	0.60	0.60	0.60	0.55
κ-MP2.X:κ-OOMP2	0.15	0.10	0.15	0.15

Table 5.5: Optimal scaling parameter for the MP3 energy contribution (c_3) for the whole S66 data set and the three subsets hydrogen bonds, dispersion and mixed.

The dispersion-bound subsection of S66 (23 data points) are of particular interest as standard MP2 is known to overbind these complexes.[214–217] This is illustrated by the high RMSD of 0.94 kcal/mol. The κ-regularized MP methods significantly improve binding: κ-MP2 with an RMSD of 0.39 kcal/mol, κ-OOMP2 with an RMSD of 0.44 kcal/mol and MP2.5:κ-OOMP2 with an RMSD of 0.13 kcal/mol. For MP2, the largest deviation is seen in the π-stacked pyridine dimer -1.97 kcal/mol; this is reduced to -0.74 kcal/mol for κ-MP2, to -0.64 kcal/mol for κ-OOMP2 and to 0.01 kcal/mol for MP2.5:κ-OOMP2. Consequently, κ-MP methods are suitable for describing dispersion-bound complexes because the regularizer damps the correlation energy appropriately.

The DFT functional ωB97M-V performs well with an RMSD of 0.15 kcal/mol and is only outperformed by MP2.5:κ-OOMP2. B3LYP-D3 performs worse with an RMSD of 0.34 kcal/mol and is also outperformed by κ-MP2. The coupled cluster method CCSD performs poorly in comparison to MP2.5:κ-OOMP2 with an RMSD of 0.70 kcal/mol (CCSD/CBS) but the scaled version SCS(MI)-CCSD performs similarly to MP2.5:κ-OOMP2 (RMSD: 0.08 kcal/mol SCS(MI)-CCSD/CBS).[465]

In summary, the top performer is MP2.5:κ-OOMP2 with an RMSD of 0.10 kcal/mol. In addition, MP2.5:κ-OOMP2 results in a smaller spread in the data and fewer outliers than the other methods (see boxplots in figure 5.2 (c) & (d)).

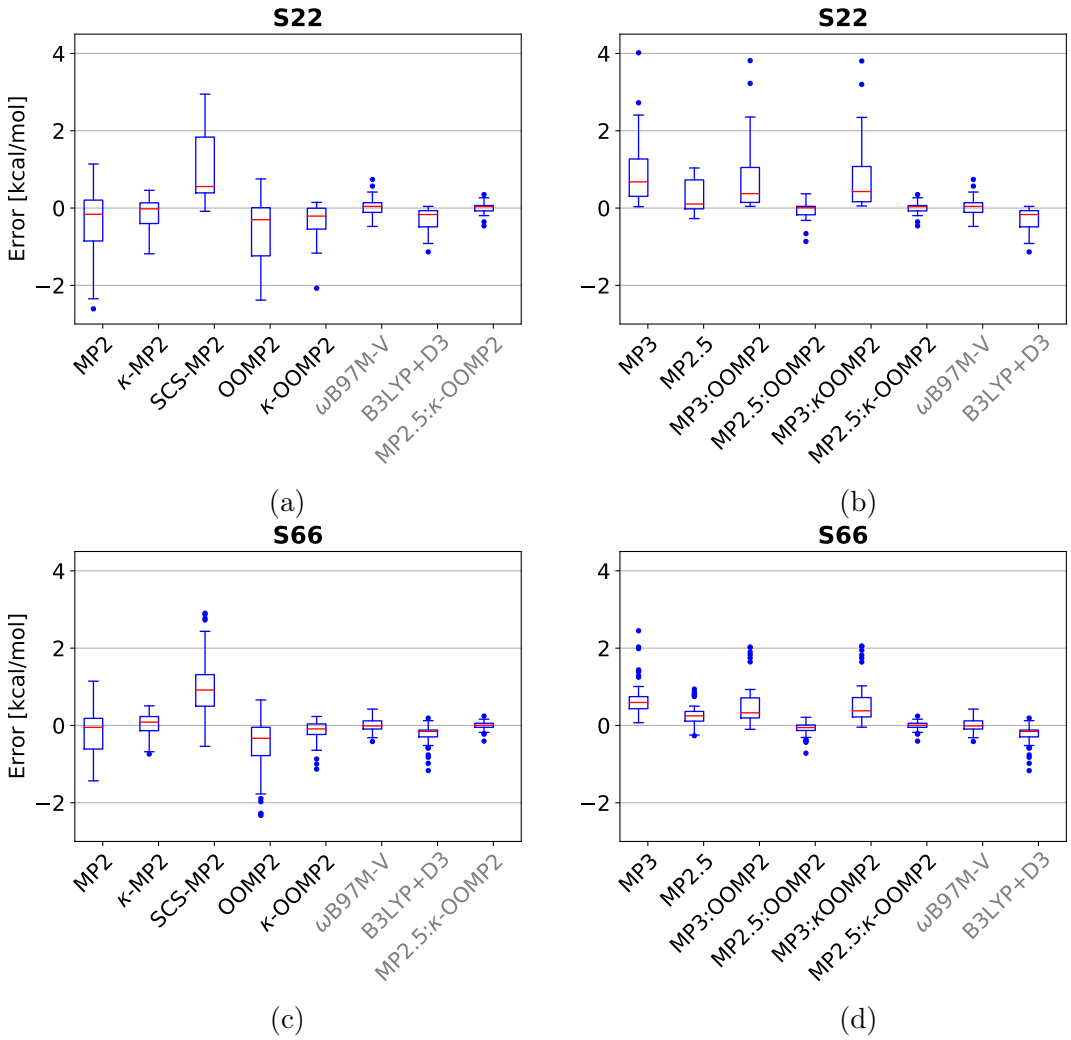

Figure 5.2: Boxplots of the S22 & S66 data-sets: (a) MP2 methods for S22, (b) MP3 methods for S22; (c) MP2 methods for S66, (d) MP3 methods for S66. Red lines mark the median deviation, boxes bound the central 50% of the data, whiskers enclose all data points within 1.5 times the inter-quartile range of the box edges, and points denote outlying data.

A24

The A24[461] benchmark set consists of 24 very small non-covalent complexes including the water-ammonia dimer and methane-ethane dimer. Among the second-order methods, only OOMP2 (RMSD: 0.13 kcal/mol) shows a considerable improvement over MP2 (RMSD: 0.17 kcal/mol). Among the third-order methods, the top performers are MP2.5:κ-OOMP2 with an RMSD of 0.09 kcal/mol, MP2.5:OOMP2 with an RMSD of 0.09 kcal/mol. ωB97M-V performs similarly with an RMSD of 0.09 kcal/mol. In contrast, CCSD performs significantly worse with an RMSD of 0.38 kcal/mol (CCSD interaction energies for A24 and HSG were taken from ref. [392] (CCSD/aTZ)). The spread in the error is smallest for MP2.5:κ-OOMP2 (see boxplots in figure D.8). Overall, MP2.5:κ-OOMP2 is the top performer.

DS14

The DS14[472] benchmark set comprises of 14 non-covalent dimers with sulfur-containing species, e.g. the water-hydrogen sulfide dimer and methane-hydrogen sulfide dimer. The largest data point is the benzene-dimethyl sulfide dimer (21 atoms). The top performer on this data set is MP2.5:κ-OOMP2 with an RMSD of 0.05 kcal/mol, significantly outperforming ωB97M-V with an RMSD of 0.13 kcal/mol. Among second-order methods κ-OOMP2 performs best with an RMSD of 0.10 kcal/mol. Standard MP2 has an RMSD of 0.33 kcal/mol; the poor performance mainly stems from overbinding of the two benzene systems (benzene-dimethyl sulfide and benzene-methanethiol). Regularization almost halves (κ-MP2 RMSD of 0.18 kcal/mol) the MP2 RMSD by improving on the two outliers (see boxplots in figure D.8), whereas orbital optimizing without regularization leads to slightly worse results (OOMP2 RMSD of 0.39 kcal/mol).

HB15

The HB15[473] benchmark set consists of 15 medium-sized ionic hydrogen bonded systems relevant to biology like the guanidinium-methanol dimer (16 atoms). The top performer is MP2.5:κ-OOMP2 with an RMSD 0.13 kcal/mol. Scaling the MP3 correlation energy and using κ-OOMP2 reference orbitals significantly improves the results from MP3 (RMSD of 0.44 kcal/mol). All second-order methods perform very similarly as neither regularization nor orbital optimization significantly improves the binding energies [e.g. MP2: 0.36 kcal/mol, κ-MP2: 0.34 kcal/mol]. It is noteworthy that all MP methods outperform the popular B3LYP functional, which has an RMSD of 0.75 kcal/mol. Charge delocalization error[500] makes these systems more challenging for DFT.

HSG

The HSG[474] data set comprises 21 NCIs relevant to protein-ligand docking. The largest data point is the butane-*N*-tert-butylformamide dimer (32 atoms). The top performer is MP2.5:κ-OOMP2 with an RMSD of 0.05 kcal/mol; runners-up are κ-OOMP2 with an RMSD

of 0.12 kcal/mol performing similarly to ωB97M-V (0.11 kcal/mol). Interestingly, in this data set neither regularization (κ-MP2: 0.29 kcal/mol) nor OOMP2 (0.28 kcal/mol) significantly improve upon standard MP2 (0.30 kcal/mol), only the combination of both is effective via κ-OOMP2.

X40

The X40[465] data set comprises 31 π-stacking, halogen bonding and hydrogen bonding interactions containing halogenated molecules (we excluded the 9 dimers containing iodide in accordance with ref. [20]). The largest system is bromobenzene-trimethylamine dimer (25 atoms). Among the second-order methods, κ-OOMP2 performs best with an RMSD of 0.28 kcal/mol; κ-MP2 performs similarly with 0.30 kcal/mol. Both improve upon standard MP2 with RMSD of 0.58 kcal/mol. Similar to other data sets, the poor performance of MP2 can be attributed to two π-stacked benzene data points, which MP2 overbinds by $\sim$2 kcal/mol (see boxplots in figure D.10). Regularization alone significantly improves the binding of those outliers (κ-MP2 has an RMSD of 0.30 kcal/mol).

Among the third-order methods, the top performer is MP3:κ-OOMP2 with an RMSD of 0.09 kcal/mol as both spin scaling and κ-OOMP2 (and OOMP2) reference orbitals improve the energetics significantly. This is illustrated by the comparison to MP2.5 (0.28 kcal/mol) and MP3:κ-OOMP2 (0.68 kcal/mol). The ωB97M-V functional performs quite well (0.22 kcal/mol), surpassing B3LYP-D3(BJ) (0.34 kcal/mol). CCSD performs worse than the top MP3 methods with an RMSD of 0.48 kcal/mol (CCSD/CBS[465]) but SCS(MI)-CCSD performs similarly (SCS(MI)-CCSD/CBS RMSD: 0.08 kcal/mol[465]). Overall, MP2.5:κ-OOMP2 is the top performer with an RMSD of 0.09 kcal/mol, which is three times lower than the best second order method (κ-OOMP2).

HW30

The HW30[475] data set contains 30 hydrocarbon-water dimer interactions including the benzene-water and butane-water dimers. Among the second-order methods, κ-MP2 performs best with an RMSD of 0.12 kcal/mol improving significantly on standard MP2 with an RMSD of 0.45 kcal/mol. Orbital optimization does improve upon MP2 with an RMSD of 0.16 kcal/mol for OOMP2. However, κ-OOMP2with a RMSD of 0.13 kcal/mol performs slightly worse than k-MP2. Among the third-order methods, the top performer is MP2.5:κ-OOMP2 with an RMSD of 0.04 kcal/mol improving upon MP2.5 (0.09 kcal/mol). The popular B3LYP-D3 (0.17 kcal/mol) and ωB97M-V (0.23 kcal/mol) perform worse than both top performing MP2 and MP3 methods. The overall top performer is MP2.5:κ-OOMP2.

NC15

The NC15[476] data set comprises 15 very small non-covalent interactions like the argon dimer. Among the second-order methods, κ-OOMP2 is the top performer (0.059 kcal/mol), even though standard also MP2 performs well (0.088 kcal/mol). Among the third-order

methods, the top performers set are MP2.5:OOMP2 (0.052 kcal/mol), MP2.5:κ-OOMP2 (0.056 kcal/mol). However, none of the perturbative methods outperform ωB97M-V (0.040 kcal/mol).

AlkBind12

The AlkBind12[477] benchmark set comprises 12 medium-sized dispersion-bound saturated and unsaturated hydrocarbon dimers including the benzene dimer. Standard MP2 systematically overbinds these dispersion-bound complexes (MSD: -0.37 kcal/mol) and consequently performs poorly with an RMSD of 0.69 kcal/mol. Both κ-OOMP2 and κ-MP2 improve upon MP2 with RMSDs of 0.24 kcal/mol and 0.43 kcal/mol, respectively. The poor performance of MP2 results mainly from one outlier, the benzene dimer, with a deviation of -2.00 kcal/mol. Notably κ-OOMP2 reduces this error to -0.48 kcal/mol. In contrast, all of the unscaled MP3 methods systematically underbind these dispersion complexes (e.g. MP3 MSD: 0.754 kcal/mol). The scaling (MP2.5) improves the RMSD to 0.30 kcal/mol and κ-OOMP2 reference orbitals in MP2.5:κ-OOMP2 further improve the results (RMSD of 0.09 kcal/mol). ωB97M-V (0.12 kcal/mol), CCSD (RMSD 0.85 kcal/mol; CCSD/CBS[477]) and SCS(MI)-CCSD (RMSD: 0.18 kcal/mol; SCS(MI)-CCSD/CBS[477]) are outperformed by MP2.5:κ-OOMP2 making it the overall top performer for this set.

CO2Nitrogen16

The CO2Nitrogen16[478] benchmark set includes 16 model complexes for the absorption of CO_2 onto eight polyheterocyclic aromatic compounds ranging from pyridine and pyrazine to 1,6-diazacoronene. However, we excluded the two largest diazacoronene data points due to difficulty obtaining MP3 energies for these systems. Among the second-order methods κ-MP2 performs best with an RMSD of 0.31 kcal/mol followed by κ-OOMP2 (0.39 kcal/mol). Standard MP2 significantly overbinds (MSD: -0.30 kcal/mol) resulting in an RMSD of 0.64 kcal/mol. Among the third-order methods, the top performer for this set is MP2.5:κ-OOMP2 with an RMSD of 0.11 kcal/mol improving upon MP2.5 (0.36 kcal/mol). Both B3LYP-D3 (0.07 kcal/mol) and ωB97M-V (0.09 kcal/mol) functionals perform significantly better than all MP methods.

HB49

The HB49[479, 499, 501] data set consists of 49 small- and medium-sized hydrogen bonding complexes. The sets includes both neutral-neutral and ion-neutral complexes and thus governs a wide range of interaction energies (3–25 kcal/mol). A typical example is the guanidinium–methanol dimer (16 atoms). Among the second-order methods, the top performer on this set is κ-OOMP2 with an RMSD of 0.18 kcal/mol, halving the RMSD in comparison to standard MP2 (0.40 kcal/mol). This is the best-performing method on this set. For comparison, with regularization alone, κ-MP2 already improves significantly upon standard MP2 with an RMSD of 0.29 kcal/mol. Among the third-order methods MP2.5:OOMP2

performs best with an RMSD of 0.20 kcal/mol and MP2.5:κ-OOMP2 performs similarly (RMSD: 0.21 kcal/mol). Both κ-OOMP2 and MP2.5:κ-OOMP2 outperform ωB97M-V (0.24 kcal/mol) and B3LYP (0.59 kcal/mol).

Ionic43

The Ionic43[480] data set comprises 43 small- to medium-sized charged non-covalent interactions (cationic-neutral, anionic-neutral and anion-cation dimer), e.g. the formate-water dimer. Among the second-order methods (and indeed all methods), the top performer is κ-OOMP2 with an RMSD of 0.53 kcal/mol improving upon both standard MP2 (0.90 kcal/mol) and κ-MP2 (0.74 kcal/mol). Among the third-order methods, MP2.5:κ-OOMP2 performs best with an RMSD of 0.63 kcal/mol. Both ωB97M-V (0.70 kcal/mol) and B3LYP (0.80 kcal/mol) perform worse than most MP methods as these systems are prone to charge delocalization error making them more challenging for DFT calculations[324]. The boxplots indicate that the error is distributed similarly in all of the top performing methods (see figure D.12).

Discussion

The accumulated NCED data category has 356 data points and the top performer is MP2.5:κ-OOMP2 with an RMSD of 0.25 kcal/mol. Notable among the second-order methods are κ-OOMP2 with an RMSD 0.33 kcal/mol and κ-MP2 with an RMSD of 0.37 kcal/mol; both improve upon standard MP2 by almost a factor of two (MP2 RMSD: 0.63 kcal/mol). This is further illustrated by figure 5.3 which shows a histogram of the absolute deviation from the reference energies for MP2, κ-MP2, κ-OOMP2 and MP2.5:κ-OOMP2. It shows how the error distribution is concentrated towards the smaller deviations, and larger deviations are significantly reduced moving from MP2 to MP2.5:κ-OOMP2. A similar picture emerges from boxplots of the NCED data category in figure 5.4. κ-MP2 reduces the spread of the data in both directions (over and underbinding) compared to MP2 but is more effective for overbinding. The quite systematic success of regularized κ-MP2 over standard MP2 is very encouraging: it appears to be a preferable choice for a wide range of NCI. The value of regularization is also clear from the fact that OOMP2 is significantly less effective than κ-OOMP2. While κ-OOMP2 outperforms κ-MP2 (overall and in 8 of 13 datasets), the energetic improvements for these mostly closed shell systems from regular MP2 to κ-OOMP2 stem mainly from the κ-regularization rather than the orbital optimization.

In contrast, scaled MP3 (i.e. with HF orbitals) removes many of the overbinding outliers at the cost of a significant underbinding bias. Interestingly, the scaled MP3 methods not only remove underbinding outliers but also decrease the spread of the error more than just the κ-regularization. These findings are consistent with the fact that adding a scaled MP3 correlation energy on top of κ-MP2 led to a very small c_3 coefficient with only marginal improvement. Both the addition of the third-order term and the κ-regularization damp the correlation energy so as to remove the overbinding.

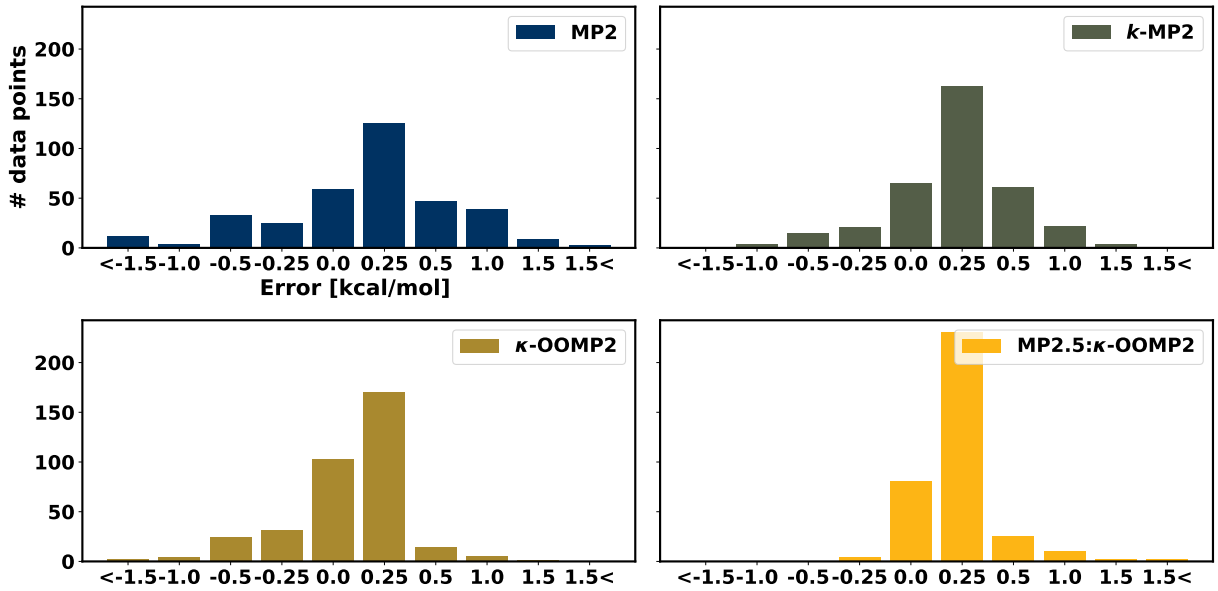

Figure 5.3: Histogram of the absolute deviation of MP2 (top left panel), κ-MP2 (top right panel), κ-OOMP2 (bottom left panel) and MP2.5:κ-OOMP2 (bottom right panel).

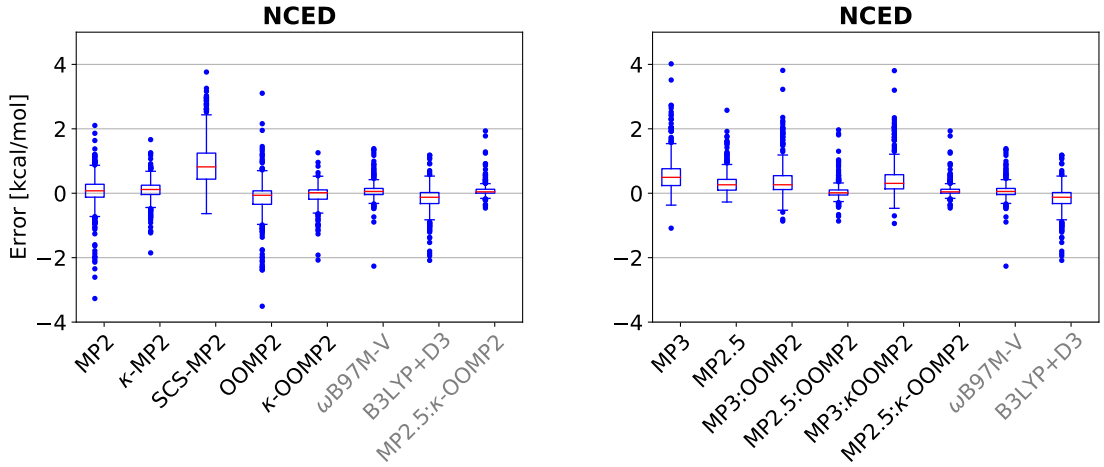

(a) (b)

Figure 5.4: Boxplots of the NCED data category for (a) MP2 methods, (b) MP3 and DFT methods. Red lines mark the median deviation, boxes bound the central 50% of the data, whiskers enclose all data points within 1.5 times the inter-quartile range of the box edges, and points denote outlying data. DFT and MP2.5:κ-OOMP2 are included in all plots for comparison.

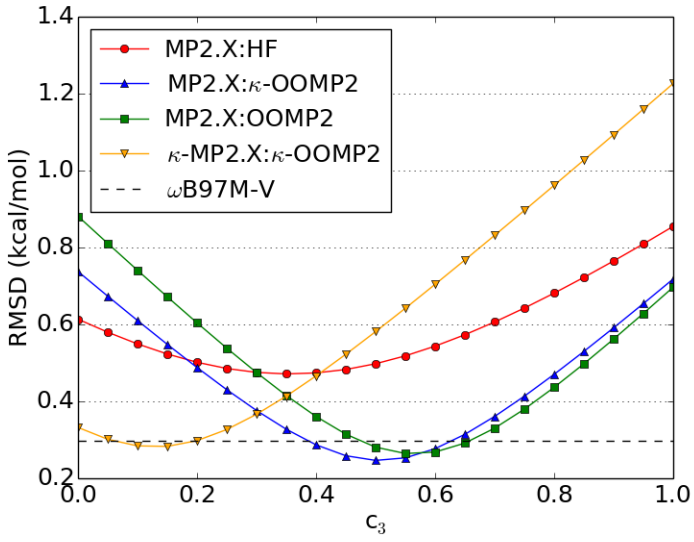

Figure 5.5: Dependence of the the root-mean square deviation on the scaling of the third-order energy (c_3) for the whole NCED data data category; in kcal/mol; for four scaled MP2.X methods (MP2.X, MP2.X:OOMP2, MP2.X:κ-OOMP2, κMP2.X:κ-OOMP2); for reference, the RMSD of ωB97M-V is depicted as a flat line.

For the third order methods, using all of NCED to train the c_3 scaling parameter leads to the conclusion that the S66 training set results are transferable to the total NCED data category: the optimal c_3 values are close to 0.5 with 0.35, 0.50, and 0.55 for MP2.X, MP2.X:κ-OOMP2, and MP2.X:OOMP2, respectively. The dependence of the RMSD with respect to c_3 for MP2.X:κ-OOMP2, and MP2.X:OOMP2 is depicted in figure 5.5. This data supports keeping the established factor of 0.5 yielding MP2.5, MP2.5:OOMP2 and MP2.5:κ-OOMP2.

The standard MP3 RMSDs are in general worse than standard MP2; there is an improvement in only 1 (HW30) out of 13 data sets. Consistent with conventional wisdom, it cannot be recommended for NCI. Both scaling the third-order energy by a factor of 0.5 (MP2.5) or changing the reference orbitals (e.g. MP3:κ-OOMP2) improves the results. The combination of both in MP2.5:κ-OOMP2 yields very high accuracy in all benchmark sets. It is the top performer in 8 out of 13 benchmark sets and among the top performing methods in the others. It outperforms CCSD in all cases and even performs similarly to SCS(MI)-CCSD, which is more expensive (iterative $\mathcal{O}(N^6)$) and the spin scaling parameters were trained to perform well on NCI. We note that MP2.5:OOMP2 has a very similar RMSD in all benchmark sets; thus it is, perhaps surprisingly, a good alternative if the κ-regularizer is not available (we shall see later that ωB97X-V orbitals are another excellent alternative).

NCD

The NCD data category includes TA13, XB18, Bauza30, XB51 augmented with the Orel26rad data set. By contrast with NCED, this class is more difficult due to self-interaction errors, and also includes open-shell cases for which HF orbitals may exhibit significant spin contamination. The results for all data sets of that category are summarized in table 5.4.

TA13

The TA13 benchmark set includes thirteen small binary radical-solvent complexes like lithium water dimer. [209] For the MP2 methods, orbital optimization is necessary in this benchmark set to remove spin-contamination of the reference orbitals as illustrated by the improvement of κ-OOMP2 (0.88 kcal/mol) over standard MP2 (using canonical UHF reference orbitals, 2.14 kcal/mol). The maximum deviation in MP2 is seen in the $HF\cdots CO^+$ dimer with -5.07 kcal/mol. However, the RMSD for MP2 can be further decreased to 1.65 kcal/mol by using a restricted-open shell HF (RO-HF) reference.[172] Among the third-order methods, the top performer is unscaled MP3:κ-OOMP2 with an RMSD of 0.63 kcal/mol and the largest deviation is seen in $H_2O\cdots Al$ dimer with 1.04 kcal/mol. Scaling of the third-order energy significantly increases the error to 0.93 kcal/mol. This stems mainly from overbinding of both the $H_2O\cdots F$ and $H_2O\cdots Cl$ with the scaled MP3 energy contribution. All complexes are sensitive to the charge delocalization error and consequently both B3LYP (3.85 kcal/mol) and ωB97M-V (2.85 kcal/mol) perform poorly. CCSD performs similarly to κ-OOMP2 with an RMSD of 0.89 kcal/mol. Overall the top performer is MP3:κ-OOMP2 with an RMSD of 0.63 kcal/mol.

XB18

The XB18[486] contains 8 halogen bonded complexes such as $Br_2\cdots$ NCH (we omitted the 10 iodide containing complexes originally included). Furthermore, we used a slightly different computational set-up: the aug-cc-PVTZ-PP basis and the corresponding ECP were used for Br[249] and the frozen core approximation was employed to harmonize with the reference values which were also generated with aug-cc-PVTZ-PP and ECP for Br.[486]

Among the second-order methods κ-MP2 (0.26 kcal/mol) performed best followed by standard MP2 (0.31 kcal/mol). Notably, orbital optimization worsens the results for both κ-OOMP2 (0.50 kcal/mol) and OOMP2 (1.01 kcal/mol). Among the third-order methods, MP2.5:κ-OOMP2 performs best (0.35 kcal/mol) performing slightly worse than the MP2 methods. The top MP methods outperform B3LYP (0.37 kcal/mol) and are similar to ωB97M-V: (0.27 kcal/mol). CCSD performs worse than most MP methods with an RMSD of 0.66 kcal/mol suggesting that the inclusion of CC triples is important for halogen bonding motifs. In contrast, SCS(MI)-CCSD performs remarkably well with an RMSD of 0.11 kcal/mol (SCS(MI)-CCSD/aQZ); RMSD adjusted to the subset investigated here. Overall, the top performing method is κ-MP2 with an RMSD of 0.26 kcal/mol.

Bauza30

The Bauza30[487, 502] data set includes 30 small halogen, chalcogen, and pnicogen bonded complexes, e.g. the $Cl^- \cdots$ BrF complex. The top performer is standard MP2 with an RMSD of 0.72 kcal/mol. Both regularization and orbital optimization increase the RMSD (κ-MP2: 0.98 kcal/mol, OOMP2: 1.76 kcal/mol). The runner-up is MP2.5:κ-OOMP2 with an RMSD of 0.88 kcal/mol which is still a significant improvement over B3LYP (RMSD: 1.87 kcal/mol). However, all MP methods perform worse than ωB97M-V with an RMSD of 0.59 kcal/mol.

CT20

The CT20[488] data set is comprised of 20 small ground state charge-transfer complexes of NF_3 with HCN, HNC, HF, or ClF. All MP2 methods perform very similarly but the top performer is κ-MP2 (0.10 kcal/mol). Among the third-order methods, MP3:OOMP2 (RMSD of 0.09 kcal/mol) and MP3:κ-OOMP2 (RMSD of 0.10 kcal/mol) also achieve virtually the same accuracy. All MP methods outperform B3LYP, which has an RMSD of 0.28 kcal/mol, but not ωB97M-V, which has an RMSD of 0.08 kcal/mol.

XB51

The XB51[486] contains 20 halogen bonded complexes such as $Br_2 \cdots$ FCCH dimer; we omitted the 31 iodide containing complexes and the HLi complex following ref. [20]. Furthermore, we used a slightly different computational set-up: the aug-cc-PVTZ-PP basis and the corresponding ECP were used for Br[249] and the frozen core approximation was employed to harmonize with the reference values which were also generated with aug-cc-PVTZ-PP and ECP for Br.[486]

Among the second-order methods, MP2 (RMSD: 0.36 kcal/mol) and κ-MP2 (0.36 kcal/mol) and κ-OOMP2 (0.36 kcal/mol) perform similarly. Interestingly both MP2 and κ-OOMP2 also slightly overbind with MSDs of -0.24 kcal/mol and -0.16 kcal/mol, respectively; but κ-MP2 underbinds with an MSD of 0.21 kcal/mol. Among the third-order methods, the top performer is MP2.5:κ-OOMP2 with an RMSD of 0.34 kcal/mol and a MSD of -0.25 kcal/mol suggesting that MP2.5:κ-OOMP2 slightly overbinds. MP2.5:κ-OOMP2 improves upon MP2.5 (0.54 kcal/mol) but is only slightly better than MP2. For comparison, B3LYP-D3 performs significantly worse with an RMSD of 1.05 kcal/mol, while but ωB97M-V performs well with an RMSD of 0.26 kcal/mol. Interestingly, both MP2.5:κ-OOMP2 and κ-OOMP2 outperform the more expensive CCSD (CCSD/aTZ) with an RMSD of 0.67 kcal/mol (adjusted to the subset investigated here).

Orel26rad

The Orel26[231] data set comprises 26 cationic radical dimer complexes of aromatic (hetero)cycles, such as $py^{\bullet+} \cdots py$ (where py is pyridine). The largest system is the tetrathia-

fulvalene dimer complex (28 atoms). We use ROHF as a reference for the MP2 results as suggested in ref. [231] due to severe spin contamination in the UHF wave function for these systems; while using UKS and UOOMP2 as those theories are less prone to spin contamination due to inclusion of electron correlation in the SCF procedure. We note that properly converging ROHF (and RO-SCF in general) can be significantly more challenging than UHF and thus is less desirable.

Among second-order methods, the top performer is κ-OOMP2 with an RMSD of 0.59 kcal/mol. κ-MP2 (RO reference) with an RMSD of 1.53 kcal/mol significantly improves on standard MP2 with an RMSD of 3.03 kcal/mol. MP2 strongly overbinds these dispersion-dominated interactions with an MSD of -2.36 kcal/mol (maximum deviation of -6.08 kcal/mol for the bithiophene dimer (π-stacked)). Interestingly, κ-regularization seems to slightly over-regularize which results in underbinding with an MSD of 1.29 kcal/mol and the maximum deviation is 2.91 kcal/mol for the thiophene dimer (π-stacked). In contrast, κ-OOMP2 only slightly overbinds with an MSD of -0.26 kcal/mol and a small and balanced spread of errors. The largest deviation is the bithiophene dimer (-1.32 kcal/mol); see boxplots in figure 5.6.

We used a more compact basis (def2-tzvpd[247, 248] and corresponding auxiliary basis[255, 496, 497]) for the MP3 calculations of the eight larger systems to reduce the computational cost (tetrathiafulvalene, thienothiophene, bifuran and bithiophene complexes; two isomers each). We checked the difference between aug-cc-pVTZ and def2-tzvpd for a few cases and the differences in the interaction energies were between 0.2–0.5 kcal/mol (pyridine dimer, thiophene and thienothiophene; see appendix D). Thus, the reported RMSDs for the MP3 methods have a mixed basis. However, the same trends hold if the larger systems are excluded. The top performer among the MP3 methods is MP2.5:κ-OOMP2 with an RMSD of 0.78 kcal/mol and an MSD of -0.58 kcal/mol. The maximum deviation is the thiophene dimer (-1.29 kcal/mol).

For context, these systems are quite challenging even for good hybrid DFT methods due to delocalization error, as illustrated by the high RMSDs of B3LYP-D3 (5.67 kcal/mol) and ωB97M-V (1.59 kcal/mol).

In summary, both MP3 and the κ-regularizer damp the correlation energy to avoid strong overbinding. κ-OOMP2 is recommended for these systems as the top performer. It restores spin-symmetry and yields accurate binding energies at moderate cost.

Discussion

The TA13 and Orel26rad results show the importance of good reference orbitals for radical and aromatic systems as a poor mean-field reference yields artificial symmetry breaking. This is illustrated by the good performance of κ-OOMP2 in both data sets. The κ-regularizer improves the energetics in both cases for OOMP2 (but for MP2 only in Orel26rad).

In the NCD data category the optimal c_3 deviates from 0.5 in several data sets: TA13 is the only data set where the unscaled MP3:κ-OOMP2 is the top performer as there is no minimum for the scaling parameter c_3 between 0.0 and 1.0. The optimal scaling for halogen

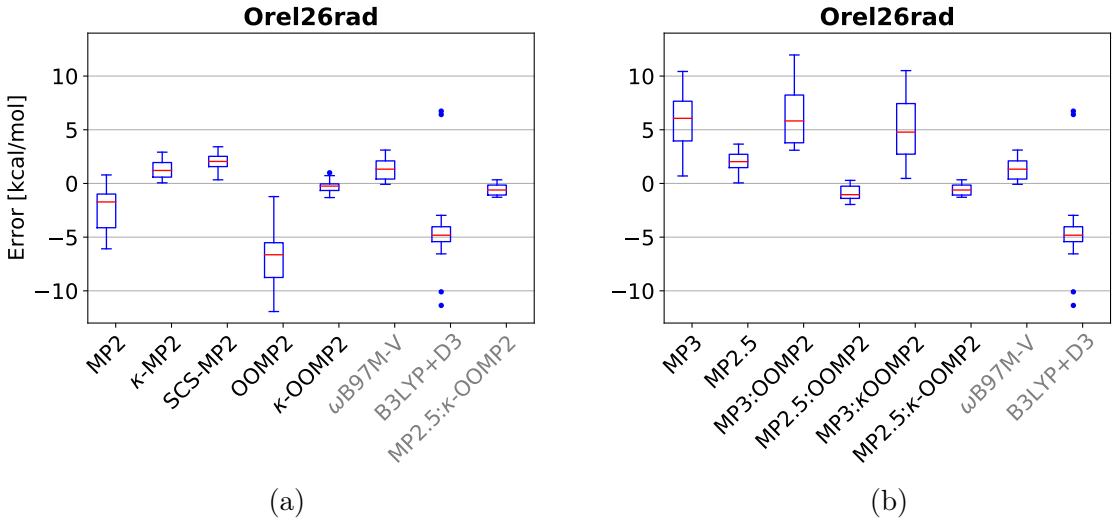

(a) (b)

Figure 5.6: Boxplots of the Orel26rad data set for (a) MP2 methods, (b) MP3 methods. Red lines mark the median deviation, boxes bound the central 50% of the data, whiskers enclose all data points within 1.5 times the inter-quartile range of the box edges, and points denote outlying data. DFT and MP2.5:κ-OOMP2 are included in all plots for comparison.

bonding seems to be around 0.7 for both M2.X:OOMP2 and MP2.X:κ-OOMP2 but 0.2 for MP2.X. Similary for CT20, the optimal c_3 parameters are 0.80 for MP2.X:κ-OOMP2, 0.85 for MP2.X:OOMP2 and 0.15 for MP2.X.

For halogen bonding, standard MP2 performs remarkably well. It is the top performer in Bauza30 and performs only slightly worse than the top performing MP3 methods in XB18 and XB51. The top performer for halogen bonding is MP2.5:κ-OOMP2 but it provides less than 0.1 kcal/mol improvement for the XB sets and performs worse than MP2 in Bauza30 and thus is not worth the higher compute cost.

Potential energy surfaces

In order to gauge any distance dependence of our conclusions on accuracy of MP2 and MP3-based methods, we investigated potential energy surface (PES) scans for a few important NCI binding motifs. For dispersion-dominated interactions we chose the benzene dimer; the reference geometries and values are taken from the NBC10 data set[481, 503]. We also use two hydrogen bonding motifs from S66x8[484]: the water dimer and methylamine (CH_3NH_2) dimer (classified as a mixed interaction).

The benzene dimer PES consists of 17 points from 3.2 to 10 Å. MP2 over-binds significantly, yielding an RMSD of 1.62 kcal/mol. The top performer is SCS-MP2 with an RMSD of 0.05 kcal/mol. Both κ-regularization (κ-MP2 0.36, κ-OOMP2 0.27) and all three MP2.5 methods also yield high accuracy (MP2.5 0.14, MP2.5:κ-OOMP2 0.13, MP2.5:OOMP2 0.08).

The PESs for MP2, κ-MP2, κ-OOMP2, MP2.5, MP2.5:κ-OOMP2 (including the CCSD(T) reference values taken from ref. [481]) are depicted in the left panel of figure 5.7. The plot shows that all methods besides standard MP2 produces accurate PESs. However, κ-MP2, κ-OOMP2, and MP2.5 underbind around the minimum, whereas MP2.5:κ-OOMP2 slightly overbinds ($\sim$0.15 kcal/mol).

Next, we investigate two hydrogen binding motifs from S66x8[484]; in both cases 8 points are taken along the PES based on the scaled equilibrium bond distance (r_0): 0.90, 0.95, 1.0, 1.05, 1.10, 1.25, 1.50, 2.0, where r_0 is 2.01 Å for the H_2O dimer and 2.28 Å for the CH_3NH_2 dimer. The top performer for the combined surfaces are κ-OOMP2, MP2.5:κ-OOMP2 and MP2.5:OOMP2 all with an RMSD of 0.04 kcal/mol. Both OOMP2 (0.10 kcal/mol) and κ-MP2 (0.11 kcal/mol) perform similarly to MP2 (0.11 kcal/mol), but SCS-MP2 performs significantly worse (0.63 kcal/mol). The PESs are depicted in figure 5.7, MP2.5 significantly underbinds around the minimum for both hydrogen bonds, MP2 underbinds for the water dimer and κ-MP2 for CH_3NH_2 dimer. κ-OOMP2 and MP2.5:κ-OOMP2 produce very accurate PES for both hydrogen bonding motifs.

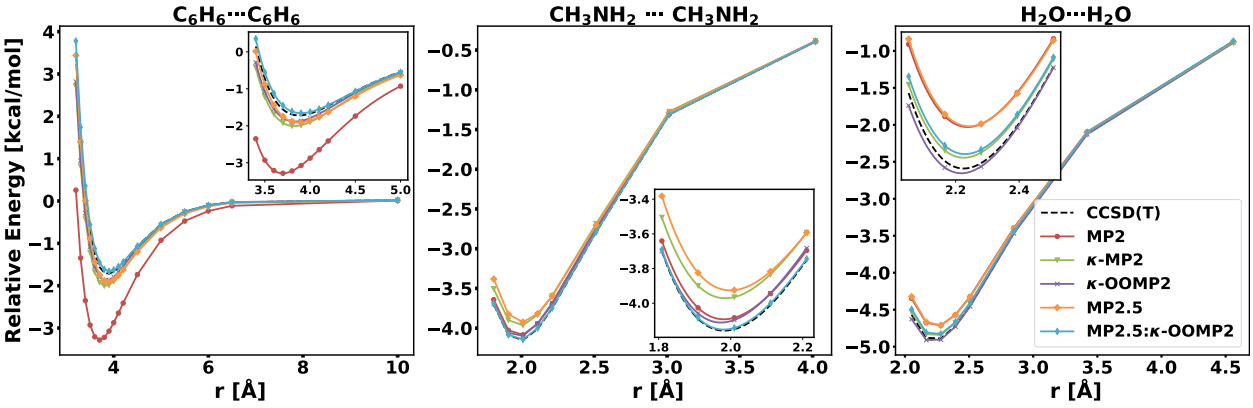

Figure 5.7: PES scan of the π-stacked benzene dimer with insets for the minimum region (geometries and reference values taken from the NBC10[481, 503] data set and PES scan of CH_3NH_2 dimer and water dimer (geometries and reference values taken from the S66x8[484] data set).

Use of KS-DFT Orbitals for MP2.X

Another possible choice for reference orbitals, which already incorporate electron correlation, are KS-DFT orbitals. Our group recently demonstrated similar performance of (κ-)OOMP2 orbitals and KS-DFT orbitals for MP3 and MP2.X methods.[490] In addition, these results were robust with respect to the functional choice; even local functionals provided a good set of reference orbitals.[490] Consequently, the MP2.X:DFT is a potential alternative, especially if (κ-)OOMP2 capabilities are not available in the software package of choice.

To this end, we tested MP3:ωB97X-V and MP2.5:ωB97X-V for a subset of data sets. We not only use classic NCI data sets as A24 and S22 but also include those where charge delocalization is more prominent like Ionic43, TA13 and Orel26rad; the results are summarized in figure 5.6. In most cases the performance of significantly better MP2.5:ωB97X-V is better than MP3:ωB97X-V (except in TA13) and thus the following discussion focuses on the former. The performance of MP2.5:ωB97X-V is comparable to MP2.5:κ-OOMP2, even slightly better in some cases. For instance, in S22, the RMSD of MP2.5:ωB97X-V is 0.08 kcal/mol, a factor of two lower than MP2.5:κ-OOMP2, which is the top performing MP method. A similar trend is observed for the A24 data set: MP2.5:ωB97X-V outperforms MP2.5:κ-OOMP2 slightly with an RMSD of 0.07 kcal/mol. We note, however, that such an error reduction occurs at an energy scale comparable to the basis set error.

Interestingly, as seen for Ionic43, TA13 and Orel26rad in figure 5.6, MP2.5:ωB97X-V works reasonably well even when the KS orbitals themselves behave poorly due to self-interaction error (SIE). For Ionic43, MP2.5:ωB97X-V performs well with an RMSD of 0.62 kcal/mol, similar to MP2.5:κ-OOMP2 (RMSD: 0.63 kcal/mol) and ωB97M-V (RMSD: 0.70 kcal/mol) but is not able to outperform the top performer κ-OOMP2 (RMSD: 0.53 kcal/mol). The TA13 data set comprises systems which are strongly affected by SIE and consequently most functionals perform poorly (e.g. ωB97M-V with an RMSD of 2.85 kcal/mol). Nonetheless, MP3:ωB97X-V performs surprisingly well with an RMSD of 0.70 kcal/mol, which is close to MP3:κ-OOMP2 (RMSD: 0.62 kcal/mol). This is surprising especially when considering the good performance of κ-OOMP2 itself (RMSD: 0.88 kcal/mol) versus the poor performance of density functionals on this set. For the Orel26rad data set we omitted the eight larger systems involving tetrathiafulvalene, thienothiophene, bifuran and bithiophene complexes due to computational cost. Consequently, we adjusted the RMSD for the other methods to that subset accordingly to assure comparability. MP2.5:ωB97X-V performs similarly to both MP2.5:κ-OOMP2 and ωB97M-V.

In summary, MP2.5:ωB97X-V is a comparable method to MP2.5:κ-OOMP2 and is also surprisingly reliable even for systems where spin-contamination is present, see table 5.7 for a detailed comparison using various metrics.

5.6 Conclusions

In summary, this work systematically assesses the influence of reference orbitals, regularization and scaling on the performance of second- and third-order Møller-Plesset perturbation theory wavefunction methods for non-covalent interactions (NCI). We employ 19 data sets (A24[461], DS14[472], HB15[473], HSG[474], S22[215], X40[465], HW30[475], NC15[476], S66[464], AlkBind12[477], CO2Nitrogen16[478], HB49[479], Ionic43[480], TA13[209], XB18[486], Bauza30[487] , CT20[488], XB51[486], Orel26rad[231]) covering a wide range of NCI. The data is sub-divided into "easy dimers" (NCED; 356 data points), and "difficult" systems (NCD) that are subject to delocalization errors in DFT and spin-contamination in UHF.

	A24	S22	Ionic43	TA13	Orel26rad
κ-MP2	0.16	0.50	0.74	2.46	1.72
κ-OOMP2	0.16	0.65	0.53	0.88	0.45
MP3:κ-OOMP2	0.20	1.38	1.09	0.62	3.94
MP2.5:κ-OOMP2	0.09	0.18	0.63	0.93	0.92
MP3:ωB97X-V	0.19	1.24	1.10	0.70	3.96
MP2.5:ωB97X-V	0.07	0.08	0.62	1.27	0.71
ωB97M-V	0.09	0.28	0.70	2.85	1.00
ωB97X-V	0.08	0.30	0.81	3.08	2.02

Table 5.6: Results of MP3:ωB97X-V and MP2.5:ωB97X-V for A24, S22, Ionic43, TA13 and Orel26rad (8 data points omitted, see main text); for reference we included the results of κ-MP2, κ-OOMP2, MP3:κ-OOMP2 and MP2.5:κ-OOMP2; RMSD in kcal/mol. For each data set all method cells are colored in a heatmap from green to yellow to red. Low RMSD are represented in green and high RMSD in red.

Method	MP2.5:κ-OOMP2			MP2.5:ωB97X-V		
Set	RMSD	MSD	MaxDev	RMSD	MSD	MaxDev
A24	0.09	0.08	0.24	0.07	0.05	0.16
S22	0.18	0.00	−0.46	0.08	0.02	−0.23
Ionic43	0.63	0.47	1.94	0.62	0.42	2.01
TA13	0.93	0.07	−2.28	1.26	−0.37	−3.64
Orel26rad	0.93	−0.82	−1.29	0.71	−0.60	−1.12

Table 5.7: Comparison (via RMSD, MSD and largest outlier (MaxDev)) of MP2.5:κ-OOMP2 and MP2.5:ωB98X-V for for A24, S22, Ionic43, TA13 and Orel26rad (8 data points omitted, see main text); in kcal/mol.

Furthermore, we include PESs from different hydrogen bonds and dispersion-bound complexes to gauge the accuracy for non-equilibrium geometries.

We test 15 perturbation theory based methods: MP2, κ-MP2, SCS-MP2, OOMP2, κ-OOMP2, MP3, MP2.5, MP3:OOMP2, MP2.5:OOMP2, MP3:κ-OOMP2, MP2.5:κ-OOMP2, and κ-MP3:κ-OOMP2, κ-MP2.5:κ-OOMP2, MP3:ωB97X-V, and MP2.5:ωB97X-V. Furthermore, we compare these methods to the density functionals ωB97M-V and B3LYP-D3 and CCSD. The main findings from this study are:

1. MP2.5:κ-OOMP2 is a very accurate method for NCI providing accurate results in nearly all data sets invested in this study (RMSD on the NCED data category: 0.25 kcal/mol). The improvement over standard MP2.5 is quite statistically significant (RMSD on the NCED data category: 0.50 kcal/mol) Furthermore, MP2.5:κ-OOMP2 performs also well for radical systems, halogen bonding and provides accurate PESs. It performs at least comparably to CCSD and even the spin-scaled CCSD method with parameters specifically optimized for NCI (SCS(MI)-CCSD[463]). Furthermore, we investigated the effect of Kohn-Sham density functional reference orbitals (using ωB97X-V[391]) for NCI as a previous study found promising results[490]. We find that ωB97X-V reference orbitals perform very similarly to using κ-OOMP2 orbitals even in NCD benchmark sets where the self-interaction error is prominent, such as Ionic43, Orel26rad and TA13.

2. We investigated the optimal scaling parameter for all scaled MP3 methods and find that a scaling factor near 0.5 is optimal for the Hartree-Fock reference and also for both OOMP2 and κ-OOMP2 reference orbitals based on the S66 [464] benchmark set (optimal c_3 values were 0.45, 0.55, and 0.60 for MP2.X, MP2.X:κ-OOMP2, and MP2.X:OOMP2, respectively). These optimized parameters were similar for the entire NCED super set (optimal c_3 values were 0.35, 0.50, and 0.55 for MP2.X, MP2.X:κ-OOMP2, and MP2.X:OOMP2, respectively)

3. Limiting ourselves to second order perturbation theory, we find the substantial improvements over MP2 are attained using a κ-MP2 with $\kappa = 1.45E_h^{-1}$, with κ-OOMP2 performing slightly better. It is noteworthy that this value was determined based on the W4-11 thermochemistry benchmark set, and was not optimized for NCI.[40] The RMSD for the NCED data category (356 data points) is 0.33 kcal/mol for κ-OOMP2 and 0.37 kcal/mol for κ-MP2; both improve upon standard MP2 by almost a factor of two (RMSD MP2: 0.63 kcal/mol). In radical systems κ-OOMP2 provides clearly better results as it removes spin-contamination of the reference and damps unphysical contributions to the correlation energy. This is illustrated by the excellent performance of κ-OOMP2 in Orel26rad (RMSD: 0.59 kcal/mol vs 1.53 kcal/mol for κ-MP2 and 3.03 kcal/mol for MP2) and TA13 (RMSD: 0.88 kcal/mol vs 2.46 kcal/mol for κ-MP2 and 2.14 kcal/mol for MP2).

4. We obtain high accuracy in a medium sized basis (aug-cc-pVTZ) with non-HF orbitals (either κ-OOMP2 or DFT) and scaling of the third-order contribution. The success of these MP2/MP3 methods versus CCSD(T) at the complete basis set (CBS) limit is encouraging, and indicates that modified double excitations can compensate for the lack of triples and basis set incompleteness. Accordingly, the scaling of the third-order methods is basis set dependent. We showed that 0.5 is optimal with a triple-zeta basis to approximate CCSD(T)/CBS results. However, a larger fraction of the third-order correlation energy is optimal when a larger basis is used or when CCSD(T) with a finite basis is used as a reference. This means that our results are broadly compatible with the recent success of MP2.8:κ-OOMP2 and MP2.8:DFT against CCSD(T) in a triple zeta basis,[286, 490] on a far more limited set of NCI tests, and some thermochemistry test sets.

Chapter 6

Computational Study of an Iron(II)-Polypyridine Electrocatalyst for CO_2 Reduction: Key Roles for Intramolecular Interactions in CO_2 Binding and Proton Transfer

6.1 Introduction

The world energy consumption is approaching a record high 15000 Mtoe. Fossil fuels are still one of the main energy sources resulting in a continuous rise of CO_2 emissions. [504] This anthropogenic emission yields unprecedented high concentration of CO_2 in the atmosphere which is one of the main driving forces of global climate change. This has focused considerable attention on artificial photosynthesis. [276, 277] The solar driven conversion of CO_2 into fuels or other chemically useful compounds, will not only mitigate the greenhouse effect but also provide a valuable method to obtain fuels in a renewable fashion. The inertness of CO_2 is illustrated by the negative one-electron reduction potential; however, coupled multi-electron and multi-proton reductions make an efficient conversion at modest potentials feasible. Unfortunately, these potentials are similar to the potential of the hydrogen evolution reaction (see Table 6.1). [155] This means that its reduction requires not only energy but also the deployment of a catalyst which is ideally substrate selective, efficient, stable and made out of earth abundant materials. Several strategies are known for efficient CO_2 conversion such as biological [157], hydrogenation [162], photochemical [505], electrochemical [506], or photoelectrochemical reduction. [155, 159, 507] Among possible products CO is one of the most economically viable. [164] It can be further utilized to synthesize fuels using the Fischer-Tropsch process [508].

One approach to reduce CO_2 is to employ heterogeneous catalysts such as earth abundant

metallic electrodes; however, the catalytic mechanisms can be difficult to study, and catalytic activities often suffer from poisoning of the electrode by the intermediates and substrate selectivity. [155, 159, 509–512] Indeed only Cu is capable of reducing CO_2 beyond CO to C1 or C2 hydrocarbons, and not selectively or with high energy efficiency. [513]

As an alternative strategy, molecular homogeneous electrocatalysts can show high selectivity, good turnover numbers, and fast catalytic rates. However, they usually operate at a high overpotential. When operated in aqueous media, proton reduction takes place at a similar potential (see table 6.1); thus, a high selectivity for the CO_2 reduction reaction (CO2RR) over the hydrogen evolution reaction (HER) is especially desirable. The catalyst acts as an electron shuttle between an electrode and CO_2 in solution. It accepts electrons and stabilizes intermediates to facilitate the transformation which results in a smaller overpotential and faster turnover rates. Many different molecular catalysts have been developed but are often based on expensive metals like Re, Ir or Ru. [155, 506] However, many notable catalysts containing earth abundant first row transition metals such as Mn, Co, Fe, Ni, Cu and Zn were developed recently. [165, 396, 397, 401, 514–517] They can be incorporated into covalent or metal organic frameworks [170, 518, 519], attached on surfaces [520, 521] or incorporated into a flow cell architecture [169] to further enhance their activity.

Table 6.1: Reduction potentials of CO_2 and proton reduction at pH = 7 versus NHE. [155, 522]

Reaction			Potential
$2\,H^+ + 2e^-$	$\longrightarrow$	H_2	$E^0 = -0.42$ V
$CO_2 + 2\,H^+ + 2\,e^-$	$\longrightarrow$	$CO + H_2O$	$E^0 = -0.53$ V
$CO_2 + e^-$	$\longrightarrow$	$CO_2^{\cdot -}$	$E^0 = -1.90$ V

In the quest for rational catalyst design, mechanistic studies of both a spectroscopic and computational nature are essential to uncover possible intermediates and intrinsic factors influencing selectivity and activity. Several molecular electrocatalysts for the two electron, two proton reduction of CO_2 to CO were studied thoroughly; most prominently, the $Re(bpy)(CO)_3Cl$ family and its derivatives. Experimental efforts include (spectro) electrochemical analysis, rapid scan Fourier-transform infrared spectroscopy (FTIR) spectroscopy during stopped-flow mixing, kinetic isotope studies and X-ray absorption spectroscopy. [523–530] In addition, a mechanism was proposed using density functional theory (DFT) calculations. [133] Further computational studies elucidated the mechanistic differences between the rhenium and manganese derivatives and explained the importance of weak Brønsted acids for the manganese catalyst. [132, 531] The second protonation was determined to be the rate limiting step which coincides with the proton dependence of the catalytic activity. The high selectivity favoring CO_2 reduction over HER is one of the main advantages of this family of catalysts. Although thermodynamics favors the formation of a hydride intermediate, the

high reaction barrier compared to the essentially barrierless CO_2 addition makes the H_2 pathway kinetically inaccessible.

Another well-studied system is $[Ni(cyclam)]^{2+}$ (cyclam = 1,4,8,11-tetraazacyclotetradecane), which was also investigated using DFT. [516, 532] A single initial reduction of the metal, followed by CO_2 binding is proposed. Next, a proton coupled electron transfer (PCET) step yields a carboxylate anion followed by the concerted second protonation and C–O bond cleavage to yield CO and H_2O. The dissociation of CO then regenerates the catalyst to close the catalytic cycle. The Ni(II)-CO species can also accept an electron and the calculated reduction potentials are much lower than for the initial reduction of the Ni(II) complex. Dissociation of CO from the reduced Ni(I)-CO species is an endergonic process. Therefore, this species was predicted to accumulate during catalysis. [532] This poisoning of the catalyst is also observed experimentally and determined to be rate-limiting [533, 534].

Iron is one of the most earth-abundant elements. Hence, it is especially desirable to use it as the central metal of a catalyst. The prominent catalyst family for the conversion of CO_2 to CO are iron porphyrin-based. They show very high turnover rates accompanied by a high selectivity for CO_2 reduction [401, 535]. The catalytic pathway for the iron tetraphenylporphyrin starts with two initial reductions of the catalyst, a recent combined spectroscopic and computational investigation revealed that both reductions are mainly ligand-centered [536]. This is followed by the formation of a CO_2 adduct, a two step protonation and dehydration. At low acid concentrations, the second protonation is the rate-limiting step. The CO release to regenerate the catalyst is coupled to another reduction. [537, 538] A computational study confirmed that the second protonation has a significantly higher barrier than the first protonation [539]. Further mechanistic studies clarified the role of the pendant phenol groups in the more active heme catalyst: the CO_2 adduct is initially stabilized by the pendant phenol groups through intramolecular hydrogen bonding. The first protonation of the CO_2 adduct is believed to involve proton transfer from the pendant phenol group, followed by reprotonation of the phenoxide ion by external phenol. Thus, the pre-positioned phenol groups act as both hydrogen bonding stabilizers and as local proton donors [382] The second protonation is assumed to occur via a PCET step with concerted cleavage of the C−O bond [382, 540].

The incorporation of proton relays like phenol groups in the secondary and outer coordination spheres is a well-established strategy in bioinspired catalyst design to control product selectivity and enhance catalytic activity. [165, 167, 401, 535, 541–547] Correct positioning of the hydrogen bonding moiety can play crucial role in tuning the activity of the catalyst for CO_2 to CO reduction. [385, 406] To this end, a recent experimental study identified a family of non-heme iron complexes $[Fe(bpy^{R}PY2\,Me)]^{2+}$ with various protic functional groups in the second coordination sphere as a viable catalysts for the conversion of CO_2 to CO in acetonitrile solutions with 11 M H_2O. [385] Among the tested compositions, the ethylamine functional group (R = NHEt) is notable for affording the $[Fe(bpy^{NHEt}PY2\,Me)L_2]^{2+}$ complex with high CO_2 to CO conversion activity, high selectivity against HER, and electrolytically stable for 12 h (see figure 6.1). Interestingly, the Fe complex bearing the more acidic hydroxyl group instead favors production of H_2 CO in a *ca.* 2:1 ratio. [385] The new catalyst features three functional partitions: a reactive metal center, a ligand-based electron reservoir, and

a secondary coordination sphere Brønsted-acidic moiety. However, the mechanistic details remain unclear. This study presents first efforts to elucidate the Fe-catalyzed CO_2 reduction mechanism using electronic structure calculations.

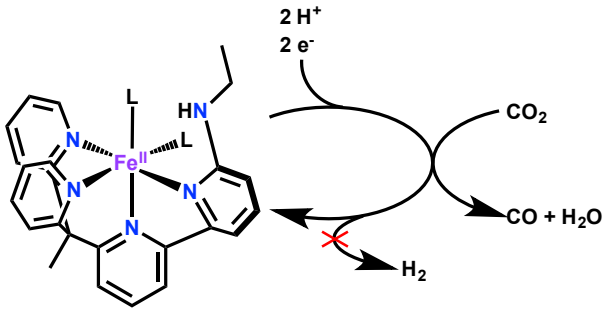

Figure 6.1: The catalytic system $[Fe(bpy^{NHEt}PY2\,Me)L_2]^{2+}$ (L = CH_3CN), a CO_2 reduction catalyst with high selectivity against hydrogen evolution reaction.

6.2 Computational Model

Density functional theory calculations were performed with the Q-Chem package [108] (version 5.0.2) using the ωB97X-D [68] and ωB97M-V [70] functionals. All reported geometries were fully optimized in the gas phase without constraints. Minimum and transition state structures were verified by having only positive, real frequency eigenvalues or having only one imaginary frequency, respectively. The geometry optimization and frequency calculations were performed with ωB97X-D and a mixed basis (def2-SVP basis for all main group elements, def2-TZVP basis set for Fe). [247] Single point calculations with the larger def2-TZVPP basis [247] using ωB97M-V [70] were used to refine the electronic structure for free energies and barrier heights. The ωB97M-V functional has performed very well in comparative assessments of density functionals for both main group [20] and transition metal [51] chemistry. The solvation energies were calculated using the C-PCM model (acetonitrile, $\epsilon = 37.5$) as implemented in Q-Chem [119]. Additional calculation were performed with B97-D [62] and B3LYP[50, 56, 57]+D3[66] to gauge functional dependency and can be found in the appendix E. CASSCF/NEVPT2 calculations were performed with Orca (version 4.0.0.2) [548] employing the RI approximation along with the def2-TZVPP basis and auxiliary basis set [497]. All molecular orbitals (MO) were plotted using an isovalue of 0.03 (blue: positive, red: negative values) and spin density using an isovalue of 0.005 (green: α spin density, yellow: β spin density).

The reaction free energies ($\Delta_R G$), activation energies ($\Delta G^{\ddagger}$), reduction potentials and pK_a values were calculated based on the standard thermodynamic cycles (see Refs [128, 130, 133, 532]). The Gibbs free energies include enthalpic contributions from the zero-point energy correction and the entropic contribution is calculated from the vibrational frequencies

at T = 298 K. Solvation energies were approximated by performing single point calculations applying the implicit C-PCM solvent model.

The calculation of pK_a values requires the Gibbs free energy of a proton, which cannot be calculated using quantum chemical methods. Therefore, we used the experimental value based on the Sackur-Tetrode equation and an estimated solvation energy of $G(H^+) = -264.6$ kcal/mol.[125, 130] Employing this experimental value makes it challenging to compute accurate pK_a values because an error of 1.36 kcal/mol leads to a deviation of 1 pK_a unit [134]. Other studies found deviations between this approach and experimental values of $\pm$ 3 units. [549] In this vein, we tested our computational protocol with two acids (CH_3COOH and phenol); in both cases the computed pK_a values were lower than the experimental ones in acetonitrile by 4 units (see table E.10). In spite of this systematic computational error, calculated relative pK_a values are more reliable because of favorable error cancellation by removing the experimental free energy of the proton. Thus, calculated pK_a values should mainly be compared against each other. Furthermore, it is important to note that electrolyses with the Fe catalysts were conducted in a solution of 11 M H_2O in acetonitrile, saturated with 1 atm of CO_2, not in pure acetonitrile.[385] These experimental conditions lead to several important complications that merit further discussion here. First, experimental pK_a values of acids in mixtures of acetonitrile and water are lower than in pure acetonitrile. [550, 551] This decrease in pK_a is not accounted for by the implicit solvent model used in our calculations. Therefore, the actual pK_a of possible intermediates under the experimental conditions should be lower than the calculated values. An overview of pK_a values and corresponding free energies for all relevant intermediates are provided in table E.11. Second, the introduction of CO_2 to the water-acetonitrile mixture lowers the effective pK_a of H_2O to 11.2. [552] This occurs via the complexation between CO_2 and OH^-, and is not accounted for in our computational model either.

Reduction potentials are reported against the ferrocene/ferrocenium (Fc/Fc^+) couple used as an internal standard. [127, 128] This method allows accurate predictions even at a modest level of theory with an accuracy of < 100 mV relative to experimental values. [128] However, other studies have shown that the errors can be larger for charged transition metal complexes and are functional-dependent. [549, 553–555]

The correct prediction of (adiabatic) spin gaps ($\Delta_{hs/ls}G = G(hs) - G(ls)$) in first row TS metal complexes is very sensitive to the choice of the density functional. Generalized gradient approximation (GGA) functionals tent to overstabilize the low-spin (ls) state whereas hybrid functionals tend to overstabilize the high-spin (hs) state. The amount of Hartree-Fock (HF) exchange plays a crucial role because it is found that spin gaps depend almost linearly on the amount of HF exchange incorporated in the functional. An increasing amount of HF exchange stabilizes the hs state. [556–559] Various studies specifically for iron complexes revealed that hybrid functionals perform better for correctly predicting the ground spin state. However, the recommended amount of HF exchange varies. [109, 557, 559, 560]. The range separated hybrid ωB97M-V (short range: 12% HF exchange) performed best in predicting both the experimentally known spin gap of $[Fe(bpy^{NHEt}PY2\,Me)L_2]^{2+}$ (L = CH_3CN) and the reduction potentials (see appendix E).

$[Fe(bpy^{NHEt}PY2\,Me)L_2]^{2+}$ has two open coordination sites, which are occupied by solvent ligands. Acetonitrile, water, or hydroxide ion are conceivable due to the experimental conditions. All three ligands occupy similar positions in the spectrochemical series. However, water not only interacts as a ligand but can also form intramolecular hydrogen bonds. This can lead to an overestimation of the dissociation energies, as hydrogen bonding might in the experiment be provided by solvent (water) molecules. The hydroxide ion is charged which results in overestimation of the binding energy to positively charged species because solvation is only taken into account implicitly. Acetonitrile solely acts as a σ-donating ligand and is not charged. Hence, it is used as the primary ligand in this study to compare the stability of different coordination numbers.

We reasoned that H_2O should be used as the main proton source for calculating reaction barriers (i.e. kinetics) involving protonation reactions, because under the experimental conditions the concentration of water is significantly higher (by a factor of roughly 10^5) than both H_3O^+ and H_2CO_3. [532]. The reaction barriers with H_2CO_3 are also presented. These kinetic barriers do not reflect the experimental catalytic system (as the concentration of carbonic acid is vanishingly small). We include them here to illustrate how barriers for the protonation steps can vary when using a stronger acid source; for example, when another acid is added to the reaction mixture. The calculated pK_a of H_2CO_3 is significantly lower than commonly used acids sources like phenol [561] or trifluoroethanol [514] (see table E.10). Therefore, the H_2CO_3 barriers should be lower than with these weaker acids.

6.3 Results and Discussion

Various reaction pathways for the catalytic reaction of $[Fe(bpy^{NHEt}PY2\,Me)L_2)]^{2+}$ are explored in this study using electronic structure calculations. The proposed reaction mechanism is depicted in figure 6.2. The paper is structured as follows: in the first part, the catalytic cycle is described step-wise starting with the initial reduction, followed by CO_2 fixation and protonation. In the second part, alternative intermediates are presented and discussed with respect to their relevance.

A consistent naming scheme is used throughout the manuscript which encodes the multiplicity (2S+1), the total charge, the iron coordination number (CN) and a consecutive number X for each intermediate step (1: initial complex, 2: CO_2 adduct, ...): $^{\textbf{multiplicity}}_{\textbf{charge}}\mathbf{X}^{\mathbf{CN}}$, e.g. $^5_2\mathbf{1}^6$ describes the initial hexacoordinated complex $[Fe(bpy^{NHEt}PY2\,Me)L_2)]^{2+}$ in the quintet spin state and overall charge 2+.

Reduction of the Initial Complex

The optimized geometry of the initial complex is illustrated in figure 6.3. The calculated and experimentally determined X-ray crystal structure show good agreement between theory and experiment using the ωB97X-D functional (see appendix table E.1). The Fe(II) compound shows a distorted octahedral coordination by a tetradentate chelating ligand

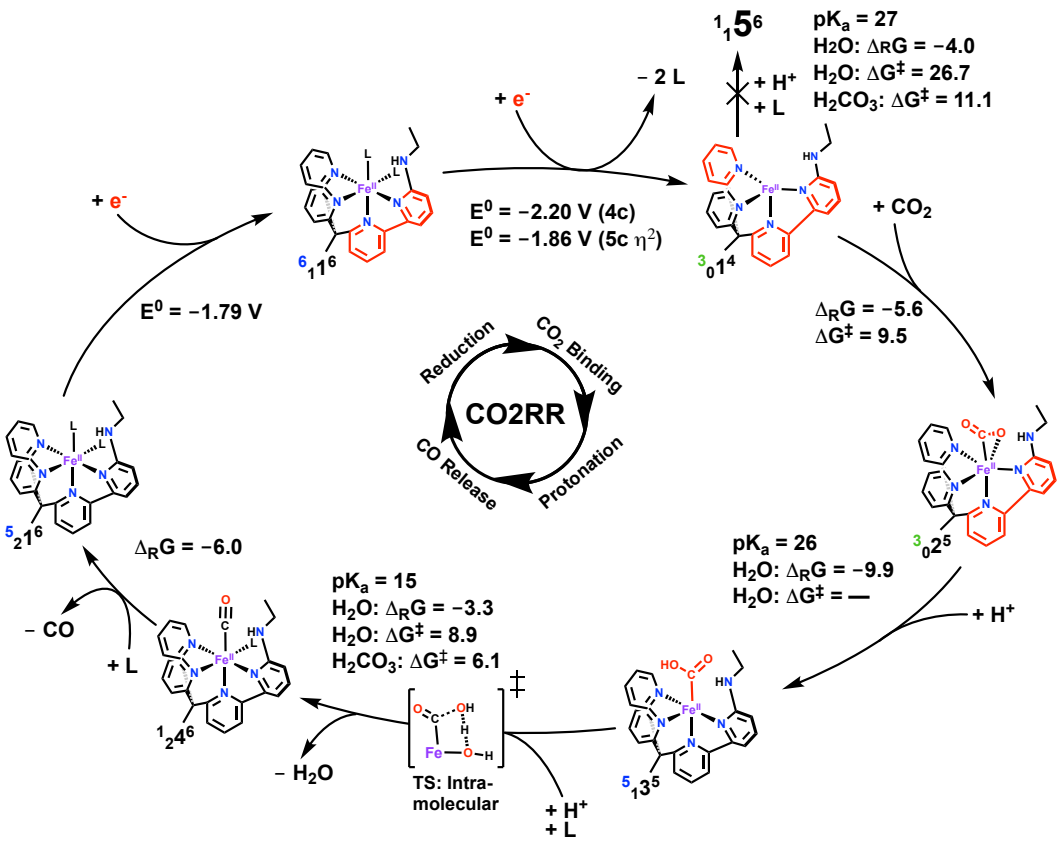

Figure 6.2: Proposed mechanism for the selective CO_2 to CO reduction using $[Fe(bpy^{NHEt}PY2\,Me)L_2)]^{2+}$. The red colored molecular moiety indicate localization of the excess electrons; reaction and activation energies in kcal/mol; reduction potentials against Fc/Fc^+; L = CH_3CN expect for the free energies and activation energies of the intramolecular protonation steps where water/hydroxide is used (see main text for justification); pK_a values were computed using L = CH_3CN.

($bpy^{NHEt}PY2\,Me$) and two solvent molecules (in this case, acetonitrile) (figure 6.3 (a)). The spin gap between high and low-spin states is only 1.5 kcal/mol with the low-spin state being higher in energy. This is in good agreement with the experimentally determined effective magnetic moment μ_{eff}=1.4 μ_B [385], which demonstrates the presence of both spin states in experimental samples and a spin gap of less than 1.0 kcal/mol.

The cyclic voltammetry (CV) of $[Fe(bpy^{NHEt}PY2\,Me)L_2)]^{2+}$ exhibits two one-electron reduction events within a narrow 0.2 V window at −1.79 V and −1.87 V versus Fc/Fc^+. [385] The calculated reduction potential of $[Fe(bpy^{NHEt}PY2\,Me)L_2)]^{2+}$, here denoted ${}^{5}_{2}1^{6}$, to yield $[Fe(bpy^{NHEt}PY2\,Me)L_2)]^{+}$, ${}^{6}_{1}1^{6}$, is −1.79 V, in excellent agreement with the experimental result; the analysis of the spin densities of the unreduced complex ${}^{5}_{2}1^{6}$ versus the one electron reduced complex ${}^{6}_{1}1^{6}$ in figures 6.3 (b) and (c) reveals a non-innocent ligand-based reduction

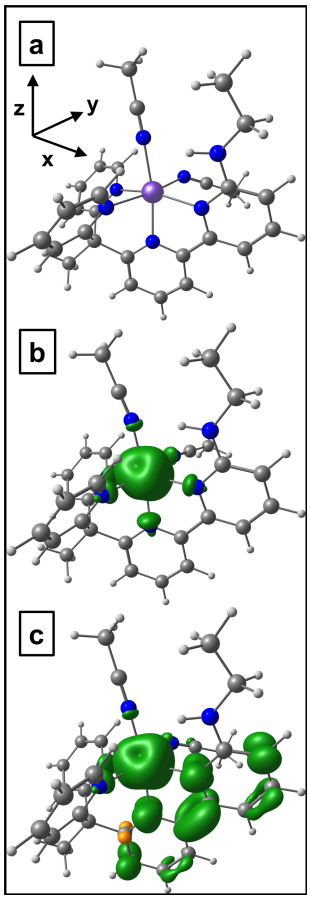

Figure 6.3: a) the optimized geometry of $[Fe(bpy^{NHEt}PY2\,Me)L_2]^{2+}$ ($^5_2 1^6$); b) spin density of $^5_2 1^6$ and c) spin densiity of the singly reduced intermediate $[Fe(bpy^{NHEt}PY2\,Me)L_2]^{+}$ ($^6_1 1^6$). In contrast to $^5_2 1^6$, the spin density on the ligand in $^6_1 1^6$ is non-zero, indicating that the first reduction is ligand-centered.

in the bpy π^*. A ligand-based reduction was also observed in all other spin states and is robust to the choice of DFT functional. A schematic MO diagram is depicted in figure 6.4 (a).

The second reduction event is accompanied by the dissociation of one or two solvent ligands. We identified two possible intermediates: the four-coordinate trigonal pyramidal complex ($[Fe(bpy^{NHEt}PY2\,Me)]^0$, $^3_0 1^4$) and the five-coordinate trigonal bipyramidal species ($[Fe(bpy^{NHEt}PY2\,Me)(\eta^2{-}NCCH_3)]^0$, $^3_0 1^4$), see figure 6.5. The ground states for both complexes $^3_0 1^4$ and $^3_0 1^5$ were calculated to be triplet states, with the corresponding quintet states calculated to be 4.5 and 1.9 kcal/mol higher in energy, respectively.

The complex $^3_0 1^5$ contains a side-on bound, bent acetonitrile ligand ($\angle(NCC) = 142.4°$), which implies a ligand-based second reduction step featuring a reduced acetonitrile in an η^2 coordination mode. Although rare, the side-on bound η^2 acetonitrile ligand has been crys-

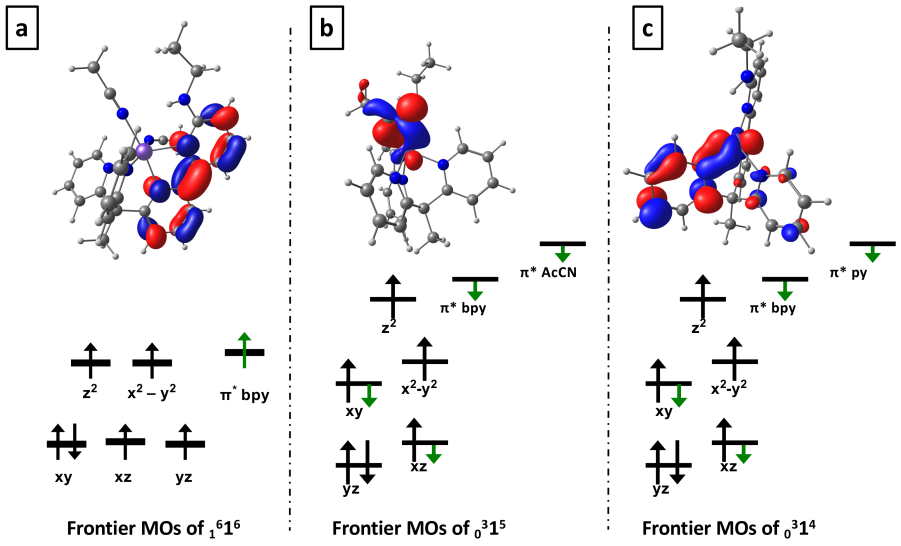

Figure 6.4: Schematic diagram of the frontier molecular orbitals of a) ${}^{6}_{1}1^{6}$ ($[\mathrm{Fe(bpy^{NHEt}PY2\,Me)L_2}]^{+}$), b) ${}^{3}_{0}1^{5}$ ($[\mathrm{Fe(bpy^{NHEt}PY2\,Me)}(\eta^2{-}\mathrm{NCCH_3})]^{0}$) and c) ${}^{3}_{0}1^{4}$ ($[\mathrm{Fe(bpy^{NHEt}PY2\,Me)}]^{0}$) including the key molecular orbitals for the reduction step. In (a) the α SOMO is a ligand centered, bpy π^*, consistent with fig. 6.3. The doubly reduced species shown in panels (b) and (c), exhibit antiferromangetic coupling between ligand and metal orbitals, leading to partial occupation and strong correlation (indicated by half-length arrows).

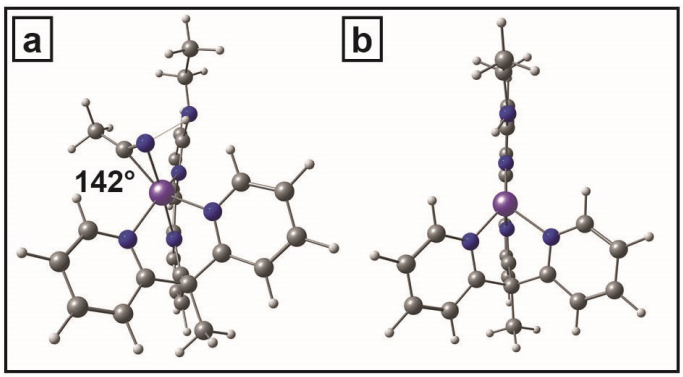

Figure 6.5: a) Geometry of five-coordinate doubly reduced complex ${}^{3}_{0}1^{5}$ ($[\mathrm{Fe(bpy^{NHEt}PY2\,Me)}(\eta^2{-}\mathrm{NCCH_3})]^{0}$) and b) the four-coordinate alternative ${}^{3}_{0}1^{4}$ ($[\mathrm{Fe(bpy^{NHEt}PY2\,Me)}]^{0}$).

tallographically observed in a number of low valent transition metal complexes, including Mo [562], W [563], Ni [564], Ir [565], and Nb [566]. The spin density plot and the β HOMO and β HOMO-1 shed light on the electronic structure: two β electrons in an acetonitrile π^* orbital and a bpy π^* orbital couple antiferromagnetically (afm) with the Fe-t_{2g} orbitals of a high spin metal center to an overall triplet state (see fig. E.1(a) & (b)). In addition, the decrease in the coordination number and η^2 coordination of CH_3CN results in a distorted ligand field. The schematic MO diagram in figure 6.4 (b) summarizes the electronic structure. Interestingly, the Mulliken spin population on iron does not decrease drastically upon reduction from ${}^5_2\mathbf{1}^6$ (3.8) to ${}^3_0\mathbf{1}^5$ (3.3). The electron density on the metal only slightly increases during the reduction process and the increase of electron density due to afm coupling is compensated by a ligand loss. The calculated reduction potential of -1.87 V is again in excellent agreement with experimental measurements.

The electronic structure of the four-coordinate complex ${}^3_0\mathbf{1}^4$ is best described as a reduced bpy and a reduced pyridine ligand resulting in a doubly reduced chelate ligand framework which couples to a high-spin Fe(II) center as illustrated by the spin density in figure 6.6. A schematic diagram of the frontier MOs of ${}^3_0\mathbf{1}^4$ is depicted in figure 6.4 (c). The species is 7.7 kcal/mol higher in energy than ${}^3_0\mathbf{1}^5$, resulting in a calculated reduction potential of -2.20 V (deviation of -330 mV from experiment). However, both isomers exhibit significant spin contamination ($<S^2>({}^3_0\mathbf{1}^4) = 3.5$, $<S^2>$ $({}^3_0\mathbf{1}^4) = 3.2$ and $<S^2>$(triplet) $= 2$). Furthermore, the energy difference between the two isomers is strongly dependent on the choice of functional: wB97M-V predicted the largest energy difference and PBE the smallest at 1.8 kcal/mol.

All hybrid functionals tend to localize the additional electron density upon both reduction steps onto the ligand suggesting a doubly reduced ligand framework which couples to a high-spin Fe(II) center. In contrast, local functionals like PBE preferably delocalize more electron density at the metal center which would suggest a stronger afm (or metal based reduction). This is illustrated by the different spin densities obtained with ωB97M-V and PBE in figure 6.6. This finding is in agreement with current literature about the physical and formal oxidation states of the central metal in reduced complexes containing redox-active ligand frameworks like Fe(II) pyridine and bpy complexes. [114, 567–569] Benchmark of density functionals against wave function methods showed in such cases a poor performance of hybrid functionals. The top performers were local functionals like PBE and TPSS which suggests that ωB97M-V is not an ideal choice for this doubly reduced intermediate. [114] Therefore, we employed CASSCF(8,7)/NEVPT2 to get insights into the static correlation in the electronic structure and an estimate of the energy difference between the two isomers (see appendix E for a detailed discussion). Both ${}^3_0\mathbf{1}^4$ and ${}^3_0\mathbf{1}^5$ revealed partial occupation numbers of the natural orbitals and confirm that these highly reduced Fe(II) pyridine complexes have some amount of static correlation.

The wave-function method predict a small gap of $\approx$2 kcal/mol and ${}^3_0\mathbf{1}^5$ to be lower in energy (see appendix E for further details). An in-depth analysis of the electronic structure of these two possible intermediates using CASSCF is beyond the scope of this work. [570–574] However, this discussion should illustrate that ${}^3_0\mathbf{1}^4$ and ${}^3_0\mathbf{1}^5$ are likely closer in energy as

predicted by the computational set up used in this study and thus are both accessible species. Overall, ${}^{3}_{0}1^{4}$ is most likely the key reactive intermediate in the catalytic cycle, and the active species for the binding and activation of CO_2 (*vide infra*). Both excess electrons are highly delocalized among the bpy π^* and py π^* and the metal center. The antiferromagnetic ordering in the electronic structure makes this intermediate challenging for KS-DFT. The ligand-based character of the reductions was reported with both experimental and computational evidence by some of us for a similar polypyridine iron catalyst. [398]

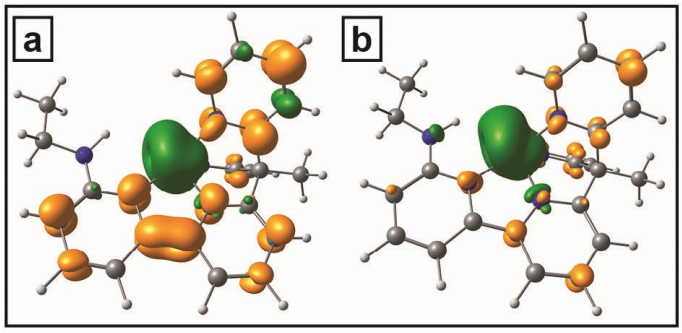

Figure 6.6: Spin density of ${}^{3}_{0}1^{4}$ ([Fe(bpy$^{\mathrm{NHEt}}$PY2Me)]^0) using the ωB97M-V (a) and the PBE (b) functionals, respectively. (α spin density green; β spin density yellow); ωB97M-V localizes most of the excess electron density in the ligand framework whereas PBE delocalizes the excess electrons strongly over both ligand and metal center resulting in significantly less spin density in the ligand moiety.

CO_2 Binding

There are four different binding modes for CO_2 to bind to a metal center: three restricted to an interaction between metal center and CO_2 and one involving a metal-ligand cooperation (MLC) (see figure 6.7). The following discussion focuses on the metal binding; metal ligand cooperation will be discussed in a later part of the manuscript.

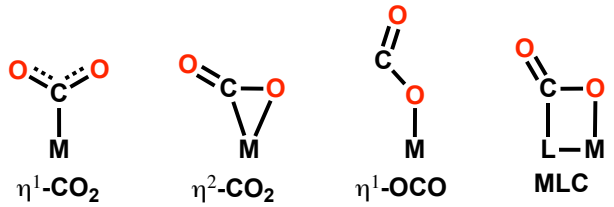

Figure 6.7: Schematic illustration of the four possible CO_2 binding modes (MLC = metal ligand cooperation).

The reaction pathway remains on the triplet surface and the lowest energy species $[Fe(bpy^{NHEt}PY2\,Me)(\eta^2{-}CO_2)]^0$ is a pentacoordinated CO_2 adduct in the η^2 binding mode ($^3_02^5$, see fig. 6.8 (a)) (the quintet species is 2.2 kcal/mol higher in energy). The OCO angle ($\angle$(OCO)) is 139°, which indicates at least partial reduction of the CO_2 fragment ($\angle$(OCO) is 134° for free $CO_2^{\cdot-}$). This is also confirmed by the spin density of $^3_02^5$ which shows significant excess spin in the CO_2 moiety (see figure S4). The $^3_02^5$ adduct is 2.4 kcal/mol lower in energy than the η^1-OCO isomer $[Fe(bpy^{NHEt}PY2\,Me)(CO_2{-}\kappa O)]^0$ ($^3_02^5(\eta^1\kappa O)$). This preference for the η^2 binding mode can be rationalized by analysing the electronic structure: the η^2 binding mode enables a σ interaction between the O lone pair and the Fe-d_{z^2} orbital (see the frontier MO in figure 6.8 (b)), a π interaction between the CO2 π^* orbital with a Fe-t_{2g} orbital (see the frontier MO in figure 6.8 (c)) and hydrogen bonding by the amine group. A dative bond σ bond is formed between the oxygen lone pair and a Fe-e_g type orbital (d_{z^2}). In total, three electrons occupy both bonding and anti bonding orbitals due to the high spin iron center. Thus, the interaction is still net stabilizing, the frontier anitbonding e_g^* (d_{z^2}) is depicted in figure 6.8 (b) (low lying bonding orbitals are depicted in figures S10 (a) and (b)). The occupied π^* orbital in the singly reduced CO_2 moiety can delocalize onto two Fe-t_{2g} orbitals which are empty in the β space (figure 6.8 (c)). This interaction motif illustrates that the Fe center remains Lewis acidic, allowing an effective coordination of the oxygen.

Both reduced complexes $^3_01^5$ and $^3_01^4$ can act as the active species to bind and activate CO_2, the energetics and kinetics involving both species are summarized in table 6.2. In a first scenario, the binding of CO_2 to $^3_01^5$ via an η^2 binding mode is slightly thermodynamically uphill and kinetically inhibited as the activation barrier is high. The geometry of the TS is illustrated in figure 6.9 (b) and involves not only the bond formation of both Fe$-CO_2$ and Fe$-$OCO bonds but also the simultaneous bond dissociation of the Fe$-$N and Fe$-$C bonds of the bound CH_3CN, rationalizing the high barrier. It is noteworthy that the amine group already forms a hydrogen bond to CO_2 at the TS. In a second scenario, CO_2 binds to $^3_01^4$ via the η^2 binding mode which is thermodynamically favorable and the activation barrier is significantly lower because CO_2 can directly bind at the axial position with favorable hydrogen bonding (see figure 6.9 (a)). In a third scenario, CO_2 can bind via a η^1-OCO. However, this is not only thermodynamically less favorable but also kinetically inaccessible. In summary the analysis of the CO_2 adducts indicate that the active species for CO_2 binding is $^3_01^4$ and the resulting adduct $^3_02^5$ binds CO_2 in the η^2 binding mode including a stabilizing hydrogen bond from the amine group.

Protonation of the CO_2 Adduct

The subsequent protonation of the reduced CO_2 significantly lowers the energy of the CO_2 π^* orbital, inducing a second charge transfer from the complex to COOH moiety. This reduction of the CO_2 ligand is reflected in the smaller O-C-O bond angle of 118° (see appendix fig E.7). Upon protonation and charge transfer the bonding situation changes from a π type interaction of the $CO_2^{\cdot-}$ to a dative bond of the CO_2H^- lone pair as a σ-donor into the Fe-d_{z^2} orbital. This causes a change of the binding mode from η^2 to η^1-COO which

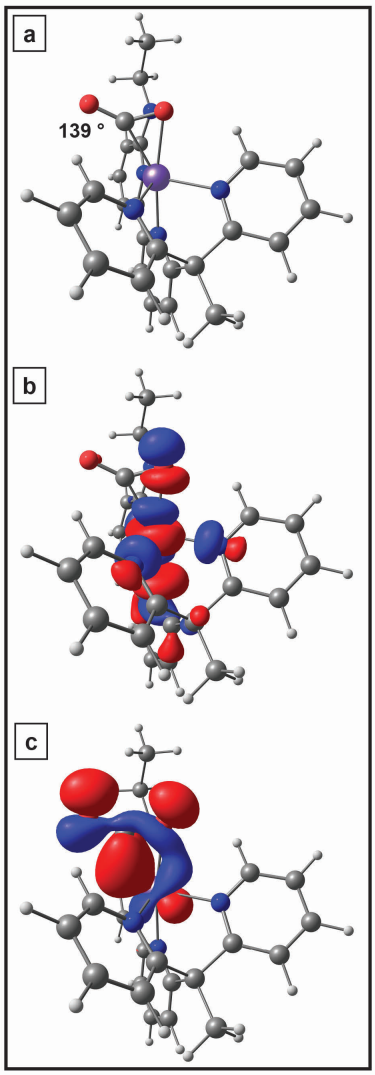

Figure 6.8: a) geometry of the CO_2 adduct ${}^{3}_{1}2^{5}$; b) MO illustrating the interaction of the oxygen lone pair with the metal d_{z2} orbital; c) MO illustrating the stabilization of the CO_2 π^* with a t_{2g} metal orbital via a π type interaction.

Table 6.2: Relative Gibbs free reaction energies and barriers for the formation of CO_2 adducts after the second reduction (energies in kcal/mol).
* using B97-D geometries because the TS could not be located with ωB97X-D.

Reaction			$\Delta_R G$	$\Delta G^{\ddagger}$
${}^{3}_{0}1^{5} + CO_2$	$\longrightarrow$	${}^{3}_{0}2^{5}(\eta^2) + CH_3CN$	2.1	25.4
${}^{3}_{0}1^{4} + CO_2$	$\longrightarrow$	${}^{3}_{0}2^{5}(\eta^2)$	−5.7	9.5
${}^{3}_{0}1^{4} + CO_2$	$\longrightarrow$	${}^{3}_{0}2^{5}(\eta^1\kappa O)$	−2.5	≈44*

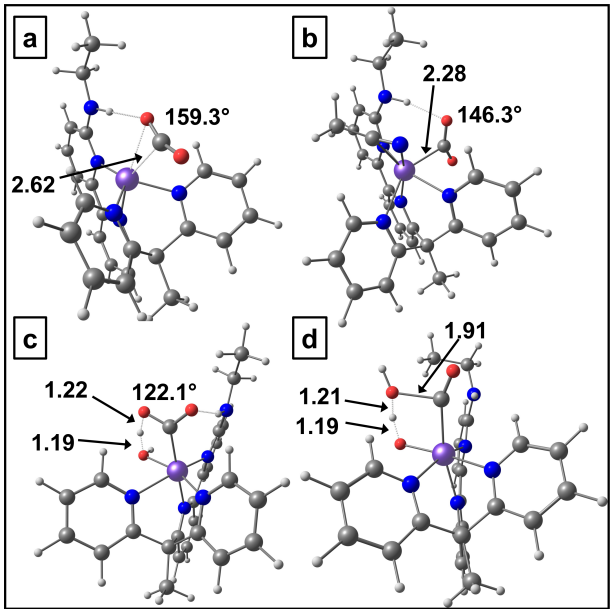

Figure 6.9: Geometries of the key transition states in the catalytic cycle: CO_2 addition to a) ${}^{3}_{0}1^{4}$, b) ${}^{3}_{0}1^{5}$, c) first protonation of ${}^{3}_{0}2^{5}$, d) second protonation of ${}^{5}_{1}3^{6}$, both protonation transition states utilize water as the proton source (distances in Å).

leads to a small high-spin (S = 2) low-spin (S = 0) gap, similar to the unreduced catalyst species. The hexacoordinated carboxy species $[Fe(bpy^{NHEt}PY2Me)(CO_2H)L]^+$ in the low-spin configuration is the most stable intermediate (${}^{1}_{1}3^{6}$). However, the two high-spin isomers lie within 1.5 kcal/mol (${}^{5}_{1}3^{5}$: 0.5 kcal/mol and ${}^{5}_{1}3^{6}$: 1.5 kcal/mol). The advantage of the high-spin surfaces is the ability to undergo rapid ligand exchange associated with a geometry conversion from trigonal-bipyramidal to octahedral.

The open axial coordination site allows the CO_2 adduct ${}^{3}_{0}2^{5}$ to coordinate a water molecule as a sixth ligand, which opens up the possibility of a *intramolecular* proton transfer using H_2O. The formation of such a precomplex is only slightly endergonic (2.5 kcal/mol). The intramolecular protonation pathway leads to two major advantages: first, a perfect alignment

of the H_2O and CO_2 molecules for the subsequent protonation due to a hydrogen- and a dative bond of the water and the hydrogen bond of the amine group (see the TS geometry in figure 6.9 (c); second, the enhancement of the Brønsted acidity of the H_2O through binding to the Lewis acidic metal center. This polarizes the O–H bond and stabilizes the resulting base. Hence, the first protonation reaction yielding ${}^{5}_{1}3^{5}$ is facile both thermodynamically (-9.9 kcal/mol) and kinetically (barrierless). The first protonation step is also barrierless on the quintet surface (see table E.3).

The second protonation is able to follow an intramolecular pathway as well. This is attributed to the fact that the energy difference between the five and six-coordinated carboxy intermediates is only 1.0 kcal/mol (*vide supra*). This facilitates the rapid ligand exchange featuring the removal of the leftover hydroxide ligand from the complex, followed by the coordination of a new water molecule. Alternatively, the hydroxide can also get protonated by another acid source in solution (e.g. H_2CO_3).

The second protonation step is accompanied by the cleavage of the C–O bond and results in H_2O and a metal carbonyl $[Fe(bpy^{NHEt}PY2\,Me)(CO)L]^{2+}$ (${}^{2}_{1}4^{6}$). The reaction is more likely to proceed on the quintet surface because it has a slightly lower barrier. However, both singlet and quintet surfaces have similar energetics and kinetics (see table 6.3). Similarly to the first protonation step, a coordinated water ligand benefits from an enhanced acidity due to the $Fe{-}OH_2$ bond and its optimized geometric alignment (see figure 6.9 (d)) yielding an exergonic process (-3.3 kcal). The intramolecular second proton transfer happens simultaneously with the heterolytic cleavage of the C–O bond and the release of one water molecule. The concerted bond formation and cleavage is crucial to compensate the kinetic penalty of the C–O bond splitting, which has been estimated to be 36 kcal/mol [532]. Thus, the intramolecular process has still a sizeable barrier with 8.9 kcal/mol. The barrier gets lowered by 2.7 kcal/mol if the proton source is H_2CO_3 which accelerates the this step by a factor of 100. In summary, an EEC mechanism is proposed with the CO_2 binding as the rate limiting step and the COOH intermediate as the resting state. The second protonation step is prohibited on the triple surface for both kinetic and thermodynamic reasons. The barrier for the second protonation is 15.4 kcal/mol, 6.5 kcal/mol larger than the barrier along the quintet surface. Additionally, the triplet carboxy intermediate is 14 kcal/mol higher in energy than the quintet carboxy intermediate ${}^{5}_{1}3^{5}$, presumably because of an less preferred intermediate spin Fe center on the triplet surface.

The high oxidation state of iron (Fe(II)) in the resulting carbonyl intermediate ${}^{1}_{2}4^{6}$ rationalizes the exergonic nature of the CO release (-6.0 kcal/mol) to regenerate ${}^{5}_{2}1^{6}$ barrierless. The interaction is mainly driven by the σ forward-donation of the CO because the π back-donation is limited by the high oxidation state of the central metal. In addition, the CO release is further enhanced by the low solubility of CO in water which promotes its direct release into gas phase thus also reducing the likelihood of catalyst poisoning at this step in the cycle (*vide infra*). The free energy diagram of the complete catalytic pathway is depicted in figure 6.10.

Table 6.3: The activation energies and pK_a values of both protonation steps. The activation and reaction free energies correspond to the intramolecular proton transfer using H_2O (reactant) & OH^- (product) as a sixth ligand. The pK_a values refer to the equilibria using acetonitrile as a ligand and experimental free energy for H^+.

Reaction					$\Delta_R G$	$\Delta G^{\ddagger}$	pK_a
${}^{3}_{0}2^{5}$	$+H_2O$	$\longrightarrow$	${}^{5}_{0}3^{6OH}$		-9.9	-	26
${}^{5}_{1}3^{5}$	$+H_2O$	$\longrightarrow$	${}^{1}_{1}4^{6OH}$	$+ H_2O$	-3.3	8.9	15
${}^{5}_{1}3^{5}$	$+H_2CO_3$+L	$\longrightarrow$	${}^{1}_{2}4^{6}$	$+ H_2O$+HCO_3^-	-1.8	6.1	15
${}^{1}_{1}3^{6}$	$+H_2O$	$\longrightarrow$	${}^{1}_{1}4^{6OH}$	$+ H_2O$	-2.8	9.9	14

Possible Pathways Towards Catalyst Degradation and Activity Decrease

A high selectivity towards CO2RR versus HER is an important feature of a CO_2 reduction catalyst and is experimentally observed for the $[Fe(bpy^{NHEt}PY2\,Me)L_2]^{2+}$ system. It is a key feature of a good catalyst and can originate either from thermodynamics [532] or kinetics [132, 133]. Furthermore, catalyst degradation tremendously reduces the efficiency of catalytic materials. Thus, both aspects should be understood and are investigated in this section.

A possible mechanism for HER involves the formation of a hydride $[HFe(bpy^{NHEt}PY2\,Me)L]$. The addition of a proton to ${}^{6}_{1}1^{6}$ results in the formation of a metal hydride intermediate (${}^{2}_{2}5^{6}$). Upon addition of the proton, a coincident oxidation of the metal center and $bpy^{\cdot -}$ takes place to form H^-. The hydride is a strong σ donor; hence, the resulting stronger d-orbital splitting stabilizes the low spin configuration. However, the formation of the complex ${}^{2}_{2}5^{6}$ is thermodynamically unfavorable and thus would require strong acidic conditions as the pK_a of the complex is negative. Thus, the formation of a hydride species can be ruled out after the first reduction step.

In contrast, the formation of a hydride species from ${}^{3}_{0}1^{4}$ is thermodynamically favorable with a pK_a of 33 which is higher than any pK_a in the CO2RR; using water as the proton source the free energy is -4.0 kcal/mol comparable to CO_2 addition. The resulting hydride species is hexacoordinated and low spin (${}^{1}_{1}5^{6}$). The two excess electrons localize to form a H^- and a Fe(II) metal center as the proton gets reduced by the two electrons delocalized over the metal and π^* orbital of the ligand framework. However, a high barrier (26.7 kcal/mol) for hydride formation with water as the proton source hinders HER kinetically. This barrier shrinks significantly (11.1 kcal/mol) using a moderately strong acid (H_2CO_3). Therefore, the main product of catalysis should be CO even when a moderately strong acid is added to the reaction mixture albeit with lower selectivity. The high selectivity even with moderately strong acids can be explained by the electronic structure of ${}^{3}_{0}1^{4}$. The highly delocalized excess electrons and the low coordination number results in a Lewis acidic and positively charged metal center. On the one hand, CO_2 has a high quadruple moment allowing for a

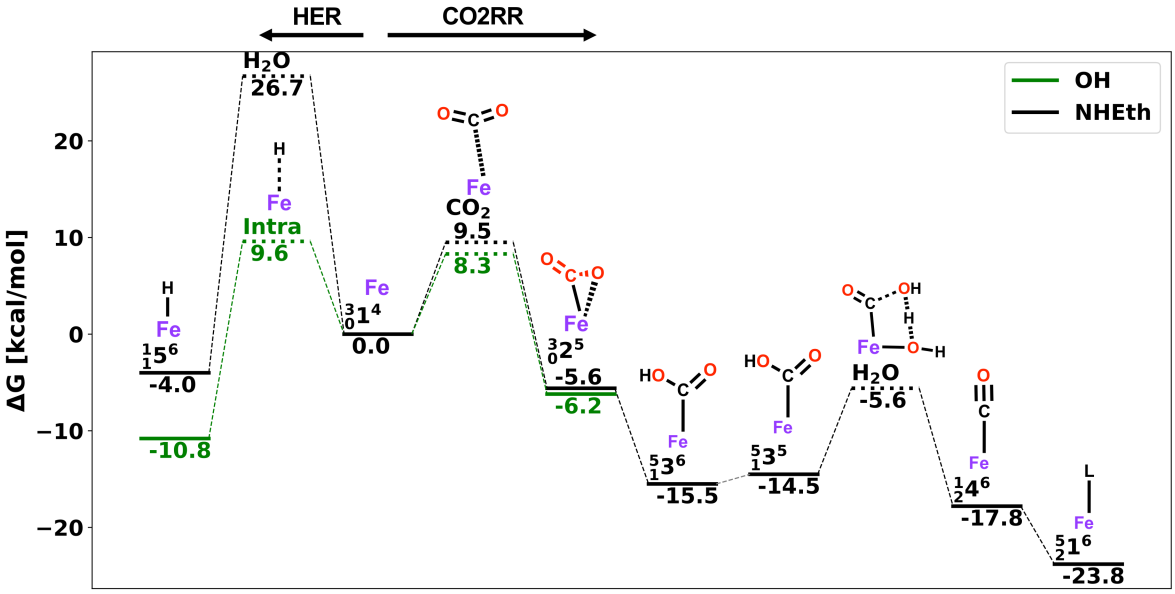

Figure 6.10: Free energy landscape of both CO2RR and HER pathways for $[Fe(bpy^{OH}PY2\,Me)L_2)]^{2+}$ (green) and $[Fe(bpy^{NHEt}PY2\,Me)L_2)]^{2+}$ (black); solid lines correspond to intermediate states and dashed line to a transition states; the sixth ligand L corresponds to CH_3CN, except for the two intramolecular protonation steps where water and hydroxide are used; assuming a rapid ligand exchange between both protonation steps (see main text for justification).

facile coordination via the oxygen resulting in a lower barrier (9.5 kcal/mol). On the other hand, the coordination of an acid (via hydrogen) to a Lewis acid metal center results in a high barrier. Thus, despite being thermodynamically favored, the addition of H^+ even with an acidic proton source (H_2CO_3) is about 15 times slower than CO_2.

A third reduction is a possible degradation pathway because the dissociation of CO from a singly reduced carbonyl intermediate is significantly endergonic ($\Delta_R G$ = 9.6 kcal/mol, but barrierless) and could consequently trap the catalyst, especially in solvents with higher CO solubility than acetonitrile. This CO poisoning was observed and proposed for the nickel cyclam system. [532, 534] A third reduction can happen at various stages of the catalytic cycle: First, the reduction of the CO_2 adduct is unlikely as the reduction potential is −2.16 V vs Fc/Fc^+ which is more negative than the two reductions of ${}^{5}_{2}1^{6}$. In addition, the protonation processes utilize H_2O as an intramolecular proton source; therefore, the lifetime of these species is expected to be short and make an additional reduction less likely. Second, the reduction of the carboxy intermediate ${}^{5}_{1}3^{5}$ yielding ${}^{4}_{0}3^{5}$ (−1.81 V) is feasible because the potential is less negative than the potential required to obtain ${}^{3}_{0}1^{5}$. Third, the carbonyl intermediate ${}^{1}_{2}4^{6}$ can readily be reduced to ${}^{4}_{1}4^{5}$ (−1.00 V) because the excess electron increases

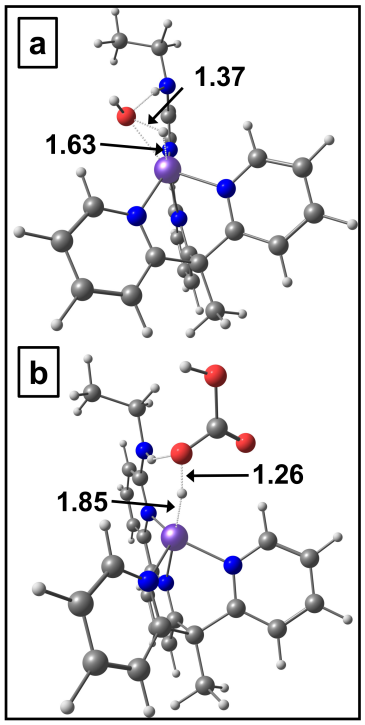

Figure 6.11: Geometries of for the transition states for a possible formation of a hydride using (a) water and (b) carbonic acid as the proton source (distances in Ångstrom).

the backbonding of CO as indicated by the red-shift of 136 cm^{-1} in the carbonyl stretching mode.

The bent acetonitrile in ${}^{3}_{0}1^{5}$ suggests a protonation of the activated acetonitrile may be possible (see figures S1 (a) & (b)). However, the protonation is kinetically inhibited using H_2O as the proton source with a barrier over 30 kcal/mol. The transition state for the possible intramolecuar protonation of the activated CH_3CN is depicted in figure E.9. Therefore, ${}^{3}_{0}1^{5}$ is kinetically inhibited for the reaction with both CO_2 and H_2O.

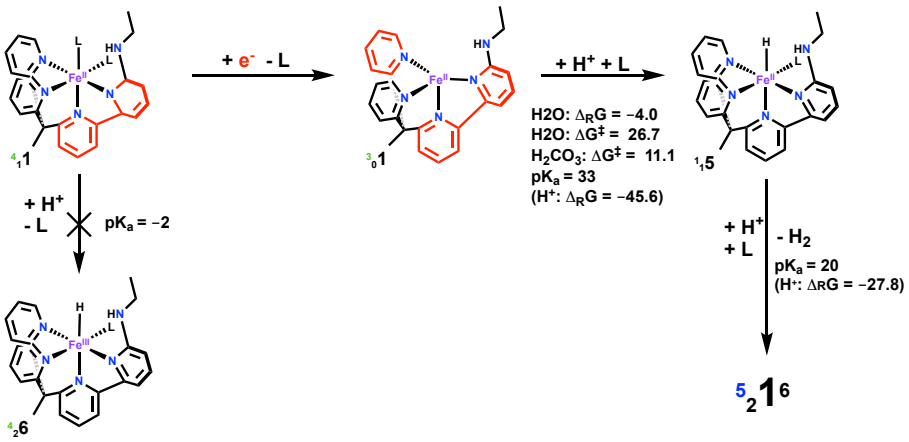

Figure 6.12: Possible HER mechanism involving $[Fe(bpy^{NHEt}PY2\,Me)L_2)]^{2+}$ starting from the doubly reduced ${}^{3}_{0}1^{4}$. The red colored molecular moiety indicate localization of the excess electrons; reaction and activation energies in kcal/mol; reduction potentials against Fc/Fc^{+}; L = CH_3CN.

6.4 Hydroxyl Substituent

The hydroxyl substituent complex $[Fe(bpy^{OH}PY2\,Me)L_2)]^{2+}$ showed a high Faradaic efficiency but low selectivity. In bulk electrolysis, significant amounts of both CO and H_2 were observed. The lower selectivity of the can be related to the increased acidity of the second coordination sphere. The doubly reduced active species ${}^{3}_{0}1^{4OH}$ has two competing pathways with similar activation barriers: an *intramolecuar* proton transfer and CO_2 addition.

On the one hand, the high acidity of the hydroxyl group opens up the possibility of an intramolecular proton transfer for ${}^{3}_{0}1^{4OH}$ from the hydroxyl group to the Fe center with an activation energy of 9.6 kcal/mol. The transition state is shown in figure 6.13 (a). This process yields a hydride which is an important intermediate for HER. On the other hand, the addiction of CO_2 to ${}^{3}_{0}1^{4OH}$ has a slightly lower barrier of 8.3 kcal/mol and results in the CO2RR pathway. The transition state is depicted in figure 6.13 (b). Thus, the stronger hydrogen bonding further facilitates CO_2 binding as the barrier is lower than for the NHEt isomers (9.5 kcal/mol) but dramatically decreases selectivity by opening up a facile HER pathway. This situation is illustrated in a free energy diagram of the two reaction pathways in figure 6.10 for both the OH and NHEt substituent.

6.5 Alternative Catalysis Cycles

In addition to the discussed catalysis cycle, two alternative pathways are conceivable which either originate due to the binding of CO_2 to an alternative species formed during the catalysis cycle or stem from an altered CO_2 binding mode. They will be described in the

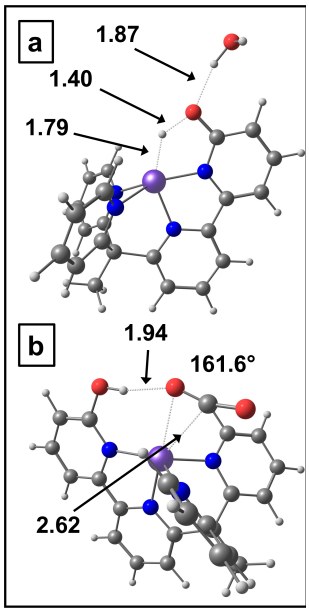

Figure 6.13: Geometries of the and key parameters of the transition states for a) intramolecular proton transfer and b) CO_2 addition of $[Fe(bpy^{OH}PY2)\,L_2Me)]^{2+}$ (distances in Å).

following section, which includes a discussion about their limitations with respect to the proposed catalytic cycle.

1. CO_2 could also bind to the singly reduced species ${}^{6}_{1}1^{6}$ by replacing a solvent ligand suggesting an ECE mechanism. The most stable isomer is a six-coordinated quartet state with CO_2 in an η^2 mode (${}^{4}_{1}2^{6}$). The CO_2 activation process is endergonic (4.6 kcal/mol) implying that the species could exist in equilibrium. The reaction barrier of this step is 13.8 kcal/mol making it the rate limiting step in this cycle. The calculated potential for the reduction of the CO_2 adduct ${}^{4}_{1}2^{6}$ to ${}^{3}_{0}2^{5}$ is -1.76 V vs Fc/Fc^{+} which is in very good agreement with the experimentally applied potential. The subsequent protonation of ${}^{3}_{0}2^{5}$ is identical to the proposed catalytic cycle. It is noteworthy that no singly reduced CO_2 adducts could be computed for the parent compound revealing that in this case the amine group is crucial for the CO_2 binding. In summary, it is both thermodynamically and kinetically less favorable to bind CO_2 after only 1 initial reduction. The rate limiting step remains the CO_2 addition and the resting states remains the carboxy adduct.

2. Alternatively to the formation of a solely metal-bound adduct, CO_2 can also cooperatively bind to the ligand framework (see figure 6.7). This was observed in several other cases e.g. pincer-type complexes [575–577] zirconium metallocene phosphinoaryloxide complex [578] as well as in catalytic processes. [579, 580] There are two conceivable ligand-based binding sites for CO_2 in this ligand framework; it can be inserted into the amine group yielding a carbamate or can bind via a reversible C–C bond to the ligand framework (see fig. 6.14).

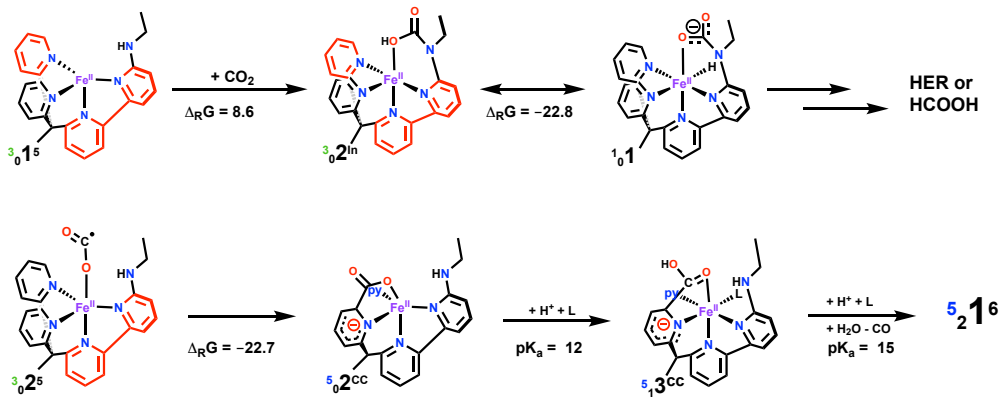

Figure 6.14: Alternative cycles involving cooperatively bound CO_2.

In a first scenario, CO_2 is bound to the amine group. However, the formation of this carbamate intermediate is not favorable in comparison to a metal bound CO_2 adduct (8.6 kcal/mol). In addition, it readily rearranges to a metal-hydride via an intramolecular proton transfer ($\Delta G_R = -22.8$ kcal/mol). The nucleophilic character of the hydride would either favor the hydrogen evolution upon addition of a second proton or the formation of formic acid over the experimentally observed CO.

In a second scenario, CO_2 can bind via a *reversible* C–C bond to a pyridine forming an sp^3-C2 carbon in the ring ($^5_0\mathbf{2}^{5CC}$ see fig. E.8). This intermediate is the most stable isomer in the CO_2 adduct isomer-space as it is more than 20 kcal/mol lower in energy than the metal bound adducts in all spin states. A mechanism using this species is conceivable via an aromatization/dearomatization sequence as the second reduction to $^3_0\mathbf{1}^4$ already breaks the aromaticity in the pyridine (*vide supra*). Both protonation steps are possible (pK_a = 12, 15) and the second protonation leads to a concerted O–H bond formation and C-C and C-O bond cleavage yielding H_2O, CO and the starting complex $^5_2\mathbf{1}^6$. The regaining of aromaticity seems to be the main driving force for the C-C bond cleavage. However, $^5_0\mathbf{2}^{5CC}$ is only accessible from $^3_0\mathbf{2}^5(\eta^1\kappa O)$ ($[Fe(bpy^{NHEt}PY2\,Me)(CO_2{-}\kappa O)]^0$) (see figure E.5) which is an unlikely intermediate. The discussion about CO_2 adducts (*vide supra*) ruled out a direct formation of the η^1-OCO adduct. But it was not possible to locate a transition state connecting to the η^2 adduct ($^3_0\mathbf{1}^5$) or binding CO_2 directly in the metal ligand cooperation (MLC) binding mode. However, the energy difference between both CO_2 adducts ($^3_0\mathbf{1}^5(\eta^2)$ and $^3_0\mathbf{2}^5(\eta^1\kappa O)$) is 2.4 kcal/mol. Therefore, if the lifetime of $^3_0\mathbf{2}^5$ would be sufficiently long, an equilibrium could form between both binding modes. This would open up the possibility to enter the CC pathway. However, the proposed cycle predicts a very facile and fast first protonation step which makes the formation of the $^5_0\mathbf{2}^{5CC}$ intermediate unlikely.

6.6 Conclusion

Electronic structure calculations were performed in order to study the electrochemical reduction of CO_2 to CO by $[Fe(bpy^{NHEt}PY2\,Me)L_2]^{2+}$. A schematic free energy diagram summarizing the results is depicted in figure 6.10. The redox active ligand framework paired with a high spin Fe(II) center allows effective delocalization of additional electrons rationalizing the reduction events at mild negative potentials. The metal center remains Lewis acidic through the reduction process because of the non-innocent chelate ligand framework and the ability to dissociate up to two solvent ligands. The high Lewis acidity of the Fe in the doubly reduced intermediate results in a high barrier for the formation of a hydride intermediate. In contrast, the binding of CO_2 is facile due to its high quadruple moment uncovering the origin of the selectivity in the kinetics. The CO_2 adduct exhibits an η^2 binding mode to maximize the π-type coupling of the singly reduced CO_2 π^* to a t_{2g}-type d-orbital. The Lewis acidity of the central metal allows further charge delocalization via a dative bond of the oxygen to the metal center. Furthermore, the amine group forms a favorable hydrogen bond to stabilize the CO_2 adduct.

The second available equatorial coordination site opens up the possibility of *intramolecular* protonation by coordination of H_2O. The formation of this precomplex facilitates protonation because not only CO_2 but also the proton source H_2O is activated due to the $Fe-OH_2$ bond. This polarizes the O–H bond and aligns both CO_2 and H_2O properly, resulting in a barrier-less first protonation. The small ligand field results in a high spin quintet surface for both protonation steps. The energy difference between the five and hexacoordinated carboxy intermediates is small which allows a rapid ligand exchange for a second intramolecular protonation. This step exhibits a concerted heterolytic cleavage of the C-O bond and the release of a water molecule. The resulting carbonyl species is only weakly bound due to the high oxidation state and weak ligand field; thus, the CO release is exergonic to recover the initial state of the catalyst. The proposed mechanism follows an EEC mechanism with the formation of the CO_2 adduct as the rate-limiting step. This rationalized the importance of the second coordination sphere.

The lower selectivity of the corresponding hydroxy-substituted complex is connected to the higher acidity of the hydroxyl group as it opens up the possibility of an intramolcular proton transfer to form a hydride intermediate. This barrier is even lower than protonation with an acid source (H_2CO_3) and has a similar magnitude than CO_2 addition. This rationalizes the experimental finding that $[Fe(bpy^{OH}PY2\,Me)L_2]^{2+}$ produces both CO and H_2.

Chapter 7

Mechanistic Insights into Co and Fe Quaterpyridine Based CO_2 Reduction Catalysts: Metal-Ligand Orbital Interaction as the Key Driving Force for Distinct Pathways

7.1 Introduction

The electrochemical reduction of CO_2 to CO is a promising pathway for sustainable fuel production via artificial photosynthesis. [153, 154, 156] The resulting carbon monoxide can be further transformed into hydrocarbons using the Fischer-Tropsch process [508], making it one of the most economically viable products of CO_2 reduction out of a variety of possible products. [164] Carbon dioxide is typically electrochemically inert, so proton coupled reductions are necessary to operate at moderate potentials. Unfortunately, the two-electron two-proton CO_2 reduction reaction (CO2RR) to CO operates at a potential similar to the less desirable hydrogen evolution reaction (HER). [155, 522] Consequently, catalysts are required which are ideally efficient (low overpotential), fast (high turnover frequency (TOF)), substrate selective (CO2RR vs HER), and cheap (earth abundant materials).

The main catalytic [155] approaches are molecular [100, 168, 397, 581, 582], heterogeneous [159, 509] and biological [583]. Heterogeneous catalysts reduce CO_2 with high current densities [584], but often suffer from poisoning and poor substrate selectivity. [155, 159, 509, 510] For example, copper is able to reduce CO_2 with a high current density but produces a variety of C1 and C2 products with ethylene and ethanol as the main products, [509, 585] making mechanistic studies difficult. [511, 513]

Homogeneous catalysts can facilitate electron transfer to CO_2 yielding lower overpotentials. Furthermore, the catalyst can stabilize various intermediates and transition states to

accelerate the transformation of CO_2. Molecular catalysts yield good TOF, a very high selectivity (over 90%), and are highly tunable. [165–167] The activity of the molecular catalyst can be dramatically improved by a novel flow cell design. Berlinguette *et al.* designed a zero-gap membrane flow reactor which produced CO (from CO_2) using a cobalt phthalocyanine catalyst, achieving a current density comparable to a heterogeneous catalyst and a selectivity of over 95%. [169] Alternatively, activity can be improved by incorporating the catalyst into metal/covalent organic frameworks [170, 171, 518, 519] or attaching the molecular catalyst onto a surface [521, 586–590].

Mechanistic insights in the catalytic pathway are invaluable for rational catalyst design as they illuminate the origin of activity and selectivity, as well as the cause of any intrinsic limitations. Both spectroscopic methods and computational chemistry should be employed to identify possible intermediates, steps in the reaction pathway, activation barriers, and rate limiting steps. Experimental tools include cyclic voltammetry (CV) [382, 591], Mössbauer, EPR [398], X-ray spectroscopy/ crystallography [525, 536], spectroelectrochemistry [592], and stopped-flow rapid mixing and transient absorption [526] (see references [99] & [100] for a detailed overview). Computational methods such as density functional theory [20, 41, 44, 51] (DFT) can provide structural and spectroscopic information on intermediates along with complete catalytic pathways by computing reaction free energies, reduction potentials, pK_a values, and barrier heights among many examples. Detailed computational studies providing mechanistic insights were conducted, for example, by Ye *et al.* for the nickel cyclam system [532] and Carter *et al.* for the rhenium/manganese tricarbonyl-bipyridine system. [132, 133, 531]

The most prominent molecular catalysts for the electrochemical reduction of CO_2 to CO are nickel cyclam [516, 534, 593, 594], rhenium/manganese tricarbonyl-bipyridine [514, 523, 527–530, 595–598] and iron porphyrins such as FeTPP (TPP = tetraphenylporphyrin) and its derivatives [380, 383, 399, 401, 535]. Both iron and cobalt catalysts are especially desirable due to the natural abundance of the central metal, and notable iron [176, 385] and cobalt [599] based catalysts were developed recently. This makes iron [600] and cobalt [601] quaterpyridine complexes especially attractive as both complexes are active CO_2 reduction catalysts with an identical ligand framework. Both catalysts are efficient and selective, meaning both catalysts (or their derivatives) find application in electrochemical [561, 602, 603] and photoelectrochemical [604] reduction of CO_2 to various products, even to CH_4 (albeit with a low Faradaic efficiency) [605]; furthermore, hybrid systems are able to operate efficiently in water.[586, 606]

Robert *et al.* [561] reported a detailed experimental mechanistic study to investigate the catalytic pathways of both Fe and Co systems. Interestingly, they proposed distinct pathways despite an identical ligand framework (see figures 7.1 (a) and (b)). Therefore, this system provides a unique opportunity to understand the role of the central metal for each step throughout a catalytic pathway. In this work, we provide a computational study where we propose detailed catalytic pathways for both metals in line with the experimental findings of reference [561] (compare figures 7.1 (a) and (b) with figures 7.3 and 7.9). Furthermore, we provide an in-depth analysis of the electronic structure of important intermediates to

understand the origin of the different pathways and reactivities, and predict the effect of ligand substituent groups on the key steps.

Experimental Findings

Robert *et al.* [561] reported two selective and efficient catalysts for the electrochemical reduction of CO_2 to CO: $[Co^{II}(qpy)(H_2O)_2]^{2+}$ and $[Fe^{II}(qpy)(H_2O)_2]^{2+}$ with qpy = 2,2′:6′,2″:6″,2‴-quaterpyridine. The cobalt catalyst shows fast turnover rates (500–33000 s^{-1}). Both are extremely selective for CO2RR over HER (>95%) and operate at low overpotentials (140–240 mV). Furthermore, both are also highly selective and active catalysts for the photochemical conversion of CO_2 to CO with selectivity and turnover numbers up to 2600. [604] Interestingly, experimental evidence suggests that the two catalysts exhibit different pathways despite the identical ligand framework. The experimentally suggested pathway for $[Co^{II}(qpy)(H_2O)_2]^{2+}$ is as follows: (i) two reductions to form a $[Co(qpy)]^0$ intermediate; (ii) binding of CO_2 resulting in a $[Co(qpy)CO_2]^0$ intermediate; (iii) two protonation steps involving the C−O bond cleavage and CO release to close the cycle (see figure 7.1 (a)). The suggested pathway for $[Fe^{II}(qpy)(H_2O)_2]^{2+}$ differs: (i) initial reduction resulting in an $[Fe(qpy)]^+$ intermediate; (ii) binding of CO_2 to form a $[Fe(qpy)CO_2]^+$ intermediate; (iii) two protonation and reduction events cleaving one C−O bond of CO_2 to form H_2O and a singly reduced $[Fe(qpy)CO]^+$ adduct; (iv) release of CO to close the cycle (see figure 7.1 (b)). The experimental evidence is summarized in the following paragraphs (potentials were reported versus SCE but are converted in this work against ferrocene/ferrocenium couple (Fc^+/Fc) for consistency using −380 mV [607]).

The cobalt based catalyst $[Co^{II}(qpy)(H_2O)_2]^{2+}$ exhibits two reduction waves at −0.95 V and −1.18 V vs Fc^+/Fc. The first reduction wave is reversible, but the second wave is only observable at low scan rates, suggesting that a slow water loss occurs before the second reduction. The addition of phenol during the CV experiments results in coordination of the acid to the metal center which shifts the second reduction wave to −1.66 V vs Fc^+/Fc. The presence of CO_2 does not induce a shift of the first reduction wave. This indicates no binding of CO_2 after only one reduction which is in contrast to the iron system. Controlled potential electrolysis (CPE) at −1.5 V in wet acetonitrile (2% water) with electrolyte ions and 3 M PhOH showed high selectivity (96% CO and 4% H_2) and a high Faradaic efficiency (FE) of 94%. $[Co^{II}(qpy)(H_2O)_2]^{2+}$ ranks among the fastest homogeneous CO_2 reduction catalysts reported to date with a TOF_{max} up to 33000 s^{-1} and an overpotential of 300 mV. This can be compared to the fastest molecular catalyst for CO_2 to CO reduction: Fe-*o*-TMA, a tetra-TMA substituted FeTPP derivative (TMA = trimethylammonio, $-NMe_3^+$), with a TOF_{max} of up to 10^6 s^{-1} at an overpotential of 220 mV.[380] A second top performing system is $[Mn(mesbpy)(CO)_3(MCN)]^+$ (mesbpy = dimesityl-2,2′-bipyridine) with a TOF_{max} 630 s^{-1} at an overpotential of 300 mV.[608] It is important to point out that both the FeTPP [380, 383, 399, 401, 402, 535–539] and Mn/Re(bpy)$(CO)_3$[132, 133, 514, 523, 527–531, 595–598, 608] systems were extensively studied and thus have optimized ligand frameworks and reaction conditions unlike the $[Co^{II}(qpy)(H_2O)_2]^{2+}$ and $[Fe^{II}(qpy)(H_2O)_2]^{2+}$ systems;

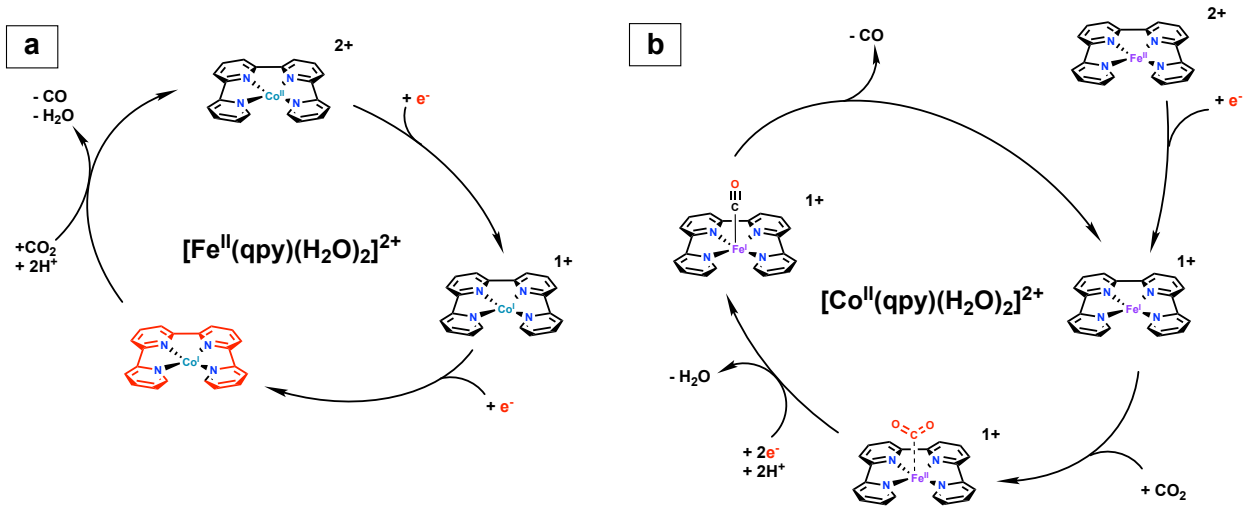

Figure 7.1: Proposed catalytic pathways by Robert *et al.* [561] for both (a) $[Fe^{II}(qpy)(H_2O)_2]^{2+}$ and (b) $[Co^{II}(qpy)(H_2O)_2]^{2+}$ based on experimental observations; the red colored molecular moiety indicates localization of the excess electrons.

see references [380],[561] and [608] for benchmarking Tafel plots including more (less active) catalysts. A second study [602] on $[Co^{II}(qpy)(H_2O)_2]^{2+}$ revealed that an alternative pathway for CO2RR under different conditions is feasible: at lower acid concentrations (0.1 M PhOH) and a higher applied potential (-1.98 V vs Fc^+/Fc), a second pathway via a triply reduced catalyst is accessible. However, both FE (77%) and selectivity against HER (77% CO and 20% H_2) are decreased.

$[Fe^{II}(qpy)(H_2O)_2]^{2+}$ exhibits a reversible first reduction wave at -1.39 V vs Fc^+/Fc and a second reversible reduction at -1.60 V vs Fc^+/Fc under argon atmosphere. The first reduction wave is positively shifted by 0.021 V and becomes irreversible upon saturation with CO_2. This suggests an EC mechanism: electron transfer (E) followed by the chemical (C) addition of CO_2 to the iron catalyst. The rate constant was estimated as 82 $s^{-1}M^{-1}$ based on the scan rate dependence of the shift (assuming pure kinetic conditions). This corresponds to an activation energy of $\sim$15 kcal/mol (using transition state theory). Catalysis is observed after the second reduction at approximately -1.60 V vs Fc^+/Fc and is enhanced with an acid (phenol). On the backward scan an oxidation wave at -1.09 V vs Fc^+/Fc was observed. The shift to more anodic potentials is attributed to a singly reduced carbonyl species $[Fe(qpy)CO]^+$. The presence of this carbonyl species is further established by CV experiments under CO atmosphere where a reversible reduction wave at -1.17 V vs Fc^+/Fc is observed, suggesting an EC sequence. In addition, a second reduction wave is observed at -1.42 V vs Fc^+/Fc which corresponds to the reduction of the singly reduced $[Fe(qpy)CO]^+$ species. CPE at -1.6 V vs Fc^+/Fc (240 mV overpotential) in wet acetonitrile (2% water) and 1 M PhOH showed that the catalyst produces CO with over 99% selectivity but with

a low Faradaic efficiency of 48%. However, the FE can be improved to 70% by irradiation with visible light during the electrolysis. It is conjectured that light promotes CO release from the $[Fe(qpy)CO]^+$ intermediate over further reduction to $[Fe(qpy)CO]^0$.

7.2 Computational Model

All quantum chemical calculations were performed with the Q-Chem package [108] (version 5.2.0) using the ωB97X-D [68] density functional for all Fe compounds and the B3LYP-D3 [50, 56, 57, 414] density functional for all Co compounds. All DFT calculations use a (75, 302) grid (75 radial shells with 302 Lebedev points on each) for the integration of the exchange-correlation functional. The reason for choosing different functionals is to ensure that the predicted reduction potentials are in good agreement with the experimentally reported values (see below for further discussion). Minima and transition state (TS) geometries were verified as stationary points by harmonic vibrational frequencies.

The geometry optimization and frequency calculations employed a mixed basis (def2-SVP for N,C,H, def2-SVPD for O and def2-TZVP basis set for Fe and Co). [247] Single point calculations were performed with the larger def2-TZVPPD basis [247] to decrease the basis set incompleteness errors, consistent with best practices. [20]

The solvation energies were calculated using the C-PCM model (acetonitrile, $\epsilon = 35.88$) as implemented in Q-Chem [119]. All molecular orbitals (MOs) were plotted using an isovalue of 0.03 (blue: positive, red: negative values) and spin densities were visualized using an isovalue of 0.005 (green: α spin density, gold: β spin density).

The reaction free energies ($\Delta_R G$), activation energies ($\Delta G^\ddagger$), reduction potentials, and pK_a values were calculated based on the standard thermodynamic cycles. [532] The Gibbs free energies include enthalpic contributions from the zero-point energy correction and the entropic contribution, which is calculated from the vibrational frequencies at T = 298 K. Solvation energies were approximated using single point calculations with the implicit C-PCM solvent model.

The gas phase rigid rotor and harmonic oscillator approximations were used for the entropic contribution to the free energies of CO_2 binding. It is known that this approach can overestimate entropies for species in solution because both translational and rotational degrees of freedom are reduced by surrounding solvent molecules. The comparison with experimental entropies (obtained via Henry's Law) indicate differences of up to 9 kcal/mol for the free energy of CO_2 in solution. [609, 610] This implies that calculated CO_2 binding free energies are too endergonic.

The calculation of accurate free energies for protonation reactions is difficult due to the poor description of the solvation energy of protons by implicit solvent models. Therefore, the experimental value based on the Sackur-Tetrode equation and an estimated solvation energy of $G_{solv}(H^+) = -264.6$ kcal/mol in acetonitrile was used.[125, 130] Studies found deviations of this approach versus experimental values of $\pm$ 3 pK_A units. [549] We tested our computational protocol for phenol: B3LYP yielded a pK_a of 24.8 and ωB97X-D 24.6 which

are 4-5 units lower than the experimental value of 29.1 in acetonitrile [551]. In spite of this systematic computational error, calculated relative pK_a values are more reliable because of favorable error cancellation by removing the experimental free energy of the proton. Thus, calculated pK_a values should mainly be compared against each other. It is important to point out that the implicit solvation model corresponds to a pure solution of acetonitrile. However, electrolysis experiments were conducted in a solution of 3 M phenol in acetonitrile, saturated with 1 atm of CO_2, not in pure acetonitrile. Therefore, the actual pK_a of possible intermediates under the experimental conditions should be lower than the calculated values due to several factors: first, experimental pK_a values of acids in mixtures of acetonitrile and water are lower than in pure acetonitrile. [550, 551] This decrease in pK_a is not accounted for by the implicit solvent model used in our calculations. Second, the introduction of CO_2 to the water-acetonitrile-phenol mixture lowers the effective pK_a of the solution. This occurs via the direct formation of carbonic acid or complexation between CO_2 and OH^-. For reference, the experimental pK_a of water-acetonitrile mixtures saturated with carbon dioxide is estimated to be 11. [552] Therefore, we report not only the pK_a value of the protonation steps but also the free energy of the protonation reaction coupled to carbonic acid. This is in line with experimental approaches of determining the overpotential which also use carbonic acid as the proton source. Even if it is assumed that phenol is involved in the rate limiting barriers (*vide supra*), the conjugated base phenolate is reprotonated by the strongest acid in the solution which is carbonic acid or aqueous CO_2. [380]

We use phenol as the main proton source for calculating reaction barriers involving protonation reactions as it was added to the reaction mixture in the CPE experiments. [561] The concentration of other proton sources (H^+ and H_2CO_3) is negligible. [532] Nonetheless, we also present the reaction barriers with H_2CO_3 for the Fe system. These kinetic barriers do not reflect the experimental conditions. We include them here to illustrate how barriers for the protonation steps decrease with a stronger acid. The calculated pK_a in acetonitrile of H_2CO_3 (13) is significantly lower than phenol (25). We note that implicit solvation models poorly describe the solvation of anions where the charge is concentrated, e.g. PhO^-. The augmentation of implicit solvent calculations with explicit water molecules improves the accuracy as it helps to account for strong short-range hydrogen bonding interactions between the anion and the solvent.[124] Hence, adding an explicit water molecule in the pK_a calculations to stabilize the conjugate base PhO^- decreases the pK_a to 22.

Reduction potentials are reported with an isodesmic scheme against the ferrocene/ ferrocenium couple used as an internal standard. [127, 128] This methods allows accurate predictions even at a modest level of theory with reported accuracy of $\sim$ 100 mV to experimental values. [128]

We used different functionals for the Fe (ωB97X-D) and Co (B3LYP) complexes as these functionals provided the best match between predicted and experimentally reported reduction potentials; see tables F.2 and F.3 in the appendix. Unfortunately, many properties [611] of transition metal systems like energetics of ligand dissociation [612, 613], adiabatic spin gaps (high spin–low spin) [614, 615] or reduction potentials [616] are sensitive to limitations of approximate Kohn-Sham DFT functionals. In particular, many observables are

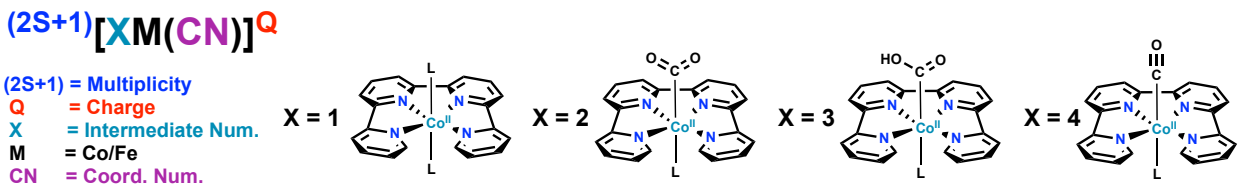

Figure 7.2: Naming scheme for intermediates used throughout the manuscript.

quite sensitive to the amount of "exact" exchange (Hartee-Fock exchange), as this parameter strongly affects the extent to which the charge delocalization error (often also described as self-interaction error) affects a given system-functional pair. [324] Thus, a separate choice of functional for each transition metal complex was necessary to accurately reproduce the experimental findings. However, our main findings like relative barrier heights, key MOs , localization of electrons upon reduction (ligand centered vs. metal centered); and CO_2 binding modes are robust to a broad spectrum of suitable functionals unless otherwise noted in the main text (see appendix F).

7.3 Results

We employ a naming scheme which encodes the spin multiplicity (2S+1), the total charge, the coordination number (CN), a consecutive number X for each intermediate step (1: initial complex, 2: CO_2 adduct, ...) and an element symbol M (M = Co, Fe) to indicate the central metal: $^{\text{multiplicity}}[\mathbf{XM}(\text{CN})]^{\text{charge}}$ (see figure 7.2). As an example, $^4[\mathbf{1Co}(6)]^{2+}$ describes the initial hexacoordinated diaqua complex $[\text{Co}^{\text{II}}(\text{qpy})(\text{H}_2\text{O})_2]^{2+}$ in the quartet spin state and overall charge 2+.

Catalytic Pathway for $[\text{Co}^{\text{II}}(\text{qpy})(\text{H}_2\text{O})_2]^{2+}$

The proposed catalytic cycle for the electrochemical reduction of CO_2 to CO with added phenol (3 M) catalyzed by $[\text{Co}(\text{qpy})(\text{H}_2\text{O})_2]^{2+}$ is depicted in figure 7.3 (see figure F.9 for a more detailed cycle including a possible third reduction). The first reduction of $[\text{Co}(\text{qpy})(\text{H}_2\text{O})_2]^{2+}$ ($^4[\mathbf{1Co}(6)]^{2+}$, figure 7.4 (a)) is a ligand based reduction in the low-lying π^* orbital of the non-innocent qpy moiety and accompanied by the loss of one aqua ligand forming $[\text{Co}(\text{qpy})(\text{H}_2\text{O})]^+$ ($^3[\mathbf{1Co}(5)]^+$). The reduction is further stabilized by an antiferromagnetic (afm) coupling to the high-spin d^7 Co(II) center, which rationalizes the low reduction potential. The electronic structure is illustrated with a schematic MO diagram in figure 7.6 (a). The calculated reduction potential is −0.78 V (vs Fc^+/Fc), which is in acceptable agreement with the experimentally measured potential (−0.95 V). The electronic structure is illustrated by the spin density plot of $^3[\mathbf{1Co}(5)]^+$ in figure 7.4 (c) and can be compared to the spin density of $^4[\mathbf{1Co}(6)]^{2+}$ in figure 7.4 (b) where the spin density is localized solely on the metal

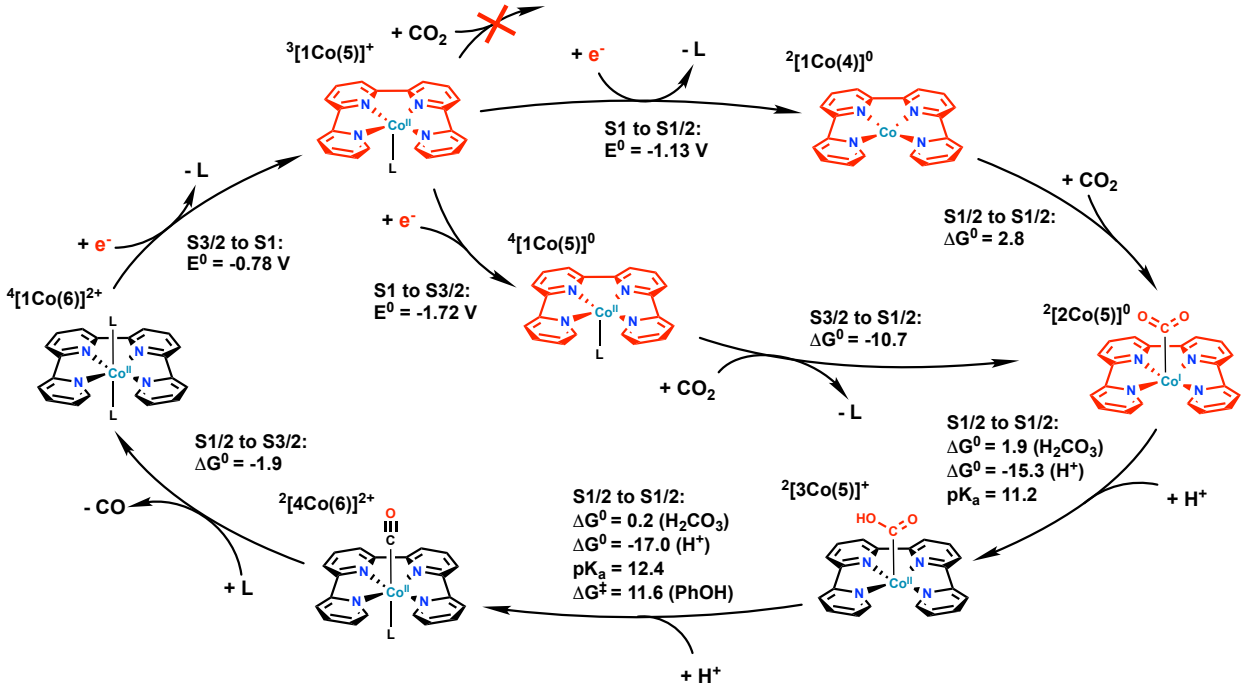

Figure 7.3: Proposed mechanism for the selective CO_2 to CO reduction using $[Co(qpy)L_2]^{2+}$; the red colored molecular moiety indicates localization of the excess electrons; reaction and activation energies in kcal/mol; reduction potentials against Fc/Fc^+; L = H_2O; see figure 7.2 for the naming conventions.

center. The ligand loss reduces the negative charge on the central metal and allows a stronger afm coupling. This seems to compensate for the weaker d orbital splitting, maintaining the high spin state.

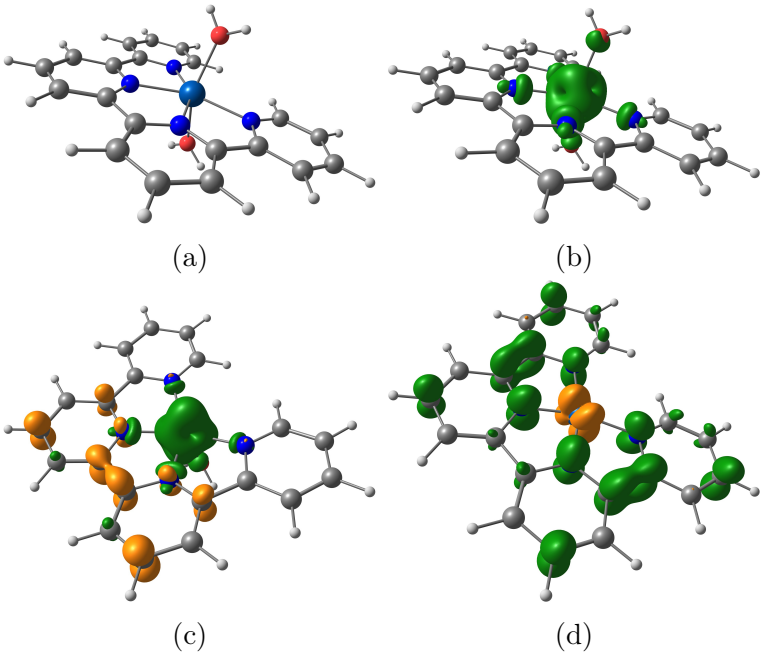

Figure 7.4: (a) Geometry of the unreduced $[Co^{II}(qpy)(H_2O)_2]^{2+}$ ($^4[\mathbf{1Co}(6)]^{2+}$); (b) Spin density of $^4[\mathbf{1Co}(6)]^{2+}$; (c) Spin density of the singly reduced intermediate $^3[\mathbf{1Co}(5)]^{+}$; (d) Spin density of the doubly reduced intermediate $^2[\mathbf{1Co}(4)]^{0}$. Green and gold colors indicate excess of α or β spin electron density, respectively.

The second reduction step is accompanied by the dissociation of the second aqua ligand to form $[Co(qpy)]^0$ ($^2[\mathbf{1Co}(4)]^0$) with a distorted square planar coordination geometry. Counterintuitively, the weaker d orbital splitting accompanies a spin transition to a low spin Co resulting in a doublet metal center with a singly occupied d_{xz} type orbital and an empty $d_{x^2-y^2}$. This surprising result can be explained by a bonding interaction between the metal and qpy ligand, which stabilizes the second excess electron. The bonding occurs due to the stabilization of the d_{xz} orbital by coupling with the qpy π^* orbital. Analysis of the electronic structure reveals that the second excess electron is strongly delocalized between metal and ligand. It can be understood as a formally doubly reduced qpy moiety (triplet π^*) and a doublet Co^{II} (d_{xz}) coupling to an overall doublet with a weak π type metal ligand bond. The HOMO in the α space is a solely qpy based π^*, but the HOMO-1 exhibits significant metal contribution (46%) and a π type bonding character between the d_{yz} (which is empty in the α space) and a qpy π^*. The electronic structure is illustrated in a schematic MO diagram in figure 7.6 (b) and the spin density plot in figure 7.4 (d). Thus, the second electron is highly delocalized between the metal and the qpy moiety and the reduction *cannot* be classified as metal or ligand based. Further evidence for the significant metal contribution in the second reduction is shown by the comparison of the doublet $^2[\mathbf{1Co}(4)]^0$ to the corresponding quartet $^4[\mathbf{1Co}(4)]^0$ (uncoupled metal doublet and ligand triplet), which localizes both excess electrons in the qpy ligand. The partial Mulliken charges on Co change by 0.4 from the quartet state to the doublet state. (The spin contamination of this broken symmetry solution is mild ($\langle S^2 \rangle$ =0.92) which also confirms small contributions of the quartet spin state and a bonding character between the Co d_{xz} and qpy π^*). Thus, the energetics and overlap of Co d_{xz} and qpy π^* allows for an efficient delocalization of the electron over both metal and ligand. The formation of this bonding interaction significantly shortens Co-N bond distances to 1.93 Å (from 2.14 Å in $^3[\mathbf{1Co}(5)]^+$) which results in a distortion of the qpy framework to avoid repulsion of two hydrogen atoms (see figure S1 (b)). In contrast, the first reduction from $^4[\mathbf{1Co}(6)]^{2+}$ to $^3[\mathbf{1Co}(5)]^+$ does not change the bond distance significantly (2.16 to 2.14 Å).

The stabilization of the second excess electron via the metal-ligand bond rationalizes the mild second reduction potential. The calculated reduction potential is -1.13 V (vs Fc/Fc^+), which is in excellent agreement with the experimentally measured potential (-1.18 V). It is noteworthy that a ligand centered first reduction was also observed in all other possible spin states; furthermore, these findings are robust with respect to different DFT functionals (for all possible spin states as well). The doubly reduced doublet species ($^2[\mathbf{1Co}(4)]^0$) was also identified as the most stable isomer among all possible doubly reduced isomers, but the degree of metal-ligand delocalization varied among different density functionals (see table F.1). However, the metal-ligand delocalization observed with the B3LYP functional is similar to multi-reference active space (CASSCF) calculations (see table F.1 and appendix F section CASSCF).

Experimentally, the first reduction wave is reversible, but the second one is irreversible and only visible at slow scan rates. Because of this, Robert *et al.* [561] assign the first reduction to be metal centered and the second reduction as ligand centered, with a slow loss of H_2O which was also hypothesized by Che *et al.* [601]. This is in contrast to our

calculations, in which the first reduction is mainly ligand based and the loss of the first aqua ligand does not change the spin at the Co center. Thus, the reorganization energy is small, and the electron transfer is fast. In contrast, the second reduction has significant metal character and also induces a spin transition from high spin to low spin. Consequently, the reorganization energy is significantly larger and the kinetics of the electron transfer more sluggish. Thus, we provide an alternative interpretation of the experimental observations. Further CV experiments with phenol revealed a binding of phenol to the complex after the first reduction and a significant shift in the second reduction wave to -1.66 V vs Fc^+/Fc (from -1.18 V). This can be compared to the calculated reduction potential of the second reduction *without* an allowed water loss: -1.72 V vs Fc^+/Fc from $^3[\mathbf{1Co}(5)]^+$ to $^4[\mathbf{1Co}(5)]^0$ (assuming the effect of H_2O and PhOH on the d orbital splitting is similar). This highlights the importance of the ligand loss and the spin transition in order to access the stable doubly reduced intermediate $^2[\mathbf{1Co}(4)]^0$.

It is noteworthy that a similar reduction pathway was observed by some of us with experimental evidence for the reduced intermediates in an iron complex with a terpyridine ligand scaffold. [398]. Both reductions are ligand based, but the second reduction is accompanied by the loss of an acetonitrile ligand and a spin transition from a low spin to intermediate spin iron (S = 2). The metal d orbital mixes strongly with the terpyridine π^* orbitals, similarly resulting in a mild reduction potential. The π^* orbitals of the qpy moiety are even lower in energy than the terpyridine moiety, which rationalizes that these orbitals are involved in both reduction steps of $[Co(qpy)(H_2O)_2]^{2+}$.

The catalyst state which binds CO_2 is most likely the doubly reduced complex $^2[\mathbf{1Co}(4)]^0$ (or $^4[\mathbf{1Co}(5)]^0$) because it was not possible to converge a singly reduced CO_2 adduct. This suggests that the catalytic pathway follows an EEC mechanism. CO_2 binds to $^2[\mathbf{1Co}(4)]^0$ in the η^1-κC binding mode to form $[Co(qpy)(CO_2{-}\kappa C)]^0$ ($^2[\mathbf{2Co}(5)]^0$) and the binding induces bending of the CO_2 $\angle$(OCO) angle of 146°, which indicates the transfer of nearly one electron into the CO_2 moiety as the $\angle$(OCO) is 134° for free $CO_2^{\bullet-}$ (see figure 7.7 (a)). It was not possible to obtain either an η^2 or η^1-κO isomer. The spin density plot of $^2[\mathbf{2Co}(5)]^0$ shows little spin polarization on both Co and CO_2 and one electron still occupies the qpy π^* (see figure 7.7 (b)). This is also confirmed by the Mulliken spin population which is approximately 0.2 for both Co and CO_2. Analysis of the MOs suggests a Co(I) in a d^8 configuration forming a dative σ bond with CO_2 via the doubly occupied d_{z^2} and the CO_2-LUMO, see figure 7.6 (c). The hybrid d_{z^2} + CO_2-π^* MO has $\sim$ 70% d_{z^2} character. The oxidation state is confirmed by a localized orbital bonding analysis [617] which localizes 3 orbitals with over 90% Co d-character and one d orbital with over 70% Co d-character. The binding is slightly endergonic but barrierless (ΔG = 2.8 kcal/mol). The lowered oxidation state makes Co a good Lewis base, and the low coordination number stabilizes the d_{z^2} orbital; both factors seem to facilitate CO_2 binding. We probed the effect of adding a single explicit water to stabilize the reduced CO_2 in $^2[\mathbf{2Co}(5)]^0$. The structure is depicted in S2 (a) and shows a more activated CO_2 as the $\angle$(OCO) slightly decreases. However, the stabilizing effect on thermodynamics is small as the formation of this complex is thermodynamically neutral. The CO_2 addition becomes significantly more exergonic (-10.7 kcal/mol) under higher acid

concentration and a more negative potential for CPE as this implies a pathway via the less stable doubly reduced $^4[\mathbf{1Co}(4)]^0$. This is in line with the experimental finding that a potential of -1.5 V vs Fc/Fc^+ is required to observe significant catalysis. Our calculation suggest that additional thermodynamic driving force is necessary as the subsequent reaction steps (protonation) are endergonic (*vide infra*).

The subsequent protonation of the CO_2 adduct $^2[\mathbf{2Co}(5)]^0$ is also barrierless using PhOH as the proton source with a pK_a of 11 and is slightly endergonic coupled to the deprotonation of H_2CO_3 (1.9 kcal/mol). Upon proton transfer, both excess electrons localize on the CO_2 moiety as the CO_2 angle of 121° indicates (see figure 7.8 (a)). The resulting anionic carboxy intermediate $[Co(qpy)(COOH)]^+$ ($^2[\mathbf{3Co}(5)]^+$) is stabilized by a dative bond to a low spin Co(II) central metal. Thus, the addition of a proton source leads to the second reduction of CO_2 via a push-pull mechanism, where the initial reduction of CO_2 is achieved by a "push" from the metal center and the second reduction arises from "pulling" of the acid associated with the first protonation. [400] If phenol is assumed to be the proton source, the catalytic cycle proceeds most likely via a phenoxide–$^2[\mathbf{3Co}(5)]^+$ complex. The phenoxide is then either reprotonated via the reaction with water and CO_2 yielding phenol and HCO_3^- or stabilized by a counter-ion (e.g. electrolyte). The free energy for the formation of this complex is estimated to be 10.6 kcal/mol (see figure F.3). Hence, this reaction step could become slow during long electrolysis experiments when the pH of the reaction increases as the concentration of CO_2 decreases.

The second protonation yields the carbonyl $[Co(qpy)(H_2O)(CO)]^{2+}$ ($^2[\mathbf{4Co}(6)]^{2+}$) and water with a pK_a of 12 which is thermodynamically neutral when coupled to the deprotonation of H_2CO_3 (0.2 kcal/mol). The protonation process is coupled to the C−O bond cleavage; the transition state exhibits a stretched C−O bond (2.12 Å) and is depicted in figure 7.8. The activation barrier for the reaction is 11.6 kcal/mol, constituting the rate limiting step in the cycle (corresponding to a rate of $\sim$20000 s^{-1}). $^2[\mathbf{4Co}(6)]^{2+}$ is not stable since the high oxidation state of the central metal allows only for a weak backbonding interaction with CO. Consequently, the dissociation of CO and regeneration of $[Co(qpy)(H_2O)_2]^{2+}$ is thermodynamically favorable ($\Delta_R G = -1.9$ kcal/mol). In total, the pathway via $^2[\mathbf{1Co}(4)]^0$ exhibits three consecutive endergonic reaction steps and is overall endergonic by 3 kcal/mol. This could explain why no catalysis is observed at -1.13 V vs Fc/Fc^+. Instead at higher acid concentration and more negative potential the less stable doubly reduced intermediate $^4[\mathbf{1Co}(5)]^0$ is accessed which makes CO_2 addition, and the whole pathway, exergonic.

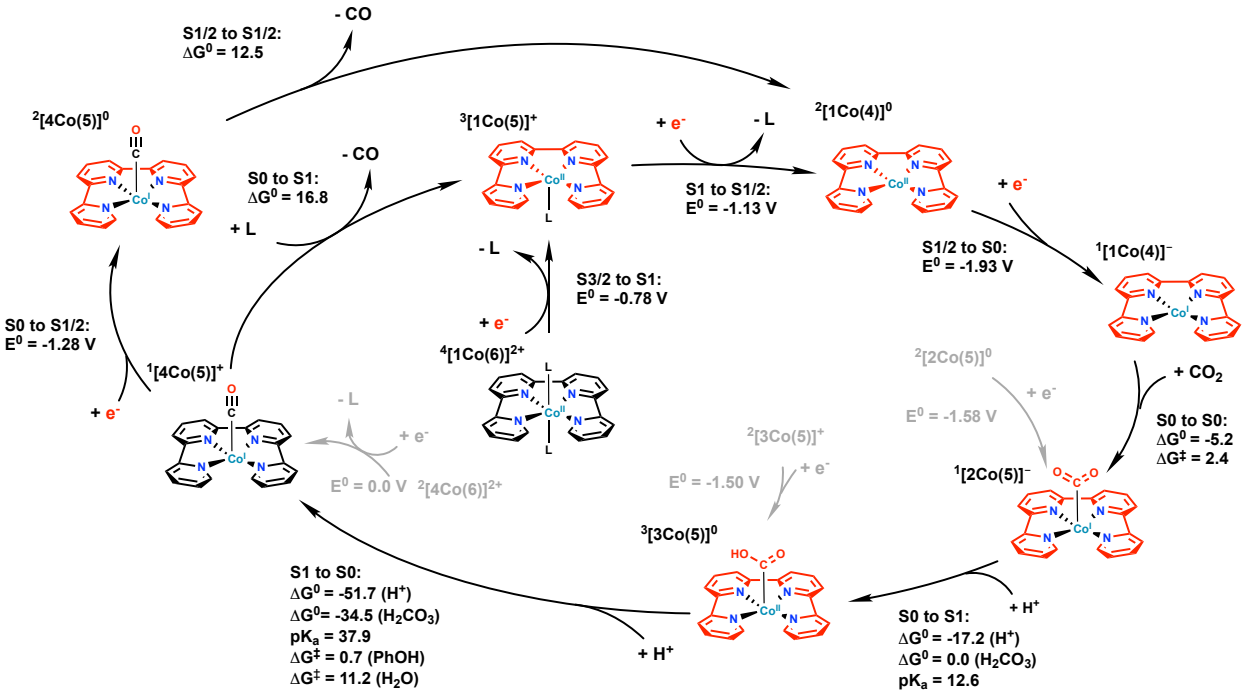

Figure 7.5: Proposed mechanism for CO_2 to CO reduction using $[Co(qpy)L_2]^{2+}$ and incorporating a third reduction; the red colored molecular moiety indicates localization of the excess electrons; reaction and activation energies in kcal/mol; reduction potentials against Fc/Fc^+; L = H_2O; grey arrows indicate connections (via reduction) to doubly reduced intermediates (see figure F.9 for the full cycle); see figure 7.2 for the naming conventions.

Increasing the applied potential to −1.98 V vs Fc^+/Fc enables CO_2 reduction at lower acid concentrations (0.1 M PhOH), albeit with a lower selectivity since a significant amount of H_2 is produced as well (*vide infra*).[602] A possible mechanism at this more negative applied potential is depicted in figure 7.5. The third reduction of the initial complex leads to $^1[\mathbf{1Co}(4)]^-$ in a singlet ground state with a doubly reduced qpy ligand (in the same orbital) and a d^8 Co(I) center. The computed reduction potential is −1.93 V vs Fc/Fc^+, which is in excellent agreement with the experimentally [602] predicted reduction potential (−1.89 V vs Fc/Fc^+). The subsequent CO_2 addition is exergonic (−5.2 kcal/mol) and has a small barrier of 2.4 kcal/mol. The adduct binds CO_2 also in a κC binding mode ($^1[\mathbf{2Co}(5)]^-$). This suggests an EEEC mechanism for CO_2 binding. The subsequent first protonation yielding $^3[\mathbf{3Co}(5)]^0$ is barrierless and thermodynamically neutral when coupled to deprotonation of H_2CO_3 with a pK_a of 13. The second protonation yielding the carbonyl complex, $^1[\mathbf{4Co}(5)]^+$, is barrierless (0.7 kcal/mol) using phenol as the proton source. The process is strongly exergonic with a pK_a of 38 and free energy of −34.5 kcal/mol (when coupled to deprotonation of H_2CO_3). The barrier remains low (11.2 kcal/mol) even with water as the proton source which explains the experimentally observed high activity without

the addition of a proton source or at low phenol concentrations. In this case the main proton source is most likely water. The driving force for the second protonation is the very stable singly reduced carbonyl which entails an extremely endergonic CO release (16.8 kcal/mol) to regenerate $^{3}[\mathbf{1Co}(5)]^{+}$. Thus, the CO release is slow, the rate limiting step in this alternative pathway and $^{1}[\mathbf{4Co}(5)]^{+}$ a persistent intermediate. The carbonyl $^{1}[\mathbf{4Co}(5)]^{+}$ is likely to accumulate during catalysis which increases the possibility for a further reduction to $^{2}[\mathbf{4Co}(5)]^{0}$ at -1.28 V vs Fc/Fc^{+}. Then, the regeneration of the catalyst is significantly less exergonic (12.5 kcal/mol). In addition, the low solubility of CO and the negative applied potential should further shift the equilibrium and facilitate the release.

In summary, an alternative pathway involving a third (and fourth reduction) is able to drive CO_2 reduction at a lower acid concentration (0.1 M versus 3 M) but a higher applied potential (1.98 V versus 1.5 V vs Fc/Fc^{+}). The second protonation and the CO release are the rate limiting processes. The stability of the carbonyl intermediate allows to drive the reaction efficiently even with water as the proton source (see figure S11(a)–(c) for the transition states). Therefore, this catalyst is able to operate efficiently under different experimental conditions by proceeding via a second mechanism. In both proposed cycles, the rate-limiting barriers are similar which is in line with the similar experimentally measured rates despite the distinct conditions.[561, 602]

A connection to the third reduction pathway is accessible at all intermediates as the reduction of the CO_2, CO_2H and CO intermediates is possible at potentials lower than -1.72 V vs Fc/Fc^{+} (the second reduction at high acid concentration, see figure F.9 for a detailed cycle including a third reduction for every intermediate). Thus, triply reduced intermediates could accumulate and could be responsible for the generation of H_2 as the selectivity in the three electron pathway is significantly lower. However, the first protonation process is barrierless, the barrier for the second protonation barrier is low and the CO release is barrierless. Therefore, it is unlikely for both $^{2}[\mathbf{4Co}(6)]^{2+}$ and $^{2}[\mathbf{3Co}(5)]^{+}$ to persist long enough in order to get further reduced. This is also in line with experimental observations as FE for CO_2 to CO conversion is 94%.

A possible HER mechanism is depicted in figure F.7, starting with a direct protonation of $^{2}[\mathbf{1Co}(4)]^{0}$. The formation of a hydride has a pK_a of 12 similarly to both protonation steps in the CO2RR cycle and is thermodynamically neutral (0.2 kcal/mol). However, it was not possible to find a transition state for the direct formation of a hydride with phenol. The acid prefers to coordinate to the metal via a dative bond (via O) which can lead to a possible protonation of a pyridine. This could either be a possible degradation pathway or HER proceeds via an unconventional pathway which is most likely not competitive with the barrierless CO_2 addition. This is in line with experimental findings as CPE experiments with the addition of phenol yield over 96% CO. The exact nature of the (minority) HER mechanism, however, is beyond the scope of this work. The formation of a hydride after three reductions via $^{1}[\mathbf{1Co}(4)]^{-}$ is exergonic with a pK_a of 18 and -7.3 kcal/mol. Furthermore, the process is barrierless (using phenol as the proton source) which can explain the significant amount of H_2 produced by this pathway.

The in-depth analysis of possible catalytic pathways is a basis for modifications to improve

the catalyst by optimizing the metal-ligand interaction for $^2[\mathbf{1Co}(4)]^0$. Performance could be altered by modifying the energy of the qpy π^* orbitals by introducing electron donating or withdrawing substituents. Table 7.1 shows the effect of three substituents ($-NH_2$, $-F$, $-CN$) on both the reduction potentials and the barrier of the (rate limiting) transition state. We assume that the introduction of the substituents do not alter the proposed mechanism. The substituent is introduced twice at the 4″ and 4‴ positions (para positions of the two inner pyridines). We probe both a positive mesomeric effect with $-NH_2$ and a negative mesomeric effect with $-CN$. The amino group raises the qpy π^* orbital energy and this consequently increases the reduction potentials significantly. Conversely, the nitrile group lowers the qpy π^* orbital energy which reduces the reduction potentials. The first reduction is more affected since it is mainly ligand based. The effect on the barriers is reversed: the amino group decreases the barrier whereas the nitrile increases the barrier. Interestingly, the fluoride group has a weak positive mesomeric effect and negative inductive effect which decreases both overpotential and the barrier mildly. Furthermore, a fluoride substituent would increase the solubility in aqueous solutions.

The amino-qpy could both decrease overpotential and increase catalytic activity more significantly by altering the pathway. The analysis of the unsubstituted complex's catalytic pathway suggested that the less stable doubly reduced $^4[\mathbf{1Co}(5)]^0$ is accessed under high acid concentrations and higher applied potentials as these conditions provide important thermodynamic driving forces for the subsequent reaction steps (*vide infra*). In case of the amino-qpy, the increase of the second reduction potential could provide enough thermodynamic driving force to drive catalysis via the four coordinated doubly reduced intermediate $^3[\mathbf{1Co}(4)]^0$ at less negative potential than the unsubstituted complex (via $^4[\mathbf{1Co}(5)]^0$). In addition, the amino substituent decreases the barrier of the rate limiting step substantially. Hence, the amino group could reduce both the overpotential and increase the rate.

Substituent	E_1	E_2	$\Delta G^{\ddagger}$
$-H$	-0.78	-1.13	11.6
$-NH_2$	-1.11	-1.31	7.9
$-CN$	-0.24	-0.79	17.7
$-F$	-0.71	-1.08	10.9

Table 7.1: Effect of introducing a substituent at the 4″ and 4‴ position of the qpy on both reduction potentials and the barrier of the second protonation (rate limiting step). Reduction potential in V versus Fc/Fc^+, activation energy in kcal/mol using phenol as the proton source.

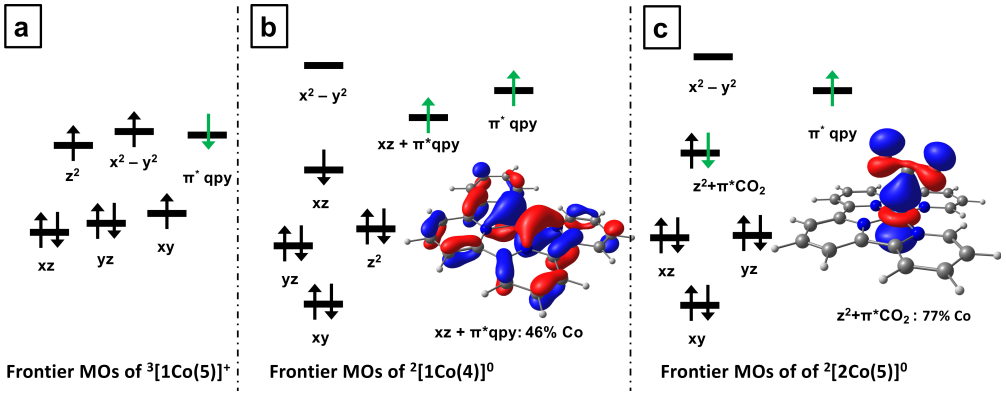

Figure 7.6: Schematic MO diagram of the important intermediates in the cycle: a) the singly reduced complex $[Co(qpy)(H_2O)]^+$ ($^3[\mathbf{1Co}(5)]^+$), b) the doubly reduced complex $[Co(qpy)]^0$ ($^2[\mathbf{1Co}(4)]^0$) and c) the CO_2 adduct $[Co(qpy)(CO_2{-}\kappa C)]^0$ ($^2[\mathbf{2Co}(5)]^0$). The green arrows indicate the extra electrons due to reduction. The MO in (b) illustrates the delocalized π type metal (d_{xz}) ligand (π^*) bond to stabilize the excess electron; the MO in panel (c) illustrates the σ type interaction of the Co-d_{z^2} orbital and the CO_2 LUMO leading to the η^1 binding mode in $[Co(qpy)(CO_2{-}\kappa C)]^0$.

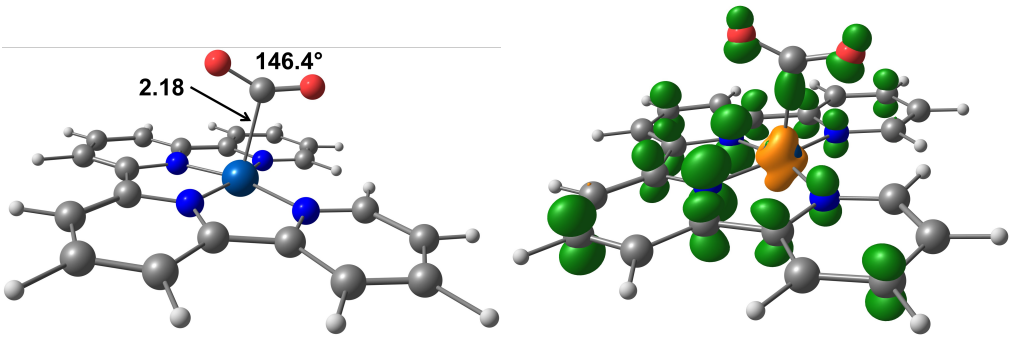

(a) (b)

Figure 7.7: (a) Geometrical parameters of $[Co(qpy)(CO_2)]^0$ ($^2[\mathbf{2Co}(5)]^0$), the doubly reduced complex that binds CO_2, with emphasis on the structural features of the CO_2 ligand; (b) Spin density of the complex, showing most spin density remains on the qpy ligand.

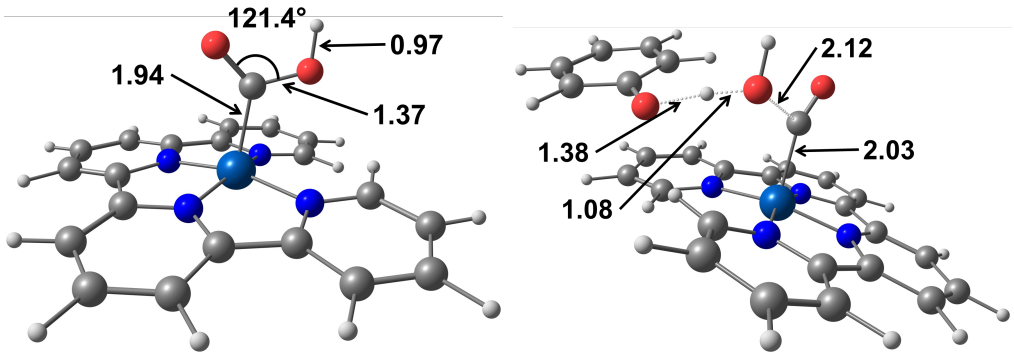

(a) (b)

Figure 7.8: (a) Geometrical parameters pertaining to $[Co(qpy)(CO_2H)]^+$ ($^2[\mathbf{3Co}(5)]^+$), highlighting the CO_2H ligand and (b) transition state for the second protonation step of $[Co(qpy)(CO_2H)]$, with phenol as the proton donor, emphasizing the structural changes of the involved species.

Catalytic Pathway for $[Fe^{II}(qpy)(H_2O)_2]^{2+}$

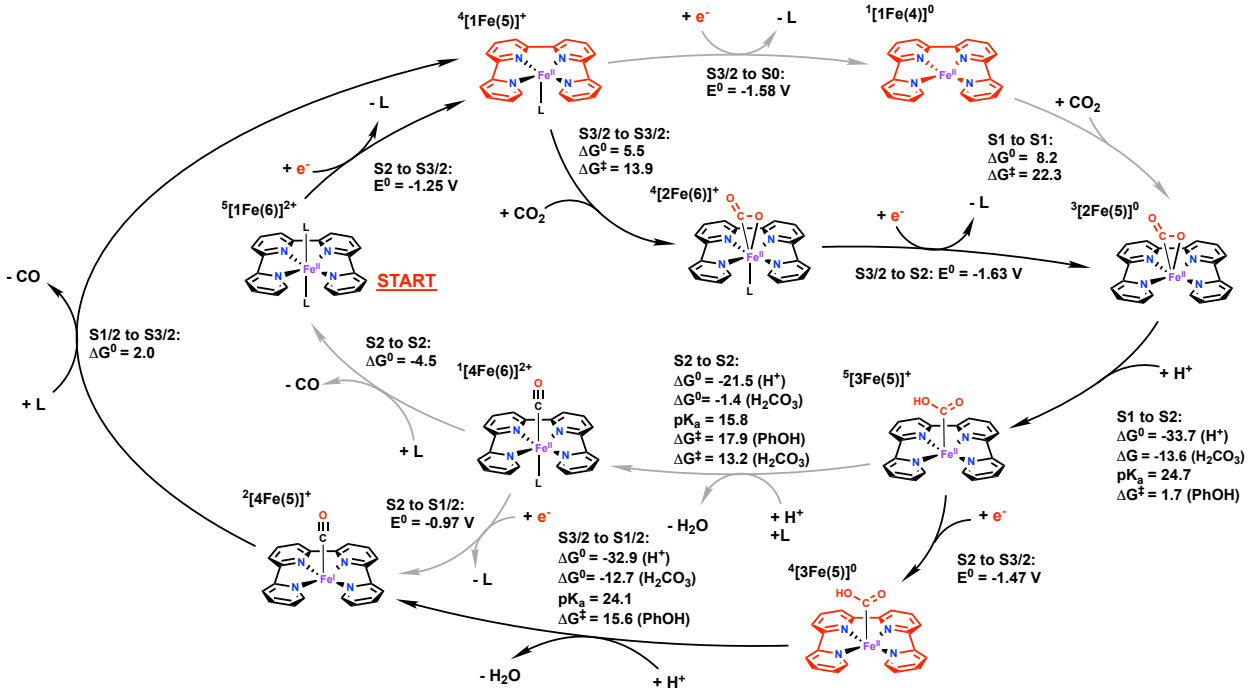

Figure 7.9: Proposed mechanism for the selective CO_2 to CO reduction using $[Fe(qpy)L_2]^{2+}$; the red colored molecular moiety indicates localization of the excess electrons; grey arrows indicate alternative competitive pathways; reaction and activation energies in kcal/mol; reduction potentials against Fc/Fc^+; L = H_2O; see figure 7.2 for the naming conventions.

The proposed catalytic cycle for CO2RR using $[Fe^{II}(qpy)(H_2O)_2]^{2+}$ is depicted in figure 7.9 (a more detailed cycle including a possible third reduction at every intermediate step can be found in figure F.10). The initial first reduction of $[Fe(qpy)(H_2O)_2]^{2+}$ (^{5}[**1Fe**(6)]$^{2+}$) to $[Fe(qpy)(H_2O)]^+$ (^{4}[**1Fe**(5)]$^+$) is a ligand based reduction in the low-lying π^* orbital of the non-innocent qpy moiety which is accompanied by the loss of one aqua ligand (see figure 7.10 (a)). The electronic structure is illustrated by the spin density plot of ^{4}[**1Fe**(5)]$^+$ in figure 7.10 (c) which exhibits an unpaired electron in the π^* of the qpy ligand framework antiferromagnetically coupled to the high spin metal (in contrast to the spin density of ^{5}[**1Fe**(6)]$^{2+}$ in figure 7.10 (b)). The electronic structure is illustrated by the schematic MO diagram in figure 7.11 (a). The calculated reduction potential is -1.25 V vs Fc/Fc^+ which is in good agreement with the experimentally measured potential (-1.39 V) but slightly less negative. This could suggest that the DFT calculation slightly overestimate the stabilization by the afm coupling. It is noteworthy that the potential of the solely ligand based reduction to the (uncoupled) sextet is -1.41 V, which is in even better agreement with the experimental potential.

The second reduction is also accompanied by a ligand loss to form $[Fe(qpy)]^0$ ($^1[\mathbf{1Fe}(4)]^0$). The square planar coordination geometry induces a spin transition on the Fe(II) from high spin (S = 2) to intermediate spin (S = 1). Unlike the cobalt catalyst, the second reduction is ligand based in a second qpy π^* orbital. The Fe contribution to both qpy π^* orbitals is small (5% & 11%). The electronic structure is best described as intermediate spin triplet Fe(II) coupled to a triplet doubly reduced qpy ligand. The electronic structure is illustrated by the spin density in figure 7.10 (d) and a schematic MO-scheme in figure 7.11 (b). This is also confirmed by CASSCF calculations as the metal ligand bonding is weaker in $^1[\mathbf{1Fe}(4)]^0$ in comparison to $^2[\mathbf{1Co}(4)]^0$ (see appendix F section CASSCF). The computed reduction potential of −1.58 V vs Fc/Fc^+ is in very good agreement with the experimentally measured potential (−1.60 V[561]). It is noteworthy, that ligand based reductions were also observed in all other possible spin states for both reduction events. Furthermore, these findings are robust with respect to different exchange-correlation functionals (see figures F.16–F.18).

Experimentally both reduction potentials are reversible with fast kinetics which suggests minimal structural reorganization. Our computational results show that both reductions are ligand based with little mixing between the iron d orbitals and qpy π^* which could explain the fast kinetics of both reductions. Hence, the Fe d orbitals are not suited to mix strongly with the π^* orbitals yielding ligand centered reductions.

The subsequent CO_2 binding is possible after either a single reduction event yielding the CO_2 adduct $[Fe(qpy)(H_2O)(\eta^2{-}CO_2)]^+$ ($^4[\mathbf{2Fe}(6)]^+$) or after two reduction events yielding $[Fe(qpy)(\eta^2{-}CO_2)]^0$ ($^3[\mathbf{2Fe}(5)]^0$). In both cases CO_2 binds in an η^2 binding mode; no η^1-κC isomer could be located as a minimum structure, and the η^1-κO isomers were significantly higher in energy (first reduction: ∼6 kcal/mol and second reduction: ∼13 kcal/mol). The binding of CO_2 induces a bending of the CO_2 angle to 147°, and the Fe−O bond distance is slightly elongated in comparison to the Fe−C bond (see figure 7.12 (a) & (c)).

The electronic structure analysis of $^4[\mathbf{2Fe}(6)]^+$ reveals a high spin (quartet) Fe center and a singly reduced $CO_2^{\cdot-}$ radical moiety (see figure 7.12 (b)). This indicates a charge transfer from the π^* orbital of the qpy into the π^* orbital of the CO_2 upon binding. The $CO_2^{\cdot-}$ moiety is stabilized by two pathways: first, by delocalizing some electron density from the CO_2-π^* into the unoccupied (in the β-space) Fe-d_{xz} via a π-type metal ligand bond; second, by a dative bond of the oxygen lone pair. This bonding situation is illustrated in the MO scheme in figure 7.11 (c) (see also figure 7.17 (b) for the MO of the dative bond). Furthermore, this binding mode was also observed both experimentally for a nickel complex [618] and in a computational study of a similar iron based catalyst by some of us [176]. The η^2 binding mode benefits from a Lewis acidic metal center due to the additional dative bond from the CO_2-oxygen and is able to stabilize the $CO_2^{\cdot-}$ moiety after a single reduction event. By contrast, iron-porphyrin based catalysts are only able to form a CO_2 adduct after multiple reductions. [380, 382]

The electronic structure of the doubly reduced CO_2 adduct $^3[\mathbf{2Fe}(5)]^0$ is similar to the singly reduced $^4[\mathbf{2Fe}(6)]^+$ –high spin Fe center and stabilized $CO_2^{\cdot-}$ moiety– as indicated by the similar O−C−O angle, Fe−C and Fe−O bond distances (see figure 7.12 (c)). The second excess electron is localized in the qpy ligand framework, and stabilized by afm coupling.

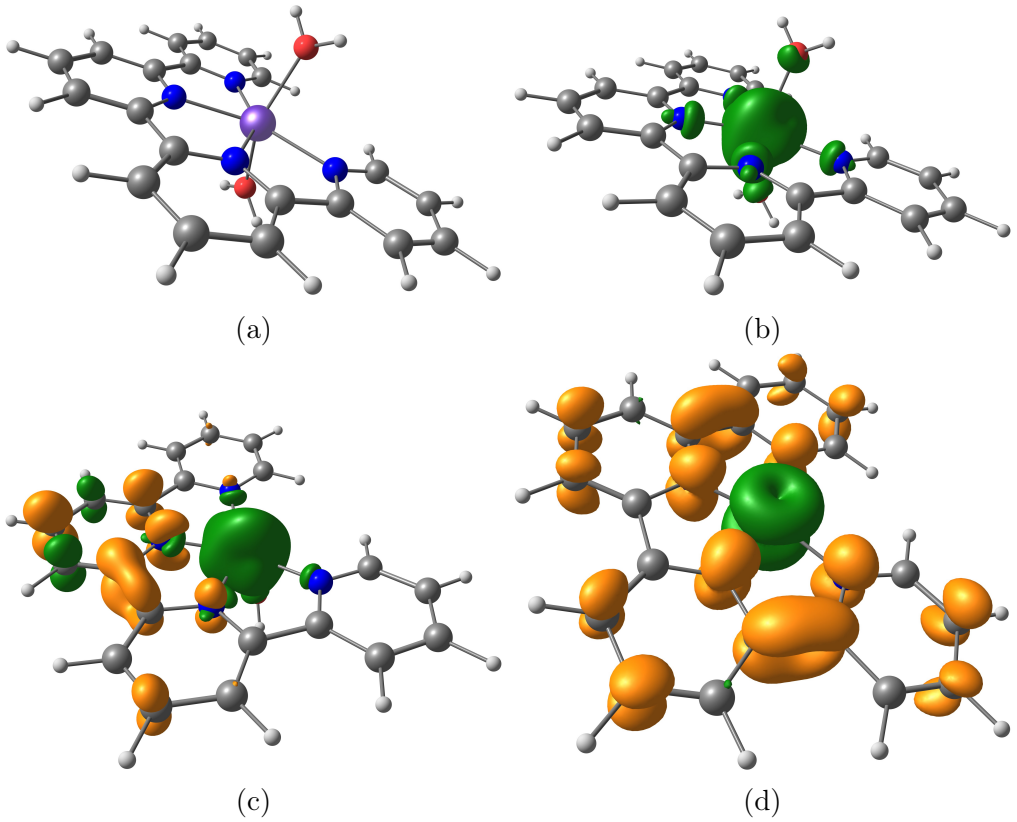

Figure 7.10: (a) Geometry of the unreduced $[Fe^{II}(qpy)(H_2O)_2]^{2+}$ (^{5}[**1Fe**(6)]$^{2+}$); (b) Spin density of ^{5}[**1Fe**(6)]$^{2+}$; (c) Spin density of the singly reduced intermediate ^{4}[**1Fe**(5)]$^{+}$; (d) Spin density of the doubly reduced intermediate ^{1}[**1Fe**(4)]^{0}. Green and gold colors indicate excess of α or β spin electron density, respectively.

Interestingly, the afm coupling to the reduced qpy ligand moiety decreases the Lewis-acidity of the Fe center. This weakens the dative bond from the CO_2 oxygen lone pair illustrated by the elongation of the Fe−O bond from 2.19 Å in ^{4}[**2Fe**(6)]$^{+}$ to 2.25 Å in ^{3}[**2Fe**(5)]^{0} despite the loss of the water ligand. We gauged the effect of adding an explicit water to stabilize the activated CO_2 for both CO_2 adducts (see figures F.2 (b) and (c)). The effect is similar in both cases: the CO_2 angle decreases further indicating a more activated CO_2 moiety.

The existence of a stable singly and doubly reduced CO_2 adduct yields two conceivable pathways: either reduction-CO_2-binding-reduction (ECE mechanism) or reduction-reduction-CO_2 binding (EEC mechanism). The binding of CO_2 is thermodynamically more favorable after the first reduction (5.5 kcal/mol versus 8.2 kcal/mol) but endergonic in both cases. However, binding after a single reduction (ECE) overcomes a significantly lower barrier (by 8.4 kcal/mol) which translates to a reaction rate that is seven orders of magnitude faster. Both transition states show similar levels of CO_2 activation with an O−C−O angle

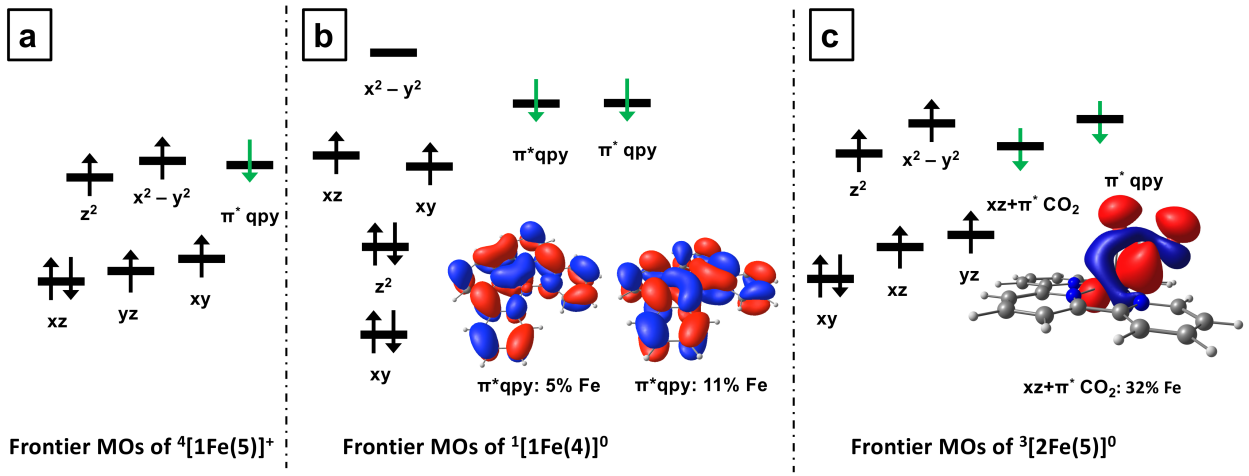

Figure 7.11: Schematic MO diagram of the important intermediates in the cycle: a) the singly reduced complex $[Fe(qpy)(H_2O)]^+$ (^{4}[**1Fe**(5)]^0), b) the doubly reduced complex $[Fe(qpy)]^0$ (^{1}[**1Co**(4)]^0) and c) the CO_2 adduct $[Fe(qpy)(\eta^2{-}CO_2]^0$ (^{3}[**2Fe**(5)]^0). The green arrows indicate the extra electrons due reduction. The MOs in (b) illustrate the mainly ligand based character of the two reductions; the MO in panel (c) illustrate the π type CO_2 LUMO Fe-d_{yz} bond in $[Fe(qpy)(\eta^2{-}CO_2)]^0$.

of 157° and a Fe−C bond distance of 2.3 Å. The weaker dative bond for the doubly reduced adduct ^{3}[**2Fe**(5)]^0 translates also to the TS: the key difference is the much shorter Fe−O bond distance in the transition state after a single reduction (see figures 7.13 (a) & (b)) and could explain the lower barrier after a single reduction. The free energy for CO_2 binding is most likely lower than the reported one due to the overestimation of the calculated entropic contribution of CO_2 (see the Computational Model section). The computed reduction potential of ^{4}[**2Fe**(6)]$^+$ to ^{3}[**2Fe**(5)]^0 is −1.63 V. This is 0.05 V higher than the predicted second reduction of the initial complex **1Fe** and should therefore be accessible.

Hence, CO_2 binding most likely occurs after a single reduction event (ECE mechanism). This is in line with experimental findings as CV experiments under CO_2 atmosphere lead to a positive shift and loss of reversibility in the first reduction wave. This suggests a chemical reaction step after the first reduction. Scan rate dependence studies showed a rate constant of 82 $s^{-1}M^{-1}$ which corresponds to a barrier of ∼15 kcal/mol similar to the computed barrier of 13.9 kcal/mol.

The subsequent protonation of the CO_2 adduct ^{3}[**2Fe**(5)]^0 yields the carboxy adduct $[Fe(qpy)(COOH)]^+$ (^{5}[**3Fe**(5)]$^+$), the protonation of the singly reduced adduct ^{4}[**2Fe**(6)]$^+$ is thermodynamically unfavorable. The protonation induces charge transfer of the second excess electron from the qpy π^* orbital into the CO_2H moiety which also causes a change in the binding mode from η^2 to η^1-κC and decreases the O−C−O binding angle to 118°.

The spin density is localized solely on the Fe-center which implies a doubly reduced CO_2H^- moiety acting as a ligand through the carbon lone pair to a high spin Fe center. The reaction is thermodynamically favorable by −13.6 kcal/mol (coupled to H_2CO_3) as indicated by the high pK_a (25), where the main driving force is to restore aromaticity in the qpy ligand. The activation energy of 1.7 kcal/mol makes this process almost barrierless; the transition state is depicted in figure 7.14 (b). The addition of a water molecule is essential to facilitate a fast protonation step. In the transition state a water molecule significantly facilitates the protonation as it stabilizes both the conjugate base and the electron localization in the CO_2 moiety. In contrast when the water molecule acts as a sixth ligand, the corresponding transition state geometry changes significantly (see figure F.5) and is higher in energy (over 10 kcal/mol).

The second protonation is accompanied by the cleavage of the C−O bond to form the carbonyl intermediate $[Fe(qpy)(H_2O)(CO)]^{2+}$(^{2}[**4Fe**(6)]$^+$) and water. The process is exergonic by −1.4 kcal/mol (coupled to H_2CO_3), but the pK_a is significantly lower (9 units) than the first protonation. The barrier is the highest in the cycle at 17.9 kcal/mol, making this step rate limiting. The transition state involves a weak interaction of the phenol with the metal center resulting in significant distortion in the complex (see figure 7.14 (c)). The high oxidation state results in a weak Fe-CO interaction making the CO release and regeneration of the catalyst exergonic and barrierless. The protonation steps are summarized in table 7.2.

The barrier for the second protonation using the stronger acid H_2CO_3 is 13.2 kcal/mol which is 4.7 kcal/mol lower than the barrier with phenol (see table 7.2 and see figure F.6 (b) for the structure of the TS). Consequently, the stronger acid should significantly increase the catalytic activity. Therefore, a stronger acid could drive the second protonation efficiently *without* a further third reduction (*vide infra*).

Reaction				pK_a	$\Delta G^\ddagger$
1 st protonation:	^{3}[**2Fe**(5)]^0 +H^+	⟶	^{5}[**3Fe**(5)]$^+$	25	1.7
2 nd protonation:	^{5}[**3Fe**(5)]$^+$ +H^+ +L	⟶	^{1}[**4Fe**(6)]$^{2+}$ +H_2O	16	17.9 (13.2)
2 nd protonation:	^{4}[**3Fe**(5)]^0 +H^+	⟶	^{2}[**4Fe**(5)]$^{1+}$ +H_2O	24	15.6

Table 7.2: Possible pathways for the protonation processes in the catalytic cycle for $[Fe^{II}(qpy)(H_2O)_2]^{2+}$. Activation energies ($\Delta G^\ddagger$) are reported in kcal/mol and use phenol as a proton source; $\Delta G^\ddagger$ reported in parenthesis correspond to activation energies with carbonic acid as a proton source.

The uptake of a third electron is possible for the doubly reduced CO_2, CO_2H or CO intermediates. All discussed pathways for a third reduction are summarized in table 7.3. The reduction of the CO_2 adduct ^{3}[**2Fe**(5)]^0 (resulting in ^{6}[**2Fe**(5)]$^-$) is unlikely as the computed reduction potential is more negative than −1.8 V. In contrast, the reduction of the carboxy intermediate ^{5}[**3Fe**(5)]$^+$ to ^{4}[**3Fe**(5)]^0 appears at a milder potential with a computed reduc-

tion potential of −1.47 V. This is 110 mV less than the potential required for the second reduction. The mild potential is readily rationalized as the qpy π^* orbitals in ^{5}[**3Fe**(5)]$^+$ are not occupied. In addition, both forward and backward reaction barriers are high (rate limiting) and consequently the ^{5}[**3Fe**(5)]$^+$ should accumulate and have a significant lifetime, making a reduction after a single protonation likely. At last, the third reduction can also occur for the carbonyl intermediate ^{1}[**4Fe**(6)]$^{2+}$ to ^{2}[**4Fe**(5)]$^+$ at a mild reduction potential of −0.97 V vs Fc^+/Fc which is in good agreement with the experimentally observed re-oxidation peak at −1.09 V. The additional electron strengthens the backbonding of the π acidic carbonyl ligand. However, CO release is exergonic and barrierless for the doubly reduced carbonyl intermediate ^{2}[**4Fe**(6)]$^+$; consequently, reduction at that stage is unlikely.

(Half)-Reaction				E^0
CO_2 intermediate:	^{3}[**2Fe**(5)]^0 +e$^-$	⟶	^{6}[**2Fe**(5)]$^-$	−1.85
CO_2H intermediate:	^{5}[**3Fe**(5)]$^+$ +e$^-$	⟶	^{4}[**3Fe**(5)]^0	−1.47
CO intermediate:	^{1}[**4Fe**(6)]$^{2+}$ +e$^-$	⟶	^{2}[**4Fe**(5)]$^+$ +L	−0.97

Table 7.3: Possible pathways for the third reduction in the catalytic cycle for $[Fe^{II}(qpy)(H_2O)_2]^{2+}$. Reduction potential are reported in V against the Fc^+/Fc couple. For reference: the computed second reduction of $[Fe^{II}(qpy)(H_2O)_2]^{2+}$ is −1.58 V (from ^{4}[**1Fe**(5)]$^+$ to ^{1}[**1Fe**(4)]^0)

.

The subsequent second protonation of the triply reduced ^{4}[**3Fe**(5)]^0 is both faster (with a barrier of 15.6 kcal/mol) and thermodynamically more favorable (with a pK_a of 24) than the second protonation after only two reductions (pK_a = 16, barrier: 17.9 kcal/mol) as the reduction not only destabilizes the reactant, but also stabilizes the product. CO release from ^{2}[**4Fe**(5)]$^+$ becomes endergonic (2.0 kcal/mol), but barrierless. Thus, the reduction of the carboxy intermediate ^{5}[**3Fe**(5)]$^+$ facilitates the second protonation step both kinetically and thermodynamically (see table 7.2) albeit at the cost of an endergonic CO release. In addition, a second reduction (fourth overall) of the carbonyl species ^{2}[**4Fe**(5)]$^+$ has a calculated potential of −1.45 V vs Fc^+/Fc which is lower than the second reduction of the initial complex, **1Fe**. The accumulation of ^{2}[**4Fe**(5)]$^+$ is observed experimentally by a reoxidation peak in the CV experiments and is likely to contribute to the low FE of that catalyst (*vide infra*). The FE was improved experimentally by irradiation with UV-light which induces a low to high spin transition and facilitates the CO release versus a further reduction of the carbonyl intermediate. These findings agree with the CV experiments under CO, where a further reduction of the singly reduced carbonyl intermediate was observed at −1.42 V to yield ^{1}[**4Fe**(5)]^0. The calculated free energy for CO dissociation from the doubly reduced carbonyl ^{1}[**4Fe**(5)]^0 is 5.0 kcal/mol which does not justify the experimental observations that ^{1}[**4Fe**(5)]^0 poisons the catalyst. However, we find that if the CO release would proceed via

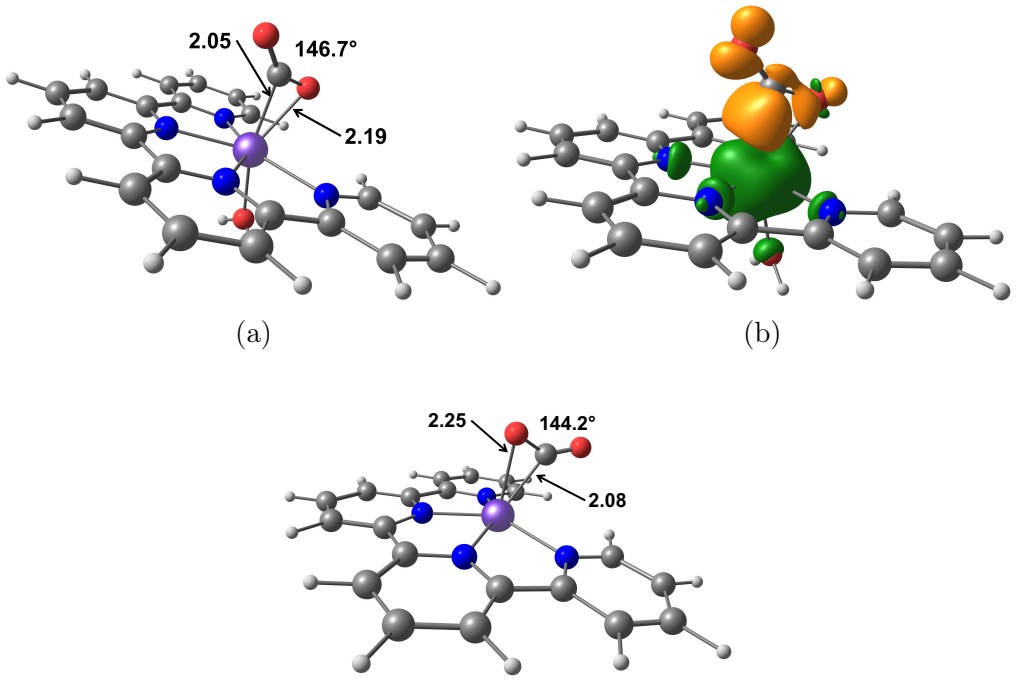

Figure 7.12: Geometrical parameters of both possible CO_2 adduct intermediates of the Iron catalyst (a) after one reduction yielding ^{4}[**2Fe**(6)]$^+$; (b) Spin density of ^{4}[**2Fe**(6)]$^+$ which indicates the formation of a $CO_2^{\cdot-}$, (c) after two reductions yielding ^{3}[**2Fe**(5)]^0.

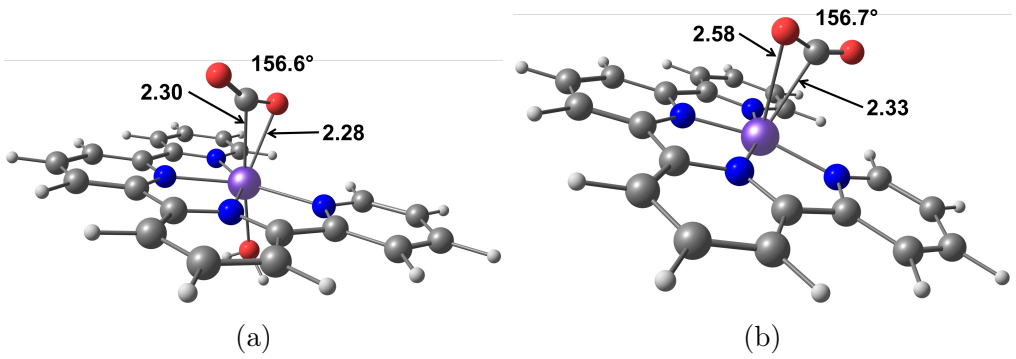

Figure 7.13: Geometrical parameters of both transition states yielding the corresponding CO_2 adducts of the iron catalyst after (a) one reduction and (b) two reductions.

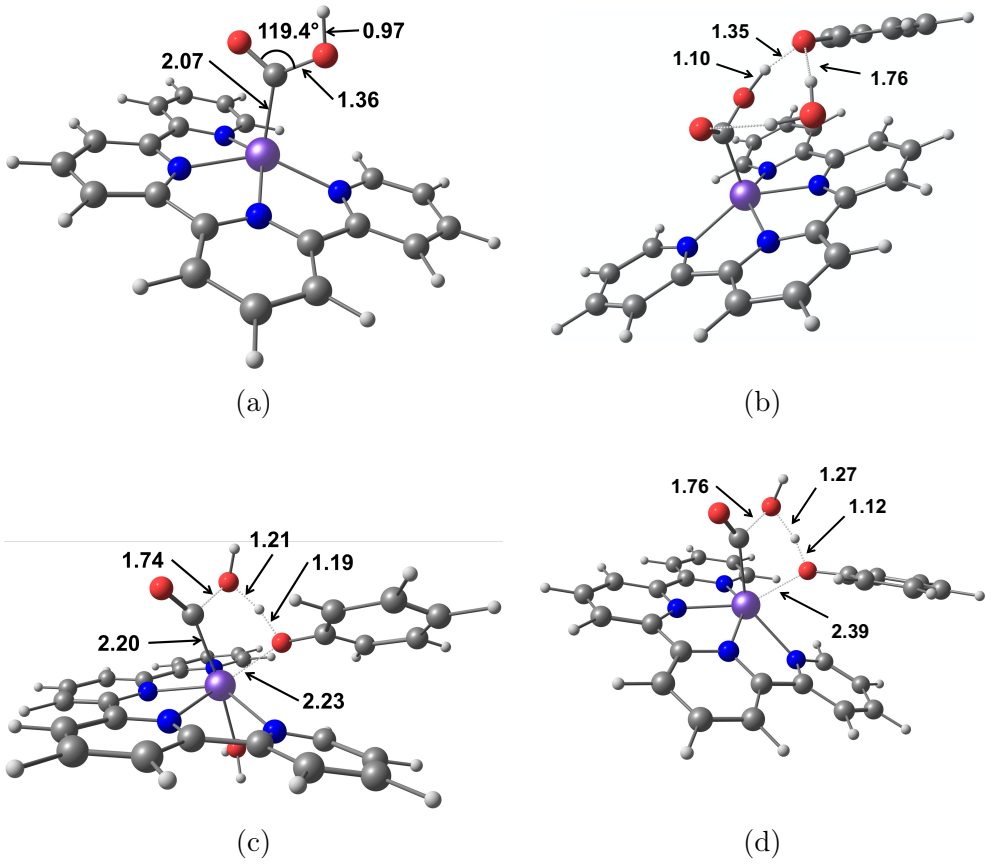

Figure 7.14: Geometrical parameters of (a) the protonated carboxy intermediate $^{5}[\mathbf{3Fe}(5)]^{2+}$; (b) the transition state for the first protonation step (quintet surface); (c) the transition state for the second protonation step using phenol as the proton source after two reduction steps (quintet surface); (d) the transition state for the second protonation step using phenol as the proton source after a third reduction (quartet surface).

a spin transition on the triplet surface, the minimum energy crossing point of the singlet and triplet surfaces along the Fe−C bond is over 20 kcal/mol higher in energy (at a Fe−C bond distance of ∼2.2 Å, see figure F.12 (a)). We further note, that $^{1}[\mathbf{4Fe}(5)]^{0}$ could be the starting point of a more sophisticated degradation pathway. This was observed for the nickel cyclam system, where the formation of a $NiCO_4$ was detected and the addition of CO scavengers increased the activity.[534] Another possibility would be the decomposition of the catalyst yielding metallic iron on the electrode. Further experimental insights are necessary to determine the exact degradation pathway. We investigated possible intermediates and found that upon binding of a second carbonyl, a partial dissociation of the qpy is observed (see figure F.12 (b)).

The analysis of a large variety of intermediates showed that two steps in the the catalytic

mechanism can proceed via different channels: (i) the binding of CO_2 can occur after one or two reductions (ECE vs EEC mechanism) – our calculations indicate that the ECE mechanism is preferred – (ii) the second protonation can occur after two reductions or after a third reduction where the latter results in a lower barrier and better thermodynamics at the cost of an endergonic CO release. The population of both channels depends on the lifetime of the carboxy intermediate $^5[\mathbf{3Fe}(5)]^+$, which should be significant due to the large barriers for both protonation steps. Hence, a third reduction at this step seems likely for $^5[\mathbf{3Fe}(5)]^+$. The rate limiting step is the second protonation. Similar barrier heights were reported by Carter *et al.* [133] for the $[Re(bpy)(CO)_3Cl]$ catalyst using a comparable computational set-up and methanol as proton source.

An important aspect of a good CO_2 reduction catalyst is the selectivity for CO2RR over HER. A possible HER mechanism is depicted in the appendix in figure F.8. The formation of a hydride from the proposed active species of the catalyst $^6[\mathbf{2Fe}(5)]^+$ is thermodynamically not favorable as the pK_a for this step is negative. If it is assumed that the CO2RR mechanism proceeds mainly via the ECE channel, then the formation of a hydride should not be possible and the catalyst can operate even in very acidic conditions with high selectivity. These findings can be related to the fact that the reductions are mainly ligand based for the Fe catalyst (*vide supra*) which yields a Lewis acidic metal center. Hence, the formation of a hydride is unfavorable. These findings are in line with the experimentally observed high selectivity of over 99% CO in the CPE experiments.[561]

The in-depth analysis of possible catalytic pathways, side reactions, and degradation pathways allows us to rationalize modifications to improve the activity: First, further facilitating the endergonic CO_2 binding after the first reduction will provide not only more driving force for CO_2 addition but also should result in a high selectivity vs HER even in acidic conditions. Thus, a modification of the ligand framework to stabilize the bound CO_2 either via a well-positioned hydrogen bonding donor, [176, 385, 406] or through electrostatic interactions [380] in the secondary coordination sphere would be beneficial. This concept is well established in bio-inspired catalyst design to enhance catalytic activity. [165, 167, 541–543, 546] Secondly, to achieve a higher FE, a singly reduced carbonyl intermediate must be avoided. However, our analysis shows that a third reduction at the carboxy intermediate is necessary to improve both kinetics and thermodynamics of the second protonation step. Alternatively, our calculations indicate that a stronger acid (e.g. H_2CO_3) is also capable of driving the second protonation efficiently *without* a third reduction; thus, avoiding the accumulation of a reduced carbonyl intermediate which deactivates a degradation pathway and increases FE.

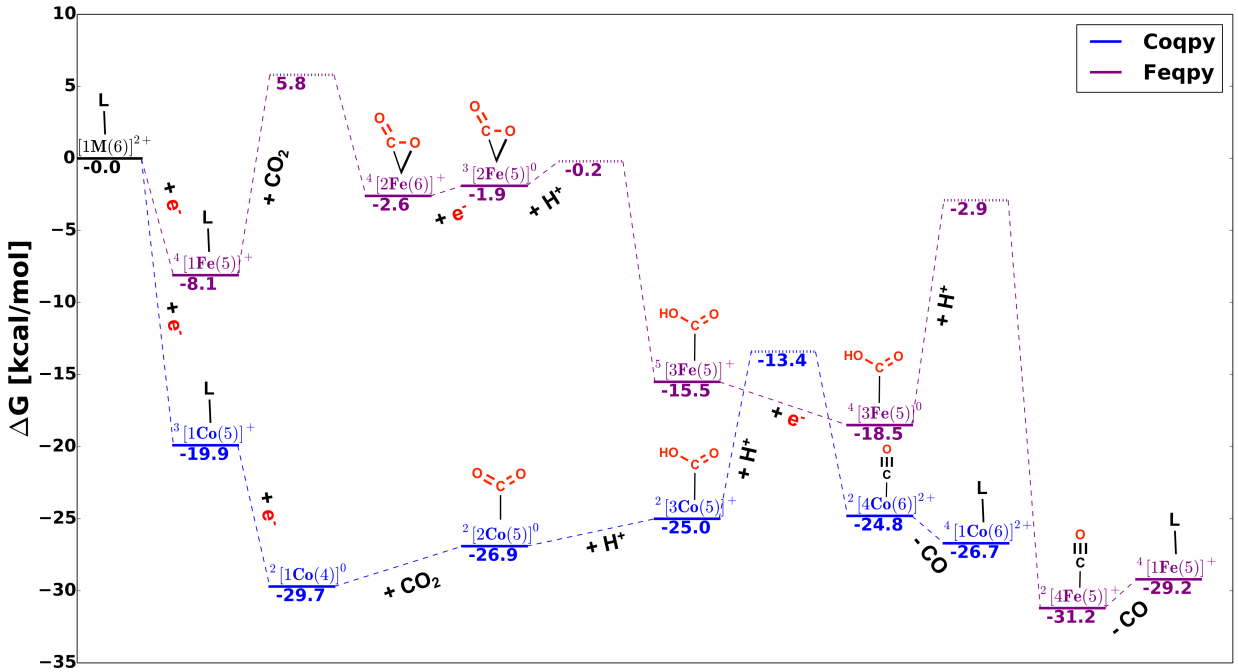

Figure 7.15: Free energy landscape of the most likely CO2RR pathways of both Coqpy and Feqpy; for the reduction steps, a potential of -1.6 V vs Fc^+/Fc is applied; for the protonation steps, phenol is used to estimate barriers and carbonic acid for free energies (see main text for justification); solid lines correspond to intermediate states and dashed lines to transition states; the energy difference for the total reaction energy in the two cycles stems from using different functionals as the pKa of H_2CO_3 is 12.6 with B3LYP-D3 and 14.7 with ωB97X-D.

7.4 Comparison and Discussion

After the in-depth analysis of each system, the Co and Fe catalysts can be compared step-wise and an energetic diagram comparing the most likely pathways of both catalyst is depicted in figure 7.15:

Reduction: The $[Co^{II}qpy(H_2O)_2]^{2+}$ catalyst exhibits a ligand-based first reduction and a highly delocalized second reduction. The second excess electron is stabilized by a π type metal ligand bond (with significant metal contribution) between a Co t_{2g} type d orbital and a qpy π^* orbital (see figure 7.16 (a)). The second reduction is accompanied by a ligand loss which induces a spin transition to a low spin state and notable rearrangement of the ligand framework (twist). These two factors could explain the experimentally observed slow kinetics for this reduction.

The reduction process for the Fe catalyst is markedly different: The $[Fe^{II}qpy(H_2O)_2]^{2+}$ catalyst exhibits two ligand based reductions in the low-lying qpy π^* orbitals (see figure 7.16 (b)). The iron d orbitals are less suitable for mixing with the qpy π^* orbitals

which results in little metal contribution to the singly and doubly reduced states. This leads to significantly more negative reduction potentials but faster kinetics. The doubly reduced intermediates of both cycles $^2[\mathbf{1Co}(4)]^0$ and $^3[\mathbf{1Fe}(4)]^0$ are contrasted in the MO diagram in figure 7.16.

CO_2 Binding: In the cobalt system, the subsequent CO_2 binding and activation is fast (barrierless) and slightly endergonic. The doubly reduced catalyst $^2[\mathbf{1Co}(4)]^0$ binds CO_2 in an η^1-κC binding mode where a low spin d^8 Co(I) center interacts with CO_2 via a σ type bond from the doubly occupied metal d_{z^2} to the CO_2 LUMO. The binding of CO_2 to a singly reduced complex was not possible suggesting an EEC mechanism for CO_2 binding.

In contrast, the Fe center remains Lewis acidic throughout the reduction process which governs CO_2 binding via an η^2 binding mode. The $CO_2^{\cdot-}$ moiety is stabilized by two pathways: first, by delocalizing some electron density from the CO_2-π^* orbital into the unoccupied (in the β-space) Fe-d_{xz} orbital via a π-type bond; second, by a dative bond from the oxygen lone pair. This allows binding and activation of CO_2 to a *singly* reduced catalyst which is supported by experimental evidence. In both cases the binding and activation process is endergonic with a significant barrier. However, CO_2 binding to a doubly reduced catalyst much slower. This can be explained by the weakened O−Fe (of the CO_2) interaction upon the second reduction which is already significant in the transition state. The computed second reduction of the singly reduced CO_2 adduct is at a similar potential as the second reduction of the catalyst. All this taken into account, CO_2 binding most likely proceeds via reduction-CO_2 binding-reduction (ECE) mechanism. Two factors can explain why the η^2 binding mode is not observed in the Co catalyst: first, the softer Co metal center; second, the additional d electron in Co (in comparison to Fe) yields doubly occupied t_{2g} type orbitals in all spin states, thus preventing a π type interaction of the CO_2 LUMO and the Co. The key MOs for both the Co and Fe CO_2 adducts are depicted in figure 7.17.

Protonation: In the Co system, the first protonation is barrierless yielding a doubly reduced COOH moiety bound to an unreduced complex. The second protonation is coupled to the C−O bond cleavage yielding a carbonyl complex and water. This step has a barrier of 11.6 kcal/mol making it rate limiting (and only barrier) in the cycle.

In the Fe system, both protonation reactions have barriers of 1.7 and 17.9 kcal/mol. The second protonation is concerted with the C−O bond cleavage and is the rate limiting step. The barriers are significantly higher for the Fe catalyst, which is in line with the reported difference in activity.

Regeneration: The subsequent CO release to regenerate the catalyst is exergonic and barrierless due to the high oxidation state of the central complex in both cases. The Co catalyst has overall only one low barrier (11.6 kcal/mol) which aligns with the high k_{cat} observed for this catalyst making it one of the fastest molecular CO_2 to CO reduction catalysts. The Fe catalyst on the other hand has two significant barriers, for CO_2 addition (13.9 kcal/mol) and the second protonation (15.6 kcal/mol) rationalizing the lower experimentally observed k_{cat}.

Possible Third Reduction: For the Co catalyst, an alternative three reduction pathway (EEEC) is feasible at a more negative potential. In addition, a third reduction is feasible

for each intermediate species at lower potentials than the initial second reduction (see figure F.9). This pathway is able to use water efficiently as the proton source but suffers from a very endergonic CO release.

For the Fe catalyst, the barriers for both protonation steps result in an accumulation of the carboxy intermediate which can be further reduced at a mild potential. The third reduction facilitates the second protonation both thermodynamically and kinetically (barrier: 15.6 kcal/mol); however, the subsequent CO release is slightly endergonic which could lead to another reduction of the carbonyl intermediate posing a dead end for catalysis. This could explain the low Faradaic efficiency of the catalyst and the increase of FE due to UV irradiation.

Possible Improvements: Based on our proposed cycle for the Co system, further tuning of the metal-ligand interaction for the doubly reduced intermediate via electron withdrawing or releasing substituents can alter both the overpotential and catalytic activity: (i) a $-$F group slightly decreases both rate limiting barrier and overpotential; (ii) a $-NH_2$ group markedly increases the reduction potential and also markedly decreases the rate limiting barrier. This opens up the possibility of entering a pathway via the four coordinated doubly reduced species (if a non coordinating acid is used). Thus, could increase k_{cat} *without* an increase of overpotential by proceeding via a different intermediate.

The ECE mechanism proposed for the Fe system makes it extremely robust against a possible HER side reaction. The analysis of a possible HER pathway revealed that the formation of a hydride intermediate from the singly reduced catalyst is only feasible under extremely acidic conditions. This opens up the possibility to operate with stronger acids without a loss in selectivity. Our calculations show that the barriers for the rate limiting second protonation is significantly lower (13.2 kcal/mol); thus, a stronger acid could drive the reaction effectively *without* a third reduction. This would increase both FE and maximum TOF by avoiding the accumulation of an carbonyl intermediate. Furthermore, the modification of the ligand framework to incorporate a moiety in the second coordination sphere could stabilize the bound CO_2 (either via electrostatics or hydrogen bonding) and should facilitate the endergonic CO_2 addition.

7.5 Conclusion

In summary, we investigated the catalytic mechanisms of the experimentally reported Fe and Co quaterpyridine molecular electrocatalysts for the two-electron, two-proton reduction of CO_2 to CO using electronic structure calculations (DFT). We report possible catalytic and degradation pathways which are in line with the detailed experimental efforts of Robert *et al.* [561]. Furthermore, we provide an in-depth analysis of the electronic structure of intermediates to understand what factors affect the different pathways of both catalysts.

The $[Co^{II}qpy(H_2O)_2]^{2+}$ catalyst exhibits a ligand-based first reduction and a highly delocalized second reduction. The CO_2 binding proceeds via η^1-κC binding mode, is only possible after two reductions, and is barrierless (EEC mechanism). The subsequent first

protonation is barrierless as well. The second protonation is rate limiting (11.6 kcal/mol) followed by a barrierless CO release. The introduction of substituents on the qpy ligand can decrease overpotential or increase the turnover rates. However, a fluorine substituent can slightly improve both and could also increase solubility in aqueous solvents. The amino substituent could also decrease overpotential and turn over rates by proceeding via a different intermediate.

The $[Fe^{II}qpy(H_2O)_2]^{2+}$ catalyst exhibits two ligand based reductions in the low-lying qpy π^* orbitals and binds CO_2 in an η^2 binding mode. This interaction enables CO_2 binding to a singly and doubly reduced catalyst. The binding of CO_2 after a single reduction is kinetically preferred, suggesting an ECE mechanism. Both protonation steps have significantly higher barriers than for the Co catalyst, and the second protonation is rate limiting (17.9 kcal/mol). A third reduction is likely to happen for the carboxy intermediate and reduces the barrier for the second protonation (15.6 kcal/mol) but results in an endergonic CO release. We show that the Fe complex could be a more efficient catalyst with a stronger acid without decreased selectivity towards CO2RR vs HER. This could prevent a third reduction and thus avoid a possible degradation pathway.

Between the two metal systems, the key difference is the more favorable metal d orbital/qpy π^* orbital interaction in the Co system. This becomes apparent when comparing the metal character of the doubly reduced intermediates in figure 7.16. In the Co catalyst, this leads to greater metal contribution in the first two reductions, resulting in milder reduction potentials and a softer metal center. The subsequent binding and activation of CO_2 relies on a metal base binding to the nucleophilic carbon of the CO_2 in an η^1-κC binding mode. Binding to a singly reduced Co catalyst was not possible since the metal center is most likely "stuck in the middle" in terms of Lewis acidity. In case of the Fe catalyst, the metal center remains Lewis acidic with mainly ligand based reductions. This leads to a different mechanism of binding and activating CO_2 via an η^2 binding mode which benefits from a Lewis acidic metal center that can bind CO_2 after a single reduction. The key MOs for both the Co and Fe CO_2 adducts are depicted in figure 7.17.

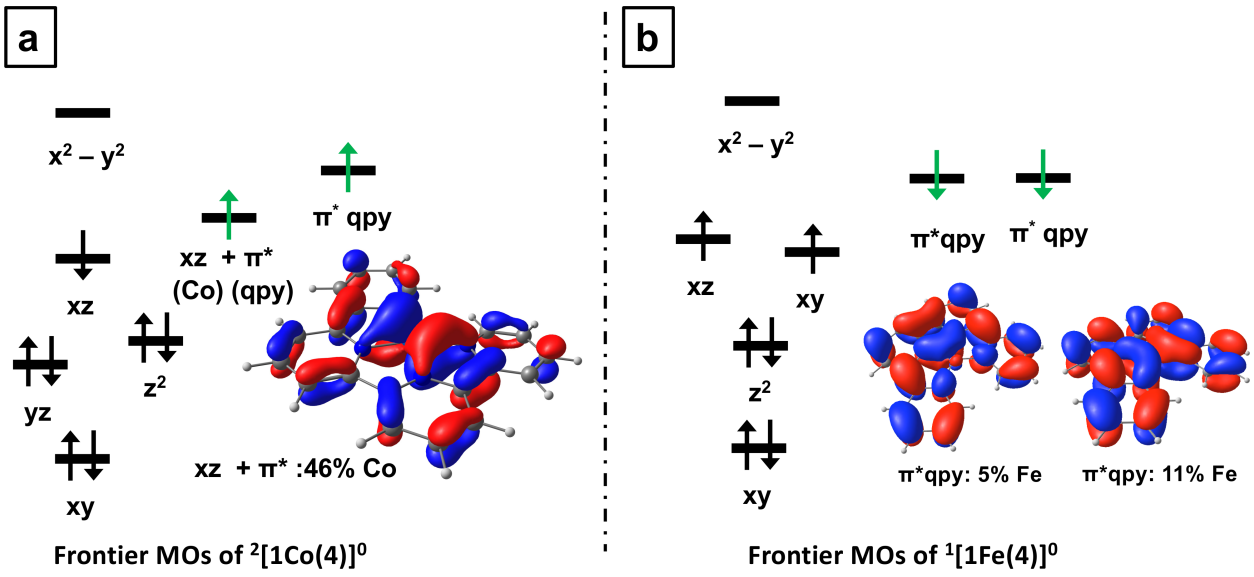

Figure 7.16: Schematic MO diagram of both doubly reduced intermediates a) $^{2}[\mathbf{1Co}(4)]^{0}$ and b) $^{1}[\mathbf{1Fe}(4)]^{0}$. The green arrows indicate the extra electrons due to both reductions. The MO shown in panel (a) illustrates the delocalized π type metal (d_{xz}) ligand (π^{*}) bond to stabilize the excess electron; the MOs in panel (b) illustrate the mainly ligand based character of the two reductions.

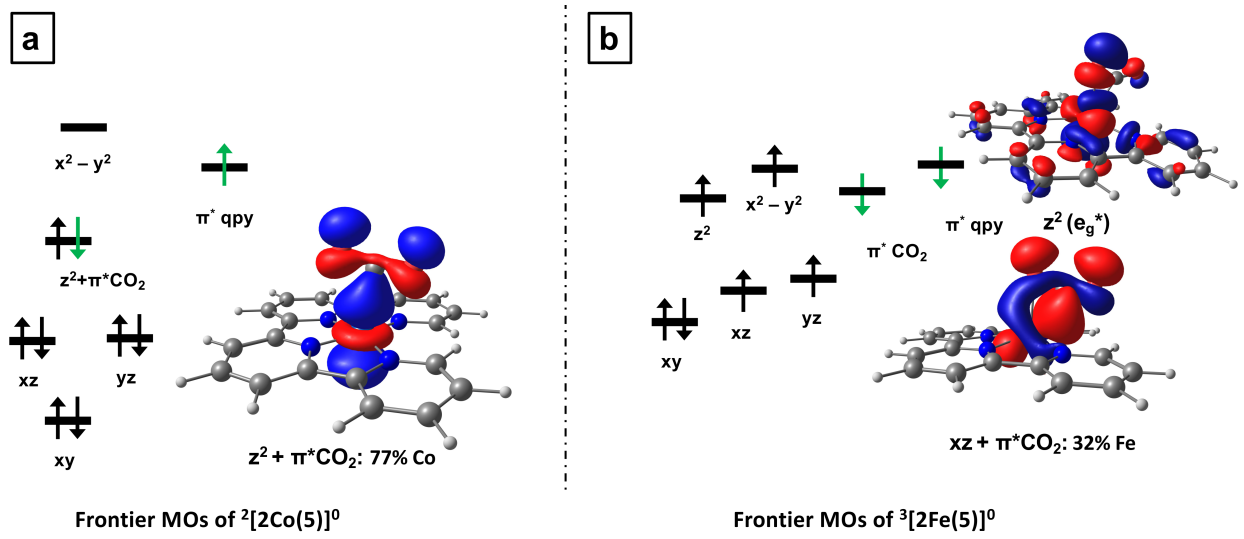

Figure 7.17: Schematic MO diagram of both doubly reduced CO_2 adducts a) ^{2}[**1Co**(4)]^0 and b) ^{3}[**1Fe**(4)]^0. The green arrows indicate the extra electrons due to both reductions. The MO in panel (a) illustrates the σ type interaction of the Co-d_{z^2} orbital and the CO_2 LUMO leading to the η^1 binding mode in the Co system; the MOs in panel (b) illustrate the two ways the CO_2 is stabilized in an η^2 binding mode in the Fe system: (i) by a π type CO_2 LUMO Fe-d_{xz} bond; (ii) by a dative O−Fe bond from the oxygen lone pair.

Chapter 8

Influence of Overpotential on an Iron Terpyridine Complex for CO_2 Reduction: A Combined Experimental and Computational Investigation

8.1 Introduction

Increasing energy demands and global climate change has motivated the need for technologies that capture and utilize atmospheric carbon dioxide (CO_2) and convert it into value-added carbon sources.[153, 156, 619] There are various possible products for the electrochemical CO_2 reduction reaction (CO2RR) such as CO, CH_3OH, CH_4; a comprehensive overview is presented in reference [163]. The two-electron two-proton reduction of CO_2 to CO is economically most viable due to its usage in the Fischer-Tropsch process.[164] The electrochemical reduction of CO_2 via artificial photosynthesis[154, 155] offers a promising way to restore balance to the carbon cycle and develop a net negative carbon footprint if these technologies can be coupled to renewable sources of electricity. In order for these goals to be realized, efficient catalysts are required to selectively drive CO_2 reduction versus the thermodynamic and kinetically competitive hydrogen evolution reaction (HER).[155, 522] The electrochemical CO_2 reduction reaction has been extensively explored across materials[160], biological[583], and molecular systems[161]. Molecular systems are of particular interest to us as they are ideal platforms that can be rationally and systematically tuned through synthetic chemistry[97, 167, 620] with a level of precision and in the absence of defects, that is unavailable to heterogeneous catalysts[160, 621]. Moreover, due to their small size relative to enzymes and their homogeneous nature, they can be investigated at an mechanistic level which aids in the understanding and directed development of improved catalytic platforms.[97, 100, 538]

Due to its abundance, iron platforms are especially desirable; the iron porphyrin platform FeTPP (TPP = tetraphenylporphyrin) is a robust and active catalyst making it a popular

framework for ligand development with a considerable amount of derivatives having been prepared in recent years.[380, 383, 399, 401, 535]. The rates of the original FeTPP platform has been improved by several order of magnitude from a 10^{2} s^{-1} to 10^{6} s^{-1} for Fe-*o*-TMA, a tetra-TMA substituted FeTPP derivative (TMA = trimethylammonio, $-NMe_3^+$). The (current) top performance of 10^{9} s^{-1} for this platform is achieved by introducing four bulky, methylimidazolium-containing groups.[407] The success story of the FeTPP system over the last decade illustrates the effectiveness of synthetic modification of the ligand platform and optimization of reaction conditions. Alternatively, simpler polypyridyl ligand platforms such as, iron-bipyridine (bpy)[176, 385] (Figure 8.1 (a)) and iron-quarterpyridine (qpy) [177, 561, 600, 602] (Figure 8.1 (c)) have received increase attention. These ligand platforms are robust under electrochemical conditions and are synthetically accessible through facile and modular routes which facilitates precise tuning of their sterics and electronics in a rational fashion. As such, the development of novel polypyridyl electrocatalysts for proton and CO_2 reduction has been a part of a larger research program between our labs.

We recently reported[398] a novel terpyridine(tpy)-based iron polypyridine complex (Figure 8.1 (b)), $[Fe(tpyPY_2Me)]^{2+}$ ($[Fe]^{2+}$), that leverages ligand non-innocence of the tpy moiety and metal-ligand cooperativity through exchange coupling. These two factors yield mild reduction potentials for the complex in comparison to other pyridine based catalysts as illustrated in Figure 8.1 (see main text for detailed explanation) and allows it to electrochemically convert CO_2 into CO at extremely low overpotentials (η), resulting in high product selectivity and rates under both organic solvents and aqueous conditions. The Faradaic efficiency for CO production (FE_{CO}), rates (k_{max}) and overpotentials of the three platforms are compared to the FeTTP platforms and summarized in Table 8.1. Comparison of these parameters for benchmarking catalytic performance clearly identifies these polypyridyl complexes as some of the best homogeneous catalysts to date but should be done with care. Determination of accurate overpotentials requires the use of the thermodynamic potential required to convert CO_2 into CO which is often unknown for the exact experimental conditions and can thus vary by over 500 mV depending on solution conditions. To normalize for this uncertainly, we give the values reported by Matsubara[552] that take into account the effect of solvent mixtures and acid additives. Similarly, estimation of kinetic performance based on maximum turnover frequency (TOF_{max}) is highly dependent on the method utilized (e.g., foot-of-the-wave analysis, peak catalytic current analysis, etc). As such, the methods used to determine the rate is indicated in Table 8.1. In order to minimize errors in rate determination for our $[Fe]^{2+}$ catalyst, we extracted the kinetic parameters directly from the averaged specific current densities for CO production obtained from variable potential CPE experiments that were conducted in triplicate as described by Saveant and coworkers.[622, 623]

In our initial study of the $[Fe(tpyPY_2Me)]^{2+}$ system, we reported the synthesis, characterization, and electrocatalytic behavior of $[Fe]^{2+}$ for CO_2RR to CO. Synthesis of the two-electron reduced product, $[Fe(tpyPY_2Me)]^{0}$ ($[Fe]^{0}$), and spectroscopic characterization allowed us to attribute its exceptional catalytic activity to its unique open-shell singlet electronic structure that results from the anti-ferromagnetic coupling of the intermediate-spin Fe(II) center (S_{Fe}=1) to a doubly reduced, triplet ligand system (S_{tpy}=1). We were able to

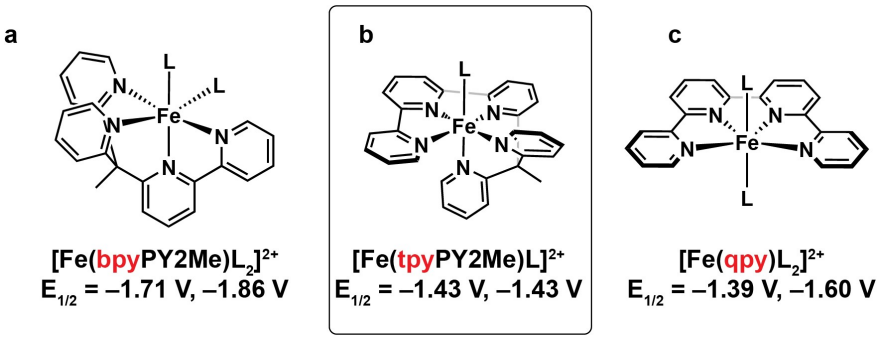

Figure 8.1: Overview of various iron-pyridine based molecular catalyst platforms for CO_2 to CO reduction and their reduction potentials: a)$[Fe(bpyPY_2Me)L_2]^{2+}$, b) $[Fe(tpyPY_2Me)L]^{2+}$ (tpy = terpyridine); c) $[Fe(qpy)L_2]^{2+}$; ; L = H_2O or CH_3CN; potential versus Fc/Fc^+.

establish that this electronic structure was responsible for the reduction of CO_2 to CO at low overpotentials, through the preparation and comparison to a series of redox-(in)active metal and ligand controls.

Table 8.1: Key benchmark metrics of the three pyridine based catalyst platforms, the FeTPP platform and a top performing derivative of that platform, the Fe-*o*-TMA; potential versus Fc/Fc^+.

Platform	F.E. [%]	TOF_{max} s^{-1}	η V	Ref.
$[Fe(bpy^{NHEt}PY2\,Me)L_2]^{2+}$	81	10^{2}	0.66	[385]
$[Fe(tpyPY_2Me)]^{2+}$	97	10^{5}	0.71	[398]
$[Fe(qpy)(H_2O)_2]^{2+}$	70	10^{2}	0.24	[561]
FeTPP	93	10^{2}	0.67	[552]
Fe-*o*-TMA	93	10^{6}	0.60	[380, 552]

However, the mechanistic pathways through which $[Fe]^{2+}$ functions are entirely unexplored. In particular, this system interestingly exhibits two distinct catalytic regimes that are potential dependent (Figure 8.2). Cyclic voltammograms collected under CO_2 atmosphere with the addition of 1 M phenol, as a proton source, shows the formation of two catalytic waves. The first regime, reaches a plateau at -1.6 V vs Fc/Fc^+ (η = 330 mV) and displays canonical S-shaped wave instructive of pure kinetic conditions without substrate consumption. At more negative applied potentials beyond -1.75 V vs Fc/Fc^+ (η = 480 mV), a second catalytic response is observed reaching a maximum current density at ca. -1.98 V vs Fc/Fc^+ (η = 710 mV). This second catalytic regime shows peak-shaped behavior

indicative of substrate consumption by the rate-determining step (Figure 8.2).

This present work aims to shed light on the mechanistic pathways using a combined experimental and computational approach. Here we propose that at low overpotentials ($\eta < 0.480$ mV), $[Fe]^{2+}$ undergoes a two electron reduction, two proton transfer mechanism (EECC) where turnover occurs through the dicationic iron complex, $[Fe]^{2+}$. At higher overpotentials ($\eta > 0.480$ mV), an additional electron transfer event becomes possible through either a step-wise or a proton coupled electron transfer (PCET) pathway, allowing for catalytic turnover from the monocationic iron complex ($[Fe]^{+}$) via an ECEC mechanism. Based on the detailed mechanistic analysis, we propose the design of improved ligand frameworks and explore their electronic structures with an energy decomposition analysis (EDA). This mechanistic analysis lays the framework for further rational optimization of theoretically driven modification of the ligand framework for increased catalytic activity.

8.2 Computational Model

In this section we briefly explain the model, its assumptions and expected errors (see appendix G for technical details). Density functional theory calculations for free energies, activation energies, reduction potential and the LOBA[617] oxidation state analysis were performed with the Q-Chem package [108] (version 5.3.0) using the ωB97X-D [68] functional with a mixed basis for the optimization and frequency calculations were performed with a mixed basis (def2-SVP basis for all main group elements, def2-TZVP basis set for Fe).[247]. This functional was chosen based on our previous study and extensive functional screening (see SI of reference [398]). Gibbs free energies (G) were used to compute reduction potentials and adiabatic spin gaps and are based on standard thermodynamic cycles see Refs [128, 130, 532]. Solvation energies were approximated by performing single point calculations applying the implicit C-PCM solvent model with the larger def2-TZVP basis for all elements[247].

Reduction potentials are reported with an isodesmic scheme against the ferrocene/ ferrocenium couple (Fc/Fc^{+}) used as an internal standard. [127, 128] This method allows accurate predictions even at a modest level of theory with reported errors within approximately ~ 100 mV (~ 4 kcal/mol) of experimental values.[128] Of particular relevance for this work, this approach has yielded accurate calculated reduction potentials in several pyridine based electro-catalysts.[176, 177, 398]

The RMSD of ωB97X-D for barrier heights is $\sim$2 kcal/mol using gas phase high level wave function methods as the reference;[20, 624] When comparing to experimental values, as done in this study, additional error arise from solvation by the implicit solvation model and simplification by the computational model versus experiment.

The calculation of accurate free energies for protonation reactions with implicit solvent models resulting in expected deviations versus experimental values of $\pm$ 3 pK_A units. [549] We tested our computational protocol for phenol ωB97X-D yielding a pK_a of 24.6 which are 4-5 pK_a units too low.[551]. In spite of this systematic computational error, calculated relative pK_a values are more reliable because of favorable error cancellation by removing

the experimental free energy of the proton. Thus, calculated pK_a values should mainly be compared against each other.

We use phenol as the main proton source for calculating reaction barriers involving protonation reactions as it was added to the reaction mixture in molar quantities for the CPE experiments. The concentration of other proton sources (H^+ and H_2CO_3) is negligible.[532] However, we report free energies of protonation reaction steps versus carbonic acid (H_2CO_3) because it is the strongest acid in solution and reprotonates phenolate (PhO^-) via complexation of CO_2 and OH^-. This approach was also used in a previous study for quarterpyridine based catalysts.[177] The calculated standard potential for the reduction reaction using carbonic acid is -1.28 V vs Fc/Fc^+ which translates to a total reaction energy of -25.0 kcal/mol at an potential of -1.82 V vs Fc/Fc^+ ($CO_2 + 2\,H_2CO_3 + 2\,e^- \longrightarrow CO + H_2O + 2\,HCO_3^-$). This is in good agreement with the experimental estimation of -1.27 V used in our previous study[398]. Matsubara[552] estimates the standard potential in wet CH_3CN depending on the mole fraction of water to be between -0.95 V– -1.63 V vs Fc/Fc^+. In contrast, using Phenol as the acid sources results in standard potential of -1.94 V vs Fc/Fc^+ and a resulting reaction free energy of 5.1 kcal/mol.

We employ the energetic span model to predict the turnover frequency (TOF) based on our calculated catalytic cycles. This model identifies the key intermediates and transition states, which control the rate of catalysis (see the corresponding section for more detail).[140].

8.3 Results and Discussion

The catalytic voltammogram of $[Fe]^{2+}$ given in Figure 8.2 clearly illustrates the formation of two catalytic waves with maximum current densities achieved at -1.66 V vs Fc/Fc^+ (η = 390 mV) and -1.98 V vs Fc/Fc^+ (η = 710 mV). We attribute this behavior to the occurrence of two distinct catalytic regimes with disparate mechanisms. In this study, we explore various reaction pathways for these two catalytic regimes in the presence of 1 M Phenol (PhOH) and 4-chlorophenol (Cl-PhOH) in order to probe the effect of the pK_a on the observed rates and to investigate the origin of selectivity of $[Fe]^{2+}$ for the CO_2RR relative to the HER. These proposed mechanisms are in line with experimental kinetic data obtained from controlled potential electrolysis (CPE) data collected with direct product detection via gas chromatography (vide infra). In order to compactly provide relevant information regarding the electronic structure of the proposed catalytic intermediates along the way, we introduce a naming scheme that incorporates the multiplicity (M, $M = 2S+1$), Charge (C), and the identity of the sixth, axial ligand (X) on the iron center: $^{M}[Fe{-}X]^{C}$; for example, $^{1}[Fe{-}L]^{2+}$ corresponds to the unreduced, hexacoordinated initial iron complex in the singlet state.

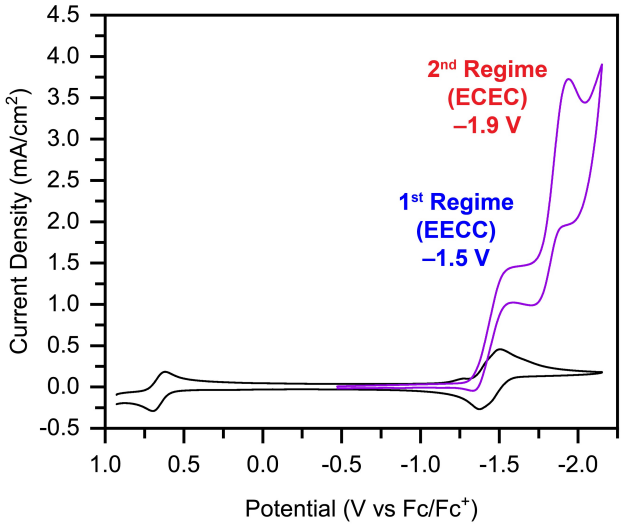

Figure 8.2: Electrochemical characterization of $^1[Fe]^{2+}$. Cyclic voltammograms of $^1[Fe]^{2+}$ collected under Ar (black) and CO_2 (purple) with the addition of 1 M phenol as a proton source. Cyclic voltammograms were collected with a scan rate of 100 mV/s with an electrolyte of 0.10 M $TBAPF_6$ dissolved in CH_3CN. The proposed two distinct mechanistic pathways for $^1[Fe]^{2+}$ that approach maximum rates at ca. -1.66 and -1.98 V vs Fc/Fc^+ and are labeled in red and blue, respectively. The first regime turns over from the 2^+ complex and undergoes a proposed EECC mechanism while the second regime at more negative potentials undergoes turnover from the 1^+ complex via an ECEC mechanism.

Low Overpotential Pathway.

Figure 8.2a shows that the current density of the first catalytic regime reaches a plateau at -1.66 V vs Fc/Fc^+ ($\eta = 390$ mV) with rates that are slower relative to the second catalytic regime. A mechanism for this first regime is illustrated in Figure 8.3 and presented in this section. First, we propose two, sequential single electron reduction steps followed by the dissociation of CH_3CN to generate the catalytically active open-shell singlet, $^1[Fe]^0$. CO_2 binding and subsequent protontation steps can then occur resulting in the loss of a water molecule and the formation of $^1[Fe{-}CO]^{2+}$. Ligand exchange with exogenous CH_3CN and CO release closes the catalytic cycle. Interestingly, the formal oxidation state of the central metal does not change during catalysis. The following sections will expand upon these proposed individual elementary steps before we build our discussion to include a proposed catalytic pathway for the second catalytic region that occurs at more negative potentials.

Reduction. The reduction pathway of $^1[Fe]^{2+}$ was established in our initial report [398]. Variable temperature NMR and Mössbauer studies established that the starting $^1[Fe]^{2+}$ complex is predominantly low-spin, Fe(II) with a small population of thermally accessible spin

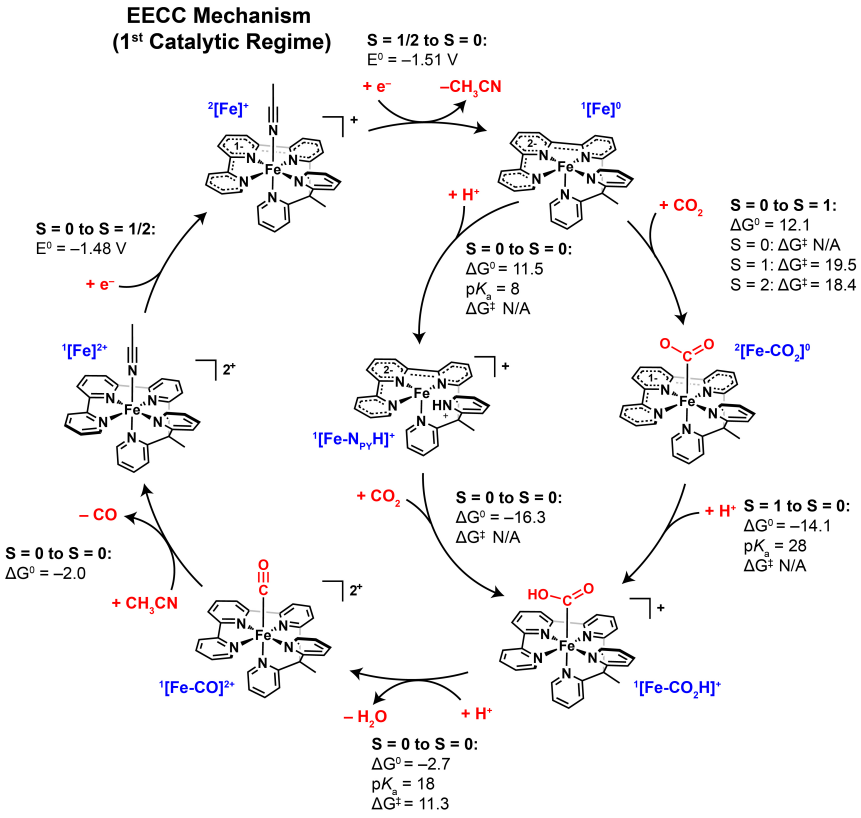

Figure 8.3: Proposed mechanistic pathways for the low overpotential regime. Starting from $^1[Fe]^{2+}$ (left side), we first propose two one-electron reduction steps followed by the dissociation of CH_3CN to generate the catalytically active open-shell singlet, $^1[Fe]^0$. CO_2 binding and subsequent protontation steps can then occur resulting in the loss of a water molecule and the formation of $^1[Fe{-}CO]^{2+}$. Ligand exchange with exogenous CH_3CN and CO release closes the catalytic cycle (outer pathway). Alternatively, direct protonation of the pyridyl arm in $^1[Fe]^0$ to give $^1[Fe{-}NH]^+$ followed by CO_2 coordination and proton transfer was found to be a competitive pathway (inner pathway). All reaction and activation energies are given in units of kcal/mol and all reduction potentials are referenced to the computed Fe/Fe^+ couple.

excited states near room temperature that we attributed to the axial distortions engendered by the rigid tpyPY2Me ligand (Figure 8.4a). The first reduction of $^1[Fe]^{2+}$ is ligand centered, with occupation of the tpy-π^* orbital with almost no excess spin density on the metal center, yielding $^2[Fe{-}L]^+$, a ground state doublet composed of an low-spin Fe(II) center and a radical $tpyPY_2Me^-$ ligand (Figure 8.4b). The addition of a second electron occupies another tpy-π^* orbital and induces a spin-state transition of the iron center from low-spin ($S_{Fe} = 0$) to intermediate-spin ($S_{Fe} = 1$) and ligand dissociation of the axially coordinated CH_3CN solvent molecule. This tetraradicaloid electronic configuration allows for strong exchange coupling of the two unpaired d electrons on the intermediate-spin iron center with the two electrons in the tpy-π^* manifolds forming an overall open-shell singlet ground state, $^1[Fe]^0$ (Figure 8.4c). The open-shell singlet electronic structure was validated by synthesizing and isolating $^1[Fe]^0$ from the chemical reduction of $^1[Fe]^{2+}$ with decamethylcobaltocene and fully characterizing the resulting coordination compound by single-crystal X-ray crystallography, NMR, Mössbauer spectroscopy, X-ray absorption spectroscopy, and DFT and CASSCF calculations. Through these spectroscopic studies and with comparison to control complexes, we were able to attribute the catalysis of $^1[Fe]^{2+}$ for the CO_2RR at mild overpotentials to this anti-ferromagnetic complex. The predicted reduction potentials for both reductions are -1.46 V and -1.51 V vs Fc/Fc^+, which are in good agreement with the experimental cyclic voltammetry data collected under argon atmosphere that show two closely spaced one-electron reduction waves centered at -1.43 V vs Fc/Fc^+. The exchange-coupling shifts the second reduction wave positive by a remarkable 640 mV relative to $[Zn(tpyPY_2Me)]^{2+}$ which employs the same redox-active tpyPY2Me ligand, but contains a Zn(II) metal center that is unable to participate in stabilization through antiferromagnetic coupling. The change in electronic structure of $^1[Fe]^{2+}$ along the reduction pathway is illustrated by the spin density plots given in Figure 8.4. The closed shell unreduced complex, $^1[Fe]^{2+}$, exhibits no excess spin as expected (Figure 8.4a). The singly reduced complex, $^2[Fe]^+$, shows spin density almost exclusively in tpy π^* orbitals of the tpyPY2Me ligand (Figure 8.4b) while the doubly reduced complex, $^1[Fe]^0$, shows spin polarization with spin density on the iron center and the π^* orbitals of the tpy moiety (Figure 8.4c).

CO_2-Binding. CO_2 coordination occurs after $^1[Fe]^{2+}$ has been reduced by two electrons and the iron center has undergone a spin-state transition and subsequent ligand dissociation of the axially bound solvent molecule. The binding of CO_2 under standard conditions is endergonic and remains on the singlet surface yielding $^1[Fe{-}CO_2]^0$. We tried to stabilize the CO_2 adduct with the addition of either explicit water molecules or electrolyte ($TBAPF_6$) but the binding remains endergonic with a free energy of +12.1 kcal/mol ($\Delta H \sim 4$ kcal/mol, see Figure G.1 a). The CO_2 is bound via the carbon atom with an angle of 127°. This is indicative of a closed shell doubly reduced CO_2 moiety and a low spin triplet Fe(II) center with a neutral tpyPY2Me ligand. The endergonic binding can be rationalized by the high stability of $^1[Fe]^0$, attributed to its anti-ferromagnetically coupled electronic structure, which yields a positive reduction potential but consequently at the cost of handicapped CO_2 binding. This is in line

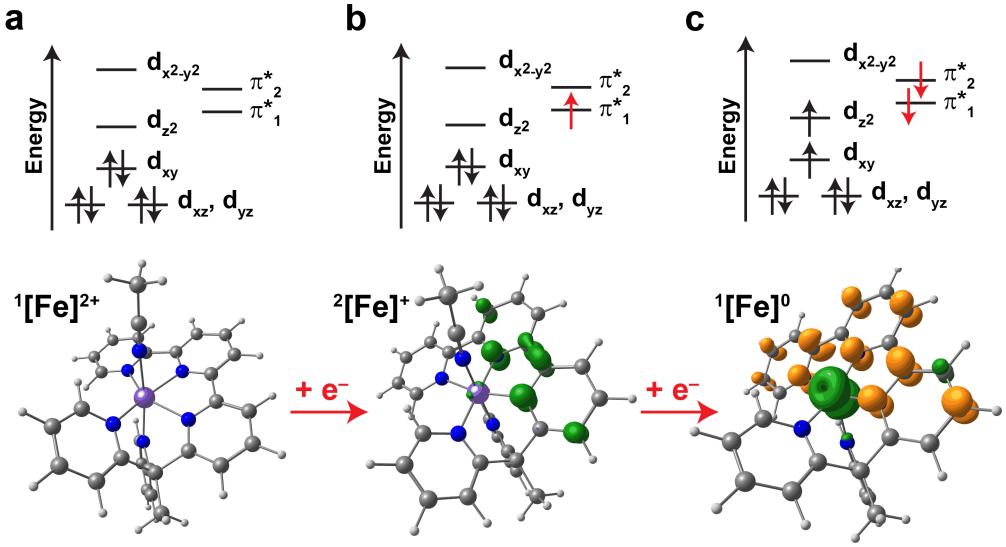

Figure 8.4: Spin densities and schematic MO diagrams: (a) unreduced complex $^1[Fe{-}L]^{2+}$ exhibiting no spin density; (b) singly reduced complex, $^1[Fe{-}L]^{2+}$, exhibiting spin density solely in the tpy ligand; (c) doubly reduced complex, $^1[Fe{-}L]^{2+}$, exhibiting spin density on both the metal center and the tpy moiety of the tpyPY2Me ligand in an exchange coupled state.

with experimental findings as high concentrations of phenol are required in order to observe CO_2 binding and subsequent catalysis. In order to probe the binding of CO_2, we attempted to measure the equilibrium constants for CO_2 binding $K_{(CO2)}$, based on the potential shift of the ligand reduction wave under Ar and CO_2 atmosphere. Under Ar atmosphere, without the addition of phenol as a proton source, there is no shift in the ligand reduction waves centered at -1.43 V vs Fc/Fc^+. When phenol (1 M) is added, a catalytic wave is formed; however, a reversible coupling could not be observed even when the experiment was performed with fast scan rates up to 50 V/s. Taken together, this suggests that CO_2 binding and thus catalysis is hampered when the system is proton limited. Interestingly, the higher spin-state surfaces [triplet ($^3[Fe]^0$) and quintet ($^5[Fe]^0$)] both exhibited much higher barriers for CO_2 binding that would effectively prevent catalysis. Thus, the open-shell singlet electronic structure of $^1[Fe]^0$ is key not only to decrease the overpotentials required for catalysis but also to facilitate CO_2 binding even though it is thermodynamically difficult. We further investigated an alternative pathway of CO_2 binding to a singly reduced intermediate ($^2[Fe]^+$). This pathway was not competitive as CO_2 coordination is even more endergonic (14.1 kcal/mol). Moreover, further reduction of this CO_2 bound intermediate ($^4[Fe{-}CO_2]^+$) is not accessible under the first catalytic regime based on the calculated redox potential of -1.81 V vs Fc/Fc^+.

Protonation. In a first scenario, the first protonation of $^2[Fe{-}CO_2]^0$ is barrierless and strongly exergonic (−14.1 kcal/mol) yielding the carboxyl intermediate, $^1[Fe{-}CO_2H]^+$. This intermediate can be best described as a CO_2H^- moiety coordinated to the Fe(II) center with the neutral tpy ligand framework. The second proton transfer step is exergonic (−2.1 kcal/mol) but with a barrier of 14.1 kcal/mol as it is coupled to the cleavage of the C−O bond and results in the loss of water and the formation of the carbonyl intermediate ($^1[Fe{-}CO]^{2+}$). The transition state geometry is depicted in Figure G.1 d. The influence of explicit solvent molecules added to the transition state geometry was probed, but we were unable to find lower barriers with the addition of exogenous water molecules.

In a second scenario, $^1[Fe]^0$ is protonated at one of the pyridine arms yielding a pyridinium intermediate, $^1[Fe{-}N_{PY}H]^+$. The calculated pK_a of 8 is quite acidic (versus a calculated pK_a of 16 for H_2CO_3); thus, the free energy of protonation coupled to carbonic acid is 11.5 kcal/mol. Previous experimental work by Matsubara shows that the pK_a of the reaction mixture is significantly lower with the addition of water. The experimental pK_a for CO_2 saturated water-acetonitrile mixtures can range from 7.8 to 16.8 where we would further expect the addition of molar quantities of phenol to further acidify the solution thus making this intermediate competitive. [552] The binding of CO_2 to $^1[Fe{-}N_{PY}H]^+$ is very exergonic and directly yields a carboxy intermediate, $^1[Fe{-}CO_2H]^+$, by skipping the high energy CO_2 adduct. This is achieved by a simultaneous intramolecular proton transfer from the pyridinium and electron transfer from the tpy upon binding of CO_2 to form CO_2H^-. The second protonation proceeds as described above, see Figure 8.3 (outer pathway).

CO Release. CO release from $^1[Fe{-}CO]^{2+}$ is exergonic and barrierless which can be attributed to the relatively high oxidation state of the iron center, which limits backbonding interactions. In addition, the low solubility of CO in CH_3CN promotes removal of CO from solution and into the gas phase. In order to further probe CO coordination and release, CVs of $^1[Fe]^{2+}$ were collected under CO atmosphere at variable scan rates (100 − 500 mV/s) and compared to data collected under Ar atmosphere. The addition of CO results in the formation of very small reductive features at −0.59 and a quantitative reductive wave at −1.23 V vs Fc/Fc^+. Additionally, the reversibility in the ligand reduction waves centered at −1.43 are lost at slower scan rates of 100 mV/s. We assign the new reduction wave at −1.23 V vs Fc/Fc^+ to the reduction of an Fe(II)-carbonyl species ($^1[Fe{-}CO]^{2+}$). This agrees well with the predicted reduction potential of −1.18 V vs Fc/Fc^+, supporting this assignment. These data suggest that CO coordination is kinetically relevant to the electrochemical response and would be consistent with an CE-type mechanism (i.e., CO binding chemical step followed by an electron-transfer step). However, when the scan rate is increased to rates faster than 100 mV/s, reversibility is restored to the ligand reduction wave, suggesting that ligand exchange is comparatively slow and can be out-competed by electron transfer. Multisegmented CV data collected under CO_2 atmosphere with the addition of 1 M phenol, do not show any significant changes or the formation of a new reductive feature that could be attributed to the build up of iron carbonyl species in the voltammograms across

one-hundred cycles. Taken together, these data support the computational findings that CO binding is weakly endergonic by 2 kcal/mol and barrierless and thus we do not observe the accumulation of iron carbonyl species under electrocatalytic conditions. Further reduction of an iron carbonyl intermediate $^{2}[\mathrm{Fe}{-}\mathrm{CO}]^{+}$ to $^{1}[\mathrm{Fe}{-}\mathrm{CO}]^{0}$ can be eliminated based on the predicted redox potential which is more negative than -2.0 V vs $\mathrm{Fc}/\mathrm{Fc}^{+}$. A similar Fe(II)-carbonyl species equipped with a comparable terpyridine and pyridyl-N-heterocyclic carbene based ligand system was synthesized and structurally characterized by ^{1}H NMR and single crystal X-ray diffraction by Miller and coworkers[625]. Chemical reduction with two equivalents of decamethylcobaltocene resulted in the dissociation of the pyridine ligand and the formation of a pentacoordinate, low-valent iron carbonyl complex that was unfortunately shown to undergo rate limiting endergonic release of CO. This hemilability of the pyridyl arm to generate a stable 18-electron complex, may be a defining feature to explain the difference in catalytic activity and speaks to the potential advantages engendered by utilizing a homoleptic tpyPY2Me ligand system.

High Overpotential Pathway.

The application of more reducing potentials beyond -1.7 V vs Fc/Fc^+ results in the formation of a second catalytic wave. A mechanism for this high overpotential regime is illustrated in Figure 8.5 and presented in detail in this section. Here we investigate three potential pathways and found two to be competitive for this high overpotential regime. In all three cases, the initial reduction steps are identical in redox potential and electronic structure to what we presented for the low overpotential pathway discussed above. However, the first electron transfer is off-pathway; where at more reducing potentials, we find that there is enough driving force to reduce the carboxy intermediate ($^1[Fe{-}CO_2H]^+$) with a predicted redox potential of -1.83 V vs Fc/Fc^+ (vide infra). This results in catalytic turnover occurring from the singly reduced, iron complex ($^1[Fe]^+$) rather than turnover from the unreduced $^1[Fe]^{2+}$. The three mechanistic pathways explored below diverge following the formation of the $^1[Fe]^0$ catalytic resting state.

The mechanism is depicted in Figure 8.5. In the first two scenarios, from the $^1[Fe]^0$ intermediate, CO_2 coordination (Figure 8.5; outer cycle) or protonation (Figure 8.5; inner cycle) can occur first as discussed above for the low overpotential regime. Both pathways are uphill by approximately 11 kcal/mol and barrierless. The two pathways converge at the formation of the CO_2H adduct, $^1[Fe{-}CO_2H]^+$, that can be further reduced at a calculated applied potential of -1.81 V vs Fc/Fc^+ yielding $^2[Fe{-}CO_2H]^0$ where the electron populates one of the low-lying tpy-π^* orbitals. The second proton transfer step to yield the carbonyl intermediate, $^2[Fe{-}CO]^+$, is strongly exergonic by -17.5 kcal/mol. Moreover, the activation barrier for the second protonation is 7.3 kcal/mol, which is 4 kcal/mol lower than the barrier for the C$-$O bond cleavage step in the low overpotential regime. The CO release becomes endergonic by 4.3 kcal/mol due to the excess electron density that is transferred from the tpy-π^* orbital to the Fe$-$CO moiety thus strengthening the backbonding to the CO ligand. Hence, the additional reductive event significantly lowers the the barrier of the second protonation at the cost of more difficult CO release. Therefore, the second protonation is not as critical as in the low over-potential regime. Depending on the pathway, either the addition of CO_2 (12.1 kcal/mol) or the protonation of the $^1[Fe{-}py{-}H]^+$ (11.5 kcal/mol) become critical steps as well. Unfortunately, it is not possible to distinguish those two pathways computationally due to the small relative energy difference of 0.6 kcal/mol and the error associated with the predictions of protonation and CO_2 addition. It is possible that both channels are populated.

In a third scenario, following the formation of $^1[Fe]^0$, a proton coupled electron transfer (PCET) pathway is possible where one of the pyridyl arms is protonated yielding $^2[Fe{-}N_{PY}H]^0$. The additional electron is localized in the pyridinium moiety, thus the electronic structure can be described as a doubly reduced tpy-π^* moiety coupled to the intermediate spin iron center and a singly reduced pyridinium. The reduction potential is acid dependent; using H_2CO_3 the calculated reduction potential is 2.14 V vs. Fc/Fc^+. However, taking non-standard concentrations into account using a similar approach to Ref. [532], we compute a shift by 0.3 V resulting in a potential of 1.84 V. For reference using H^+ the computed reduction potential

is 1.17 V vs Fc/Fc^+. Next, CO_2 can bind to $^2[Fe{-}N_{PY}H]^0$ to directly yield $^2[Fe{-}CO_2H]^0$ in an intramolecular proton and electron transfer with a free energy of −12.0 kcal/mol and thus also "skipping" the high energy CO_2 adduct intermediate. The role of proton transfer during catalysis was examined by measuring the H/D kinetic isotope effects at both catalytic regimes using C_6H_5OH or C_6D_5OD as the proton source. Experimentally, normal primary H/D kinetic isotope effects were observed under both catalytic regimes (k_H/k_D of 1.59 and 1.22, respectively), suggesting that proton transfer is involved in the rate determining step, thus supporting the protonation-first pathways, and excluding the CO_2-first mechanism.

Kinetic analysis of proposed mechanistic pathways.

The free energy landscape summarizing the total catalytic cycle is depicted in Figure 8.6. Following elucidation of the possible reaction pathways for CO_2 reduction across both potential-dependent regimes, we next sought to compare experimentally determined kinetic data against computationally derived turnover frequencies (TOFs) obtained from the energetic span computational model developed by Kozuch and coworkers.[140]. The energetic span model was employed to identify key intermediates and transition states, which control the rate of catalysis. This model connects the free energy landscape of the DFT based catalytic cycles with the experimentally measured TOFs using Eyring transition state theory. The model identifies TOF-determining transition states (TDTS) and the TOF-determining intermediates (TDI) and computes rates based on the energetic span of these two states.[140] Often there are various intermediates with a significant influence on the catalytic rates. This can be quatified in this model by the degree of TOF control (donated as X_{TOF})[138], which describes how the TOF varies by a small change in energy of that intermediate or transition state. The range of X_{TOF} is between 0 and 1, where 0 denotes that the species has no influence on the TOF and 1 denotes that the species solely controls the TOF (see references [140] and [142] for the exact mathematical definitions).[142, 626]

Experimental kinetic parameters were obtained from variable controlled potential (CPE) experiments as described by Saveant and co-workers[622, 623]. Short-term (5 min; Figure 8.7) and long-term (1 h) CPE experiments were performed where the products (CO and H_2) were detected and quantified by gas chromatography for the long-term CPE experiments conducted in an air-tight electrochemical cell. The observed rate constants (k_{obs}) at each applied potential were extracted from the average specific current densities taken across the entire electrolysis experiment and were then compared to the computed rates obtained from the energetic span model. To further probe the influence of the proton transfer step on the observed rates, PhOH (see Figure S6), and Cl-PhOH, which is approximately one pK_a unit more acidic (in water), were utilized.

First, we explored the kinetics of the low overpotential regime (Potential window of −1.40 − −1.75 V vs Fc/Fc^+). CPE data collected at applied potentials between −1.42 − −1.72 V vs Fc/Fc^+ overlay closely with the voltammogram collected under CO_2 atmosphere with 1 M PhOH (Figure 8.7a). Current densities were stable across the entire electrolysis (Figure 8.7b) and reached a plateau at ca. −1.6 V vs Fc/Fc^+ with an average current

density of 1.53 mA/cm^2 which corresponds to a TOF of 1.74 x 10^5 s^{-1} (Figure 8.7c). When the more acidic, Cl-PhOH was added as the proton donor, the maximum TOF of the first catalytic regime increased to 5.50 x 10^5 s^{-1}, a three-fold increase in observed rate relative to the data obtained with phenol as the proton source (Figure 8.7d) without loss of product selectivity. Analysis of this catalytic regime with the energetic span model shows that the catalytic rate is solely controlled by the second protonation step (C−O bond cleavage to release water) as the key rate limiting intermediate and transition state are both associate with the second protonation. The carboxy intermediate, $^1[Fe{-}CO_2H]^+$, is the TDI and the second protonation barrier is the TDTS both with X_{TOF} values close to 1. Based on this analysis, a TOF of 400 s^{-1} is predicted. This is slower than the experimentally determined TOF of 1.74 x 10^5; however, this translates to an energy difference of ∼3.5 kcal/mol which is still within acceptable agreement. Furthermore, when Cl-PhOH is utilized as the acid source, the barrier is lowered by 1.1 kcal/mol which translates to a rate increase by one order of magnitude. The stronger acid lowers the TDTS which leads to an increase in the importance of the CO_2 binding step which is illustrated by the change in the degree of TOF control: The X_{TOF} of both the TDI ($^1[Fe{-}CO_2]^+$) and TDTS decreases from 0.98 to 0.86 and the CO_2 binding step is increasingly important for the rate as the X_{TOF} increases to 0.14 from 0.02. Distinction between the protonation first or CO_2 binding first pathways by this kinetic analysis was not possible because both options occur before the rate determining protonation step.

Application of more negative onset potentials between −1.81 and −2.01 V vs Fc/Fc$^+$ allowed us to probe the kinetics of the second, high overpotential regime. Tight correlations between averaged current densities from the CPE experiments with the cyclic voltammograms collected under CO_2 atmosphere with PhOH (Figure 8.7a) or Cl-PhOH was observed. Peak current density of 4.0 mV/cm^2 was reached at −2.01 V vs Fc/Fc$^+$ which corresponds to a maximum TOF of 1.05 x 10^6 s^{-1}. Addition of 1 M Cl-PhOH as the proton source results in a smaller rate enhancement with a maximum TOF of 1.5 x 10^6 s^{-1}, representing only a 1.4-fold enhancement relative to PhOH, about half of what was observed in the low overpotential regime (Figure 8.7d). Catalytic Tafel plots comparing the two acids are presented in Figure 8.7d. In addition, there is still a proton dependence on the rate limiting step as illustrated by the normal, primary H/D kinetic isotope effect.

Next, the energetic span model was then applied to predict the rates for the three possible mechanistic pathways proposed for the high overpotential regime. These rates are then compared to the experimentally determined TOFs. The three pathways are given in Figure 8.5 and are illustrated in a free energy diagram (Figure 8.5) to allow for more direct comparison. From the $^1[Fe]^0$ catalytic resting state, the iron complex can either go through: (1) a CO_2 coordination first pathway to give the η^2 CO_2 complex ($^2[Fe{-}CO_2]^0$); (2) a protonation first pathway to generate the cationic pyridinium intermediate, $^1[Fe{-}N_{PY}H]^+$; or a PCET pathway to generate a similar neutral pyridinium species, $^2[Fe{-}N_{PY}H]^0$.

A TOF of 16000 s^{-1} is predicted for the CO_2 binding first pathway. The TOF is completely controlled by the CO_2 coordination step as the reduction of $^1[Fe{-}CO_2H]^+$ to $^2[Fe{-}CO_2H]^0$ lowers the (previously rate limiting) barrier for the second protonation by

6.6 kcal/mol from 13.9 to 7.3 kcal/mol. This shrinks the X_{TOF} for both $^1[Fe{-}CO_2H]^1$ and the transition state for the second protonation to 0. The CO_2 first pathway can be eliminated because CO_2 coordination is shown by the energetic span model to be entirely rate limiting and thus fails to explain the experimentally observed normal, primary H/D kinetic isotope effect and a large catalytic enhancement with the addition of more acidic proton donors.

Next, for the protonation first pathway, we predict a TOF that is almost 3 orders of magnitude slower than what we observed experimentally (11000 s^{-1}). Additionally, we find that the cycle is solely controlled by the first protonation of $^1[Fe]^0$ to give the pyridinium intermediate, $^1[Fe{-}N_{PY}H]^+$. The protonation first pathway would account for the primary kinetic isotope effect but not the rate enhancement upon addition of stronger acids as the energetic span model predicts the same rate regardless of if PhOH or Cl-PhOH are utilized as the proton source.

The TOF predicted for the PCET pathway of 1.4 x 10^7 s^{-1} resulted in the closest match to the experimentally measured value of 1.05 x 10^6 s^{-1} with the pathway being controlled by both the PCET step as well as the second protonation of $^2[Fe{-}CO_2H]^0$ as both have X_{TOF} coefficients close to 0.5. The chloro-substituted phenol lowers the barrier for the second protonation by 2.6 kcal/mol. However, only the PCET pathway is kinetically controlled by this transition state increasing the TOF from 1.4 x 10^7 s^{-1} to 2.6 x 10^7 s^{-1}. This increase is smaller than the increase in the low overpotential regime despite a stronger effect on barrier lowering. This can be understood by the lower X_{TOF} of that step in the low versus high overpotential regime. Taking together the experimental and computational findings, these data suggest that the PCET pathway is the more likely mechanism for the high overpotential regime.

Selectivity versus HER.

Achieving selectivity for CO_2 reduction over the reduction of protons to H_2 is critical. The HER is a competitive side reaction across a similar potential window to the CO_2RR and is highly dependent on the presence and strength of the proton source.[97] The generation of an iron hydride under reducing conditions in the presence of a proton donor can thus shift the catalyst selectivity away from CO production and toward the formation of H_2. It is therefore important to understand the kinetic and thermodynamic barriers associated with the protonation of the reduced iron center.

In our proposed pathway there are two critical intermediates through which the formation of a hydride is feasible. The first possibility is the direct protonation of the iron center of the doubly reduced intermediate, $^1[Fe]^0$. The other possibility is the rearrangement of the pyridinium intermediate, $^1[Fe{-}N_{PY}H]^+$, to a metal hydride. In both cases, high activation barriers prevent these side reactions and explain the high product selectivity for CO_2 reduction to CO that is observed experimentally. The direct formation of a hydride $^1[Fe{-}H]^+$ from $^1[Fe]^0$ albeit thermodynamically favorable with a free energy of −6.1 kcal/mol, is kinetically inhibited with a high activation barrier of 24.5 kcal/mol. The rearrangement of $^1[Fe{-}N_{PY}H]^+$ to $^1[Fe{-}H]^+$, is more exergonic (−17.5 kcal/mol); however, this pathway is

also inhibited by a larger activation barrier of 21.4 kcal/mol. In both cases, the high barriers can be rationalized by the electronic structure of $^1[Fe]^0$: the metal center stabilizes the two ligand reductions through antiferromagnetic coupling and thus the metal center remains Lewis acidic. This is illustrated by the coordination of acid (e.g., PhOH or H_2CO_3) to $^1[Fe]^0$ in which the acid prefers to bind via the oxygen atom to the iron center which then facilitates the protonation of the pyridyl arm, but blocks the metal center from protonation. Therefore, the formation of a metal-hydride is prohibited by steep kinetic barriers ultimately shutting down pathways to hydrogen production (see Figure G.3 for both HER transition states). The difference between the rate limiting transition state in CO_2RR and the barrier for hydride formation is $\sim$10 kcal/mol which implies that $^1[Fe]^{2+}$ should remain selective for the CO_2RR even when stronger acids are used as proton donors. This is illustrated by using 4-nitro-phenol, an even stronger acid (two pK_a units stronger than Cl-PhOH), with a barrier of 19.3 kcal/mol for the formation of a hydride. We explored this possibility and in all cases we do not detect any hydrogen formation experimentally. However, 4-nitro-phenol was also redox-active at the potentials applied, which prevented also the formation of CO.

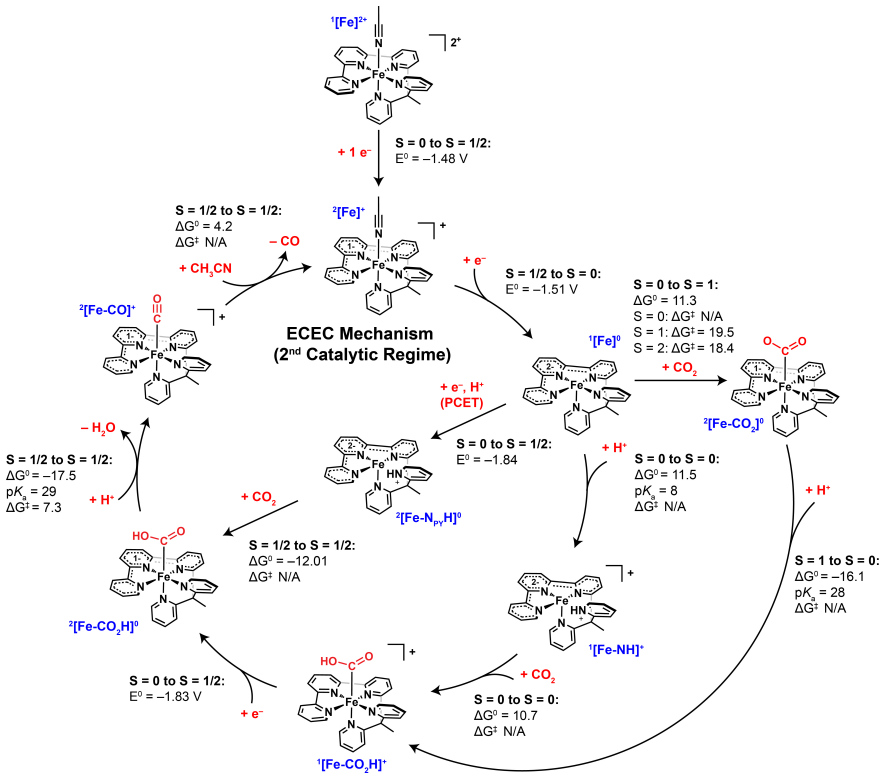

Figure 8.5: Proposed mechanistic cycles for the high overpotential regime. The high overpotential catalytic regime turns over from ^{2}[Fe]$^+$ following an initial induction period. Single-electron reduction of ^{2}[Fe]$^+$ gives the catalytic resting state, ^{1}[Fe]^0. Following formation of ^{1}[Fe]^0, the pathway diverges in three directions. CO_2 binding can occur first followed by protonation to give ^{1}[CO_2H]$^+$ (outer pathway) or protonation-first can occur followed by CO_2 coordination (inner pathway). The ^{1}[Fe–CO_2H]$^+$ intermediate can then be further reduced to ^{2}[Fe–CO_2H]^0 and following the final protonation step and loss of water generates the carbonyl complex, ^{2}[Fe–CO]$^+$ which regenerates ^{2}[Fe]$^+$ following ligand exchange. We additionally explore the possibility of overcoming the high energy barriers associated with either CO_2 binding or protonation of ^{1}[Fe]^0 by undergoing a PCET pathway to generate ^{2}[Fe–N_{PY}H]^0 (center pathway). All reaction and activation energies are given in units of kcal/mol and all reduction potentials are referenced to the computed Fe/Fe$^+$ couple.

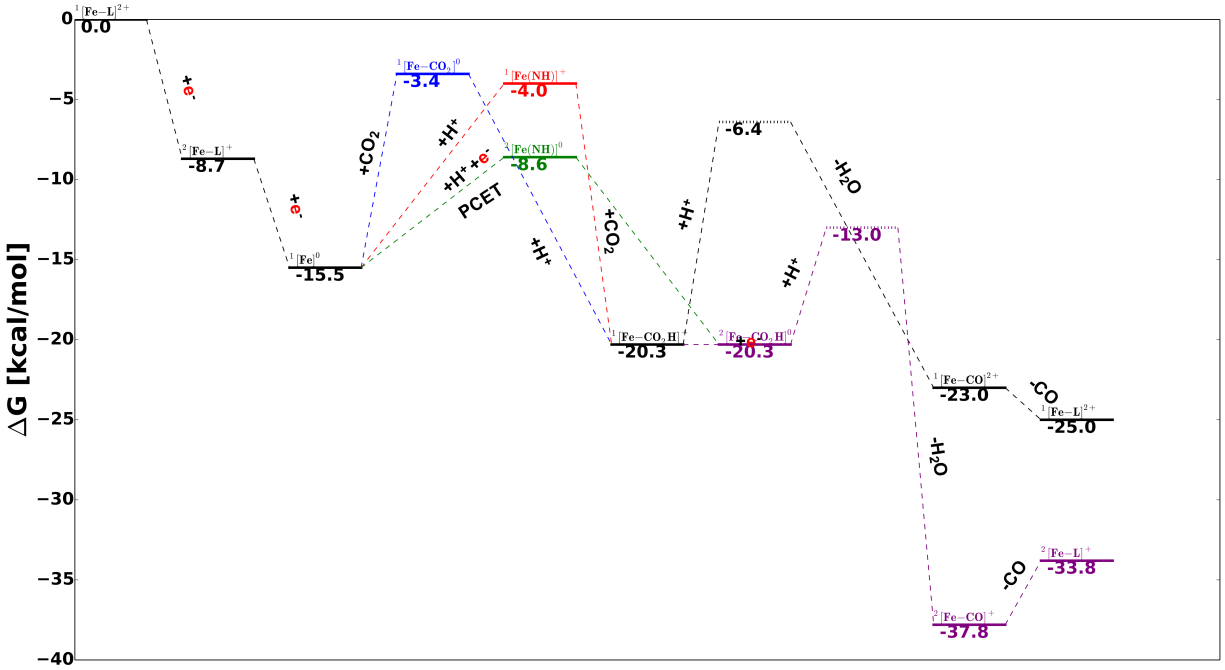

Figure 8.6: Free energy landscape of CO_2RR (both regimes). For the reduction steps, a potential of -1.8 V vs Fc^+/Fc is applied; for the protonation steps, phenol is used to estimate barriers and carbonic acid for free energies (see main text for justification); solid lines correspond to intermediate states and dashed lines to transition states.

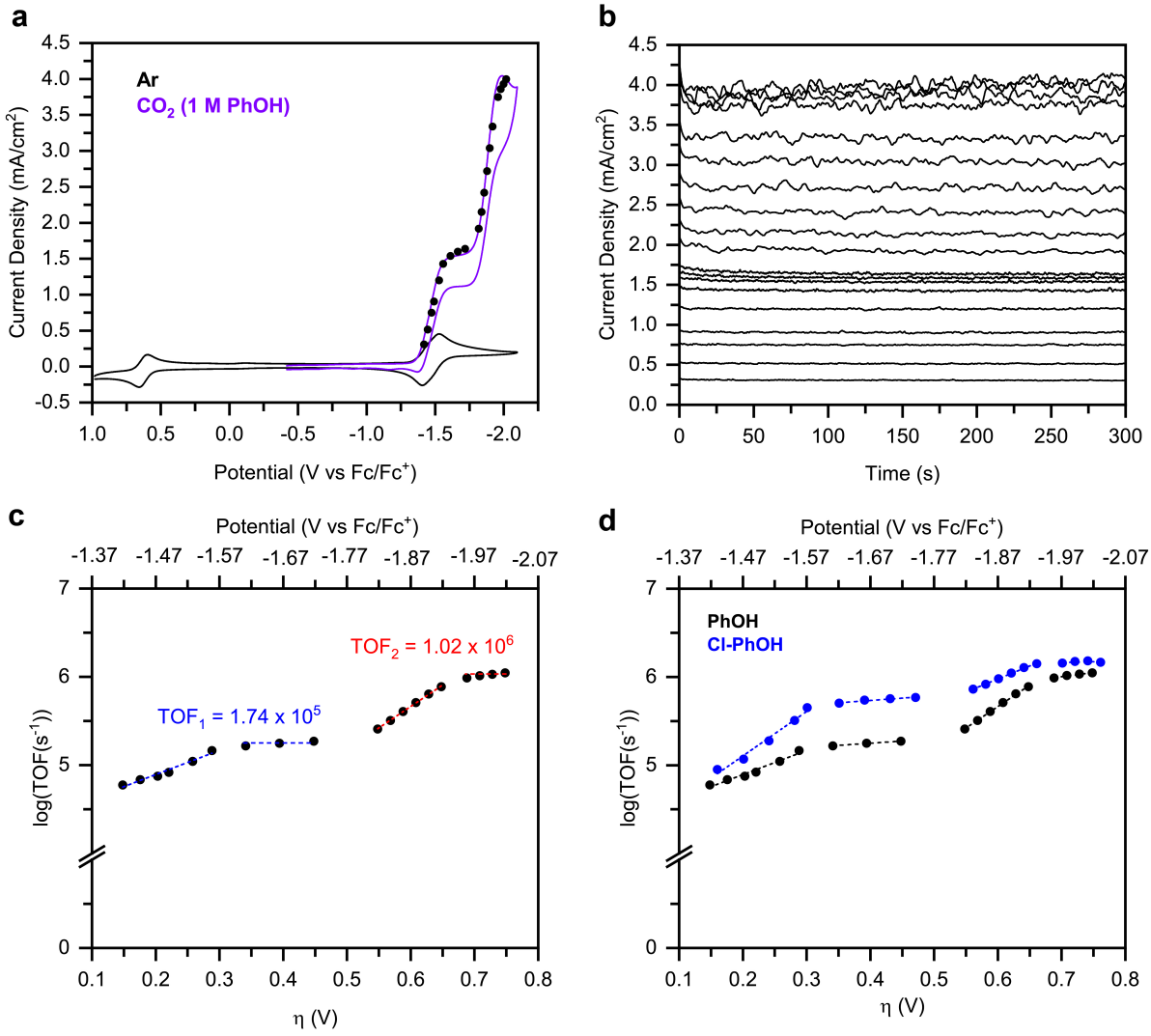

Figure 8.7: Kinetic analysis of $^1[Fe]^{2+}$ (a) Cyclic voltammograms of $^1[Fe]^{2+}$ in the absence (black) and presence (purple) of CO_2 with 1 M phenol. Average current densities extracted from the controlled potential electrolysis experiments (b) are overlayed on the catalytic CV (black dots) (c) Catalytic Tafel plot for $^1[Fe]^{2+}$ obtained from CPE experiments with 1 M phenol. (d) Comparison of catalytic Tafel plots obtained with 1 M PhOH or Cl-PhOH. CPE experiments were collected in an electrolyte of 0.10 M $TBAPF_6$ dissolved in acetonitrile

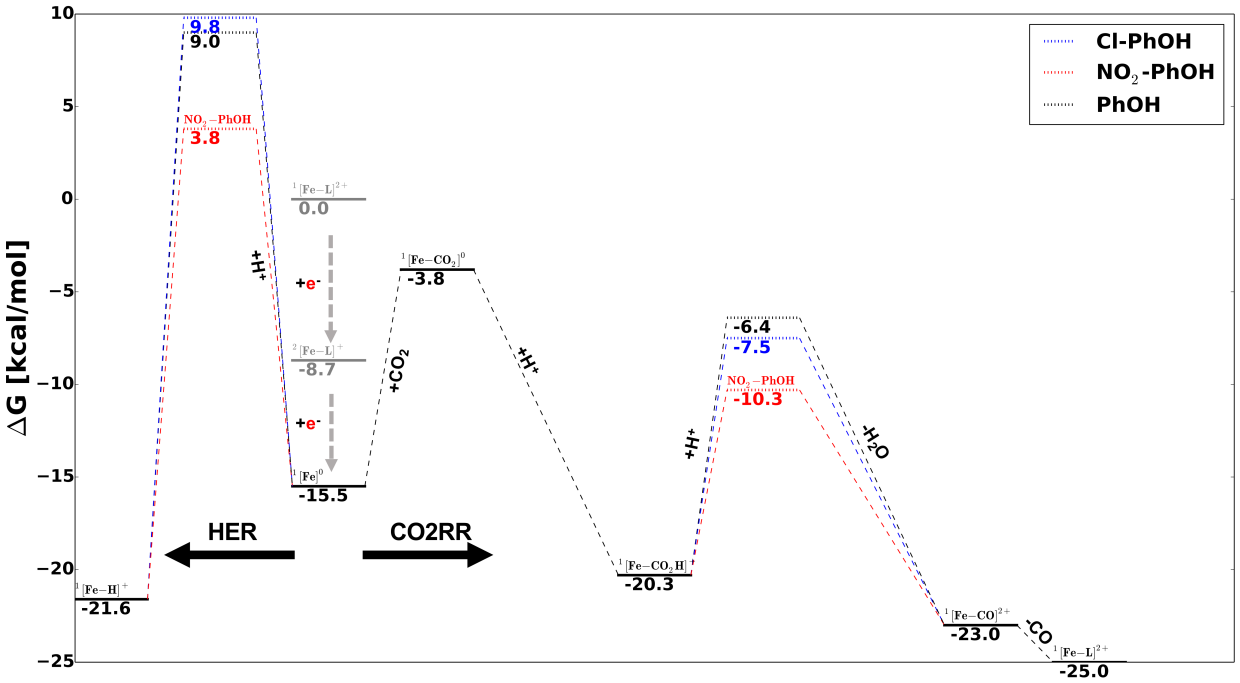

Figure 8.8: Free energy landscape of the CO_2RR (low overpotential regime) and HER pathways; for the reduction steps, a potential of -1.8 V vs Fc^+/Fc is applied; for the protonation steps, phenol is used to estimate barriers and carbonic acid for free energies (see main text for justification); solid lines correspond to intermediate states and dashed lines to transition structures.

Rational Catalyst Design Driven by Mechanistic Insights.

Based on the mechanistic studies we identified several critical intermediates and transition states. This directed us to propose improved ligand designs that ideally stabilize several critical intermediates. The key takeaways from the kinetic analysis are: first, the low overpotential regime is solely controlled by the second protonation step, even when stronger acids are used. Thus, modifications must either lower the energy of the transition state or decrease the stability of the carboxy intermediate. Second, the high overpotential regime is mainly controlled by either the CO_2 adduct or the formation of the pyridinium intermediate, especially when stronger acids are used as the proton source. Thus, an optimal modification should have a positive effect on both the CO_2 binding and second protonation. On the basis of our detailed mechanistic investigation, we propose rationally designed synthetic modifications to the tpyPY2Me ligand to further increase the catalytic performance of the iron complex. Synthetic modification to the pyridine moiety is the most promising for two reasons: first, it does not affect the initial reduction potentials and the crucial antiferromagnetic coupling of $^1[Fe]^0$; second, substituents can affect all critical intermediates by stabilizing the bound CO_2 adduct, increasing the pK_a of the pyridine itself for protonation and PCET, and then stabilizing the transition state for the second protonation (Figure 8.9 for investigated candidates).

In order to gain quantitative insights, we use ALMO-EDA(solv)[174] to understand how a specific modification stabilizes the reduced CO_2 adduct. We employ a difference-in-difference-approach where we compare the change in interaction energy and EDA terms using the unsubstituted tpyPY2Me ligand as the reference. We investigate hydrogen bonding ($-$OH and $-NH_2$) and ionic stabilization ($-N(CH_3)_3^+$) as both moieties are known to facilitate CO_2 binding in other CO2RR catalysts (see figure 8.9).[167, 176, 380, 385, 401, 403] The EDA decomposition of that change in interaction energy is crucial for understanding the exact stabilization pathway as substituents affect the reduced CO_2 not only directly via a non-covalent interaction but also indirectly via substituent effects. Both pathway often have distinct EDA fingerprints and thus can be distinguished by an EDA scheme. This was recently shown by us for an iron tetraphenylporphyrin catalyst.[174] The chosen reference fragmentation of the complex is a doubly reduced CO_2^{2-} and an unreduced catalyst. This fragmentation is more suitable for this type of complex as the O$-$C$-$O bond angle of 124° indicates a transfer of both electrons into the CO_2 moiety. The alternative choice, a neutral but bent CO_2 fragment and a doubly reduced metal complex will be solely dominated by the geometry distortion term see reference [174] for a more detailed discussion. Thus, this interaction energy decomposed by the EDA scheme corresponds to the stabilization of the doubly reduced CO_2^{2-} dianion by the unreduced catalyst. It is important to point out that this is just a part of the total free energy of CO_2 addition.

The EDA results are given in Figure 8.10 a and show that the interaction is dominated by electrostatic interactions with significant charge transfer contributions. The short Fe$-$C bond distance of 2.05 Å rationalizes the high Pauli repulsion. The change in interactions energies as well as each EDA component for each substituent relative to the unsubstituted

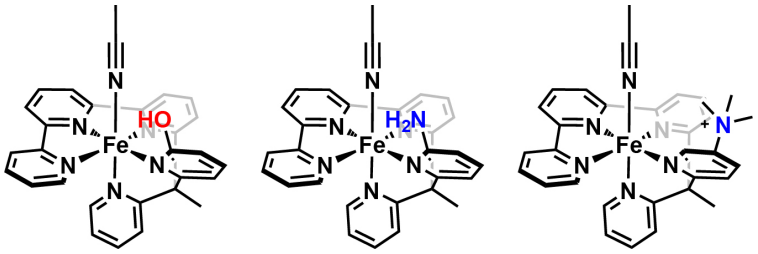

Figure 8.9: Chemical structures of second-sphere functionalized polypyridyl catalysts for improved performance based on our mechanistic understanding

complex is depicted in Figure 8.10 b.

The ortho hydroxy substituent (*o*-OH) strengthens the interaction by 77.1 kJ/mol (18.5 kcal/mol). The main driving force is additional favorable electrostatic interaction, which is also supplemented by favorable contributions from polarization and charge transfer, which are typical of an hydrogen bonding fingerprint.[83] The large increase in Pauli repulsion can be attributed to the repulsion of the diffuse lone pairs of the CO_2 moiety and the hydroxy group. Interestingly, this intermediate was not stable without freezing the hydroxy OH bond as it otherwise directly protonates the CO_2 moiety. The ortho amino substituent has a much smaller stabilizing effect of -22.5 kJ/mol (5.4 kcal/mol). The favorable electrostatic interaction cannot overcome the additional Pauli repulsion of the amino substituent and the CO_2^{2-} moiety. Lastly, the charged trimethylamino (TMA) moiety had to be placed at the meta position due to the bulkiness of the group. The EDA results demonstrate how this group provides a purely electrostatic stabilization; however, the solvation screens most of the interaction to yield an overall stabilization of -44.6 kJ/mol (-10.7 kcal/mol).

The ortho hydrogen donating substituents have another advantage: They can stabilize the transition state for the second protonation step by forming hydrogen bonds. These interactions lower the transition state (see Figure G.4 b) for the *o*-OH by 1.3 kcal/mol which translates to an order of magnitude faster TOF in the low overpotential regime (similar effect to the use of stronger acids).

8.4 Conclusions

In summary, inspired by the excellent catalytic activity of $[Fe(tpyPY_2Me)]^{2+}$, we investigated the mechanistic pathways through which it electrochemically converts CO_2 into CO. Cyclic voltammograms collected under CO_2 atmosphere displayed the formation of two distinct catalytic regimes with maximum current densities achieved at -1.66 V vs Fc/Fc^+ (η = 390 mV) and -1.98 V vs Fc/Fc^+ (η = 710 mV). For the low overpotential regime, the computed pathway shows that $^1[Fe]^{2+}$ first undergoes two, single-electron reduction steps to generate the five-coordinate open-shell singlet, $^1[Fe]^0$. From $^1[Fe]^0$, we show that the order of

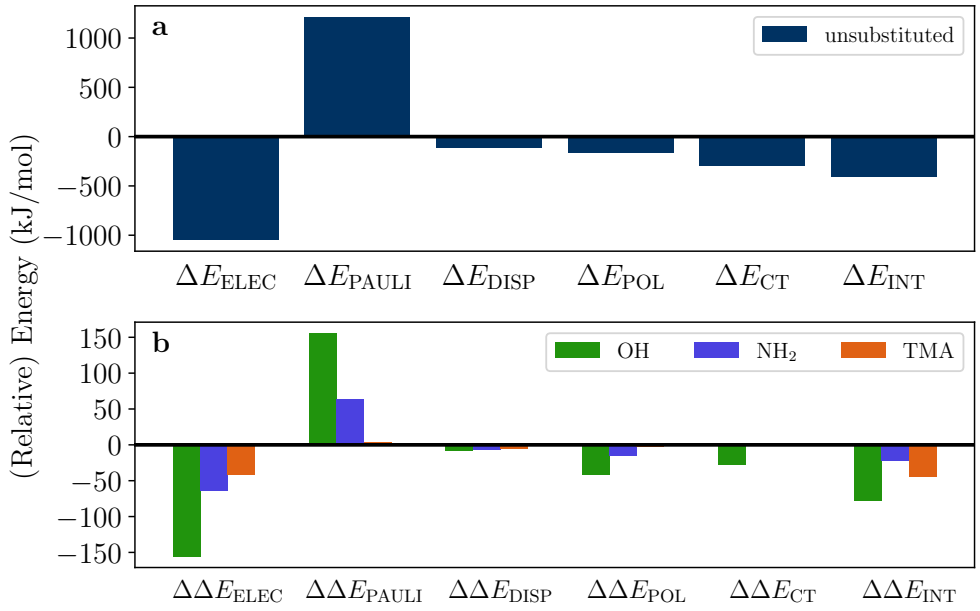

Figure 8.10: ALMO-EDA(solv) results for CO_2 adduct $^1[Fe{-}CO_2]^0$: (a) the unsubstituted adduct; (b) differential (ALMO-EDA(solv) results for three different substituents $-OH$, $-NH_2$ and $-N(CH_3)_3{}^+$ (TMA) ; energies in kJ/mol.

CO_2 addition or protonation is flexible and experimentally indistinguishable with both steps having comparable calculated barriers. We find that both CO_2 binding and protonation of the pyridine arm are feasible steps with similar endergonic free energies. In any case, the rate limiting step was found to be the second protonation step resulting in cleavage of the C−O bond with subsequent CO release being barrierless and exergonic. Analysis of the complete low overpotential regime revealed that catalysis is solely controlled by the carboxyl intermediate ($^1[Fe{-}CO_2H]^+$) and the transition state for the second protonation step. Consequently, the use of a stronger proton source, such as Cl-PhOH, resulted in three-fold increase in the rate of catalysis without any loss in product selectivity.

Computational analysis of the high overpotential regime shows a similar two initial electron transfer steps; however, at more reducing potentials, the first reduction is off-pathway, allowing for turnover from $^2[Fe]^1$ rather than $^1[Fe]^{2+}$ as is observed in the low overpotential regime. Following formation of the catalytic resting state, $^1[Fe]^0$, we computationally probed three mechanistic pathways and compared them to experimental kinetic data and results obtained from the energetic span model. From this analysis, we identified the PCET pathway of one of the pyridine arms as the most consistent mechanism. This intermediate readily binds CO_2 and rearranged into a singly reduced carbonyl intermediate. The additional electron greatly facilitates the second protonation step explaining the increased rates

observed for the higher overpotential regime. Analysis of the cycle showed that both the PCET and the second protonation steps control the rate of catalysis. As such, similar to the low overpotential regime, the use of a more acidic proton source increases the rate of catalysis, but to a lesser degree. The stronger acid only lowers the barrier for the second protonation; however this step has less influence on the turnover frequency and thus the effect of acid pK_a is lower (see Figure G.5 for a complete overview).

Finally, the mechanistic insights gained from this study identified the pyridyl arms as promising targets for further optimization of the catalytic performance of this system. The pyridyl arms are not involved in stabilizing the excess electron density in the reduction events and thus any modifications should not alter the reduction potential of $^1[Fe]^{2+}$, which is already optimally matched to the standard redox potential for the conversation of CO_2. The introduction of hydrogen bond donors into the second coordination sphere can further greatly stabilize the CO_2 adduct and lower the transition state for the second protonation step, both of which are critical intermediates for fast catalysis. Moreover, we also expect that the substituent effects can help to stabilize the pyridinium intermediate; therefore, this synthetic modification has the potential to improve catalysis in all proposed cycles for both the low and high overpotential regimes.

Bibliography

(1) Dirac, P. A. M. Quantum mechanics of many-electron systems. *Proc. R. Soc. A* **1929**, *123*, 714–733.

(2) Simões, A. Dirac's Claim and the Chemists. *Phys. Perspect.* **2002**, *4*, 253–266.

(3) Head-Gordon, M. Quantum chemistry and molecular processes. *J. Phys. Chem.* **1996**, *100*, 13213–13225.

(4) Friesner, R. A. Ab initio quantum chemistry: Methodology and applications. *Proc. Natl. Acad. Sci. U.S.A.* **2005**, *102*, 6648–6653.

(5) Neese, F.; Atanasov, M.; Bistoni, G.; Maganas, D.; Ye, S. Chemistry and quantum mechanics in 2019: give us insight and numbers. *J. Am. Chem. Soc.* **2019**, *141*, 2814–2824.

(6) Dral, P. O. Quantum chemistry in the age of machine learning. *J. Phys. Chem* **2020**, *11*, 2336–2347.

(7) Cao, Y.; Romero, J.; Olson, J. P.; Degroote, M.; Johnson, P. D.; Kieferová, M.; Kivlichan, I. D.; Menke, T.; Peropadre, B.; Sawaya, N. P., et al. Quantum chemistry in the age of quantum computing. *Chem. Rev.* **2019**, *119*, 10856–10915.

(8) Sakurai, J. J.; Commins, E. D., *Modern quantum mechanics, revised edition*; American Association of Physics Teachers: 1995.

(9) Szabo, A.; Ostlund, N. S., *Modern quantum chemistry: introduction to advanced electronic structure theory*; Courier Corporation: 2012.

(10) Cramer, C. J., *Essentials of computational chemistry: theories and models*; John Wiley & Sons: 2013.

(11) Jensen, F., *Introduction to computational chemistry*, 3rd ed.; John wiley & sons: 2017.

(12) Lin, L.; Lu, J., *A mathematical introduction to electronic structure theory*; SIAM: 2019.

(13) Schrödinger, E. An undulatory theory of the mechanics of atoms and molecules. *Phys. Rev.* **1926**, *28*, 1049.

(14) Born, M.; Oppenheimer, R. Zur quantentheorie der molekeln. *Ann. Phys.* **1927**, *389*, 457–484.

(15) Head-Gordon, M.; Maslen, P. E.; White, C. A. A tensor formulation of many-electron theory in a nonorthogonal single-particle basis. *J. Chem. Phys* **1998**, *108*, 616–625.

(16) Shavitt, I.; Bartlett, R. J., *Many-body methods in chemistry and physics: MBPT and coupled-cluster theory*; Cambridge university press: 2009.

(17) Echenique, P.; Alonso, J. L. A mathematical and computational review of Hartree–Fock SCF methods in quantum chemistry. *Mol. Phys.* **2007**, *105*, 3057–3098.

(18) Koch, W.; Holthausen, M. C., *A chemist's guide to density functional theory*; John Wiley & Sons: 2015.

(19) Capelle, K. A bird's-eye view of density-functional theory. *Braz. J. Phys.* **2006**, *36*, 1318–1343.

(20) Mardirossian, N.; Head-Gordon, M. Thirty years of density functional theory in computational chemistry: an overview and extensive assessment of 200 density functionals. *Mol. Phys.* **2017**, *115*, 2315–2372.

(21) Hartree, D. R.; Hartree, W. Self-consistent field, with exchange, for beryllium. *Proc. R. Soc. A* **1935**, *150*, 9–33.

(22) Slater, J. C. The theory of complex spectra. *Phys. Rev.* **1929**, *34*, 1293.

(23) Condon, E. The theory of complex spectra. *Phys. Rev.* **1930**, *36*, 1121.

(24) Roothaan, C. C. J. New developments in molecular orbital theory. *Rev. Mod. Phys.* **1951**, *23*, 69.

(25) Pople, J. A.; Nesbet, R. K. Self-consistent orbitals for radicals. *J. Chem. Phys* **1954**, *22*, 571–572.

(26) Lee, J.; Head-Gordon, M. Distinguishing artificial and essential symmetry breaking in a single determinant: Approach and application to the C 60, C 36, and C 20 fullerenes. *Phys. Chem. Chem. Phys.* **2019**, *21*, 4763–4778.

(27) Head-Gordon, M.; Pople, J. A. Optimization of wave function and geometry in the finite basis Hartree-Fock method. *J. Phys. Chem.* **1988**, *92*, 3063–3069.

(28) Van Voorhis, T.; Head-Gordon, M. A geometric approach to direct minimization. *Mol. Phys.* **2002**, *100*, 1713–1721.

(29) Stoll, H.; Wagenblast, G.; Preuβ, H. On the use of local basis sets for localized molecular orbitals. *Theor. Chim. Acta* **1980**, *57*, 169–178.

(30) Gianinetti, E.; Raimondi, M.; Tornaghi, E. Modification of the Roothaan equations to exclude BSSE from molecular interaction calculations. *Int. J. Quantum Chem.* **1996**, *60*, 157–166.

(31) Khaliullin, R. Z.; Head-Gordon, M.; Bell, A. T. An efficient self-consistent field method for large systems of weakly interacting components. *J. Chem. Phys* **2006**, *124*, 204105.

(32) Horn, P. R.; Head-Gordon, M. Polarization contributions to intermolecular interactions revisited with fragment electric-field response functions. *J. Chem. Phys.* **2015**, *143*, 114111.

(33) Mao, Y.; Ge, Q.; Horn, P. R.; Head-Gordon, M. On the Computational Characterization of Charge-Transfer Effects in Noncovalently Bound Molecular Complexes. *J. Chem. Theory Comput.* **2018**, *14*, 2401–2417.

(34) Møller, C.; Plesset, M. S. Note on an approximation treatment for many-electron systems. *Phys. Rev.* **1934**, *46*, 618.

(35) Cremer, D. Møller–Plesset perturbation theory: from small molecule methods to methods for thousands of atoms. *Wiley Interdiscip. Rev. Comput. Mol. Sci.* **2011**, *1*, 509–530.

(36) Bartlett, R. J.; Musiał, M. Coupled-cluster theory in quantum chemistry. *Rev. Mod. Phys.* **2007**, *79*, 291.

(37) Bartlett, R. J. Coupled-cluster theory and its equation-of-motion extensions. *Wiley Interdiscip. Rev. Comput. Mol. Sci.* **2012**, *2*, 126–138.

(38) Hylleraas, E. A. Über den Grundterm der Zweielektronenprobleme von H^-, He, Li^+, Be^{++} usw. *Z. Phys.* **1930**, *65*, 209–225.

(39) Neese, F.; Schwabe, T.; Kossmann, S.; Schirmer, B.; Grimme, S. Assessment of Orbital-Optimized, Spin-Component Scaled Second-Order Many-Body Perturbation Theory for Thermochemistry and Kinetics. *J. Chem. Theory Comput.* **2009**, *5*, 3060–3073.

(40) Lee, J.; Head-Gordon, M. Regularized Orbital-Optimized Second-Order Möller-Plesset Perturbation Theory: A Reliable Fifth-Order-Scaling Electron Correlation Model with Orbital Energy Dependent Regularizers. *J. Chem. Theory Comput.* **2018**, *14*, 5203–5219.

(41) Hohenberg, P.; Kohn, W. Inhomogeneous electron gas. *Phys. Rev.* **1964**, *136*, B864.

(42) Bloch, F. Bemerkung zur Elektronentheorie des Ferromagnetismus und der elektrischen Leitfähigkeit. *Z. Phys.* **1929**, *57*, 545–555.

(43) Laricchia, S.; Constantin, L. A.; Fabiano, E.; Della Sala, F. Laplacian-level kinetic energy approximations based on the fourth-order gradient expansion: global assessment and application to the subsystem formulation of density functional theory. *J. Chem. Theory Comput.* **2014**, *10*, 164–179.

(44) Kohn, W.; Sham, L. J. Self-consistent equations including exchange and correlation effects. *Phys. Rev.* **1965**, *140*, A1133.

(45) Parr, R. G.; Yang, W., *Density-functional theory of atoms and molecules. International Series of Monographs on Chemistry*, 1994.

(46) Perdew, J. P.; Ruzsinszky, A.; Tao, J.; Staroverov, V. N.; Scuseria, G. E.; Csonka, G. I. Prescription for the design and selection of density functional approximations: More constraint satisfaction with fewer fits. *J. Chem. Phys* **2005**, *123*, 062201.

(47) Dirac, P. A. In *Mathematical proceedings of the Cambridge philosophical society*, 1930; Vol. 26, pp 376–385.

(48) Perdew, J. P.; Wang, Y. Accurate and simple analytic representation of the electron-gas correlation energy. *Phys. Rev. B* **1992**, *45*, 13244.

(49) Perdew, J. P.; Burke, K.; Ernzerhof, M. Generalized gradient approximation made simple. *Phys. Rev. Lett.* **1996**, *77*, 3865.

(50) Becke, A. D. Density-functional exchange-energy approximation with correct asymptotic behavior. *Phys. Rev. A* **1988**, *38*, 3098.

(51) Chan, B.; Gill, P. M.; Kimura, M. Assessment of DFT methods for transition metals with the TMC151 compilation of data sets and comparison with accuracies for main-group chemistry. *J. Chem. Theory Comput.* **2019**, *15*, 3610–3622.

(52) Tao, J.; Perdew, J. P.; Staroverov, V. N.; Scuseria, G. E. Climbing the density functional ladder: Nonempirical meta–generalized gradient approximation designed for molecules and solids. *Phys. Rev. Lett.* **2003**, *91*, 146401.

(53) Wang, Y.; Jin, X.; Haoyu, S. Y.; Truhlar, D. G.; He, X. Revised M06-L functional for improved accuracy on chemical reaction barrier heights, noncovalent interactions, and solid-state physics. *Proc. Natl. Acad. Sci.* **2017**, *114*, 8487–8492.

(54) Polo, V.; Kraka, E.; Cremer, D. Electron correlation and the self-interaction error of density functional theory. *Mol. Phys.* **2002**, *100*, 1771–1790.

(55) Lundberg, M.; Siegbahn, P. E. M. Quantifying the effects of the self-interaction error in DFT: When do the delocalized states appear? *J. Chem. Phys.* **2005**, *122*, 224103.

(56) Becke, A. D. Density-functional thermochemistry. III. The role of exact exchange. *J. Chem. Phys.* **1993**, *98*, 5648–5652.

(57) Lee, C.; Yang, W.; Parr, R. G. Development of the Colle-Salvetti correlation-energy formula into a functional of the electron density. *Phys. Rev. B* **1988**, *37*, 785.

(58) Harvey, J. N. On the accuracy of density functional theory in transition metal chemistry. *Annu. Rep. Prog. Chem., Sect. C: Phys. Chem.* **2006**, *102*, 203–226.

(59) Leininger, T.; Stoll, H.; Werner, H.-J.; Savin, A. Combining long-range configuration interaction with short-range density functionals. *Chem. Phys. Lett.* **1997**, *275*, 151–160.

(60) Iikura, H.; Tsuneda, T.; Yanai, T.; Hirao, K. A long-range correction scheme for generalized-gradient-approximation exchange functionals. *J. Chem. Phys* **2001**, *115*, 3540–3544.

(61) Chai, J.-D.; Head-Gordon, M. Systematic optimization of long-range corrected hybrid density functionals. *J. Chem. Phys* **2008**, *128*, 084106.

(62) Grimme, S. Semiempirical GGA-type density functional constructed with a long-range dispersion correction. *J. Comput. Chem.* **2006**, *27*, 1787–1799.

(63) Mardirossian, N.; Head-Gordon, M. Survival of the most transferable at the top of Jacob's ladder: Defining and testing the ωB97M(2) double hybrid density functional. *J. Chem. Phys* **2018**, *148*, 241736.

(64) Haoyu, S. Y.; He, X.; Li, S. L.; Truhlar, D. G. MN15: A Kohn–Sham global-hybrid exchange–correlation density functional with broad accuracy for multi-reference and single-reference systems and noncovalent interactions. *Chem. Sci.* **2016**, *7*, 5032–5051.

(65) Kristyán, S.; Pulay, P. Can (semi) local density functional theory account for the London dispersion forces? *Chem. Phys. Lett* **1994**, *229*, 175–180.

(66) Grimme, S.; Antony, J.; Ehrlich, S.; Krieg, H. A consistent and accurate ab initio parametrization of density functional dispersion correction (DFT-D) for the 94 elements H-Pu. *J. Chem. Phys* **2010**, *132*, 154104.

(67) Brandenburg, J. G.; Grimme, S. In *Prediction and Calculation of Crystal Structures*; Springer: 2013, pp 1–23.

(68) Chai, J.-D.; Head-Gordon, M. Long-range corrected hybrid density functionals with damped atom-atom dispersion corrections. *Phys. Chem. Chem. Phys.* **2008**, *10*, 6615–6620.

(69) Vydrov, O. A.; Van Voorhis, T. Nonlocal van der Waals density functional: The simpler the better. *J. Chem. Phys* **2010**, *133*, 244103.

(70) Mardirossian, N.; Head-Gordon, M. ωB97M-V: A combinatorially optimized, range-separated hybrid, meta-GGA density functional with VV10 nonlocal correlation. *J. Chem. Phys* **2016**, *144*, 214110.

(71) Noodleman, L.; Norman Jr, J. G.; Osborne, J. H.; Aizman, A.; Case, D. A. Models for ferredoxins: electronic structures of iron-sulfur clusters with one, two, and four iron atoms. *J. Am. Chem. Soc.* **1985**, *107*, 3418–3426.

(72) Noodleman, L.; Davidson, E. R. Ligand spin polarization and antiferromagnetic coupling in transition metal dimers. *Chemical physics* **1986**, *109*, 131–143.

(73) Yamaguchi, K.; Fueno, T.; Ueyama, N.; Nakamura, A.; Ozaki, M. Antiferromagnetic spin couplings between iron ions in iron-sulfur clusters. A localized picture by the spin vector model. *Chem. Phys. Lett.* **1989**, *164*, 210–216.

(74) Neese, F. Definition of corresponding orbitals and the diradical character in broken symmetry DFT calculations on spin coupled systems. *J. Phys. Chem. Solids* **2004**, *65*, 781–785.

(75) Neese, F. A critical evaluation of DFT, including time-dependent DFT, applied to bioinorganic chemistry. *J. Biol. Inorg. Chem.* **2006**, *11*, 702–711.

(76) Heisenberg, W. Zur Theorie des Ferromagnetismus. *Z. Phys.* **1928**, *49*, 619–636.

(77) Soda, T.; Kitagawa, Y.; Onishi, T.; Takano, Y.; Shigeta, Y.; Nagao, H.; Yoshioka, Y.; Yamaguchi, K. Ab initio computations of effective exchange integrals for H–H, H–He–H and Mn2O2 complex: comparison of broken-symmetry approaches. *Chem. Phys. Lett.* **2000**, *319*, 223–230.

(78) Ruiz, E.; Cano, J.; Alvarez, S.; Alemany, P. Broken symmetry approach to calculation of exchange coupling constants for homobinuclear and heterobinuclear transition metal complexes. *J. Comput. Chem.* **1999**, *20*, 1391–1400.

(79) Orio, M.; Pantazis, D. A.; Petrenko, T.; Neese, F. Magnetic and spectroscopic properties of mixed valence manganese (III, IV) dimers: a systematic study using broken symmetry density functional theory. *Inorg. Chem.* **2009**, *48*, 7251–7260.

(80) Pantazis, D. A. Meeting the challenge of magnetic coupling in a triply-bridged chromium dimer: Complementary broken-symmetry density functional theory and multireference density matrix renormalization group perspectives. *J. Chem. Theory Comput.* **2019**, *15*, 938–948.

(81) Li, Z.; Guo, S.; Sun, Q.; Chan, G. K.-L. Electronic landscape of the P-cluster of nitrogenase as revealed through many-electron quantum wavefunction simulations. *Nat. Chem.* **2019**, *11*, 1026–1033.

(82) Andrés, J.; Ayers, P. W.; Boto, R. A.; Carbó-Dorca, R.; Chermette, H.; Cioslowski, J.; Contreras-García, J.; Cooper, D. L.; Frenking, G.; Gatti, C., et al. Nine questions on energy decomposition analysis. *J. Comput. Chem.* **2019**, *40*, 2248–2283.

(83) Khaliullin, R. Z.; Cobar, E. A.; Lochan, R. C.; Bell, A. T.; Head-Gordon, M. Unravelling the Origin of Intermolecular Interactions Using Absolutely Localized Molecular Orbitals. *J. Phys. Chem. A* **2007**, *111*, 8753–8765.

(84) Horn, P. R.; Mao, Y.; Head-Gordon, M. Probing non-covalent interactions with a second generation energy decomposition analysis using absolutely localized molecular orbitals. *Phys. Chem. Chem. Phys.* **2016**, *18*, 23067–23079.

(85) Mao, Y.; Loipersberger, M.; Horn, P. R.; Das, A.; Demerdash, O.; Levine, D. S.; Prasad Veccham, S.; Head-Gordon, T.; Head-Gordon, M. From Intermolecular Interaction Energies and Observable Shifts to Component Contributions and Back Again: A Tale of Variational Energy Decomposition Analysis. *Annu. Rev. Phys. Chem* **2021**, *72*, 641–666.

(86) Horn, P. R.; Mao, Y.; Head-Gordon, M. Defining the contributions of permanent electrostatics, Pauli repulsion, and dispersion in density functional theory calculations of intermolecular interaction energies. *J. Chem. Phys.* **2016**, *144*, 114107.

(87) Khaliullin, R. Z.; Bell, A. T.; Head-Gordon, M. Analysis of charge transfer effects in molecular complexes based on absolutely localized molecular orbitals. *J. Chem. Phys* **2008**, *128*, 184112.

(88) Veccham, S. P.; Lee, J.; Mao, Y.; Horn, P. R.; Head-Gordon, M. A non-perturbative pairwise-additive analysis of charge transfer contributions to intermolecular interaction energies. *Phys. Chem. Chem. Phys.* **2021**, *23*, 928–943.

(89) Dewar, J. A review of the pi-complex theory. *Bull. Soc. Chim. Fr.* **1951**, *18*, C71–C79.

(90) Chatt, J.; Duncanson, L. A. 586. Olefin co-ordination compounds. Part III. Infra-red spectra and structure: attempted preparation of acetylene complexes. *J. Chem. Soc.* **1953**, 2939–2947.

(91) Mao, Y.; Head-Gordon, M. Probing blue-shifting hydrogen bonds with adiabatic energy decomposition analysis. *J. Phys. Chem* **2019**, *10*, 3899–3905.

(92) Odoh, S. O.; Cramer, C. J.; Truhlar, D. G.; Gagliardi, L. Quantum-chemical characterization of the properties and reactivities of metal–organic frameworks. *Chem. Rev.* **2015**, *115*, 6051–6111.

(93) Santoro, S.; Kalek, M.; Huang, G.; Himo, F. Elucidation of mechanisms and selectivities of metal-catalyzed reactions using quantum chemical methodology. *Acc. Chem. Res.* **2016**, *49*, 1006–1018.

(94) Eisenstein, O.; Milani, J.; Perutz, R. N. Selectivity of C–H activation and competition between C–H and C–F bond activation at fluorocarbons. *Chem. Rev.* **2017**, *117*, 8710–8753.

(95) Yang, Y.-F.; Hong, X.; Yu, J.-Q.; Houk, K. Experimental–computational synergy for selective Pd (II)-catalyzed C–H activation of aryl and alkyl groups. *Acc. Chem. Res.* **2017**, *50*, 2853–2860.

(96) Maji, R.; Mallojjala, S. C.; Wheeler, S. E. Chiral phosphoric acid catalysis: from numbers to insights. *Chem. Soc. Rev.* **2018**, *47*, 1142–1158.

(97) Kinzel, N. W.; Werlé, C.; Leitner, W. Transition Metal Complexes as Catalysts for the Electroconversion of CO2: An Organometallic Perspective. *Angew. Chem. Int. Ed.* **2021**, *60*, 11628–11686.

(98) Noyori, R.; Richmond, J. P. Ethical conduct in chemical research and publishing. *Adv. Synth. Catal.* **2013**, *355*, 3–9.

(99) Lee, K. J.; Elgrishi, N.; Kandemir, B.; Dempsey, J. L. Electrochemical and spectroscopic methods for evaluating molecular electrocatalysts. *Nat. Rev. Chem.* **2017**, *1*, 1–14.

(100) Francke, R.; Schille, B.; Roemelt, M. Homogeneously catalyzed electroreduction of carbon dioxide-methods, mechanisms, and catalysts. *Chem. Rev.* **2018**, *118*, 4631–4701.

(101) Harvey, J. N.; Himo, F.; Maseras, F.; Perrin, L. Scope and challenge of computational methods for studying mechanism and reactivity in homogeneous catalysis. *ACS Catal.* **2019**, *9*, 6803–6813.

(102) Rudshteyn, B.; Weber, J.; Coskun, D.; Devlaminck, P. A.; Zhang, S.; Reichman, D. R.; Shee, J.; Friesner, R. Calculation of Metallocene Ionization Potentials via Auxiliary Field Quantum Monte Carlo: Towards Benchmark Quantum Chemistry for Transition Metals. *ChemRxiv* **2021**, DOI: `10.26434/chemrxiv.14751684.v1`.

(103) Shee, J.; Loipersberger, M.; Hait, D.; Lee, J.; Head-Gordon, M. Revealing the nature of electron correlation in transition metal complexes with symmetry breaking and chemical intuition. *J. Chem. Phys* **2021**, *154*, 194109.

(104) Hait, D.; Tubman, N. M.; Levine, D. S.; Whaley, K. B.; Head-Gordon, M. What levels of coupled cluster theory are appropriate for transition metal systems? a study using near-exact quantum chemical values for 3d transition metal binary compounds. *J. Chem. Theory Comput.* **2019**, *15*, 5370–5385.

(105) Werner, H.-J.; Schütz, M. An efficient local coupled cluster method for accurate thermochemistry of large systems. *J. Chem. Phys* **2011**, *135*, 144116.

(106) Riplinger, C.; Neese, F. An efficient and near linear scaling pair natural orbital based local coupled cluster method. *J. Chem. Phys* **2013**, *138*, 034106.

(107) Liakos, D. G.; Guo, Y.; Neese, F. Comprehensive benchmark results for the domain based local pair natural orbital coupled cluster method (DLPNO-CCSD (T)) for closed-and open-shell systems. *J. Phys. Chem. A* **2019**, *124*, 90–100.

(108) Shao, Y. et al. Advances in molecular quantum chemistry contained in the Q-Chem 4 program package. *Mol. Phys.* **2015**, *113*, 184–215.

(109) Verma, P.; Varga, Z.; Klein, J. E.; Cramer, C. J.; Que, L.; Truhlar, D. G. Assessment of electronic structure methods for the determination of the ground spin states of Fe (II), Fe (III) and Fe (IV) complexes. *Phys. Chem. Chem. Phys.* **2017**, *19*, 13049–13069.

(110) Reiher, M. Theoretical study of the Fe (phen) 2 (NCS) 2 spin-crossover complex with reparametrized density functionals. *Inorg. Chem.* **2002**, *41*, 6928–6935.

(111) Ioannidis, E. I.; Kulik, H. J. Ligand-field-dependent behavior of meta-GGA exchange in transition-metal complex spin-state ordering. *J. Phys. Chem. A* **2017**, *121*, 874–884.

(112) Grimme, S. Improved second-order Møller-Plesset perturbation theory by separate scaling of parallel- and antiparallel-spin pair correlation energies. *J. Chem. Phys.* **2003**, *118*, 9095–9102.

(113) Pantazis, D. A.; Orio, M.; Petrenko, T.; Zein, S.; Bill, E.; Lubitz, W.; Messinger, J.; Neese, F. A New Quantum Chemical Approach to the Magnetic Properties of Oligonuclear Transition-Metal Complexes: Application to a Model for the Tetranuclear Manganese Cluster of Photosystem II. *Chem. Eur. J.* **2009**, *15*, 5108–5123.

(114) Milko, P.; Iron, M. A. On the innocence of bipyridine ligands: how well do DFT functionals fare for these challenging spin systems? *J. Chem. Theory Comput.* **2014**, *10*, 220–235.

(115) Ortuño, M. A.; Cramer, C. J. Multireference electronic structures of Fe–pyridine (diimine) complexes over multiple oxidation states. *J. Phys. Chem. A* **2017**, *121*, 5932–5939.

(116) Boys, S. F.; Bernardi, F. The calculation of small molecular interactions by the differences of separate total energies. Some procedures with reduced errors. *Mol. Phys.* **1970**, *19*, 553–566.

(117) Halkier, A.; Helgaker, T.; Jørgensen, P.; Klopper, W.; Koch, H.; Olsen, J.; Wilson, A. K. Basis-set convergence in correlated calculations on Ne, N2, and H2O. *Chem. Phys. Lett.* **1998**, *286*, 243–252.

(118) Li, W.-L.; Lininger, C. N.; Chen, K.; Vaissier Welborn, V.; Rossomme, E.; Bell, A. T.; Head-Gordon, M.; Head-Gordon, T. Critical Role of Thermal Fluctuations for CO Binding on Electrocatalytic Metal Surfaces. *JACS Au* **2021**, *ASAP*.

(119) Truong, T. N.; Stefanovich, E. V. A new method for incorporating solvent effect into the classical, ab initio molecular orbital and density functional theory frameworks for arbitrary shape cavity. *Chem. Phys. Lett.* **1995**, *240*, 253–260.

(120) Barone, V.; Cossi, M. Quantum calculation of molecular energies and energy gradients in solution by a conductor solvent model. *J. Phys. Chem. A* **1998**, *102*, 1995–2001.

(121) Bondi, A. v. van der Waals volumes and radii. *J. Phys. Chem.* **1964**, *68*, 441–451.

(122) Marenich, A. V.; Cramer, C. J.; Truhlar, D. G. Universal solvation model based on solute electron density and on a continuum model of the solvent defined by the bulk dielectric constant and atomic surface tensions. *J. Phys. Chem. B* **2009**, *113*, 6378–6396.

(123) Marenich, A. V.; Olson, R. M.; Kelly, C. P.; Cramer, C. J.; Truhlar, D. G. Self-consistent reaction field model for aqueous and nonaqueous solutions based on accurate polarized partial charges. *J. Chem. Theory Comput.* **2007**, *3*, 2011–2033.

(124) Kelly, C. P.; Cramer, C. J.; Truhlar, D. G. Adding explicit solvent molecules to continuum solvent calculations for the calculation of aqueous acid dissociation constants. *J. Phys. Chem. A* **2006**, *110*, 2493–2499.

(125) Alongi, K. S.; Shields, G. C. Theoretical calculations of acid dissociation constants: a review article. *Annu Rep Comput Chem* **2010**, *6*, 113–138.

(126) Isse, A. A.; Gennaro, A. Absolute potential of the standard hydrogen electrode and the problem of interconversion of potentials in different solvents. *J. Phys. Chem. B* **2010**, *114*, 7894–7899.

(127) Fu, Y.; Liu, L.; Yu, H.-Z.; Wang, Y.-M.; Guo, Q.-X. Quantum-chemical predictions of absolute standard redox potentials of diverse organic molecules and free radicals in acetonitrile. *J. Am. Chem. Soc.* **2005**, *127*, 7227–7234.

(128) Konezny, S. J.; Doherty, M. D.; Luca, O. R.; Crabtree, R. H.; Soloveichik, G. L.; Batista, V. S. Reduction of systematic uncertainty in DFT redox potentials of transition-metal complexes. *J. Phys. Chem. C* **2012**, *116*, 6349–6356.

(129) Seybold, P. G.; Shields, G. C. Computational estimation of pKa values. *Wiley Interdiscip. Rev. Comput. Mol. Sci.* **2015**, *5*, 290–297.

(130) Kelly, C. P.; Cramer, C. J.; Truhlar, D. G. Single-ion solvation free energies and the normal hydrogen electrode potential in methanol, acetonitrile, and dimethyl sulfoxide. *J. Phys. Chem. B* **2007**, *111*, 408–422.

(131) Song, J.; Klein, E. L.; Neese, F.; Ye, S. The mechanism of homogeneous CO2 reduction by Ni (cyclam): Product selectivity, concerted proton–electron transfer and C–O bond cleavage. *Inorg. Chem.* **2014**, *53*, 7500–7507.

(132) Riplinger, C.; Sampson, M. D.; Ritzmann, A. M.; Kubiak, C. P.; Carter, E. A. Mechanistic contrasts between manganese and rhenium bipyridine electrocatalysts for the reduction of carbon dioxide. *J. Am. Chem. Soc.* **2014**, *136*, 16285–16298.

(133) Keith, J. A.; Grice, K. A.; Kubiak, C. P.; Carter, E. A. Elucidation of the selectivity of proton-dependent electrocatalytic CO2 reduction by fac-Re(bpy)$(CO)_3$Cl. *J. Am. Chem. Soc.* **2013**, *135*, 15823–15829.

(134) Liptak, M. D.; Shields, G. C. Accurate pKa calculations for carboxylic acids using complete basis set and Gaussian-n models combined with CPCM continuum solvation methods. *J. Am. Chem. Soc.* **2001**, *123*, 7314–7319.

(135) Muckerman, J. T.; Skone, J. H.; Ning, M.; Wasada-Tsutsui, Y. Toward the accurate calculation of pKa values in water and acetonitrile. *Biochim Biophys Acta Bioenerg* **2013**, *1827*, 882–891.

(136) Solis, B. H.; Hammes-Schiffer, S. Theoretical analysis of mechanistic pathways for hydrogen evolution catalyzed by cobaloximes. *Inorg. Chem.* **2011**, *50*, 11252–11262.

(137) Christiansen, J. A. In *Advances in Catalysis*; Elsevier: 1953; Vol. 5, pp 311–353.

(138) Kozuch, S.; Shaik, S. A combined kinetic- quantum mechanical model for assessment of catalytic cycles: Application to cross-coupling and Heck reactions. *J. Am. Chem. Soc.* **2006**, *128*, 3355–3365.

(139) Kozuch, S.; Shaik, S. Kinetic-quantum chemical model for catalytic cycles: the Haber-Bosch process and the effect of reagent concentration. *J. Phys. Chem. A* **2008**, *112*, 6032–6041.

(140) Kozuch, S.; Shaik, S. How to conceptualize catalytic cycles? The energetic span model. *Acc. Chem. Res.* **2011**, *44*, 101–110.

(141) Campbell, C. T. Finding the Rate-Determining Step in a Mechanism: Comparing DeDonder Relations with the "Degree of Rate Control". *J. Catal.* **2001**, *204*, 520–524.

(142) Uhe, A.; Kozuch, S.; Shaik, S. Automatic analysis of computed catalytic cycles. *J. Comput. Chem.* **2011**, *32*, 978–985.

(143) Burns, M.; Essafi, S.; Bame, J. R.; Bull, S. P.; Webster, M. P.; Balieu, S.; Dale, J. W.; Butts, C. P.; Harvey, J. N.; Aggarwal, V. K. Assembly-line synthesis of organic molecules with tailored shapes. *Nature* **2014**, *513*, 183–188.

(144) Bergeler, M.; Simm, G. N.; Proppe, J.; Reiher, M. Heuristics-guided exploration of reaction mechanisms. *J. Chem. Theory Comput.* **2015**, *11*, 5712–5722.

(145) Dewyer, A. L.; Argüelles, A. J.; Zimmerman, P. M. Methods for exploring reaction space in molecular systems. *Wiley Interdiscip. Rev. Comput. Mol. Sci.* **2018**, *8*, e1354.

(146) Kitchin, J. R. Machine learning in catalysis. *Nat. Catal.* **2018**, *1*, 230–232.

(147) Yang, W.; Fidelis, T. T.; Sun, W.-H. Machine learning in catalysis, from proposal to practicing. *ACS omega* **2019**, *5*, 83–88.

(148) Dos Passos Gomes, G.; Pollice, R.; Aspuru-Guzik, A. Navigating through the maze of homogeneous catalyst design with machine learning. *Trends Chem.* **2021**.

(149) Agency, U. S. E. P. Global greenhouse gas emissions data., 2021.

(150) Stein, T. Carbon dioxide peaks near 420 parts per million at Mauna Loa observatory., 2021.

(151) Hall-Spencer, J. M.; Rodolfo-Metalpa, R.; Martin, S.; Ransome, E.; Fine, M.; Turner, S. M.; Rowley, S. J.; Tedesco, D.; Buia, M.-C. Volcanic carbon dioxide vents show ecosystem effects of ocean acidification. *Nature* **2008**, *454*, 96–99.

(152) Vol'Pin, M.; Kolomnikov, I. In *Coordination Chemistry–XIV*; Elsevier: 1973, pp 567–581.

(153) Lewis, N. S.; Nocera, D. G. Powering the planet: Chemical challenges in solar energy utilization. *Proc. Natl. Acad. Sci. U.S.A.* **2006**, *103*, 15729–15735.

(154) Gust, D.; Moore, T. A.; Moore, A. L. Solar fuels via artificial photosynthesis. *Acc. Chem. Res.* **2009**, *42*, 1890–1898.

(155) Appel, A. M. et al. Frontiers, Opportunities, and Challenges in Biochemical and Chemical Catalysis of CO2 Fixation. *Chem. Rev.* **2013**, *113*, 6621–6658.

(156) De Luna, P.; Hahn, C.; Higgins, D.; Jaffer, S. A.; Jaramillo, T. F.; Sargent, E. H. What would it take for renewably powered electrosynthesis to displace petrochemical processes? *Science* **2019**, *364*, eaav3506.

(157) Schuchmann, K.; Müller, V. Direct and reversible hydrogenation of CO2 to formate by a bacterial carbon dioxide reductase. *Science* **2013**, *342*, 1382–1385.

(158) Vu, N.-N.; Kaliaguine, S.; Do, T.-O. Critical aspects and recent advances in structural engineering of photocatalysts for sunlight-driven photocatalytic reduction of CO2 into fuels. *Adv. Funct. Mater.* **2019**, *29*, 1901825.

(159) Zhao, G.; Huang, X.; Wang, X.; Wang, X. Progress in catalyst exploration for heterogeneous CO 2 reduction and utilization: a critical review. *J. Mater. Chem. A* **2017**, *5*, 21625–21649.

(160) Long, C.; Li, X.; Guo, J.; Shi, Y.; Liu, S.; Tang, Z. Electrochemical reduction of CO2 over heterogeneous catalysts in aqueous solution: recent progress and perspectives. *Small Methods* **2019**, *3*, 1800369.

(161) Elouarzaki, K.; Kannan, V.; Jose, V.; Sabharwal, H. S.; Lee, J.-M. Recent trends, benchmarking, and challenges of electrochemical reduction of CO2 by molecular catalysts. *Adv. Energy Mater.* **2019**, *9*, 1900090.

(162) Wang, W.; Wang, S.; Ma, X.; Gong, J. Recent advances in catalytic hydrogenation of carbon dioxide. *Chem. Soc. Rev.* **2011**, *40*, 3703–3727.

(163) Sun, Z.; Ma, T.; Tao, H.; Fan, Q.; Han, B. Fundamentals and challenges of electrochemical CO2 reduction using two-dimensional materials. *Chem* **2017**, *3*, 560–587.

(164) Verma, S.; Kim, B.; Jhong, H.-R.; Ma, S.; Kenis, P. J. A gross-margin model for defining technoeconomic benchmarks in the electroreduction of CO2. *ChemSusChem* **2016**, *9*, 1972–1979.

(165) Roy, S.; Sharma, B.; Pécaut, J.; Simon, P.; Fontecave, M.; Tran, P. D.; Derat, E.; Artero, V. Molecular cobalt complexes with pendant amines for selective electrocatalytic reduction of carbon dioxide to formic acid. *J. Am. Chem. Soc.* **2017**, *139*, 3685–3696.

(166) Savéant, J.-M. Proton Relays in Molecular Catalysis of Electrochemical Reactions: Origin and Limitations of the Boosting Effect. *Angew. Chem. Int. Ed.* **2019**, *58*, 2125–2128.

(167) Nichols, A. W.; Machan, C. W. Secondary-Sphere Effects in Molecular Electrocatalytic CO2 Reduction. *Front. Chem.* **2019**, *7*, 397.

(168) Savéant, J.-M. Molecular catalysis of electrochemical reactions. Mechanistic aspects. *Chem. Rev.* **2008**, *108*, 2348–2378.

(169) Ren, S.; Joulié, D.; Salvatore, D.; Torbensen, K.; Wang, M.; Robert, M.; Berlinguette, C. P. Molecular electrocatalysts can mediate fast, selective CO2 reduction in a flow cell. *Science* **2019**, *365*, 367–369.

(170) Lin, S.; Diercks, C. S.; Zhang, Y.-B.; Kornienko, N.; Nichols, E. M.; Zhao, Y.; Paris, A. R.; Kim, D.; Yang, P.; Yaghi, O. M.; Chang, C. J. Covalent organic frameworks comprising cobalt porphyrins for catalytic CO2 reduction in water. *Science* **2015**, *349*, 1208–1213.

(171) Wang, H. et al. Recent progress in covalent organic framework thin films: fabrications, applications and perspectives. *Chem. Soc. Rev.* **2019**, *48*, 488–516.

(172) Loipersberger, M.; Lee, J.; Mao, Y.; Das, A. K.; Ikeda, K.; Thirman, J.; Head-Gordon, T.; Head-Gordon, M. Energy Decomposition Analysis for Interactions of Radicals: Theory and Implementation at the MP2 Level with Application to Hydration of Halogenated Benzene Cations and Complexes between CO2–· and Pyridine and Imidazole. *J. Phys. Chem. A* **2019**, *123*, 9621–9633.

(173) Loipersberger, M.; Mao, Y.; Head-Gordon, M. Variational Forward-Backward Charge Transfer Analysis Based on Absolutely Localized Molecular Orbitals: Energetics and Molecular Properties. *J. Chem. Theory Comput.* **2020**, *16*, 1073–1089.

(174) Mao, Y.; Loipersberger, M.; Kron, K.; Derrick, J. S.; Chang, C.; Sharada, S. M.; Head-Gordon, M. Consistent inclusion of continuum solvation in energy decomposition analysis: theory and application to molecular CO_2 reduction catalysts. *Chem. Sci* **2021**, *12*, 1398–1414.

(175) Loipersberger, M.; Bertels, L. W.; Lee, J.; Head-Gordon, M. Exploring the Limits of Second- and Third-Order Møller-Plesset Perturbation Theory for Non-Covalent Interactions: Revisiting MP2.5 and Assessing the Importance of Regularization and Reference Orbitals. *J. Chem. Theory Comput.* **2021**, just accepted.

(176) Loipersberger, M.; Zee, D. Z.; Panetier, J. A.; Chang, C. J.; Long, J. R.; Head-Gordon, M. Computational Study of an Iron(II) Polypyridine Electrocatalyst for CO2 Reduction: Key Roles for Intramolecular Interactions in CO2 Binding and Proton Transfer. *Inorg. Chem.* **2020**, *59*, 8146–8160.

(177) Loipersberger, M.; Cabral, D. G. A.; Chu, D. B. K.; Head-Gordon, M. Mechanistic Insights into Co and Fe Quaterpyridine-Based CO_2 Reduction Catalysts: Metal–Ligand Orbital Interaction as the Key Driving Force for Distinct Pathways. *J. Am. Chem. Soc.* **2021**, *143*, 744–763.

(178) Stone, A., *The Theory of Intermolecular Forces*; Oxford University Press: 2013.

(179) Scheiner, S., *Noncovalent forces*; Springer: 2015; Vol. 19.

(180) Müller-Dethlefs, K.; Hobza, P. Noncovalent Interactions: A Challenge for Experiment and Theory. *Chem. Rev.* **2000**, *100*, 143–168.

(181) Rose, G. D.; Wolfenden, R. Hydrogen Bonding, Hydrophobicity, Packing, and Protein Folding. *Annu. Rev. Biophys.* **1993**, *22*, 381–415.

(182) Hubbard, R. E.; Kamran Haider, M. Hydrogen bonds in proteins: role and strength. *e LS* **2010**.

(183) Grabowski, S. J. What is the covalency of hydrogen bonding? *Chem. Rev.* **2011**, *111*, 2597–2625.

(184) Meyer, F.; Dubois, P. Halogen bonding at work: recent applications in synthetic chemistry and materials science. *CrystEngComm* **2013**, *15*, 3058–3071.

(185) Steiner, T. The Hydrogen Bond in the Solid State. *Angew. Chem. Int. Ed.* **2002**, *41*, 48–76.

(186) Toste, F. D.; Sigman, M. S.; Miller, S. J. Pursuit of Noncovalent Interactions for Strategic Site-Selective Catalysis. *Acc. Chem. Res.* **2017**, *50*, 609–615.

(187) Neel, A. J.; Hilton, M. J.; Sigman, M. S.; Toste, F. D. Exploiting non-covalent π interactions for catalyst design. *Nature* **2017**, *543*, 637–646.

(188) Phipps, M. J.; Fox, T.; Tautermann, C. S.; Skylaris, C.-K. Energy decomposition analysis approaches and their evaluation on prototypical protein–drug interaction patterns. *Chem. Soc. Rev.* **2015**, *44*, 3177–3211.

(189) Pastorczak, E.; Corminboeuf, C. Perspective: Found in translation: Quantum chemical tools for grasping non-covalent interactions. *J. Chem. Phys.* **2017**, *146*, 120901.

(190) Zhao, L.; von Hopffgarten, M.; Andrada, D. M.; Frenking, G. Energy decomposition analysis. *WIREs: Comput. Mol. Sci.* **2018**, *8*, e1345.

(191) Morokuma, K. Molecular orbital studies of hydrogen bonds. III. C=O··· H–O hydrogen bond in H_2CO··· H_2O and H_2CO··· $2H_2O$. *J. Chem. Phys.* **1971**, *55*, 1236–1244.

(192) Kitaura, K.; Morokuma, K. A new energy decomposition scheme for molecular interactions within the Hartree-Fock approximation. *Int. J. Quantum Chem.* **1976**, *10*, 325–340.

(193) Morokuma, K. Why do molecules interact? The origin of electron donor-acceptor complexes, hydrogen bonding and proton affinity. *Acc. Chem. Res.* **1977**, *10*, 294–300.

(194) Ziegler, T.; Rauk, A. On the Calculation of Bonding Energies by the Hartree Fock Slater Method. *Theor. Chem. Acc.* **1977**, *46*, 1–10.

(195) Ziegler, T.; Rauk, A. A Theoretical Study of the Ethylene-Metal Bond in Complexes between Cu^+, Ag^+, Pt^0, or Pt^{2+} and Ethylene, Based on Hartree-Fock-Slater Transition-State Method. *Inorg. Chem.* **1979**, *18*, 1558–1565.

(196) Stoll, H.; Wagenblast, G.; Preuβ, H. On the use of local basis sets for localized molecular orbitals. *Theor. Chem. Acc.* **1980**, *57*, 169–178.

(197) Mo, Y.; Gao, J.; Peyerimhoff, S. D. Energy decomposition analysis of intermolecular interactions using a block-localized wave function approach. *J. Chem. Phys.* **2000**, *112*, 5530–5538.

(198) Mo, Y.; Song, L.; Lin, Y. Block-localized wavefunction (BLW) method at the density functional theory (DFT) level. *J. Phys. Chem. A* **2007**, *111*, 8291–8301.

(199) Mo, Y.; Bao, P.; Gao, J. Energy decomposition analysis based on a block-localized wavefunction and multistate density functional theory. *Phys. Chem. Chem. Phys.* **2011**, *13*, 6760–6775.

(200) Horn, P. R.; Sundstrom, E. J.; Baker, T. A.; Head-Gordon, M. Unrestricted absolutely localized molecular orbitals for energy decomposition analysis: Theory and applications to intermolecular interactions involving radicals. *J. Chem. Phys.* **2013**, *138*, 134119.

(201) Mao, Y.; Horn, P. R.; Head-Gordon, M. Energy decomposition analysis in an adiabatic picture. *Phys. Chem. Chem. Phys.* **2017**, *19*, 5944–5958.

(202) Ge, Q.; Mao, Y.; Head-Gordon, M. Energy decomposition analysis for exciplexes using absolutely localized molecular orbitals. *J. Chem. Phys.* **2018**, *148*, 064105.

(203) Ge, Q.; Head-Gordon, M. Energy decomposition analysis for excimers using absolutely localized molecular orbitals within time-dependent density functional theory and configuration interaction with single excitations. *J. Chem. Theory Comput.* **2018**, *14*, 5156–5168.

(204) Gonthier, J. F.; Thirman, J.; Head-Gordon, M. Understanding Non-Covalent Interactions: Correlated Energy Decomposition Analysis and Applications to Halogen Bonding. *Chimia* **2018**, *72*, 193–198.

(205) Yoo, S.; Aprà, E.; Zeng, X. C.; Xantheas, S. S. High-Level Ab Initio Electronic Structure Calculations of Water Clusters $(H_2O)_{16}$ and $(H_2O)_{17}$: A New Global Minimum for $(H_2O)_{16}$. *J. Phys. Chem. Lett.* **2010**, *1*, 3122–3127.

(206) Mardirossian, N.; Lambrecht, D. S.; McCaslin, L.; Xantheas, S. S.; Head-Gordon, M. The Performance of Density Functionals for Sulfate-Water Clusters. *J. Chem. Theory Comput.* **2013**, *9*, 1368–1380.

(207) Feyereisen, M.; Fitzgerald, G.; Komornicki, A. Use of approximate integrals in ab initio theory. An application in MP2 energy calculations. *Chem. Phys. Lett.* **1993**, *208*, 359–363.

(208) Bernholdt, D. E.; Harrison, R. J. Large-scale correlated electronic structure calculations: the RI-MP2 method on parallel computers. *Chem. Phys. Lett.* **1996**, *250*, 477–484.

(209) Tentscher, P. R.; Arey, J. S. Binding in Radical-Solvent Binary Complexes: Benchmark Energies and Performance of Approximate Methods. *J. Chem. Theory Comput.* **2013**, *9*, 1568–1579.

(210) Su, P.; Li, H. Energy decomposition analysis of covalent bonds and intermolecular interactions. *J. Chem. Phys* **2009**, *131*, 014102.

(211) Thirman, J.; Head-Gordon, M. Electrostatic Domination of the Effect of Electron Correlation in Intermolecular Interactions. *J. Phys. Chem. Lett.* **2014**, *5*, 1380.

(212) Thirman, J.; Head-Gordon, M. An energy decomposition analysis for second-order Møller–Plesset perturbation theory based on absolutely localized molecular orbitals. *J. Chem. Phys* **2015**, *143*, 084124.

(213) Schütz, M.; Rauhut, G.; Werner, H.-J. Local treatment of electron correlation in molecular clusters: Structures and stabilities of $(H_2O)_n$, $n = 2 - 4$. *J. Phys. Chem. A* **1998**, *102*, 5997–6003.

(214) Sherrill, C. D.; Takatani, T.; Hohenstein, E. G. An Assessment of Theoretical Methods for Nonbonded Interactions: Comparison to Complete Basis Set Limit Coupled-Cluster Potential Energy Curves for the Benzene Dimer, the Methane Dimer, Benzene–Methane, and Benzene–H2S. *J. Phys. Chem. A* **2009**, *113*, 10146–10159.

(215) Jurečka, P.; Šponer, J.; Černý, J.; Hobza, P. Benchmark database of accurate (MP2 and CCSD(T) complete basis set limit) interaction energies of small model complexes, DNA base pairs, and amino acid pairs. *Phys. Chem. Chem. Phys.* **2006**, *8*, 1985–1993.

(216) Janowski, T.; Ford, A. R.; Pulay, P. Accurate correlated calculation of the intermolecular potential surface in the coronene dimer. *Mol. Phys.* **2010**, *108*, 249–257.

(217) Tkatchenko, A.; DiStasio, R. A.; Head-Gordon, M.; Scheffler, M. Dispersion-corrected Møller–Plesset second-order perturbation theory. *J. Chem. Phys.* **2009**, *131*, 094106.

(218) Schneider, W. B.; Bistoni, G.; Sparta, M.; Saitow, M.; Riplinger, C.; Auer, A. A.; Neese, F. Decomposition of Intermolecular Interaction Energies within the Local Pair Natural Orbital Coupled Cluster Framework. *J. Chem. Theory Comput.* **2016**, *12*, 4778–4792.

(219) Altun, A.; Saitow, M.; Neese, F.; Bistoni, G. Local Energy Decomposition of Open-Shell Molecular Systems in the Domain-Based Local Pair Natural Orbital Coupled Cluster Framework. *J. Chem. Theory Comput.* **2019**, *15*, 1616–1632.

(220) Altun, A.; Neese, F.; Bistoni, G. Effect of Electron Correlation on Intermolecular Interactions: A Pair Natural Orbitals Coupled Cluster Based Local Energy Decomposition Study. *J. Chem. Theory Comput.* **2018**, *15*, 215–228.

(221) Bistoni, G. Finding chemical concepts in the Hilbert space: Coupled cluster analyses of noncovalent interactions. *WIREs: Comput. Mol. Sci.* **2020**, *10*, e1442.

(222) Parker, T. M.; Burns, L. A.; Parrish, R. M.; Ryno, A. G.; Sherrill, C. D. Levels of symmetry adapted perturbation theory (SAPT). I. Efficiency and performance for interaction energies. *J. Chem. Phys.* **2014**, *140*, 094106.

(223) Jeziorski, B.; Moszynski, R.; Szalewicz, K. Perturbation theory approach to intermolecular potential energy surfaces of van der Waals complexes. *Chem. Rev.* **1994**, *94*, 1887–1930.

(224) Szalewicz, K. Symmetry-adapted perturbation theory of intermolecular forces. *WIREs: Comput. Mol. Sci.* **2012**, *2*, 254–272.

(225) Hohenstein, E. G.; Jaeger, H. M.; Carrell, E. J.; Tschumper, G. S.; Sherrill, C. D. Accurate Interaction Energies for Problematic Dispersion-Bound Complexes: Homogeneous Dimers of NCCN, P2, and PCCP. *J. Chem. Theory Comput.* **2011**, *7*, 2842–2851.

(226) Parrish, R. M.; Hohenstein, E. G.; Sherrill, C. D. Tractability gains in symmetry-adapted perturbation theory including coupled double excitations: CCD+ST(CCD) dispersion with natural orbital truncations. *J. Chem. Phys* **2013**, *139*, 174102.

(227) Thirman, J.; Head-Gordon, M. Efficient Implementation of Energy Decomposition Analysis for Second-Order Møller-Plesset Perturbation Theory and Application to Anion-pi Interactions. *J. Phys. Chem. A* **2017**, *121*, 717–728.

(228) Lee, M. S.; Maslen, P. E.; Head-Gordon, M. Closely approximating second-order Møller–Plesset perturbation theory with a local triatomics in molecules model. *J. Chem. Phys.* **2000**, *112*, 3592–3601.

(229) DiStasio, R. A.; Jung, Y.; Head-Gordon, M. A Resolution-Of-The-Identity Implementation of the Local Triatomics-In-Molecules Model for Second-Order Møller–Plesset Perturbation Theory with Application to Alanine Tetrapeptide Conformational Energies. *J. Chem. Theory Comput.* **2005**, *1*, 862–876.

(230) Azar, R. J.; Head-Gordon, M. An energy decomposition analysis for intermolecular interactions from an absolutely localized molecular orbital reference at the coupled-cluster singles and doubles level. *J. Chem. Phys.* **2012**, *136*, 024103.

(231) Steinmann, S. N.; Corminboeuf, C. Exploring the limits of density functional approximations for interaction energies of molecular precursors to organic electronics. *J. Chem. Theory Comput* **2012**, *8*, 4305–4316.

(232) Mason, K. A.; Pearcy, A. C.; Attah, I. K.; Platt, S. P.; Aziz, S. G.; El-Shall, M. S. Gas phase hydration of halogenated benzene cations. Is it hydrogen or halogen bonding? *Phys. Chem. Chem. Phys.* **2017**, *19*, 18603–18611.

(233) Kamrath, M. Z.; Relph, R. A.; Johnson, M. A. Vibrational Predissociation Spectrum of the Carbamate Radical Anion, $C_5H_5N\text{-}CO_2^-$, Generated by Reaction of Pyridine with $(CO_2)_m^-$. *J. Am. Chem. Soc.* **2010**, *132*, 15508–15511.

(234) Craig, S. M.; Johnson, C. J.; Ranasinghe, D. S.; Perera, A.; Bartlett, R. J.; Berman, M. R.; Johnson, M. A. Vibrational Characterization of Radical Ion Adducts between Imidazole and CO_2. *J. Phys. Chem. A* **2018**, *122*, 3805–3810.

(235) Amos, R. D.; Andrews, J. S.; Handy, N. C.; Knowles, P. J. Open-shell Møller–Plesset perturbation theory. *Chem. Phys. Lett.* **1991**, *185*, 256–264.

(236) Murray, C.; Davidson, E. R. Perturbation theory for open shell systems. *Chem. Phys. Lett.* **1991**, *187*, 451–454.

(237) Hubač, I.; Čársky, P. Correlation energy of open-shell systems. Application of the many-body Rayleigh-Schrödinger perturbation theory in the restricted Roothaan-Hartree-Fock formalism. *Phys. Rev. A* **1980**, *22*, 2392–2399.

(238) Lee, T. J.; Jayatilaka, D. An open-shell restricted Hartree-Fock perturbation theory based on symmetric spin orbitals. *Chem. Phys. Lett.* **1993**, *201*, 1–10.

(239) Knowles, P. J.; Andrews, J. S.; Amos, R. D.; Handy, N. C.; Pople, J. A. Restricted Møller-Plesset theory for open-shell molecules. *Chem. Phys. Lett.* **1991**, *186*, 130–136.

(240) Lauderdale, W. J.; Stanton, J. F.; Gauss, J.; Watts, J. D.; Bartlett, R. J. Many-body perturbation theory with a restricted open-shell Hartree-Fock reference. *Chem. Phys. Lett.* **1991**, *187*, 21–28.

(241) Nagata, T.; Takahashi, O.; Saito, K.; Iwata, S. Basis set superposition error free self-consistent field method for molecular interaction in multi-component systems: Projection operator formalism. *J. Chem. Phys.* **2001**, *115*, 3553–3560.

(242) Löwdin, P.-O. On the non-orthogonality problem connected with the use of atomic wave functions in the theory of molecules and crystals. *J. Chem. Phys.* **1950**, *18*, 365–375.

(243) Handy, N. C.; Schaefer III, H. F. On the evaluation of analytic energy derivatives for correlated wave functions. *J. Chem. Phys.* **1984**, *81*, 5031–5033.

(244) Seeger, R.; Pople, J. A. Self-consistent molecular orbital methods. XVIII. Constraints and stability in Hartree-Fock theory. *J. Chem. Phys.* **1977**, *66*, 3045–3050.

(245) Tozer, D. J.; Andrews, J. S.; Amos, R. D.; Handy, N. C. Gradient theory applied to restricted (open-shell) Møller–Plesset theory. *Chem. Phys. Lett.* **1992**, *199*, 229–236.

(246) Rhee, Y. M.; DiStasio, R. A.; Lochan, R. C.; Head-Gordon, M. Analytical gradient of restricted second-order Møller–Plesset correlation energy with the resolution of the identity approximation, applied to the TCNE dimer anion complex. *Chem. Phys. Lett.* **2006**, *426*, 197–203.

(247) Weigend, F.; Ahlrichs, R. Balanced basis sets of split valence, triple zeta valence and quadruple zeta valence quality for H to Rn: Design and assessment of accuracy. *Phys. Chem. Chem. Phys* **2005**, *7*, 3297–3305.

(248) Rappoport, D.; Furche, F. Property-optimized Gaussian basis sets for molecular response calculations. *J. Chem. Phys* **2010**, *133*, 134105.

(249) Peterson, K. A.; Figgen, D.; Goll, E.; Stoll, H.; Dolg, M. Systematically convergent basis sets with relativistic pseudopotentials. II. Small-core pseudopotentials and correlation consistent basis sets for the post-d group 16-18 elements. *J. Chem. Phys.* **2003**, *119*, 11113–11123.

(250) Dunning Jr, T. H. Gaussian basis sets for use in correlated molecular calculations. I. The atoms boron through neon and hydrogen. *J. Chem. Phys.* **1989**, *90*, 1007–1023.

(251) Kendall, R. A.; Dunning, T. H.; Harrison, R. J. Electron affinities of the row atoms revisited. Systematic basis sets and wave functions. *J. Chem. Phys* **1992**, *96*, 6796–6806.

(252) Woon, D. E.; Dunning Jr, T. H. Gaussian basis sets for use in correlated molecular calculations. III. The atoms aluminum through argon. *J. Chem. Phys.* **1993**, *98*, 1358–1371.

(253) Weigend, F.; Köhn, A.; Hättig, C. Efficient use of the correlation consistent basis sets in resolution of the identity MP2 calculations. *J. Chem. Phys.* **2002**, *116*, 3175–3183.

(254) Hättig, C. Optimization of auxiliary basis sets for RI-MP2 and RI-CC2 calculations: Core–valence and quintuple-ζ basis sets for H to Ar and QZVPP basis sets for Li to Kr. *Phys. Chem. Chem. Phys.* **2005**, *7*, 59–66.

(255) Hellweg, A.; Rappoport, D. Development of new auxiliary basis functions of the Karlsruhe segmented contracted basis sets including diffuse basis functions (def2-SVPD, def2-TZVPPD, and def2-QVPPD) for RI-MP2 and RI-CC calculations. *Phys. Chem. Chem. Phys* **2015**, *17*, 1010–1017.

(256) Manna, D.; Kesharwani, M. K.; Sylvetsky, N.; Martin, J. M. Conventional and explicitly correlated ab initio benchmark study on water clusters: revision of the BEGDB and WATER27 datasets. *J. Chem. Theory Comput.* **2017**, 3136–3152.

(257) Sokalski, W.; Hariharan, P.; Kaufman, J. J. A self-consistent field interaction energy decomposition study of 12 hydrogen-bonded dimers. *J. Phys. Chem.* **1983**, *87*, 2803–2810.

(258) Levine, D. S.; Horn, P. R.; Mao, Y.; Head-Gordon, M. Variational Energy Decomposition Analysis of Chemical Bonding. 1. Spin-Pure Analysis of Single Bonds. *J. Chem. Theory Comput* **2016**, *12*, 4812–4820.

(259) Levine, D. S.; Head-Gordon, M. Energy decomposition analysis of single bonds within Kohn–Sham density functional theory. *Proceedings of the National Academy of Sciences* **2017**, *114*, 12649–12656.

(260) Tentscher, P. R.; Arey, J. S. On the nature of interactions of radicals with polar molecules. *J. Phys. Chem. A* **2013**, *117*, 12560–12568.

(261) Ramos-Cordoba, E.; Lambrecht, D. S.; Head-Gordon, M. Charge-transfer and the hydrogen bond: Spectroscopic and structural implications from electronic structure calculations. *Faraday Discuss.* **2011**, *150*, 345–362.

(262) Khaliullin, R. Z.; Bell, A. T.; Head-Gordon, M. Electron donation in the water–water hydrogen bond. *Chem.-Eur. J.* **2009**, *15*, 851–855.

(263) Meot-Ner, M. The Ionic Hydrogen Bond. *Chem. Rev.* **2005**, *105*, 213–284.

(264) R., D. G.; Shing, H. P.; Lars, K.; C., L. A.; Roberto, M.; Pierangelo, M.; Peter, P.; Giuseppe, R.; Kari, R. *Pure Appl. Chem.* **2013**, *85*, 1711–1713.

(265) Clark, T.; Hennemann, M.; Murray, J. S.; Politzer, P. Halogen bonding: the σ-hole. *J. Mol. Model.* **2007**, *13*, 291–296.

(266) Clark, T.; Heßelmann, A. The coulombic σ-hole model describes bonding in $CX_3I\cdots Y^-$ complexes completely. *Phys. Chem. Chem. Phys.* **2018**, *20*, 22849–22855.

(267) Huber, S. M.; Jimenez-Izal, E.; Ugalde, J. M.; Infante, I. Unexpected trends in halogen-bond based noncovalent adducts. *ChemComm* **2012**, *48*, 7708–7710.

(268) Grabowski, S. J. Hydrogen and halogen bonds are ruled by the same mechanisms. *Phys. Chem. Chem. Phys.* **2013**, *15*, 7249–7259.

(269) Wang, C.; Danovich, D.; Mo, Y.; Shaik, S. On The Nature of the Halogen Bond. *J. Chem. Theory Comput.* **2014**, *10*, 3726–3737.

(270) Thirman, J.; Engelage, E.; Huber, S. M.; Head-Gordon, M. Characterizing the interplay of Pauli repulsion, electrostatics, dispersion and charge transfer in halogen bonding with energy decomposition analysis. *Phys. Chem. Chem. Phys.* **2018**, *20*, 905–915.

(271) Angarov, V.; Kozuch, S. On the σ, π and δ Hole Interactions: a Molecular Orbital Overview. *New J. Chem* **2018**, *42*, 1413–1422.

(272) Ang, S. J.; Mak, A. M.; Wong, M. W. Nature of halogen bonding involving systems, nitroxide radicals and carbenes: a highlight of the importance of charge transfer. *Phys. Chem. Chem. Phys.* **2018**, *20*, 26463–26478.

(273) Řezáč, J.; de la Lande, A. On the role of charge transfer in halogen bonding. *Phys. Chem. Chem. Phys.* **2017**, *19*, 791–803.

(274) Nepal, B.; Scheiner, S. $NX\cdots Y$ halogen bonds. Comparison with $NH\cdots Y$ H-bonds and $CX\cdots Y$ halogen bonds. *Phys. Chem. Chem. Phys.* **2016**, *18*, 18015–18023.

(275) Benz, S.; Poblador-Bahamonde, A. I.; Low-Ders, N.; Matile, S. Catalysis with Pnictogen, Chalcogen, and Halogen Bonds. *Angew. Chem. Int. Ed.* **2018**, *130*, 5506–5510.

(276) Concepcion, J. J.; House, R. L.; Papanikolas, J. M.; Meyer, T. J. Chemical approaches to artificial photosynthesis. *Proc. Natl. Acad. Sci.* **2012**, *109*, 15560–15564.

(277) Alstrum-Acevedo, J. H.; Brennaman, M. K.; Meyer, T. J. Chemical Approaches to Artificial Photosynthesis. 2. *Inorg. Chem.* **2005**, *44*, 6802–6827.

(278) Barton, E. E.; Rampulla, D. M.; Bocarsly, A. B. Selective Solar-Driven Reduction of CO_2 to Methanol Using a Catalyzed *p*-GaP Based Photoelectrochemical Cell. *J. Am. Chem. Soc.* **2008**, *130*, 6342–6344.

(279) Bocarsly, A. B.; Gibson, Q. D.; Morris, A. J.; L'Esperance, R. P.; Detweiler, Z. M.; Lakkaraju, P. S.; Zeitler, E. L.; Shaw, T. W. Comparative Study of Imidazole and Pyridine Catalyzed Reduction of Carbon Dioxide at Illuminated Iron Pyrite Electrodes. *ACS Catal.* **2012**, *2*, 1684–1692.

(280) DeLuca, M. J.; Niu, B.; Johnson, M. A. Photoelectron spectroscopy of $(CO_2)_n^-$ clusters with 2≤n≤13: Cluster size dependence of the core molecular ion. *J. Chem. Phys.* **1988**, *88*, 5857–5863.

(281) Shin, J.-W.; Hammer, N. I.; Johnson, M. A.; Schneider, H.; Glöß, A.; Weber, J. M. An Infrared Investigation of the $(CO_2)_n^-$ Clusters: Core Ion Switching from Both the Ion and Solvent Perspectives. *J. Phys. Chem. A* **2005**, *109*, 3146–3152.

(282) Thompson, M. C.; Weber, J. M. Enhancement of infrared activity by moving electrons through bonds — The case of CO_2 anion and carboxylate. *Chem. Phys. Lett.* **2017**, *683*, 586–590.

(283) Han, S. Y.; Chu, I.; Kim, J. H.; Song, J. K.; Kim, S. K. Photoelectron spectroscopy and ab initio study of mixed cluster anions of $[(CO_2)_{1-3}(Pyridine)_{1-6}]^-$: Formation of a covalently bonded anion core of $(C_5H_5N^-CO_2)^-$. *J. Chem. Phys.* **2000**, *113*, 596–601.

(284) Lee, J.; Head-Gordon, M. Two single-reference approaches to singlet biradicaloid problems: Complex, restricted orbitals and approximate spin-projection combined with regularized orbital-optimized Møller-Plesset perturbation theory. *J. Chem. Phys.* **2019**, *150*, 244106.

(285) Goerigk, L.; Grimme, S. Double-hybrid density functionals. *WIREs Comput. Mol. Sci.* **2014**, *4*, 576–600.

(286) Bertels, L. W.; Lee, J.; Head-Gordon, M. Third-Order Møller–Plesset Perturbation Theory Made Useful? Choice of Orbitals and Scaling Greatly Improves Accuracy for Thermochemistry, Kinetics, and Intermolecular Interactions. *J. Phys. Chem. Lett.* **2019**, *10*, 4170–4176.

(287) Miessler, G.; Fischer, P.; Tarr, D., *Inorganic Chemistry*, 5th ed.; Pearson Education: 2014.

(288) Elian, M.; Hoffmann, R. Bonding capabilities of transition metal carbonyl fragments. *Inorg. Chem* **1975**, *14*, 1058–1076.

(289) Ziegler, T.; Rauk, A. Carbon monoxide, carbon monosulfide, molecular nitrogen, phosphorus trifluoride, and methyl isocyanide as. sigma. donors and. pi. acceptors. A theoretical study by the Hartree-Fock-Slater transition-state method. *Inorg. Chem* **1979**, *18*, 1755–1759.

(290) Dapprich, S.; Frenking, G. Investigation of donor-acceptor interactions: A charge decomposition analysis using fragment molecular orbitals. *J. Phys. Chem.* **1995**, *99*, 9352–9362.

(291) Ehlers, A. W.; Dapprich, S.; Vyboishchikov, S. F.; Frenking, G. Structure and Bonding of the Transition-Metal Carbonyl Complexes $M(CO)_5L$ (M= Cr, Mo, W) and $M(CO)_3L$ (M= Ni, Pd, Pt; L= CO, SiO, CS, N_2, NO^+, CN^-, NC^-, HCCH, CCH_2, CH_2, CF_2, H_2). *Organometallics* **1996**, *15*, 105–117.

(292) Matito, E.; Solà, M. The role of electronic delocalization in transition metal complexes from the electron localization function and the quantum theory of atoms in molecules viewpoints. *Coord. Chem. Rev.* **2009**, *253*, 647–665.

(293) Mond, L.; Langer, C.; Quincke, F. L.–Action of carbon monoxide on nickel. *J. Chem. Soc., Trans.* **1890**, *57*, 749–753.

(294) Cotton, F. Metal carbonyls: some new observations in an old field. *Progr. Inorg. Chem* **1976**, *21*, 1–28.

(295) Herrmann, W. A. 100 years of metal carbonyls: a serendipitous chemical discovery of major scientific and industrial impact. *J. Organomet. Chem.* **1990**, *383*, 21–44.

(296) Lin, J. T.; Hagen, G. P.; Ellis, J. E. Highly reduced organometallics. 9. Synthesis and characterization of the tetrasodium tetracarbonylmetalates(4-) of chromium, molybdenum, and tungsten, $Na_4M(CO)_4$: their reactions with weak acids to generate $H_2M_2(CO)_8^{2-}$(M = Cr, Mo, and W). *J. Am. Chem. Soc.* **1983**, *105*, 2296–2303.

(297) Lupinetti, A. J.; Strauss, S. H.; Frenking, G. In *Progress in Inorganic Chemistry*; John Wiley & Sons, Ltd: 2007, pp 1–112.

(298) Bauschlicher, C. W.; Ricca, A. On the interaction of CO and NH_3 with BH_3 and BF_3. *Chem. Phys. Lett* **1995**, *237*, 14–19.

(299) Stephan, D. W.; Erker, G. Frustrated Lewis pair chemistry of carbon, nitrogen and sulfur oxides. *Chem. Sci.* **2014**, *5*, 2625–2641.

(300) Wu, X.; Zhao, L.; Jin, J.; Pan, S.; Li, W.; Jin, X.; Wang, G.; Zhou, M.; Frenking, G. Observation of alkaline earth complexes $M(CO)_8$ (M= Ca, Sr, or Ba) that mimic transition metals. *Science* **2018**, *361*, 912–916.

(301) Wu, X.; Zhao, L.; Jiang, D.; Fernández, I.; Berger, R.; Zhou, M.; Frenking, G. Barium as honorary transition metal in action: Experimental and theoretical study of $Ba(CO)^+$ and $Ba(CO)^-$. *Angew. Chem. Int. Ed.* **2018**, *57*, 3974–3980.

(302) Allen, A. D.; Senoff, C. V. Nitrogenopentammineruthenium(II) complexes. *Chem. Commun.* **1965**, 621–622.

(303) Bazhenova, T.; Shilov, A. Nitrogen fixation in solution. *Coord. Chem. Rev.* **1995**, *144*, 69–145.

(304) MacKay, B. A.; Fryzuk, M. D. Dinitrogen Coordination Chemistry: On the Biomimetic Borderlands. *Chem. Rev.* **2004**, *104*, 385–402.

(305) Laplaza, C. E.; Cummins, C. C. Dinitrogen Cleavage by a Three-Coordinate Molybdenum(III) Complex. *Science* **1995**, *268*, 861–863.

(306) Yandulov, D. V.; Schrock, R. R. Catalytic Reduction of Dinitrogen to Ammonia at a Single Molybdenum Center. *Science* **2003**, *301*, 76–78.

(307) Tanabe, Y.; Nishibayashi, Y. Developing more sustainable processes for ammonia synthesis. *Coord. Chem. Rev.* **2013**, *257*, 2551–2564.

(308) Anderson, J. S.; Rittle, J.; Peters, J. C. Catalytic conversion of nitrogen to ammonia by an iron model complex. *Nature* **2013**, *501*, 84–87.

(309) MacLeod, K. C.; Holland, P. L. Recent developments in the homogeneous reduction of dinitrogen by molybdenum and iron. *Nat. Chem.* **2013**, *5*, 559–565.

(310) Fajardo, J.; Peters, J. C. Catalytic Nitrogen-to-Ammonia Conversion by Osmium and Ruthenium Complexes. *J. Am. Chem. Soc.* **2017**, *139*, 16105–16108.

(311) Foster, S. L.; Bakovic, S. I. P.; Duda, R. D.; Maheshwari, S.; Milton, R. D.; Minteer, S. D.; Janik, M. J.; Renner, J. N.; Greenlee, L. F. Catalysts for nitrogen reduction to ammonia. *Nat. Catal.* **2018**, *1*, 490–500.

(312) Chen, J. G. et al. Beyond fossil fuel–driven nitrogen transformations. *Science* **2018**, *360*.

(313) Stevens, W. J.; Fink, W. H. Frozen fragment reduced variational space analysis of hydrogen bonding interactions. Application to the water dimer. *Chem. Phys. Lett.* **1987**, *139*, 15–22.

(314) Bagus, P. S.; Hermann, K.; Bauschlicher Jr, C. W. A new analysis of charge transfer and polarization for ligand–metal bonding: Model studies of Al_4CO and Al_4NH_3. *J. Chem. Phys.* **1984**, *80*, 4378–4386.

(315) Reed, A. E.; Weinhold, F. Natural bond orbital analysis of near-Hartree–Fock water dimer. *J. Chem. Phys.* **1983**, *78*, 4066–4073.

(316) Reed, A. E.; Curtiss, L. A.; Weinhold, F. Intermolecular interactions from a natural bond orbital, donor-acceptor viewpoint. *Chem. Rev.* **1988**, *88*, 899–926.

(317) Liang, W.; Head-Gordon, M. An exact reformulation of the diagonalization step in electronic structure calculations as a set of second order nonlinear equations. *J. Chem. Phys.* **2004**, *120*, 10379–10384.

(318) Bagus, P. S.; Hermann, K.; Bauschlicher Jr, C. W. On the nature of the bonding of lone pair ligands to a transition metal. *J. Chem. Phys.* **1984**, *81*, 1966–1974.

(319) Bauschlicher Jr, C. W.; Bagus, P. S.; Nelin, C. J.; Roos, B. O. The nature of the bonding in XCO for X= Fe, Ni, and Cu. *J. Chem. Phys.* **1986**, *85*, 354–364.

(320) Berquist, E.; Lambrecht, D. A First Principles Approach for Partitioning Linear Response Properties into Additive and Cooperative Contributions., 10.26434/chemrxiv.5773968.v1.

(321) Lambrecht, D. S. Generalizing energy decomposition analysis to response properties to inform expedited predictive models. *Comput. Theor. Chem.* **2019**, *1149*, 24–30.

(322) Mao, Y.; Demerdash, O.; Head-Gordon, M.; Head-Gordon, T. Assessing ion-water interactions in the AMOEBA force field using energy decomposition analysis of electronic structure calculations. *J. Chem. Theory Comput.* **2016**, *12*, 5422–5437.

(323) Löwdin, P.-O. In *Advances in quantum chemistry*; Elsevier: 1970; Vol. 5, pp 185–199.

(324) Hait, D.; Head-Gordon, M. Delocalization errors in density functional theory are essentially quadratic in fractional occupation number. *J. Phys. Chem. Lett* **2018**, *9*, 6280–6288.

(325) Gordy, W.; Ring, H.; Burg, A. B. Microwave Determination of the Structure of Borine Carbonyl and of the Nuclear Moments of the Stable Boron Isotopes. *Phys. Rev.* **1950**, *78*, 512–517.

(326) Bethke, G. W.; Wilson, M. K. Vibrational Spectrum of Borine Carbonyl. *J. Chem. Phys.* **1957**, *26*, 1118–1130.

(327) Jacobsen, H.; Berke, H.; Döring, S.; Kehr, G.; Erker, G.; Fröhlich, R.; Meyer, O. Lewis Acid Properties of Tris(pentafluorophenyl)borane. Structure and Bonding in L–B(C_6F_5)$_3$ Complexes. *Organometallics* **1999**, *18*, 1724–1735.

(328) Rossomme, E. C.; Lininger, C. N.; Bell, A. T.; Head-Gordon, T.; Head-Gordon, M. Electronic structure calculations permit identification of the driving forces behind frequency shifts in transition metal monocarbonyls. *Phys. Chem. Chem. Phys.* **2020**, *22*, 781–798.

(329) Goldman, A. S.; Krogh-Jespersen, K. Why Do Cationic Carbon Monoxide Complexes Have High C- O Stretching Force Constants and Short C- O Bonds? Electrostatic Effects, Not σ-Bonding. *J. Am. Chem. Soc.* **1996**, *118*, 12159–12166.

(330) Lupinetti, A. J.; Fau, S.; Frenking, G.; Strauss, S. H. Theoretical Analysis of the Bonding between CO and Positively Charged Atoms. *J. Phys. Chem. A* **1997**, *101*, 9551–9559.

(331) Chen, M.; Zhang, Q.; Zhou, M.; Andrada, D. M.; Frenking, G. Carbon Monoxide Bonding With BeO and $BeCO_3$: Surprisingly High CO Stretching Frequency of $OCBeCO_3$. *Angew. Chem. Int. Ed.* **2015**, *54*, 124–128.

(332) Thompson, C. A.; Andrews, L. Noble Gas Complexes with BeO: Infrared Spectra of NG-BeO (NG = Ar, Kr, Xe). *J. Am. Chem. Soc.* **1994**, *116*, 423–424.

(333) Mitoraj, M. P.; Michalak, A.; Ziegler, T. A Combined Charge and Energy Decomposition Scheme for Bond Analysis. *J. Chem. Theory Comput.* **2009**, *5*, 962–975.

(334) Nakashima, K.; Zhang, X.; Xiang, M.; Lin, Y.; Lin, M.; Mo, Y. Block-localized wavefunction energy decomposition (BLW-ED) analysis of σ/π interactions in metal-carbonyl bonding. *J. Theory Comput. Chem.* **2008**, *7*, 639–654.

(335) Bistoni, G.; Rampino, S.; Scafuri, N.; Ciancaleoni, G.; Zuccaccia, D.; Belpassi, L.; Tarantelli, F. How π back-donation quantitatively controls the CO stretching response in classical and non-classical metal carbonyl complexes. *Chem. Sci.* **2016**, *7*, 1174–1184.

(336) Frenking, G.; Loschen, C.; Krapp, A.; Fau, S.; Strauss, S. H. Electronic structure of CO–an exercise in modern chemical bonding theory. *J. Comput. Chem.* **2007**, *28*, 117–126.

(337) Belpassi, L.; Infante, I.; Tarantelli, F.; Visscher, L. The chemical bond between Au (I) and the noble gases. Comparative study of NgAuF and $NgAu^+$ (Ng= Ar, Kr, Xe) by density functional and coupled cluster methods. *J. Am. Chem. Soc.* **2008**, *130*, 1048–1060.

(338) Bistoni, G.; Belpassi, L.; Tarantelli, F. Advances in Charge Displacement Analysis. *J. Chem. Theory Comput.* **2016**, *12*, 1236–1244.

(339) Radius, U.; Bickelhaupt, F. M.; Ehlers, A. W.; Goldberg, N.; Hoffmann, R. Is CO a special ligand in organometallic chemistry? Theoretical investigation of AB, $Fe(CO)_4AB$, and $Fe(AB)_5$ (AB= N_2, CO, BF, SiO). *Inorg. Chem* **1998**, *37*, 1080–1090.

(340) Ehlers, A. W.; Baerends, E. J.; Bickelhaupt, F. M.; Radius, U. Alternatives to the CO Ligand: Coordination of the Isolobal Analogues BF, BNH_2, $BN(CH_3)_2$, and BO- in Mono- and Binuclear First-Row Transition Metal Complexes. *Chem.: Eur. J.* **1998**, *4*, 210–221.

(341) Xu, L.; Li, Q.-S.; Xie, Y.; King, R. B.; Schaefer, H. F. Prospects for Making Organometallic Compounds with BF Ligands: Fluoroborylene Iron Carbonyls. *Inorg. Chem.* **2010**, *49*, 1046–1055.

(342) Fantuzzi, F.; Cardozo, T. M.; Nascimento, M. A. C. Nature of the chemical bond and origin of the inverted dipole moment in boron fluoride: A generalized valence bond approach. *J. Phys. Chem. A* **2015**, *119*, 5335–5343.

(343) Zhao, L.; Hermann, M.; Schwarz, W. E.; Frenking, G. The Lewis electron-pair bonding model: modern energy decomposition analysis. *Nat. Rev. Chem.* **2019**, *3*, 48–63.

(344) Timms, P. Boron-fluorine chemistry. I. Boron monofluoride and some derivatives. *J. Am. Chem. Soc.* **1967**, *89*, 1629–1632.

(345) Timms, P. Boron-fluorine chemistry. II. Reaction of boron monofluoride with acetylenes. *J. Am. Chem. Soc.* **1968**, *90*, 4585–4589.

(346) Drance, M. J.; Sears, J. D.; Mrse, A. M.; Moore, C. E.; Rheingold, A. L.; Neidig, M. L.; Figueroa, J. S. Terminal coordination of diatomic boron monofluoride to iron. *Science* **2019**, *363*, 1203–1205.

(347) De Jong, G. T.; Bickelhaupt, F. M. Catalytic carbon-halogen bond activation: trends in reactivity, selectivity, and solvation. *J. Chem. Theory Comput.* **2007**, *3*, 514–529.

(348) Varghese, J. J.; Mushrif, S. H. Origins of complex solvent effects on chemical reactivity and computational tools to investigate them: a review. *React. Chem. Eng.* **2019**, *4*, 165–206.

(349) Tomasi, J.; Persico, M. Molecular interactions in solution: an overview of methods based on continuous distributions of the solvent. *Chem. Rev.* **1994**, *94*, 2027–2094.

(350) Cramer, C. J.; Truhlar, D. G. Implicit solvation models: equilibria, structure, spectra, and dynamics. *Chem. Rev.* **1999**, *99*, 2161–2200.

(351) Tomasi, J.; Mennucci, B.; Cammi, R. Quantum mechanical continuum solvation models. *Chem. Rev.* **2005**, *105*, 2999–3094.

(352) Klamt, A.; Schürmann, G. COSMO: a new approach to dielectric screening in solvents with explicit expressions for the screening energy and its gradient. *J. Chem. Soc. Perkin Trans. 2* **1993**, *1993*, 799–805.

(353) Klamt, A. The COSMO and COSMO-RS solvation models. *WIREs: Comput. Mol. Sci.* **2011**, *1*, 699–709.

(354) Cossi, M.; Rega, N.; Scalmani, G.; Barone, V. Energies, structures, and electronic properties of molecules in solution with the C-PCM solvation model. *J. Comput. Chem.* **2003**, *24*, 669–681.

(355) Cances, E.; Mennucci, B.; Tomasi, J. A new integral equation formalism for the polarizable continuum model: Theoretical background and applications to isotropic and anisotropic dielectrics. *J. Chem. Phys.* **1997**, *107*, 3032–3041.

(356) Mennucci, B.; Cances, E.; Tomasi, J. Evaluation of solvent effects in isotropic and anisotropic dielectrics and in ionic solutions with a unified integral equation method: theoretical bases, computational implementation, and numerical applications. *J. Phys. Chem. B* **1997**, *101*, 10506–10517.

(357) Chipman, D. M. Reaction field treatment of charge penetration. *J. Chem. Phys.* **2000**, *112*, 5558–5565.

(358) Lange, A. W.; Herbert, J. M. Polarizable continuum reaction-field solvation models affording smooth potential energy surfaces. *J. Phys. Chem. Lett.* **2010**, *1*, 556–561.

(359) Lange, A. W.; Herbert, J. M. A smooth, nonsingular, and faithful discretization scheme for polarizable continuum models: The switching/Gaussian approach. *J. Chem. Phys.* **2010**, *133*, 244111.

(360) Cramer, C. J.; Truhlar, D. G. A universal approach to solvation modeling. *Acc. Chem. Res.* **2008**, *41*, 760–768.

(361) Marenich, A. V.; Cramer, C. J.; Truhlar, D. G. Generalized born solvation model SM12. *J. Chem. Theory Comput.* **2013**, *9*, 609–620.

(362) Fattebert, J.-L.; Gygi, F. Density functional theory for efficient ab initio molecular dynamics simulations in solution. *J. Comput. Chem.* **2002**, *23*, 662–666.

(363) Fattebert, J.-L.; Gygi, F. First-principles molecular dynamics simulations in a continuum solvent. *Int. J. Quant. Chem.* **2003**, *93*, 139–147.

(364) Scherlis, D. A.; Fattebert, J.-L.; Gygi, F.; Cococcioni, M.; Marzari, N. A unified electrostatic and cavitation model for first-principles molecular dynamics in solution. *J. Chem. Phys.* **2006**, *124*, 074103.

(365) Dziedzic, J.; Helal, H. H.; Skylaris, C.-K.; Mostofi, A. A.; Payne, M. C. Minimal parameter implicit solvent model for ab initio electronic-structure calculations. *Europhys. Lett.* **2011**, *95*, 43001.

(366) Stein, C. J.; Herbert, J. M.; Head-Gordon, M. The Poisson–Boltzmann model for implicit solvation of electrolyte solutions: Quantum chemical implementation and assessment via Sechenov coefficients. *J. Chem. Phys.* **2019**, *151*, 224111.

(367) Prentice, J. C.; Aarons, J.; Womack, J. C.; Allen, A. E.; Andrinopoulos, L.; Anton, L.; Bell, R. A.; Bhandari, A.; Bramley, G. A.; Charlton, R. J., et al. The ONETEP linear-scaling density functional theory program. *J. Chem. Phys.* **2020**, *152*, 174111.

(368) Phipps, M. J.; Fox, T.; Tautermann, C. S.; Skylaris, C.-K. Energy decomposition analysis based on absolutely localized molecular orbitals for large-scale density functional theory calculations in drug design. *J. Chem. Theory Comput.* **2016**, *12*, 3135–3148.

(369) Phipps, M.; Fox, T.; Tautermann, C.; Skylaris, C.-K. Intuitive Density Functional Theory-Based Energy Decomposition Analysis for Protein–Ligand Interactions. *J. Chem. Theory Comput.* **2017**, *13*, 1837–1850.

(370) Cammi, R.; del Valle, F. O.; Tomasi, J. Decomposition of the interaction energy with counterpoise corrections to the basis set superposition error for dimers in solution. Method and application to the hydrogen fluoride dimer. *Chem. Phys.* **1988**, *122*, 63–74.

(371) Contador, J.; Aguilar, M.; Sánchez, M.; del Valle, F. O. A theoretical study of hydrogen-bonded complexes in solution: BSSE and decomposition of interaction energy. *J. Mol. Struct.: THEOCHEM* **1994**, *314*, 229–239.

(372) Gora, R. W.; Bartkowiak, W.; Roszak, S.; Leszczynski, J. Intermolecular interactions in solution: Elucidating the influence of the solvent. *J. Chem. Phys.* **2004**, *120*, 2802–2813.

(373) Fedorov, D. G.; Kitaura, K. Pair interaction energy decomposition analysis. *J. Comput. Chem.* **2007**, *28*, 222–237.

(374) Fedorov, D. G.; Kitaura, K. Extending the power of quantum chemistry to large systems with the fragment molecular orbital method. *J. Phys. Chem. A* **2007**, *111*, 6904–6914.

(375) Fedorov, D. G.; Kitaura, K. Energy decomposition analysis in solution based on the fragment molecular orbital method. *J. Phys. Chem. A* **2012**, *116*, 704–719.

(376) Su, P.; Liu, H.; Wu, W. Free energy decomposition analysis of bonding and nonbonding interactions in solution. *J. Chem. Phys.* **2012**, *137*, 034111.

(377) Su, P.; Jiang, Z.; Chen, Z.; Wu, W. Energy decomposition scheme based on the generalized Kohn–Sham scheme. *J. Phys. Chem. A* **2014**, *118*, 2531–2542.

(378) Su, P.; Tang, Z.; Wu, W. Generalized Kohn-Sham energy decomposition analysis and its applications. *WIREs: Comput. Mol. Sci.* **2020**, e1460.

(379) Mao, Y.; Levine, D. S.; Loipersberger, M.; Horn, P. R.; Head-Gordon, M. Probing Radical-Molecule Interactions with a Second Generation Energy Decomposition Analysis of DFT Calculations Using Absolutely Localized Molecular Orbitals. *Phys. Chem. Chem. Phys.* **2020**, *22*, 12867–12885.

(380) Azcarate, I.; Costentin, C.; Robert, M.; Savéant, J.-M. Through-space charge interaction substituent effects in molecular catalysis leading to the design of the most efficient catalyst of CO2-to-CO electrochemical conversion. *J. Am. Chem. Soc.* **2016**, *138*, 16639–16644.

(381) Seo, H.; Katcher, M. H.; Jamison, T. F. Photoredox activation of carbon dioxide for amino acid synthesis in continuous flow. *Nat. Chem.* **2017**, *9*, 453–456.

(382) Costentin, C.; Passard, G.; Robert, M.; Savéant, J.-M. Pendant acid–base groups in molecular catalysts: H-bond promoters or proton relays? Mechanisms of the conversion of CO2 to CO by electrogenerated iron (0) porphyrins bearing prepositioned phenol functionalities. *J. Am. Chem. Soc.* **2014**, *136*, 11821–11829.

(383) Costentin, C.; Robert, M.; Savéant, J.-M.; Tatin, A. Efficient and selective molecular catalyst for the CO2-to-CO electrochemical conversion in water. *Proc. Natl. Acad. Sci.* **2015**, *112*, 6882–6886.

(384) Zee, D. Z.; Chantarojsiri, T.; Long, J. R.; Chang, C. J. Metal-Polypyridyl Catalysts for Electro- and Photochemical Reduction of Water to Hydrogen. *Acc. Chem. Res* **2015**, *48*, 2027–2036.

(385) Zee, D. Z.; Nippe, M.; King, A. E.; Chang, C. J.; Long, J. R. Tuning Second Coordination Sphere Interactions in Polypyridyl–Iron Complexes to Achieve Selective Electrocatalytic Reduction of Carbon Dioxide to Carbon Monoxide. *Inorg. Chem.* **2020**, *59*, 5206–5217.

(386) Yang, L.; Adam, C.; Nichol, G. S.; Cockroft, S. L. How much do van der Waals dispersion forces contribute to molecular recognition in solution? *Nat. Chem.* **2013**, *5*, 1006–1010.

(387) Tkatchenko, A.; DiStasio Jr, R. A.; Car, R.; Scheffler, M. Accurate and efficient method for many-body van der Waals interactions. *Phys. Rev. Lett.* **2012**, *108*, 236402.

(388) Rappé, A. K.; Casewit, C. J.; Colwell, K.; Goddard III, W. A.; Skiff, W. M. UFF, a full periodic table force field for molecular mechanics and molecular dynamics simulations. *J. Am. Chem. Soc.* **1992**, *114*, 10024–10035.

(389) Mantina, M.; Valero, R.; Cramer, C. J.; Truhlar, D. G., *Atomic radii of the elements*; CRC Press London: 2013; Vol. 94.

(390) Pascual-ahuir, J.-L.; Silla, E.; Tunon, I. GEPOL: An improved description of molecular surfaces. III. A new algorithm for the computation of a solvent-excluding surface. *J. Comput. Chem.* **1994**, *15*, 1127–1138.

(391) Mardirossian, N.; Head-Gordon, M. ωB97X-V: A 10-parameter, range-separated hybrid, generalized gradient approximation density functional with nonlocal correlation, designed by a survival-of-the-fittest strategy. *Phys. Chem. Chem. Phys* **2014**, *16*, 9904–9924.

(392) Burns, L. A.; Faver, J. C.; Zheng, Z.; Marshall, M. S.; Smith, D. G.; Vanommeslaeghe, K.; MacKerell Jr, A. D.; Merz Jr, K. M.; Sherrill, C. D. The BioFragment Database (BFDb): An open-data platform for computational chemistry analysis of noncovalent interactions. *J. Chem. Phys* **2017**, *147*, 161727.

(393) Goerigk, L.; Hansen, A.; Bauer, C.; Ehrlich, S.; Najibi, A.; Grimme, S. A look at the density functional theory zoo with the advanced GMTKN55 database for general main group thermochemistry, kinetics and noncovalent interactions. *Phys. Chem. Chem. Phys.* **2017**, *19*, 32184–32215.

(394) Mao, Y.; Shao, Y.; Dziedzic, J.; Skylaris, C.-K.; Head-Gordon, T.; Head-Gordon, M. Performance of the AMOEBA water model in the vicinity of QM solutes: A diagnosis using energy decomposition analysis. *J. Chem. Theory Comput.* **2017**, *13*, 1963–1979.

(395) Gill, P. M.; Johnson, B. G.; Pople, J. A. A standard grid for density functional calculations. *Chem. Phys. Lett.* **1993**, *209*, 506–512.

(396) Chen, L.; Guo, Z.; Wei, X.-G.; Gallenkamp, C.; Bonin, J.; Anxolabéhère-Mallart, E.; Lau, K.-C.; Lau, T.-C.; Robert, M. Molecular catalysis of the electrochemical and photochemical reduction of CO2 with earth-abundant metal complexes. Selective production of CO vs HCOOH by switching of the metal center. *J. Am. Chem. Soc.* **2015**, *137*, 10918–10921.

(397) Takeda, H.; Cometto, C.; Ishitani, O.; Robert, M. Electrons, photons, protons and earth-abundant metal complexes for molecular catalysis of CO2 reduction. *ACS Catal.* **2017**, *7*, 70–88.

(398) Derrick, J. S.; Loipersberger, M.; Chatterjee, R.; Iovan, D. A.; Smith, P. T.; Chakarawet, K.; Yano, J.; Long, J. R.; Head-Gordon, M.; Chang, C. J. Metal–Ligand Cooperativity via Exchange Coupling Promotes Iron-Catalyzed Electrochemical CO_2 Reduction at Low Overpotentials. *J. Am. Chem. Soc.* **2020**, *142*, 20489–20501.

(399) Hammouche, M.; Lexa, D.; Savéant, J.; Momenteau, M. Catalysis of the electrochemical reduction of carbon dioxide by iron ("0") porphyrins. *J. Electroanal. Chem.* **1988**, *249*, 347–351.

(400) Bhugun, I.; Lexa, D.; Savéant, J.-M. Catalysis of the electrochemical reduction of carbon dioxide by iron (0) porphyrins: Synergystic effect of weak Brönsted acids. *J. Am. Chem. Soc.* **1996**, *118*, 1769–1776.

(401) Costentin, C.; Drouet, S.; Robert, M.; Savéant, J.-M. A Local Proton Source Enhances CO2 Electroreduction to CO by a Molecular Fe Catalyst. *Science* **2012**, *338*, 90–94.

(402) Azcarate, I.; Costentin, C.; Robert, M.; Savéant, J.-M. Dissection of electronic substituent effects in multielectron–multistep molecular catalysis. Electrochemical CO2-to-CO conversion catalyzed by iron porphyrins. *J. Phys. Chem. C* **2016**, *120*, 28951–28960.

(403) Ambre, R. B.; Daniel, Q.; Fan, T.; Chen, H.; Zhang, B.; Wang, L.; Ahlquist, M. S.; Duan, L.; Sun, L. Molecular engineering for efficient and selective iron porphyrin catalysts for electrochemical reduction of CO_2 to CO. *Chem. Commun.* **2016**, *52*, 14478–14481.

(404) Okabe, Y.; Lee, S. K.; Kondo, M.; Masaoka, S. Syntheses and CO_2 reduction activities of π-expanded/extended iron porphyrin complexes. *J. Bio. Inorg. Chem.* **2017**, *22*, 713–725.

(405) Gagliardi, L. G.; Castells, C. B.; Rafols, C.; Rosés, M.; Bosch, E. Static Dielectric Constants of Acetonitrile/Water Mixtures at Different Temperatures and Debye-Hückel A and a 0 B Parameters for Activity Coefficients. *J. Chem. Eng. Data* **2007**, *52*, 1103–1107.

(406) Nichols, E. M.; Derrick, J. S.; Nistanaki, S. K.; Smith, P. T.; Chang, C. J. Positional effects of second-sphere amide pendants on electrochemical CO2 reduction catalyzed by iron porphyrins. *Chem. Sci.* **2018**, *9*, 2952–2960.

(407) Khadhraoui, A.; Gotico, P.; Boitrel, B.; Leibl, W.; Halime, Z.; Aukauloo, A. Local ionic liquid environment at a modified iron porphyrin catalyst enhances the electrocatalytic performance of CO 2 to CO reduction in water. *Chem. Commun.* **2018**, *54*, 11630–11633.

(408) Romero, N. A.; Nicewicz, D. A. Organic photoredox catalysis. *Chem. Rev.* **2016**, *116*, 10075–10166.

(409) Shaw, M. H.; Twilton, J.; MacMillan, D. W. Photoredox catalysis in organic chemistry. *J. Org. Chem.* **2016**, *81*, 6898–6926.

(410) Kron, K. J.; Gomez, S. J.; Mao, Y.; Cave, R. J.; Mallikarjun Sharada, S. Computational Analysis of Electron Transfer Kinetics for CO2 Reduction with Organic Photoredox Catalysts. *J. Phys. Chem. A* **2020**, *124*, 5359–5368.

(411) Marcus, R. A. Electron transfer reactions in chemistry. Theory and experiment. *Rev. Mod. Phys.* **1993**, *65*, 599.

(412) Wu, Q.; Van Voorhis, T. Direct optimization method to study constrained systems within density-functional theory. *Phys. Rev. A* **2005**, *72*, 024502.

(413) Wu, Q.; Van Voorhis, T. Direct calculation of electron transfer parameters through constrained density functional theory. *J. Phys. Chem. A* **2006**, *110*, 9212–9218.

(414) Grimme, S.; Ehrlich, S.; Goerigk, L. Effect of the damping function in dispersion corrected density functional theory. *J. Comput. Chem.* **2011**, *32*, 1456–1465.

(415) Krishnan, R.; Binkley, J. S.; Seeger, R.; Pople, J. A. Self-consistent molecular orbital methods. XX. A basis set for correlated wave functions. *J. Chem. Phys.* **1980**, *72*, 650–654.

(416) Hammett, L. P. The effect of structure upon the reactions of organic compounds. Benzene derivatives. *J. Am. Chem. Soc.* **1937**, *59*, 96–103.

(417) Cohen, A. J.; Mori-Sánchez, P.; Yang, W. Insights into current limitations of density functional theory. *Science* **2008**, *321*, 792–794.

(418) Wang, Y.; Liu, M.; Gao, J. Enhanced receptor binding of SARS-CoV-2 through networks of hydrogen-bonding and hydrophobic interactions. *Proc. Natl. Acad. Sci. U.S.A* **2020**, *117*, 13967–13974.

(419) Thirman, J.; Head-Gordon, M. Electrostatic domination of the effect of electron correlation in intermolecular interactions. *J. Phys. Chem. Lett.* **2014**, *5*, 1380–1385.

(420) Sinnokrot, M. O.; Valeev, E. F.; Sherrill, C. D. Estimates of the ab initio limit for π-π interactions: The benzene dimer. *J. Am. Chem. Soc.* **2002**, *124*, 10887–10893.

(421) Altun, A.; Neese, F.; Bistoni, G. HFLD: A Nonempirical London Dispersion-Corrected Hartree–Fock Method for the Quantification and Analysis of Noncovalent Interaction Energies of Large Molecular Systems. *J. Chem. Theory Comput.* **2019**, *15*, 5894–5907.

(422) Lochan, R. C.; Jung, Y.; Head-Gordon, M. Scaled Opposite Spin Second Order Møller-Plesset Theory with Improved Physical Description of Long-Range Dispersion Interactions. *J. Phys. Chem. A* **2005**, *109*, 7598–7605.

(423) Goldey, M.; Head-Gordon, M. Attenuating Away the Errors in Inter- and Intramolecular Interactions from Second-Order Møller-Plesset Calculations in the Small Aug-cc-pVDZ Basis Set. *J. Phys. Chem. Lett.* **2012**, *3*, 3592–3598.

(424) Goldey, M.; Dutoi, A.; Head-Gordon, M. Attenuated second-order Møller-Plesset perturbation theory: performance within the aug-cc-pVTZ basis. *Phys. Chem. Chem. Phys.* **2013**, *15*, 15869–15875.

(425) Goldey, M. B.; Belzunces, B.; Head-Gordon, M. Attenuated MP2 with a Long-Range Dispersion Correction for Treating Nonbonded Interactions. *J. Chem. Theor. Comput.* **2015**, *11*, 4159–4168.

(426) Lochan, R. C.; Head-Gordon, M. Orbital-optimized opposite-spin scaled second-order correlation: An economical method to improve the description of open-shell molecules. *J. Chem. Phys* **2007**, *126*, 164101.

(427) Bozkaya, U.; Turney, J. M.; Yamaguchi, Y.; Schaefer III, H. F.; Sherrill, C. D. Quadratically convergent algorithm for orbital optimization in the orbital-optimized coupled-cluster doubles method and in orbital-optimized second-order Møller-Plesset perturbation theory. *J. Chem. Phys.* **2011**, *135*, 104103.

(428) Farnell, L.; Pople, J. A.; Radom, L. Structural predictions for open-shell systems: a comparative assessment of ab initio procedures. *J. Phys. Chem.* **1983**, *87*, 79–82.

(429) Nobes, R. H.; Pople, J. A.; Radom, L.; Handy, N. C.; Knowles, P. J. Slow convergence of the Møller-Plesset perturbation series: the dissociation energy of hydrogen cyanide and the electron affinity of the cyano radical. *Chem. Phys. Lett.* **1987**, *138*, 481–485.

(430) Gill, P. M. W.; Pople, J. A.; Radom, L.; Nobes, R. H. Why does unrestricted Møller-Plesset perturbation theory converge so slowly for spin-contaminated wave functions? *J. Chem. Phys.* **1988**, *89*, 7307–7314.

(431) Jensen, F. A remarkable large effect of spin contamination on calculated vibrational frequencies. *Chem. Phys. Lett.* **1990**, *169*, 519–528.

(432) Soydaş, E.; Bozkaya, U. Assessment of Orbital-Optimized MP2.5 for Thermochemistry and Kinetics: Dramatic Failures of Standard Perturbation Theory Approaches for Aromatic Bond Dissociation Energies and Barrier Heights of Radical Reactions. *J. Chem. Theory Comput.* **2015**, *11*, 1564–1573.

(433) Stück, D.; Head-Gordon, M. Regularized orbital-optimized second-order perturbation theory. *J. Chem. Phys.* **2013**, *139*, 244109.

(434) Sharada, S. M.; Stück, D.; Sundstrom, E. J.; Bell, A. T.; Head-Gordon, M. Wavefunction stability analysis without analytical electronic Hessians: application to orbital-optimised second-order Møller-Plesset theory and VV10-containing density functionals. *Mol. Phys.* **2015**, *113*, 1802–1808.

(435) Coulson, C. A.; Fischer, I. XXXIV. Notes on the molecular orbital treatment of the hydrogen molecule. *Philos. Mag.* **1949**, *40*, 386–393.

(436) Karton, A.; Daon, S.; Martin, J. M. W4-11: A high-confidence benchmark dataset for computational thermochemistry derived from first-principles W4 data. *Chem. Phys. Lett.* **2011**, *510*, 165–178.

(437) Zipse, H. In *Radicals in Synthesis I*, Gansäuer, A., Ed.; Springer Berlin Heidelberg: Berlin, Heidelberg, 2006, pp 163–189.

(438) Jung, Y.; Lochan, R. C.; Dutoi, A. D.; Head-Gordon, M. Scaled opposite-spin second order Møller-Plesset correlation energy: An economical electronic structure method. *J. Chem. Phys.* **2004**, *121*, 9793–9802.

(439) Grimme, S. Accurate Calculation of the Heats of Formation for Large Main Group Compounds with Spin-Component Scaled MP2 Methods. *J. Phys. Chem. A* **2005**, *109*, 3067–3077.

(440) Distasio Jr., R. A.; Head-Gordon, M. Optimized spin-component scaled second-order Møller-Plesset perturbation theory for intermolecular interaction energies. *Mol. Phys.* **2007**, *105*, 1073–1083.

(441) Lochan, R. C.; Shao, Y.; Head-Gordon, M. Quartic-Scaling Analytical Energy Gradient of Scaled Opposite-Spin Second-Order Møller-Plesset Perturbation Theory. *J. Chem. Theory Comput.* **2007**, *3*, 988–1003.

(442) Grimme, S. Semiempirical hybrid density functional with perturbative second-order correlation. *J. Chem. Phys.* **2006**, *124*, 034108.

(443) Chai, J.-D.; Head-Gordon, M. Long-range corrected double-hybrid density functionals. *J. Chem. Phys.* **2009**, *131*, 174105.

(444) Kozuch, S.; Martin, J. M. L. DSD-PBEP86: in search of the best double-hybrid DFT with spin-component scaled MP2 and dispersion corrections. *Phys. Chem. Chem. Phys.* **2011**, *13*, 20104–20107.

(445) Najibi, A.; Goerigk, L. A Comprehensive Assessment of the Effectiveness of Orbital Optimization in Double-Hybrid Density Functionals in the Treatment of Thermochemistry, Kinetics, and Noncovalent Interactions. *J. Phys. Chem. A* **2018**, *122*, 5610–5624.

(446) Urban, L.; Thompson, T.; Ochsenfeld, C. A scaled explicitly correlated F12 correction to second-order Møller–Plesset perturbation theory. *J. Chem. Phys* **2021**, *154*, 044101.

(447) Goldey, M.; Head-Gordon, M. Separate Electronic Attenuation Allowing a Spin-Component-Scaled Second-Order Møller-Plesset Theory to Be Effective for Both Thermochemistry and Noncovalent Interactions. *J. Phys. Chem. B* **2014**, *118*, 6519–6525.

(448) Gráfová, L.; Pitoňák, M.; Řezáč, J.; Hobza, P. Comparative Study of Selected Wave Function and Density Functional Methods for Noncovalent Interaction Energy Calculations Using the Extended S22 Data Set. *J. Chem. Theory Comput.* **2010**, *6*, 2365–2376.

(449) Riley, K. E.; Platts, J. A.; Řezáč, J.; Hobza, P.; Hill, J. G. Assessment of the Performance of MP2 and MP2 Variants for the Treatment of Noncovalent Interactions. *J. Phys. Chem. A* **2012**, *116*, 4159–4169.

(450) Pitoňák, M.; Neogrády, P.; Černý, J.; Grimme, S.; Hobza, P. Scaled MP3 Non-Covalent Interaction Energies Agree Closely with Accurate CCSD(T) Benchmark Data. *ChemPhysChem* **2009**, *10*, 282–289.

(451) Riley, K. E.; Řezáč, J.; Hobza, P. The performance of MP2.5 and MP2.X methods for nonequilibrium geometries of molecular complexes. *Phys. Chem. Chem. Phys.* **2012**, *14*, 13187–13193.

(452) Sedlak, R.; Riley, K. E.; Řezáč, J.; Pitoňák, M.; Hobza, P. MP2.5 and MP2.X: Approaching CCSD(T) Quality Description of Noncovalent Interaction at the Cost of a Single CCSD Iteration. *ChemPhysChem* **2013**, *14*, 698–707.

(453) Suliman, S.; Pitoňák, M.; Cernusak, I.; Louis, F. On the applicability of the MP2. 5 approximation for open-shell systems. Case study of atmospheric reactivity. *Comput. Theor. Chem.* **2020**, *1186*, 112901.

(454) Bozkaya, U. Orbital-optimized third-order Møller-Plesset perturbation theory and its spin-component and spin-opposite scaled variants: Application to symmetry breaking problems. *J. Chem. Phys.* **2011**, *135*, 224103.

(455) Soydaş, E.; Bozkaya, U. Assessment of Orbital-Optimized Third-Order Møller-Plesset Perturbation Theory and Its Spin-Component and Spin-Opposite Scaled Variants for Thermochemistry and Kinetics. *J. Chem. Theory Comput.* **2013**, *9*, 1452–1460.

(456) Bozkaya, U.; Sherrill, C. D. Orbital-optimized MP2.5 and its analytic gradients: Approaching CCSD(T) quality for noncovalent interactions. *J. Chem. Phys.* **2014**, *141*, 204105.

(457) Bozkaya, U. Orbital-Optimized MP3 and MP2.5 with Density-Fitting and Cholesky Decomposition Approximations. *J. Chem. Theory Comput.* **2016**, *12*, 1179–1188.

(458) Purvis, G. D.; Bartlett, R. J. A full coupled-cluster singles and doubles model: The inclusion of disconnected triples. *J. Chem. Phys.* **1982**, *76*, 1910–1918.

(459) Scuseria, G. E.; Janssen, C. L.; Schaefer, H. F. An efficient reformulation of the closed-shell coupled cluster single and double excitation (CCSD) equations. *J. Chem. Phys.* **1988**, *89*, 7382–7387.

(460) Raghavachari, K.; Trucks, G. W.; Pople, J. A.; Head-Gordon, M. A fifth-order perturbation comparison of electron correlation theories. *Chem. Phys. Lett.* **1989**, *157*, 479–483.

(461) Rezác, J.; Hobza, P. Describing noncovalent interactions beyond the common approximations: How accurate is the "gold standard," CCSD (T) at the complete basis set limit? *J. Chem. Theory Comput* **2013**, *9*, 2151–2155.

(462) Small, D. W. Remarkable Accuracy of an O(N^6) Perturbative Correction to Opposite-Spin CCSD: Are Triples Necessary for Chemical Accuracy in Coupled Cluster? *J. Chem. Theory Comput.* **2020**, *16*, 4014–4020.

(463) Pitoňák, M.; Řezáč, J.; Hobza, P. Spin-component scaled coupled-clusters singles and doubles optimized towards calculation of noncovalent interactions. *Phys. Chem. Chem. Phys.* **2010**, *12*, 9611–9614.

(464) Rezác, J.; Riley, K. E.; Hobza, P. S66: A well-balanced database of benchmark interaction energies relevant to biomolecular structures. *J. Chem. Theory Comput* **2011**, *7*, 2427–2438.

(465) Rezac, J.; Riley, K. E.; Hobza, P. Benchmark calculations of noncovalent interactions of halogenated molecules. *J. Chem. Theory Comput* **2012**, *8*, 4285–4292.

(466) Ren, X. G.; Rinke, P.; Joas, C.; Scheffler, M. Random-phase approximation and its applications in computational chemistry and materials science. *J. Mat. Sci.* **2012**, *47*, 7447–7471.

(467) Chen, G. P.; Voora, V. K.; Agee, M. M.; Balasubramani, S. G.; Furche, F. In; Annu. Rev. Phys. Chem, Vol. 68, 2017, pp 421–445.

(468) Modrzejewski, M.; Yourdkhani, S.; Klimess, J. Random Phase Approximation Applied to Many-Body Noncovalent Systems. *J. Chem. Theory Comput.* **2020**, *16*, 427–442.

(469) Ren, X. G.; Rinke, P.; Scuseria, G. E.; Scheffler, M. Renormalized second-order perturbation theory for the electron correlation energy: Concept, implementation, and benchmarks. *Phys. Rev. B* **2013**, *88*, 035120.

(470) Dixit, A.; Claudot, J.; Lebegue, S.; Rocca, D. Improving the Efficiency of Beyond-RPA Methods within the Dielectric Matrix Formulation: Algorithms and Applications to the A24 and S22 Test Sets. *J. Chem. Theory Comput* **2017**, *13*, 5432–5442.

(471) Su, H.; Wang, H.; Wang, H. Y.; Lu, Y. X.; Zhu, Z. D. Description of noncovalent interactions involving pi-system with high precision: An assessment of RPA, MP2, and DFT-D methods. *J. Comput. Chem* **2019**, *40*, 1643–1651.

(472) Mintz, B. J.; Parks, J. M. Benchmark interaction energies for biologically relevant noncovalent complexes containing divalent sulfur. *J. Phys. Chem. A* **2012**, *116*, 1086–1092.

(473) Rezác, J.; Hobza, P. Advanced corrections of hydrogen bonding and dispersion for semiempirical quantum mechanical methods. *J. Chem. Theory Comput* **2012**, *8*, 141–151.

(474) Faver, J. C.; Benson, M. L.; He, X.; Roberts, B. P.; Wang, B.; Marshall, M. S.; Kennedy, M. R.; Sherrill, C. D.; Merz Jr, K. M. Formal estimation of errors in computed absolute interaction energies of protein- ligand complexes. *J. Chem. Theory Comput* **2011**, *7*, 790–797.

(475) Copeland, K. L.; Tschumper, G. S. Hydrocarbon/water interactions: Encouraging energetics and structures from DFT but disconcerting discrepancies for Hessian indices. *J. Chem. Theory Comput* **2012**, *8*, 1646–1656.

(476) Smith, D. G.; Jankowski, P.; Slawik, M.; Witek, H. A.; Patkowski, K. Basis set convergence of the post-CCSD (T) contribution to noncovalent interaction energies. *J. Chem. Theory Comput* **2014**, *10*, 3140–3150.

(477) Granatier, J.; Pitonak, M.; Hobza, P. Accuracy of several wave function and density functional theory methods for description of noncovalent interaction of saturated and unsaturated hydrocarbon dimers. *J. Chem. Theory Comput* **2012**, *8*, 2282–2292.

(478) Li, S.; Smith, D. G.; Patkowski, K. An accurate benchmark description of the interactions between carbon dioxide and polyheterocyclic aromatic compounds containing nitrogen. *Phys. Chem. Chem. Phys.* **2015**, *17*, 16560–16574.

(479) Boese, A. D. Assessment of coupled cluster theory and more approximate methods for hydrogen bonded systems. *J. Chem. Theory Comput* **2013**, *9*, 4403–4413.

(480) Lao, K. U.; Schäffer, R.; Jansen, G.; Herbert, J. M. Accurate description of intermolecular interactions involving ions using symmetry-adapted perturbation theory. *J. Chem. Theory Comput* **2015**, *11*, 2473–2486.

(481) Marshall, M. S.; Burns, L. A.; Sherrill, C. D. Basis set convergence of the coupled-cluster correction, δ MP2 CCSD (T): Best practices for benchmarking non-covalent interactions and the attendant revision of the S22, NBC10, HBC6, and HSG databases. *J. Chem. Phys.* **2011**, *135*, 194102.

(482) Crittenden, D. L. A systematic CCSD (T) study of long-range and noncovalent interactions between benzene and a series of first-and second-row hydrides and rare gas atoms. *J. Phys. Chem. A* **2009**, *113*, 1663–1669.

(483) Witte, J.; Goldey, M.; Neaton, J. B.; Head-Gordon, M. Beyond energies: Geometries of nonbonded molecular complexes as metrics for assessing electronic structure approaches. *J. Chem. Theory Comput* **2015**, *11*, 1481–1492.

(484) Brauer, B.; Kesharwani, M. K.; Kozuch, S.; Martin, J. M. The S66x8 benchmark for noncovalent interactions revisited: Explicitly correlated ab initio methods and density functional theory. *Phys. Chem. Chem. Phys.* **2016**, *18*, 20905–20925.

(485) Rezac, J.; Huang, Y.; Hobza, P.; Beran, G. J. Benchmark calculations of three-body intermolecular interactions and the performance of low-cost electronic structure methods. *J. Chem. Theory Comput* **2015**, *11*, 3065–3079.

(486) Kozuch, S.; Martin, J. M. Halogen bonds: Benchmarks and theoretical analysis. *J. Chem. Theory Comput* **2013**, *9*, 1918–1931.

(487) Bauza, A.; Alkorta, I.; Frontera, A.; Elguero, J. On the reliability of pure and hybrid DFT methods for the evaluation of halogen, chalcogen, and pnicogen bonds involving anionic and neutral electron donors. *J. Chem. Theory Comput* **2013**, *9*, 5201–5210.

(488) Steinmann, S. N.; Piemontesi, C.; Delachat, A.; Corminboeuf, C. Why are the interaction energies of charge-transfer complexes challenging for DFT? *J. Chem. Theory Comput* **2012**, *8*, 1629–1640.

(489) Xantheas, S. S. On the importance of the fragment relaxation energy terms in the estimation of the basis set superposition error correction to the intermolecular interaction energy. *J. Chem. Phys* **1996**, *104*, 8821–8824.

(490) Rettig, A.; Hait, D.; Bertels, L. W.; Head-Gordon, M. Third-Order Møller–Plesset Theory Made More Useful? The Role of Density Functional Theory Orbitals. *J. Chem. Theory Comput* **2020**.

(491) Hait, D.; Head-Gordon, M. How accurate is density functional theory at predicting dipole moments? An assessment using a new database of 200 benchmark values. *J. Chem. Theory Comput* **2018**, *14*, 1969–1981.

(492) Hait, D.; Head-Gordon, M. How accurate are static polarizability predictions from density functional theory? An assessment over 132 species at equilibrium geometry. *Phys. Chem. Chem. Phys* **2018**, *20*, 19800–19810.

(493) Hait, D.; Liang, Y. H.; Head-Gordon, M. Too big, too small, or just right? A benchmark assessment of density functional theory for predicting the spatial extent of the electron density of small chemical systems. *J. Chem. Phys* **2021**, *154*, 074109.

(494) Ishikawa, T.; Sakakura, K.; Mochizuki, Y. RI-MP3 calculations of biomolecules based on the fragment molecular orbital method. *J. Comput. Chem* **2018**, *39*, 1970–1978.

(495) Lee, J.; Lin, L.; Head-Gordon, M. Systematically improvable tensor hypercontraction: Interpolative separable density-fitting for molecules applied to exact exchange, second-and third-order Møller–Plesset perturbation theory. *J. Chem. Theory Comput* **2019**, *16*, 243–263.

(496) Weigend, F.; Häser, M.; Patzelt, H.; Ahlrichs, R. RI-MP2: optimized auxiliary basis sets and demonstration of efficiency. *Chem. Phys. Lett* **1998**, *294*, 143–152.

(497) Hellweg, A.; Hättig, C.; Höfener, S.; Klopper, W. Optimized accurate auxiliary basis sets for RI-MP2 and RI-CC2 calculations for the atoms Rb to Rn. *Theor. Chem. Acc* **2007**, *117*, 587–597.

(498) Weigend, F.; Furche, F.; Ahlrichs, R. Gaussian basis sets of quadruple zeta valence quality for atoms H–Kr. *J. Chem. Phys* **2003**, *119*, 12753–12762.

(499) Boese, A. D. Basis set limit coupled-cluster studies of hydrogen-bonded systems. *Mol. Phys.* **2015**, *113*, 1618–1629.

(500) Gräfenstein, J.; Cremer, D. The self-interaction error and the description of non-dynamic electron correlation in density functional theory. *Theor. Chem. Acc* **2009**, *123*, 171–182.

(501) Boese, A. D. Density functional theory and hydrogen bonds: are we there yet? *ChemPhysChem* **2015**, *16*, 978–985.

(502) Otero-De-La-Roza, A.; Johnson, E. R.; DiLabio, G. A. Halogen bonding from dispersion-corrected density-functional theory: the role of delocalization error. *J. Chem. Theory Comput* **2014**, *10*, 5436–5447.

(503) Takatani, T.; Sherrill, C. D. Performance of spin-component-scaled Møller–Plesset theory (SCS-MP2) for potential energy curves of noncovalent interactions. *Phys. Chem. Chem. Phys.* **2007**, *9*, 6106–6114.

(504) Global Energy Statistical Yearbook Total energy consumption., 2019.

(505) Habisreutinger, S. N.; Schmidt-Mende, L.; Stolarczyk, J. K. Photocatalytic Reduction of CO2 on TiO2 and Other Semiconductors. *Angew. Chem., Int. Ed.* **2013**, *52*, 7372–7408.

(506) Grice, K. A.; Kubiak, C. P., *Chapter Five - Recent Studies of Rhenium and Manganese Bipyridine Carbonyl Catalysts for the Electrochemical Reduction of CO_2*; Advances in Inorg. Chem. Vol. 66; Academic Press: 2014, pp 163–188.

(507) Qiao, J.; Liu, Y.; Hong, F.; Zhang, J. A review of catalysts for the electroreduction of carbon dioxide to produce low-carbon fuels. *Chem. Soc. Rev.* **2014**, *43*, 631–675.

(508) De Klerk, A.; Furimsky, E. Catalysis in the refining of Fischer–Tropsch syncrude. *Platinum Metals Rev* **2011**, *55*, 263–267.

(509) Kuhl, K. P.; Cave, E. R.; Abram, D. N.; Jaramillo, T. F. New insights into the electrochemical reduction of carbon dioxide on metallic copper surfaces. *Energy Environ. Sci.* **2012**, *5*, 7050–7059.

(510) Lee, C. H.; Kanan, M. W. Controlling H+ vs CO2 Reduction Selectivity on Pb Electrodes. *ACS Catal.* **2015**, *5*, 465–469.

(511) Goodpaster, J. D.; Bell, A. T.; Head-Gordon, M. Identification of Possible Pathways for C-C Bond Formation during Electrochemical Reduction of CO2: New Theoretical Insights from an Improved Electrochemical Model. *J. Phys. Chem. Lett* **2016**, *7*, 1471–1477.

(512) Medina-Ramos, J.; Pupillo, R. C.; Keane, T. P.; DiMeglio, J. L.; Rosenthal, J. Efficient Conversion of CO2 to CO Using Tin and Other Inexpensive and Easily Prepared Post-Transition Metal Catalysts. *J. Am. Chem. Soc.* **2015**, *137*, 5021–5027.

(513) Garza, A. J.; Bell, A. T.; Head-Gordon, M. Mechanism of CO2 reduction at copper surfaces: Pathways to C2 products. *ACS Catal.* **2018**, *8*, 1490–1499.

(514) Smieja, J. M.; Sampson, M. D.; Grice, K. A.; Benson, E. E.; Froehlich, J. D.; Kubiak, C. P. Manganese as a Substitute for Rhenium in CO2 Reduction Catalysts: The Importance of Acids. *Inorg. Chem.* **2013**, *52*, 2484–2491.

(515) Wang, M.; Torbensen, K.; Salvatore, D.; Ren, S.; Joulié, D.; Dumoulin, F.; Mendoza, D.; Lassalle-Kaiser, B.; Işci, U.; Berlinguette Curtis P. Berlinguette, M. R. CO 2 electrochemical catalytic reduction with a highly active cobalt phthalocyanine. *Nat. Commun* **2019**, *10*, 1–8.

(516) Beley, M.; Collin, J. P.; Ruppert, R.; Sauvage, J. P. Electrocatalytic reduction of carbon dioxide by nickel cyclam2+ in water: study of the factors affecting the efficiency and the selectivity of the process. *J. Am. Chem. Soc.* **1986**, *108*, 7461–7467.

(517) Wu, Y.; Jiang, J.; Weng, Z.; Wang, M.; Broere, D. L. J.; Zhong, Y.; Brudvig, G. W.; Feng, Z.; Wang, H. Electroreduction of CO2 Catalyzed by a Heterogenized Zn-Porphyrin Complex with a Redox-Innocent Metal Center. *ACS Cent. Sci.* **2017**, *3*, 847–852.

(518) Hod, I.; Sampson, M. D.; Deria, P.; Kubiak, C. P.; Farha, O. K.; Hupp, J. T. Fe-Porphyrin-Based Metal-Organic Framework Films as High-Surface Concentration, Heterogeneous Catalysts for Electrochemical Reduction of CO2. *ACS Catal.* **2015**, *5*, 6302–6309.

(519) Kornienko, N.; Zhao, Y.; Kley, C. S.; Zhu, C.; Kim, D.; Lin, S.; Chang, C. J.; Yaghi, O. M.; Yang, P. Metal-Organic Frameworks for Electrocatalytic Reduction of Carbon Dioxide. *J. Am. Chem. Soc.* **2015**, *137*, 14129–14135.

(520) Elgrishi, N.; Griveau, S.; Chambers, M. B.; Bedioui, F.; Fontecave, M. Versatile functionalization of carbon electrodes with a polypyridine ligand: metallation and electrocatalytic H^+ and CO2 reduction. *Chem. Commun.* **2015**, *51*, 2995–2998.

(521) Oh, S.; Gallagher, J. R.; Miller, J. T.; Surendranath, Y. Graphite-Conjugated Rhenium Catalysts for Carbon Dioxide Reduction. *J. Am. Chem. Soc.* **2016**, *138*, 1820–1823.

(522) Kumar, B.; Llorente, M.; Froehlich, J.; Dang, T.; Sathrum, A.; Kubiak, C. P. Photochemical and photoelectrochemical reduction of CO2. *Annual review of physical chemistry* **2012**, *63*, 541–569.

(523) Smieja, J. M.; Kubiak, C. P. Re(bipy-tBu)(CO)3Cl–improved Catalytic Activity for Reduction of Carbon Dioxide: IR-Spectroelectrochemical and Mechanistic Studies. *Inorg. Chem.* **2010**, *49*, 9283–9289.

(524) Smieja, J. M.; Benson, E. E.; Kumar, B.; Grice, K. A.; Seu, C. S.; Miller, A. J. M.; Mayer, J. M.; Kubiak, C. P. Kinetic and structural studies, origins of selectivity, and interfacial charge transfer in the artificial photosynthesis of CO. *Proc. Natl. Acad. Sci.* **2012**, *109*, 15646–15650.

(525) Benson, E. E.; Sampson, M. D.; Grice, K. A.; Smieja, J. M.; Froehlich, J. D.; Friebel, D.; Keith, J. A.; Carter, E. A.; Nilsson, A.; Kubiak, C. P. The Electronic States of Rhenium Bipyridyl Electrocatalysts for CO2 Reduction as Revealed by X-ray Absorption Spectroscopy and Computational Quantum Chemistry. *Angew. Chem., Int. Ed.* **2013**, *52*, 4841–4844.

(526) Sampson, M. D.; Froehlich, J. D.; Smieja, J. M.; Benson, E. E.; Sharp, I. D.; Kubiak, C. P. Direct observation of the reduction of carbon dioxide by rhenium bipyridine catalysts. *Energy. Environ. Sci.* **2013**, *6*, 3748–3755.

(527) Sampson, M. D.; Nguyen, A. D.; Grice, K. A.; Moore, C. E.; Rheingold, A. L.; Kubiak, C. P. Manganese Catalysts with Bulky Bipyridine Ligands for the Electrocatalytic Reduction of Carbon Dioxide: Eliminating Dimerization and Altering Catalysis. *J. Am. Chem. Soc.* **2014**, *136*, 5460–5471.

(528) Machan, C. W.; Sampson, M. D.; Chabolla, S. A.; Dang, T.; Kubiak, C. P. Developing a Mechanistic Understanding of Molecular Electrocatalysts for CO2 Reduction using Infrared Spectroelectrochemistry. *Organometallics* **2014**, *33*, 4550–4559.

(529) Machan, C. W.; Stanton, C. J.; Vandezande, J. E.; Majetich, G. F.; Schaefer, H. F.; Kubiak, C. P.; Agarwal, J. Electrocatalytic Reduction of Carbon Dioxide by Mn(CN)(2,2'-bipyridine)(CO)3: CN Coordination Alters Mechanism. *Inorg. Chem.* **2015**, *54*, 8849–8856.

(530) Sung, S.; Li, X.; Wolf, L. M.; Meeder, J. R.; Bhuvanesh, N. S.; Grice, K. A.; Panetier, J. A.; Nippe, M. Synergistic Effects of Imidazolium-Functionalization on fac-Mn (CO) 3 Bipyridine Catalyst Platforms for Electrocatalytic Carbon Dioxide Reduction. *J. Am. Chem. Soc.* **2019**, *141*, 6569–6582.

(531) Riplinger, C.; Carter, E. A. Influence of weak Brønsted acids on electrocatalytic CO2 reduction by manganese and rhenium bipyridine catalysts. *ACS Catal.* **2015**, *5*, 900–908.

(532) Song, J.; Klein, E. L.; Neese, F.; Ye, S. The Mechanism of Homogeneous CO2 Reduction by Ni(cyclam): Product Selectivity, Concerted Proton-Electron Transfer and C-O Bond Cleavage. *Inorg. Chem.* **2014**, *53*, 7500–7507.

(533) Kelly, C. A.; Mulazzani, Q. G.; Venturi, M.; Blinn, E. L.; Rodgers, M. A. J. The Thermodynamics and Kinetics of CO2 and H+ Binding to Ni(cyclam)+ in Aqueous Solution. *J. Am. Chem. Soc.* **1995**, *117*, 4911–4919.

(534) Froehlich, J. D.; Kubiak, C. P. The homogeneous reduction of CO2 by [Ni (cyclam)]+: increased catalytic rates with the addition of a CO scavenger. *J. Am. Chem. Soc.* **2015**, *137*, 3565–3573.

(535) Costentin, C.; Passard, G.; Robert, M.; Savéant, J.-M. Ultraefficient homogeneous catalyst for the CO2-to-CO electrochemical conversion. *Proc. Natl. Acad. Sci.* **2014**, *111*, 14990–14994.

(536) Römelt, C.; Song, J.; Tarrago, M.; Rees, J. A.; van Gastel, M.; Weyhermüller, T.; DeBeer, S.; Bill, E.; Neese, F.; Ye, S. Electronic Structure of a Formal Iron(0) Porphyrin Complex Relevant to CO2 Reduction. *Inorg. Chem.* **2017**, *56*, 4745–4750.

(537) Bonin, J.; Maurin, A.; Robert, M. Molecular catalysis of the electrochemical and photochemical reduction of CO2 with Fe and Co metal based complexes. Recent advances. *Coord. Chem. Rev.* **2017**, *334*, 184–198.

(538) Fukuzumi, S.; Lee, Y.-M.; Ahn, H. S.; Nam, W. Mechanisms of catalytic reduction of CO 2 with heme and nonheme metal complexes. *Chemical science* **2018**, *9*, 6017–6034.

(539) Davethu, P. A.; de Visser, S. P. CO2 Reduction on an Iron-Porphyrin Center: A Computational Study. *J. Phys. Chem. A* **2019**, *123*, 6527–6535.

(540) Costentin, C.; Drouet, S.; Passard, G.; Robert, M.; Savéant, J.-M. Proton-Coupled Electron Transfer Cleavage of Heavy-Atom Bonds in Electrocatalytic Processes. Cleavage of a C-O Bond in the Catalyzed Electrochemical Reduction of CO2. *J. Am. Chem. Soc.* **2013**, *135*, 9023–9031.

(541) Haviv, E.; Azaiza-Dabbah, D.; Carmieli, R.; Avram, L.; Martin, J. M.; Neumann, R. A thiourea tether in the second coordination sphere as a binding site for CO2 and a proton donor promotes the electrochemical reduction of CO2 to CO catalyzed by a rhenium bipyridine-type complex. *J. Am. Chem. Soc.* **2018**, *140*, 12451–12456.

(542) Hong, D.; Tsukakoshi, Y.; Kotani, H.; Ishizuka, T.; Kojima, T. Visible-Light-Driven Photocatalytic CO2 Reduction by a Ni(II) Complex Bearing a Bioinspired Tetradentate Ligand for Selective CO Production. *J. Am. Chem. Soc.* **2017**, *139*, 6538–6541.

(543) Dubey, A.; Nencini, L.; Fayzullin, R. R.; Nervi, C.; Khusnutdinova, J. R. Bio-Inspired Mn(I) Complexes for the Hydrogenation of CO2 to Formate and Formamide. *ACS Catal.* **2017**, *7*, 3864–3868.

(544) Dutta, A.; Lense, S.; Hou, J.; Engelhard, M. H.; Roberts, J. A. S.; Shaw, W. J. Minimal Proton Channel Enables H2 Oxidation and Production with a Water-Soluble Nickel-Based Catalyst. *J. Am. Chem. Soc.* **2013**, *135*, 18490–18496.

(545) Schmeier, T. J.; Dobereiner, G. E.; Crabtree, R. H.; Hazari, N. Secondary Coordination Sphere Interactions Facilitate the Insertion Step in an Iridium(III) CO2 Reduction Catalyst. *J. Am. Chem. Soc.* **2011**, *133*, 9274–9277.

(546) Ngo, K. T.; McKinnon, M.; Mahanti, B.; Narayanan, R.; Grills, D. C.; Ertem, M. Z.; Rochford, J. Turning on the Protonation-First Pathway for Electrocatalytic CO2 Reduction by Manganese Bipyridyl Tricarbonyl Complexes. *J. Am. Chem. Soc.* **2017**, *139*, 2604–2618.

(547) DuBois, D. L. Development of Molecular Electrocatalysts for Energy Storage. *Inorg. Chem.* **2014**, *53*, 3935–3960.

(548) Neese, F. The ORCA program system. *Interdiscip. Rev. Comput. Mol. Sci* **2012**, *2*, 73–78.

(549) Bhattacharjee, A.; Andreiadis, E. S.; Chavarot-Kerlidou, M.; Fontecave, M.; Field, M. J.; Artero, V. A Computational Study of the Mechanism of Hydrogen Evolution by Cobalt(Diimine-Dioxime) Catalysts. *Chem.: Eur. J* **2013**, *19*, 15166–15174.

(550) Aktaş, A. H.; Şanlı, N.; Pekcan, G. Spectrometric Determination of pK. *Acta Chim. Slov* **2006**, *53*, 214–218.

(551) Raamat, E.; Kaupmees, K.; Ovsjannikov, G.; Trummal, A.; Kütt, A.; Saame, J.; Koppel, I.; Kaljurand, I.; Lipping, L.; Rodima, T. Acidities of strong neutral Brønsted acids in different media. *Journal of Physical Organic Chemistry* **2013**, *26*, 162–170.

(552) Matsubara, Y. Unified Benchmarking of Electrocatalysts in Noninnocent Second Coordination Spheres for CO2 Reduction. *ACS Energy Lett.* **2019**, *4*, 1999–2004.

(553) Roy, L. E.; Jakubikova, E.; Guthrie, M. G.; Batista, E. R. Calculation of One-Electron Redox Potentials Revisited. Is It Possible to Calculate Accurate Potentials with Density Functional Methods? *J. Phys. Chem. A* **2009**, *113*, 6745–6750.

(554) Roy, L. E.; Batista, E. R.; Hay, P. J. Theoretical Studies on the Redox Potentials of Fe Dinuclear Complexes as Models for Hydrogenase. *Inorg. Chem.* **2008**, *47*, 9228–9237.

(555) Canaguier, S.; Fourmond, V.; Perotto, C. U.; Fize, J.; Pecaut, J.; Fontecave, M.; Field, M. J.; Artero, V. Catalytic hydrogen production by a Ni-Ru mimic of NiFe hydrogenases involves a proton-coupled electron transfer step. *Chem. Commun.* **2013**, *49*, 5004–5006.

(556) Salomon, O.; Reiher, M.; Hess, B. A. Assertion and validation of the performance of the B3LYP* functional for the first transition metal row and the G2 test set. *J. Chem. Phys.* **2002**, *117*, 4729–4737.

(557) Swart, M. Accurate Spin-State Energies for Iron Complexes. *J. Chem. Theory Comput* **2008**, *4*, 2057–2066.

(558) Ioannidis, E. I.; Kulik, H. J. Towards quantifying the role of exact exchange in predictions of transition metal complex properties. *J. Chem. Phys.* **2015**, *143*, 034104.

(559) Kepp, K. P. Theoretical Study of Spin Crossover in 30 Iron Complexes. *Inorg. Chem.* **2016**, *55*, 2717–2727.

(560) Droghetti, A.; Alfè, D.; Sanvito, S. Assessment of density functional theory for iron(II) molecules across the spin-crossover transition. *J. Chem. Phys.* **2012**, *137*, 124303.

(561) Cometto, C.; Chen, L.; Lo, P.-K.; Guo, Z.; Lau, K.-C.; Anxolabéhère-Mallart, E.; Fave, C.; Lau, T.-C.; Robert, M. Highly selective molecular catalysts for the CO2-to-CO electrochemical conversion at very low overpotential. Contrasting Fe vs Co quaterpyridine complexes upon mechanistic studies. *ACS Catalysis* **2018**, *8*, 3411–3417.

(562) Wright, T. C.; Wilkinson, G.; Motevalli, M.; Hursthouse, M. B. (η 2-Acetonitrile) bis (η 5-cyclopentadienyl) molybdenum (II): the first structurally characterized complex containing an η 2-nitrile ligand. *J. Chem. Soc., Dalton Trans.* **1986**, 2017–2019.

(563) Barrera, J.; Sabat, M.; Harman, W. D. Crystal structure of an. eta. 2-acetonitrile complex of tungsten (II): acetonitrile as a four-electron donor. *J. Am. Chem. Soc.* **1991**, *113*, 8178–8180.

(564) Garcia, J. J.; Jones, W. D. Reversible Cleavage of Carbon- Carbon Bonds in Benzonitrile Using Nickel (0). *Organometallics* **2000**, *19*, 5544–5545.

(565) Chetcuti, P. A.; Knobler, C. B.; Hawthorne, M. F. Formation of. eta. 2-side-bonded aryl nitrile complexes from 4-metallaisoxazolin-5-one species and their application in the thermal and photochemical activation of carbon-hydrogen bonds. *Organometallics* **1988**, *7*, 650–660.

(566) Lorente, P.; Carfagna, C.; Etienne, M.; Donnadieu, B. Alkyne and Nitrile as $\eta 2$ (3e) Ligands in [Tris (pyrazolyl) borato] niobium (I) Complexes. Synthesis, Structure, and Coupling Reaction. *Organometallics* **1996**, *15*, 1090–1092.

(567) Butschke, B.; Fillman, K. L.; Bendikov, T.; Shimon, L. J. W.; Diskin-Posner, Y.; Leitus, G.; Gorelsky, S. I.; Neidig, M. L.; Milstein, D. How Innocent are Potentially Redox Non-Innocent Ligands? Electronic Structure and Metal Oxidation States in Iron-PNN Complexes as a Representative Case Study. *Inorg. Chem.* **2015**, *54*, 4909–4926.

(568) Schlimgen, A. W.; Heaps, C. W.; Mazziotti, D. A. Entangled Electrons Foil Synthesis of Elusive Low-Valent Vanadium Oxo Complex. *J. Phys. Chem. Lett* **2016**, *7*, 627–631.

(569) Ortuño, M. A.; Cramer, C. J. Multireference Electronic Structures of Fe-Pyridine(diimine) Complexes over Multiple Oxidation States. *J. Phys. Chem. A* **2017**, *121*, 5932–5939.

(570) Sayfutyarova, E. R.; Sun, Q.; Chan, G. K.-L.; Knizia, G. Automated construction of molecular active spaces from atomic valence orbitals. *J. Chem. Theory Comput* **2017**, *13*, 4063–4078.

(571) Khedkar, A.; Roemelt, M. Active Space Selection Based on Natural Orbital Occupation Numbers From N-Electron Valence Perturbation Theory. *J. Chem. Theory Comput* **2019**.

(572) Stein, C. J.; Reiher, M. Automated selection of active orbital spaces. *J. Chem. Theory Comput* **2016**, *12*, 1760–1771.

(573) Stein, C. J.; Reiher, M. Automated identification of relevant frontier orbitals for chemical compounds and processes. *CHIMIA* **2017**, *71*, 170–176.

(574) Stein, C. J.; Reiher, M. autoCAS: A Program for Fully Automated Multiconfigurational Calculations. *J. Comput. Chem.* **2019**, *40*, 2216–2226.

(575) Vogt, M.; Gargir, M.; Iron, M. A.; Diskin-Posner, Y.; Ben-David, Y.; Milstein, D. A New Mode of Activation of CO2 by Metal-Ligand Cooperation with Reversible C-C and M-O Bond Formation at Ambient Temperature. *Chem.–Eur. J.* **2012**, *18*, 9194–9197.

(576) Vogt, M.; Nerush, A.; Diskin-Posner, Y.; Ben-David, Y.; Milstein, D. Reversible CO2 binding triggered by metal-ligand cooperation in a rhenium(i) PNP pincer-type complex and the reaction with dihydrogen. *Chem. Sci.* **2014**, *5*, 2043–2051.

(577) Stichauer, R.; Helmers, A.; Bremer, J.; Rohdenburg, M.; Wark, A.; Lork, E.; Vogt, M. Rhenium(I) Triscarbonyl Complexes with Redox-Active Amino- and Iminopyridine Ligands: Metal-Ligand Cooperation as Trigger for the Reversible Binding of CO2 via a Dearmomatization/Rearomatization Reaction Sequence. *Organometallics* **2017**, *36*, 839–848.

(578) Flynn, S. R.; Wass, D. F. Transition Metal Frustrated Lewis Pairs. *ACS Catal.* **2013**, *3*, 2574–2581.

(579) Balaraman, E.; Gunanathan, C.; Zhang, J.; Shimon, L. J. W.; Milstein, D. Efficient hydrogenation of organic carbonates, carbamates and formates indicates alternative routes to methanol based on CO2 and CO. *Nat. Chem.* **2011**, *3*, 609–614.

(580) Sieh, D.; Lacy, D. C.; Peters, J. C.; Kubiak, C. P. Reduction of CO2 by Pyridine Monoimine Molybdenum Carbonyl Complexes: Cooperative Metal-Ligand Binding of CO2. *Chem.–Eur. J.* **2015**, *21*, 8497–8503.

(581) Dalle, K. E.; Warnan, J.; Leung, J. J.; Reuillard, B.; Karmel, I. S.; Reisner, E. Electro- and solar-driven fuel synthesis with first row transition metal complexes. *Chem. Rev.* **2019**, *119*, 2752–2875.

(582) Zhang, B.; Sun, L. Artificial photosynthesis: opportunities and challenges of molecular catalysts. *Chem. Soc. Rev.* **2019**, *48*, 2216–2264.

(583) Razzak, S. A.; Ali, S. A. M.; Hossain, M. M.; deLasa, H. Biological CO2 fixation with production of microalgae in wastewater–a review. *Renew. Sustain. Energy Rev* **2017**, *76*, 379–390.

(584) García de Arquer, F. P. et al. CO2 electrolysis to multicarbon products at activities greater than 1 A cm^{-1}. *Science* **2020**, *367*, 661–666.

(585) Hori, Y.; Kikuchi, K.; Murata, A.; Suzuki, S. Production of methane and ethylene in electrochemical reduction of carbon dioxide at copper electrode in aqueous hydrogencarbonate solution. *Chem. Lett.* **1986**, *15*, 897–898.

(586) Wang, M.; Chen, L.; Lau, T.-C.; Robert, M. A hybrid Co quaterpyridine complex/carbon nanotube catalytic material for CO2 reduction in water. *Angew. Chem. Int. Ed.* **2018**, *57*, 7769–7773.

(587) Kaminsky, C. J.; Wright, J.; Surendranath, Y. Graphite-conjugation enhances porphyrin electrocatalysis. *ACS Catal.* **2019**, *9*, 3667–3671.

(588) Zhu, M.; Chen, J.; Huang, L.; Ye, R.; Xu, J.; Han, Y.-F. Covalently grafting cobalt porphyrin onto carbon nanotubes for efficient CO2 electroreduction. *Angew. Chem. Int. Ed.* **2019**, *58*, 6595–6599.

(589) Zhanaidarova, A.; Jones, S. C.; Despagnet-Ayoub, E.; Pimentel, B. R.; Kubiak, C. P. Re (tBu-bpy)(CO) 3Cl Supported on Multi-Walled Carbon Nanotubes Selectively Reduces CO2 in Water. *J. Am. Chem. Soc.* **2019**, *141*, 17270–17277.

(590) Smith, P. T.; Nichols, E. M.; Cao, Z.; Chang, C. J. Hybrid Catalysts for Artificial Photosynthesis: Merging Approaches from Molecular, Materials, and Biological Catalysis. *Acc. Chem. Res.* **2020**, *53*, 575–587.

(591) Costentin, C.; Savéant, J.-M. Concepts and tools for mechanism and selectivity analysis in synthetic organic electrochemistry. *Proc. Natl. Acad. Sci. U.S.A.* **2019**, *116*, 11147–11152.

(592) Machan, C. W. Recent advances in spectroelectrochemistry related to molecular catalytic processes. *Curr Opin Electrochem* **2019**, *15*, 42–49.

(593) Fisher, B. J.; Eisenberg, R. Electrocatalytic reduction of carbon dioxide by using macrocycles of nickel and cobalt. *J. Am. Chem. Soc.* **1980**, *102*, 7361–7363.

(594) Beley, M.; Collin, J.-P.; Ruppert, R.; Sauvage, J.-P. Nickel (II)-cyclam: an extremely selective electrocatalyst for reduction of CO 2 in water. *ChemComm* **1984**, 1315–1316.

(595) Hawecker, J.; Lehn, J.-M.; Ziessel, R. Electrocatalytic reduction of carbon dioxide mediated by Re (bipy)(CO) 3 Cl (bipy= 2, 2'-bipyridine). *ChemComm* **1984**, 328–330.

(596) Chabolla, S. A.; Machan, C. W.; Yin, J.; Dellamary, E.; Sahu, S.; Gianneschi, N.; Gilson, M.; Tezcan, F.; Kubiak, C. Bio-inspired CO2 reduction by a rhenium tricarbonyl bipyridine-based catalyst appended to amino acids and peptidic platforms: incorporating proton relays and hydrogen-bonding functional groups. *Faraday Discuss.* **2017**, *198*, 279–300.

(597) Matson, B. D.; McLoughlin, E. A.; Armstrong, K. C.; Waymouth, R. M.; Sarangi, R. Effect of Redox Active Ligands on the Electrochemical Properties of Manganese Tricarbonyl Complexes. *Inorg. Chem.* **2019**, *58*, 7453–7465.

(598) Myren, T. H.; Alherz, A.; Thurston, J. R.; Stinson, T. A.; Huntzinger, C. G.; Musgrave, C. B.; Luca, O. R. Mn-Based Molecular Catalysts for the Electrocatalytic Disproportionation of CO_2 into CO and CO_3^-. *ACS Catal.* **2020**, *10*, 1961–1968.

(599) Su, X.; McCardle, K. M.; Chen, L.; Panetier, J. A.; Jurss, J. W. Robust and Selective Cobalt Catalysts Bearing Redox-Active Bipyridyl-N-heterocyclic Carbene Frameworks for Electrochemical CO2 Reduction in Aqueous Solutions. *ACS Catal.* **2019**, *9*, 7398–7408.

(600) Che, C.-M.; Chan, C.-W.; Yang, S.-M.; Guo, C.-X.; Lee, C.-Y.; Peng, S.-M. Synthesis, properties and crystal structures of iron-(II) and-(III) complexes of 2, 2': 6', 2 ": 6 ", 2"'-quaterpyridine. *J. Chem. Soc., Dalton Trans.* **1995**, 2961–2966.

(601) Lam, K.-M.; Wong, K.-Y.; Yang, S.-M.; Che, C.-M. Cobalt and nickel complexes of 2, 2': 6', 2": 6", 2"'-quaterpyridine as catalysts for electrochemical reduction of carbon dioxide. *J. Chem. Soc., Dalton Trans.* **1995**, 1103–1107.

(602) Cometto, C.; Chen, L.; Anxolabéhère-Mallart, E.; Fave, C.; Lau, T.-C.; Robert, M. Molecular electrochemical catalysis of the CO2-to-CO conversion with a Co complex: A cyclic voltammetry mechanistic investigation. *Organometallics* **2018**, *38*, 1280–1285.

(603) Guo, Z.; Chen, G.; Cometto, C.; Ma, B.; Zhao, H.; Groizard, T.; Chen, L.; Fan, H.; Man, W.-L.; Yiu, S.-M.; Lau, K.-C.; Lau, T.-C.; Robert, M. Selectivity control of CO versus HCOO- production in the visible-light-driven catalytic reduction of CO 2 with two cooperative metal sites. *Nat. Catal.* **2019**, *2*, 801–808.

(604) Guo, Z.; Cheng, S.; Cometto, C.; Anxolabéhère-Mallart, E.; Ng, S.-M.; Ko, C.-C.; Liu, G.; Chen, L.; Robert, M.; Lau, T.-C. Highly efficient and selective photocatalytic CO2 reduction by iron and cobalt quaterpyridine complexes. *J. Am. Chem. Soc.* **2016**, *138*, 9413–9416.

(605) Cometto, C.; Chen, L.; Mendoza, D.; Lassalle-Kaiser, B.; Lau, T.-C.; Robert, M. An Iron Quaterpyridine Complex as Precursor for the Electrocatalytic Reduction of CO2 to Methane. *ChemSusChem* **2019**, *12*, 4500–4505.

(606) Pati, P. B.; Wang, R.; Boutin, E.; Diring, S.; Jobic, S.; Barreau, N.; Odobel, F.; Robert, M. Photocathode functionalized with a molecular cobalt catalyst for selective carbon dioxide reduction in water. *Nat. Commun* **2020**, *11*, 1–9.

(607) Pavlishchuk, V. V.; Addison, A. W. Conversion constants for redox potentials measured versus different reference electrodes in acetonitrile solutions at 25°C. *Inorg. Chim. Acta* **2000**, *298*, 97–102.

(608) Sampson, M. D.; Kubiak, C. P. Manganese electrocatalysts with bulky bipyridine ligands: Utilizing Lewis acids to promote carbon dioxide reduction at low overpotentials. *J. Am. Chem. Soc.* **2016**, *138*, 1386–1393.

(609) Garza, A. J.; Pakhira, S.; Bell, A. T.; Mendoza-Cortes, J. L.; Head-Gordon, M. Reaction mechanism of the selective reduction of CO_2 to CO by a tetraaza $[Co^{II} N_4 H]^{2+}$ complex in the presence of protons. *Phys. Chem. Chem. Phys.* **2018**, *20*, 24058–24064.

(610) Garza, A. J.; Bell, A. T.; Head-Gordon, M. Is subsurface oxygen necessary for the electrochemical reduction of CO2 on copper? *J. Phys. Chem. Lett.* **2018**, *9*, 601–606.

(611) Jensen, K. P.; Roos, B. O.; Ryde, U. Performance of density functionals for first row transition metal systems. *J. Chem. Phys.* **2007**, *126*, 014103.

(612) Moltved, K. A.; Kepp, K. P. Chemical bond energies of 3d transition metals studied by density functional theory. *J. Chem. Theory Comput* **2018**, *14*, 3479–3492.

(613) Moltved, K. A.; Kepp, K. P. The Metal Hydride Problem of Computational Chemistry: Origins and Consequences. *J. Phys. Chem. A* **2019**, *123*, 2888–2900.

(614) Jensen, K. P.; Cirera, J. Accurate computed enthalpies of spin crossover in iron and cobalt complexes. *J. Phys. Chem. A* **2009**, *113*, 10033–10039.

(615) Cirera, J.; Via-Nadal, M.; Ruiz, E. Benchmarking density functional methods for calculation of state energies of first row spin-crossover molecules. *Inorg. Chem.* **2018**, *57*, 14097–14105.

(616) Arumugam, K.; Becker, U. Computational redox potential predictions: applications to inorganic and organic aqueous complexes, and complexes adsorbed to mineral surfaces. *Minerals* **2014**, *4*, 345–387.

(617) Thom, A. J.; Sundstrom, E. J.; Head-Gordon, M. LOBA: a localized orbital bonding analysis to calculate oxidation states, with application to a model water oxidation catalyst. *Phys. Chem. Chem. Phys.* **2009**, *11*, 11297–11304.

(618) Aresta, M.; Nobile, C. F.; Albano, V. G.; Forni, E.; Manassero, M. New nickel–carbon dioxide complex: synthesis, properties, and crystallographic characterization of (carbon dioxide)-bis (tricyclohexylphosphine) nickel. *ChemComm* **1975**, 636–637.

(619) Nguyen, V.-H.; Nguyen, B.-S.; Jin, Z.; Shokouhimehr, M.; Jang, H. W.; Hu, C.; Singh, P.; Raizada, P.; Peng, W.; Lam, S. S., et al. Towards artificial photosynthesis: Sustainable hydrogen utilization for photocatalytic reduction of CO2 to high-value renewable fuels. *Chem. Eng. J* **2020**, 126184.

(620) Luo, Y.-H.; Dong, L.-Z.; Liu, J.; Li, S.-L.; Lan, Y.-Q. From molecular metal complex to metal-organic framework: The CO2 reduction photocatalysts with clear and tunable structure. *Coord. Chem. Rev.* **2019**, *390*, 86–126.

(621) Sun, L.; Reddu, V.; Fisher, A. C.; Wang, X. Electrocatalytic reduction of carbon dioxide: opportunities with heterogeneous molecular catalysts. *Energy Environ. Sci.* **2020**, *13*, 374–403.

(622) Costentin, C.; Drouet, S.; Robert, M.; Savéant, J.-M. Turnover numbers, turnover frequencies, and overpotential in molecular catalysis of electrochemical reactions. Cyclic voltammetry and preparative-scale electrolysis. *J. Am. Chem. Soc.* **2012**, *134*, 11235–11242.

(623) Costentin, C.; Drouet, S.; Robert, M.; Savéant, J.-M. Correction to Turnover Numbers, Turnover Frequencies, and Overpotential in Molecular Catalysis of Electrochemical Reactions. Cyclic Voltammetry and Preparative-Scale Electrolysis. *J. Am. Chem. Soc.* **2012**, *134*, 19949–19950.

(624) Karton, A.; O'Reilly, R. J.; Radom, L. Assessment of theoretical procedures for calculating barrier heights for a diverse set of water-catalyzed proton-transfer reactions. *J. Phys. Chem. A* **2012**, *116*, 4211–4221.

(625) Gonell, S.; Lloret-Fillol, J.; Miller, A. J. An Iron Pyridyl-Carbene Electrocatalyst for Low Overpotential CO2 Reduction to CO. *ACS Catal.* **2020**, *11*, 615–626.

(626) Kozuch, S. A refinement of everyday thinking: the energetic span model for kinetic assessment of catalytic cycles. *Wiley Interdiscip. Rev. Comput. Mol. Sci.* **2012**, *2*, 795–815.

Appendix A

MP2-EDA for Radicals

A.1 Long-Range Behavior of each Energy Component

The asymptotic behaviors of the four energy components are shown in Fig. A.1. All terms show the correct behavior in the long range: frozen interaction and charge transfer decay exponentially, while polarization and dispersion show $1/r^4$ and $1/r^6$ decay, respectively. The test system for frozen and polarization energy is a single fragment Li atom with an external charge, and dispersion and charge transfer are examined on a Li$\cdots$He complex (doublet). These tests are analogous to those employed previously for closed-shell MP2-ALMO-EDA. [212]

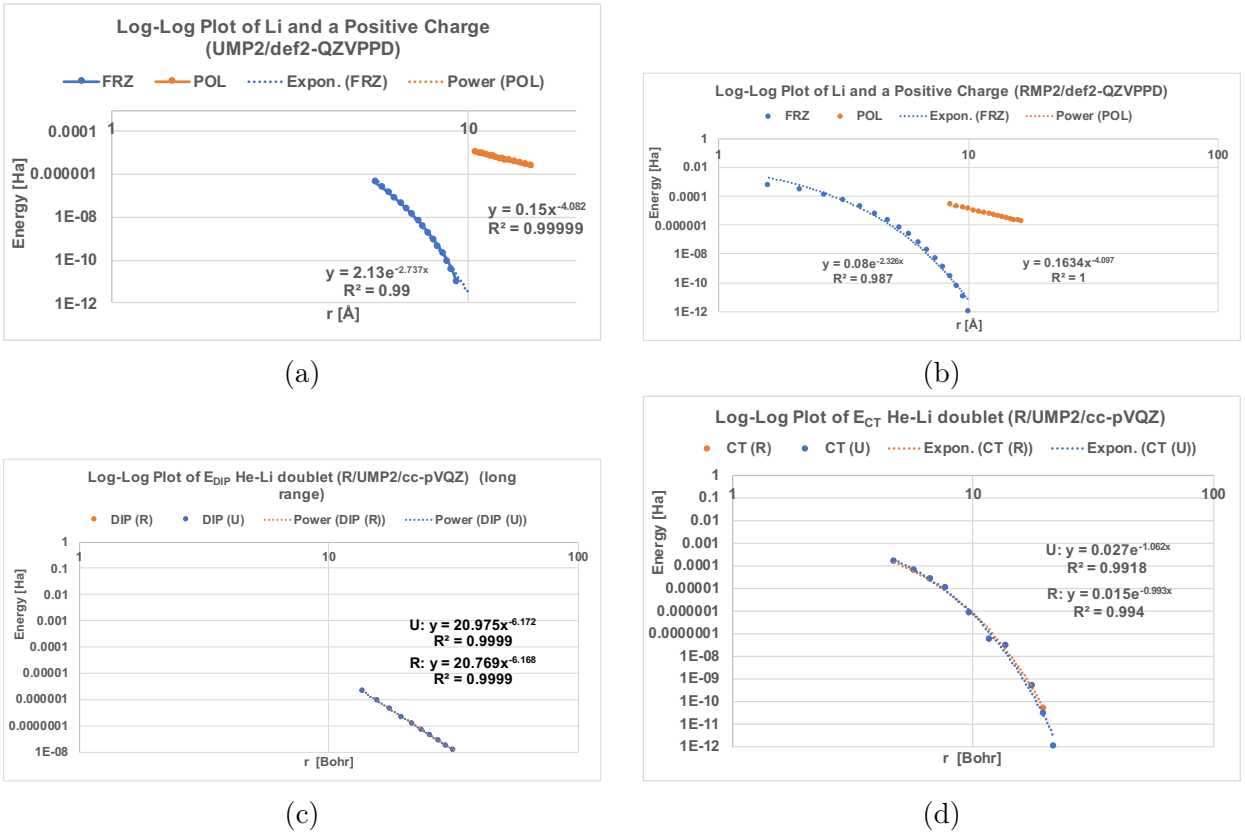

Figure A.1: a) Log-Log plot for the decay of both the frozen and polarization terms for a Li atom interacting with an external charge (UMP2); b) Log-Log plot for the decay of both the frozen and polarization terms for the same Li$^\bullet$–external charge complex (RMP2); c) Log-Log plot for the decay of dispersion energy for the He$\cdots$Li$^\bullet$ complex with both UMP2 and RMP2; d) Log-Log plot for the decay of charge transfer energy for the Li$^\bullet$–external charge complex with both UMP2 and RMP2.

A.2 TA13 Benchmark Set

All geometries and reference interaction energies were taken from Ref. [209]. All calculations were performed with the aug-cc-pVTZ basis and the RI-aug-cc-pVTZ auxiliary basis for all elements except Li and Be for which RI-cc-pVQZ was employed. [250–254] Both UMP2-EDA (Table A.1) and RMP2-EDA (Table A.2) results are provided below.

Table A.1: UMP2-EDA results for the TA13 benchmark set (all energies in kJ/mol). Errors in total interaction energies are evaluated against the reference values given in Ref. [209].

Complex	ΔE_{FRZ}^{HF}	ΔE_{POL}^{HF}	ΔE_{CT}^{HF}	ΔE_{INT}^{HF}	ΔE_{FRZ}^{MP2}	ΔE_{POL}^{MP2}	ΔE_{DISP}^{MP2}	ΔE_{CT}^{MP2}	ΔE_{INT}^{MP2}	ΔE_{INT}	Error
H2O-Al	58.25	-63.84	-9.60	-15.19	25.89	-8.75	-20.72	-7.04	-10.63	-25.82	5.94
H2O-Be+	63.04	-292.48	-36.06	-265.49	39.76	-13.81	-12.04	-7.10	6.81	-258.68	9.94
H2O-Br	20.98	-6.90	-8.73	5.35	8.46	-2.80	-12.82	-8.28	-15.44	-10.09	4.64
HOH CH3	4.31	-1.97	-2.82	-0.48	2.50	-0.98	-5.39	-2.13	-5.99	-6.48	0.59
H2O-Cl	20.76	-5.55	-9.55	5.66	28.57	-22.49	-12.08	-9.59	-15.58	-9.93	5.51
H2O-F	47.00	-5.31	-17.94	23.75	13.58	-4.73	-11.66	-19.17	-21.97	1.78	17.80
H2O-Li	27.50	-62.48	-7.34	-42.31	13.00	-3.73	-8.01	-4.16	-2.91	-45.22	6.60
H2O-HNH2+	-24.56	-47.72	-23.66	-95.94	21.24	-6.91	-13.48	-9.00	-8.15	-104.09	-3.35
H2O-NH3+	-27.38	-18.63	-11.12	-57.13	13.11	-3.35	-12.16	-11.24	-13.63	-70.77	5.99
FH-BH2	5.88	-6.57	-9.29	-9.99	5.11	-2.22	-5.56	-3.67	-6.34	-16.32	0.57
HF-CO+	85.64	-100.15	-71.59	-86.10	20.13	-8.96	-23.01	-45.31	-57.15	-143.24	-21.20
FH-NH2	-4.68	-16.56	-14.83	-36.08	17.57	-7.43	-9.88	-5.89	-5.63	-41.71	-0.55
FH-OH	-4.41	-8.63	-6.74	-19.78	10.10	-3.32	-6.58	-4.16	-3.97	-23.75	1.11

Table A.2: RMP2-EDA results for the TA13 benchmark set (all energies in kJ/mol). Errors in total interaction energies are evaluated against the reference values given in Ref. [209].

Complex	ΔE^{HF}_{FRZ}	ΔE^{HF}_{POL}	ΔE^{HF}_{CT}	ΔE^{HF}_{INT}	ΔE^{MP2}_{FRZ}	ΔE^{MP2}_{POL}	ΔE^{MP2}_{DISP}	ΔE^{MP2}_{CT}	ΔE^{MP2}_{INT}	ΔE_{INT}	Error
H_2O-Al	70.88	-74.52	-9.78	-13.42	26.00	-11.59	-21.50	-6.96	-14.05	-27.47	4.29
H_2O-Be^+	63.01	-291.17	-37.22	-265.38	39.78	-15.69	-11.80	-5.53	6.77	-258.61	10.01
H_2O-Br	20.82	-5.88	-9.44	5.50	8.04	-2.62	-12.91	-8.19	-15.69	-10.19	4.54
$HOH-CH_3$	4.49	-1.89	-3.00	-0.40	2.34	-1.00	-5.49	-2.11	-6.26	-6.66	0.41
H_2O-Cl	20.75	-4.59	-10.16	6.00	8.15	-2.48	-12.19	-9.51	-16.03	-10.02	5.42
H_2O-F	47.29	-4.10	-17.39	25.81	13.33	-5.44	-11.70	-18.95	-22.76	3.05	19.07
H_2O-Li	27.46	-62.41	-7.32	-42.27	13.03	-3.78	-8.00	-4.15	-2.89	-45.16	6.66
$H_2O-HNH_2^+$	-25.09	-47.72	-23.69	-96.50	21.91	-7.15	-13.50	-8.92	-7.65	-104.15	-3.41
$H_2O-NH_3^+$	-27.03	-17.46	-11.51	-56.00	12.76	-4.02	-12.26	-11.25	-14.76	-70.76	6.00
$FH-BH_2$	5.94	-6.09	-9.65	-9.80	5.12	-2.56	-5.56	-3.63	-6.63	-16.43	0.46
$HF-CO^+$	79.22	-89.60	-81.56	-91.94	42.25	-12.19	-22.14	-35.83	-27.91	-119.86	2.18
$FH-NH_2$	-4.71	-16.46	-14.66	-35.83	17.56	-7.54	-9.88	-5.97	-5.83	-41.66	-0.50
FH−OH	-4.42	-8.59	-6.66	-19.67	10.08	-3.36	-6.58	-4.19	-4.06	-23.73	1.07

A.3 Complexes between Halogenated Benzene Radical Cation and Water

All geometries were fully optimized using ωB97X-D[68]/def2-TZVPPD[247, 248] in the gas phase with no constraints. An ECP was used for iodine. [249] The RMP2-EDA results for F-, Cl-, and Br-substituted benzene radical cations were calculated with aug-cc-pVTZ and its corresponding RI basis, while for iodobenzene the def2-TZVPPD basis set (with RI-def2-TZVPPD) and an ECP were employed. The full results are presented in Table A.3. For comparison, we also performed DFT-based ALMO-EDA using ωB97M-V [70] with the same choice of basis sets for these complexes, whose results are shown in Table A.4. To make the results comparable to those of RMP2-EDA, the original ALMO scheme [83] was employed, and the use of fragment electric response functions (FERFs) [32] for polarization makes a small difference (e.g. 0.5 kJ/mol for the hydrogen-bonded complex of water chlorobenzene radical cation). The dominant complementary occupied-virtual orbital pairs (COVPs) for the bromobenzene radical cation–water complexes (Fig. A.2) were also generated at the ωB97M-V/aug-cc-pVTZ level of theory.

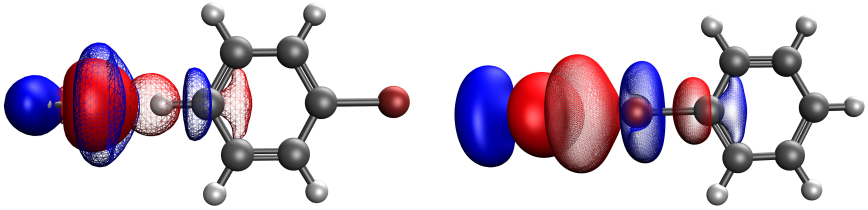

(a) (b)

Figure A.2: The main COVP for (a) the hydrogen-bonded form of the $H_2O\cdots C_6H_5Br^{+\bullet}$ complex, and (b) the halogen-bonded form of the same complex (filled: donor orbital; meshed: acceptor orbital).

Table A.3: RMP2-EDA results for the halogenated benzene radical cations interacting with H_2O. All energies are in kJ/mol, and the reference values for total interaction energies were calculated at the ωB97M(2)/def2-TZVPPD level of theory.

Complex	ΔE_{FRZ}^{HF}	ΔE_{POL}^{HF}	ΔE_{CT}^{HF}	ΔE_{INT}^{HF}	ΔE_{FRZ}^{MP2}	ΔE_{POL}^{MP2}	ΔE_{DISP}^{MP2}	ΔE_{CT}^{MP2}	ΔE_{INT}^{MP2}	ΔE_{INT}	ΔE_{REF}	Error
Hydro Bz-F	-23.65	-9.36	-3.10	-36.12	9.12	-1.91	-8.09	-2.80	-3.68	-39.80	-39.84	-0.04
Hydro Bz-Cl	-22.85	-8.79	-2.87	-34.51	9.68	-1.69	-7.92	-2.64	-2.57	-37.07	-37.45	-0.38
Hydro Bz-Br	-22.62	-8.53	-2.75	-33.90	10.13	-1.56	-7.81	-2.55	-1.79	-35.69	-38.58	-2.89
Hydro Bz-I	-21.53	-7.72	-2.89	-32.15	12.14	-0.94	-6.97	-2.58	1.63	-30.51	-32.70	-2.19
Halo Bz-F	-14.32	-1.25	-0.12	-15.70	-0.34	-0.32	-2.74	-0.36	-3.76	-19.46	-19.42	0.03
Halo Bz-Cl	-15.22	-5.70	-2.61	-23.53	4.33	-1.52	-9.18	-2.92	-9.28	-32.81	-33.36	-0.55
Halo Bz-Br	-14.88	-8.40	-3.75	-27.02	5.79	-2.18	-11.12	-3.95	-11.46	-38.48	-38.16	0.32
Halo Bz-I	-15.22	-13.54	-5.09	-33.84	8.14	-3.32	-12.49	-5.56	-13.25	-47.09	-46.80	0.28

Table A.4: Comparison of RMP2-EDA against DFT-based ALMO-EDA (unrestricted, with ωB97M-V/aug-cc-pVTZ) for the halogenated benzene radical cation–water complexes. All energies are in kJ/mol, and the reference values for total interaction energies were obtained using ωB97M(2)/def2-TZVPPD.

Complex	ΔE_{FRZ}^{DFT}	ΔE_{POL}^{DFT}	ΔE_{DISP}^{DFT}	ΔE_{CT}^{DFT}	ΔE_{INT}^{DFT}	Error
Hydro Bz-F	-17.33	-9.84	-7.89	-4.99	-40.04	0.20
Hydro Bz-Cl	-16.19	-9.07	-7.72	-4.59	-37.58	0.13
Hydro Bz-Br	-15.53	-8.68	-7.63	-4.39	-36.23	-2.35
Hydro Bz-I	-14.19	-7.64	-6.88	-4.27	-32.98	0.28
Halo Bz-F	-14.66	-1.62	-2.92	-0.22	-19.42	-0.05
Halo Bz-Cl	-13.05	-6.71	-8.29	-4.44	-32.49	-0.87
Halo Bz-Br	-12.67	-9.83	-9.93	-6.22	-38.65	0.49
Halo Bz-I	-11.55	-15.84	-12.63	-7.98	-48.00	1.20
Complex	ΔE_{FRZ}^{MP2}	ΔE_{POL}^{MP2}	ΔE_{DISP}^{MP2}	ΔE_{CT}^{MP2}	ΔE_{INT}^{MP2}	Error
Hydro Bz-F	-14.54	-11.27	-8.09	-5.90	-39.80	-0.04
Hydro Bz-Cl	-13.17	-10.47	-7.92	-5.51	-37.07	-0.38
Hydro Bz-Br	-12.49	-10.08	-7.81	-5.30	-35.69	-2.89
Hydro Bz-I	-9.39	-8.66	-6.97	-5.47	-30.49	-2.19
Halo Bz-F	-14.66	-1.58	-2.74	-0.48	-19.46	0.03
Halo Bz-Cl	-10.89	-7.22	-9.18	-5.53	-32.81	-0.55
Halo Bz-Br	-9.08	-10.58	-11.12	-7.70	-38.48	0.32
Halo Bz-I	-7.07	-16.86	-12.49	-10.65	-47.07	0.28

A.4 Anionic CO_2 radical N-heterocycle complexes

All reference total interaction energies were obtained with ωB97M(2)/def2-QZVPPD and the corresponding auxiliary basis set. The EDA results were obtained with RMP2/aug-cc-pVTZ (with the corresponding RI basis) and the results are presented in Table A.5. For comparison, we also performed DFT-based ALMO-EDA with ωB97M-V/aug-cc-pVTZ and the results are shown in Table A.6. As for the previous set of systems in Sec. A.3, the original ALMO scheme was employed for DFT-based EDA calculations, and the use of FERFs also makes an insignificant difference (e.g. 2 kJ/mol for the hydrogen-bonded Im−$CO_2^{-\bullet}$ complex). The plots electron density / spin density (Fig. A.3) and the dominant COVP (Fig. A.4) were also generated with ωB97M-V/aug-cc-pVTZ.

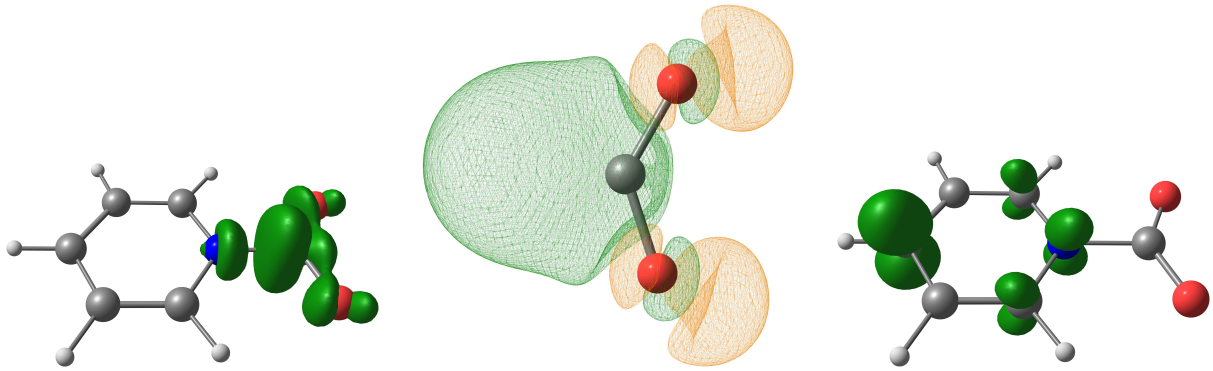

(a) (b) (c)

Figure A.3: (a) RO-HF spin density at the frozen level for the carbamate Py−$CO_2^{-\bullet}$; (b) density difference plot for a $CO_2^{-\bullet}$ radical anion with and without a partial negative charge located 1.5 Å away from the carbon atom (green indicates density depletion and yellow indicates enhancement); (c) fully unconstrained RO-HF spin density for the carbamate Py−$CO_2^{-\bullet}$.

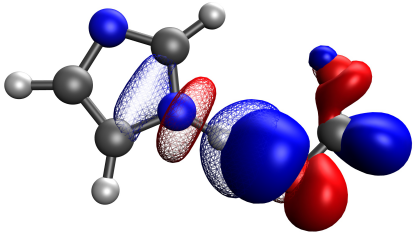

Figure A.4: Most significant COVP for charge transfer in the hydrogen-bonded Im−$CO_2^{-\bullet}$ complex (filled: donor orbital; meshed: acceptor orbital).

Table A.5: RMP2-EDA results for the Py$-CO_2^{+\bullet}$ and Im$-CO_2^{+\bullet}$ complexes. The binding mode is denoted by either (H) for hydrogen bonding or (C) for the carbamate motif. All energies are in kJ/mol and the reference total interaction energies were obtained using ωB97M(2)/def2-QZVPPD.

Complex	ΔE_{FRZ}^{HF}	ΔE_{POL}^{HF}	ΔE_{CT}^{HF}	ΔE_{INT}^{HF}	ΔE_{FRZ}^{MP2}	ΔE_{POL}^{MP2}	ΔE_{DISP}^{MP2}	ΔE_{CT}^{MP2}	ΔE_{INT}^{MP2}	ΔE_{INT}	ΔE_{REF}	Error
Im$-CO_2^{-\bullet}$(H)	-35.65	-43.30	-15.79	-94.74	36.22	-12.70	-22.02	-11.00	-9.50	-104.24	-105.11	0.87
Py$-CO_2^{-\bullet}$ (C)	1276.30	-871.68	-506.94	-102.32	261.26	-95.76	-128.95	-68.32	-31.77	-134.09	-140.49	6.39
Im$BH_2-CO_2^{-\bullet}$(H)	-42.48	-53.69	-19.77	-115.95	38.94	-15.17	-22.98	-12.35	-11.58	-127.53	-128.47	0.94
ImOH$-CO_2^{-\bullet}$ (H)	-38.45	-44.03	-16.41	-98.89	37.28	-13.17	-21.55	-11.04	-8.48	-107.36	-107.72	0.35
Py$BH_2-CO_2^{-\bullet}$(C)	1135.35	-749.09	-578.24	-191.98	234.95	-79.90	-118.37	-79.10	-42.45	-234.43	-241.30	6.87
PyOH$-CO_2^{-\bullet}$(C)	1301.15	-912.34	-463.32	-74.51	267.84	-81.92	-122.73	-95.11	-31.96	-106.46	-113.67	7.20
Im$-CO_2^{-\bullet}$ (C)	1447.40	-1043.19	-454.56	-50.35	288.65	-97.25	-120.48	-41.26	29.62	-20.73	-27.36	6.63
Py$-CO_2^{-\bullet}$ (H)	-9.14	-28.07	-5.29	-42.51	19.80	-5.18	-17.28	-6.29	-8.96	-51.46	-52.51	1.05

Table A.6: Comparison of RMP2-EDA against DFT-based ALMO-EDA (unrestricted, with ωB97M-V/aug-cc-pVTZ) for the Py$-CO_2^{+\bullet}$ and Im$-CO_2^{+\bullet}$ complexes. The binding mode is denoted by either (H) for hydrogen bonding or (C) for the carbamate motif. All energies are in kJ/mol and reference total interaction energies are obtained using ωB97M(2)/def2-QZVPPD.

Complex	ΔE_{FRZ}^{DFT}	ΔE_{POL}^{DFT}	ΔE_{DISP}^{DFT}	ΔE_{CT}^{DFT}	ΔE_{INT}^{DFT}	Error
Im$-CO_2^{-\bullet}$(H)	-18.07	-41.41	-21.58	-21.94	-103.00	2.12
Py$-CO_2^{-\bullet}$ (C)	1270.86	-820.03	-84.05	-513.13	-146.35	-5.87
Im$BH_2-CO_2^{-\bullet}$(H)	-25.65	-52.01	-21.77	-26.94	-126.37	2.10
ImOH$-CO_2^{-\bullet}$ (H)	-19.82	-42.45	-20.99	-24.59	-107.85	-0.14
Py$BH_2-CO_2^{-\bullet}$(C)	1122.99	-710.59	-81.94	-575.88	-245.43	-4.13
PyOH$-CO_2^{-\bullet}$ (C)	1297.68	-869.18	-84.71	-462.33	-118.54	-4.87
Im$-CO_2^{-\bullet}$ (C)	1448.52	-1003.49	-82.44	-399.41	-36.83	-9.47
Py$-CO_2^{-\bullet}$ (H)	0.82	-25.02	-18.90	-8.16	-51.26	1.26
Complex	ΔE_{FRZ}^{MP2}	ΔE_{POL}^{MP2}	ΔE_{DISP}^{MP2}	ΔE_{CT}^{MP2}	ΔE_{INT}^{MP2}	Error
Im$-CO_2^{-\bullet}$(H)	0.57	-56.01	-22.02	-26.79	-104.24	0.87
Py$-CO_2^{-\bullet}$ (C)	1537.56	-967.44	-128.95	-575.26	-134.09	6.39
Im$BH_2-CO_2^{-\bullet}$(H)	-3.54	-68.87	-22.98	-32.12	-127.53	0.94
ImOH$-CO_2^{-\bullet}$ (H)	-1.17	-57.19	-21.55	-27.45	-107.36	0.35
Py$BH_2-CO_2^{-\bullet}$(C)	1370.30	-828.99	-118.37	-657.35	-234.43	6.87
PyOH$-CO_2^{-\bullet}$ (C)	1568.99	-994.26	-122.73	-558.43	-106.46	7.20
Im$-CO_2^{-\bullet}$ (C)	1736.05	-1140.44	-120.48	-495.83	-20.73	6.63
Py$-CO_2^{-\bullet}$ (H)	10.65	-33.24	-17.28	-11.58	-51.46	1.05

Appendix B

Variational Forward-Backward Charge Transfer Analysis

B.1 Additional results for BH_3 complexes

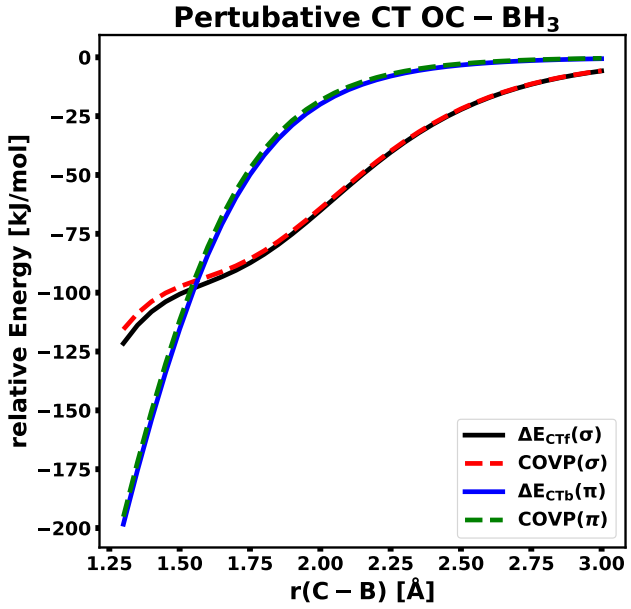

Figure B.1: Decay of the total forward and backward CT energies (ΔE_{CTf} and ΔE_{CTb}) obtained from perturbative CT analysis [87] with respect to the C−B distance. The forward CT energy is well reproduced by the stabilization energy associated while the σ-type COVP and backward CT energy by that of π-type COVP.

Table B.1: Decomposition of the frozen interaction energy at the minimum-energy structures using the "quasiclassical" scheme [86, 322] (energies in kJ/mol).

	ΔE_{Elec}	ΔE_{Pauli}	ΔE_{Disp}
H_3N-BH_3	-354.14	497.52	-31.13
$OC-BH_3$	-299.40	667.26	-35.75

Table B.2: Vertical ALMO-EDA results for $OC-BH_3$ with the B97-D[62] and ωB97X-D[68] functionals. Energies in kJ/mol and distances in Å.

	ΔE_{Frz}	ΔE_{Pol}	ΔE_{CTf}	ΔE_{CTb}	ΔE_{CT}	ΔE_{Tot}	r(B−C)
B97-D	331.6	-284.7	-99.8	-120.8	-227.6	-180.8	1.527
ωB97X-D	312.7	-281.2	-101.9	-99.6	-205.4	-173.9	1.523

Table B.3: Adiabatic ALMO-EDA molecular properties results for the $OC-BH_3$ complex. For the free CO, r(CO) = 1.134 Å and ν_{CO}= 2130 cm^{-1} (B97-D) and r(CO) = 1.123 Å and ν_{CO}= 2248 cm^{-1} (ωB97X-D).

		r(CB) [Å]	Δr(CO) [Å]	$\Delta\nu_{CO}$ [cm^{-1}]
B97-D	Frz	3.25	-0.001	9
	Pol	3.19	-0.001	10
	CTf	1.84	-0.010	103
	CTb	1.54	0.002	28
	Tot	1.53	0.006	-3
ωB97X-D	Frz	3.14	-0.001	10
	Pol	2.97	-0.001	13
	CTf	1.73	-0.011	116
	CTb	1.55	-0.002	40
	Tot	1.52	0.001	14

B.2 Additional results for complexes between CO and BeY (Y = O or CO_3)

(a) (b)

Figure B.2: Electron density difference between the Pol and Frz states (plotted with isovalue 0.01 a.u.) for (a) OC−BeO and (b) CO−BeO. Green and gold colors indicate the enhancement and depletion of electron density, respectively.

Table B.4: Decomposition of the frozen interaction energy at the minimum-energy structures of the CO−BeY complexes using the "quasiclassical" scheme with the B3LYP functional (energies in kJ/mol).

	ΔE_{Elec}	ΔE_{Pauli}	ΔE_{Disp}
OC−BeO	-115.89	134.36	-7.04
CO−BeO	-62.37	100.99	-7.22
OC−$BeCO_3$	-103.35	124.82	-8.80
CO−$BeCO_3$	-53.24	86.65	-6.46

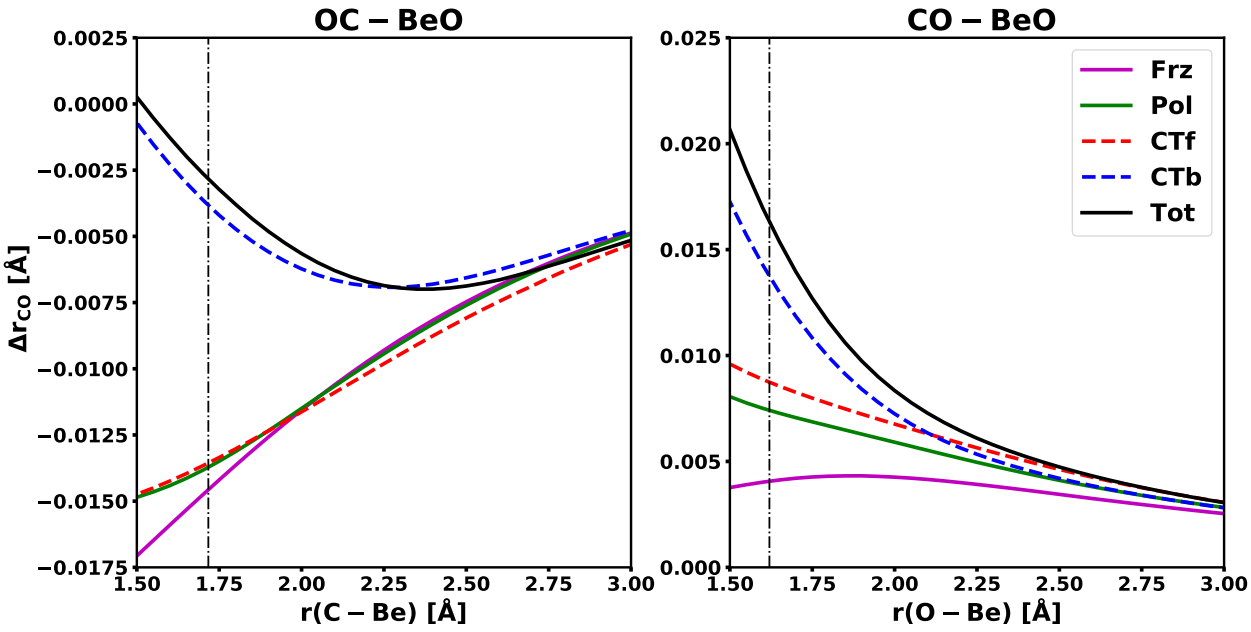

Figure B.3: Shifts in C−O bond length (Δr(CO)) as a function of the intermolecular distance for OC−BeO (left panel) and CO−BeO (right panel). The geometry of the complex is relaxed on each PES at each given X−Be distance. The black dashed lines indicate the full equilibrium distance for each complex.

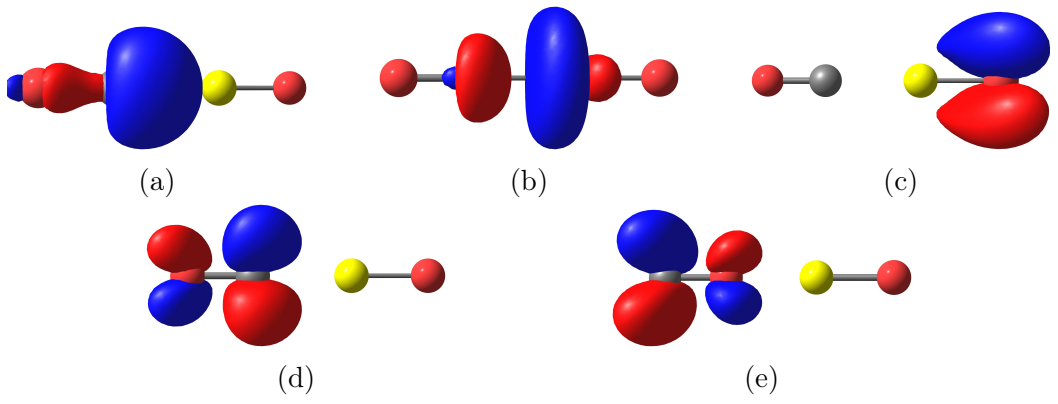

Figure B.4: Key COVPs illustrating the σ and π donations in OC−BeO: (a) σ-donor, (b) σ-acceptor, (c) π-donor, and (d) π-acceptor. Panel (e) shows the π-acceptor orbital in the κO complex CO−BeO.

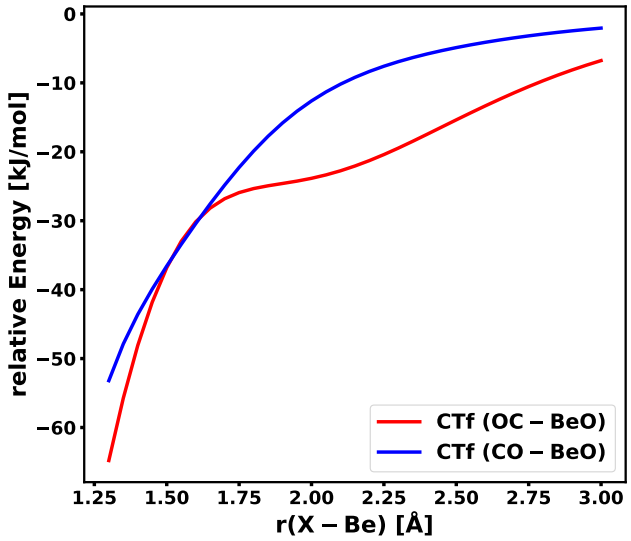

Figure B.5: Decay of the forward CT stabilization energy ($E_{\mathrm{CTf}} - E_{\mathrm{Pol}}$) with the intermolecular (X−Be) distance for the κC and κO isomers.

Table B.5: Vertical ALMO-EDA results for the four CO−BeY complexes using B97-D and ωB97X-D (energies in kJ/mol).

		ΔE_{Frz}	ΔE_{Pol}	ΔE_{CTf}	ΔE_{CTb}	ΔE_{CT}	ΔE_{Tot}
B97-D	OC−BeO	28.1	-111.3	-24.9	-70.0	-98.1	-181.3
	CO−BeO	50.9	-81.0	-28.7	-37.8	-69.4	-99.5
	OC−$BeCO_3$	19.4	-94.9	-27.4	-25.0	-53.8	-129.3
	CO−$BeCO_3$	31.4	-65.9	-26.0	-9.7	-36.1	-70.6
ωB97X-D	OC−BeO	2.1	-96.2	-23.2	-32.7	-57.2	-151.3
	CO−BeO	22.9	-68.6	-23.2	-13.1	-36.6	-82.3
	OC−$BeCO_3$	0.0	-82.5	-25.6	-9.0	-34.7	-117.2
	CO−$BeCO_3$	20.1	-63.0	-23.3	-4.6	-27.9	-70.8

Table B.6: Adiabatic ALMO-EDA molecular properties results for the four X−BeY adducts using **B97-D**. The distances are in Å and the frequency shifts are in cm^{-1}. For the free CO, r(CO) = 1.134 Å and ν_{CO}= 2130 cm^{-1}.

		OC−BeO	CO−BeO	OC−$BeCO_3$	CO−$BeCO_3$
r(CO)	Frz	1.124	1.137	1.126	1.137
r(CO)	Pol	1.121	1.140	1.121	1.140
r(CO)	CTf	1.121	1.142	1.121	1.142
r(CO)	CTb	1.134	1.152	1.126	1.142
r(CO)	Full	1.136	1.159	1.127	1.146
r(X-Be)	Frz	2.24	2.51	2.40	2.60
r(X-Be)	Pol	1.86	1.85	1.92	1.90
r(X-Be)	CTf	1.85	1.76	1.90	1.78
r(X-Be)	CTb	1.73	1.71	1.82	1.84
r(X-Be)	Full	1.72	1.62	1.80	1.72
$\Delta\nu_{CO}$	Frz	94	-21	78	-20
$\Delta\nu_{CO}$	Pol	140	-37	131	-38
$\Delta\nu_{CO}$	CTf	138	-50	132	-53
$\Delta\nu_{CO}$	CTb	19	-170	69	-64
$\Delta\nu_{CO}$	Full	4	-227	56	-109

Table B.7: Adiabatic ALMO-EDA molecular properties results for the four X−BeY adducts using **ωB97X-D**. The distances are in Å and the frequency shifts are in cm^{-1}. For the free CO, r(CO) = 1.123 Å and ν_{CO}= 2248 cm^{-1}.

		OC−BeO	CO−BeO	OC−$BeCO_3$	CO−$BeCO_3$
r(CO)	Frz	1.112	1.127	1.114	1.127
r(CO)	Pol	1.110	1.130	1.110	1.130
r(CO)	CTf	1.847	1.132	1.110	1.132
r(CO)	CTb	1.115	1.132	1.111	1.131
r(CO)	Full	1.116	1.134	1.111	1.132
r(X-Be)	Frz	2.18	2.18	2.31	2.33
r(X-Be)	Pol	1.87	1.87	1.92	1.87
r(X-Be)	CTf	1.11	1.11	1.89	1.75
r(X-Be)	CTb	1.77	1.77	1.88	1.85
r(X-Be)	Full	1.75	1.75	1.85	1.73
$\Delta\nu_{CO}$	Frz	104	-34	86	-34
$\Delta\nu_{CO}$	Pol	138	-52	127	-56
$\Delta\nu_{CO}$	CTf	139	-62	131	-68
$\Delta\nu_{CO}$	CTb	75	-73	117	-57
$\Delta\nu_{CO}$	Full	66	-100	116	-72

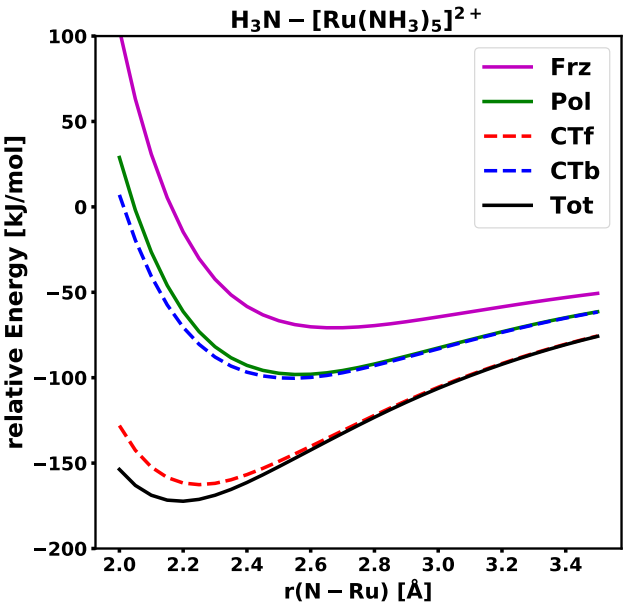

Figure B.6: Potential energy surface for each ALMO-EDA intermediate state for $H_3N{-}[Ru(NH_3)_5]^{2+}$.

B.3 Additional results for complexes between $[Ru(II)(NH_3)_5]^{2+}$ and π-acidic ligand series

Table B.8: Decomposition of the frozen interaction energy at the minimum-energy structures of the transition metal complexes using the "quasiclassical" scheme with the B3LYP functional (energies are in kJ/mol).

	ΔE_{Elec}	ΔE_{Pauli}	ΔE_{Disp}
$NN{-}[Ru(NH_3)_5]^{2+}$	-240.89	420.96	-19.66
$OC{-}[Ru(NH_3)_5]^{2+}$	-485.79	796.45	-27.54
$FB{-}[Ru(NH_3)_5]^{2+}$	-700.15	1060.49	-43.26
$NN{-}[Fe(NH_3)_5]^{2+}$	-166.33	264.22	-15.46
$NN{-}[Tc(NH_3)_5]^{+}$	-326.24	622.11	-32.07

Table B.9: Vertical ALMO-EDA results (in kJ/mol) for the transition metal complexes using the B3LYP, B97-D and ωB97X-D functionals. ΔE_{PCTf} and ΔE_{PCTb} refer to the forward and backward CT energies calculated using the perturbative CT analysis.

	ΔE_{Frz}	ΔE_{Pol}	ΔE_{CTf}	ΔE_{CTb}	ΔE_{CT}	ΔE_{Tot}	ΔE_{PCTf}	ΔE_{PCTb}
				B3LYP				
NN−$[Ru(NH_3)_5]^{2+}$	160.4	-70.1	-95.0	-99.5	-212.7	-122.4	-90.8	-103.1
OC−$[Ru(NH_3)_5]^{2+}$	283.1	-119.6	-190.0	-155.8	-392.8	-229.2	-181.5	-170.8
FB−$[Ru(NH_3)_5]^{2+}$	317.1	-171.0	-284.7	-130.0	-477.2	-331.1	-271.0	-139.2
NN−$[Fe(NH_3)_5]^{2+}$	82.4	-57.1	-42.1	-53.2	-100.9	-75.6	-38.5	-51.0
NN−$[Tc(NH_3)_5]^{+}$	263.8	-75.0	-94.6	-277.4	-414.7	-225.9	-90.1	-412.5
				B97-D				
NN−$[Ru(NH_3)_5]^{2+}$	156.8	-68.0	-103.0	-117.2	-244.5	-155.7	-107.9	-170.5
OC−$[Ru(NH_3)_5]^{2+}$	273.0	-117.3	-201.8	-173.5	-431.5	-275.8	-216.4	-248.2
FB−$[Ru(NH_3)_5]^{2+}$	298.3	-170.7	-299.2	-141.1	-510.3	-382.6	-334.2	-182.6
NN−$[Fe(NH_3)_5]^{2+}$	77.0	-55.2	-46.8	-76.8	-134.1	-112.3	-48.1	-112.5
NN−$[Tc(NH_3)_5]^{+}$	259.6	-75.7	-103.5	-300.7	-455.0	-271.1	-106.5	-717.7
				ωB97X-D				
NN−$[Ru(NH_3)_5]^{2+}$	138.1	-67.8	-92.7	-88.5	-196.5	-126.2	-75.7	-60.5
OC−$[Ru(NH_3)_5]^{2+}$	257.5	-118.3	-188.4	-147.1	-378.9	-239.7	-149.9	-112.3
FB−$[Ru(NH_3)_5]^{2+}$	294.2	-175.9	-282.8	-122.3	-461.7	-343.4	-210.0	-98.1
NN−$[Fe(NH_3)_5]^{2+}$	65.5	-56.5	-40.7	-44.7	-89.7	-80.7	-30.1	-29.1
NN−$[Tc(NH_3)_5]^{+}$	239.1	-70.0	-91.4	-258.0	-388.1	-219.0	-76.0	-189.3

Table B.10: Metal-ligand distance [r(M−X)] and bond length of the diatomic ligand [r(X−Y)] (both in Å) evaluated on the Pol, CTf, CTb, and Tot surfaces using **B97-D**. In the isolated state, r(N−N) = 1.099 Å, r(C−O) = 1.134 Å, r(B−F) = 1.279 Å.

	r(M-X)				r(X-Y)			
Complex	Pol	CTf	CTb	Tot	Pol	CTf	CTb	Tot
NN−$[Ru(NH_3)_5]^{2+}$	2.713	2.285	2.236	1.899	1.098	1.096	1.105	1.120
OC−$[Ru(NH_3)_5]^{2+}$	2.614	2.189	2.184	1.836	1.126	1.122	1.137	1.154
FB−$[Ru(NH_3)_5]^{2+}$	2.729	2.118	2.327	1.858	1.256	1.247	1.264	1.279
NN−$[Fe(NH_3)_5]^{2+}$	2.857	2.857	2.046	1.820	1.099	1.097	1.106	1.116
NN−$[Tc(NH_3)_5]^{+}$	2.992	2.390	2.079	1.853	1.098	1.096	1.128	1.149

Table B.11: Adiabatic ALMO-EDA results with **B97-D** for the shifts in the vibrational frequency of N_2, CO, and BF ($\Delta\nu_{XY}$ in cm^{-1}) when associated with the transition metal moieties. In the isolated state, ν_{NN} = 2372 cm^{-1}, ν_{CO} = 2130 cm^{-1}, ν_{BF} = 1344 cm^{-1}.

	$\Delta\nu_{XY}$			
Complex	Pol	CTf	CTb	Tot
NN−$[Ru(NH_3)_5]^{2+}$	12	33	-72	-202
OC−$[Ru(NH_3)_5]^{2+}$	72	119	-28	-111
FB−$[Ru(NH_3)_5]^{2+}$	133	220	110	154
NN−$[Fe(NH_3)_5]^{2+}$	4	21	-87	-183
NN−$[Tc(NH_3)_5]^{+}$	8	34	-252	-393

Table B.12: Metal-ligand distance [r(M−X)] and bond length of the diatomic ligand [r(X−Y)] (both in Å) evaluated on the Pol, CTf, CTb, and Tot surfaces using **ωB97X-D**. In the isolated state, r(N−N) = 1.088 Å, r(C−O) = 1.123 Å, r(B−F) = 1.266 Å.

	r(M-X)				r(X-Y)			
Complex	Pol	CTf	CTb	Tot	Pol	CTf	CTb	Tot
NN−$[Ru(NH_3)_5]^{2+}$	2.564	2.296	2.329	1.959	1.087	1.086	1.089	1.097
OC−$[Ru(NH_3)_5]^{2+}$	2.555	2.194	2.225	1.856	1.114	1.112	1.120	1.134
FB−$[Ru(NH_3)_5]^{2+}$	2.619	2.143	2.344	1.869	1.242	1.236	1.247	1.262
NN−$[Fe(NH_3)_5]^{2+}$	2.471	2.241	2.216	1.964	1.087	1.087	1.088	1.091
NN−$[Tc(NH_3)_5]^{+}$	2.558	2.361	2.090	1.869	1.086	1.086	1.108	1.124

Table B.13: Adiabatic ALMO-EDA results with **ωB97X-D** for the shifts in the vibrational frequency of N_2, CO, and BF ($\Delta\nu_{XY}$ in cm^{-1}) when associated with the transition metal moieties. In the isolated state, ν_{NN} = 2493 cm^{-1}, ν_{CO} = 2248 cm^{-1}, ν_{BF} = 1400 cm^{-1}.

	$\Delta\nu_{XY}$			
Complex	Pol	CTf	CTb	Tot
NN−$[Ru(NH_3)_5]^{2+}$	15	29	-21	-106
OC−$[Ru(NH_3)_5]^{2+}$	83	114	16	-74
FB−$[Ru(NH_3)_5]^{2+}$	165	215	152	135
NN−$[Fe(NH_3)_5]^{2+}$	10	20	-5	-42
NN−$[Tc(NH_3)_5]^{+}$	22	28	-195	-337

Appendix C

Consistent Inclusion of Continuum Solvation in Energy Decomposition Analysis: Theory and Application to Molecular CO_2 Reduction Catalysts

C.1 Additional results for the validation of ALMO-EDA(solv)

Table C.1: Strength (in kJ/mol) of internal QM electrostatics ($\Delta E^{(0)}_{\mathrm{ELEC}}$) and the effect of solute-solvent electrostatic interaction on binding ($\Delta E^{\mathrm{el}}_{\mathrm{SOL}}$) for $Na^+\cdots Cl^-$ separated by 20 Å calculated with ωB97X-V/def2-TZVPPD and IEF-PCM with varying dielectric constants. $\Delta E^{(\mathrm{s})}_{\mathrm{ELEC}} = \Delta E^{(0)}_{\mathrm{ELEC}} + \Delta E^{\mathrm{el}}_{\mathrm{SOL}}$ is the effective (screened) electrostatic interaction in the solution phase.

ϵ	$\Delta E^{(0)}_{\mathrm{ELEC}}$	$\Delta E^{\mathrm{el}}_{\mathrm{SOL}}$	$\Delta E^{(\mathrm{s})}_{\mathrm{ELEC}}$	$\Delta E^{(0)}_{\mathrm{ELEC}}/\Delta E^{(\mathrm{s})}_{\mathrm{ELEC}}$
1	-69.47	0	-69.47	1.0
10	-69.47	62.52	-6.94	10.0
20	-69.47	65.99	-3.47	20.0
40	-69.47	67.73	-1.74	40.0
80	-69.47	68.60	-0.87	79.9

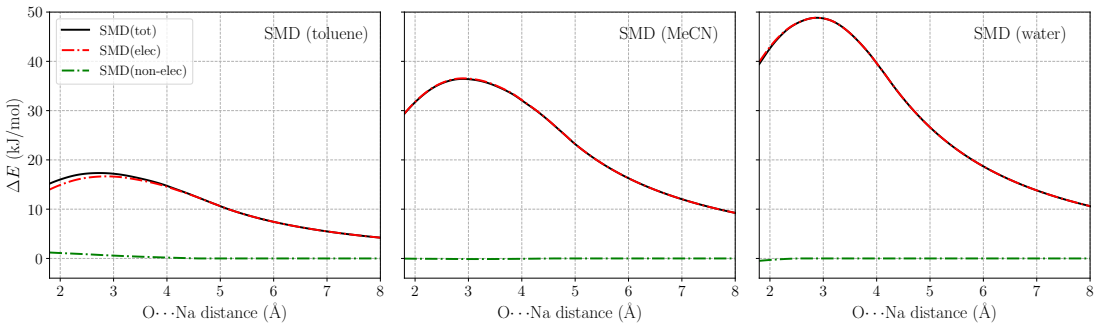

Figure C.1: Electrostatic and non-electrostatic components (in kJ/mol) of the solvent contribution (ΔE_{SOL}) to the $H_2O\cdots Na^+$ interaction with the $O\cdots Na^+$ distance ranging from 1.8 to 8.0 Å, with solvents toluene, MeCN, and water modeled by SMD.

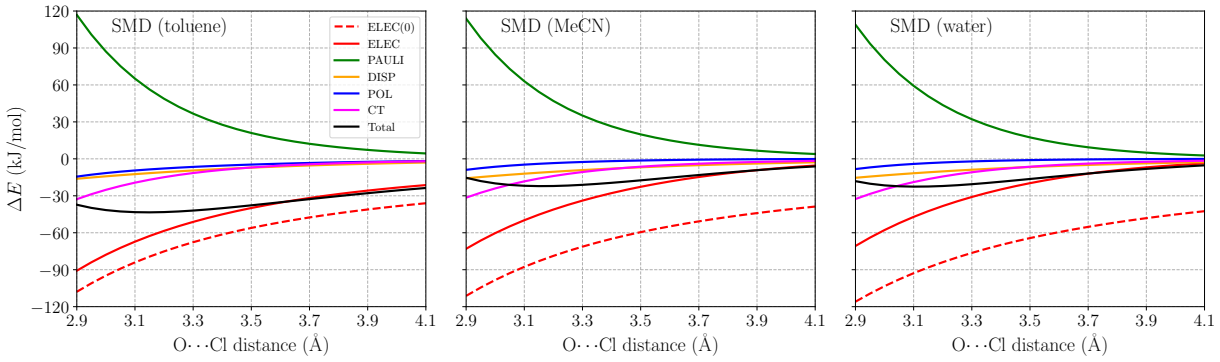

Figure C.2: ALMO-EDA(sol) results (in kJ/mol) for the $H_2O\cdots Cl^-$ complex in toluene, acetonitrile (MeCN), and water solutions with the $O\cdots Cl^-$ distance ranging from 2.9 to 4.1 Å. All calculations are performed using ωB97X-V/def2-TZVPPD with solvents described by the SMD model. Terms in ALMO-EDA(sol) are represented with solid lines while the internal electrostatic interaction, denoted as "ELEC(0)", is shown in a dashed line.

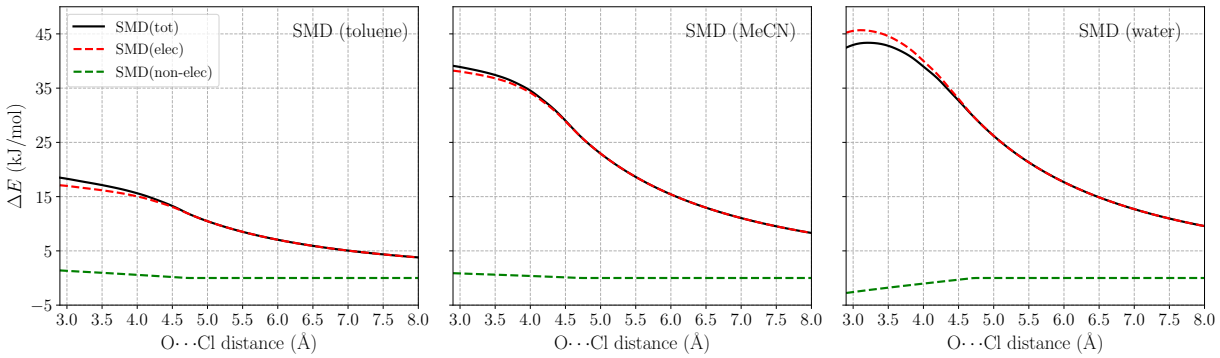

Figure C.3: Electrostatic and non-electrostatic components (in kJ/mol) of the solvent contribution (ΔE_{SOL}) to the $H_2O\cdots Cl^-$ interaction with the $O\cdots Cl^-$ distance ranging from 2.9 to 8.0 Å, with solvents toluene, MeCN, and water modeled by SMD.

C.2 Additional results for the [FeTPP($CO_2^{\bullet -}$)] derivatives

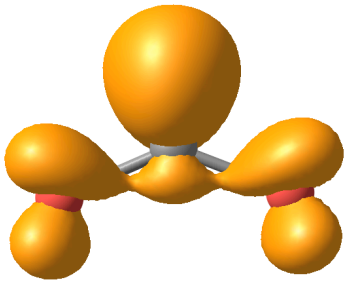

Figure C.4: Spin density of $CO_2^{\bullet -}$ (isovalue: 0.08 a.u.) optimized with ωB97X-V/def2-TZVPP).

Table C.2: Geometry distortion (GD) term for the CO_2 fragment with different fragmentation schemes (in kJ/mol).

Fragment	ΔE_{GD}
CO_2	206.6
$CO_2^{\cdot -}$	0.6

Table C.3: Fe−CO_2 bond length (in Å) for all CO_2 adducts investigated in this study. All geometries are optimized with ωB97X-V/def2-TZVPP with PCM model for the CH_3CN solvent ($\epsilon = 35.88$).

Complex	r(Fe−C)
$[FeTPP(CO_2)]^{2-}$	2.08
[Fe-*p*-SUL-$(CO_2)]^{4-}$	2.09
[Fe-*p*-TMA-$(CO_2)]^{0}$	2.10
[Fe-*o*-TMA-$(CO_2)]^{0}$	2.06
[Fe-*o*-OH-$(CO_2)]^{2-}$	2.01
$[FeTPPF10(CO_2)]^{2-}$	2.10
[Fe-imid-$(CO_2)]^{-}$	2.07
[Fe-imid2-$(CO_2)]^{0}$	2.00

Table C.4: ALMO-EDA(solv) results (in kJ/mol) with ωB97X-V/def2-TZVPP and PCM solvent (CH_3CN, $\epsilon = 35.88$) for all the different derivatives of the doubly reduced FeTPP−CO_2 adducts studied in this work.

Complex	ELEC	PAULI	DISP	POL	CT	INT
$[FeTPP(CO_2)]^{2-}$	-363.4	634.2	-66.2	-135.4	-123.0	-53.8
$[FeTPPF10(CO_2)]^{2-}$	-343.1	594.9	-66.0	-127.1	-106.0	-47.3
[Fe-*o*-OH-$(CO_2)]^{2-}$	-542.4	848.7	-88.5	-168.3	-167.5	-117.9
[Fe-*p*-OH-$(CO_2)]^{2-}$	-357.3	626.9	-66.1	-134.2	-111.7	-42.5
[Fe-*p*-TMA-$(CO_2)]^{0}$	-296.2	451.2	-71.7	-47.3	-111.0	-75.0
[Fe-*o*-TMA-$(CO_2)]^{0}$	-379.3	545.7	-96.2	-59.5	-129.7	-119.0
[Fe-*p*-SUL-$(CO_2)]^{4-}$	-343.1	613.9	-66.1	-132.6	-119.7	-47.6
[Fe-*o*-imid-$(CO_2)]^{-}$	-449.3	748.0	-100.0	-153.0	-149.2	-103.1
[Fe-*o*-imid2-$(CO_2)]^{0}$	-1005.4	955.3	-131.2	-201.4	-176.1	-197.3
[Fe-*o*-imid2-$(CO_2)]^{2-}$(NH-ref) [a]	-504.0	827.1	-91.3	-163.7	-155.5	-87.4

[a] The [Fe-*o*-imid2-$(CO_2)]^{2-}$(NH-ref) corresponds the reference calculation to separate the effect of the amino hydrogen bonds and the methylimidazolium. We replaced the methylimidazolium with methyl and kept the bond distances for both hydrogen bonds frozen.

Table C.5: Gas phase ALMO-EDA results with ωB97X-V/def2-TZVPP (in kJ/mol) for the selected derivatives of the doubly reduced FeTPP$-CO_2$ complexes.

Complex	ELEC	PAULI	DISP	POL	CT	INT
$[FeTPP(CO_2)]^{2-}$	-135.5	600.6	-64.8	-182.2	-126.7	128.5
[Fe-*p*-SUL-$(CO_2)]^{4-}$	150.4	625.2	-65.8	-179.9	-121.8	408.1
[Fe-*o*-TMA-$(CO_2)]^0$	-401.0	444.6	-72.0	-95.1	-110.3	-233.8

C.3 Additional results for the substituted terphenyl$\cdots CO_2$ complexes

Below we show the ALMO-EDA results for the reactant and product states of the substituted terphenyl$\cdots CO_2$ complex (carrying -1 charge) evaluated at the ωB97X-V/def2-TZVPD (Tables C.6) and C.7) and B3LYP-D3(BJ)/6-311G(d,p) levels of theory with or without solvent. Comparing the results in Table C.7 and Table C.9, we found that B3LYP-D3(BJ)/6-311G(d,p) produces much larger CT energies than ωB97X-V/def2-TZVPD for the product-state complexes when the solvent is absent. The differences in reactant state, on the other hand, are much more moderate. We ascribe this discrepancy to the more substantial delocalization error associated with the B3LYP functional,[324, 417] which, as shown in our previous work,[379] can result in substantial overestimation of the CT component in ALMO-EDA (and correspondingly the total binding energy). Using the range-separated hybrid ωB97X-V functional, on the other hand, considerably reduces the spurious charge delocalization, and results in unconstrained SCF solutions for the reactant and product states in which the excess electron is well-localized on the terphenyl and CO_2 moieties, respectively. Table C.10 shows the fragment Mulliken populations in the *fully relaxed* reactant and product states given by these two levels of theory. It reveals that the charge population on the CO_2 moiety largely deviates from -1 when calculated with B3LYP-D3(BJ) in vacuum, which, however, does not occur when ωB97X-V is employed. Interestingly, with the presence of SMD solvent, the ALMO-EDA results at these two different levels of theory become more comparable (see Tables C.6 and C.8), indicating that the solvent environment assists in stabilizing the charge-separated reactant and product states and mitigates the spurious charge delocalization associated with the B3LYP-D3(BJ)/6-311G(d,p) model chemistry. This further demonstrates the value of incorporating solvation effects in ALMO-EDA calculations for intermolecular complexes in solution, since otherwise the EDA results will suffer from artifacts caused by the unrealistic gas phase environment. The differences between the CT energies given by these two levels of theory now mainly arise from the larger basis set superposition error (BSSE) associated with the smaller 6-311G(d,p) basis set.

Table C.6: ALMO-EDA(solv) results with **ωB97X-V/def2-TZVPD** (in kJ/mol) for the reactant- and product-state complexes of the electron-transfer reaction from terphenyl$^{\bullet-}$ to CO_2 **in CH_2Cl_2** ($\epsilon = 8.93$, described by the SMD model).

	Reactant state					
	ELEC	PAULI	DISP	POL	CT	INT
$-NMe_2$	-14.32	24.63	-21.27	-1.26	-2.81	-15.02
$-OH$	-12.61	21.31	-18.85	-1.06	-2.52	-13.73
$-CH_3$	-13.52	22.01	-17.99	-1.07	-2.58	-13.15
$-H$	-12.75	22.06	-19.29	-1.10	-2.62	-13.70
$-Br$	-11.92	22.27	-19.5	-1.10	-2.60	-12.86
$-CF_3$	-11.79	21.90	-19.56	-1.09	-2.50	-13.04
$-NO_2$	-10.81	21.12	-19.09	-1.03	-2.21	-12.02
	Product state					
	ELEC	PAULI	DISP	POL	CT	INT
$-NMe_2$	8.97	12.44	-16.80	-1.55	-1.10	1.96
$-OH$	5.79	13.28	-16.96	-1.56	-1.14	-0.58
$-CH_3$	5.97	13.44	-17.12	-1.60	-1.16	-0.46
$-H$	4.78	13.52	-17.04	-1.56	-1.15	-1.44
$-Br$	0.65	13.78	-17.07	-1.61	-1.17	-5.42
$-CF_3$	-1.26	14.02	-17.15	-1.60	-1.16	-7.15
$-NO_2$	-4.97	14.42	-17.19	-1.67	-1.20	-10.61

Table C.7: ALMO-EDA results (in kJ/mol) with **ωB97X-V/def2-TZVPD** for the reactant- and product-state complexes of the electron-transfer reaction from terphenyl$^{\bullet-}$ to CO_2 **in the gas phase**.

	Reactant state					
	ELEC	PAULI	DISP	POL	CT	INT
$-NMe_2$	-19.05	26.29	-21.29	-3.58	-3.16	-20.80
$-OH$	-17.53	22.69	-18.81	-3.17	-2.81	-19.64
$-CH_3$	-17.71	23.75	-18.05	-3.31	-2.99	-18.31
$-H$	-17.35	23.41	-19.28	-3.35	-2.93	-19.50
$-Br$	-15.84	23.61	-19.52	-2.80	-2.85	-17.39
$-CF_3$	-15.32	22.92	-19.59	-2.69	-2.70	-17.38
$-NO_2$	-15.25	22.90	-19.39	-2.86	-2.57	-17.17
	Product state					
	ELEC	PAULI	DISP	POL	CT	INT
$-NMe_2$	35.10	15.16	-17.09	-24.87	-1.43	6.88
$-OH$	19.27	16.00	-17.25	-23.20	-1.53	-6.72
$-CH_3$	20.32	16.16	-17.43	-23.78	-1.56	-6.29
$-H$	15.58	16.26	-17.36	-22.84	-1.55	-9.92
$-Br$	-2.11	16.53	-17.42	-24.83	-1.63	-29.46
$-CF_3$	-12.37	16.80	-17.50	-24.06	-1.64	-38.77
$-NO_2$	-27.95	17.22	-17.57	-25.04	-1.73	-55.07

Table C.8: ALMO-EDA(solv) results with **B3LYP-D3(BJ)/6-311G(d,p)** (in kJ/mol) for the reactant- and product-state complexes of the electron-transfer reaction from terphenyl$^{\bullet-}$ to CO_2 **in CH_2Cl_2** (ϵ = 8.93, described by the SMD model). Note that counterpoise correction is *not* applied in these calculations since it is currently incompatible with the SMD model.

	Reactant state					
	ELEC	PAULI	DISP	POL	CT	INT
$-NMe_2$	-9.44	17.40	-19.38	-0.41	-8.54	-20.37
$-OH$	-8.47	15.08	-17.22	-0.34	-7.34	-18.29
$-CH_3$	-9.04	15.57	-16.60	-0.35	-7.43	-17.85
$-H$	-8.32	15.49	-17.45	-0.36	-7.53	-18.16
$-Br$	-7.67	15.98	-18.11	-0.37	-7.44	-17.61
$-CF_3$	-7.77	15.74	-17.95	-0.31	-7.36	-17.65
$-NO_2$	-7.05	15.40	-18.02	-0.27	-7.16	-17.10
	Product state					
	ELEC	PAULI	DISP	POL	CT	INT
$-NMe_2$	13.42	3.76	-9.72	-1.29	-11.04	-4.87
$-OH$	10.61	4.07	-9.90	-1.26	-11.69	-8.18
$-CH_3$	10.35	4.14	-9.99	-1.30	-11.95	-8.75
$-H$	9.30	4.16	-9.98	-1.26	-12.08	-9.85
$-Br$	5.62	4.19	-10.10	-1.31	-12.20	-13.81
$-CF_3$	3.86	4.19	-10.17	-1.30	-12.33	-15.75
$-NO_2$	0.24	4.32	-10.30	-1.38	-19.09	-26.21

Table C.9: ALMO-EDA results (in kJ/mol) with **B3LYP-D3(BJ)/6-311G(d,p)** (counterpoise-corrected) for the reactant- and product-state complexes of the electron-transfer reaction from terphenyl$^{\bullet-}$ to CO_2 **in the gas phase**.

	Reactant state					
	ELEC	PAULI	DISP	POL	CT	INT
$-NMe_2$	-14.43	18.81	-19.40	-2.10	-2.87	-19.99
$-OH$	-13.88	16.31	-17.23	-1.96	-2.22	-18.99
$-CH_3$	-13.33	16.94	-16.63	-2.04	-2.83	-17.89
$-H$	-13.34	16.71	-17.48	-2.08	-2.42	-18.61
$-Br$	-11.92	17.19	-18.14	-1.68	-2.43	-16.98
$-CF_3$	-11.64	16.65	-17.98	-1.56	-2.29	-16.82
$-NO_2$	-10.19	16.30	-18.05	-1.22	-2.01	-15.16
	Product state					
	ELEC	PAULI	DISP	POL	CT	INT
$-NMe_2$	45.95	2.49	-9.72	-22.72	-8.98	7.02
$-OH$	30.65	2.68	-9.90	-20.77	-11.07	-8.42
$-CH_3$	29.77	2.73	-10.00	-21.43	-14.66	-13.59
$-H$	25.44	2.74	-9.98	-20.37	-15.60	-17.76
$-Br$	8.37	2.77	-10.11	-22.30	-23.77	-45.03
$-CF_3$	-2.01	2.75	-10.17	-21.38	-31.86	-62.67
$-NO_2$	-18.18	2.86	-10.30	-22.56	-74.96	-123.14

Table C.10: Mulliken charge population (e^-) on the CO_2 moiety in the fully relaxed reactant and product states of the terphenyl$\cdots CO_2$ complex with different substituent groups. The calculations are performed at the B3LYP-D3(BJ)/6-311G(d,p) and ωB97X-V/def2-TZVPD levels of theory, without and with the SMD solvation model. The results show that gas-phase B3LYP-D3(BJ)/6-311G(d,p) calculations suffer from spurious charge transfer from $CO_2^{\bullet-}$ to the terphenyl moiety.

	B3LYP-D3(BJ) (vacuum)		ωB97X-V (vacuum)	
group	reactant	product	reactant	product
$-NMe_2$	-0.004	-0.753	0.010	-0.994
$-OH$	-0.004	-0.737	0.005	-0.989
$-H$	-0.004	-0.699	0.002	-0.989
$-CH_3$	-0.010	-0.706	0.008	-0.989
$-Br$	-0.001	-0.645	0.012	-0.985
$-CF_3$	0.000	-0.599	0.013	-0.986
$-NO_2$	0.004	-0.423	0.012	-0.981
	B3LYP-D3(BJ) (CH_2Cl_2)		ωB97X-V (CH_2Cl_2)	
group	reactant	product	reactant	product
$-NMe_2$	0.002	-0.977	0.014	-0.999
$-OH$	0.001	-0.974	0.009	-0.996
$-H$	0.001	-0.973	0.006	-0.995
$-CH_3$	-0.004	-0.974	0.013	-0.995
$-Br$	0.003	-0.972	0.013	-0.994
$-CF_3$	0.003	-0.972	0.015	-0.995
$-NO_2$	0.007	-0.716	0.020	-0.993

Table C.11: Differential interaction energies (in kJ/mol) between the reactant and product complexes ($\Delta\Delta E_{\mathrm{INT}}$) and the differences between the monomer energies in the reactant and product complexes (ΔE_{PREP}, including contributions from both geometric distortion and change in electronic configuration). Ignoring the entropic contributions the free energy driving force for the electron transfer (ET) reaction can be approximated by $\Delta E_{\mathrm{ET}} = \Delta\Delta E_{\mathrm{INT}} + \Delta E_{\mathrm{PREP}}$.

	$\Delta\Delta E_{\mathrm{INT}}$	ΔE_{PREP}	ΔE_{ET}
$-NMe_2$	16.98	-50.45	-33.47
$-OH$	13.15	-32.45	-19.30
$-CH_3$	12.69	-20.82	-8.13
$-H$	12.26	-11.12	1.14
$-Br$	7.44	5.54	12.98
$-CF_3$	5.89	25.72	31.61
$-NO_2$	1.41	74.33	75.74

Appendix D

Exploring the Limits of Second- and Third-Order Møller-Plesset Perturbation Theory for Non-Covalent Interactions: Importance of Regularization and Reference Orbitals

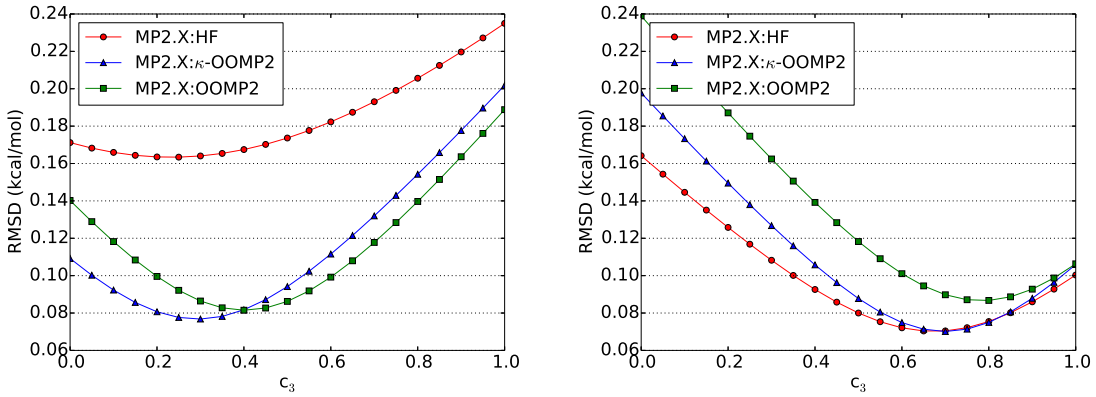

Figure D.1: Dependence of the the root-mean square deviation on the scaling of the third-order energy (c_3) in the A24 data set aTZ with CBS reference (a); aTZ with aTZ reference (b); RMSD in kcal/mol; four scaled MP2.X methods (MP2.X, MP2.X:OOMP2, MP2.X:κ-OOMP2).

D.1 Optimal c_3 Coefficients

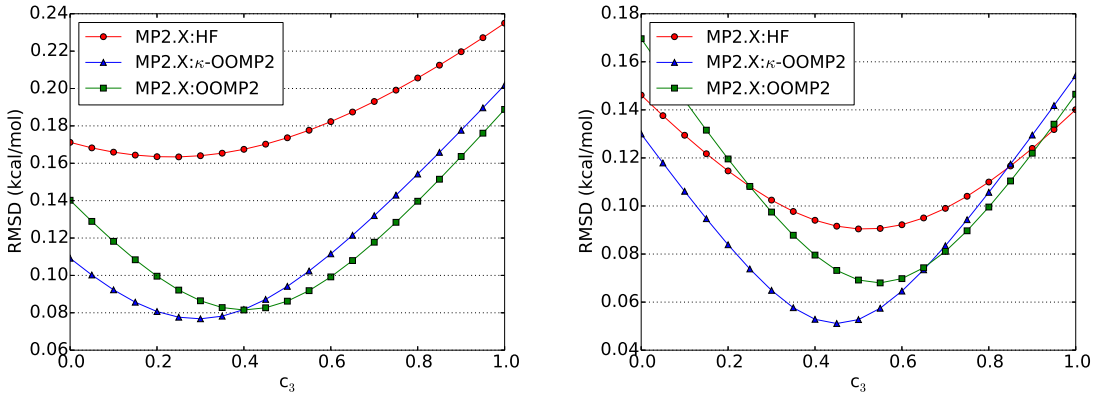

Figure D.2: Dependence of the the root-mean square deviation on the scaling of the third-order energy (c_3) in the A24 data set aTZ with CBS reference (a); aQZ with CBS reference (b); RMSD in kcal/mol; four scaled MP2.X methods (MP2.X, MP2.X:OOMP2, MP2.X:κ-OOMP2).

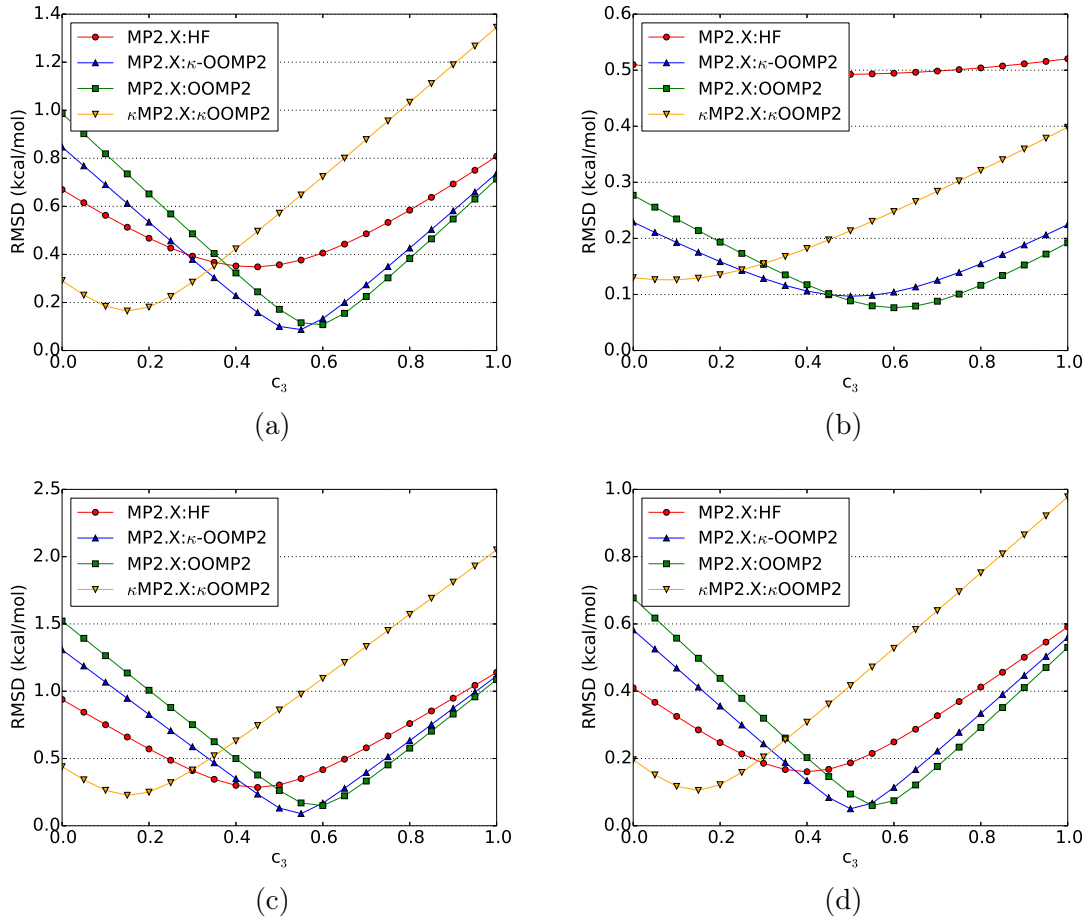

Figure D.3: Dependence of the the root-mean square deviation on the scaling of the third-order energy (c_3) in the S66 data set (a) and the three subgroups hydrogen bonding (b), dispersion (c) and mixed (d); RMSD in kcal/mol; four scaled MP2.X methods (MP2.X, MP2.X:OOMP2, MP2.X:κ-OOMP2, κMP2.X:κ-OOMP2).

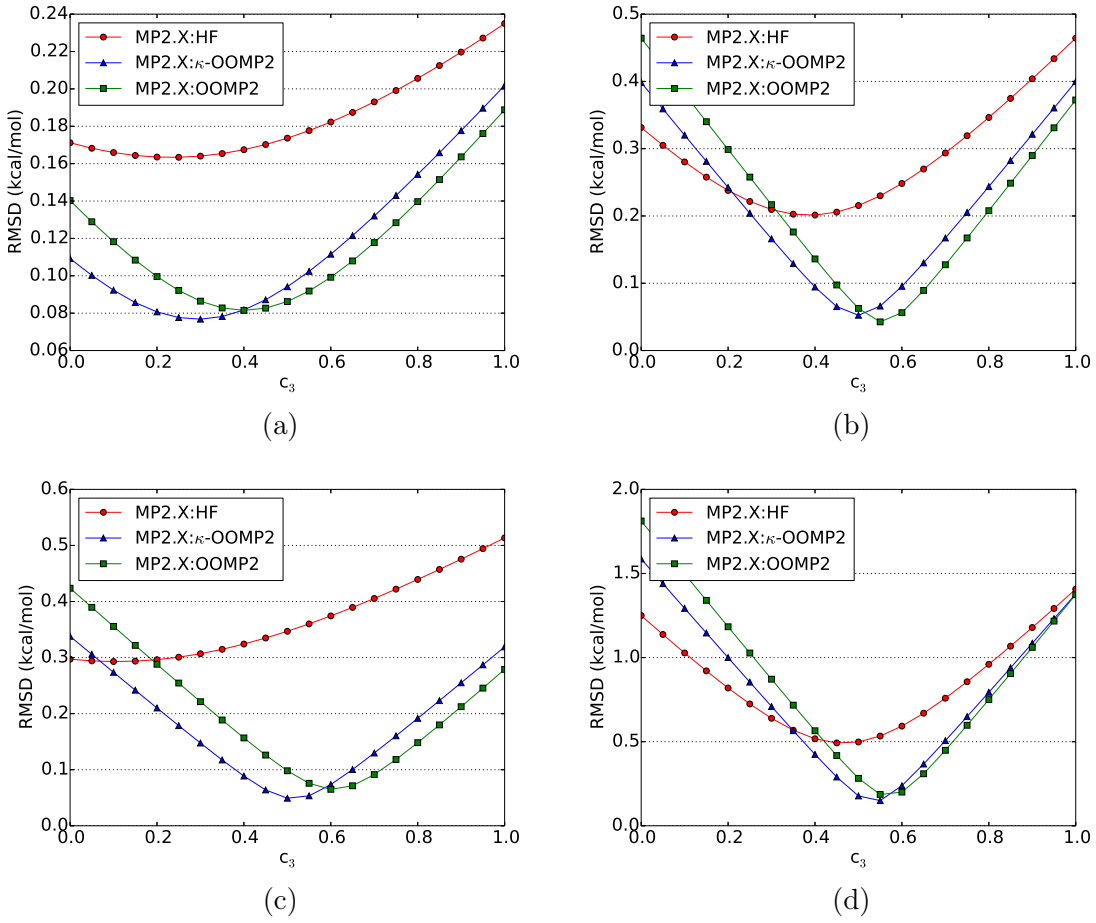

Figure D.4: Dependence of the the root-mean square deviation on the scaling of the third-order energy (c_3) in the A24 (a), DS14 (b), HSG (c) and S22 (d) data sets; RMSD in kcal/mol; four scaled MP2.X methods (MP2.X, MP2.X:OOMP2, MP2.X:κ-OOMP2, κMP2.X:κ-OOMP2).

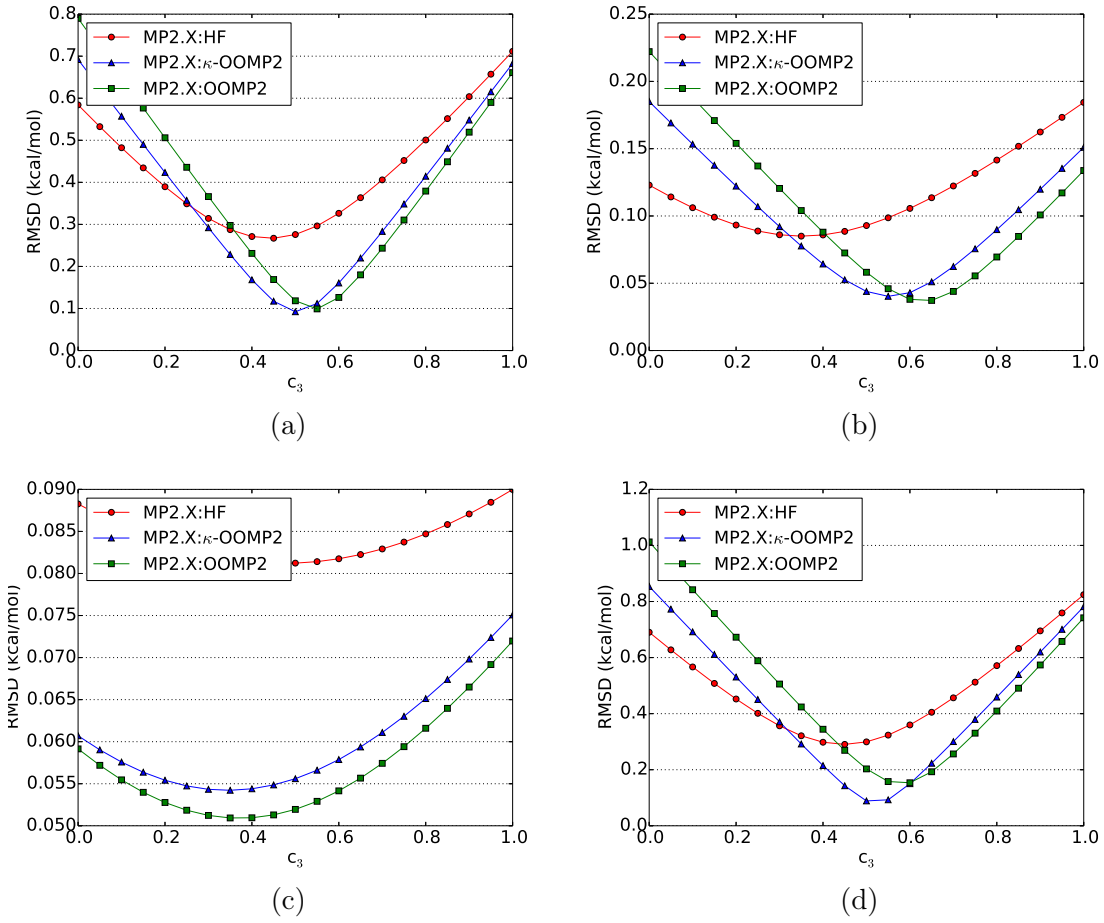

Figure D.5: Dependence of the the root-mean square deviation on the scaling of the third-order energy (c_3) in the X40 (a), HW30 (b), NC15 (c) and AlkBind12 (d) data sets; RMSD in kcal/mol; four scaled MP2.X methods (MP2.X, MP2.X:OOMP2, MP2.X:κ-OOMP2, κMP2.X:κ-OOMP2).

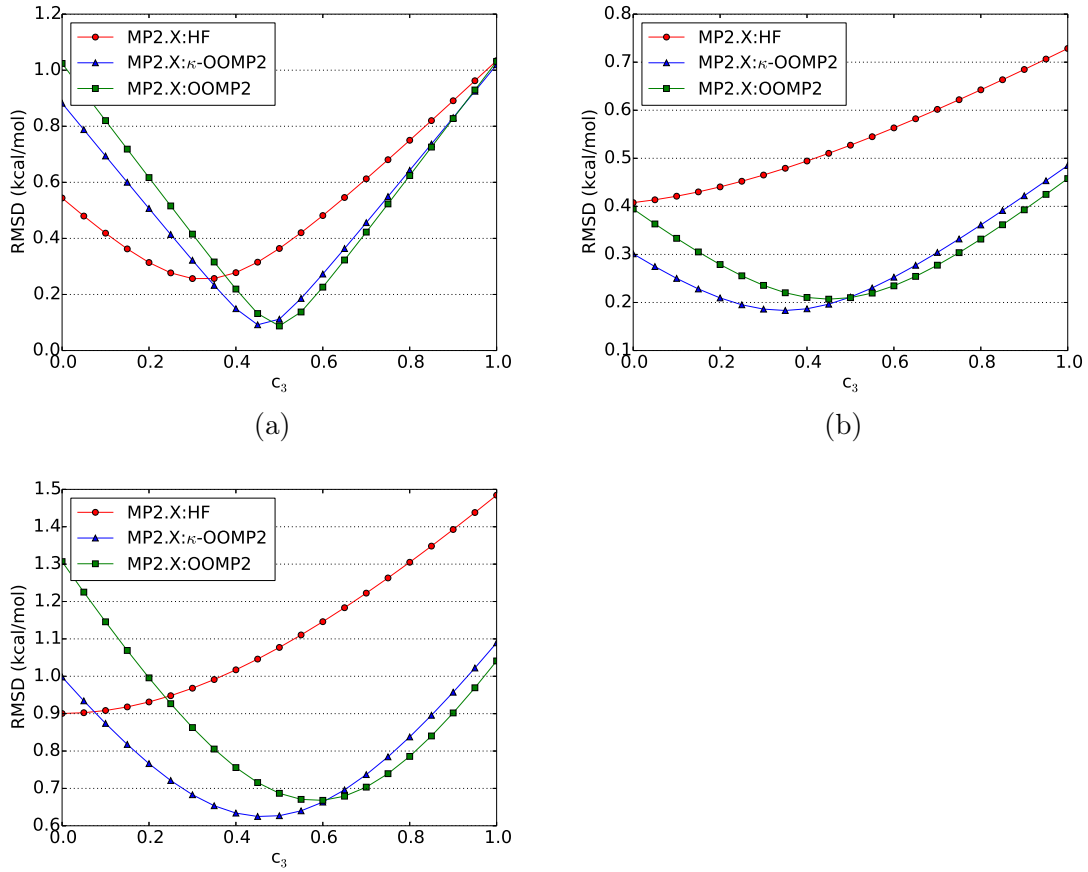

Figure D.6: Dependence of the the root-mean square deviation on the scaling of the third-order energy (c_3) in the CO2Nitrogen16 (a), HB49 (b) and Ionic43 (c) data sets; RMSD in kcal/mol; four scaled MP2.X methods (MP2.X, MP2.X:OOMP2, MP2.X:κ-OOMP2, κMP2.X:κ-OOMP2).

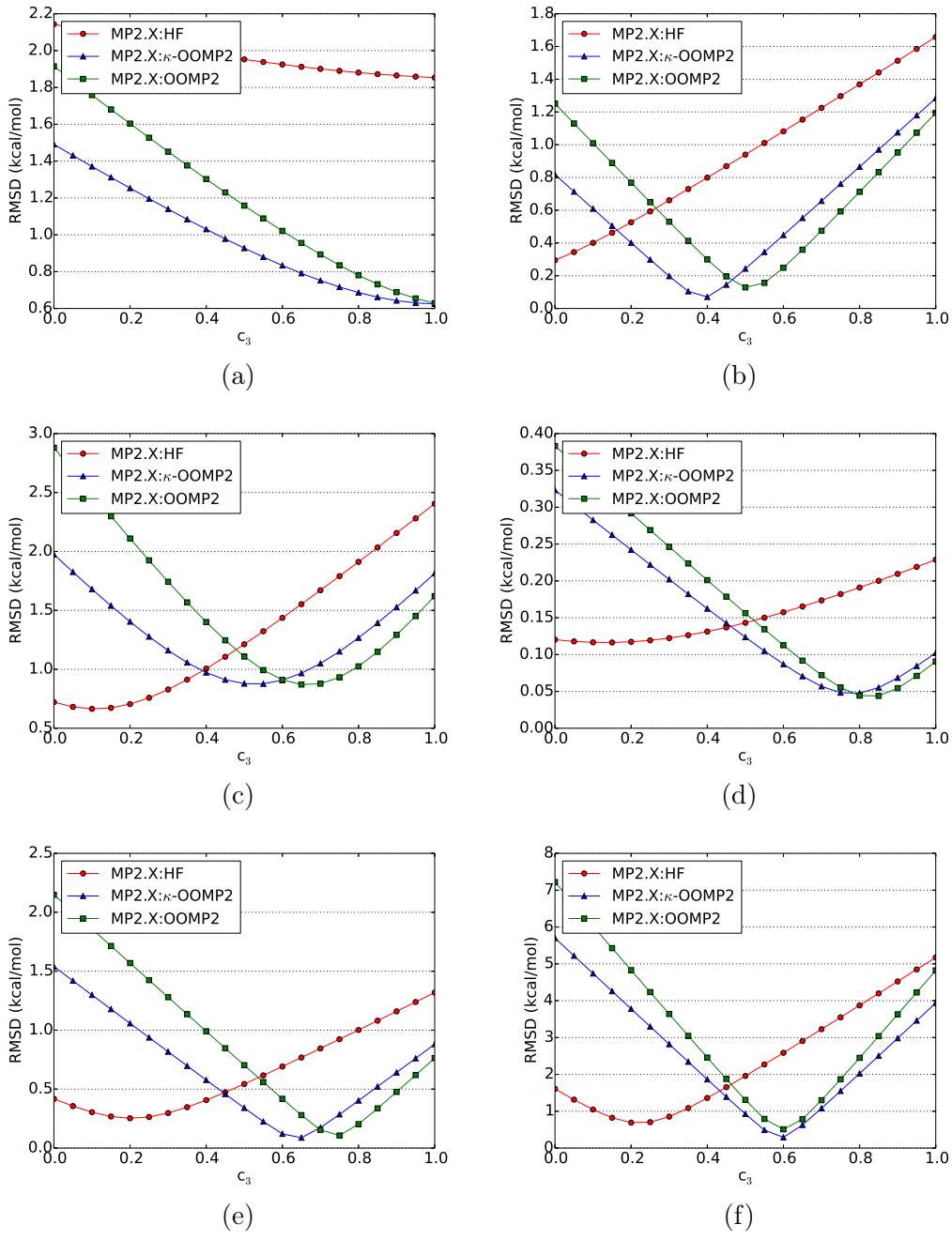

Figure D.7: Dependence of the the root-mean square deviation on the scaling of the third-order energy (c_3) in the TA13 (a), HB49 (b), Bauza30 (c), CT20 (d) data sets, XB51 (e) and Orel26rad (f); RMSD in kcal/mol; four scaled MP2.X methods (MP2.X, MP2.X:OOMP2, MP2.X:κ-OOMP2, κMP2.X:κ-OOMP2).

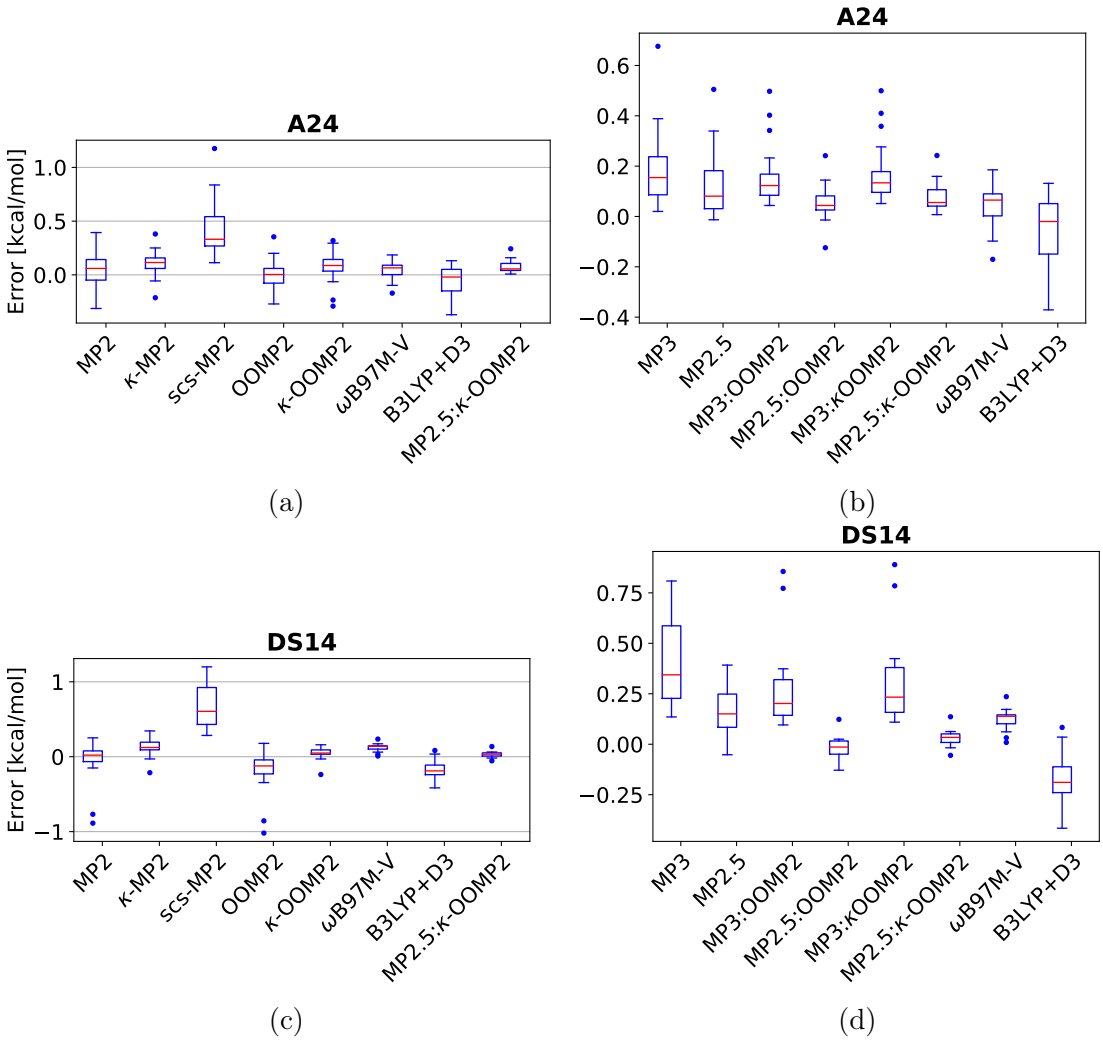

Figure D.8: Box-plots of the data-sets A24: (a) MP2 methods, (b) MP3 methods; DS14: (c) MP2 methods, (d) MP3 methods. Red lines mark the median deviation, boxes bound the central 50% of the data, whiskers enclose all data points within 1.5 times the inter-quartile range of the box edges, and points denote outlying data.

D.2 Box Plots

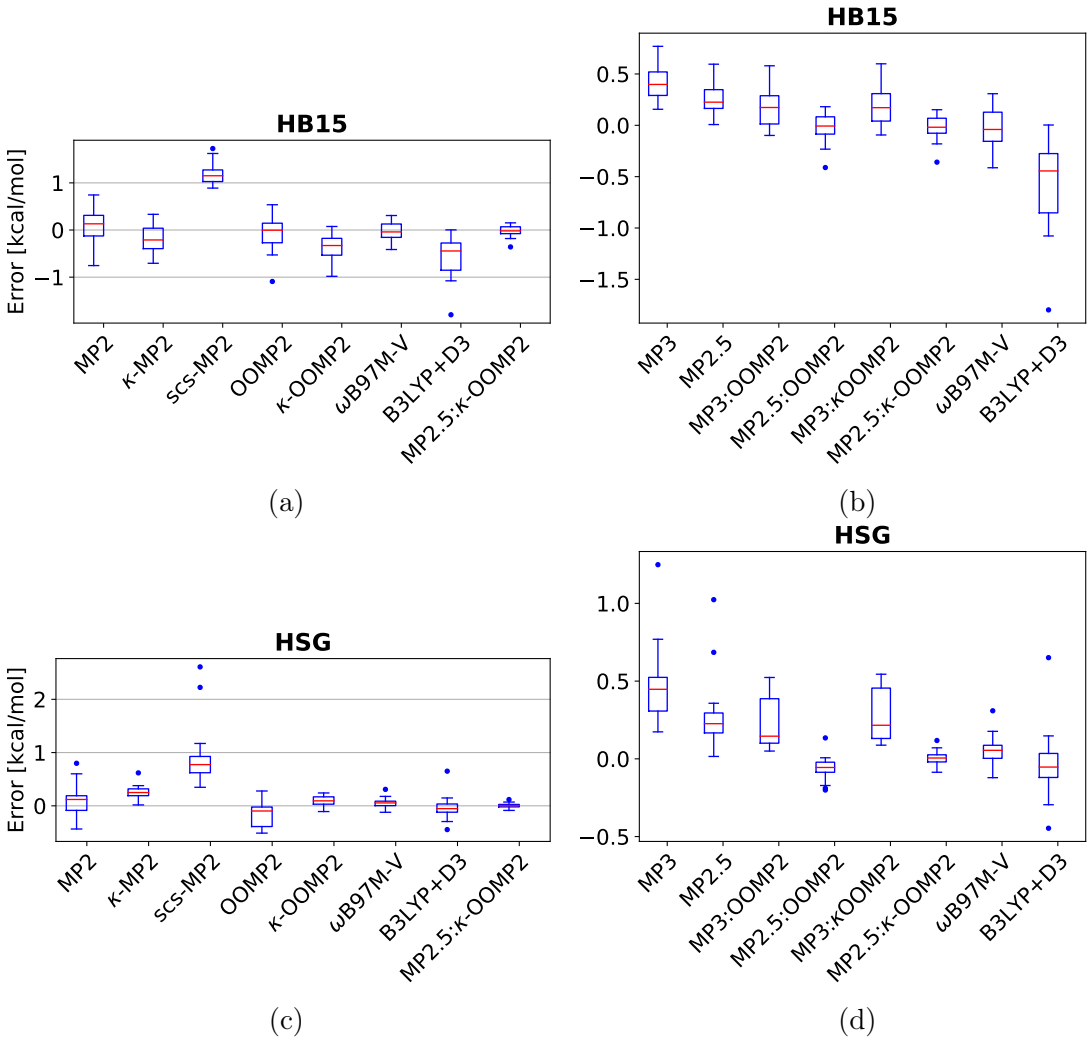

Figure D.9: Box-plots of the data-sets HB15: (a) MP2 methods, (b) MP3 methods; HSG: (c) MP2 methods, (d) MP3 methods. Red lines mark the median deviation, boxes bound the central 50% of the data, whiskers enclose all data points within 1.5 times the inter-quartile range of the box edges, and points denote outlying data.

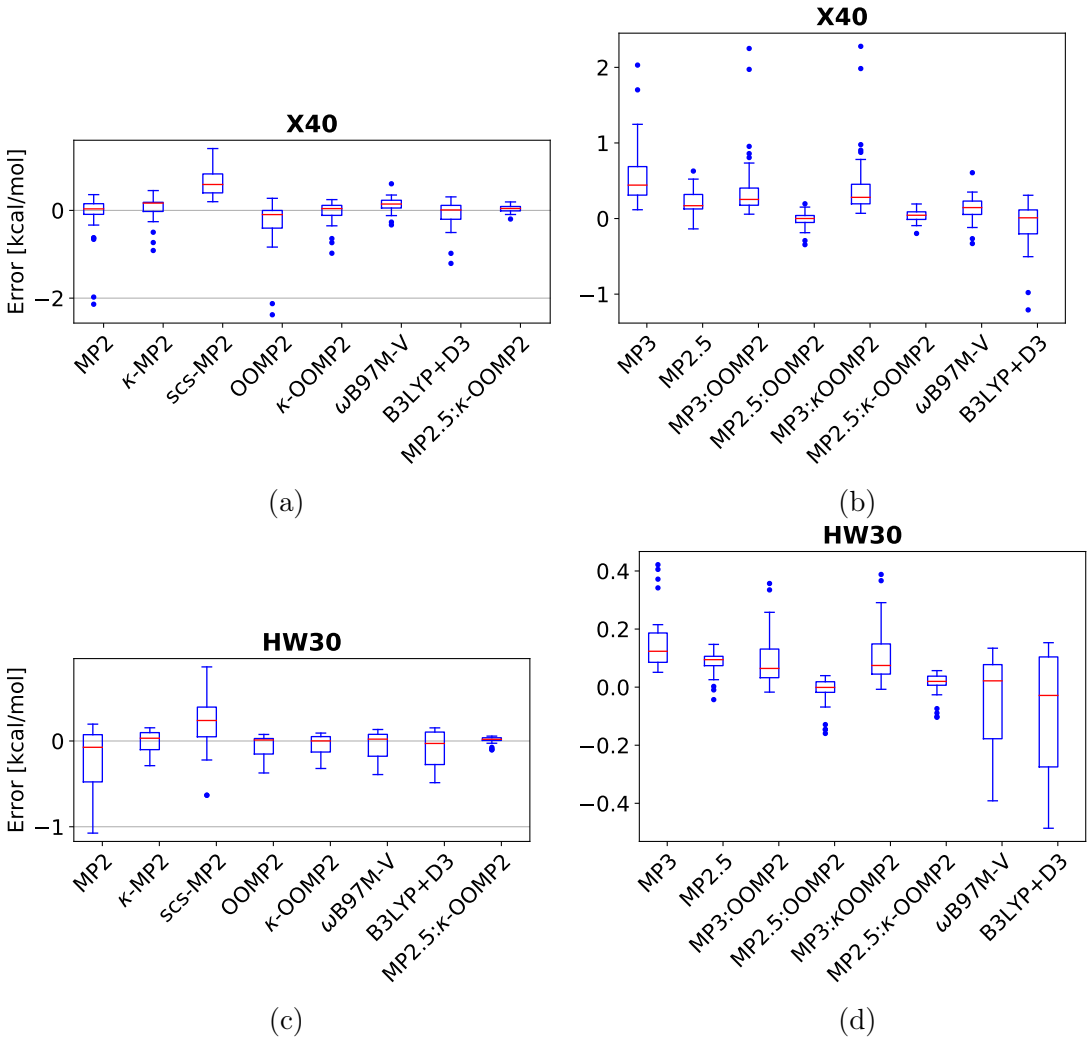

Figure D.10: Box-plots of the data-sets X40: (a) MP2 methods, (b) MP3 methods; HW30: (c) MP2 methods, (d) MP3 methods. Red lines mark the median deviation, boxes bound the central 50% of the data, whiskers enclose all data points within 1.5 times the inter-quartile range of the box edges, and points denote outlying data.

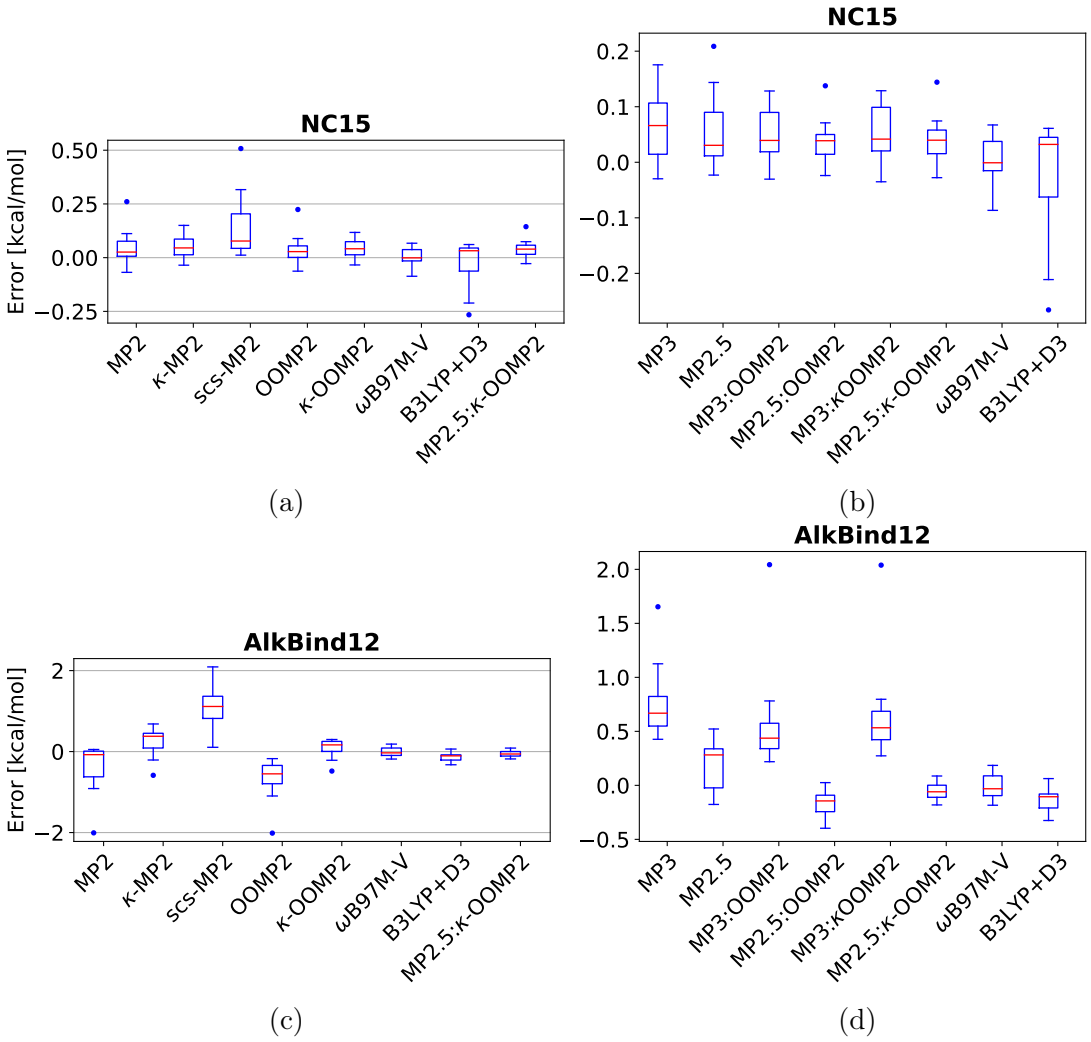

Figure D.11: Box-plots of the data-sets NC15: (a) MP2 methods, (b) MP3 methods; AlkBind12: (c) MP2 methods, (d) MP3 methods. Red lines mark the median deviation, boxes bound the central 50% of the data, whiskers enclose all data points within 1.5 times the inter-quartile range of the box edges, and points denote outlying data.

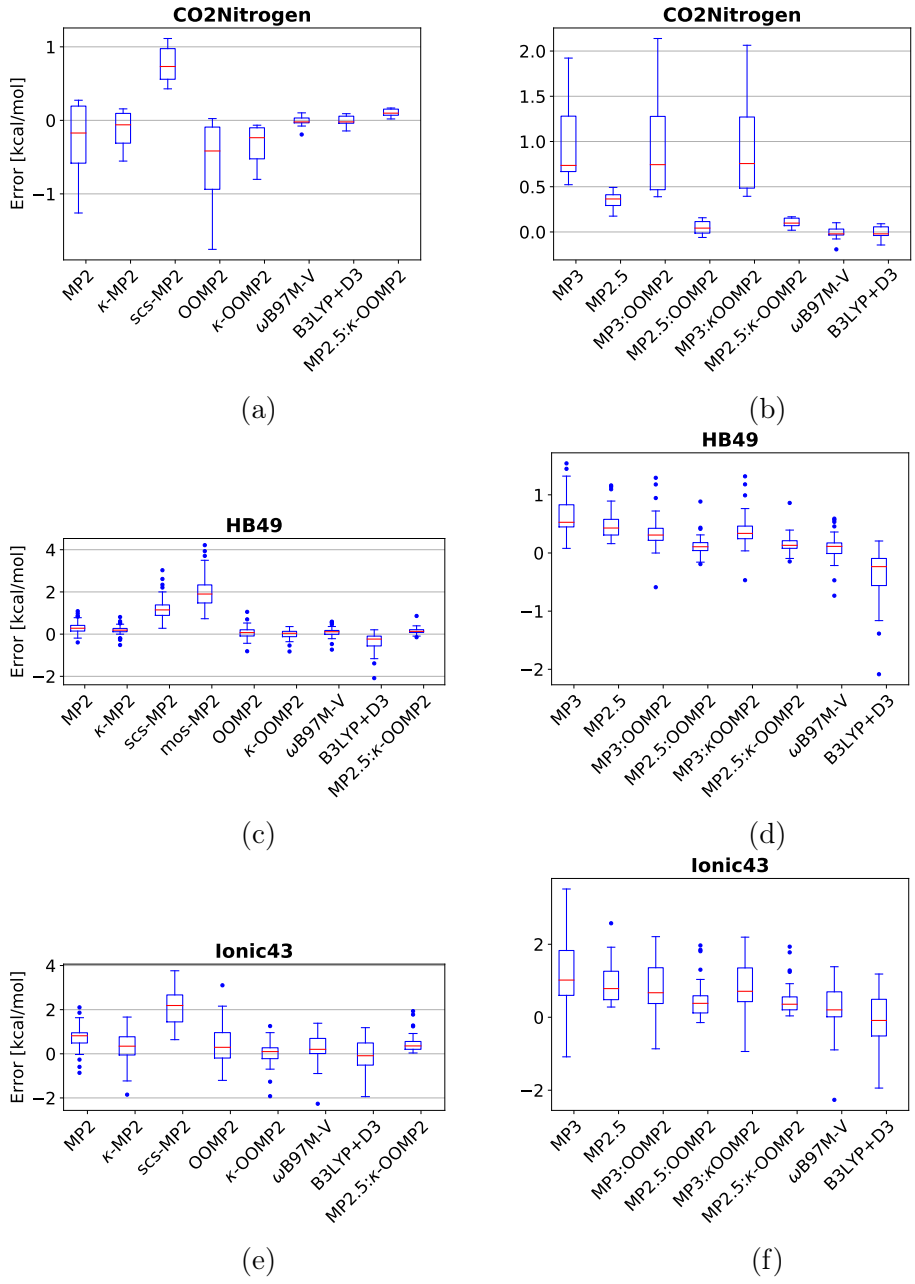

Figure D.12: Box-plots of the data-sets CO2Nitrogen16: (a) MP2 methods, (b) MP3 methods; HB49: (c) MP2 methods, (d) MP3 methods; Ionic43: (e) MP2 methods, (f) MP3 methods. Red lines mark the median deviation, boxes bound the central 50% of the data, whiskers enclose all data points within 1.5 times the inter-quartile range of the box edges, and points denote outlying data.

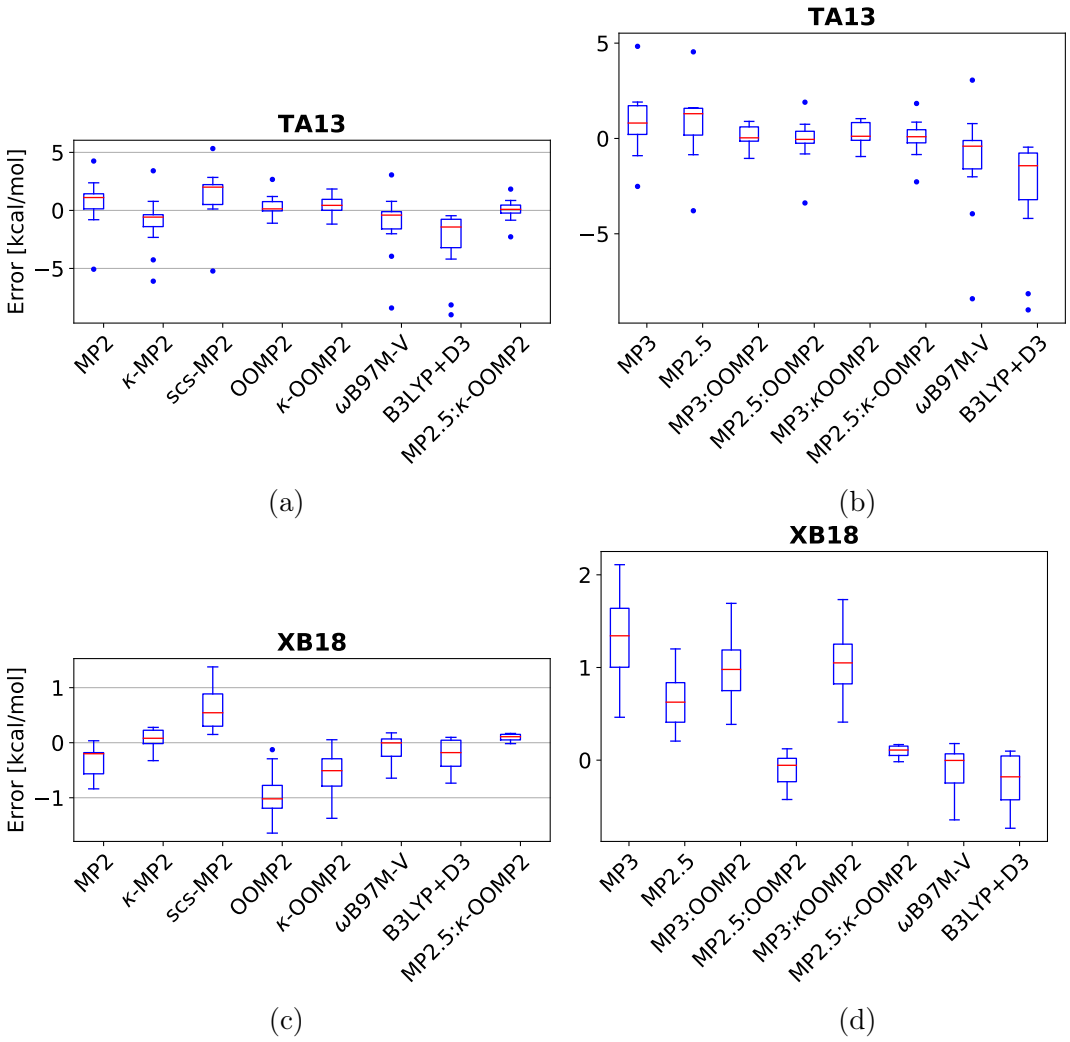

Figure D.13: Box-plots of the data-sets TA13: (a) MP2 methods, (b) MP3 methods; XB18: (c) MP2 methods, (d) MP3 methods. Red lines mark the median deviation, boxes bound the central 50% of the data, whiskers enclose all data points within 1.5 times the inter-quartile range of the box edges, and points denote outlying data.

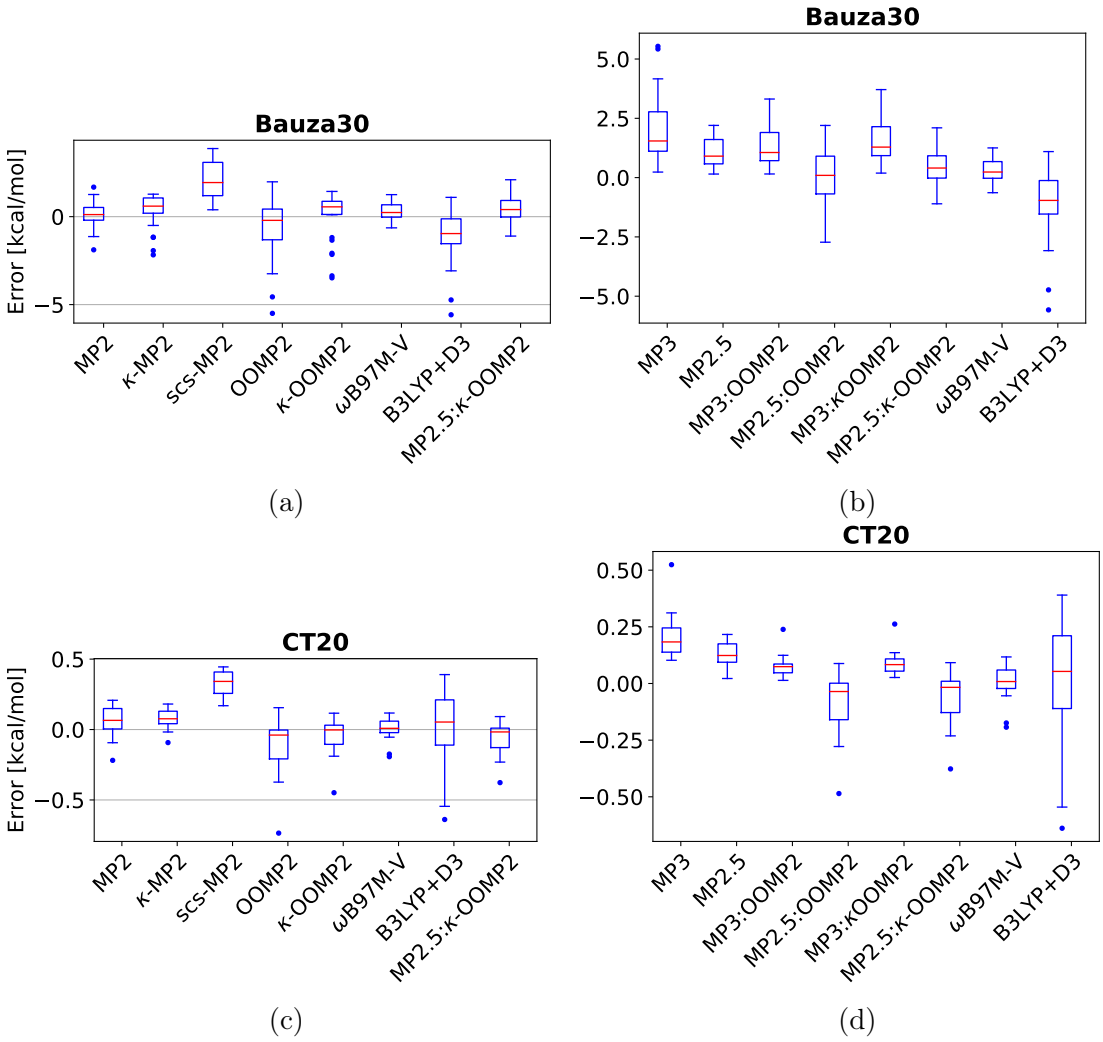

Figure D.14: Box-plots of the data-sets Bauza30: (a) MP2 methods, (b) MP3 methods; XB18: (c) MP2 methods, (d) MP3 methods. Red lines mark the median deviation, boxes bound the central 50% of the data, whiskers enclose all data points within 1.5 times the inter-quartile range of the box edges, and points denote outlying data.

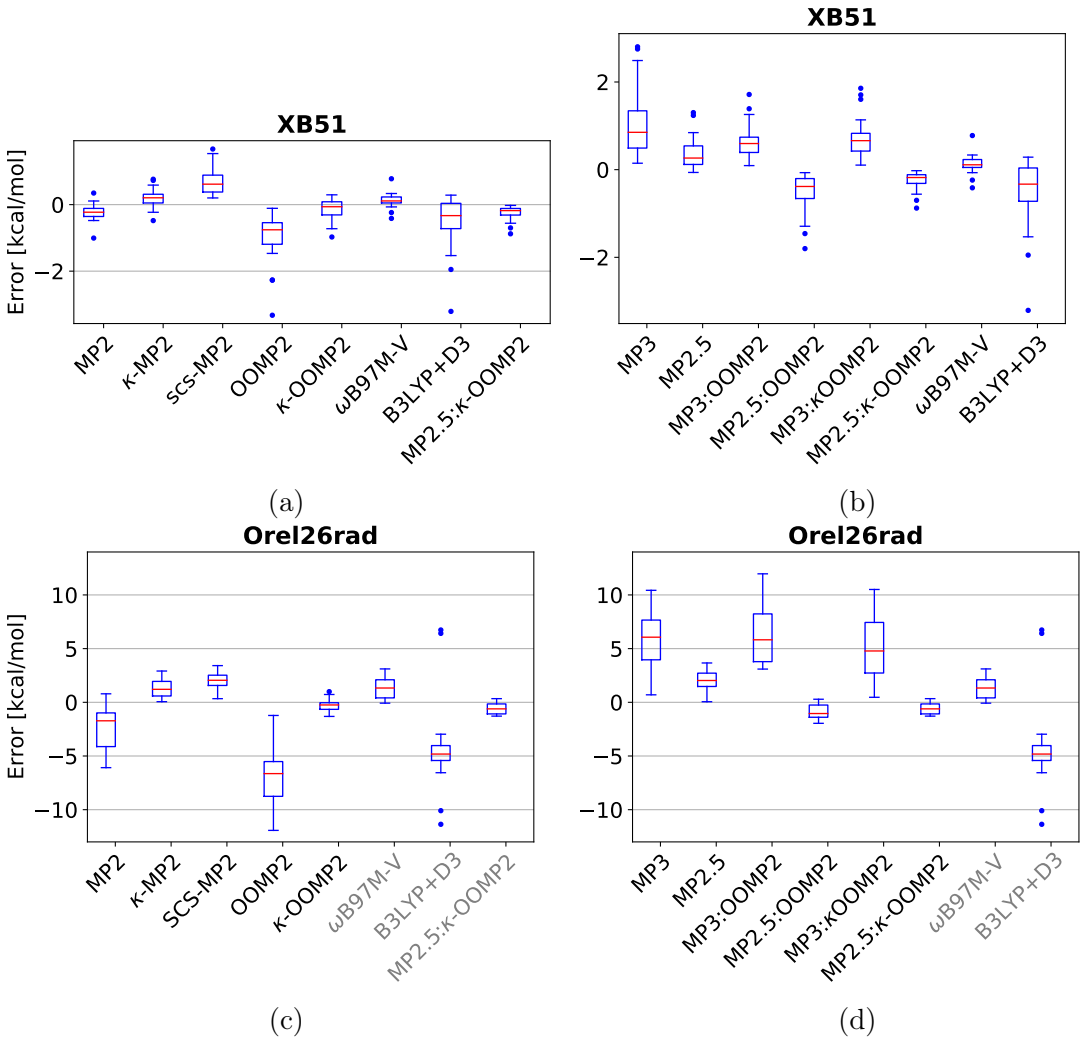

Figure D.15: Box-plots of the data-sets XB51: (a) MP2 methods, (b) MP3 methods; Orel26rad: (c) MP2 methods, (d) MP3 methods. Red lines mark the median deviation, boxes bound the central 50% of the data, whiskers enclose all data points within 1.5 times the inter-quartile range of the box edges, and points denote outlying data.

Appendix E

Computational Study of an Iron(II)-Polypyridine Electrocatalyst for CO_2 Reduction: Key Roles for Intramolecular Interactions in CO_2 Binding and Proton Transfer

E.1 Comparison of Different DFT functional

Table E.1: Comparison of the crystal structure of the initital complex ${}^{5}_{0}1^{6}$ with the optimized geometries of the three functionals used in this study.

Functional	∠(py-fe-bpy) (N_{axial}) [°]	r_{CC} (bpy) [Å]	$r_{Fe\text{-}O}$ (OTf_{ax}) [Å]	$r_{Fe\text{-}N}$ (bpy_{ax}) [Å]	$r_{Fe\text{-}N}$ (py_{x}) [Å]
ωB97X-D	104.4	1.492	2.045	2.162	2.240
crystal data	110.2	1.485	2.087	2.109	2.169

Table E.2: Adiabatic spin gap ($\Delta_{hs/ls}G = G(hs) - G(ls)$) ${}^{3}_{0}1^{5}$ to ${}^{3}_{0}1^{4}$ using different functionals.

DFT functional	$\Delta_{hs/ls}G$
ωB97M-V	-1.5
ωB97X-D	-3.6
B97-D	$+4.2$
B3LYP/D3	-3.0

Table E.3: Key reaction of the catalytic cycle using ωB97M-V with the constraint of remaining on the high spin (quintet) surface. The activation energy correspond to the intramolecular proton transfer using H_2O/OH^- as a sixth ligand; The pK_a values refer to the equilibria using acetonitrile as a ligand and experimental free energy for H^+; L corresponds to CH_3CN; all energies is kcal/mol and reduction potentials versus the Fc/Fc^+) couple.

Reaction			$\Delta_R G$	$\Delta G^{\ddagger}$	pK_a	E^0
${}^{5}_{2}1^{6}$+e$^-$	$\longrightarrow$	${}^{6}_{1}1^{6}$				-1.79
${}^{6}_{1}1^{6}$+e$^-$	$\longrightarrow$	${}^{5}_{0}1^{5}$ +L				-1.94
${}^{6}_{1}1^{6}$+e$^-$	$\longrightarrow$	${}^{5}_{0}1^{4}$ +2L				-2.38
${}^{5}_{0}1^{4}$+CO_2	$\longrightarrow$	${}^{5}_{0}2^{5}$	-7.3	8.5		
${}^{5}_{0}2^{5}$ +H^+	$\longrightarrow$	${}^{5}_{1}3^{5}$		-	28	
${}^{5}_{1}3^{5}$ +H^+ + L	$\longrightarrow$	${}^{1}_{2}4^{6}$ +H_2O		10.1	16	
${}^{1}_{2}4^{6}$ +L	$\longrightarrow$	${}^{5}_{2}1^{6}$ +CO	-6.0			

Table E.4: Adibatic quintet-triplet gap using ωB97M-V for the both 4 (${}_{0}1^{4}$) and 5 (${}_{0}1^{5}$) coordinated isomers of doubly reduced complex, the doubly reduced CO_2 adduct (${}_{0}2^{5}$) and the carboxy intermediate (${}_{0}3^{5}$) (free energies in kcal/mol).

DFT functional	Δ(G(S=5/2)$-$G(S=3/2))
${}_{0}1^{4}$	-4.2
${}_{0}1^{5}$	-1.9
${}_{0}2^{5}$	-2.4
${}_{0}2^{5}$ (TS)	-3.2
${}_{0}3^{5}$	14.0

Table E.5: Key reaction of the catalytic cycle using ω**B97X-D**. The activation energy correspond to the intramolecular proton transfer using H_2O/OH^- as a sixth ligand; The pK_a values refer to the equilibria using acetonitrile as a ligand and experimental free energy for H^+; L corresponds to CH_3CN; all energies is kcal/mol and reduction potentials versus the Fc/Fc^+) couple.

Reaction			$\Delta_R G$	$\Delta G^{\ddagger}$	pK_a	E^0
${}^{5}_{2}1^{6}+e^-$	$\longrightarrow$	${}^{6}_{1}1^{6}$				-1.76
${}^{6}_{1}1^{6}+e^-$	$\longrightarrow$	${}^{3}_{0}1^{5}$ +L				-1.71
${}^{6}_{1}1^{6}+e^-$	$\longrightarrow$	${}^{3}_{0}1^{4}$ +2L				-1.99
${}^{3}_{0}1^{4}+CO_2$	$\longrightarrow$	${}^{3}_{0}2^{5}$	-2.6	12.3		
${}^{3}_{0}2^{5}$ $+H^+$	$\longrightarrow$	${}^{5}_{1}3^{5}$		-	26	
${}^{5}_{1}3^{5}$ $+H^+$ + L	$\longrightarrow$	${}^{1}_{2}4^{6}$ $+H_2O$		10.1	16	
${}^{1}_{2}4^{6}$ +L	$\longrightarrow$	${}^{5}_{2}1^{6}$ +CO	-6.1			

Table E.6: Key reaction of the catalytic cycle using **B3LYP-D3**. The activation energy correspond to the intramolecular proton transfer using H_2O/OH^- as a sixth ligand; The pK_a values refer to the equilibria using acetonitrile as a ligand and experimental free energy for H^+; L corresponds to CH_3CN; all energies is kcal/mol and reduction potentials versus the Fc/Fc^+) couple.

Reaction			$\Delta_R G$	$\Delta G^{\ddagger}$	pK_a	E^0
${}^{5}_{2}1^{6}+e^-$	$\longrightarrow$	${}^{6}_{1}1^{6}$				-1.65
${}^{6}_{1}1^{6}+e^-$	$\longrightarrow$	${}^{3}_{0}1^{5}$ +L				-1.83
${}^{6}_{1}1^{6}+e^-$	$\longrightarrow$	${}^{3}_{0}1^{4}$ +2L				-1.91
${}^{3}_{0}1^{4}+CO_2$	$\longrightarrow$	${}^{3}_{0}2^{5}$	-0.4	9.0		
${}^{3}_{0}2^{5}$ $+H^+$	$\longrightarrow$	${}^{5}_{1}3^{5}$		-	22	
${}^{5}_{1}3^{5}$ $+H^+$ + L	$\longrightarrow$	${}^{1}_{2}4^{6}$ $+H_2O$		6.7	18	
${}^{1}_{2}4^{6}$ +L	$\longrightarrow$	${}^{5}_{2}1^{6}$ +CO	-3.8			

Table E.7: Key reaction of the catalytic cycle using **B97-D**. The activation energy correspond to the intramolecular proton transfer using H_2O/OH^- as a sixth ligand; The pK_a values refer to the equilibria using acetonitrile as a ligand and experimental free energy for H^+; L corresponds to CH_3CN; all energies is kcal/mol and reduction potentials versus the Fc/Fc^+) couple.

Reaction			$\Delta_R G$	$\Delta G^{\ddagger}$	pK_a	E^0
${}^{5}_{2}1^{6}+e^-$	$\longrightarrow$	${}^{6}_{1}1^{6}$				-1.63
${}^{6}_{1}1^{6}+e^-$	$\longrightarrow$	${}^{3}_{0}1^{5}$ +L				-1.15
${}^{6}_{1}1^{6}+e^-$	$\longrightarrow$	${}^{3}_{0}1^{4}$ +2L				-1.06
${}^{3}_{0}1^{4}+CO_2$	$\longrightarrow$	${}^{3}_{0}2^{5}$	2.5	9.4		
${}^{3}_{0}2^{5}$ $+H^+$	$\longrightarrow$	${}^{5}_{1}3^{5}$		-	14	
${}^{5}_{1}3^{5}$ $+H^+$ + L	$\longrightarrow$	${}^{1}_{2}4^{6}$ $+H_2O$		3.7	27	
${}^{1}_{2}4^{6}$ +L	$\longrightarrow$	${}^{5}_{2}1^{6}$ +CO	9.5			

E.2 Doubly Reduced Intermediates

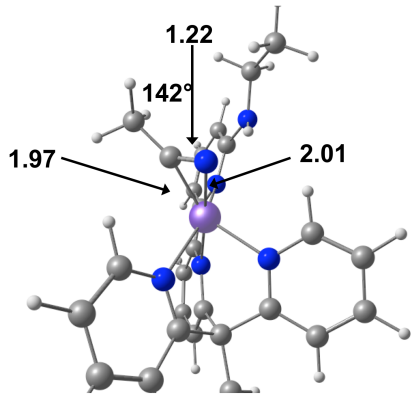

(a)

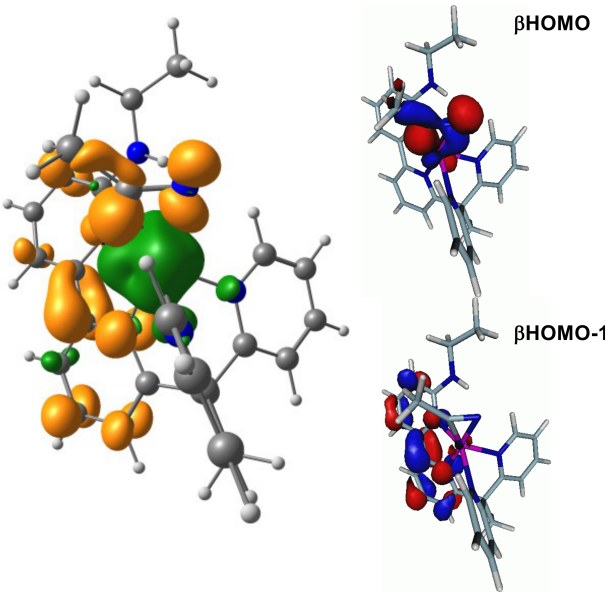

(b)

Figure E.1: (a) Geometry of ${}^{3}_{0}1^{5}$ with an η^2 coordinated CH_3CN, for comparison: free CH_3CN r(CN) = 1.16 Å vs. in the complex r(CN) = 1.22 Å; (b) Spin density and βHOMO and βHOMO-1 of doubly reduced complex ${}^{3}_{0}1^{5}$.

In order to obtain comparable electronic energies and active spaces a loosely bound CH_3CN ligand was added to ${}^{3}_{0}1^{4}$. For the initial CASSCF calculation an active space of 15 electrons in 15 orbitals for the triplet state was employed. The active space consisted of 5 metal 3d orbitals and 5 occupied and 5 unoccupied π orbitals in the ligand framework using

Table E.8: Isomerization energy from ${}^3_0\mathrm{1}^5$ to ${}^3_0\mathrm{1}^4$ using different functionals (positive values indicates that ${}^3_0\mathrm{1}^5$ is lower in energy).

DFT functional	ΔG
ωB97M-V	7.7
ωB97X-D	6.5
B97-D	2.1
PW6B95	2.4
B3LYP	2.0
TPSSh	2.8
PBE	1.8

the ICE-CI algorithm. The quasi restricted orbitals of a B97-D high spin (septet) were used as guess orbitals. All orbital with occupation numbers close to two and zero were removed from the active space except the fifth d-orbital. Subsequently, a CAS(8,7)/NEVPT2 was employed to account for both static and dynamic correlation using the regular CI solver.

The active space includes the five 3d orbitals, a bpy π^* and a py π^* in case of ${}^3_0\mathrm{1}^4$ and a CH_3CN π^*. The converged natural orbitals including their occupation number (NOON) are depicted in figs. E.2 and E.3. The NOONs of both species are summarized in tab. E.9 deviation from integers (0,1 or 2) confirms a significant amount of static correlation and an antiferromagnetic ordering. They show significant orbital entanglement of the two metal d-orbital and the two π^* ligand orbitals moieties.

In case of ${}^3_0\mathrm{1}^4$: first, a metal d_{xy} (distorted) with a pyridine π^* forming a π bond whereas both bonding (1.22 fig. E.2 (g)) and anitbonding (0.78 fig. E.2 (l)) orbitals are significantly occupied; second, a metal d_{xz} (distorted) with a bpy π^* forming a π bond whereas both bonding (1.20 fig. E.2 (h)) and anitbonding (0.80 fig. E.2 (k)) orbitals are significantly occupied.

In case of ${}^3_0\mathrm{1}^5$: first, a metal d_{yz} (distorted) with a acetonitrile π^* forming a π bond whereas both bonding (1.62 fig. E.3 (g)) and anitbonding (0.38 fig. E.3 (l)) orbitals are significantly occupied; second, a metal d_{xz} (distorted) with a bpy π^* forming a π bond whereas both bonding (1.16 fig. E.3 (h)) and anitbonding (0.84 fig. E.3 (k)) orbitals are significantly occupied.

This approach yields a free energy difference in the Gas phase using corrections from DFT frequency calculations of 2.2 kcal/mol (${}^3_0\mathrm{1}^5$). The gap is expected to shrink further since ${}^3_0\mathrm{1}^4$ should have a larger solvation energy.

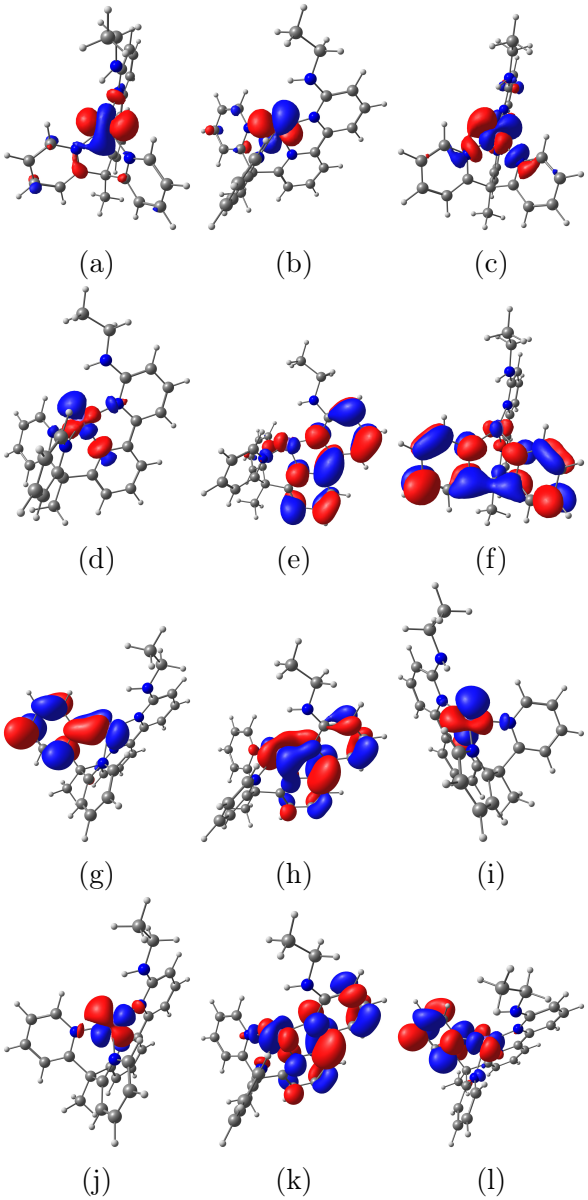

Figure E.2: MOs of ${}^{3}_{0}1^{4}$ before and after the CASSCF calculation. a)–f) unrestricted natural orbitals of the septet spin state g) NOON: 1.22 h) NOON: 1.20 i) NOON: 1.00 j) NOON: 1.00 k) NOON: 0.80 l) NOON: 0.78

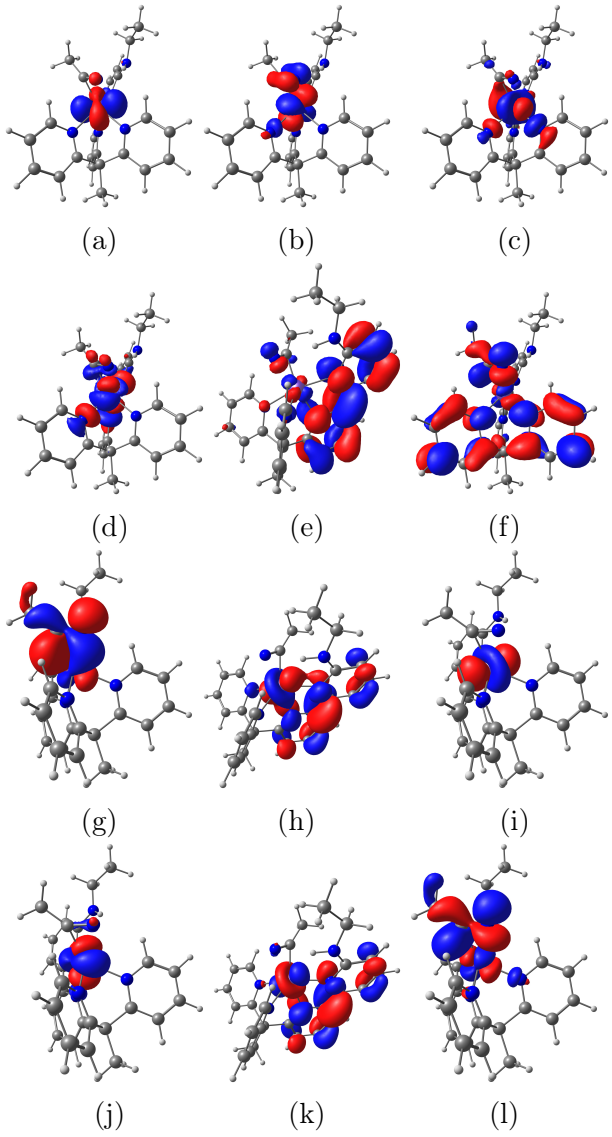

Figure E.3: MOs of ${}^{3}_{0}1^{5}$ before and after the CASSCF calculation. a)–f) unrestricted natural orbitals of the septet spin state g) NOON: 1.00 h) NOON: 1.62 i) NOON: 1.16 j) NOON: 1.00 k) NOON: 0.84 l) NOON: 0.36

Complex	NOON (d-orbital)	NOON (delocalized)
${}^{3}_{0}1^{4}$	211	1.22, 1.20, 0.80, 0.78
${}^{3}_{0}1^{5}$	211	1.62, 1.16, 0.84, 0.38

Table E.9: Natural orbital occupation number (NOON) of the CASSCF calculations.

E.3 Further Information about pK_a values

Table E.10: Comparison of free energies and computed pK_a values acetonitrile to experimental values taken from Ref. [551] using the experimental solvation energy for H^+

Reaction			$\Delta_R G$	pK_a (comp.)	pK_a (exp.) in CH_3CN	pK_a (exp.) in H_2O
PhO^-+H^+	$\longrightarrow$	PhOH	−34.2	25	29	10
$CH_3COO^-+H^+$	$\longrightarrow$	CH_3COOH	−27.3	20	24	5
$CF_3CH_2O^-+H^+$	$\longrightarrow$	CF_3CH_2COH	−43.4	32		

Table E.11: The activation energies and pK_a values of both protonation steps. The activation and reaction free energies correspond to the intramolecular proton transfer using H_2O/OH^- as a sixth ligand. The pK_a values refer to the equilibria using acetonitrile as a ligand and experimental free energy for H^+.

Reaction					$\Delta_R G$	pK_a
${}^{3}_{0}2^{5}$	$+H^+$	$\longrightarrow$	${}^{5}_{1}3^{5}$		−35.3	26
${}^{5}_{1}3^{5}$	$+H^+ + L$	$\longrightarrow$	${}^{1}_{2}4^{6}$	$+ H_2O$	−20.2	15
${}^{1}_{1}3^{6}$	$+H^+$	$\longrightarrow$	${}^{1}_{2}4^{6}$	$+ H_2O$	−19.2	14
${}^{3}_{0}1^{4}$	$+H^+ + L$	$\longrightarrow$	${}^{1}_{1}4^{6}$		−45.6	32
${}^{1}_{1}4^{6}$	$+H^+ + L$	$\longrightarrow$	${}^{5}_{2}1^{6}$	$+H_2$	−27.8	20
$HCO_3{}^-+H^+$	$\longrightarrow$	H_2CO_3			−18.4	13
OH^-+H^+	$\longrightarrow$	H_2O			−63.5	47

E.4 Additional Information about Intermediates in the Cycle

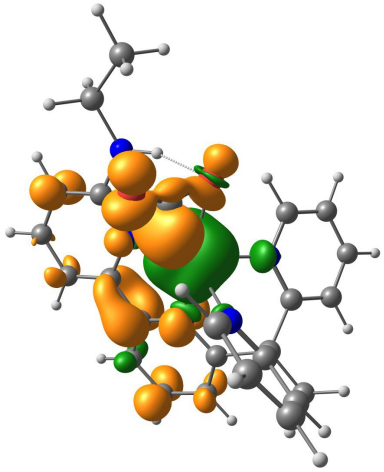

Figure E.4: Spin density the doubly reduced η^2 CO_2 adduct ${}^{3}_{0}1^{5}$.

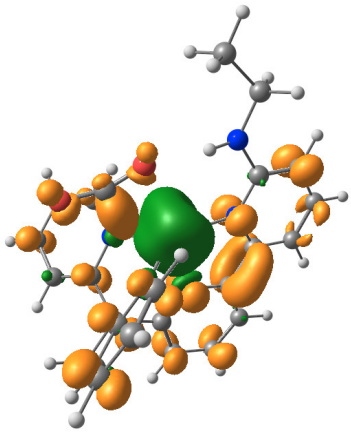

Figure E.5: Spin density the transition state forming the doubly reduced η^2 CO_2 adduct ${}^{3}_{0}1^{5}$.

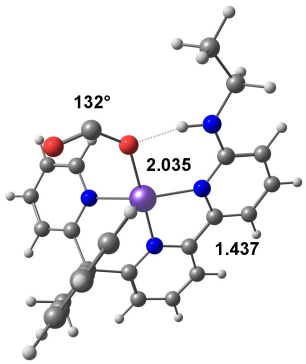

Figure E.6: Geometry of the κ-O CO_2 adduct ${}^{3}_{0}3^{5}$ (distances in Å).

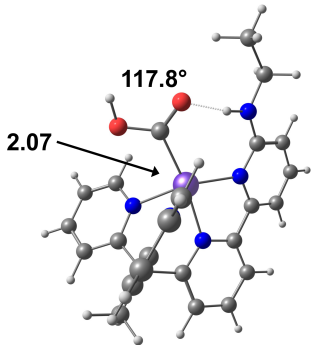

Figure E.7: Geometry of ${}^{5}_{1}3^{5}$ (distances in Å).

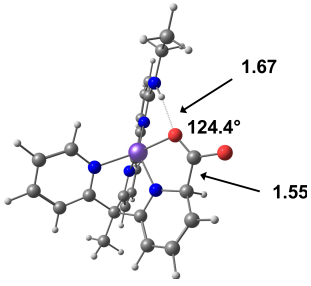

Figure E.8: Geometry of for a CO2 adduct involving metal ligand cooperation $({}^{5}_{0}2^{5CC})$(distances in Å).

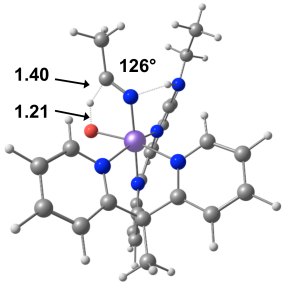

Figure E.9: Geometry of the transition state of a protonation of the activated acetonitrile using H_2O as the proton source (distances in Å). The barrier is over 30 kcal/mol.

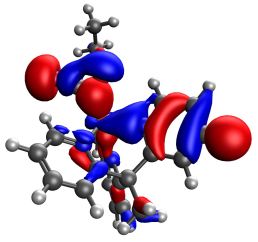

(a)

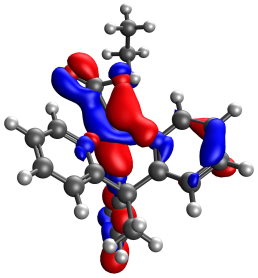

(b)

Figure E.10: Bonding orbitals illustrating the dative σ bond of the CO_2 adduct $[Fe(bpy^{NHEt}PY2\,Me)(\eta^2{-}CO_2)]^0$ $({}^3_0 2^5)$.

Appendix F

Mechanistic Insights into Co and Fe Quaterpyridine Based CO_2 Reduction Catalysts: Metal-Ligand Orbital Interaction as the Key Driving Force for Distinct Pathways

F.1 Additional Information on Possible Intermediates

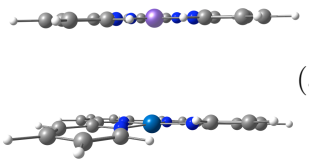

(a)

(b)

Figure F.1: Side view of (a) the doubly reduced $[Fe(qpy)]^0$ intermediate $^2[\mathbf{1Fe}(4)]^0$ and (b) the doubly reduced $[Co(qpy)]^0$ intermediate $^3[\mathbf{1Co}(4)]^0$.

Functional	% HF exchange	$<S^2>$	χ(Co)
B97-D	0	0.75	0.1
PBE10	10	0.77	0.0
B3LYP	20	0.92	0.29
MN15	44	0.82	0.15
ωB97M-V	15*	1.45	0.75
ωB97X-D	22.2*	1.33	0.65
CASSCF(5,6)	100	0.75	0.33

Table F.1: Mulliken spin population of the Co center (χ(Co)) of the doubly reduced initial complex $[Co(qpy)]^0$ in the doublet spin state (^{2}[**1Co**(4)]^0) for a variety of different DFT functionals. (*short range)

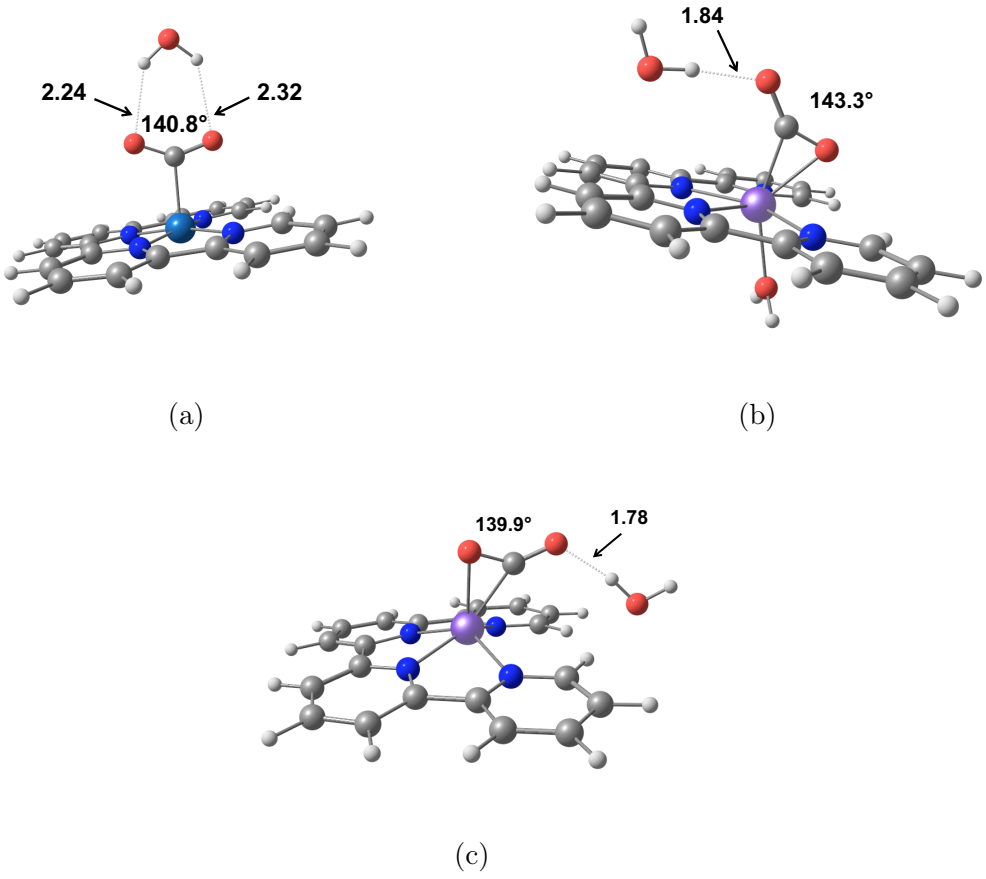

(a) (b)

(c)

Figure F.2: Geometrical parameters of all three CO_2 adducts discussed in the cycle with an explicit water added to stabilze the CO_2 (a) ^{2}[**2Co**(5)]^0; (b) ^{4}[**2Fe**(6)]$^+$; (c) ^{3}[**2Fe**(5)]^0.

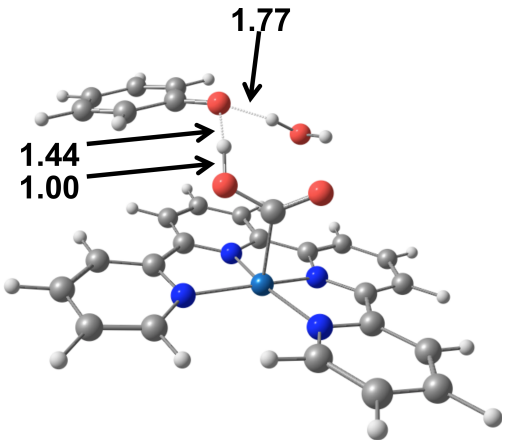

Figure F.3: Geometrical parameters for a phenoxide complex after the first protonation yielding $^{2}[\mathbf{3Co}(5)]^{+}$. Note that this is only a minimum when the carboxy O-H distance is frozen and thus the frequency calculation has a negative frequency. The free energy for the formation of this complex from $^{2}[\mathbf{2Co}(4)]^{0}$, H_2O and PhOH is 10.6.

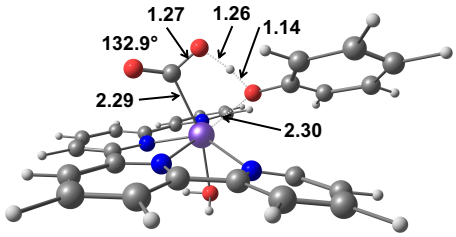

Figure F.4: Geometrical parameters for the Transition state of the first protonation of $^{3}[\mathbf{2Fe}(5)]^{0}$ where the water molecule acts as a ligand.

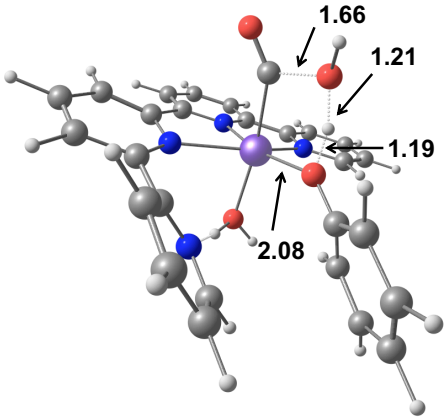

Figure F.5: Geometrical parameters for the Transition state of the second protonation of $^{5}[\mathbf{3Fe}(5)]^{+}$ where the water molecule acts as a ligand.

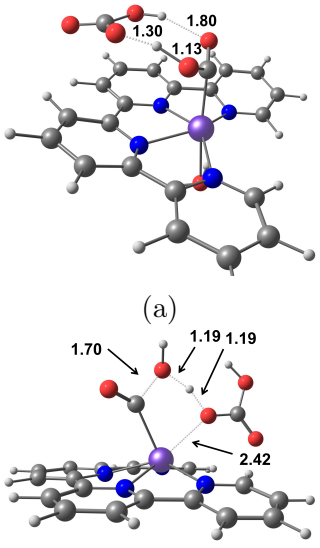

Figure F.6: Geometrical parameters of (a) the transition state of the first protonation step and (b) the transition step of the second protonation step using phenol as the acid source after two reduction steps for the Fe-catalyst ($[Fe^{II}(qpy)(H_2O)_2]^{2+}$).

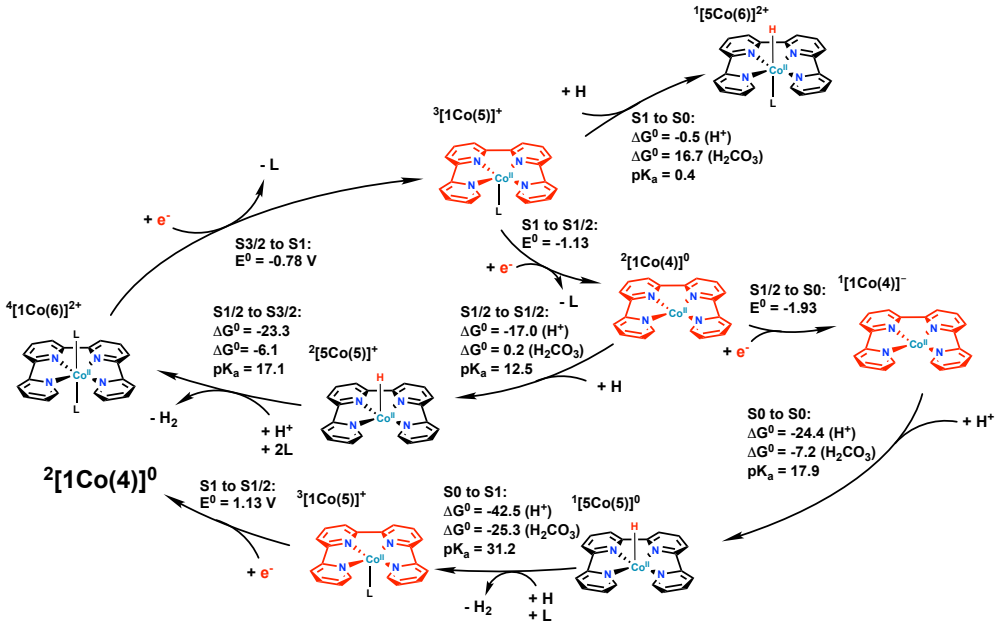

Figure F.7: Proposed mechanism for the a possible HER mechanism using $[Co(qpy)L_2]^{2+}$; the species 5Co corresponds to a metal hydride (Co−H); the red colored molecular moiety indicate localization of the excess electrons; reaction in kcal/mol; reduction potentials in V against Fc/Fc^+; L = H_2O.

F.2 HER

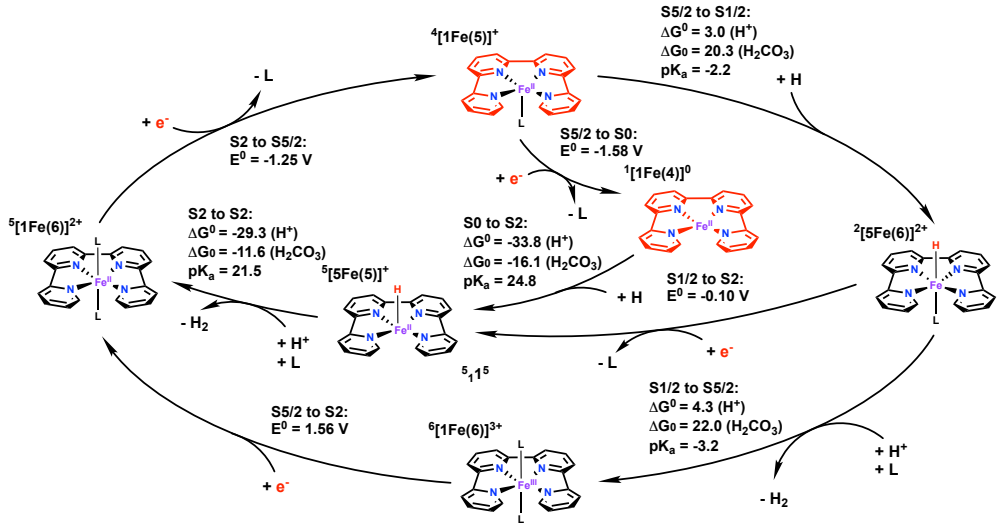

Figure F.8: Proposed mechanism for the a possible HER mechanism using $[Fe(qpy)L_2]^{2+}$; the species 5Fe corresponds to a metal hydride (Fe−H); the red colored molecular moiety indicate localization of the excess electrons; reaction in kcal/mol; reduction potentials in V against Fc/Fc^+; L = H_2O.

F.3 Full Cycles Including a Third Reduction

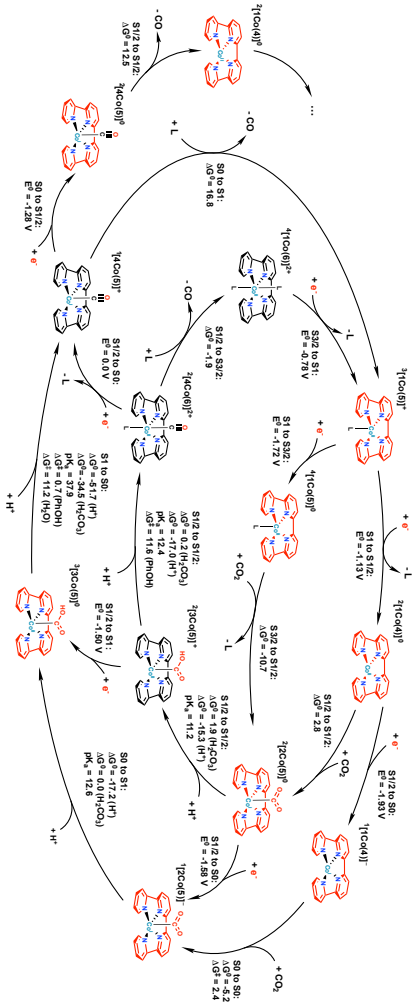

Figure F.9: Proposed mechanism for the selective CO_2 to CO reduction including a possible third reduction using $[Co(qpy)L_2]^{2+}$; the red colored molecular moiety indicate localization of the excess electrons; reaction in kcal/mol; reduction potentials in V against Fc/Fc^+; $L = H_2O$.

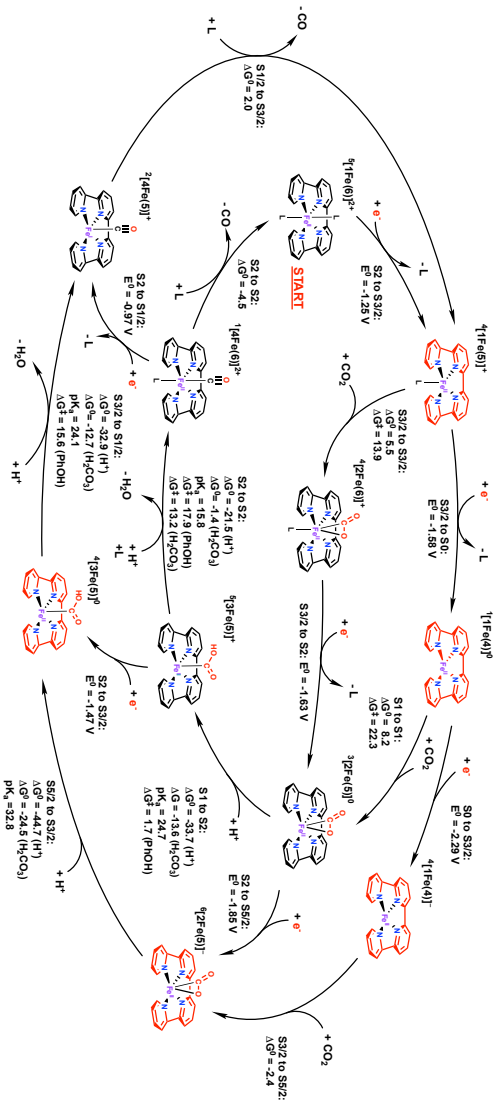

Figure F.10: Proposed mechanism for the selective CO_2 to CO reduction including a possible third reduction using $[Fe(qpy)L_2]^{2+}$; the red colored molecular moiety indicate localization of the excess electrons; reaction in kcal/mol; reduction potentials in V against Fc/Fc^+; $L = H_2O$.

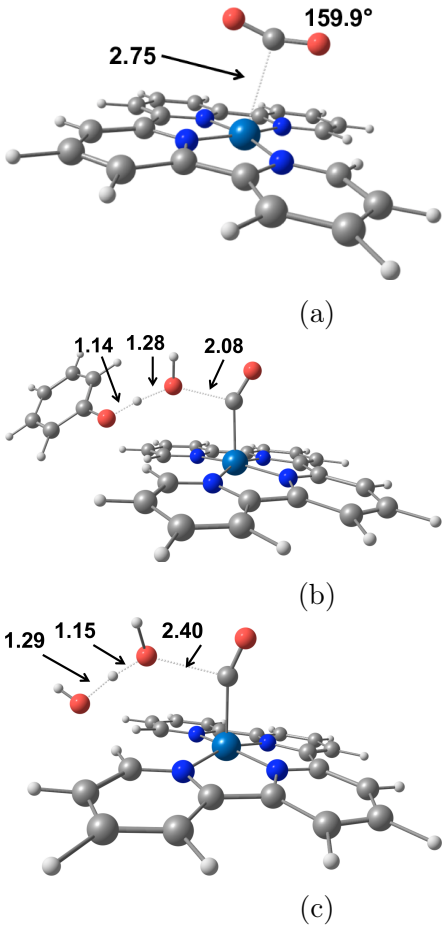

Figure F.11: Geometrical parameters of the transition states for the EEEC pathway (a) the transition of the CO_2 addition yielding $[Co(qpy)(CO_2{-}\kappa C)]^{-1}$ (S=0) (after three reductions); (b) the transition step of the second protonation step using phenol as the acid source steps yielding $[Co(qpy)CO]^0$(S=0) (after three reduction); c) using water as the acid source (distances in Å).

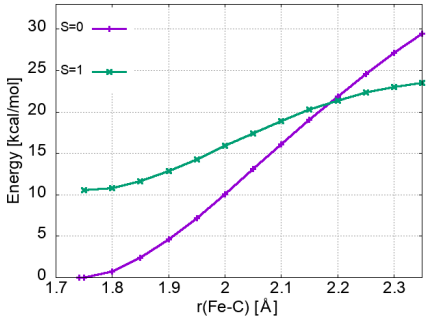

(a)

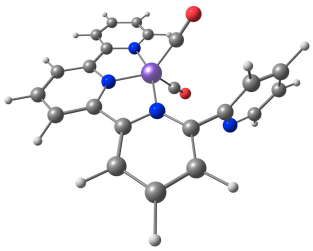

(b)

Figure F.12: (a) Possible doubly reduced di-carbonyl (S = 0) intermediate resulting in a partial dissociation of the qpy ligand; (b) relaxed PES scan for the doubly reduced singlet and triplet carbonyl complexes $^{1}[\mathbf{4Fe}(5)]^{0}$ (purple) and $^{3}[\mathbf{4Fe}(5)]^{0}$ (green); energy relative to the singlet minimum at 1.74 Å.

F.4 Functional Dependency

For all cobalt cycles the B3LYP geometries, and for all iron cycles the ωB97X-D geometries were used. The reduction potentials in table F.2 show that for the cobalt catalyst B3LYP-D3 predicts the reduction potentials with good accuracy. Both ωB97X-D and TPSSh-D3 predict the reduction potentials with acceptable accuracy (within 350 mV) whereas ωB97X-D systematically overestimates the potentials and TPSSh-D3 systematically underestimates the potentials. The reduction potentials in table F.3 show that for the iron catalyst, both range separated hybrids ωB97X-D and ωB97M-V reproduce experimental results with high accuracy. The three hybrid functionals seem to systematically underestimate the reduction potentials and predict overly large changes in redox potentials between first and second reductions e.g B3LYP-D3: 0.49 V or PBE0-D3: 0.68 V versus experiment: 0.23 V. This suggests that the relative stability between the first and second reduction is underestimated.

Based on the reduction potentials, ωB97X-D is most acceptable to describe both systems. The energetics (reduction potentials, free energies and pK_a values) and kinetics for both systems are summarized in tables F.4 and F.5. The key findings from the main manuscript remain valid: lower rate limiting barrier and lower overpotential in the Co catalyst, higher pK_a for the protonation in the Fe catalyst and similar relative pK_a for the two protonation steps in the Co cycle (compare tables F.4 and F.6). The negative reduction potentials for the Co catalyst can be rationalized with table F.1 and the CASSCF calculations (see section CASSCF), the ωB97X-D functional underestimates the metal ligand coupling for $^2[\mathbf{1Co}(4)]^0$ and thus is not optimal to describe the cobalt catalyst.

Other functionals are not satisfactory for both systems simultaneously. For instance, the B3LYP functional describes the Co system best based on the reduction potentials and the comparison to the CASSCF calculations (table F.1) and the cycle is summarized in table F.6. But unfortunately B3LYP-D3 describes the iron system quite poorly (see table F.7). First, the reduction potentials are too positive and the reduction window is too wide: 0.49 V versus 0.23 V experimentally. Second, the predicted barrier for the CO_2 addition after the first reduction is $\Delta G^\dagger$ = 10.9 kcal/mol versus the experimentally estimated $\Delta G^\dagger$ = 15 kcal/mol. Third, the CO release after a third reduction is significantly endergonic (ΔG = +8.5 kcal/mol) which makes a fourth reduction likely whereupon CO release becomes even more unlikely (ΔG = 15.1 kcal/mol). This is in contrast to the experimental observation that suggest a three electron pathway. Since B3LYP-D3's prediction of the reduction potentials of the carbonyl intermediates deviate by more than −500 mV, this suggests that B3LYP-D3 overestimates the stability of these iron carbonyls which could rationalize the very endergonic CO release.

Even so, we note that the comparison of both cycles with B3LYP-D3 (see tables F.6 and F.7) shows that many conclusions from the main text hold true despite its poor performance for the iron system: the rate limiting barrier is lower in the Co system but the pK_a's are higher in the Fe system. However, B3LYP-D3 predicts a slightly different cycle for the iron system: First, the addition of CO_2 has almost identical barriers after the first and second reduction and thus both pathways are feasible. The reason that the barriers are comparable is most

likely linked to the stability of the doubly reduced intermediate $^{1}[\mathbf{1Fe}(0)]^{0}$. B3LYP-D3 seems to underestimate the relative stability (dV is 0.49) of this intermediate which consequently also results in a smaller barrier for the subsequent CO_2 addition after the second reduction. Second, a third reduction becomes a degradation pathway.

The ωB97M-V functional is one of the top performing functionals in an extensive benchmark study [20] and consequently was also employed in this study. It is able to accurately predict the reduction potentials for the iron system (including the carbonyls) but slightly underestimates the barrier for the CO_2 addition after the first reduction. Furthermore, the functional predicts the same pathway for the iron system: a larger barrier for CO_2 addition after the second reduction, similar relative pK_a values and a feasible CO release after a third reduction (see table F.9). For the Co system, the functional systematically overestimates the reduction potentials by more than -500 mV and the reduction window is also slightly too wide (dV = 380 mV). Similarly to ωB97X-D, the too-negative reduction potentials can be rationalized with the predicted weak metal-ligand coupling for $^{2}[\mathbf{1Co}(4)]^{0}$ by ωB97M-V as shown in table F.1 and the CASSCF calculations (see section CASSCF), and thus ωB97M-V is not optimal to describe the cobalt system. However the comparison of both metals in tables F.8 and F.9 shows similar conclusions to those drawn in the main manuscript: same relative pK_a values for both Co and Fe intermediates, larger pK_a values for the iron system but smaller rate-limiting barrier in the Co cycle.

In summary, this discussion has provided detailed justification for the unfortunate necessity of using different functionals for the two systems. However, both geometries and electronic configurations are more robust to a range of DFT functionals. This is illustrated by the spin densities of singly ($[\mathbf{1Fe}(5)]^{+}$, $[\mathbf{1Co}(5)]^{+}$) and doubly ($[\mathbf{1Fe}(4)]^{0}$, $[\mathbf{1Co}(4)]^{0}$) reduced intermediates for all viable spin states. The figures F.13 to F.21 show that the non-innocence of the qpy ligand in both reduction steps for both metal is confirmed with a local functional (B97-D), a hybrid functional (B3LYP-D3) and a range separated functional (ωB97X-D). The key molecular orbitals from the main text are also robust with respect to different hybrid functionals as figure F.19 illustrates (aside from $^{2}[\mathbf{1Co}(4)]^{0}$). B3LYP MOs have a slightly higher metal contribution in comparison to ωB97X-D; but the electronic configuration is identical and the central conclusion of the main manuscript remain valid when comparing the MOs for the same functional (aside from $^{2}[\mathbf{1Co}(4)]^{0}$). We employed multi-reference wave function calculations for $^{2}[\mathbf{1Co}(4)]^{0}$ and $^{1}[\mathbf{1Fe}(4)]^{0}$ to get better insights into their electronic structure (see section CASSCF). The binding mode of the CO_2 adducts is also not sensitive to the choice of density functional: $^{2}[\mathbf{2Co}(5)]^{0}$ converges to an η^{1}-κC binding mode with both B3LYP and ωB97X-D even when an η^{2} start geometry is used and vice versa, $^{3}[\mathbf{2Fe}(5)]^{0}$ converges to an η^{2} binding mode; the final structures are depicted in figures F.20 and F.21.

Reaction			E^0
ωB97X-D			
$^4[\mathbf{1Co}(6)]^{2+} + e^-$	$\longrightarrow$	$^3[\mathbf{1Co}(5)]^{+} + L$	-1.14
$^3[\mathbf{1Co}(5)]^{+} + e^-$	$\longrightarrow$	$^2[\mathbf{1Co}(4)]^{0} + L$	-1.48
B3LYP-D3			
$^4[\mathbf{1Co}(6)]^{2+} + e^-$	$\longrightarrow$	$^3[\mathbf{1Co}(5)]^{+} + L$	-0.78
$^3[\mathbf{1Co}(5)]^{+} + e^-$	$\longrightarrow$	$^2[\mathbf{1Co}(4)]^{0} + L$	-1.13
ωB97M-V			
$^4[\mathbf{1Co}(6)]^{2+} + e^-$	$\longrightarrow$	$^3[\mathbf{1Co}(5)]^{+} + L$	-1.34
$^3[\mathbf{1Co}(5)]^{+} + e^-$	$\longrightarrow$	$^2[\mathbf{1Co}(4)]^{0} + L$	-1.72
PBE0-D3			
$^4[\mathbf{1Co}(6)]^{2+} + e^-$	$\longrightarrow$	$^3[\mathbf{1Co}(5)]^{+} + L$	-0.86
$^3[\mathbf{1Co}(5)]^{+} + e^-$	$\longrightarrow$	$^2[\mathbf{1Co}(4)]^{0} + L$	-1.42
TPSSh-D3			
$^4[\mathbf{1Co}(6)]^{2+} + e^-$	$\longrightarrow$	$^3[\mathbf{1Co}(5)]^{+} + L$	-0.77
$^3[\mathbf{1Co}(5)]^{+} + e^-$	$\longrightarrow$	$^2[\mathbf{1Co}(4)]^{0} + L$	-0.95

Table F.2: Reduction potentials for $[Co^{II}(qpy)(H_2O)_2]^{2+}$ using different DFT functionals; reduction potentials in V versus the Fe^+/Fc couple (experimental reduction potentials for reference: -0.95 V & -1.18 V); L = H_2O.

Reaction			E^0
ωB97X-D			
$^5[\mathbf{1Fe}(6)]^{2+} + e^-$	$\longrightarrow$	$^4[\mathbf{1Fe}(5)]^{+} + L$	-1.25
$^4[\mathbf{1Fe}(5)]^{+} + e^-$	$\longrightarrow$	$^1[\mathbf{1Fe}(4)]^{0} + L$	-1.58
B3LYP-D3			
$^5[\mathbf{1Fe}(6)]^{2+} + e^-$	$\longrightarrow$	$^4[\mathbf{1Fe}(5)]^{+} + L$	-0.94
$^4[\mathbf{1Fe}(5)]^{+} + e^-$	$\longrightarrow$	$^1[\mathbf{1Fe}(4)]^{0} + L$	-1.41
ωB97M-V			
$^5[\mathbf{1Fe}(6)]^{2+} + e^-$	$\longrightarrow$	$^4[\mathbf{1Fe}(5)]^{+} + L$	-1.39
$^4[\mathbf{1Fe}(5)]^{+} + e^-$	$\longrightarrow$	$^1[\mathbf{1Fe}(4)]^{0} + L$	-1.58
PBE0-D3			
$^5[\mathbf{1Fe}(6)]^{2+} + e^-$	$\longrightarrow$	$^4[\mathbf{1Fe}(5)]^{+} + L$	-0.98
$^4[\mathbf{1Fe}(5)]^{+} + e^-$	$\longrightarrow$	$^1[\mathbf{1Fe}(4)]^{0} + L$	-1.66
TPSSh-D3			
$^5[\mathbf{1Fe}(6)]^{2+} + e^-$	$\longrightarrow$	$^4[\mathbf{1Fe}(5)]^{+} + L$	-0.92
$^4[\mathbf{1Fe}(5)]^{+} + e^-$	$\longrightarrow$	$^1[\mathbf{1Fe}(4)]^{0} + L$	-1.31

Table F.3: Reduction potentials for $[Fe^{II}(qpy)(H_2O)_2]^{2+}$ using different DFT functionals; reduction potentials in V versus the Fe^+/Fc couple (experimental reduction potentials for reference: -1.39 V & -1.60 V); L = H_2O.

Reaction			E^0	$\Delta_R G^0$	pK_a	$\Delta G^{\ddagger}$
$^4[\mathbf{1Co}(6)]^{2+}$ +e^-	$\longrightarrow$	$^3[\mathbf{1Co}(5)]^{+}$ +L	−1.14			
$^3[\mathbf{1Co}(5)]^{+}$ +e^-	$\longrightarrow$	$^2[\mathbf{1Co}(4)]^{0}$ +L	−1.48			
$^2[\mathbf{1Co}(4)]^{0}$ + CO_2	$\longrightarrow$	$^2[\mathbf{2Co}(5)]^{0}$		8.5		
$^2[\mathbf{2Co}(5)]^{0}$ +H^+	$\longrightarrow$	$^4[\mathbf{3Co}(5)]^{+}$ +L			16	
$^2[\mathbf{3Co}(5)]^{+}$ +H^+ +L	$\longrightarrow$	$^2[\mathbf{4Co}(6)]^{2+}$ +H_2O			17	10.8
$^2[\mathbf{4Co}(6)]^{2+}$ +L	$\longrightarrow$	$^4[\mathbf{1Fe}(6)]^{2+}$ +CO		−6.8		

Table F.4: ω**B97X-D**: reaction of the catalytic cycle for $[Co^{II}(qpy)(H_2O)_2]^{2+}$. Activation energies ($\Delta G^{\ddagger}$) and Gibbs free reaction energies ($\Delta_R G^0$) are reported in kcal/mol and barriers for protonation use Phenol as a proton source; reduction potentials in V versus the Fe^+/Fc couple (experimental reduction potentials for reference: −0.95 V & −1.18 V); L = H_2O.

Reaction			E^0	$\Delta_R G^0$	pK_a	$\Delta G^{\ddagger}$
$^5[\mathbf{1Fe}(6)]^{2+}$ +e^-	$\longrightarrow$	$^4[\mathbf{1Fe}(5)]^{+}$ +L	−1.25			
$^4[\mathbf{1Fe}(5)]^{+}$ +e^-	$\longrightarrow$	$^1[\mathbf{1Fe}(4)]^{0}$ +L	−1.58			
$^6[\mathbf{1Fe}(5)]^{+}$ + CO_2	$\longrightarrow$	$^4[\mathbf{2Fe}(6)]^{+}$		5.5		13.9
$^3[\mathbf{1Fe}(4)]^{0}$ +CO_2 +L	$\longrightarrow$	$^3[\mathbf{2Fe}(6)]^{0}$		8.2		22.3
$^4[\mathbf{2Fe}(6)]^{+}$ +e^-	$\longrightarrow$	$^3[\mathbf{2Fe}(5)]^{0}$ +L	−1.63			
$^3[\mathbf{2Fe}(5)]^{0}$ +H^+	$\longrightarrow$	$^5[\mathbf{3Fe}(5)]^{+}$			25	1.7
$^5[\mathbf{3Fe}(5)]^{+}$ +e^-	$\longrightarrow$	$^4[\mathbf{3Fe}(5)]^{0}$	−1.47			
$^4[\mathbf{3Fe}(5)]^{0}$ +H^+	$\longrightarrow$	$^2[\mathbf{4Fe}(5)]^{+}$ +H_2O			24	15.6
$^2[\mathbf{4Fe}(5)]^{+}$ +L	$\longrightarrow$	$^4[\mathbf{1Fe}(5)]^{+}$ +CO		2.0		
$^1[\mathbf{4Fe}(5)]^{0}$	$\longrightarrow$	$^1[\mathbf{1Fe}(4)]^{0}$ +CO		5.0		
$^1[\mathbf{4Fe}(6)]^{2+}$+e^-	$\longrightarrow$	$^2[\mathbf{4Fe}(5)]^{+}$ +L	−0.97			
$^2[\mathbf{4Fe}(5)]^{+}$+e^-	$\longrightarrow$	$^1[\mathbf{4Fe}(5)]^{0}$	−1.45			

Table F.5: ω**B97X-D**: reaction of the catalytic cycle for $[Fe^{II}(qpy)(H_2O)_2]^{2+}$. Activation energies ($\Delta G^{\ddagger}$) and Gibbs free reaction energies ($\Delta_R G^0$) are reported in kcal/mol and barriers for protonation use Phenol as a proton source; reduction potentials in V versus the Fe^+/Fc couple (experimental reduction potentials for reference: −1.39 V & −1.60 V and −1.17 V & −1.42 V under CO atmosphere); L = H_2O.

Reaction			E^0	$\Delta_R G^0$	pK_a	$\Delta G^\ddagger$
$^4[\mathbf{1Co}(6)]^{2+}$ +e^-	$\longrightarrow$	$^3[\mathbf{1Co}(5)]^+$ +L	−0.78			
$^3[\mathbf{1Co}(5)]^+$ +e^-	$\longrightarrow$	$^2[\mathbf{1Co}(4)]^0$ +L	−1.13			
$^2[\mathbf{1Co}(4)]^0$ + CO_2	$\longrightarrow$	$^2[\mathbf{2Co}(5)]^0$		2.8		
$^2[\mathbf{2Co}(5)]^0$ +H^+	$\longrightarrow$	$^4[\mathbf{3Co}(5)]^+$ +L			11	
$^2[\mathbf{3Co}(5)]^+$ +H^+ +L	$\longrightarrow$	$^2[\mathbf{4Co}(6)]^{2+}$ +H_2O			12	11.6
$^2[\mathbf{4Co}(6)]^{2+}$ +L	$\longrightarrow$	$^4[\mathbf{1Fe}(6)]^{2+}$ +CO		−1.9		

Table F.6: **B3LYP-D3**: reaction of the catalytic cycle for $[Co^{II}(qpy)(H_2O)_2]^{2+}$. Activation energies ($\Delta G^\ddagger$) and Gibbs free reaction energies ($\Delta_R G^0$) are reported in kcal/mol and barriers for protonation use Phenol as a proton source; reduction potentials in V versus the Fe^+/Fc couple (experimental reduction potentials for reference: −0.95 V & −1.18 V); L = H_2O.

Reaction			E^0	$\Delta_R G^0$	pK_a	$\Delta G^\ddagger$
$^5[\mathbf{1Fe}(6)]^{2+}$ +e^-	$\longrightarrow$	$^4[\mathbf{1Fe}(5)]^+$ +L	−0.94			
$^4[\mathbf{1Fe}(5)]^+$ +e^-	$\longrightarrow$	$^1[\mathbf{1Fe}(4)]^0$ +L	−1.41			
$^4[\mathbf{1Fe}(5)]^+$ + CO_2	$\longrightarrow$	$^4[\mathbf{2Fe}(6)]^+$		8.9		10.9
$^1[\mathbf{1Fe}(4)]^0$ +CO_2	$\longrightarrow$	$^3[\mathbf{2Fe}(5)]^0$		7.3		10.4
$^4[\mathbf{2Fe}(6)]^+$ +e^-	$\longrightarrow$	$^3[\mathbf{2Fe}(5)]^0$ +L	−1.34			
$^3[\mathbf{2Fe}(5)]^0$ +H^+	$\longrightarrow$	$^5[\mathbf{3Fe}(5)]^+$			20	2.4
$^5[\mathbf{3Fe}(5)]^+$ +H^+	$\longrightarrow$	$^1[\mathbf{4Fe}(6)]^{2+}$			15	14.8
$^1[\mathbf{4Fe}(6)]^{2+}$ +L	$\longrightarrow$	$^5[\mathbf{1Fe}(6)]^{2+}$ +CO		−3.2		
$^2[\mathbf{4Fe}(5)]^+$ +L	$\longrightarrow$	$^4[\mathbf{1Fe}(5)]^+$ +CO		8.5		
$^1[\mathbf{4Fe}(5)]^0$	$\longrightarrow$	$^1[\mathbf{1Fe}(4)]^0$ +CO		15.1		
$^1[\mathbf{4Fe}(6)]^{2+}$+e^-	$\longrightarrow$	$^2[\mathbf{4Fe}(5)]^+$ +L	−0.43			
$^2[\mathbf{4Fe}(5)]^+$+e^-	$\longrightarrow$	$^1[\mathbf{4Fe}(5)]^0$	−1.13			

Table F.7: **B3LYP-D3**: reaction of the catalytic cycle for $[Fe^{II}(qpy)(H_2O)_2]^{2+}$. Activation energies ($\Delta G^\ddagger$) and Gibbs free reaction energies ($\Delta_R G^0$) are reported in kcal/mol and barriers for protonation use Phenol as a proton source; reduction potentials in V versus the Fe^+/Fc couple (experimental reduction potentials for reference: −1.39 V & −1.60 V and −1.17 V & −1.42 V under CO atmosphere); L = H_2O.

Reaction			E^0	$\Delta_R G^0$	pK_a	$\Delta G^{\ddagger}$
$^4[\mathbf{1Co}(6)]^{2+}$ +e^-	$\longrightarrow$	$^3[\mathbf{1Co}(5)]^{+}$ +L	−1.34			
$^3[\mathbf{1Co}(5)]^{+}$ +e^-	$\longrightarrow$	$^2[\mathbf{1Co}(4)]^{0}$ +L	−1.72			
$^2[\mathbf{1Co}(4)]^{0}$ + CO_2	$\longrightarrow$	$^2[\mathbf{2Co}(5)]^{0}$		5.3		
$^2[\mathbf{2Co}(5)]^{0}$ +H^+	$\longrightarrow$	$^4[\mathbf{3Co}(5)]^{+}$ +L			16	
$^2[\mathbf{3Co}(5)]^{+}$ +H^+ +L	$\longrightarrow$	$^2[\mathbf{4Co}(6)]^{2+}$ +H_2O			16	8.4
$^2[\mathbf{4Co}(6)]^{2+}$ +L	$\longrightarrow$	$^4[\mathbf{1Fe}(6)]^{2+}$ +CO		−9.8		

Table F.8: ω**B97M-V**: reaction of the catalytic cycle for $[Co^{II}(qpy)(H_2O)_2]^{2+}$. Activation energies ($\Delta G^{\ddagger}$) and Gibbs free reaction energies ($\Delta_R G^0$) are reported in kcal/mol and barriers for protonation use Phenol as a proton source; reduction potentials in V versus the Fe^+/Fc couple (experimental reduction potentials for reference: −0.95 V & −1.18 V); L = H_2O.

Reaction			E^0	$\Delta_R G^0$	pK_a	$\Delta G^{\ddagger}$
$^5[\mathbf{1Fe}(6)]^{2+}$ +e^-	$\longrightarrow$	$^4[\mathbf{1Fe}(5)]^{+}$ +L	−1.39			
$^4[\mathbf{1Fe}(5)]^{+}$ +e^-	$\longrightarrow$	$^1[\mathbf{1Fe}(4)]^{0}$ +L	−1.71			
$^4[\mathbf{1Fe}(5)]^{+}$ + CO_2	$\longrightarrow$	$^4[\mathbf{2Fe}(6)]^{+}$		3.2		11.6
$^1[\mathbf{1Fe}(4)]^{0}$ +CO_2	$\longrightarrow$	$^3[\mathbf{2Fe}(5)]^{0}$		5.3		19.6
$^4[\mathbf{2Fe}(6)]^{+}$ +e^-	$\longrightarrow$	$^3[\mathbf{2Fe}(5)]^{0}$ +L	−1.78			
$^3[\mathbf{2Fe}(5)]^{0}$ +H^+	$\longrightarrow$	$^5[\mathbf{3Fe}(5)]^{+}$			24	0.0
$^5[\mathbf{3Fe}(5)]^{+}$ +e^-	$\longrightarrow$	$^4[\mathbf{3Fe}(5)]^{0}$	−1.51			
$^4[\mathbf{3Fe}(5)]^{0}$ +H^+	$\longrightarrow$	$^2[\mathbf{4Fe}(5)]^{+}$ +H_2O			19	12.8
$^2[\mathbf{4Fe}(5)]^{+}$ +L	$\longrightarrow$	$^4[\mathbf{1Fe}(5)]^{+}$ +CO		−1.3		
$^1[\mathbf{4Fe}(5)]^{0}$	$\longrightarrow$	$^1[\mathbf{1Fe}(4)]^{0}$ +CO		3.5		
$^1[\mathbf{4Fe}(6)]^{2+}$+e^-	$\longrightarrow$	$^2[\mathbf{4Fe}(5)]^{+}$ +L	−1.23			
$^2[\mathbf{4Fe}(5)]^{+}$+e^-	$\longrightarrow$	$^1[\mathbf{4Fe}(5)]^{0}$	−1.62			

Table F.9: ω**B97M-V**: reaction of the catalytic cycle for $[Fe^{II}(qpy)(H_2O)_2]^{2+}$. Activation energies ($\Delta G^{\ddagger}$) and Gibbs free reaction energies ($\Delta_R G^0$) are reported in kcal/mol and barriers for protonation use Phenol as a proton source; reduction potentials in V versus the Fe^+/Fc couple (experimental reduction potentials for reference: −1.39 V & −1.60 V and −1.17 V & −1.42 V under CO atmosphere); L = H_2O.

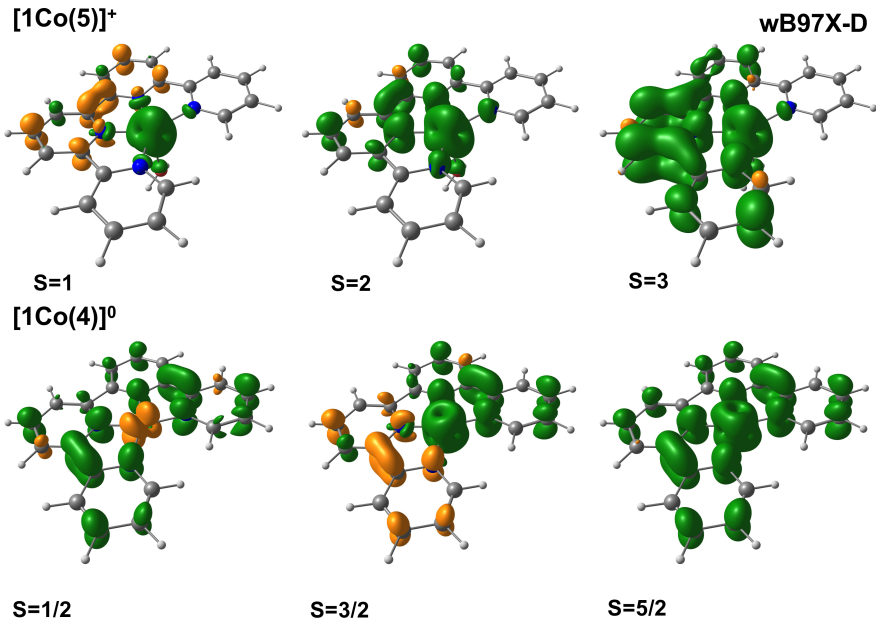

Figure F.13: Spin densities for all viable spin states for both $[\mathbf{1Co}(5)]^{+}$ and $[\mathbf{1Co}(4)]^{0}$ using ωB97X-D (isovalue:0.05).

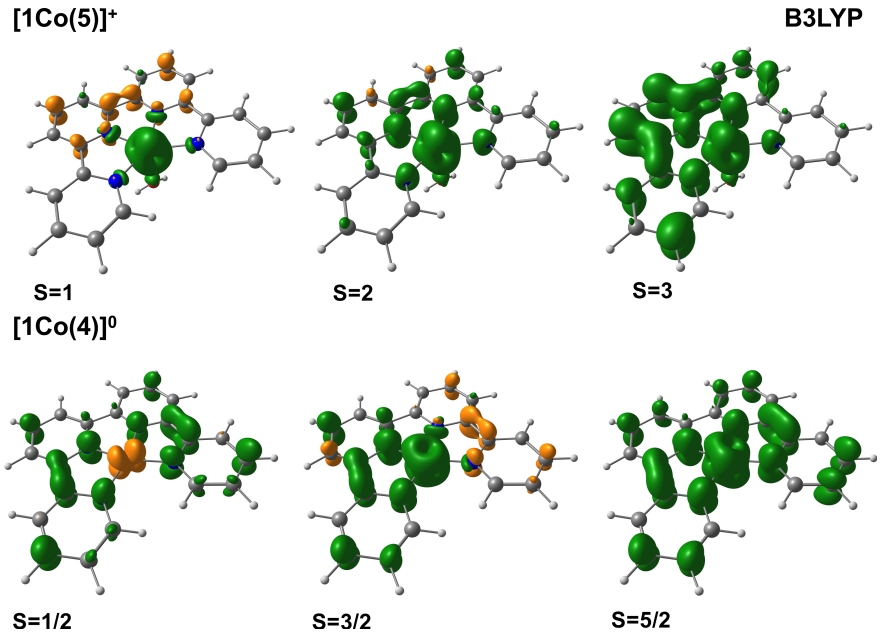

Figure F.14: Spin densities for all viable spin states for both $[\mathbf{1Co}(5)]^{+}$ and $[\mathbf{1Co}(4)]^{0}$ using B3LYP (isovalue:0.05).

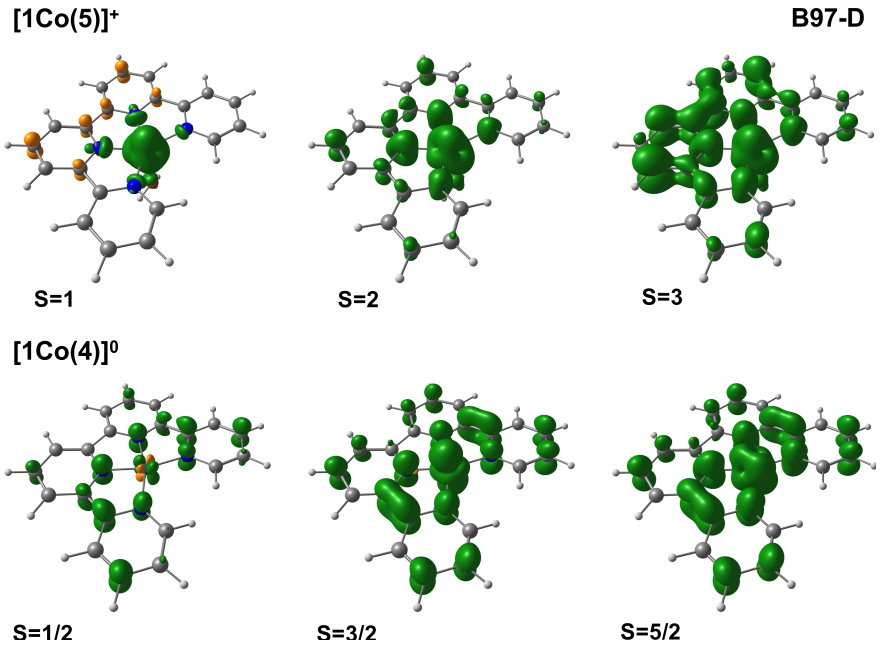

Figure F.15: Spin densities for all viable spin states for both $[\mathbf{1Co}(5)]^{+}$ and $[\mathbf{1Co}(4)]^{0}$ using B97-D (isovalue:0.05).

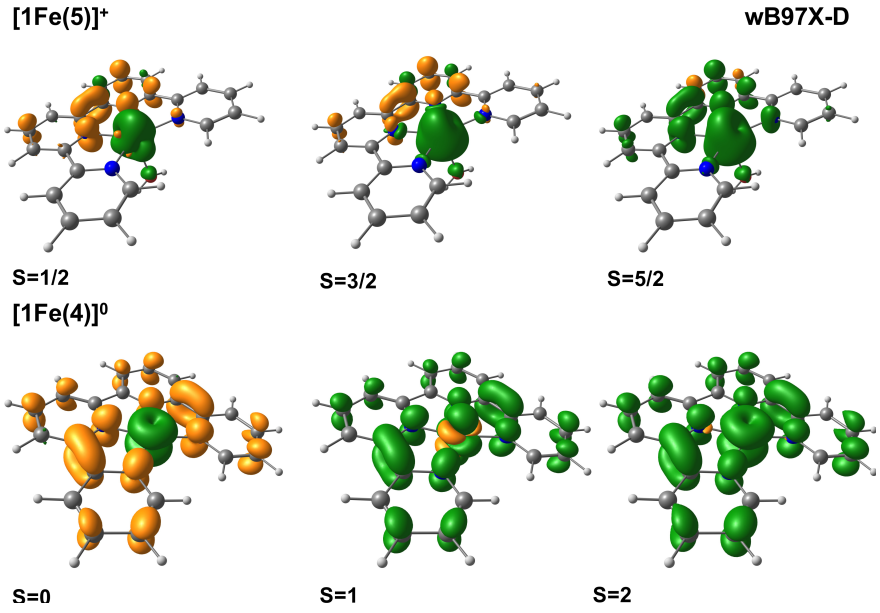

Figure F.16: Spin densities for all viable spin states for both $[\mathbf{1Fe}(5)]^{+}$ and $[\mathbf{1Fe}(4)]^{0}$ using ωB97X-D (isovalue:0.05).

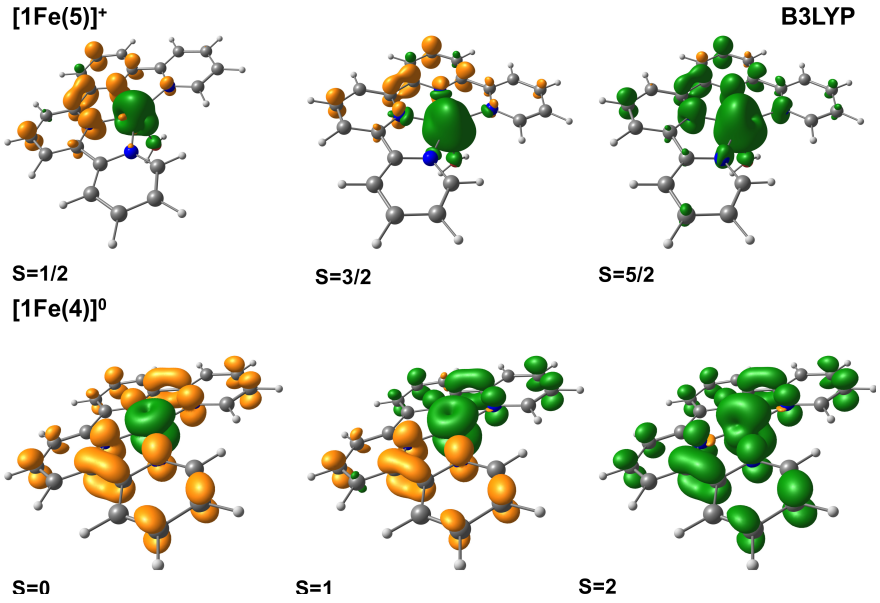

Figure F.17: Spin densities for all viable spin states for both $[\mathbf{1Fe}(5)]^{+}$ and $[\mathbf{1Fe}(4)]^{0}$ using B3LYP (isovalue:0.05).

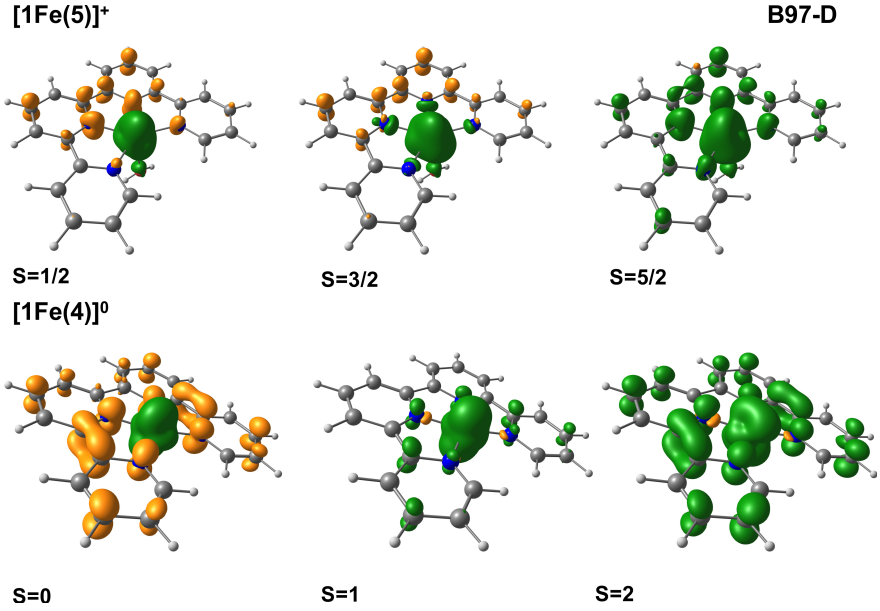

Figure F.18: Spin densities for all viable spin states for both $[\mathbf{1Fe}(5)]^{+}$ and $[\mathbf{1Fe}(4)]^{0}$ using B97-D (isovalue:0.05).

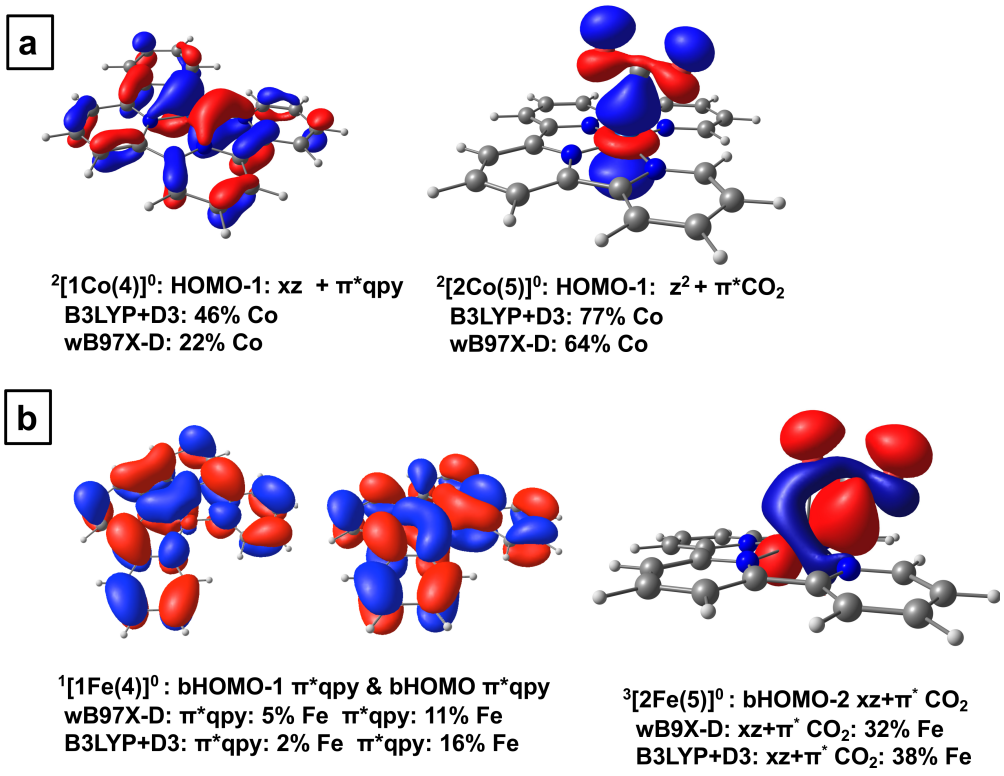

Figure F.19: Functional dependence of the key molecular orbitals of: (a) ^{2}[**1Co**(4)]^0 and ^{2}[**2Co**(5)]^0; (b) ^{1}[**1Fe**(4)]^0 and ^{3}[**2Fe**(5)]^0.

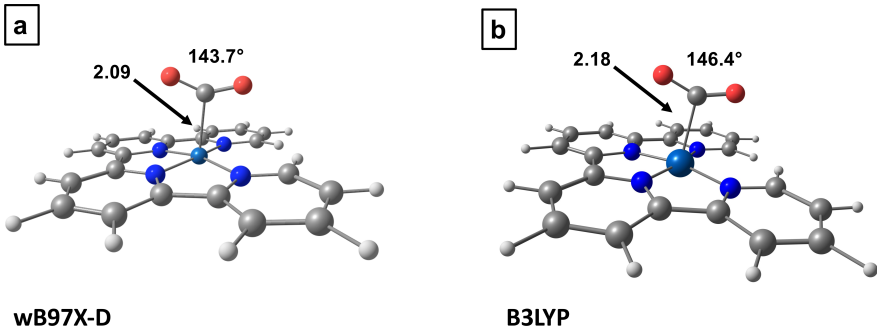

Figure F.20: Functional dependence of the structure of ^{2}[**2Co**(5)]^0.

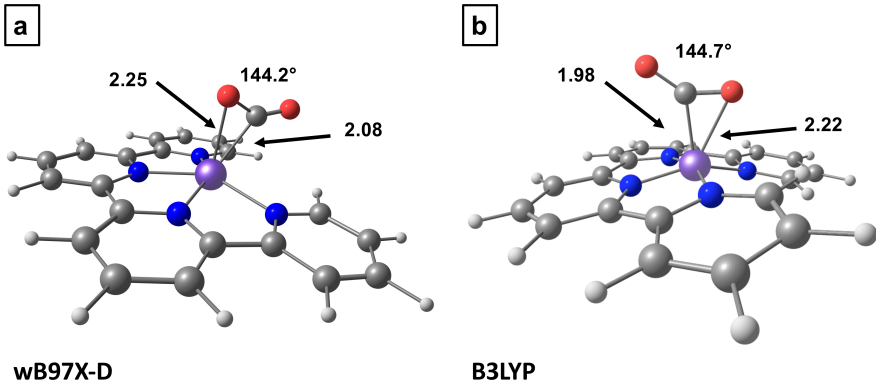

Figure F.21: Functional dependence of the structure of $^{3}[\mathbf{2Fe}(5)]^{0}$.

F.5 CASSCF

We used the complete active space self-consistent field method (CASSCF) to get more insight in metal ligand coupling of the doubly reduced intermediates $^2[\mathbf{1Co}(4)]^0$ and $^1[\mathbf{1Fe}(4)]^0$. These CASSCF calculations were performed with Orca (version 4.0.0.2) [548] employing the RI approximation along with the def2-TZVP basis and auxiliary basis set [497] (see zip file for a sample input). The quasi restricted orbitals of a high spin (Co: S = 5/2, Fe: S = 2) DFT B97-D[62] calculation served as initial guess orbitals. All molecular orbitals were plotted using an isovalue of 0.03 (blue: positive, red: negative values).

We used identical active spaces for the CASSCF calculations of both doubly reduced intermediates to probe the coupling of the ligand and metal orbitals: the two metal d-orbtials capable of mixing with the qpy π^* d_{xz} and d_{yz}; the two occupied π^* and two more additional π^* resulting in a CASSCF(5,6) set-up for $^2[\mathbf{1Co}(4)]^0$ and CASSCF(4,6) set-up for $^1[\mathbf{1Fe}(4)]^0$. We acknowledge that an in-depth analysis of these complicated electronic structures using active space methods is involved and beyond the scope of this work.[570–573]

The Natural orbital occupation number (NOON) of the converged CASSCF calculations of both species are summarized in table F.10 and the natural orbitals are depicted in figures F.22 and F.23. They exhibit significant deviation from integers (0,1 or 2) which confirms a significant amount of static correlation and an antiferromagnetic ordering. This finding explains the broken symmetry solution observed in the DFT calculations (see main text). The natural orbitals reveal different degrees of entanglement of the two metal d-orbital and the two qpy π^* orbitals for the two different metals.

In case of $^2[\mathbf{1Co}(4)]^0$: first, the metal d_{xz} and a qpy π^* are forming a π bond whereas both bonding (1.49 figure F.22 (b)) and anitbonding (0.51 figure F.22 (c)) orbitals are significantly occupied. The interaction is net bonding and shows a delocalization of the electrons onto both ligand and metal. Second, a doubly occupied metal d_{yz} (1.96 figure F.22 (a)) and singly occupied qpy π^* (1.01 figure F.22 (d)).

In case of $^1[\mathbf{1Fe}(4)]^0$: first, a metal d_{xz} and a qpy π^* forming a π bond whereas both bonding (1.34 figure F.23 (a)) and anitbonding (0.66 figure F.23 (d)) are occupied. The bond is weaker in comparison to the $^2[\mathbf{1Co}(4)]^0$ which implies more localization of the electrons on the metal and ligand, respectively. Second, two non-bonding mixed metal d_{yz} and qpy π^* orbitals (1.16 fig. F.23 (b) and 0.84 fig. F.23 (c)) implying essentially an uncoupled d-electron and qpy π^* electron.

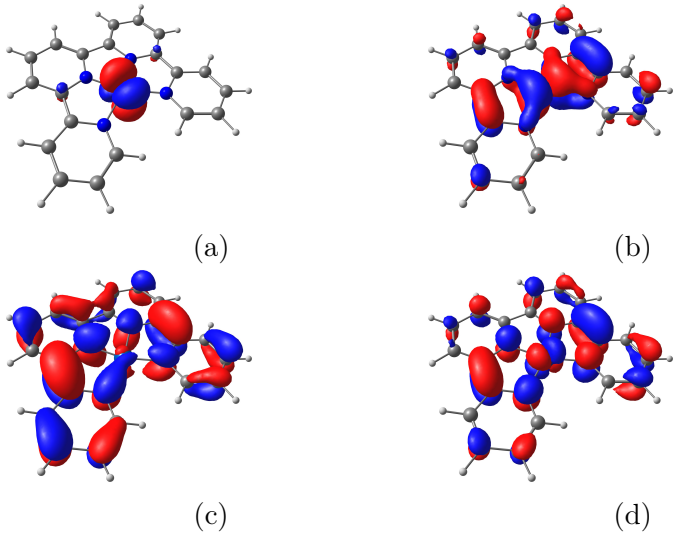

Figure F.22: Natural Orbitals of $^{2}[\mathbf{1Co}(4)]^{0}$: a) NOON: 1.96 b) NOON: 1.49 c) NOON: 1.01 d) NOON: 0.51.

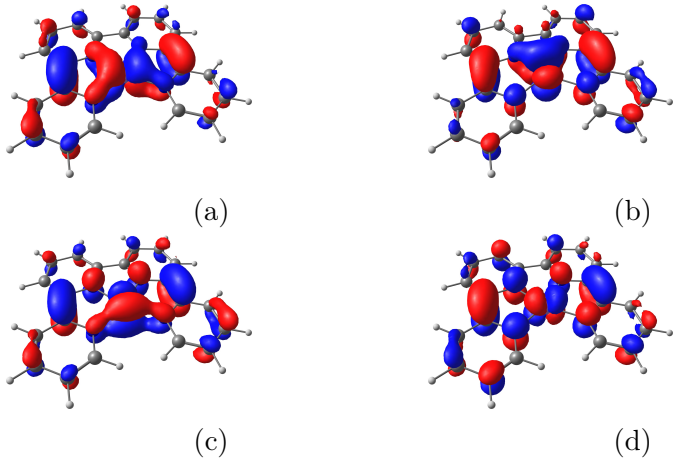

Figure F.23: Natural Orbitals of $^{1}[\mathbf{1Fe}(4)]^{0}$: a) NOON: 1.34 b) NOON: 1.14 c) NOON: 0.86 d) NOON: 0.66.

Complex	NOON			
$^{2}[\mathbf{1Co}(4)]^{0}$	1.96	1.49	1.01	0.51
$^{1}[\mathbf{1Fe}(4)]^{0}$	1.34	1.14	0.86	0.66

Table F.10: Natural orbital occupation number (NOON) of the CASSCF calculations of the two doubly reduced intermediates.

Appendix G

Influence of Overpotential on an Iron Terpyridine Complex for CO_2 Reduction: A Combined Experimental and Computational Investigation

Density functional theory calculations for spin gaps, redox potential and the LOBA analysis were performed with the Q-Chem package [108] (version 5.2.0) using the ωB97X-D [68] functional. Geometries were optimized in the gas phase with no constraints. The structures were verified as minimum with the vibrational frequencies. The geometry optimization and frequency calculations were performed with ωB97X-D and a mixed basis (def2-SVP basis for all main group elements, def2-TZVP basis set for Fe). [247] The electronic structure was refined with the def2-TZVPP basis [247] single point calculations. The solvation energies were calculated using the C-PCM model (acetonitrile, $\epsilon = 37.5$) as implemented in Q-Chem [119]. The numerical integration of the XC functional was on a (75, 302) grid (75 radial shells with 302 Lebedev points).

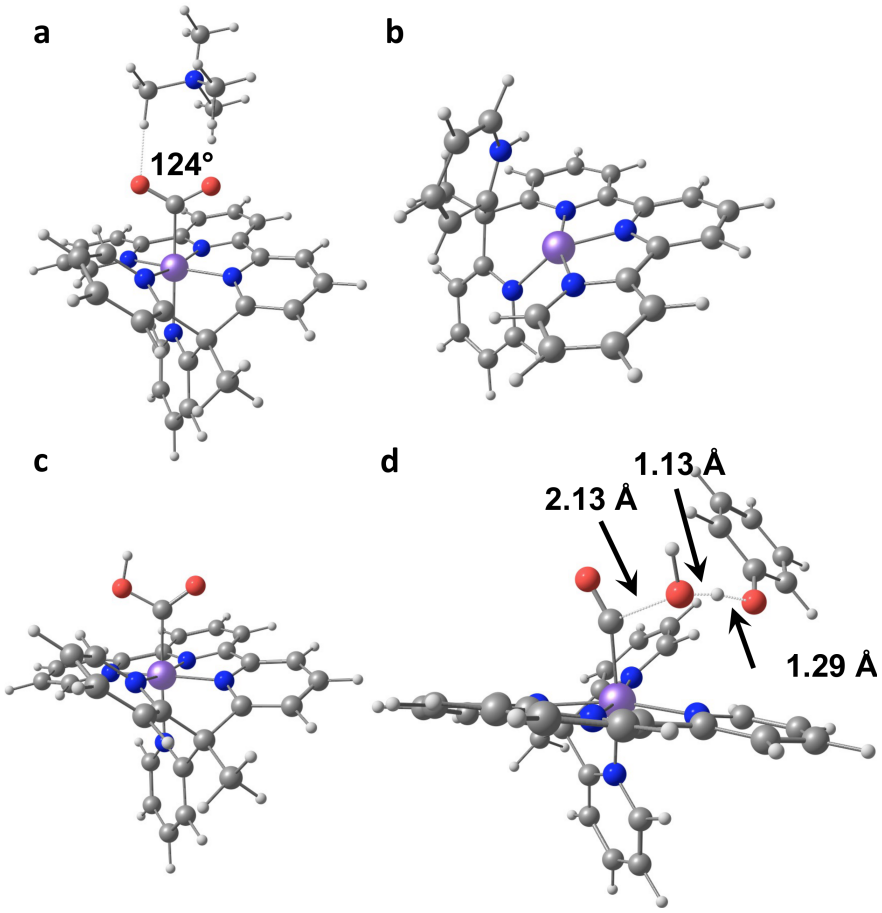

Figure G.1: Geometry of key intermediates of the low overpotential mechanism: a) CO_2 adduct $^1[Fe{-}CO_2]^0$ including a counterion; b) pyridinium intermediate $^1[Fe{-}N_{PY}H]^1$; carboxy intermediate $^1[Fe{-}CO_2H]^1$; d) transition state for the second protonation

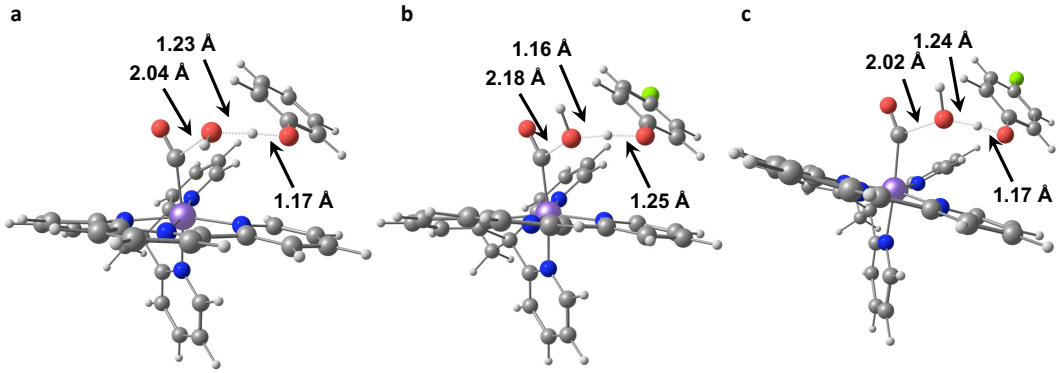

Figure G.2: Transition states for the second protonation: a) after a third redcution; b) with Cl-PhOH after two reductions; c) with Cl-PhOH after three reductions.

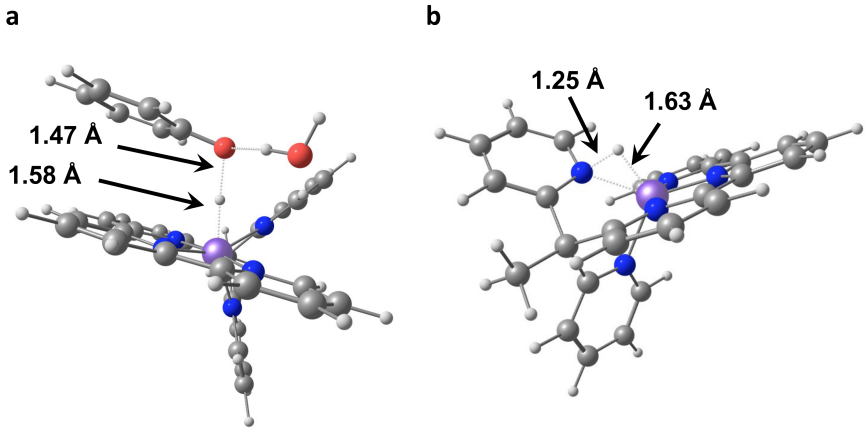

Figure G.3: Transition states for the formation of a hydride: a) directly from the acid source (PhOH); b) an intramolecular via a pyridinium.

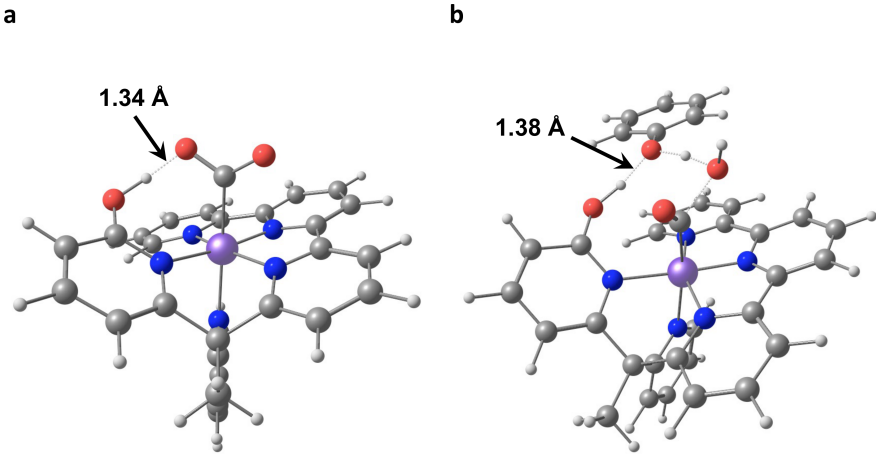

Figure G.4: Key intermediate for the OH substituted pyridine: a) CO_2 adduct; b) transition state for the second protonation.

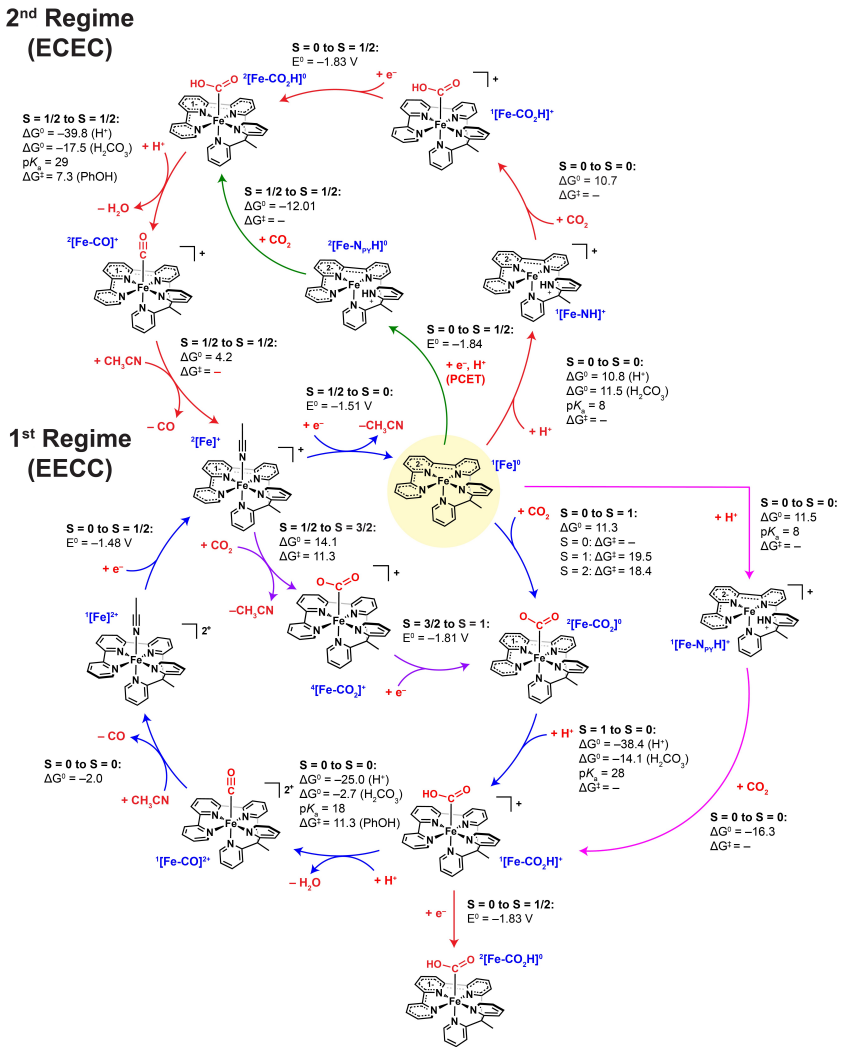

Figure G.5: Complete mechanistic pathways investigated for the first catalytic regime (low overpotential; bottom half) and the second catalytic regime (high overpotential; top half). For the low overpotential regime we probed: (1) a CO_2 binding first pathway (blue arrows), (2) protonation first pathway (magenta arrows), and (3) CO_2 binding to the singly reduced complex, $^2[Fe]^+$ (purple arrows). For the high overpotential regime, catalysis turns over from $^2[Fe]^+$. Single-electron reduction of $^2[Fe]^+$ gives the catalytic resting state, $^1[Fe]^0$ highlighted in yellow. Following formation of $^1[Fe]^0$, the pathway diverges in three directions. CO_2 binding can occur first followed by protonation to give $^1[CO_2H]^+$ (blue arrows) or protonation-first can occur followed by CO_2 coordination (red arrows). The $^1[Fe{-}CO_2H]^+$ intermediate can then be further reduced to $^2[Fe{-}CO_2H]^0$ and following the final protonation step and loss of water generates the carbonyl complex, $^2[Fe{-}CO]^+$ which regenerates $^2[Fe]^+$ following ligand exchange. We additionally explore the possibility of overcoming the high energy barriers associated with either Co_2 binding or protonation of $^1[Fe]^0$ by undergoing a PCET pathway to generate $^2[Fe{-}N_{PY}H]^0$ (green arows). All reaction and activation energies are given in units of kcal/mol and all reduction potentials are referenced to the computed Fe/Fe^+ couple.